Epidote U–Pb geochronology and isotope geochemistry to trace the hydration of the continental crust in orogens

Inaugural dissertation
of the Faculty of Science,
University of Bern

presented by

Veronica Peverelli

from Chiasso

Supervisor of the doctoral thesis:
Prof. Dr. Alfons Berger
Prof. Dr. Marco Herwegh

Institute of Geological Sciences

Epidote U–Pb geochronology and isotope geochemistry to trace the hydration of the continental crust in orogens

Inaugural dissertation
of the Faculty of Science,
University of Bern

presented by

Veronica Peverelli

from Chiasso

Supervisor of the doctoral thesis :
Prof. Dr. Alfons Berger
Prof. Dr. Marco Herwegh
Institute of Geological Sciences

Accepted by the Faculty of Science.

Bern, 31.08.2022

The Dean
Prof. Dr. M. Herwegh

Abstract

This work investigates epidote veins in crystalline rocks to date fluid circulation in the granitic continental crust, and to gain insight into fluid pathways and sources. Fluids are crucial in the tectono-metamorphic evolution of rocks because they control deformation processes, mineral reactions and heat transfer. Earth's continental crust is dominated by primarily water-poor granitic rocks. The observation that granitoids in many orogens (e.g., Alps, Himalayas) contain metamorphic hydrous minerals attests to the introduction of fluids into these primarily "dry" rocks. However, whether this occurred during prograde, peak or retrograde metamorphism is often unclear. One way to reconstruct the timing of fluid circulation is by dating veining events. In addition to time constraints, many vein-filling minerals return useful information regarding fluid sources and pathways by stable and radiogenic isotope geochemistry.

We assess and demonstrate the potential of epidote [i.e., $Ca_2Al_2(Al,Fe^{3+})Si_3O_{12}(OH)$] in veins to date and trace hydration of the granitic continental crust of the Alps from Permian to Miocene times. Epidote U–Pb geochronology is made possible by combining U–Pb isotope measurements by laser ablation inductively coupled plasma mass spectrometry (LA-ICP-MS) with the Tera–Wasserburg diagram. This approach is suitable for high-initial Pb minerals like epidote, and it returns geologically meaningful ages dating the formation of epidote during veining. Allanite (i.e., REE-rich monoclinic epidote) is used as an LA-ICP-MS reference material with no noticeable matrix effects at the available analytical precision. This is a fundamental aspect of U–Pb dating by *in-situ* techniques, because no well-characterized epidote standard exists for U–Pb isotope analyses, and uncorrected matrix-effects cause grossly inaccurate U–Pb ages in high-initial Pb minerals. The application of this new protocol for epidote U–Pb dating to selected case studies establishes epidote as a powerful geochronometer and fluid tracer in the granitic continental crust.

One group of investigated epidote-bearing veins are located in an inverted passive continental margin (i.e., Err nappe) in the eastern Swiss Alps. Surprisingly, in the Err nappe, such epidote veins formed in Late Cretaceous to Paleocene times during the compressional and extensional phases of the Eo-Alpine orogeny, and not during rifting. Epidote Pb–Sr isotope geochemistry

reveals that the epidote-forming fluids interacted with carbonatic rocks during percolation into the crust along extensional faults, and O–H isotope data in epidote suggest that the fluids originated as modified seawater with the addition of a sedimentary-water component.

The second group of studied epidote veins are from the Aar Massif, the inverted European passive continental margin. Here, epidote veins were produced by pre-orogenic Permian and syn-orogenic Miocene fluid circulation events. Hydrogen isotope data of Permian epidote indicates a meteoric origin for the Permian fluids, which likely percolated into the crust along rift-related normal faults and modified its hydrogen isotope composition interacting with syn-rift sediments.

The combination of epidote U–Pb geochronology and Pb–Sr isotope geochemistry with microstructural analysis and trace element data also reveals epidote dissolution–precipitation processes during viscous granular flow in an epidote-quartz vein. Such processes are mediated by a combination of recycled and newly added fluids, whose mixed isotope composition is recorded by newly precipitated syn-kinematic epidote. This study demonstrates that epidote is an active participant in deformation processes in deforming polymineralic aggregates.

This work demonstrates that the application of the newly developed protocol for epidote U–Pb dating, coupled with microstructural analysis, trace element data and isotope geochemistry, allows to characterize fluid circulation in inverted passive continental margins from rifting and across orogenic cycles. Epidote is ubiquitous in Earth's crust: not only as metamorphic mineral, but also in ore deposits, in geothermal fields, and as alteration mineral in basalts and feldspars. The application of the tools presented here to epidote from other geological contexts may further establish this mineral as the key tracer of low-temperature fluid circulation.

Acknowledgements

This thesis is part of the project “Fluids and new fluid tracers in water under-saturated continental crust: From rifting to tectonic inversion” funded by the Swiss National Science Foundation, to which I am thankful for making my PhD possible.

My deepest gratitude goes to my first supervisor Alfons Berger for his guidance, teaching, advice, infinite patience, open door, and – last but certainly not least –the great opportunity to work with him on this fantastic project. Sincere thanks also to my second supervisor Marco Herwegh for welcoming me – a lab rat and overall geochemical outlier – in the Tectonics and Structural Geology group, and for enriching my work by bringing very much needed structural perspective into it. I have been so lucky to have two supervisors who supported me, allowed me to make mistakes and learn, and – most importantly – constructively challenged me. For all this, THANK YOU!
I can never thank enough the IfG colleagues with whom I have had the pleasure of working and learn from: Martin Wille, Daniela Rubatto, Tanya Ewing, Thomas Pettke, Francesca Piccoli, Pierre Lanari, Igor M. Villa, Klaus Mezger, Daniel Rufer, Jörg Hermann and Pete Tollan. Many thanks to Andreas Mulch (SBiK and Goethe University, Frankfurt) and Benita Putlitz (University of Lausanne) for their collaboration, scientific input and interest in this project. Sincere thanks to Matthias Konrad-Schmolke for reviewing my thesis, and to Nagra for granting access to the GTS.

And the last paragraph is for my IfG friends and dwellers who made the social aspect of my PhD fun to the point that I had to isolate in Ticino to finish writing this thesis. I acknowledge my colleagues’ wisdom, which is no adumbration but rather and *a fortiori* a source of inspiration and motivation. Many thanks to chocolate, Friday’s G factor, Tulsi Tuesday, Warteck Friday, Ronnie James Dio, Grand Magus, System of a Down, coffee and my cat. My brain deeply thanks sugar. Thanks to my office mates for their patience, and you’re welcome for me helping you broaden your intralingual cursing vocabulary. Thanks to the professor who, eight years ago, encouraged me to achieve my potential, and thanks to me for listening to her. To myself, fifteen years ago.

चक दे

"We must not forget that when radium was discovered no one knew that it would prove useful in hospitals. The work was one of pure science. And this is a proof that scientific work must not be considered from the point of view of the direct usefulness of it. It must be done for itself, for the beauty of science, and then there is always the chance that a scientific discovery may become like the radium a benefit for mankind."

Marie Salomea Skłodowska–Curie, 1867–1934

Table of contents

List of Tables

List of Figures

1. Introduction

1.1 General introduction

Geological and planetary processes are intimately connected to the availability and the mobility of fluids (e.g., Bodnar, 2005; Jamtveit and Austrheim, 2010). These are crucial not only from a pure scientific perspective aiming at a better understanding of the evolution of our planet, but also because they have a direct impact on everyday life: from the basic need to access potable water to economic mineralization and geothermal energy (e.g., Bodnar, 2005; Kesler, 2005; Chambefort and Stefánsson, 2020). This would not be possible without plate tectonics. In the context of the associated geochemical and tectono-metamorphic evolution of Earth, the role of fluids cannot be emphasized enough in that they exert predominant control on mass and heat transfer, on deformation processes and on metamorphic reactions (e.g., Yardley, 2009; Jamtveit and Austrheim, 2010). Hence, a comprehensive investigation of orogenies cannot bypass a thorough characterization of fluid circulation in the rocks involved in tectono-metamorphic processes. Fluids in subduction zones have been intensely studied, given their importance in earthquake generation, arc magmatism and the deep cycle of volatile species (e.g., Peacock, 1990; Scambelluri and Philippot, 2001; Rubatto and Hermann, 2003; Manning, 2004; Hermann et al., 2006; Rüpke et al., 2004; Piccoli et al., 2016; 2019; Halpaap et al., 2019; Manning and Frezzotti, 2020; Vho et al., 2020). Conversely, fluid circulation in the granitic continental crust in orogens has received less attention, mostly targeting economic deposits (e.g., Cline and Bodnar, 1991; Pettke et al., 2000; Tannock et al., 2020a; 2020b).

Characterizing hydrothermal activity in granitoids – which dominate Earth's continental crust – is a key step to understand the tectono-metamorphic evolution of the continental crust. Not only do these rocks bear evidence for retrograde and prograde metamorphism, but they are also often highly deformed in presence of fluids (e.g., Ferry, 1979; Marquer et al., 1985; Morad et al., 2010; Goncalves et al., 2012; Wehrens et al., 2016; 2017; Bellahsen et al., 2019; Airaghi et al., 2020). Because granitoids are primarily water-poor, this raises a fundamental question: when and how were fluids introduced into these rather "dry" lithologies? By answering such a question, one may address the issue of whether deformation occurs where fluids are already present, or it is deformation itself that determines how granitoids are hydrated. The implications for our

understanding the tectonic evolution of the continental crust are enormous because hydrothermal alteration mechanically weakens granitoids (e.g., Wintsch et al., 1995; Tullis et al., 1996; Holyoke and Tullis, 2006; Oliot et al., 2010; Bellahsen et al., 2019; Airaghi et al., 2020; Malatesta et al., 2021). This is mainly related to rock-softening reactions of feldspar saussuritization and sericitization, which facilitate deformation through (1) increase in modal abundance of mechanically soft sheet silicates, (2) grain-size reduction by substitution of large feldspar grains by minute alteration minerals, and (3) storage of water in hydrous alteration minerals (e.g., Ferry, 1979; Fitz Gerald and Stünitz, 1993; Stünitz and Fitz Gerald, 1993; Wintsch et al., 1995; Tullis et al., 1996; Morad et al., 2010; Oliot et al., 2010). Therefore, determining the timing of fluid circulation in granitoids is a central piece of information that grants more comprehensive insight into orogenic processes in the continental crust. Besides temporal constraints, consideration of the fluid sources and pathways enhances our appreciation of the water cycle in the continental crust.

Determining when a geological event occurred relies on absolute geochronology. The year 2013 marked one hundred years since the foundation of "isotope geochronology" through the seminal work of Frederick Soddy and Arthur Holmes (e.g., Condon and Schmitz, 2013). Since then, with the developments of new analytical techniques and the establishment of new minerals as geochronometers, the temporal description of the evolution of Earth and its reservoirs has become more and more detailed. In fact, linking geochronological data (or "dates") to the geological record is a fundamental aspect, also at the base of why ages can be extracted from some minerals but not from others. What makes an "age" is the geological interpretation of a date (e.g., Schoene et al., 2013). As an example, feldspar alteration minerals often comprise K-bearing sheet silicates (e.g., Morad et al., 2010). However, two challenges exist if one aims at obtaining geologically meaningful ages from these minerals: (1) they are small and, as such, (2) they are easily affected by post-crystallization fluid–mineral processes and consequent isotopic resetting (e.g., Villa and Williams, 2013). Hence, what is the geological meaning of a date obtained from K/Ar dating of white mica in feldspar alteration, and does it help us to unravel hydration of granitoids?

This raises another crucial point in absolute geochronology: different geochronometers may be suitable to date different processes. For instance, emplacement ages of granitoids in the Aar Massif (central Swiss Alps) are returned by zircon U–Pb dating, whilst the Rb–Sr system in magmatic biotite records fluid–rock interaction in Alpine times (e.g., Abrecht and Schaltegger, 1988;

Schaltegger, 1990; Schaltegger and Corfu, 1992; Challandes et al., 2008; Rolland et al., 2009; Gaynor et al., 2022; Ruiz et al., in press). Although the weakening of the granitic continental crust cannot be assuredly dated directly in feldspar alteration, some hydrous minerals in veins and clefts are often datable, and return the timing of mineralization and fluid circulation (e.g., Berger et al., 2013; Bergemann et al., 2017; Ricchi et al., 2019; Gnos et al., 2021).

In the Alps, while some datable minerals are typical of orogenic or magmatic stages (e.g., chlorite, zircon, allanite; Schaltegger and Corfu, 1992; Herwegh et al., 2022; and references therein), some others are rather unspecific: one such mineral is epidote [$Ca_2Al_2(Al,Fe^{3+})Si_3O_{12}(OH)$]. Besides being a typical greenschist-facies metamorphic mineral (e.g., Grapes and Hoskin, 2004), epidote is also a common product of retrograde metamorphism and veining processes (e.g., Franz and Liebscher, 2004; Morad et al., 2010). In addition to being widespread in Earth's crust, this mineral has a crystal structure that allows for complex geochemistry (Franz and Liebscher, 2004; Frei et al., 2004). Elements like U, Pb and Sr can substitute for Ca in epidote (Frei et al., 2004), which may thus be used as a U–Pb geochronometer and whose Pb, Sr, O and H isotope compositions may return information on fluid pathways. The combination of these isotope systems may shed light on the lithologies with which the epidote-forming fluids interacted during percolation and on the fluid sources (e.g., Marquer and Burkhard, 1992; Pettke et al., 2000; Campos-Alvarez et al., 2010; Diamond et al., 2018; Vho et al., 2020; Grambling et al., 2021). Finally, an appealing characteristic of epidote as a potential geochronometer and fluid tracer in orogens is that it behaves in a brittle fashion during deformation (Franz and Liebscher, 2004). This is an important aspect in the interpretation of epidote U–Pb dates. It has been shown for other geochronometers (e.g., monazite; Seydoux-Guillaume et al., 2012; Grand'Homme et al., 2017) that dynamic recrystallization can reset the U–Pb isotope system, which thus reflects the time of deformation.

However, the role and behavior of epidote during deformation of granitic rocks are not fully characterized. In addition, the feasibility of epidote U–Pb dating remains to be established by employing suitable analytical techniques and scientific approaches. If indeed feasible, epidote geochronology may reveal so-far undetected fluid circulation events in the granitic continental crust of the Alps, and shed light into the timing of hydrothermal alteration of granitoids relative to the Alpine orogeny. The implications for deformation processes of pre-orogenic hydration of

granitoids are far-reaching: it would confirm that Alpine orogenesis did not affect fresh and mechanically strong granitoids, but rather hydrothermally altered and softened rocks that were preconditioned for deformation.

1.2 Scientific questions and structure of the thesis

This thesis aims at characterizing hydration of the granitic continental crust of the Alps using epidote in veins to date and trace fluid circulation. The study locations are the Grimsel Pass area (Aar Massif) and the Albula Pass area (Err nappe), in the central and eastern Swiss Alps, respectively. The Aar Massif and the Err nappe represent the inverted passive continental margins of the European and Adriatic plate, respectively, which experienced Mesozoic rifting tectonic inversion in the Cretaceous and were involved in the Alpine orogeny in the Tertiary (e.g., Handy et al., 1996; Herwegh et al., 2017). In granitoids in both areas, epidote is ubiquitous as rock-forming greenschist-facies mineral, as alteration mineral in saussuritic feldspar and as vein-filling mineral. Before this thesis, epidote had never been dated in the study areas. Building on the general introduction given above, the following scientific questions are addressed in the thesis' chapters:

1 Can epidote be used as a U–Pb geochronometer dating vein formation?
2 Did pre-orogenic fluid-driven alteration and rock softening occur in granitoids in the continental crust of the Alps?
3 Can we enhance our understanding of hydration of the granitic continental crust in the Alps and the fluid cycle therein by using epidote as a geochronometer and fluid tracer?
4 What are the behavior and the role of epidote as fluid tracer during deformation of polymineralic tectonites in granitoids?

In addition to the present introduction (Chapter 1), this thesis is subdivided into five chapters and one appendix. A brief description of each is given in the following.

Chapter 2: U–Pb geochronology of epidote by laser ablation inductively coupled plasma mass spectrometry (LA-ICP-MS) as a tool for dating hydrothermal-vein formation

This chapter describes the newly developed protocol for U–Pb dating of epidote by LA-ICP-MS, which is used throughout the thesis for dating epidote vein formation. The first part of the chapter

outlines the challenges of epidote U–Pb geochronology: these are mainly related to (1) high initial Pb contents, and (2) lack of an epidote standard for U–Pb isotope measurements by LA-ICP-MS. We show that (1) is overcome by applying the Tera–Wasserburg approach (Tera and Wasserburg, 1972), and (2) by using a magmatic allanite as reference material. This allows to obtain geologically meaningful ages from suitable epidote samples, dating epidote crystallization during vein formation. This manuscript was published in March 2021 in *Geochronology*.

Chapter 3: Epidote U–Pb geochronology and Pb–Sr–O–H isotope geochemistry reveal Eo-Alpine fluid circulation in the Err nappe (Eastern Swiss Alps)

In this chapter, epidote U–Pb geochronology is combined with epidote Pb, Sr, O and H isotope geochemistry to determine the timing of fluid circulation in granitoids in the Albula Pass area, and to assess the potential epidote-forming fluid pathways/sources. Our results reveal surprising and unexpected Late Cretaceous and Paleocene veining events related to the Eo-Alpine orogeny. Lead and Sr isotope data indicate that the fluids interacted with carbonatic rocks of the Ela nappe before reaching the veins' host granitoid. Oxygen and H isotope geochemistry suggests that the fluids originated as modified seawater or brackish water. This manuscript is in preparation for submission to *Chemical Geology*.

Chapter 4: Epidote U–Pb geochronology and H isotope geochemistry trace pre-orogenic hydration of mid-crustal granitoids

This chapter focuses on the hydration of the Aar Massif and contains the pivotal results of this thesis. Epidote veins from Grimsel Pass (southern Aar Massif) returned pre-orogenic Permian ages, providing evidence that fluid circulation affected the Aar Massif granitoids long before their structural imprint during the Alpine orogeny. Hydrogen isotope data agree with the Permian fluids having a meteoric origin and percolating into the granitoids along syn-rift faults during Permian transtension. These data are discussed against others presented in Chapter 2, which attest to syn-orogenic Miocene fluid circulation in the area and confirm that hydration of the Aar Massif granitoids was a multi-stage process. The fluid pathways of the Miocene epidote-forming fluids cannot be constrained possibly because of dissolution–precipitation processes in Miocene epidote (see Chapter 5). This chapter proves that the hydrothermal alteration and weakening of the granitic continental crust of the Aar Massif started ca. 260 myr before the onset of Alpine deformation. In

addition, it confirms that epidote can record and retain isotope data across deformation events during orogeny. This manuscript was published in June 2022 in *GEOLOGY*.

Chapter 5: Epidote dissolution–precipitation during viscous granular flow: a micro-chemical and isotope study

This chapter deals with the deformation mechanisms of epidote. By combining microstructural analysis, major and trace element data, and Pb–Sr isotope geochemistry, we demonstrate the occurrence of dissolution–precipitation of epidote, occurring together with quartz dynamic recrystallization during viscous granular flow in an epidote-quartz (±biotite) vein. We propose that the process is mediated by a mixture of internally recycled and newly added external fluids, moving throughout the deforming polymineralic aggregate via dynamic granular fluid pump (see Fusseis et al., 2009). This mechanism mediates fluid and mass transfer, and promotes the chemical homogenization of the dissolved and reprecipitated epidote material. This manuscript is under review for publication in the EGU journal *Solid Earth*.

Chapter 6: Conclusions

This final chapter summarizes the main results of this thesis and the implications of the findings.

Appendix

The Appendix of this thesis includes a sample list with all data available for each, and references to electronic appendices.

References

Abrecht, J., Schaltegger, U., 1988. Aplitic intrusions in the Central Aar massif basement: geology, petrography and Rb/Sr data. Eclogae Geol. Helv. 81, 227–239. http://doi.org/10.5169/seals-166177

Airaghi, L., Bellahsen, N., Dubacq, B., Chew, D., Rosenberg, C., Janots, E., Waldner, M., Magnin, V., 2020. Pre-orogenic upper crustal softening by lower greenschist facies metamorphic reactions in granites of the central Pyrenees. J. Metamorph. Geol. 38, 183–204. https://doi.org/10.1111/jmg.12520

Bellahsen, N., Bayet, L., Denele, Y., Waldner, M., Airaghi, L., Rosenberg, C., Dubacq, B., Mouthereau, F., Bernet, M., Pik, R., Lahfid, A., Vacherat, A., 2019. Shortening of the axial zone, pyrenees: Shortening sequence, upper crustal mylonites and crustal strength. Tectonophysics 766, 433–452. https://doi.org/10.1016/j.tecto.2019.06.002

Bergemann, C., Gnos, E., Berger, A., Whitehouse, M., Mullis, J., Wehrens, P., Pettke, T., Janots, E., 2017. Th-Pb ion probe dating of zoned hydrothermal monazite and its implications for repeated shear zone activity: An example from the central alps, Switzerland. Tectonics 36, 671–689. https://doi.org/10.1002/2016TC004407

Berger, A., Gnos, E., Janots, E., Whitehouse, M., Soom, M., Frei, R., Waight, T.E., 2013. Dating brittle tectonic movements with cleft monazite: Fluid-rock interaction and formation of REE minerals. Tectonics 32, 1176–1189. https://doi.org/10.1002/tect.20071

Bodnar, R.J., 2005. Fluids in Planetary Systems. Elements 1(1), 9–12. https://doi.org/10.2113/gselements.1.1.9

Campos-Alvarez, N.O., Samson, I.M., Fryer, B.J., Ames, D.E., 2010. Fluid sources and hydrothermal architecture of the Sudbury Structure: Constraints from femtosecond LA-MC-ICP-MS Sr isotopic analysis of hydrothermal epidote and calcite. Chem. Geol. 278, 131–150. https://doi.org/10.1016/j.chemgeo.2010.09.006

Challandes, N., Marquer, D., Villa, I.M., 2008. P-T-t modelling, fluid circulation, and 39Ar-40Ar and Rb-Sr mica ages in the Aar Massif shear zones (Swiss Alps). Swiss J. Geosci. 101, 269–288. https://doi.org/10.1007/s00015-008-1260-6

Chambefort, I., Stefánsson, A., 2020. Fluids in Geothermal Systems. Elements 16(6), 407–411. https://doi.org/10.2138/gselements.16.6.407

Cline, J.S., Bodnar, R.J., 1991. Can Economic Porphyry Copper Mineralization be Generated by a Typical Calc-Alkaline Melt? J. Geophys. Res. 96 (B5), 8113–8126.

Condon, D.J., Schmitz, M.D., 2013. One Hundred Years of Isotope Geochronology, and Counting. Elements 9(1), 15–17. https://doi.org/10.2113/gselements.9.1.15

Diamond, L.W., Wanner, C., Waber, H.N., 2018. Penetration depth of meteoric water in orogenic geothermal systems. Geology 46, 1083–1066. https://doi.org/10.1130/G45394.1

Ferry, J.M., 1979. Reaction mechanisms, physical conditions, and mass transfer during hydrothermal alteration of mica and feldspar in granitic rocks from south-central Maine, USA. Contrib. to Mineral. Petrol. 68, 125–139. https://doi.org/10.1007/BF00371895

Franz, G., Liebscher, A., 2004. Physical and Chemical Properties of the Epidote Minerals-An Introduction-. Rev. Mineral. Geochemistry 56, 1–81. https://doi.org/10.2138/gsrmg.56.1.1

Frei, D., Liebscher, A., Franz, G., Dulski, P., 2004. Trace element geochemistry of epidote minerals. Rev. Mineral. Geochemistry 56, 553–605. https://doi.org/10.2138/gsrmg.56.1.553

Fusseis, F., Regenauer-Lieb, K., Liu, J., Hough, R.M., De Carlo, F., 2009. Creep cavitation can establish a dynamic granular fluid pump in ductile shear zones. Nature 459, 974–977. https://doi.org/10.1038/nature08051

Gaynor, S.P., Schaltegger, U., 2022. The importance of high precision in the evaluation of U-Pb zircon age spectra 603, 120913. https://doi.org/10.1016/j.chemgeo.2022.120913

Gerald, J.D.F., Stünitz, H., 1993. Deformation of granitoids at low metamorphic grade. I: Reactions and grain size reduction. Tectonophys. 221, 269–297. https://doi.org/10.1016/0040-1951(93)90163-E

Gnos, E., Mullis, J., Ricchi, E., Bergemann, C.A., Janots, E., Berger, A., 2021. Episodes of fissure formation in the Alps : connecting quartz fluid inclusion , fissure monazite age , and fissure orientation data. Swiss J. Geosci. https://doi.org/10.1186/s00015-021-00391-9

Goncalves, P., Oliot, E., Marquer, D., Connolly, J.A.D., 2012. Role of chemical processes on shear zone formation: An example from the grimsel metagranodiorite (Aar massif, Central Alps). J. Metamorph. Geol. 30, 703–722. https://doi.org/10.1111/j.1525-1314.2012.00991.x

Grand'Homme, A., Janots, E., Seydoux-Guillaume, A.M., Guillaume, D., Magnin, V., Hövelmann, J., Höschen, C., Boiron, M.C., 2018. Mass transport and fractionation during monazite alteration by anisotropic replacement. Chem. Geol. 484, 51–68. https://doi.org/10.1016/j.chemgeo.2017.10.008

Grapes, R.H., Hoskin, P.W.O., 2004. Epidote group minerals in low-medium pressure metamorphic terranes. Rev. Mineral. Geochemistry 56, 301–345. https://doi.org/10.2138/gsrmg.56.1.301

Hermann, J., Spandler, C., Hack, A., Korsakov, A. V., 2006. Aqueous fluids and hydrous melts in high-pressure and ultra-high pressure rocks: Implications for element transfer in subduction zones. Lithos 92, 399–417. https://doi.org/10.1016/j.lithos.2006.03.055

Halpaap, F., Rondenay, S., Perrin, A., Goes, S., Ottemöller, L., Austrheim, H., Shaw, R., Eeken, T., 2019. Earthquakes track subduction fluids from slab source to mantle wedge sink. Sci. Adv. 5 (4), 1–13. DOI: 10.1126/sciadv.aav7369

Handy, M.R., Herwegh, M., Kamber, B.S., Tietz, R., Villa, I.M., 1996. Geochronologic, petrologic and kinematic constraints on the evolution of the Err-Platta boundary, part of a fossil continent-ocean suture in the Alps (eastern Switzerland). Schweizerische Mineral. und Petrogr. Mitteilungen 76, 453–474.

Herwegh, M., Berger, A., Baumberger, R., Wehrens, P., Kissling, E., 2017. Large-Scale Crustal-Block-Extrusion During Late Alpine Collision. Sci. Rep. 7, 1–10. https://doi.org/10.1038/s41598-017-00440-0

Holyoke, C.W., Tullis, J., 2006. The interaction between reaction and deformation: An experimental study using a biotite + plagioclase + quartz gneiss. J. Metamorph. Geol. 24, 743–762. https://doi.org/10.1111/j.1525-1314.2006.00666.x

Jamtveit, B., Austrheim, A., 2005. Metamorphism: The role of fluids. Elements 6(3), 153–158. https://doi.org/10.2113/gselements.6.3.153

Kesler, S.E., 2005. Ore-forming fluids. Elements 1(1), 13–18. https://doi.org/10.2113/gselements.1.1.13

Malatesta, C., Crispini, L., Ildefonse, B., Federico, L., Lisker, F., Läufer, A., 2021. Microstructures of epidote-prehnite bearing damaged granitoids (northern Victoria Land, Antarctica): clues for the interaction between faulting and hydrothermal fluids. J. Struct. Geol. 147. https://doi.org/10.1016/j.jsg.2021.104350

Manning, C.E., 2004. The chemistry of subduction-zone fluids. EPSL 223, 1–16. https://doi.org/10.1016/j.epsl.2004.04.030

Manning, C.E., Frezzotti, M.L., 2020. Subduction-zone fluids. Elements 16(6), 395–400. https://doi.org/10.2138/gselements.16.6.395

Marquer, D., Gapais, D., Capdevila, R., 1985. Comportement chimique et orthogneissification d'une granodiorite en facies schistes verts (Massif de l'Aar, Alpes Centrales). Bull. Mineral. 108, 209–221. https://doi.org/10.3406/bulmi.1985.7869

Marquer, D., Burkhard, M., 1992. Fluid circulation, progressive deformation and mass-transfer processes in the upper crust: the example of basement-cover relationships in the External Crystalline Massifs, Switzerland. J. Struct. Geol. 14 (8–9), 1047–1057. https://doi.org/10.1016/0191-8141(92)90035-U

Peacock, S.M., 1990. Fluid Processes in Subduction Zones. Science 248(4953), 329–337. DOI: 10.1126/science.248.4953.32

Pettke, T., Diamond, L.W., Kramers, J.D., 2000. Mesothermal gold lodes in the north-western Alps: A review of genetic constraints from radiogenic isotopes. Eur. J. Mineral. 12, 213–230. https://doi.org/10.1127/ejm/12/1/0213

Piccoli, F., Vitale Brovarone, A., Beyssac, O., Martinez, I., Ague, J.J., Chaduteau, C., 2016. Carbonation by fluid-rock interactions at high-pressure conditions: Implications for carbon cycling in subduction zones. Earth Planet. Sci. Lett. 445, 146–159. https://doi.org/10.1016/j.epsl.2016.03.045

Piccoli, F., Hermann, J., Pettke, T., Connolly, J.A.D., Kempf, E.D., Vieira Duarte, J.F., 2019. Subducting serpentinites release reduced, not oxidized, aqueous fluids. Sci. Rep. 9, 1–7. https://doi.org/10.1038/s41598-019-55944-8

Ricchi, E., Bergemann, C.A., Gnos, E., Berger, A., Rubatto, D., Whitehouse, M.J., 2019. Constraining deformation phases in the Aar Massif and the Gotthard Nappe (Switzerland) using Th-Pb crystallization ages of fissure monazite-(Ce). Lithos 342–343, 223–238. https://doi.org/10.1016/j.lithos.2019.04.014

Rolland, Y., Cox, S.F., Corsini, M., 2009. Constraining deformation stages in brittle-ductile shear zones from combined field mapping and 40Ar/39Ar dating: The structural evolution of the Grimsel Pass area (Aar Massif, Swiss Alps). J. Struct. Geol. 31, 1377–1394. https://doi.org/10.1016/j.jsg.2009.08.003

Rubatto, D., Hermann, J., 2003. Zircon formation during fluid circulation in eclogites (Monviso, Western Alps): Implications for Zr and Hf budget in subduction zones. Geochim. Cosmochim. Acta 67, 2173–2187. https://doi.org/10.1016/S0016-7037(02)01321-2

Ruiz, M., Schaltegger, U., Gaynor, S.P., Chiaradia, M., Abrecht, J., Gisler, C., Giovanoli, F., Wiederkehr, M., in press. Reassessing the intrusive tempo and magma genesis of the late Variscan Aar batholith: U-Pb geochronology, trace element and initial Hf isotope composition of zircon. Swiss J. Geosci.

Rüpke, L.H., Phipps, J., Hort, M., Connolly, J.A.D., 2004. Serpentine and the subduction zone water cycle. EPSL 223, 17–34. https://doi.org/10.1016/j.epsl.2004.04.018

Scambelluri, M., Philippot, P., 2001. Deep fluids in subduction zones. Lithos 55, 213–227. https://doi.org/10.1016/S0024-4937(00)00046-3

Schaltegger, U., 1990. Post-magmatic resetting of Rb-Sr whole rock ages - a study in the Central Aar Granite (Central Alps, Switzerland). Geol. Rundschau 79, 709–724. https://doi.org/10.1007/BF01879210

Schaltegger, U., Corfu, F., 1992. The age and source of late Hercynian magmatism in the central Alps: evidence from precise U-Pb ages and initial Hf isotopes. Contrib. to Mineral. Petrol. 111, 329–344. https://doi.org/10.1007/BF00311195

Seydoux-Guillaume, A., Montel, J., Bingen, B., Bosse, V., Parseval, P. De, Paquette, J., Janots, E., Wirth, R., 2012. Low-temperature alteration of monazite: Fluid mediated coupled dissolution–precipitation, irradiation damage, and disturbance of the U–Pb and Th–Pb chronometers. Chem. Geol. 330–331, 140–158. https://doi.org/10.1016/j.chemgeo.2012.07.031

Stünitz, H., Gerald, J.D.F., 1993. Deformation of granitoids at low metamorphic grade. II: Granular flow in albite-rich mylonites. Tectonophys. 221, 299–324. https://doi.org/10.1016/0040-1951(93)90164-F

Tannock, L., Herwegh, M., Berger, A., Liu, J., Regenauer-lieb, K., 2020a. The Effects of a Tectonic Stress Regime Change on Crustal-Scale Fluid Flow at the Heyuan Geothermal Fault, South China. Tectonophys. 781, 228399. https://doi.org/10.1016/j.tecto.2020.228399

Tannock, L., Herwegh, M., Berger, A., Liu, J., Lanari, P., Regenauer-Lieb, K., 2020b. Microstructural analyses of a giant quartz reef in south China reveal episodic brittle-ductile fluid transfer. J. Struct. Geol. 130, 103911. https://doi.org/10.1016/j.jsg.2019.103911

Tera, F., Wasserburg, G.J., 1972. U-Th-Pb systematics in three Apollo 14 basalts and the problem of initial Pb in lunar rocks. Earth Planet. Sci. Lett. 14, 281–304. https://doi.org/https://doi.org/10.1016/0012-821X(72)90128-8

Tullis, J., Yund, R., Farver, J., 1996. Deformation-enhanced fluid distribution in feldspar aggregates and implications for ductile shear zones. Geology 24, 63–66. https://doi.org/10.1130/0091-7613(1996)024<0063:DEFDIF>2.3.CO;2

Vho, A., Lanari, P., Rubatto, D., Hermann, J., 2020. Tracing fluid transfers in subduction zones: An integrated thermodynamic and δ18O fractionation modelling approach. Solid Earth 11, 307–328. https://doi.org/10.5194/se-11-307-2020

Villa, I.M., Williams, M.L. (2013). Geochronology of Metasomatic Events. In: Metasomatism and the Chemical Transformation of Rock. Lecture Notes in Earth System Sciences. Springer, Berlin, Heidelberg. https://doi.org/10.1007/978-3-642-28394-9_6

Wehrens, P., Berger, A., Peters, M., Spillmann, T., Herwegh, M., 2016. Deformation at the frictional-viscous transition: Evidence for cycles of fluid-assisted embrittlement and ductile deformation in the granitoid crust. Tectonophysics 693, 66–84. https://doi.org/10.1016/j.tecto.2016.10.022

Wehrens, P., Baumberger, R., Berger, A., Herwegh, M., 2017. How is strain localized in a meta-granitoid, mid-crustal basement section? Spatial distribution of deformation in the central Aar massif (Switzerland). J. Struct. Geol. 94, 47–67. https://doi.org/10.1016/j.jsg.2016.11.004

Wintsch, R.P., Christoffersen, R., Kronenberg, A.K., 1995. Fluid-rock reaction weakening of fault zones. J. Geophys. Res. 100. https://doi.org/10.1029/94jb02622

Yardley, B.W.D., 2009. The role of water in the evolution of the continental crust. J. Geol. Soc. 166, 585–600. https://doi.org/10.1144/0016-76492008-101

2.

U–Pb geochronology of epidote by laser ablation inductively coupled plasma mass spectrometry (LA-ICP-MS) as a tool for dating hydrothermal-vein formation

Veronica Peverelli[1], Tanya Ewing[1], Daniela Rubatto[1,2], Martin Wille[1], Alfons Berger[1], Igor M. Villa[1,3], Pierre Lanari[1], Thomas Pettke[1]& Marco Herwegh[1]

[1]*Institute of Geological Sciences, University of Bern, Switzerland*

[2]*Institute of Earth Sciences, University of Lausanne, Switzerland*

[3]*Dipartimento di Scienze dell'Ambiente e della Terra, University of Milano-Bicocca, Italy*

Published in *Geochronology*: https://doi.org/10.5194/gchron-3-123-2021

"An experiment is a question which science poses to Nature and a measurement is the recording of Nature's answer."

Max Planck, 1858–1947

ABSTRACT Epidote – here defined as minerals belonging to the epidote–clinozoisite solid solution – is a low-μ (μ = $^{238}U/^{204}Pb$) mineral occurring in a variety of geological environments, participating in many metamorphic reactions and stable throughout a wide range of pressure–temperature conditions. Despite containing fair amounts of U, its use as a U–Pb geochronometer has been hindered by the commonly high contents of initial Pb with isotopic compositions that cannot be assumed *a priori*. We present U–Pb geochronology of hydrothermal-vein epidote spanning a wide range of Pb (3.9–190 µg g^{-1}), Th (0.01–38 µg g^{-1}) and U (2.6–530 µg g^{-1}) contents and with μ values between 7–510 from the Albula area (eastern Swiss Alps), from the Grimsel area (central Swiss Alps) and from the Heyuan fault (Guangdong province, China). The investigated epidote samples show appreciable fractions of initial Pb contents (f_{206} = 0.7–1.0) – i.e., relative to radiogenic Pb – that vary to different extents. A protocol has been developed for *in situ* U–Pb dating of epidote by spot-analysis laser ablation inductively coupled plasma mass spectrometry (LA-ICP-MS) with a magmatic allanite as primary reference material. The suitability of the protocol and the reliability of the measured isotopic ratios have been ascertained by independent measurements of $^{238}U/^{206}Pb$ and $^{207}Pb/^{206}Pb$ ratios respectively by quadrupole and multicollector ICP-MS applied to epidote micro-separates digested and diluted in acids. For age calculation, we used the Tera–Wasserburg ($^{207}Pb/^{206}Pb$ *versus* $^{238}U/^{206}Pb$) diagram, which does not require corrections for initial Pb and provides the initial $^{207}Pb/^{206}Pb$ ratio. Petrographic and microstructural data indicate that the calculated ages date the crystallization of vein epidote from a hydrothermal fluid and that the U–Pb system was not reset to younger ages by later events. Vein epidote from the Albula area formed in the Paleocene (62.7 ± 3.0 Ma) and is related to Alpine greenschist-facies metamorphism. The Miocene (19.2 ± 4.3 Ma and 16.9 ± 3.7 Ma) epidote veins from the Grimsel area formed during the Handegg deformation phase (22–17 Ma) of the Alpine evolution of the Aar Massif. Identical initial $^{207}Pb/^{206}Pb$ ratios reveal homogeneity in Pb isotopic compositions of the fluid across ca. 100 m. Vein epidote from the Heyuan fault is Cretaceous in age (107.2 ± 8.9 Ma) and formed during the early movements of the fault. In situ U–Pb analyses of epidote returned reliable ages of otherwise undatable epidote-quartz veins. The Tera–Wasserburg approach has proven pivotal for *in situ* U–Pb dating of epidote and the decisive aspect for low age uncertainties is the variability in intra-sample initial Pb fractions.

2.1. Introduction

Linking petrological and structural information to the timing of geological events is crucial to better constrain the sequence of geodynamic processes. In this context, the role of fluids in the continental crust is particularly relevant because they mediate and influence deformation and metamorphism (e.g., Wyllie, 1977; Etheridge et al., 1983; Johannes, 1984; Pennacchioni and Cesare, 1997; Malaspina et al., 2011; Wehrens et al., 2016). The formation of a hydrothermal vein represents a specific deformation and hydration event in the geological history of the host rock, during which the vein-filling minerals record the geochemical signature of the mineralizing fluid (e.g., Elburg et al., 2002; Barker et al., 2009; Bons et al., 2012; Parrish et al., 2018; Ricchi et al., 2019; 2020). By combining different geochemical and geochronological techniques to suitable vein-filling minerals it is therefore possible to determine when the vein formed and the isotopic signature of the fluids for insight into their origin (e.g., Pettke et al., 2000; Barker et al., 2006; Elburg et al., 2002).

The epidote–clinozoisite solid solution [$Ca_2Al_3Si_3O_{12}(OH)$–$Ca_2Al_2Fe^{3+}Si_3O_{12}(OH)$], hereafter referred to as epidote, produces common rock-forming and vein-filling minerals (e.g., Bird and Spieler, 2004; Franz and Liebscher, 2004; Guo et al., 2014; Zanoni et al., 2016). Epidote is stable over a wide range of pressure–temperature conditions and in a multitude of magmatic, metamorphic and hydrothermal mineral assemblages (Bird and Spieler, 2004; Enami et al., 2004; Grapes and Hoskin, 2004; Schmidt and Poli, 2004). Its complex crystal structure incorporates a large variety of elements, enabling the measurements of trace element (e.g., Frei et al., 2004) and isotopic (e.g., Guo et al., 2014) signatures. Uranium and thorium are readily accepted into the epidote structure, with contents that are highly variable but generally in trace element levels (Frei et al., 2004). Hence, attempts have been made at using it as a geochronometer by step-wise leaching Pb–Pb dating (e.g., Buick et al., 1999) and thermal ionization mass spectrometry (TIMS) U–Pb dating (e.g., Oberli et al., 2004). Buick et al. (1999) constrained the timing of vein formation and that of subsequent fluid pulses in garnet-epidote-quartz veins in the Reynolds Range (central Australia). Oberli et al. (2004; their Sect. 5.3 and their Fig. 5) obtained a U–Pb age of magmatic epidote from the Bergell pluton (eastern Central Alps) and identified epidote formation as a late-stage process during the solidification of the pluton. However, these techniques allow microstructural control only if sampling by micro-drilling is viable. Epidote could provide valuable geochronological and isotopic information where no other datable minerals are available. Good

examples are epidote-quartz veins that are widespread in the Alps (e.g., Aar Massif and Albula area). Syn-kinematic epidote in breccias associated with rift-related faults in the Campos basin (southeastern Brazil) may highlight successive phases of fault movement (Savastano et al., 2017). In the Zermatt-Saas Zone (Western Alps), epidote is a peak-pressure rock-forming mineral in epidote-bearing rodingites (Zanoni et al., 2016) and it may help to better constrain the *P–T–d–t* paths related to pressure-peak metamorphism.

This contribution discusses the applicability of *in situ* U–Pb dating to minerals compositionally within the epidote–clinozoisite solid solution. To our knowledge, no analytical protocols have been proposed in this respect. To fill this gap, we present U–Pb ages measured in hydrothermal-vein epidote by LA-ICP-MS using a magmatic allanite for standardization, following a protocol similar to that applied to apatite U–Pb dating (e.g., Odlum and Stockli, 2019; 2020). The main issues related to the proposed geochronometer and addressed in this contribution are (1) the suitability of magmatic allanite as the most closely matrix-matched reference material for LA-ICP-MS U–Pb dating of epidote in spot-analysis mode, (2) the applicability of the protocol with respect to the different contents of initial Pb fractions (i.e., relative to radiogenic Pb in total Pb) and U in the studied samples and (3) the effects on age precision of the interplay between analyzed volumes and preservation of chemical variability. The Tera–Wasserburg diagram proves to be the key tool for successful epidote U–Pb geochronology, allowing to add minerals of the epidote–clinozoisite solid solution to the list of low-μ U–Pb geochronometers. Notably, by investigating epidote on its own, it is possible to combine U–Pb ages and isotopic systematics with data from trace element analyses and other isotopic systems; this may permit to reconstruct fluid flow and its origin with information that is all provided by a single mineral.

2.1.1. The challenges of investigating epidote as a geochronometer

Along with relevant amounts of U^{4+} and Th^{4+} as Ca substitution in the A site and of U^{6+} as Al or Fe substitution in the M site (Frei et al., 2004), high contents of initial Pb are incorporated by epidote during crystallization. This causes the dilution of ingrown radiogenic Pb, whose precise measurements are imperative for U–Pb geochronology, and makes epidote a low parent-to-daughter or low-μ phase (i.e., μ < ca. 2000; Romer, 2001; Romer and Xiao, 2005). U–Pb dating of initial Pb-rich minerals can proceed in two ways depending on whether or not the isotopic composition of the initial Pb is known or can be reasonably assumed. Assumptions can be based

on the modeled evolution of global Pb isotopic compositions such as those proposed by Cumming and Richards (1975) and Stacey and Kramers (1975). In the first case, a correction for initial Pb can be applied, and an initial Pb-corrected U–Pb age can be calculated from the measured U(±Th)–Pb isotopic ratios of each analysis (Williams, 1998). However, age inaccuracies due to wrong assumptions regarding initial Pb isotopic compositions can be significant (see Romer, 2001; Romer and Xiao, 2005). An initial Pb-correction can be applied if the contents of ^{204}Pb – the only non-radiogenic lead isotope – can be measured precisely, which is not always the case (e.g., because of the analytical technique employed). Hence, if no other dating method is viable (e.g., too low Th contents hampering Th–Pb dating), the best solution for dating of low-μ phases is to use a regression through the analyses uncorrected for initial Pb on the Tera–Wasserburg diagram (Tera and Wasserburg, 1972), which plots measured ^{207}Pb/^{206}Pb *versus* ^{238}U/^{206}Pb ratios. Its advantages are that (1) it does not require corrections for initial Pb isotopic compositions, (2) it provides the initial ^{207}Pb/^{206}Pb ratio itself in addition to an initial Pb-corrected U–Pb age, and (3) it gives an estimate of the fractions of initial lead relative to those of radiogenic Pb in each analysis (Tera and Wasserburg, 1972; Ludwig, 1998). This approach is based on the hypothesis that multiple analyses are performed on material of the same age sharing the same initial Pb isotopic composition. If these criteria are met, one regression is defined by the alignment of the measurements of ^{207}Pb/^{206}Pb *vs.* ^{238}U/^{206}Pb ratios, whose lower intercept with the concordia yields the age of the sample. If the hypotheses prove to be wrong (e.g., multiple mineral generations or co-genetic minerals with different initial Pb isotopic compositions; e.g., Romer and Siegesmund, 2003), this is highlighted by the statistical parameters of the regression. The fraction of initial Pb in each analysis can be estimated from the proximity of individual data points to the upper ^{207}Pb/^{206}Pb intercept of the regression (Tera and Wasserburg, 1972; Ludwig, 1998) which gives the initial ^{207}Pb/^{206}Pb ratio of the sample. The regression in the Tera–Wasserburg diagram is better constrained and yields more precise ages if the variability in initial Pb and U contents is high enough to produce spread-out data points. Epidote minerals are commonly characterized by chemical zoning (Franz and Liebscher, 2004), which may also result in variability in initial Pb fractions and U contents and promote spread of the data points along the Tera–Wasserburg regression.

A suitable technique for in situ U–Th–Pb dating is LA-ICP-MS in spot-analysis mode, provided that U/Pb and Th/Pb elemental fractionation at the ablation site (downhole fractionation, DF) is

appropriately corrected for over ablation time by relying on an external reference material (e.g., Sylvester, 2005; Košler, 2007; McFarlane et al., 2016). Since DF is matrix dependent (e.g., Sylvester, 2005; Košler, 2007; Sylvester, 2008; El Korh, 2014), a matrix-matched reference material is most commonly used. To date, no reference epidote exists, posing the problem of correction for DF of $^{238}U/^{206}Pb$ ratios measured in epidote, crucial for accurate age determinations by LA-ICP-MS (Horstwood et al., 2016). One way to date epidote by LA-ICP-MS would be by dynamic (raster) ablation with a non-matrix-matched reference material (e.g., Darling et al., 2012). However, large-enough areas within epidote grains are frequently not available for dynamic ablation. A mineral with a matrix that closely matches that of epidote is allanite. After early work by ID–TIMS (e.g., Barth et al., 1994), magmatic allanite has been dated by SIMS (e.g., Catlos et al., 2000) and in recent years it has been successfully characterized and dated by U–Th–Pb LA-ICP-MS (e.g., Gregory et al., 2007; 2012; El Korh, 2014; Smye et al., 2014). Several allanite samples have been proposed as suitable primary reference materials for LA-ICP-MS dating (e.g., Gregory et al., 2007; Smye et al., 2014). Allanite [$(Ca, REE, Th)_2(Fe^{3+}, Al)_3Si_3O_{12}(OH)$] is the REE-rich member of the epidote mineral group with ThO_2 contents of 2–3 wt% and U concentrations often below 1000 ppm (Gieré and Sorensen, 2004; and references therein), and it is a promising candidate as a closely matrix-matched reference material for minerals of the epidote–clinozoisite solid solution. The possible issues in the use of allanite as reference material for accurate U–Th–Pb geochronology are mostly related to local isotopic heterogeneity, excess ^{206}Pb due to incorporation of ^{230}Th during crystallization, variable contents of initial Pb and disturbance of the geochronometer by secondary processes (e.g., hydrothermal alteration; Gregory et al., 2007; Darling et al., 2012; Smye et al., 2014; Burn et al., 2017). Nevertheless, these issues can be largely avoided by careful selection of spot analyses referring to backscattered electron (BSE) images, and by identifying and excluding problematic analyses from calculations.

A disadvantage of U–Pb analyses by LA-ICP-MS is the large isobaric interference on mass 204 by ^{204}Hg of the carrier gas. A correction for such an interference in order to apply a ^{204}Pb-correction – whether based on measurements of the initial Pb isotopic composition in the same mineral or in coexisting ones (e.g., Cenki-Tok et al., 2014) – is complex (e.g., Storey et al., 2006). For this reason, and considering that epidote-bearing veins may not include other minerals suitable to determine the initial Pb isotopic composition, the application of the Tera–Wasserburg approach is preferable. In this study, epidote ages and initial $^{207}Pb/^{206}Pb$ ratios are assessed from the Tera–

Wasserburg diagram. If initial $^{207}Pb/^{206}Pb$ ratios are consistent with modeled values of initial Pb isotopic compositions (e.g., Stacey and Kramers, 1975), then an accurate $^{238}U/^{206}Pb$ age can be obtained by averaging single-spot ages, which are calculated from each analysis corrected for initial Pb by applying a ^{207}Pb-correction (i.e., weighted average ^{207}Pb-corrected $^{238}U/^{206}Pb$ age; see Williams, 1998).

2.2. Geological context and field relations

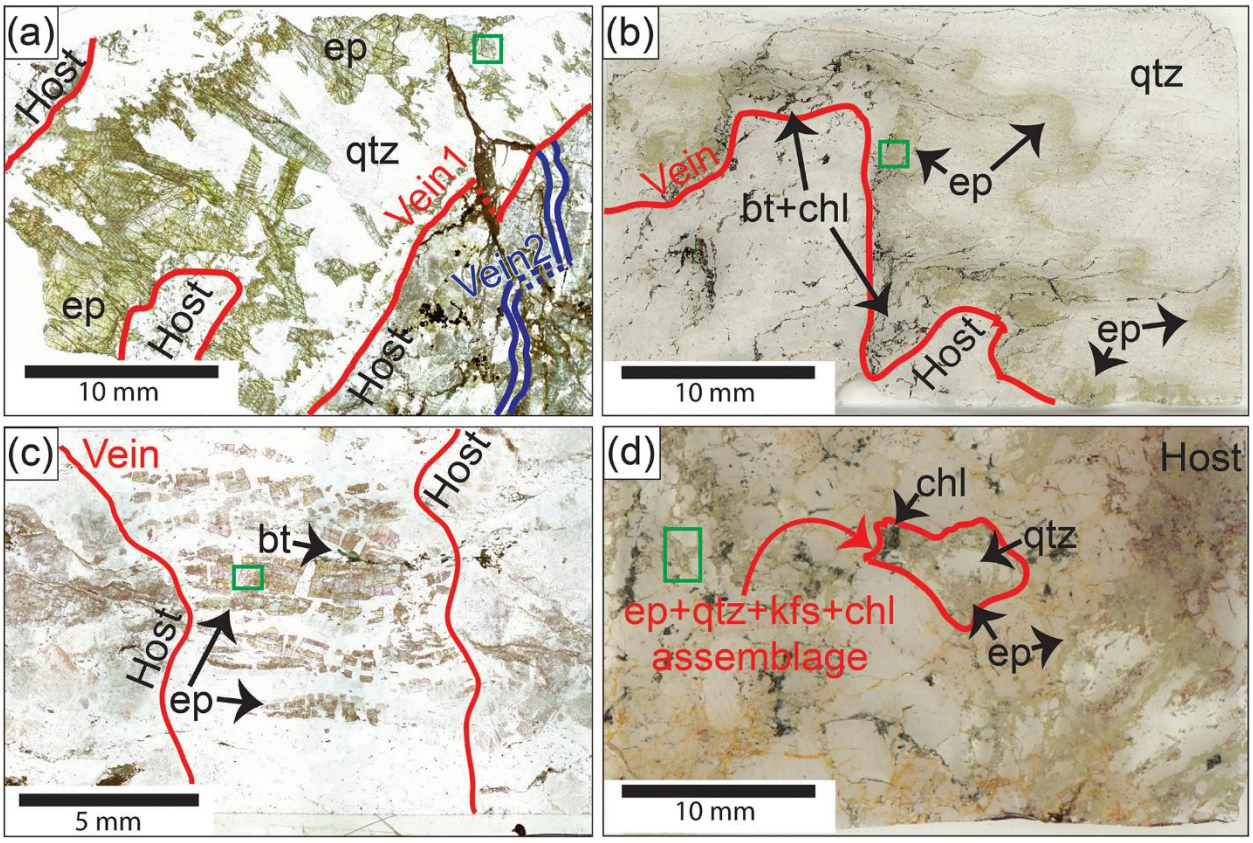

Fig. 2.1 *Scans of thin sections of (a) Albula-1, (b) Grimsel-1, (c) Grimsel-2 and (d) Heyuan-1 samples. (a) and (b): plane polarized light on petrographic microscope; (c) and (d): plane light. Green rectangles indicate the location of the BSE images shown in Fig. 2.2. bt = biotite; chl = chlorite; ep = epidote; kfs = K-feldspar; plg = plagioclase; qtz = quartz.*

Hydrothermal epidote veins (Fig. 2.1) were sampled at Albula Pass (eastern Swiss Alps), at Grimsel Pass (central Swiss Alps) and at the Heyuan Fault (Guangdong Province, China). Although there are no precise anticipated ages for the selected epidote samples, the well-constrained tectonic histories of the sampling areas and of the lithologies hosting the studied epidote-bearing veins allow to verify whether or not the obtained ages are geologically reasonable. The Albula area is located in the upper Err nappe, close to the tectonic contact with the Ela nappe. It belongs to the Austroalpine domain, the basement of the former Adriatic continental margin

(e.g., Froitzheim and Eberli, 1990; Froitzheim et al., 1994). The most common lithology in the Err basement is the Albula Granite, a granodiorite of Variscan to post-Variscan age (e.g., Manatschal and Nievergelt, 1997; Incerpi et al., 2017) and in which epidote ± quartz veins are widespread. In the late Carboniferous and early Permian, the Albula Granite intruded into the metamorphic basement of the Err nappe at < 3 km depth (Mohn et al., 2011; and references therein). Subsequently, the Lower Austroalpine was involved in the Jurassic rifting that led to the break-up of Pangea (e.g., Manatschal et al., 2000). During the Alpine orogeny, the Err nappe mainly recorded the deformation resulting from the W- to NW-directed vergence of the Austroalpine domain from Cretaceous until early Cenozoic times and was only weakly affected by the Cenozoic tectonics, when temperatures reached ca. 300 °C (i.e., lower-greenschist facies conditions; e.g., Froitzheim and Manatschal, 1996; Mohn et al., 2011; Epin et al., 2017). Sample Albula-1 was collected at coordinates 46°34'36"N/9°48'06"E and has not been described in previous studies.

The Grimsel area is in the Aar Massif, one of the External Crystalline Massifs of the Alps (Rolland et al., 2009; Wehrens et al., 2017; Herwegh et al., 2020). Here, epidote-quartz veins are common in the Central Aar granite and in the Grimsel granodiorite, which during the earliest Permian intruded into a polycyclic basement bearing evidence of Ordovician metamorphism and Variscan overprint (Schaltegger and Corfu, 1992; Berger et al., 2017). After being affected by the Jurassic rifting, the Aar Massif was involved in the continent–continent collision during the Alpine orogeny, as demonstrated by the presence of anastomosing high-strain shear zones of Alpine age (e.g., Goncalves et al., 2012; Wehrens et al., 2017). Metamorphism at greenschist facies conditions reached 450 ± 30 °C at 0.6 ± 0.1 kbar in this area (Challandes et al., 2008; Goncalves et al., 2012). The Alpine history of the Aar Massif is subdivided into three phases: (1) the Handegg phase (22–17 Ma; Challandes et al., 2008), with stable green biotite in the shear zones (Challandes et al., 2008; Rolland et al., 2009; Herwegh et al., 2017; Wehrens et al., 2017); (2) the Oberaar phase in the southern Aar Massif (14–3.4 Ma; Hofmann et al., 2004; Rolland et al., 2009), with white mica and chlorite stable in the shear zones, and metastable biotite (Herwegh et al., 2017; Wehrens et al., 2017); (3) the Pfaffenchopf phase in the northern Aar Massif (< 12 Ma; Herwegh et al., 2020). The epidote-quartz veins analyzed in this study were sampled in the Nagra Felslabor tunnel at Grimsel Pass. As these veins are only visible within the tunnel, their relationships with Alpine structures and between each other are not known. Samples Grimsel-1 and Grimsel-2 have not been previously described and they were sampled at a distance of ca. 100 m from each other, close to the "F100"

and “BK cavern” locations in Fig. 1.2 of Schneeberger et al. (2019; see also Figs. 4A1 and 5.2 of this thesis), respectively.

The Heyuan Fault is a crustal-scale fault that formed in Mesozoic times as a low-angle normal fault, but is currently active under a transpressive regime (Tannock et al., 2020a; 2020b). The footwall of this fault mainly consists of the Xinfengjiang pluton (the eastern portion of the Fogang batholith), a late Jurassic biotite granite that intruded into the basement of Proterozoic to Silurian age during the Yanshanian orogeny (Li et al., 2007; Tannock et al., 2020a; 2020b). Epidote veins are located in the mylonites at the transition between undeformed granite and fault zone (Tannock et al., 2020a). The hanging wall is composed of a quartz-sericite ultracataclasite/phyllonite in contact with a quartz reef and finally abutted by the sedimentary “Red Beds” of Cretaceous age (Tannock et al., 2020a). Since the epidote veins are either pre- or syn-kinematic with respect to the mylonites (Tannock et al., 2020b), we infer that the epidote veins cannot be older than the pluton itself, but they are also among the earliest structures related to the early movements of the Heyuan Fault (Tannock et al., 2020a; 2020b). Epidote veins are absent in the footwall cataclasite and in the quartz reef, which formed after the mylonite. Syn-kinematic epidote veins formed at a temperature of ca. 330 °C as indicated by the white mica composition in the mylonites (Tannock et al., 2020a). Sample Heyuan-1 is discussed in Tannock et al. (2020a; 2020b) and its sampling location is shown in Fig. 1 of Tannock et al. (2020a; their sample HY17-5).

2.3. Methods

Except where stated, sample preparation and measurements were carried out in the laboratory facilities of the Institute of Geological Sciences, University of Bern, Switzerland.

2.3.1. Imaging and screening methods for sample selection

Thin (30 µm) and thick (50–60 µm) sections were inspected by petrographic and electron microscopy, respectively on a ZEISS Axioplan microscope and on a ZEISS EVO50 SEM using BSE imaging (ca. 1 nA beam current, 20 kV accelerating voltage, working distance 8.5–10.0 mm). BSE images were used to plan analysis spots – all of the same size – within epidote grains so as to avoid mixing of different zonings in each single measurement, as well as mineral and fluid inclusions. Contents of major elements were measured by electron probe micro-analyzer (EPMA) using a JEOL-8200 microprobe at the Institute of Geological Sciences (University of Bern) with

15 KeV accelerating voltage, 10 nA specimen current and 2 µm electron beam diameter. The following natural and synthetic standards were used for calibration: wollastonite (SiO_2), olivine (MgO), anorthite (CaO, Al_2O_3), garnet (FeO), Topaz (F), tephroite (MnO), tugtupite (Cl), rutile (TiO_2) and celestite (SrO). Structural formula was calculated based on 12.5 oxygen cations.

REE, U, Th and Pb contents of epidote samples were measured on thin (30 µm) or thick (50–60 µm) sections, pre-cleaned with ethanol. Concentrations in sample Albula-1 were measured on a Geolas Pro 193 nm ArF excimer laser (Coherent, USA) coupled with an ELAN DRCe quadrupole ICP–MS (QMS; Perkin Elmer, USA) at the Institute of Geological Sciences (University of Bern). Instrument optimization and measurement procedures [similar to those reported in Pettke et al. (2012)] employed an ablation rate of ca. 0.1 µm *per* laser pulse, 10 Hz, and beam sizes between 24 and 60 µm, the largest possible to minimize limits of detection and to avoid inclusions and fractures. Ablation was done in a 1 l min^{-1} He-0.008 l min^{-1} H_2 atmosphere. Concentrations in samples Grimsel-1, Grimsel-2 and Heyuan-1 were measured on a RESOlutionSE 193 nm excimer laser system (Applied Spectra, USA) equipped with a S-155 large-volume constant-geometry chamber (Laurin Technic, Australia) coupled with an Agilent 7900 ICP-QMS. Ablation was carried out in He atmosphere, which was allowed to mix with Ar carrier gas for transport to the ICP-MS. Repetition rate was 5 Hz, at spot sizes between 20 and 50 µm. On both systems, analytical conditions were optimized on NIST SRM612 so as to keep ThO production rate < 0.2 % and Th/U sensitivity ratio of 0.97–1.0, the latter indicative of robust plasma conditions. GSD-1G from USGS was employed as the external standard whereas quality control was monitored by measuring SRM612 from NIST measured as an unknown. A true-time linear drift correction was applied by bracketing standardization. Data acquired on both systems were reduced off-line using SILLS (Guillong et al., 2008), with the sum of measured total oxides (98.3 % for epidote and 100 % for SRM NIST612) used for internal standardization (compare Halter et al., 2002). Limits of detection were rigorously calculated for each element in each analysis employing the formulation detailed in Pettke et al. (2012). The U-Th-Pb data are in Table 2.6 at the end of the chapter.

2.3.2. U–Pb geochronology by LA–ICP–MS

TABLE 2.1

Measurement conditions on Agilent 7900 for U–Th–Pb isotopic data by LA-ICP-MS.

RF power	14 June 2019: 1280 W
	23 July 2019: 1320 W
	16 January 2020: 1380 W
Fluence	3 J cm^{-2}
Repetition rate	5 Hz
Cell gas flow	14 June and 23 July 2019: 3 ml min^{-1} N_2 and 3500 ml min^{-1} He
	16 January 2020: 3 ml min^{-1} N_2 and 400 ml min^{-1} He
Sensitivity on mass 232 in NIST612	14 June 2019: 4150 cps ppm^{-1}
(beam size 50 µm, fluence 2.5 J cm^{-2},	23 July 2019: 4410 cps ppm^{-1}
repetition rate 5 Hz, scan rate 5 µm s^{-1})	16 January 2020: 3590 cps ppm^{-1}
232/238 ratio	> 0.97
248/232 ratio	< 0.002
Background	30 s
Pre-cleaning	14 June and 23 July 2029: 10 pulses; beam size 64 µm
	16 January 2020: 10 pulses; beam size 30 µm
Ablation time (beam size 50 µm)	40 s
Measured masses	206, 207, 208, 232, 238
(all dwell times 40 ms)	
Primary reference material	Tara allanite (Smye et al., 2014)
Secondary reference materials	14 June 2019: CAP^b allanite
	23 July 2019 and 16 January 2020: CAP and AVC allanite

TABLE 2.2

Reference data of Tara allanite for normalization of U–Th–Pb isotopic data by LA-ICP-MS, and published U–Pb Tera–Wasserburg ages of CAP^{b}, CAP and AVC allanite secondary reference materials. The ratios for Tara allanite are averages calculated from the measurements by Smye et al. (2014) by ID-TIMS; one measurement was excluded (see text). Uncertainties are given in brackets and are calculated as 2 standard errors. Subscript r = radiogenic ratio; subscript i = initial; superscript a = U–Pb age used as reference in this contribution (see Sect. 2.5.1 for details). (a) = calculated from five ID-TIMS data of Smye et al. (2014), unanchored regression; (b) = from Burn et al. (2017); (c) = from Gregory et al. (2007).

	Tara allanite	**CAP^{b} allanite**	**CAP allanite**	**AVC allanite**
$(^{206}Pb/^{238}U)_r$	0.0678 (0.0008)	-	-	-
$(^{207}Pb/^{235}U)_r$	0.5020 (0.0173)	-	-	-
$(^{208}Pb/^{232}U)_r$	0.0195 (0.0021)	-	-	-
$(^{207}Pb/^{206}U)_r$	0.0537 (0.0016)	-	-	-
$(^{207}Pb/^{206}U)_i$	0.866 (0.079)	-	-	-
Reference U–Pb age^{a}	420 ± 16 Ma (a)	284.9 ± 2.8 Ma (b)	275.0 ± 4.7 Ma (c)	289.6 ± 5.6 Ma (c)

Isotopic measurements of U, Th and Pb were performed on thin/thick sections for epidote and on acryl grain mounts for allanite. To minimize surface contamination, the thin/thick sections were cleaned with ethanol, and the grain mounts with ethanol and 5 % HNO_3. Measurements of U, Th and Pb isotopic ratios were performed with a Resonetics RESOlutionSE 193 nm excimer laser system (Applied Spectra, USA) equipped with a S-155 large-volume constant-geometry chamber (Laurin Technic, Australia) coupled with an Agilent 7900 ICP-QMS. The suitability of analytical conditions (Table 2.1) was checked in each session by performing preliminary analyses on secondary reference materials of known ages – namely CAP^{b} (for details see Burn et al., 2017), CAP and AVC allanite (for details see Barth et al., 1994; Gregory et al., 2007) – and comparing them to their published U–Pb ages (see Table 2.2). Low fluence of 3 J s^{-2}, low repetition rate of 5 Hz and large spot size of 50 µm were combined to ensure a slow increase in depth/diameter ratio of the laser crater during a 40 s ablation time, hence to minimize elemental (U/Th/Pb) DF. An additional session was carried out with a laser spot of 30 µm and the same laser conditions. The aim was to assess the effects of using a smaller spot size on the correction for DF (see Chew et al., 2014) and to explore whether the use of allanite as primary reference material can still provide accurate data at these conditions. If so, this would extend the applicability of the present protocol to smaller epidote grains. For this test, we selected two samples: the one also used for solution

ICP-MS measurements (sample Abula-1; see Sect. 2.3.3), and the one with the smallest averaged analytical errors on $^{238}U/^{206}Pb$ and $^{207}Pb/^{206}Pb$ ratios (sample Grimsel-1). The 30 µm analyses were done in the same areas and crystals analyzed in the previous sessions after polishing the thin/thick sections to remove the condensation blankets around the ablation craters.

In all sessions, Tara allanite (see Gregory et al., 2007; Smye et al., 2014) is chosen as primary reference material because it is the most homogenous allanite in terms of U–Th–Pb isotopes and the most promising reference material for U–Pb geochronology (Gregory et al., 2007; Smye et al., 2014; Burn et al., 2017; Liao et al., 2020). Tara allanite reference isotopic ratios and their uncertainties (Table 2.2) were calculated by averaging five of the six ID-TIMS measurements reported by Smye et al. (2014), excluding the measurement that yielded the youngest U–Pb age outside uncertainty. The analytical sequence involved measurements of the reference Tara allanite interspersed between 3–9 sample measurements including allanite secondary reference materials for quality control. Analysis spots in allanite were planned based on BSE images to avoid chemical and isotopic heterogeneity (i.e., mixing of zoning) within each single analysis, and inclusions (e.g., rare < 1 µm sized thorite; Smye et al., 2014). A few analyses were however intentionally placed on fluid inclusions and across zoning in sample Albula-1 to ascertain that these features would not compromise the use of this sample for solution ICP-MS (see Sects. 2.3.3 and 2.4.3).

Raw data were treated in the software Iolite (version 7.08) by the VisualAge_UcomPbine Data Reduction Scheme (Chew et al., 2014), and the correction for DF was carried out by selecting an exponential function. Iolite fits this function to model the measured DF on the analyses of the primary reference material, and then applies it to all unknown analyses to correct them for DF. The quality of signals and that of the correction for DF were considered to determine the validity of each measurement. Assessing the quality of signals implies inspection of the laser signal of each isotope across each measurement to discard – partially or entirely – those that are contaminated by impurities such as mineral or fluid inclusions, or that show isotopic heterogeneity during ablation. The accuracy of DF correction depends on the ablation behavior being the same between primary reference material and sample, and is assessed by the unknowns giving flat $^{206}Pb/^{238}U$ ratios across the ablation once corrected for DF. Although we do not apply an initial Pb correction for age calculation, correcting the time-resolved DF-corrected $^{206}Pb/^{238}U$ ratios for

initial Pb ensures that no sloping results from zoning in initial Pb contents, which can be prominent in minerals with high initial Pb contents. A ^{208}Pb-correction is therefore applied to each analysis of the epidote unknowns using initial ^{207}Pb/^{206}Pb and ^{208}Pb/^{206}Pb ratios obtained from preliminary Tera–Wasserburg diagrams. This and the subsequent normalization of the measured ratios based on the reference values of the primary reference material ensure that the ^{238}U/^{206}Pb and ^{207}Pb/^{206}Pb ratios used in the Tera–Wasserburg diagrams are true values, and that the U–Pb age calculated with these ratios is accurate. Since the isotopic fractionation between ^{207}Pb and ^{206}Pb is negligible (e.g., Burn et al., 2017), we address the suitability of the DF correction based on allanite as primary reference material only on ^{206}Pb/^{238}U ratios. A ^{207}Pb-correction was applied to the primary reference material (i.e., Tara allanite) by the VisualAge_UcomPbine Data Reduction Scheme (DRS) before it was used for normalization (Chew et al., 2014) using an initial ^{207}Pb/^{206}Pb value of 0.866 ± 0.079 obtained from a Tera–Wasserburg diagram plotting five ID-TIMS analyses by Smye et al. (2014), since it has been shown that initial ^{207}Pb/^{206}Pb ratios of allanite can deviate from model values (e.g., Cenki-Tok et al., 2014). The uncertainties on the ^{238}U/^{206}Pb and ^{207}Pb/^{206}Pb ratios obtained from the VisualAge_UcomPbine DRS (Chew et al., 2014) include an overall propagated uncertainty coming from the reproducibility of the primary reference material. Isoplot 3.7.5 (Ludwig, 2012) was used for age calculations. Age determination of epidote samples and allanite

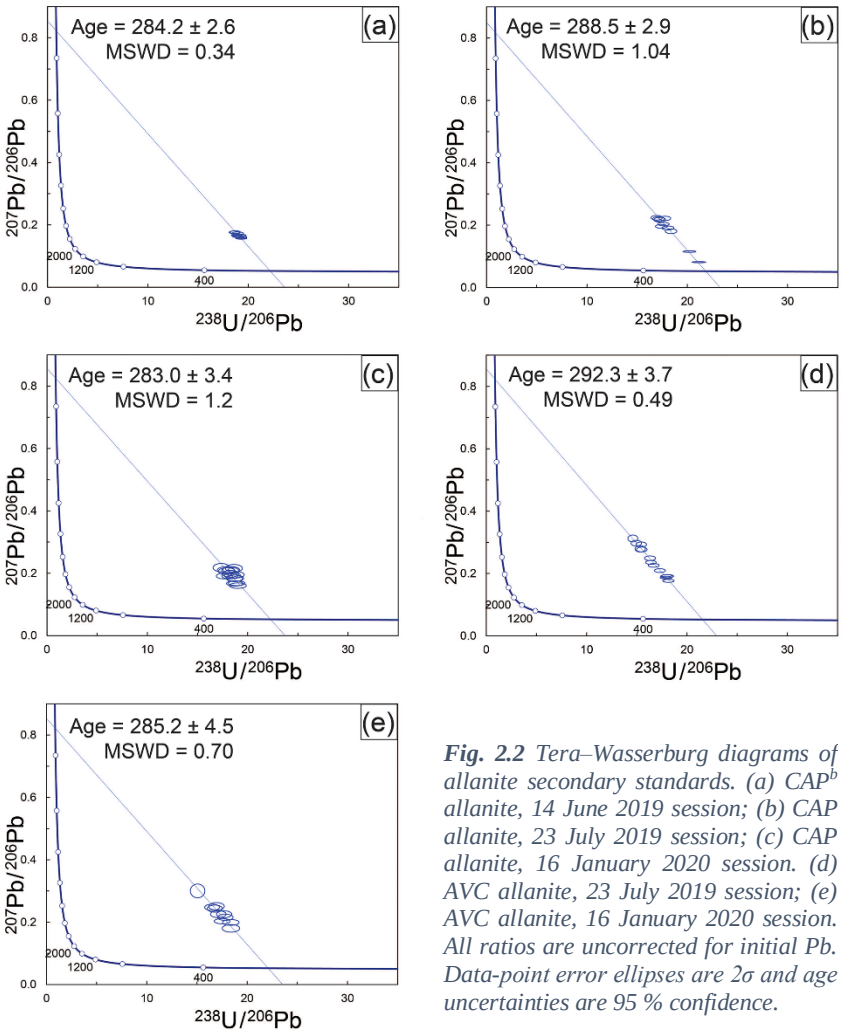

Fig. 2.2 *Tera–Wasserburg diagrams of allanite secondary standards. (a) CAP[b] allanite, 14 June 2019 session; (b) CAP allanite, 23 July 2019 session; (c) CAP allanite, 16 January 2020 session. (d) AVC allanite, 23 July 2019 session; (e) AVC allanite, 16 January 2020 session. All ratios are uncorrected for initial Pb. Data-point error ellipses are 2σ and age uncertainties are 95 % confidence.*

TABLE 2.3

U–Pb LA-ICP-MS ages of allanite secondary reference materials measured in three analytical sessions in this study. Age uncertainties are 95 % confidence. (a) = regression anchored to a $^{207}Pb/^{206}Pb$ value of 0.854 ± 0.015 (275 Ma; Stacey and Kramers, 1975); (b) = unanchored regression.

		CAP[b] allanite	CAP allanite	AVC allanite
14 June 2019	**Regression U–Pb age [Ma]**	284.2 ± 2.6 (a) MSWD = 0.34 274 ± 29 (b) MSWD = 0.33	-	-
	Weighted average U–Pb age [Ma]	284.2 ± 2.0 MSWD = 0.34	-	-
23 July 2019	**Regression U–Pb age [Ma]**	-	288.5 ± 2.9 (a) MSWD = 1.04 286.9 ± 5.2 (b) MSWD = 1.11	292.4 ± 3.7 (a) MSWD = 0.49 293.2 ± 7.4 (b) MSWD = 0.53
	Weighted average U–Pb age [Ma]	-	288.6 ± 2.3 MSWD = 1.03	292.2 ± 2.3 MSWD = 0.48
20 January 2020	**Regression U–Pb age [Ma]**	-	283.0 ± 3.4 (a) MSWD = 1.2 299 ± 20 (b) MSWD = 1.14	285.2 ± 4.5 (a) MSWD = 0.70 283 ± 16 (b) MSWD = 0.78
	Weighted average U–Pb age [Ma]	-	282.5 ± 3.2 MSWD = 1.2	285.1 ± 3.5 MSWD = 0.69

secondary reference materials relies on the Tera–Wasserburg approach (Tera and Wasserburg, 1972; Ludwig, 1998). Since the initial Pb isotopic composition of CAP, CAP[b] and AVC allanite is known and consistent with a modeled two-stage evolution of initial Pb isotopic compositions (Barth et al., 1994; Gregory et al., 2007; Burn et al., 2017), we ensured better age precision by anchoring the Tera–Wasserburg regressions of these allanite samples to an initial $^{207}Pb/^{206}Pb$ ratio of 0.854 ± 0.015 (275 Ma; Stacey & Kramers, 1975) and calculated their weighted average ^{207}Pb-corrected $^{238}U/^{206}Pb$ ages using the same value. Regression and weighted average ^{207}Pb-corrected $^{238}U/^{206}Pb$ ages of allanite secondary reference materials are summarized in Table 2.3, and their Tera–Wasserburg diagrams are presented in Fig. 2.2. The U–Pb isotope data are in Table 2.7 at the end of the chapter.

2.3.3. Solution ICP-MS

Independent measurements of $^{238}U/^{206}Pb$ and $^{207}Pb/^{206}Pb$ ratios were performed on two epidote micro-separates to check their consistency with U–Pb isotopic data measured by LA-ICP-MS and hence the reliability of the latter data. The material was separated from the epidote-quartz vein of

sample Albula-1, which is the one with the lowest degree of deformation and largest epidote crystals (see Sect. 2.4.1). Clean and pure epidote grains were handpicked under a binocular microscope. The epidote separates were pre-cleaned with MilliQ™ water. Based on LA-ICP-MS U and Pb concentration data, four sample aliquots – two from each epidote micro-separate and each corresponding to ca. 300 ng of total Pb – were weighed in acid-cleaned Teflon beakers and dissolved following the procedure of Nägler and Kamber (1996). Samples were leached with aqua regia at 120 °C for two days. The leachate was transferred into a second pre-cleaned Teflon beaker. To ensure complete dissolution a concentrated HF:HNO_3 (3:1 by volume) was added to the supernatant, and the beakers were placed on a heating plate at 90 °C for two days. After drying, 2 ml of 6.4 M HCl were added, and the beakers were placed on a heating plate at 150 °C for two days. The same procedure was applied to standard AGV-2 (Weis et al., 2006) as well as to two blanks, and complete dissolution was achieved for all samples and standards. Finally, the samples were dissolved in 1 ml 0.5 M HNO_3.

To determine $^{238}U/^{206}Pb$ ratios, a 10 % aliquot of digested samples and standards was further diluted with 0.5 M HNO_3 up to a final volume of 10 ml. Two solutions with two different dilution factors were prepared from each sample aliquot and were analyzed on a 7700x Agilent™ quadrupole ICP-MS at the Department of Geography, University of Bern, Switzerland. Standard AGV-2 (Weis et al., 2006) was used to correct for instrumental fractionation and to check accuracy of measurements. Final sample concentrations of ^{206}Pb, ^{207}Pb and ^{238}U (for both dilution factors of each sample aliquot) and their corresponding analytical uncertainties as relative standard deviations – solely based on counting statistics – were calculated by referring to a calibration curve based on three dilution factors of AGV-2 standard. The $^{238}U/^{206}Pb$ ratio and uncertainty as 2 SE of each sample aliquot were calculated with Isoplot 3.7.5 (Ludwig, 2012) as weighted average values between the $^{238}U/^{206}Pb$ ratios calculated from the measurements of both dilution factors, which were the same within uncertainty for all sample aliquots. The remaining sample material was dried and re-dissolved in 0.5 ml 1 M HNO_3 for Sr–Pb column chemistry using a pre-cleaned Sr-spec™ resin (Horwitz et al., 1992). After loading, the sample matrix was eluted from the column with 1.5 ml 1 M HNO_3 while Sr and Pb were retained on the column. The Sr and Pb fractions were eluted with 1 ml of 0.01 M HNO_3 and 8 ml of 0.01 M HCl respectively, following Villa (2009) and Quistini et al. (2017). After drying, the Pb fraction was dissolved and further diluted in 0.5 M HNO_3 for measurement of Pb isotopes on a Thermo Fisher Neptune Plus MC-ICP-MS.

Measurements were carried out in dry plasma mode using a CETAC Aridus 2 desolvating system. Thallium was added to samples and standards to correct for instrumental mass fractionation with repeated measurements of NIST SRM981 to quantify the external reproducibility of the measurements (Villa, 2009); the measured Pb isotopic composition was indistinguishable from those reported by Rehkämper and Mezger (2000). The four pairs of isotopic ratios measured by solution ICP-MS are only compared to the Tera–Wasserburg diagram based on LA-ICP-MS data (50 µm spot size) and are not used to calculate an age because the statistical robustness of a regression based on only four data points is limited.

2.4. Results

2.4.1. Petrography and U–Th–Pb contents of samples selected for U–Pb geochronology

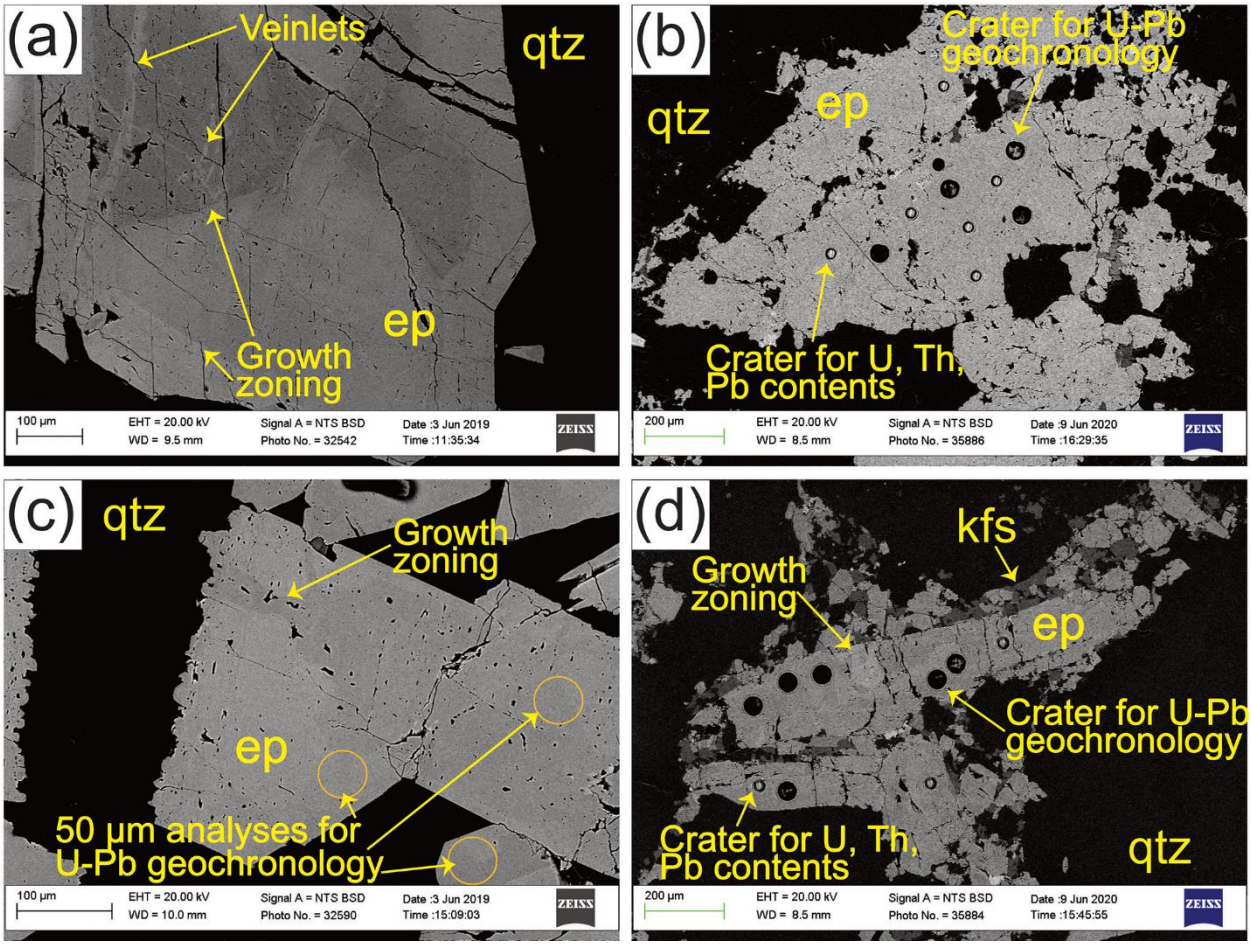

Fig. 2.3 *BSE images of (a) Albula-1, (b) Grimsel-1, (c) Grimsel-2 and (d) Heyuan-1 epidote. The specific epidote grain shown in panel (a) was not analyzed. The locations of the BSE images are indicated by the green rectangles in Fig. 2.1. bt = biotite; chl = chlorite; ep = epidote; kfs = K-feldspar; plg = plagioclase; qtz = quartz.*

Four samples were selected for this contribution mainly based on (1) size of epidote grains in order to use the largest laser beam possible for LA-ICP-MS and (2) U contents that are both as high and as variable as possible within the sample. Larger laser beams maximize the precision of U–Pb geochronology measurements. High U contents ensure higher contents of uranogenic Pb isotopes and therefore improve the precision of U and Pb isotopic measurements; their variability contributes to a larger spread of the analyses in Tera–Wasserburg diagrams for well-constrained regressions. The studied samples have epidote components (X_{Epi}) between 0.52–0.98 (calculated as $Fe^{3+}/(Al + Fe^{3+} - 2)$; Cr < limit of detection) and ΣREE between 3.3–210 µg g^{-1}.

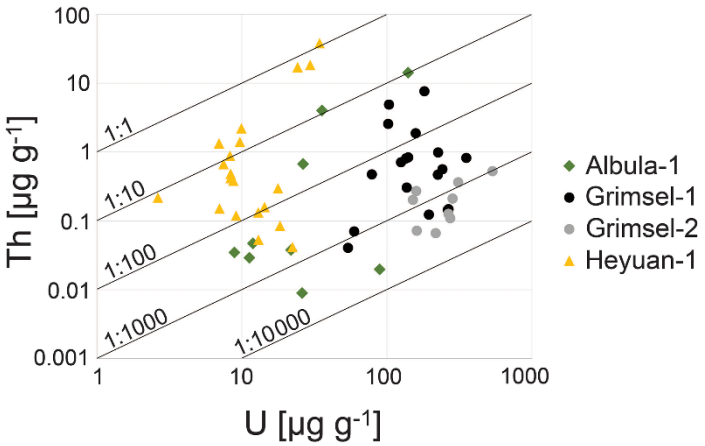

Fig. 2.4 *Th and U contents of the analyzed epidote samples.*

One sample from the Albula area, sample Albula-1, was selected for U–Pb geochronology. Two veins can be recognized (Fig. 2.1a), both crosscutting the host rock with sharp boundaries:

(1) 2–3 cm wide epidote-quartz-plagioclase vein (Vein1). Epidote grains are elongated, with lengths between ca. 0.5 mm along the vein boundaries to ca. 1 cm towards the center of the vein, with an aspect ratio up to ca. 7:1. Fractures are common and grains are euhedral to subhedral. Quartz is fractured and plagioclase is limited to a ca. 2 mm wide portion along the vein boundaries, associated with the smallest epidote grains. U contents of epidote range between 3.7–89 µg g^{-1} (Table 2.6). Th contents are 0.01–0.05 µg g^{-1} (19/25 measurements are below the limits of detection of 0.03–0.07 µg g^{-1} with a spot size of 24 µm and 0.003 µg g^{-1} with a 60 µm spot size). Pb contents are 3.9–62 µg g^{-1}, total Pb/U ratios 0.14–10 and μ values 7–510.

(2) ca. 1 mm wide epidote-quartz-plagioclase vein (Vein2). Epidote grains range between a few µm to 2 mm in diameter, most being fractured and euhedral to subhedral. Epidote grains of ca. 1–2 mm in diameter are mantled by thin layers of µm-sized anhedral epidote grains. Quartz subgrains resulting from recrystallization and plagioclase wrap the epidote grains. U contents of epidote are 26–140 µg g^{-1} (Table 2.6), and Th contents 0.67–14 µg g^{-1}. Pb contents range from 24–64 µg g^{-1}, Pb/U ratios from 0.46–1.7 and μ values from 43–160.

BSE images of epidote (Fig. 2.3a) reveal growth zoning and intra-grain veinlets resulting from interaction with a secondary fluid. Sample Albula-1 was selected for solution ICP-MS given the large size of epidote grains.

Sample Grimsel-1 (Fig. 2.1b) displays a folded epidote-quartz vein crosscutting a weakly deformed portion of the host rock. Epidote grains are generally prismatic and range between a few µm to ca. 2 mm in size. They are mostly subhedral to anhedral and cracked, and they form clusters with no preferential grain orientation. Quartz subgrains indicate dynamic recrystallization via subgrain rotation. Green biotite and rare chlorite are associated with the epidote-bearing vein. Epidote in BSE images (Fig. 2.3b) exhibits weak patchy zonation towards the rims and the presence of porosity. K-feldspar is recognized in epidote cracks. U contents are 54–350 µg g^{-1} (Table 2.6), and Th contents are 0.04–4.9 µg g^{-1}. Pb contents range between 79–190 µg g^{-1}, with Pb/U ratios from 0.45–1.7 and μ values between 41–160.

Sample Grimsel-2 (Fig. 2.1c) consists of an epidote-quartz-biotite vein cutting through a weakly deformed sector of the host rock. The vein boundaries are sharp and non-linear. Euhedral to subhedral epidote grains are cracked by stretching-induced fracturing, with single fragments ranging from a few µm to ca. 3 mm in size. Epidote grains can be estimated to have had an aspect ratio up to ca. 6:1 before fracturing. Quartz is recrystallized by subgrain rotation. Biotite grain sizes range between ca. 100–500 µm. BSE images (Fig. 2.3c) show that epidote exhibits regular growth zoning. Epidote contains 109–535 µg g^{-1} of U and 0.07–0.53 µg g^{-1} of Th (Table 2.6). Pb contents range from 51–97 µg g^{-1}, Pb/U ratios are 0.20–0.86 and μ values 83–510.

Sample Heyuan-1 (Fig. 2.1d) is characterized by an epidote-quartz-K-feldspar-chlorite assemblage that fills pockets cutting through the granite-forming minerals or interstitial among the magmatic minerals. The sample is crosscut by quartz ± hematite veins (see Fig. 4c in Tannock et al., 2020b). Epidote is variably shaped, from elongated without preferential orientation to prismatic. Epidote ranges between tens of µm to ca. 2 mm in length and forms clusters of euhedral to anhedral crystals. Quartz associated with epidote is mostly recrystallized, as indicated by the presence of quartz subgrains. Some mm sized quartz grains, however, display undulose extinction. Chlorite associated with epidote forms interstitial aggregates of ca. 500–1000 µm in size. Growth zoning of epidote is recognized from BSE images (Fig. 2.3d) and K-feldspar is intertwined with smaller-sized epidote grains along the boundaries of larger ones, as well as with quartz filling epidote fractures. The measured U content of Heyuan-1 epidote is 2.6–34 µg g^{-1} (Table 2.6). Th

contents range between 0.04–38 µg g^{-1}, with most analyses below 10 µg g^{-1}. Pb contents are 9.4–27 µg g^{-1}, Pb/U ratios range between 0.42–4.4 and μ values between 16–190.

In summary, among the four samples selected for U–Pb geochronology, measured U contents of epidote are highly variable (2.6–530 µg g^{-1}; n = 80; Table 2.6), and the intra-sample variability in U concentrations is ca. one order of magnitude (Fig. 2.4). Samples Albula-1 and Heyuan-1 both contain a few to tens of µg g^{-1} of U, whereas samples Grimsel-1 and Grimsel-2 have higher U contents of hundreds of µg g^{-1}. Thorium concentrations span four orders of magnitude (0.01–38 µg g^{-1}; n = 56). Samples with similar U concentrations display different Th contents, creating variability in Th/U ratios. Pb contents are 3.9–190 µg g^{-1}, and Pb/U ratios span between 0.14–10, each sample varying to different extents. With only 4/88 Th measurements above 10 µg g^{-1} (one in sample Albula-1 and three in sample Heyuan-1), Th–Pb geochronology is not viable. All epidote samples exhibit μ values well below 2000.

2.4.2. Testing Tara allanite as a reference material for epidote U–Pb geochronology

To assess the validity of allanite as primary reference material for epidote dating, we compared the DF correction of $^{206}Pb/^{238}U$ ratios over the ablation time using Tara allanite as reference for CAP^b allanite (Burn et al., 2017) as matrix-matched (Fig. 2.5a), for Plesovice zircon (Sláma et al., 2008) as non-matrix-matched (Fig. 2.5b), and for epidote as closely matrix-matched (Fig 2.6). An accurate correction for DF produces flat time-resolved lines of DF-corrected $^{206}Pb/^{238}U$ ratios for unknowns: sloping or more complex shaped curves indicate either zoning in initial Pb contents or that the DF correction is not compensating for the difference in matrix. As expected, CAP^b allanite

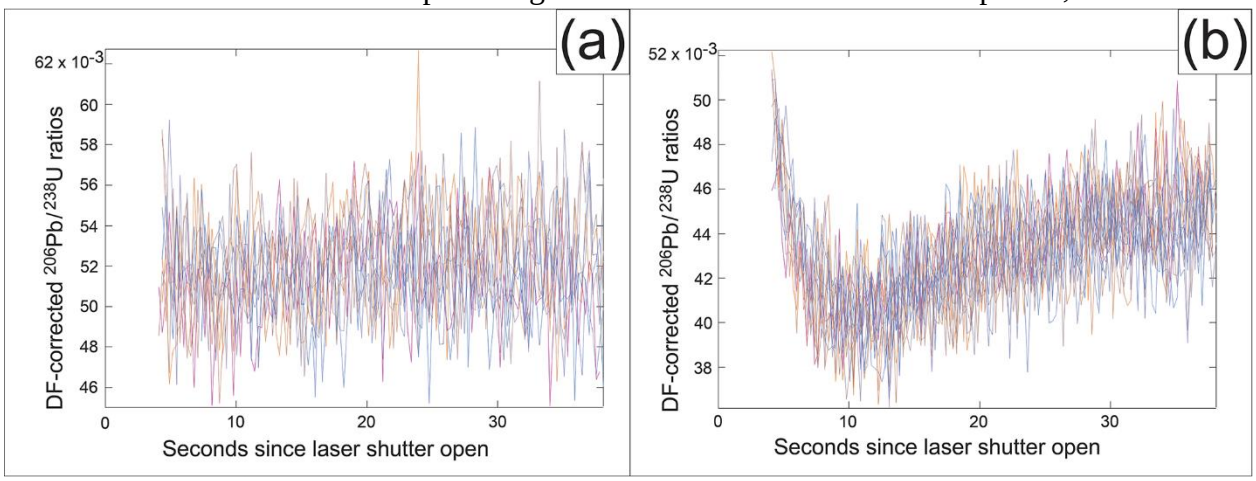

Fig. 2.5 *$^{206}Pb/^{238}U$ ratios measured by LA-ICP-MS corrected for downhole fractionation (DF) of (a) CAP^b allanite and (b) Plesovice zircon with Tara allanite as primary reference material. Each individual line represents one analysis. Measurements are with a 50 µm spot size. The DF-corrected $^{206}Pb/^{238}U$ ratios include both initial and radiogenic Pb.*

has DF-corrected $^{206}Pb/^{238}U$ ratios that are flat when standardized to Tara allanite (Fig. 2.5a, both measured with a 50 µm spot). Some of the DF-corrected $^{238}U/^{206}Pb$ ratios measured in Albula-1 and Grimsel-1 epidotes did not display a flat trend, and we therefore applied a ^{208}Pb correction to verify if this was due to zoning in initial Pb contents. The fact that the majority (122 out of 127

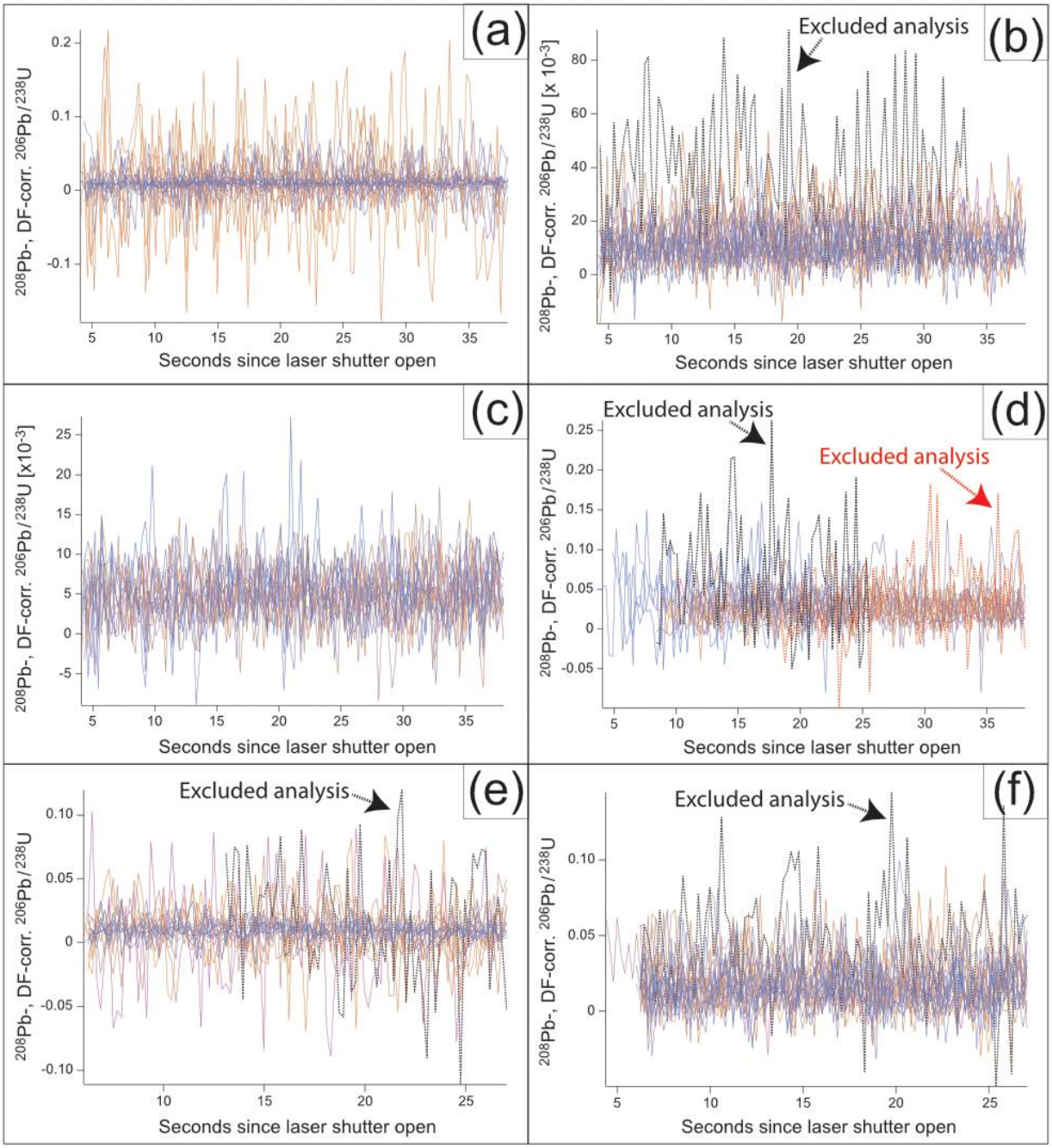

Fig. 2.6 *^{208}Pb-corrected $^{206}Pb/^{238}U$ ratios measured by LA-ICP-MS corrected for downhole fractionation (DF) of (a) Albula-1, (b) Grimsel-1, (c) Grimsel-2, (d) Heyuan-1, (e) Albula-1 and (f) Grimsel-1 epidote samples with Tara allanite as primary reference material. Each individual line represents one analysis. Measurements are with spot sizes of 50 µm (a-d) and of 30 µm (e-f).*

analyses) of ^{208}Pb- and DF-corrected time-resolved ^{206}Pb/^{238}U ratios are flat (Fig. 2.6) indicates similar ablation behavior and downhole fractionation of U from Pb between epidote and allanite for our analytical setup, and accurate correction for DF in epidote by using Tara allanite as primary reference material with both 50 µm (Fig. 2.6a-d) and 30 µm (Fig. 2.6e-f) spot sizes. The analyses whose ^{208}Pb- and DF-corrected time-resolved ^{206}Pb/^{238}U ratios are not flat or do not overlap with all other analyses were excluded from age calculation (see Sect. 2.4.3) as they could indicate either analytical instability during ablation or a different initial Pb isotopic composition. In contrast, the distinct ablation behavior of (Plesovice) zircon is revealed by complex shaped DF-corrected ^{238}U/^{206}Pb ratios even with a 50 µm spot (Fig. 2.5b; also see Fig. 6 of Burn et al., 2017).

2.4.3. Laser ablation ICP-MS U–Pb data of unknown samples

Uncertainties on LA-ICP-MS ^{238}U/^{206}Pb and ^{207}Pb/^{206}Pb ratios are 2 standard errors (2 SE), and all age uncertainties calculated with Isoplot are 95 % confidence.

A total of twenty-two spot analyses were measured in sample Albula-1 with a 50 µm spot (Table 2.7). ^{238}U/^{206}Pb ratios are 0.535–33.2 with uncertainties of 2–4 %. ^{207}Pb/^{206}Pb ratios are 0.586–0.837 ± 0.8–2 % (Table 2.7). No analyses were excluded as all ^{208}Pb- and DF-corrected time-resolved ^{206}Pb/^{238}U ratios are flat and overlap (Fig. 2.6a). A Tera–Wasserburg regression based on all data points (Fig. 2.7a) yields an intercept age of 62.7 ± 3.0 Ma (MSWD = 1.6) with a ^{207}Pb/^{206}Pb intercept of 0.8334 ± 0.0043. The good spread of the data points along the regression line reflects variable fractions of initial Pb (f_{206} = 0.69–1.0; Table 2.7). The small MSWD value indicates that there is no resolvable age difference between the two veins at the stated analytical precision. In fact, if the analyses from the two veins are considered separately, the Tera–Wasserburg ages of Vein1 and Vein2 are 67.6 ± 5.0 Ma (n = 18) and 58.9 ± 3.8 Ma (n = 4), which overlap within uncertainty. The initial ^{207}Pb/^{206}Pb ratio of Albula-1 epidote indicated by the Tera-Wasserburg diagram is within uncertainty of the model value of 0.840 ± 0.015 at 63 Ma (Stacey & Kramers, 1975). By using this model initial ratio for a ^{207}Pb-correction, the weighted average ^{207}Pb-corrected ^{238}U/^{206}Pb age is 65.0 ± 2.5 Ma (MSWD = 0.91). Eighteen additional measurements were carried out in sample Albula-1 (10 in Vein1 and eight in Vein2) with a spot size of 30 µm. Analysis 8 (Table 2.7) was excluded from age calculation because it was considered unreliable based on its ^{208}Pb- and DF-corrected time-resolved ^{206}Pb/^{238}U ratio (Fig. 2.6e). The Tera–Wasserburg diagram based on 17 analyses with a 30 µm spot yields an intercept age of 65.9

± 4.6 Ma and a $^{207}Pb/^{206}Pb$ intercept of 0.8308 ± 0.0087 (MSWD = 1.4). Both values are within uncertainty of those obtained with a spot size of 50 µm. By combining the 50 and 30 µm datasets, an intercept age of 63.9 ± 2.6 Ma is obtained with an initial $^{207}Pb/^{206}Pb$ ratio of 0.8331 ± 0.0039 (MSWD = 1.6). Given the consistency of the measured U–Pb data (i.e., no isotopic heterogeneity given by fluid inclusions and zonation even with different spot sizes), sample Albula-1 is considered suitable for solution ICP–MS (see Sect. 2.4.4).

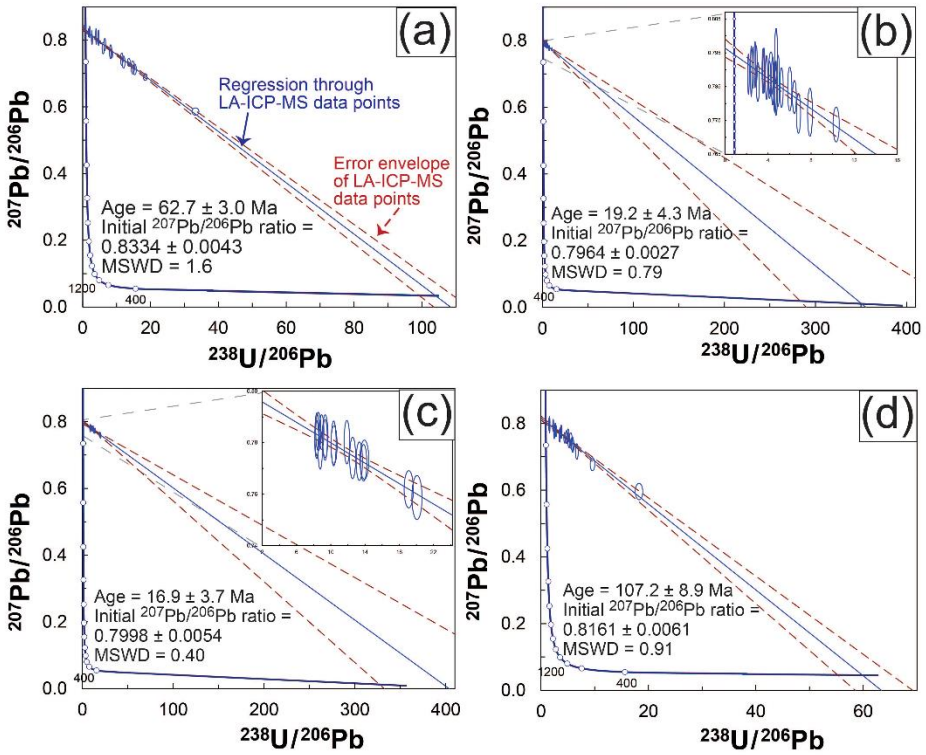

Fig. 2.7 *Tera–Wasserburg diagrams of (a) Albula-1, (b) Grimsel-1, (c) Grimsel-2 and (d) Heyuan-1 epidote samples with 50 µm measurements. All ratios are uncorrected for initial Pb. Ages are calculated from the lower intercept of the regressions through the analyses with the concordia, whereas initial $^{207}Pb/^{206}Pb$ ratios are calculated from the upper intercept of the regressions with the y-axis. Data-point error ellipses are 2σ and age uncertainties are 95 % confidence. Error envelopes are plotted with Isoplot 3.7.5 (Ludwig, 2012).*

Twenty-three 50 µm analyses were carried out in sample Grimsel-1. Analysis 14 (Table 2.7) was excluded as its ^{208}Pb- and DF-corrected time-resolved $^{206}Pb/^{238}U$ ratio does not overlap with all other analyses (Fig. 2.6b), possibly indicating a different initial Pb isotopic composition. Twenty-two analyses define a regression in a Tera–Wasserburg diagram (Fig. 2.7b) with an intercept age of 19.2 ± 4.3 Ma (MSWD = 0.79) and a $^{207}Pb/^{206}Pb$ intercept of 0.7964 ± 0.0027. All data points plot close to the y-axis ($^{238}U/^{206}Pb$ ratios = 1.10–10.3 ± 2–4 %; $^{207}Pb/^{206}Pb$ ratios = 0.774–0.794 ± 0.5–0.8 %; Table 2.7), indicating high and nearly invariable initial Pb fractions (f_{206} = 0.97–1.0; Table 2.7) in all measurements. The initial $^{207}Pb/^{206}Pb$ value is outside uncertainty of the model initial $^{207}Pb/^{206}Pb$ ratio of 0.837 ± 0.015 at 19 Ma of Stacey and Kramers (1975). Hence, a ^{207}Pb-correction with the modeled ratio would yield an inaccurate weighted average ^{207}Pb-corrected

$^{238}U/^{206}Pb$ age; thus this sample can only be dated by the Tera–Wasserburg approach. Twenty-five additional measurements were made with a spot size of 30 µm. Analysis 13 (Table 2.7) is excluded based on its ^{208}Pb- and DF-corrected time-resolved $^{206}Pb/^{238}U$ ratio not overlapping with the other analyses (Fig. 2.6f). The Tera–Wasserburg age based on 22 analyses is 17 ± 10 Ma with MSWD of 1.3. The initial $^{207}Pb/^{206}Pb$ of 0.7863 ± 0.0049 is slightly outside uncertainty of that obtained with a spot size of 50 µm. The age obtained by combining the analyses with 50 and 30 µm spot sizes is 15.2 ± 6.5 Ma with an initial $^{207}Pb/^{206}Pb$ ratio of 0.7918 ± 0.0037. However, MSWD of the combined dataset is 2.6, much higher than those obtained from the analyses with constant spot size, indicating that the two datasets should be treated separately.

Sixteen 50 µm analyses of sample Grimsel-2 define a regression in the Tera–Wasserburg diagram (Fig. 2.7c) yielding an age of 16.9 ± 3.7 Ma (MSWD = 0.40). No analyses were excluded before age calculation (Fig. 2.6c). The spread along the regression is limited and the data points are close to the y-axis ($^{238}U/^{206}Pb$ ratios = 8.35–20.1 ± 2–3 %; $^{207}Pb/^{206}Pb$ ratios = 0.759–0.784 ± 0.7–0.9 %; Table 2.7), indicating high and similar fractions of initial Pb in all analyses (f_{206} = 0.95–0.98; Table 2.6). The initial $^{207}Pb/^{206}Pb$ ratio of 0.7998 ± 0.0054 is outside uncertainty of the model initial $^{207}Pb/^{206}Pb$ value of 0.837 ± 0.015 at 17 Ma (Stacey and Kramers, 1975), which cannot be used for a ^{207}Pb-correction. The Tera–Wasserburg approach is therefore the only viable to date this sample.

Twenty-three analyses were carried out in sample Heyuan-1 with a spot size of 50 µm, and analyses 22 and 23 (Table 2.7) were excluded based on the anomalous ^{208}Pb- and DF-corrected time-resolved $^{206}Pb/^{238}U$ ratios (Fig. 2.6d). Twenty-one analyses define a regression (Fig. 2.7d) with an age of 107.2 ± 8.9 Ma (MSWD = 0.91). Initial Pb fractions are highly variable in the different measurements (f_{206} = 0.71–0.99; Table 2.7) yielding appreciable spread along the regression ($^{238}U/^{206}Pb$ ratios = 0.753–18.2 ± 3–4 %; $^{207}Pb/^{206}Pb$ ratios = 0.596–0.809 ± 2–3 %; Table 2.7). The initial $^{207}Pb/^{206}Pb$ ratio of 0.8161 ± 0.0061 indicated by the upper intercept is outside uncertainty of the modeled initial $^{207}Pb/^{206}Pb$ value of 0.843 ± 0.015 at 107 Ma (Stacey and Kramers, 1975). Thus, the age of this sample is best determined from the Tera-Wasserburg regression.

On a final note, we have calculated Tera–Wasserburg regression ages of the presented epidote samples by using a different primary reference material: CAP^b (June 2019; reference values from Burn et al., 2017) and CAP (July 2019 and January 2020; reference values from Barth et al., 1994)

allanite. The resulting epidote U–Pb ages remain within uncertainty identical to those calculated with Tara allanite as primary reference material (Table 2.4).

TABLE 2.4

Tera–Wasserburg U–Pb ages of epidote samples with CAP[b] (14 June 2019) and CAP (23 July 2019) allanite as primary reference materials. Measurements are with a 50 µm spot size. Age uncertainties are 95 % confidence.

	Albula-1	**Grimsel-1**	**Grimsel-1**	**Heyuan-1**
14 June 2019	61.1 ± 2.8 MSWD = 1.6 n = 22	18.8 ± 4.3 MSWD = 0.78 n = 22	16.5 ± 3.5 MSWD = 0.39 n = 16	-
23 July 2019	-	-	-	101.7 ± 8.9 MSWD = 0.87 n = 21

2.4.4. Solution ICP-MS U–Pb data

Uncertainties on solution ICP-MS $^{238}U/^{206}Pb$ and $^{207}Pb/^{206}Pb$ ratios are 2 standard errors (2 SE). For measurements by solution ICP-MS of $^{238}U/^{206}Pb$ and $^{207}Pb/^{206}Pb$ ratios in Albula-1 epidote, ca. 30 mg of material were necessary to ensure ca. 300 ng of total Pb. $^{238}U/^{206}Pb$ ratios range between 3.04–3.67 with uncertainties between 0.8–1.6 %, and $^{207}Pb/^{206}Pb$ ratios between 0.81319–0.81674 ± 0.03–0.04 ‰ (Table 2.5). The uncertainties on solution ICP-MS $^{238}U/^{206}Pb$ ratios are lower than those measured by LA-ICP-MS with a 50 µm spot size by a factor of 2.5, and a decrease by a factor of 13–100 occurs in analytical uncertainties on $^{207}Pb/^{206}Pb$ ratios. The two aliquots from each epidote micro-separate (A–B and C–D in Table 2.6) yield identical ratios within uncertainty. $^{238}U/^{206}Pb$ and $^{207}Pb/^{206}Pb$ ratios display minor spread in a Tera–Wasserburg diagram (Fig. 2.7). In comparison to LA-ICP-MS data, the intra-sample variability of solution ICP-MS

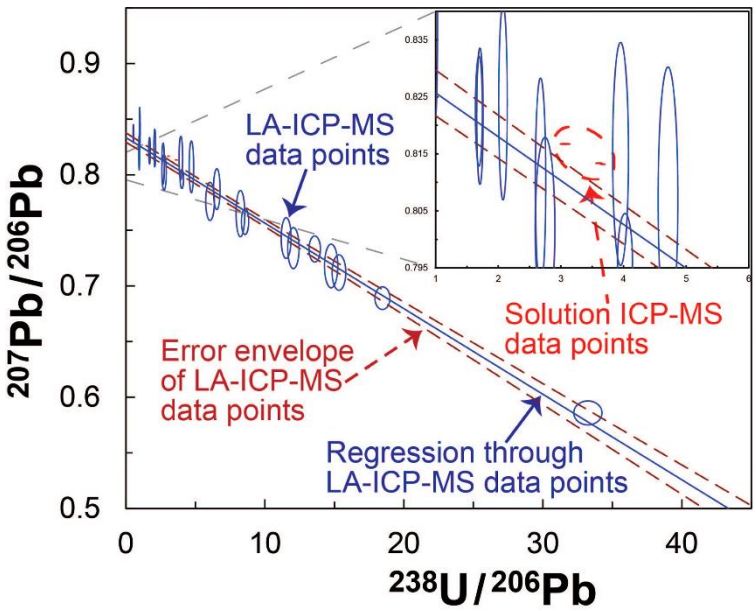

Fig. 2.8 *Tera–Wasserburg diagram showing the comparison between laser ablation ICP–MS and solution ICP–MS data points. The error envelope of LA-ICP-MS data points is plotted with Isoplot 3.7.5 (Ludwig, 2012). All ratios are uncorrected for initial Pb. Data-point error ellipses are 2σ.*

$^{238}U/^{206}Pb$ and $^{207}Pb/^{206}Pb$ ratios is only 2 % and 14 % respectively, attesting to homogenization of initial Pb fractions in the micro-separates. This confirms that no statistically robust Tera-Wasserburg regression can be calculated from the solution ICP-MS data alone. The $^{238}U/^{206}Pb$ and $^{207}Pb/^{206}Pb$ ratios measured by solution ICP-MS overlap with individual LA-ICP-MS data points (50 µm spot; Fig. 2.8).

TABLE 2.5

$^{238}U/^{206}Pb$ and $^{207}Pb/^{206}Pb$ ratios measured by solution ICP-MS. Uncertainties are 2 standard errors (2 SE).

	Albula-1_A	**Albula-1_B**	**Albula-1_C**	**Albula-1_D**
$^{238}U/^{206}Pb$	3.67	3.61	3.04	3.08
2 SE	0.03	0.04	0.04	0.05
$^{207}Pb/^{206}Pb$	0.81319	0.81337	0.81674	0.81674
2 SE	0.00004	0.00003	0.00003	0.00003

2.5. Discussion

2.5.1. CAP^{b}, CAP and AVC allanite as quality control

Although allanite geochronology is beyond the scope of this contribution, analyses of CAP^{b}, CAP and AVC allanite provide a quality control on U–Pb measurements during the analytical sessions. The epidote samples analyzed in this study contain too little Th for Th–Pb geochronology and we only explore epidote as a U–Pb geochronometer. For this reason, although the usual reference ages for allanite are Th–Pb ages, we check the reliability of our U–Pb measurements of allanite secondary reference materials by comparing them to published U–Pb ages (see Table 2.2) rather than their Th–Pb reference ages. In fact, ages from the two systems differ for these allanite samples likely due to excess ^{206}Pb and open-system behavior of the U–Pb system as opposed to the Th–Pb one (Barth et al., 1994; Oberli et al., 2004; Gregory et al., 2007; 2012; Darling et al., 2012; El Korh, 2014; Smye et al., 2014; Burn et al., 2017). Although this is a relevant issue in allanite geochronology *per se*, it does not impact the usefulness of allanite as secondary reference material for U–Pb dating in that it is the reproducibility of measured U–Pb ages in comparison with published values that confirms the reliability of U–Pb measurements. Tera–Wasserburg and weighted average ^{207}Pb-corrected $^{238}U/^{206}Pb$ ages determined from our analyses of CAP^{b}, CAP and AVC allanite (Table 2.3) in all analytical sessions are overall consistent with their published U–Pb ages, attesting to the reliability of our U–Pb measurements. AVC allanite analyzed in two

sessions provided Tera–Wasserburg ages of 292.4 ± 3.7 Ma and 285.2 ± 4.5 Ma and identical weighted average ^{207}Pb-corrected ^{238}U/^{206}Pb ages. Our AVC allanite ages are within uncertainty of the Tera–Wasserburg age of 289.6 ± 5.6 Ma of Gregory et al. (2007). CAP^{b} allanite (Burn et al., 2017) was used in one session, yielding a Tera–Wasserburg age of 284.2 ± 2.6 Ma and a weighted average ^{207}Pb-corrected ^{238}U/^{206}Pb age of 284.2 ± 2.0 Ma, both within uncertainty of those calculated by Burn et al. (2017) of respectively 284.9 ± 2.8 Ma and 283.8 ± 2.8 Ma. CAP allanite was used in two sessions returning intercept ages of 288.5 ± 2.9 Ma and 283.0 ± 3.4 Ma, with comparable weighted average ^{207}Pb-corrected ^{238}U/^{206}Pb ages. Our CAP U–Pb ages are within uncertainty of or close to the U–Pb age of 275.0 ± 4.7 Ma determined by SHRIMP by Gregory et al. (2007). The ages of CAP^{b}, CAP and AVC allanite obtained from unanchored Tera-Wasserburg regressions through our data are identical to those obtained from the anchored regressions but less precise (Table 2.3). We acknowledge that the Tera–Wasserburg age of 288.5 ± 2.9 Ma obtained from CAP allanite in the July 2019 session is slightly outside uncertainty of that reported by Gregory et al. (2007). However, we do not regard this difference outside uncertainty of ca. 2 % as significant given the complications of U–Pb age determinations of CAP allanite (e.g., Barth et al., 1994; Burn et al., 2017), and given the fact that AVC allanite used in the same session yielded an age within uncertainty of that measured by Gregory et al. (2007), attesting to reliable U–Pb measurements.

The values of excess variance calculated by Isoplot 3.7.5 (Ludwig, 2012) from the ^{207}Pb-corrected ages of CAP and AVC allanite samples in all analytical sessions conducted between July 2019 and October 2020 are respectively 1.9 and 2.2 % (2σ). These values are considered reasonable estimates of the long-term reproducibility, but they are not propagated onto our epidote ages because (1) they are not directly applicable to Tera–Wasserburg regression ages and (2) the effect of the propagation would be negligible.

2.5.2. Tara allanite as reference material for LA-ICP-MS dating of epidote

The presented data confirm that Tara allanite is an appropriate primary reference material for U–Pb dating of epidote by LA-ICP-MS in spot-analysis mode. The primary reference material is used to correct the measured isotopic ratios for DF, which is crucial to obtain reliable U–Pb geochronology by LA-ICP-MS (Horstwood et al., 2016). In this respect, 122 out of 127 analyses of epidote yield ^{208}Pb- and DF-corrected ^{206}Pb/^{238}U ratios that are flat and that overlap throughout

ablation time, demonstrating that the correction for DF is accurately carried out by using Tara allanite with a spot size of 50 µm and even 30 µm (Fig. 2.6). This is corroborated by the fact that the Tera–Wasserburg ages and initial $^{207}Pb/^{206}Pb$ ratios of Albula-1 and Grimsel-1 epidotes with a 30 µm spot remain consistent with the dataset with a 50 µm spot size. However, in both epidote samples age precision decreases with a spot of 30 µm. In the case of Grimsel-1 epidote, this is expected because the poor spread in $^{238}U/^{206}Pb$ and $^{207}Pb/^{206}Pb$ ratios, combined with larger analytical uncertainties of the 30 µm measurements, leads to an even more poorly constrained regression than that with a 50 µm spot size. Thanks to the larger spread in plotted ratios of Albula-1 epidote, the effects of the lower analytical precision with a 30 µm spot size are less dramatic but still noticeable. The flat and overlapping trends of most ^{208}Pb- and DF-corrected time-resolved $^{206}Pb/^{238}U$ ratios of sample Grimsel-1 (Fig. 2.6b and f) indicate that the fact that its initial $^{207}Pb/^{206}Pb$ ratios are slightly outside uncertainty when measured with different spot sizes cannot be due to inaccurate correction for DF.

2.5.3. Validation of $^{238}U/^{206}Pb$ and $^{207}Pb/^{206}Pb$ ratios by solution ICP-MS and considerations on analyzed volumes versus age precision

The consistency between the datasets acquired by different techniques lends support to the accuracy of our LA-ICP-MS data and of the calculated Tera–Wasserburg ages. The minor variability of $^{238}U/^{206}Pb$ ratios measured by solution ICP-MS data despite the high analytical precision with respect to LA-ICP-MS acquisitions is expected because sample preparation for solution ICP-MS requires homogenization of ca. 9×10^9 µm^3 (ca. 30 mg of material). By comparison, with LA-ICP-MS homogenization occurred over a volume of ca. $20–24\times10^3$ µm^3, as the measured depth of the LA-ICP-MS craters is between 10–12 µm. With decreasing spread in the plotted LA-ICP-MS $^{238}U/^{206}Pb$ and $^{207}Pb/^{206}Pb$ ratios, the regression becomes less constrained. Epidote samples Grimsel-1 and Grimsel-2 give larger uncertainties than Albula-1 and Heyuan-1 epidote because of the more limited spread in their LA-ICP-MS data points despite having higher U and Pb contents and hence better counting statistics. This suggests that higher analytical precision alone does not ensure better age precision unless it is accompanied by a large-enough data-point spread on the Tera Wasserburg diagram. It also confirms that epidote samples with relatively low U and Pb contents should not be automatically considered unsuitable for U–Pb geochronology.

It is therefore crucial that the spot size of LA-ICP-MS analyses represent a compromise ensuring sufficient analytical precision and the smallest extent possible of sample homogenization in order to preserve the variability in initial Pb contents. It should be noted that the analyzed samples are characterized by variable Th/U ratios (Fig. 2.4). The fractionation of Th from U is commonly attributed to oxidizing conditions (e.g., Frei et al., 2004). It is thus possible that the variability in initial Pb fractions of each individual epidote vein might be determined by physico-chemical conditions upon epidote crystallization, such as oxidizing conditions or re-equilibration along fluid pathways.

2.5.4. Isotopic composition of initial Pb

Among the epidote samples analyzed in this study, only Albula-1 epidote gives an initial $^{207}Pb/^{206}Pb$ ratio that overlaps within uncertainty with the model value of Stacey & Kramers (1975). Accordingly, the weighted average ^{207}Pb-corrected $^{238}U/^{206}Pb$ age of sample Albula-1 is within uncertainty of its Tera–Wasserburg age. Epidote from all other samples yielded Tera–Wasserburg initial $^{207}Pb/^{206}Pb$ ratios that deviate from model values, indicating non-negligible additions of inherited radiogenic components to the initial Pb. Radiogenic Pb components can be inherited by the fluid at its source and/or during circulation and re-equilibration with rocks along its pathway containing U-Th-bearing minerals (e.g., Romer, 2001). The weighted average ^{207}Pb-corrected $^{238}U/^{206}Pb$ ages of epidote Grimsel-1, Grimsel-2 and Heyuan-1 calculated by assuming a model initial $^{207}Pb/^{206}Pb$ ratio would be grossly inaccurate, implying that these three samples can only be dated with a Tera–Wasserburg regression. These considerations confirm the Tera–Wasserburg approach as the most suitable – and often the only viable – for accurate U–Pb dating of low-μ phases such as epidote (see Romer, 2001; Romer and Xiao, 2005; Odlum and Stockli, 2019; 2020).

2.5.5. Geological constraints on epidote U–Pb ages

To evaluate the geological accuracy of the U–Pb ages calculated from epidote in the veins presented above we consider other geochronological constraints on the deformation history of their respective host rocks. Albula-1 epidote gives a Paleocene age of 62.7 ± 3.0 Ma. Although, to our knowledge, no isotope geochronology is available in the Albula region, our epidote U–Pb age is consistent with geodynamic events taking place in its surroundings. For example, the Err–Platta

system was investigated by Handy et al. (1996) and their D2 – in the stability field of epidote – is dated 80–67 Ma (K/Ar on white mica); epidote growth is also observed in the post-D2 deformation (Handy et al., 1996). A rutile U–Pb age of 63.0 ± 3.0 Ma was calculated by Picazo et al. (2019) from the Malenco–Margna boundary (Passo d'Ur, ca. 90 km south-southeast of the Albula area; Fig. 1a in Picazo et al., 2019) dating the stacking of the nappes associated with metamorphism at high pressure.

Sample Grimsel-1 yielded initial $^{207}Pb/^{206}Pb$ ratios that differ outside uncertainty when measured with different spot sizes (50 *vs.* 30 µm). Although minimal, the difference in initial $^{207}Pb/^{206}Pb$ ratios given by the 50 and 30 µm measurements might indicate isotopic heterogeneity or unreliability of the 30 µm dataset. The 30 µm analyses were carried out in the same epidote grains as the 50 µm ones and no textural evidence (e.g., zoning) supports isotopic heterogeneity. Therefore, we regard the 30 µm dataset as questionable from a technical standpoint and only discuss the results obtained from the 50 µm dataset. Epidote U–Pb ages in samples Grimsel-1 and Grimsel-2 yield (early) Miocene ages of 19.2 ± 4.3 Ma and 16.9 ± 3.7 Ma, respectively. These ages are within uncertainty of each other and can be attributed to the early deformation in the area between 22–17 Ma (Handegg phase; Challandes et al., 2008; Rolland et al., 2009). This is corroborated by the presence of green biotite associated with epidote in the epidote-bearing veins (Challandes et al., 2008; Rolland et al., 2009; Herwegh et al., 2017; Wehrens et al., 2017). Notably, Grimsel-1 and Grimsel-2 epidote samples yield initial $^{207}Pb/^{206}Pb$ ratios that are identical within uncertainty and indicate an inherited radiogenic component. This implies that the Pb isotopic signature of the circulating fluid(s) was homogenously re-equilibrated over a ca. 100 m distance.

Epidote of sample Heyuan-1 yields an age of 107.2 ± 8.9 Ma, which is (early) Cretaceous and consistent with the earliest movements of the Heyuan Fault. This is supported by the sample being crosscut by an earliest-generation quartz vein associated with hematite, as the formation of quartz veins post-dates that of epidote veins across the Heyuan fault but is related to the early phases of faulting (Tannock et al., 2020a; 2020b).

2.5.6. Epidote ages as time of crystallization in low-temperature veins

Having established that the calculated epidote U–Pb ages are consistent with geological events that affected the host rocks, we now discuss whether these ages can be truly considered representative of epidote crystallization. The highest temperatures recorded by the deformation

events that affected the meta-granitoid rocks hosting the analyzed epidote veins at Albula Pass, at Grimsel Pass and at the Heyuan Fault are respectively 300 °C (Mohn et al., 2011), 450 ± 30 °C (Challandes et al., 2008; Goncalves et al., 2012) and 330 °C (Tannock et al., 2020a). All these temperatures are well below 685–750 °C, proposed by Dahl (1997) as the range for the closure temperature of Pb diffusion in epidote. Nevertheless, resetting of the U–Pb geochronometer can occur independently of temperature-controlled diffusion via fluid-mediated dissolution–precipitation processes, which can be assessed with BSE imaging. Albula-1 and Grimsel-2 epidotes display growth zoning, which is regarded as primary zoning and thus lack of significant elemental diffusion (Franz and Liebscher, 2004). Since care was taken to avoid mixing of different zoning domains in each single analysis – including those associated with secondary veinlets – and considering that the MSWD values of the calculated epidote ages are all close to or below 1 (i.e., only one epidote generation can be distinguished at the stated analytical precision), we can conclude that the ages of Albula-1 and Grimsel-2 epidote date their crystallization and therefore the formation of the epidote-bearing veins.

The epidote-bearing vein in sample Grimsel-1 is folded; epidote does not display prominent zoning, and it is fractured and porous. This may raise questions as to whether the age of 19.2 ± 4.3 Ma dates the formation of Grimsel-1 epidote or the resetting of the U–Pb geochronometer by interaction with a fluid assisting the Alpine deformation. However, epidote is associated with green biotite, hinting that the vein epidote formed during the Handegg phase (22–17 Ma) in the stability field of green biotite (Challandes et al., 2008; Rolland et al., 2009; Herwegh et al., 2017; Wehrens et al., 2017). Therefore, the age of 19.2 ± 4.3 Ma is interpreted as the crystallization age of epidote. The minor presence of chlorite may indicate that the subsequent folding of the vein may have occurred at the end of the Handegg phase or at the beginning of the Oberaar phase with the onset of chlorite crystallization (Herwegh et al., 2017; Wehrens et al., 2017).

In sample Heyuan-1, epidote is present in pockets filled by an epidote-quartz(-chlorite) assemblage. This microstructure might suggest a magmatic origin of epidote, and consequently that epidote might have formed in the Jurassic as a magmatic mineral and that the U–Pb system was reset by ingression of fluids related to the first movements of the Heyuan Fault. However, a magmatic origin of the epidote can be ruled out based on the association of epidote with chlorite instead of biotite (i.e., the magmatic phyllosilicate stable in the Xinfengjiang pluton; Li et al., 2007; Tannock et al., 2020a; 2020b) Coexistence with chlorite is consistent with the temperature of

mylonitization during Heyuan normal faulting (330 °C; Tannock et al., 2020a). Furthermore, the Th/U ratios measured in Heyuan-1 epidote are << 1, whereas the Fogang Batholith – which comprises the Xinfengjiang pluton – has Th/U ratios >> 1 (Li et al., 2007). This lands support to a non-magmatic origin of the studied epidote because epidote generally reflects the trace element composition of its host rock (Frei et al., 2004). We thus conclude that all epidote U–Pb ages presented in this study date the crystallization of the epidote grains that formed during low-temperature fluid circulation.

2.6. Concluding remarks and future prospects

This contribution presents a protocol to determine U–Pb ages and initial $^{207}Pb/^{206}Pb$ compositions of epidote (i.e., epidote–clinozoisite solid solution), that is highly but variably enriched in initial Pb. This includes preliminary screening of the material to verify the presence of sufficiently high U contents (mainly between 7–310 µg g^{-1} in our samples) and intra-sample chemical variability. If these geochemical characteristics are ascertained, measurements by spot-analysis LA-ICP-MS using a quadrupole mass spectrometer can allow U–Pb ages to be determined with uncertainties between ca. 5–20 %, the lowest precision being related to poor variability in initial Pb fractions. It is demonstrated that epidote and allanite have similar downhole fractionation of Pb from U during LA-ICP-MS spot analysis, and the consistency between the data measured by LA-ICP-MS and solution ICP-MS corroborates the accuracy of $^{238}U/^{206}Pb$ and $^{207}Pb/^{206}Pb$ ratios for epidote samples determined by using Tara allanite as primary reference material. We have shown that all effects due to downhole fractionation are accurately corrected for even with a spot size as small as 30 µm by using Tara allanite as primary reference material. Therefore, the lack of a standard that is perfectly matrix-matched to epidote does not prevent U–Pb dating of the epidote–clinozoisite solid solution by spot-analysis LA-ICP-MS with precision between ca. 5–20 %. The geological significance of the ages is verified against the geological evolution of the areas of origin of the epidote samples. In each sample, the obtained ages are interpreted as dating epidote crystallization during hydrothermal-vein formation.

The key strategy for U–Pb dating of epidote is the Tera–Wasserburg regression through data uncorrected for initial Pb. U–Pb geochronology of epidote is most successful when the epidote samples display large-enough variability in initial Pb fractions – even when high analytical precision is achieved – which may be related to variable physico-chemical conditions during the

crystallization of vein-filling epidote. Although it is recommended that the largest spot size possible be used to ensure good counting statistics, it is imperative that geochemical heterogeneity be preserved among the different analyses in order to obtain a well-constrained Tera–Wasserburg regression and a small age uncertainty. An unexpected perk highlighted by the present study is that relatively low U contents (i.e., tens of µg g^{-1}) do not necessarily hamper age determinations at a geologically useful precision provided that the spread of $^{238}U/^{206}Pb$ and $^{207}Pb/^{206}Pb$ ratios is large enough.

This study presents a protocol that can be readily applied to date epidote-bearing hydrothermal veins and to assess initial Pb isotopic variability of the epidote-forming fluid. Better insight can now be gained from the application of epidote U–Pb dating into the mechanisms that led to the hydration of the continental crust in the Aar Massif and in the Err nappe. This study represents the base from which further developments may allow to date high-*P* epidote-bearing veins in subducted oceanic units and to determine at the same time where the vein-forming fluid originated thanks to the combination of trace element, age and isotopic data measured in epidote. Multiple phases of fault re-activation may be identified in fault-plane epidote. Whether or not plagioclase recrystallization in metamorphosed granitoid rocks is linked to the formation of epidote-bearing veins may be solved by measuring U–Pb ages and initial Pb isotopic compositions in epidote, which has proven its potential to become an invaluable geochemical, isotopic and geochronological tool.

TABLE 2.6

Concentrations of Pb, Th and U, Th/U and Pb/U ratios, and μ values measured by laser ablation ICP–MS with the trace element protocol in Appendix A. The symbol < is followed by limits of detection (calculated for each element in each measurement individually following the formulation in Pettke et al., 2012). μ values are calculated from total Pb and total U contents by considering an isotopic abundance of 1.4 % for ^{204}Pb and 93 % for ^{238}U. N/A = non-applicable. Contents of Pb, Th and U are in µg g^{-1}; ratios are adimensional.

Sample Albula-1 Vein1					
Pb	**Th**	**U**	**Th/U**	**Pb/U**	**$\mu = {}^{238}U/{}^{204}Pb$**
17	0.02	89	0.0002	0.20	360
19	0.04	22	0.002	0.87	81
6.5	<0.03	11	N/A	0.60	120
7.9	0.05	12	0.004	0.66	110
7.9	0.03	8.9	0.004	0.89	80
3.9	<0.01	28	N/A	0.14	510
9.7	<0.005	28	N/A	0.35	210
18	<0.02	7.1	N/A	2.5	28
21	0.03	11	0.003	1.8	39
11	<0.004	16	N/A	0.70	100
8.2	<0.07	11	N/A	0.74	96
8.5	<0.03	3.7	N/A	2.3	31
7.5	<0.05	4.5	N/A	1.7	43
10	<0.05	5.9	N/A	1.7	42
16	<0.04	5.5	N/A	2.8	25
24	<0.06	8.3	N/A	2.9	25
5.7	<0.03	23	N/A	0.25	290
61	<0.01	6.0	N/A	10	6.9
46	<0.005	7.5	N/A	6.1	12
9.0	<0.02	3.7	N/A	2.4	29
6.4	<0.06	12	N/A	0.51	140
8.3	0.01	26	0.0003	0.32	220
7.6	<0.01	27	N/A	0.28	260
6.9	<0.01	9.6	N/A	0.72	99
25	<0.003	4.3	N/A	5.9	12
Sample Albula-1 Vein2					
Pb	**Th**	**U**	**Th/U**	**Pb/U**	**$\mu = {}^{238}U/{}^{204}Pb$**
44	0.67	26	0.03	1.7	43
64	14	140	0.10	0.46	160
24	4.0	36	0.11	0.69	100
Sample Grimsel-1					
Pb	**Th**	**U**	**Th/U**	**Pb/U**	**$\mu = {}^{238}U/{}^{204}Pb$**
130	0.12	190	0.001	0.68	100
150	7.6	180	0.04	0.83	85
170	0.15	270	0.001	0.64	110
150	0.99	230	0.004	0.67	110
130	0.47	79	0.01	1.6	44

130	<0.09	130	N/A	1.0	70
150	0.82	350	0.002	0.44	160
97	0.07	60	0.001	1.6	44
170	0.71	130	0.01	1.3	52
87	0.30	140	0.002	0.64	110
170	0.56	240	0.002	0.72	99
150	2.6	100	0.03	1.4	49
170	0.47	220	0.002	0.78	91
93	4.9	100	0.05	0.90	79
190	0.81	140	0.01	1.4	50
78	1.9	160	0.01	0.49	140
180	0.14	260	0.001	0.68	104
93	0.04	54	0.001	1.7	41
150	0.84	140	0.01	1.1	65

Sample Grimsel-2

Pb	Th	U	Th/U	Pb/U	$\mu = {}^{238}U/{}^{204}Pb$
75	0.07	220	0.0003	0.34	210
68	0.27	160	0.002	0.43	170
75	0.20	150	0.001	0.49	140
51	<0.06	120	N/A	0.42	170
62	<0.05	120	N/A	0.53	130
74	0.07	160	0.0004	0.46	150
97	0.11	270	0.0004	0.35	200
95	0.13	270	0.0005	0.36	200
65	0.21	280	0.001	0.23	310
88	<0.02	180	N/A	0.50	140
93	<0.03	110	N/A	0.86	83
75	0.53	535	0.001	0.14	510
62	0.36	310	0.001	0.20	350

Sample Heyuan-1

Pb	Th	U	Th/U	Pb/U	$\mu = {}^{238}U/{}^{204}Pb$
19	0.48	8.4	0.06	2.2	32
12	0.30	18	0.02	0.68	100
16	0.38	8.7	0.04	1.8	39
15	0.42	8.4	0.05	1.8	39
27	0.67	7.5	0.09	3.6	20
16	0.05	13	0.004	1.2	57
21	17	24	0.70	0.86	82
20	38	34	1.10	0.58	120
26	0.08	18	0.004	1.4	50
17	0.15	7.0	0.02	2.4	29
16	1.4	9.7	0.14	1.7	42
19	0.13	13	0.01	1.5	49
23	18	30	0.62	0.78	90
17	0.12	9.1	0.01	1.8	39
17	1.3	7.0	0.19	2.4	29
24	0.16	14	0.01	1.6	43

22	2.2	9.9	0.22	2.2	32
8.2	0.04	22	0.002	0.37	190
18	0.88	8.3	0.11	2.2	31
12	0.22	2.6	0.08	4.4	16

TABLE 2.7

$^{238}U/^{206}Pb$ and $^{207}Pb/^{206}Pb$ ratios, and their uncertainties as 2 standard errors (2 SE) measured by LA–ICP–MS. f206 is calculated using the initial $^{207}Pb/^{206}Pb$ indicated by the Tera–Wasserburg diagrams. (a) = 50 µm spot size; (b) = 30 µm spot size.

Sample Albula-1 (a)					
Vein1					
Analysis	**$^{238}U/^{206}Pb$**	**2 SE**	**$^{207}Pb/^{206}Pb$**	**2 SE**	**f_{206}**
1	12.05	0.33	0.734	0.015	0.87
2	8.237	0.258	0.765	0.017	0.91
3	3.953	0.103	0.815	0.016	0.98
4	0.535	0.013	0.8368	0.0067	1.0
5	0.996	0.028	0.841	0.016	1.0
6	0.952	0.025	0.820	0.013	0.98
7	1.691	0.046	0.8225	0.0079	0.99
8	1.707	0.041	0.8216	0.0098	0.98
9	15.33	0.40	0.712	0.013	0.85
10	4.024	0.097	0.7961	0.0069	0.95
11	6.540	0.188	0.787	0.015	0.94
12	11.53	0.29	0.743	0.015	0.89
13	4.710	0.129	0.807	0.019	0.97
14	2.747	0.128	0.802	0.013	0.96
15	2.076	0.056	0.824	0.014	0.99
16	14.77	0.39	0.718	0.016	0.85
17	2.675	0.068	0.810	0.015	0.97
18	6.053	0.253	0.776	0.014	0.93
Vein2					
Analysis	**$^{238}U/^{206}Pb$**	**2 SE**	**$^{207}Pb/^{206}Pb$**	**2 SE**	**f_{206}**
19	13.59	0.33	0.7332	0.0096	0.87
20	33.24	0.83	0.5858	0.0088	0.69
21	18.46	0.44	0.689	0.0083	0.82
22	8.576	0.213	0.7578	0.0094	0.90
Sample Albula-1 (b)					
Vein1					
Analysis	**$^{238}U/^{206}Pb$**	**2 SE**	**$^{207}Pb/^{206}Pb$**	**2 SE**	**f_{206}**
1	2.762	0.107	0.839	0.025	1.0
2	13.91	0.58	0.737	0.027	0.89
3	5.035	0.213	0.794	0.028	0.96
4	4.102	0.143	0.788	0.013	0.95
5	4.706	0.168	0.799	0.015	0.96
6	8.569	0.338	0.763	0.028	0.92

7	6.510	0.309	0.782	0.025	0.94
8	3.236	0.157	0.778	0.038	0.94
9	14.08	0.62	0.710	0.030	0.85
10	13.37	0.59	0.735	0.032	0.88
Vein2					
Analysis	**$^{238}U/^{206}Pb$**	**2 SE**	**$^{207}Pb/^{206}Pb$**	**2 SE**	**f_{206}**
11	17.79	0.70	0.686	0.015	0.83
12	21.90	0.81	0.639	0.017	0.77
13	14.99	0.54	0.703	0.015	0.85
14	10.54	0.77	0.740	0.017	0.89
15	9.940	0.356	0.743	0.016	0.89
16	21.70	0.80	0.658	0.018	0.79
17	26.21	0.96	0.639	0.017	0.77
18	7.107	0.263	0.776	0.013	0.93
Sample Grimsel-1 (a)					
Analysis	**$^{238}U/^{206}Pb$**	**2 SE**	**$^{207}Pb/^{206}Pb$**	**2 SE**	**f_{206}**
1	3.049	0.121	0.7864	0.0047	0.99
2	2.593	0.059	0.7906	0.005	0.99
3	4.929	0.114	0.7867	0.0062	0.99
4	10.33	0.23	0.7738	0.0042	0.97
5	7.896	0.181	0.7774	0.0058	0.97
6	4.268	0.178	0.7888	0.0053	0.99
7	2.443	0.055	0.7895	0.0061	0.99
8	2.189	0.057	0.7887	0.0049	0.99
9	3.615	0.081	0.7898	0.0054	0.99
10	4.429	0.098	0.7867	0.0058	0.99
11	2.789	0.062	0.7915	0.0056	0.99
12	3.542	0.080	0.7896	0.0054	0.99
13	4.647	0.119	0.785	0.0063	0.98
14	1.098	0.024	0.7937	0.0042	1.0
15	4.137	0.098	0.787	0.0045	0.99
16	6.826	0.158	0.7771	0.0048	0.97
17	2.912	0.067	0.7916	0.0045	0.99
18	5.258	0.127	0.7847	0.0048	0.98
19	4.737	0.112	0.7836	0.0058	0.98
20	6.449	0.145	0.7819	0.004	0.98
21	4.746	0.106	0.7941	0.0066	1.0
22	6.020	0.159	0.7843	0.0053	0.98
23	3.862	0.086	0.7877	0.0053	0.99
Sample Grimsel-1 (b)					
Analysis	**$^{238}U/^{206}Pb$**	**2 SE**	**$^{207}Pb/^{206}Pb$**	**2 SE**	**f_{206}**
1	5.018	0.166	0.7792	0.0096	0.99
2	2.533	0.090	0.7839	0.0094	1.0
3	6.575	0.220	0.785	0.011	1.0
4	2.674	0.086	0.7852	0.0089	1.0
5	5.266	0.180	0.763	0.012	0.97
6	2.089	0.070	0.7777	0.0074	0.99

7	4.640	0.155	0.783	0.011	1.0
8	1.895	0.065	0.7855	0.0091	1.0
9	5.339	0.177	0.7667	0.0085	0.98
10	4.684	0.158	0.781	0.0086	0.99
11	6.973	0.233	0.780	0.011	0.99
12	2.123	0.077	0.7867	0.0085	1.0
13	1.077	0.036	0.7842	0.007	1.0
14	2.168	0.070	0.783	0.01	1.0
15	2.913	0.093	0.7794	0.0085	0.99
16	2.461	0.079	0.7769	0.009	0.99
17	2.685	0.086	0.7874	0.009	1.0
18	2.357	0.078	0.7771	0.0098	0.99
19	3.840	0.131	0.777	0.010	0.99
20	7.032	0.232	0.7703	0.0095	0.98
21	5.862	0.196	0.7687	0.0099	0.98
22	3.611	0.117	0.7763	0.0065	0.99
23	4.572	0.178	0.7781	0.0099	0.99
24	3.636	0.132	0.7779	0.0090	0.99
25	3.347	0.123	0.7804	0.0080	0.99

Sample Grimsel-2 (a)

Analysis	$^{238}U/^{206}Pb$	**2 SE**	$^{207}Pb/^{206}Pb$	**2 SE**	f_{206}
1	13.83	0.31	0.7722	0.0058	0.96
2	19.11	0.44	0.7619	0.0059	0.95
3	13.34	0.30	0.7728	0.0061	0.96
4	8.929	0.215	0.7841	0.0055	0.98
5	12.56	0.284	0.7741	0.0066	0.97
6	11.88	0.27	0.7802	0.0069	0.97
7	8.376	0.189	0.7832	0.0068	0.98
8	8.547	0.248	0.7843	0.0061	0.98
9	13.93	0.43	0.7734	0.0062	0.96
10	10.37	0.29	0.7791	0.0061	0.97
11	8.353	0.188	0.7812	0.0060	0.98
12	9.346	0.262	0.7825	0.0068	0.98
13	20.07	0.48	0.7587	0.0070	0.95
14	9.329	0.218	0.7811	0.0065	0.98
15	8.765	0.200	0.7774	0.0063	0.97
16	10.34	0.23	0.7797	0.0071	0.97

Sample Heyuan-1 (a)

Analysis	$^{238}U/^{206}Pb$	**2 SE**	$^{207}Pb/^{206}Pb$	**2 SE**	f_{206}
1	5.040	0.155	0.764	0.016	0.93
2	3.565	0.108	0.772	0.012	0.94
3	5.907	0.174	0.734	0.017	0.89
4	4.958	0.160	0.757	0.012	0.92
5	2.655	0.071	0.785	0.013	0.96
6	5.244	0.187	0.742	0.012	0.90
7	3.499	0.098	0.764	0.016	0.93
8	6.676	0.209	0.716	0.019	0.87

9	4.409	0.132	0.757	0.013	0.92
10	2.793	0.117	0.777	0.014	0.95
11	9.578	0.349	0.678	0.016	0.82
12	3.772	0.119	0.775	0.016	0.95
13	4.751	0.165	0.759	0.016	0.93
14	5.525	0.217	0.749	0.019	0.91
15	5.827	0.180	0.739	0.017	0.90
16	1.513	0.050	0.797	0.016	0.98

References

Barker, S. L. L., Cox, S. F., Eggins, S. M. and Gagan, M. K.: Microchemical evidence for episodic growth of antitaxial veins during fracture-controlled fluid flow, Earth Planet. Sci. Lett., 250(1–2), 331–344, doi:10.1016/j.epsl.2006.07.051, 2006.

Barker, S. L. L., Bennett, V. C., Cox, S. F., Norman, M. D. and Gagan, M. K.: Sm-Nd, Sr, C and O isotope systematics in hydrothermal calcite-fluorite veins: Implications for fluid-rock reaction and geochronology, Chem. Geol., 268(1–2), 58–66, doi:10.1016/j.chemgeo.2009.07.009, 2009.

Barth, S., Oberli, F. and Meier, M.: Th-Pb versus U-Pb isotope systematics in allanite from co-genetic rhyolite and granodiorite: implications for geochronology, Earth Planet. Sci. Lett., 124(1–4), 149–159, doi:10.1016/0012-821X(94)00073-5, 1994.

Berger, A., Mercolli, I., Herwegh, M., Gnos, E.: Geological Map of the Aar Massif, Tavetsch and Gotthard Nappes. – Geol. spec. Map 1:100 000, explanatory notes 129, Federal Office of Topography swisstopo, 2017.

Bird, D.K., Spieler, A.R.: Epidote in Geothermal Systems, Rev. Mineral. Geochemistry 56, 235–300, https://doi.org/10.2138/gsrmg.56.1.235, 2004.

Bons, P. D., Elburg, M. A. and Gomez-Rivas, E.: A review of the formation of tectonic veins and their microstructures, J. Struct. Geol., 43, 33–62, doi:10.1016/j.jsg.2012.07.005, 2012.

Buick, I. S., Frei, R. and Cartwright, I.: The timing of high-temperature retrogression in the Reynolds Range, central Australia: Constraints from garnet and epidote Pb-Pb dating, Contrib. to Mineral. Petrol., 135(2–3), 244–254, doi:10.1007/s004100050510, 1999.

Burn, M., Lanari, P., Pettke, T. and Engi, M.: Non-matrix-matched standardisation in LA-ICP-MS analysis: General approach, and application to allanite Th-U-Pb dating, J. Anal. At. Spectrom., 32(7), 1359–1377, doi:10.1039/c7ja00095b, 2017.

Catlos, E. J., Sorensen, S. S. and Harrison, T. M.: Th-Pb ion-microprobe dating of allanite, Am. Mineral., 85(5–6), 633–648, doi:10.2138/am-2000-5-601, 2000.

Cenki-Tok, B., Darling, J. R., Rolland, Y., Dhuime, B. and Storey, C. D.: Direct dating of mid-crustal shear zones with synkinematic allanite: New in situ U-Th-Pb geochronological approaches applied to the Mont Blanc massif, Terra Nov., 26(1), 29–37, doi:10.1111/ter.12066, 2014.

Challandes, N., Marquer, D. and Villa, I. M.: P-T-t modelling, fluid circulation, and 39Ar-40Ar and Rb-Sr mica ages in the Aar Massif shear zones (Swiss Alps), Swiss J. Geosci., 101(2), 269–288, doi:10.1007/s00015-008-1260-6, 2008.

Chew, D. M., Petrus, J. A. and Kamber, B. S.: U-Pb LA-ICPMS dating using accessory mineral standards with variable common Pb, Chem. Geol., 363, 185–199, doi:10.1016/j.chemgeo.2013.11.006, 2014.

Cumming, G.L., Richards, J.R.: Ore lead isotope ratios in a continuously changing Earth, Earth Planet. Sci. Lett. 150, 277-290, 1975.

Dahl, P.S.: A crystal-chemical basis for Pb retention and fission-track annealing systematics in U-bearing mineral, with implications for geochronology, Earth Planet. Sci. Lett. 150, 277–290, 1997.

Darling, J. R., Storey, C. D. and Engi, M.: Allanite U-Th-Pb geochronology by laser ablation ICPMS, Chem. Geol., 292–293(April 2016), 103–115, doi:10.1016/j.chemgeo.2011.11.012, 2012.

El Korh, A.: Ablation behaviour of allanites during U-Th-Pb dating using a quadrupole ICP-MS coupled to a 193nm excimer laser, Chem. Geol., 371, 46–59, doi:10.1016/j.chemgeo.2014.01.021, 2014.

Elburg, M.A., Bons, P.D., Foden, J., Passchier, C.W.: The origin of fibrous veins: constraints from geochemistry, in: Deformation Mechanisms, Rheology and Tectonics: Current Status and Future Perspectives, Geological Society of London, special publication, Vol. 200, pp. 103-118, 2002.

Enami, M., Liou, J. G. and Mattinson, C. G.: Epidote minerals in high P/T metamorphic terranes: Subduction zone and high- to ultrahigh-pressure metamorphism, Rev. Mineral. Geochemistry, 56, 347–398, doi:10.2138/gsrmg.56.1.347, 2004.

Epin, M. E., Manatschal, G. and Amann, M.: Defining diagnostic criteria to describe the role of rift inheritance in collisional orogens: the case of the Err-Platta nappes (Switzerland), Swiss J. Geosci., 110(2), 419–438, doi:10.1007/s00015-017-0271-6, 2017.

Etheridge, M. A., Wall, V. J. and Vernon, R. H.: The role of the fluid phase during regional metamorphism and deformation, J. Metamorph. Geol., 1(3), 205–226, doi:10.1111/j.1525-1314.1983.tb00272.x, 1983.

Franz, G. and Liebscher, A.: Physical and Chemical Properties of the Epidote Minerals-An Introduction-, Rev. Mineral. Geochemistry, 56(1), 1–81, doi:10.2138/gsrmg.56.1.1, 2004.

Frei, D., Liebscher, A., Franz, G. and Dulski, P.: Trace element geochemistry of epidote minerals, Rev. Mineral. Geochemistry, 56(January), 553–605, doi:10.2138/gsrmg.56.1.553, 2004.

Froitzheim, N. and Eberli, G. P.: Extensional detachment faulting in the evolution of a Tethys passive continental margin, Eastern Alps, Switzerland, Geol. Soc. Am. Bull., 102(9), 1297–1308, doi:10.1130/0016-7606(1990)102<1297:EDFITE>2.3.CO;2, 1990.

Froitzheim, N., Schmid, S.M. and Conti, P.: Repeated change from crustal shortening to orogen-parallel extension in the Austroalpine units of Graubünden, Eclogae Geologicae Helvetiae, 87(2), 559-612, 1994.

Froitzheim, N. and Manatschal, G.: Kinematics of Jurassic rifting, mantle exhumation, and passive-margin formation in the Austroalpine and Penninic nappes (eastern Switzerland), Bull. Geol. Soc. Am., 108(9), 1120–1133, doi:10.1130/0016-7606(1996)108<1120:KOJRME>2.3.CO;2, 1996.

Gieré, R. and Sorensen, S. S.: Allanite and other: REE-rich epidote-group minerals, Rev. Mineral. Geochemistry, 56(January 2004), 431–493, doi:10.2138/gsrmg.56.1.431, 2004.

Goncalves, P., Oliot, E., Marquer, D. and Connolly, J. A. D.: Role of chemical processes on shear zone formation: An example from the Grimsel metagranodiorite (Aar massif, Central Alps), J. Metamorph. Geol., 30(7), 703–722, doi:10.1111/j.1525-1314.2012.00991.x, 2012.

Grapes, R. H. and Hoskin, P. W. O.: Epidote group minerals in low-medium pressure metamorphic terranes, Rev. Mineral. Geochemistry, 56(1993), 301–345, doi:10.2138/gsrmg.56.1.301, 2004.

Gregory, C. J., Rubatto, D., Allen, C. M., Williams, I. S., Hermann, J. and Ireland, T.: Allanite micro-geochronology: A LA-ICP-MS and SHRIMP U-Th-Pb study, Chem. Geol., 245(3–4), 162–182, doi:10.1016/j.chemgeo.2007.07.029, 2007.

Gregory, C. J., Rubatto, D., Hermann, J., Berger, A. and Engi, M.: Allanite behaviour during incipient melting in the southern Central Alps, Geochim. Cosmochim. Acta, 84, 433–458, doi:10.1016/j.gca.2012.01.020, 2012.

Guillong, M., Meier, D. L., Allan, M. M., Heinrich, C. A. and Yardley, B. W. D.: SILLS: A Matlab-Based Program for the Reduction of Laser Ablation ICP–MS Data of Homogeneous Materials and Inclusions, Mineral. Assoc. Canada Short Course, 40(June 2015), 328–333, 2008.

Guo, S., Ye, K., Yang, Y., Chen, Y., Zhang, L., Liu, J., Mao, Q. and Ma, Y.: In situ Sr isotopic analyses of epidote: Tracing the sources of multi-stage fluids in ultrahigh-pressure eclogite (Ganghe, Dabie terrane), Contrib. to Mineral. Petrol., 167(2), 1–23, doi:10.1007/s00410-014-0975-9, 2014.

Halter, W. E., Pettke, T., Heinrich, C. A. and Rothen-Rutishauser, B.: Major to trace element analysis of melt inclusions by laser-ablation ICP-MS: Methods of quantification, Chem. Geol., 183(1–4), 63–86, doi:10.1016/S0009-2541(01)00372-2, 2002.

Handy, M.R., Herwegh, M., Kamber, B.S., Tietz, R. and Villa, I.M.: Geochronologic, petrologic and kinematic constraints on the evolution of the Err-Platta boundary, part of a fossil continent-ocean suture in the Alps (eastern Switzerland), Schweizerische Mineral. und Petrogr. Mitteilungen, 76, 453-474, 1996.

Herwegh, M., Berger, A., Baumberger, R., Wehrens, P. and Kissling, E.: Large-Scale Crustal-Block-Extrusion During Late Alpine Collision, Sci. Rep., 7(1), 1–10, doi:10.1038/s41598-017-00440-0, 2017.

Herwegh, M., Berger, A., Glotzbach, C., Wangenheim, C., Mock, S., Wehrens, P., Baumberger, R., Egli, D. and Kissling, E.: Late stages of continent-continent collision: Timing, kinematic evolution, and exhumation of the Northern rim (Aar Massif) of the Alps, Earth-Science Rev., 200(November 2019), 102959, doi:10.1016/j.earscirev.2019.102959, 2020.

Hofmann, B. A., Helfer, M., Diamond, L. W., Villa, I. M., Frei, R. and Eikenberg, J.: Topography-driven hydrothermal breccia mineralization of Pliocene age at Grimsel Pass, Aar massif, Central Swiss Alps, Schweizerische Mineral. und Petrogr. Mitteilungen, 84(3), 271–302, 2004.

Horn, I., Rudnick, R. L. and McDonough, W. F.: Precise elemental and isotope ratio determination by simultaneous solution nebulization and laser ablation-ICP-MS: Application to U-Pb geochronology, Chem. Geol., 164(3–4), 281–301, doi:10.1016/S0009-2541(99)00168-0, 2000.

Horstwood, M. S. A., Košler, J., Gehrels, G., Jackson, S. E., McLean, N. M., Paton, C., Pearson, N. J., Sircombe, K., Sylvester, P., Vermeesch, P., Bowring, J. F., Condon, D. J. and Schoene, B.: Community-Derived Standards for LA-ICP-MS U-(Th-)Pb Geochronology – Uncertainty Propagation, Age Interpretation and Data Reporting, Geostand. Geoanalytical Res., 40(3), 311–332, doi:10.1111/j.1751-908X.2016.00379.x, 2016.

Horwitz, E. P., Dietz, M. L., & Chiarizia, R.: The application of novel extraction chromatographic materials to the characterization of radioactive waste solutions, Journal of Radioanalytical and Nuclear Chemistry 161, 575–583, 1992.

Incerpi, N., Martire, L., Manatschal, G. and Bernasconi, S. M.: Evidence of hydrothermal fluid flow in a hyperextended rifted margin: the case study of the Err nappe (SE Switzerland), Swiss J. Geosci., 110(2), 439–456, doi:10.1007/s00015-016-0235-2, 2017.

Johannes, W.: Beginning of melting in the granite system Qz-Or-Ab-An-H2O, Contrib. to Mineral. Petrol., 86(3), 264–273, doi:10.1007/BF00373672, 1984.

Košler, J.: Laser ablation ICP-MS - A new dating tool in Earth science, Proc. Geol. Assoc., 118(1), 19–24, doi:10.1016/S0016-7878(07)80043-5, 2007.

Li, X. H., Li, Z. X., Li, W. X., Liu, Y., Yuan, C., Wei, G. and Qi, C.: U-Pb zircon, geochemical and Sr-Nd-Hf isotopic constraints on age and origin of Jurassic I- and A-type granites from central Guangdong, SE China: A major igneous event in response to foundering of a subducted flat-slab?, Lithos, 96(1–2), 186–204, doi:10.1016/j.lithos.2006.09.018, 2007.

Ludwig, K. R.: On the treatment of concordant uranium-lead ages, Geochim. Cosmochim. Acta, 62(4), 665–676, doi:10.1016/S0016-7037(98)00059-3, 1998.

Ludwig, K. R.: User's Manual for A Geochronological Toolkit for Microsoft Excel Berkeley Geochronology Center, Options, (5), 2012.

Malaspina, N., Scambelluri, M., Pennacchioni, G. and Spagnolo, C.: Fluid-induced plastic deformation in the crustal Austroalpine system (Western Italian Alps): A petrologic and fluid inclusion analysis, Ital. J. Geosci., 130(1), 61–74, doi:10.3301/IJG.2010.24, 2011.

Manatschal, G. and Nievergelt, P.: A continent-ocean transition recorded in the Err and Platta nappes (Eastern Switzerland), Eclogae Geol. Helv., 90(1), 3–27, 1997.

Manatschal, G., Marquer, D. and Früh-Green, G. L.: Channelized fluid flow and mass transfer along a rift-related detachment fault (Eastern Alps, Southeast Switzerland), Bull. Geol. Soc. Am., 112(1), 21–33, doi:10.1130/0016-7606(2000)112<21:CFFAMT>2.0.CO;2, 2000.

Mcfarlane, C. R. M.: Allanite U–Pb geochronology by 193 nm LA ICP-MS using NIST610 glass for external calibration, Chem. Geol., 438, 91–102, doi:10.1016/j.chemgeo.2016.05.026, 2016.

Mohn, G., Manatschal, G., Masini, E. and Müntener, O.: Rift-related inheritance in orogens: A case study from the Austroalpine nappes in Central Alps (SE-Switzerland and N-Italy), Int. J. Earth Sci., 100(5), 937–961, doi:10.1007/s00531-010-0630-2, 2011.

Nägler, T. F. and Kamber, B. S.: A new silicate dissolution procedure for isotope studies on garnet and other rock forming minerals, Schweizerische Mineral. und Petrogr. Mitteilungen, 76(1), 75–80, doi:10.5169/seals-57688, 1996.

Oberli, F., Meier, M., Berger, A., Rosenberg, C. L. and Gieré, R.: U-Th-Pb and 230Th/238U disequilibrium isotope systematics: Precise accessory mineral chronology and melt evolution tracing in the Alpine Bergell intrusion, Geochim. Cosmochim. Acta, 68(11), 2543–2560, doi:10.1016/j.gca.2003.10.017, 2004.

Odlum, M. L. and Stockli, D. F.: Thermotectonic Evolution of the North Pyrenean Agly Massif During Early Cretaceous Hyperextension Using Multi-mineral U-Pb Thermochronometry, Tectonics, 38(5), 1509–1531, doi:10.1029/2018TC005298, 2019.

Odlum, M. L. and Stockli, D. F.: Geochronologic constraints on deformation and metasomatism along an exhumed mylonitic shear zone using apatite U-Pb, geochemistry, and microtextural analysis, Earth Planet. Sci. Lett., 538, 116177, doi:10.1016/j.epsl.2020.116177, 2020.

Parrish, R. R., Parrish, C. M. and Lasalle, S.: Vein calcite dating reveals Pyrenean orogen as cause of Paleogene deformation in southern England, J. Geol. Soc. London., 175(3), 425–442, doi:10.1144/jgs2017-107, 2018.

Pennacchioni, G. and Cesare, B.: Ductile-brittle transition in pre-Alpine amphibolite facies mylonites during evolution from water-present to water-deficient conditions (Mont Mary nappe, Italian Western Alps), J. Metamorph. Geol., 15(6), 777–791, doi:10.1111/j.1525-1314.1997.00055.x, 1997.

Pettke, T., Diamond, L. W. and Kramers, J. D.: Mesothermal gold lodes in the north-western Alps: A review of genetic constraints from radiogenic isotopes, Eur. J. Mineral., 12(1), 213–230, doi:10.1127/ejm/12/1/0213, 2000.

Pettke, T., Oberli, F., Audétat, A., Guillong, M., Simon, A. C., Hanley, J. J. and Klemm, L. M.: Recent developments in element concentration and isotope ratio analysis of individual fluid inclusions by laser ablation single and multiple collector ICP-MS, Ore Geol. Rev., 44, 10–38, doi:10.1016/j.oregeorev.2011.11.001, 2012.

Picazo, S. M., Ewing, T. A. and Müntener, O.: Paleocene metamorphism along the Pennine–Austroalpine suture constrained by U–Pb dating of titanite and rutile (Malenco, Alps), Swiss J. Geosci., 112(2–3), 517–542, doi:10.1007/s00015-019-00346-1, 2019.

Romer, R. L. and Siegesmund, S.: Why allanite may swindle about its true age, Contrib. to Mineral. Petrol., 146(3), 297–307, doi:10.1007/s00410-003-0494-6, 2003.

Quistini, S., Oddone, M., and Villa. I.M.: Sustainability of aquifers in Mali: Sr and Pb isotopic signatures and tritium ages, Abstract, SGI Congress, Pisa, 22-9, p. 25, 2017.

Rehkämper, M. and Mezger, K.: Investigation of matrix effects for Pb isotope ratio measurements by multiple collector ICP-MS: Verification and application of optimized analytical protocols, J. Anal. At. Spectrom., 15(11), 1451–1460, doi:10.1039/b005262k, 2000.

Ricchi, E., Bergemann, C. A., Gnos, E., Berger, A., Rubatto, D. and Whitehouse, M. J.: Constraining deformation phases in the Aar Massif and the Gotthard Nappe (Switzerland) using Th-Pb crystallization ages of fissure monazite-(Ce), Lithos, 342–343, 223–238, doi:10.1016/j.lithos.2019.04.014, 2019.

Ricchi, E., Bergemann, C., Gnos, E., Berger, A., Rubatto, D., Whitehouse, M. and Walter, F.: Cenozoic deformation in the Tauern Window (Eastern Alps, Austria) constrained by in-situ Th-Pb dating of fissure monazite, Solid Earth Discuss., 11, 437-467. https://doi.org/10.5194/se-11-437-2020, 2020.

Rolland, Y., Cox, S. F. and Corsini, M.: Constraining deformation stages in brittle-ductile shear zones from combined field mapping and 40Ar/39Ar dating: The structural evolution of the Grimsel Pass area (Aar Massif, Swiss Alps), J. Struct. Geol., 31(11), 1377–1394, doi:10.1016/j.jsg.2009.08.003, 2009.

Romer, R. L.: Lead incorporation during crystal growth and the misinterpretation of geochronological data from low-238U/204Pb metamorphic minerals, Terra Nov., 13(4), 258–263, doi:10.1046/j.1365-3121.2001.00348.x, 2001.

Romer, R. L. and Xiao, Y.: Initial Pb-Sr(-Nd) isotopic heterogeneity in a single allanite-epidote crystal: Implications of reaction history for the dating of minerals with low parent-to-daughter ratios, Contrib. to Mineral. Petrol., 148(6), 662–674, doi:10.1007/s00410-004-0630-y, 2005.

Savastano, V. L. M., Schmitt, R. da S., Araújo, M. N. C. de and Inocêncio, L. C.: Rift brittle deformation of SE-Brazilian continental margin: Kinematic analysis of onshore structures relative to the transfer and accommodation zones of southern Campos Basin, J. Struct. Geol., 94, 136–153, doi:10.1016/j.jsg.2016.11.012, 2017.

Schaltegger, U. and Corfu, F.: The age and source of late Hercynian magmatism in the central Alps: evidence from precise U-Pb ages and initial Hf isotopes, Contrib. to Mineral. Petrol., 111(3), 329–344, doi:10.1007/BF00311195, 1992.

Schmidt, M. W. and Poli, S.: Magmatic epidote, Rev. Mineral. Geochemistry, 56(January 2004), 399–430, doi:10.2138/gsrmg.56.1.399, 2004.

Schneeberger, R., Kober, F., Lanyon, G. W., Mäder, U. K., Spillmann, T. and Blechschmidt, I.: Grimsel Test Site: Revisiting the site-specific geoscientific knowledge, [online] Available from: www.nagra.ch, 2019.

Sláma, J., Košler, J., Condon, D. J., Crowley, J. L., Gerdes, A., Hanchar, J. M., Horstwood, M. S. A., Morris, G. A., Nasdala, L., Norberg, N., Schaltegger, U., Schoene, B., Tubrett, M. N. and Whitehouse, M. J.: Plešovice zircon - A new natural reference material for U-Pb and Hf isotopic microanalysis, Chem. Geol., 249(1–2), 1–35, doi:10.1016/j.chemgeo.2007.11.005, 2008.

Smye, A. J., Roberts, N. M. W., Condon, D. J., Horstwood, M. S. A. and Parrish, R. R.: Characterising the U-Th-Pb systematics of allanite by ID and LA-ICPMS: Implications for geochronology, Geochim. Cosmochim. Acta, 135, 1–28, doi:10.1016/j.gca.2014.03.021, 2014.

Spiegel, C., Siebel, W., Frisch, W. and Berner, Z.: Nd and Sr isotopic ratios and trace element geochemistry of epidote from the Swiss Molasse Basin as provenance indicators: Implications for the reconstruction of the exhumation history of the Central Alps, Chem. Geol., 189(3–4), 231–250, doi:10.1016/S0009-2541(02)00132-8, 2002.

Stacey, J. S. and Kramers, J. D.: Approximation of terrestrial lead isotope evolution by a two-stage model, Earth Planet. Sci. Lett., 26(2), 207–221, doi:10.1016/0012-821X(75)90088-6, 1975.

Sylvester, P. J.: Laser Ablation ICP-MS Developments and Trends for 2003, Geostand. Geoanalytical Res., 29(1), 41–52, doi:10.1111/j.1751-908x.2005.tb00654.x, 2005.

Storey, C. D., Jeffries, T. E. and Smith, M.: Common lead-corrected laser ablation ICP – MS U – Pb systematics and geochronology of titanite, , 227, 37–52, 2006.

Sylvester, P.: Matrix effects in laser ablation-ICP-MS, in: Laser ablation ICP-MS in the earth sciences: Current practices and outstanding issues, Mineralogical Association of Canada, Vol. 40, 67-78, 2008.

Tannock, L., Herwegh, M., Berger, A., Liu, J., Lanari, P. and Regenauer-Lieb, K.: Microstructural analyses of a giant quartz reef in south China reveal episodic brittle-ductile fluid transfer, J. Struct. Geol., 130(October 2019), 103911, doi:10.1016/j.jsg.2019.103911, 2020a.

Tannock, L., Herwegh, M., Berger, A., Liu, J. and Regenauer-lieb, K.: The Effects of a Tectonic Stress Regime Change on Crustal-Scale Fluid Flow at the Heyuan Geothermal Fault, South China., Tectonophys., 781(July 2019), 228399, doi:10.1016/j.tecto.2020.228399, 2020b.

Tera, F. and Wasserburg, G. J.: U-Th-Pb systematics in three Apollo 14 basalts and the problem of initial Pb in lunar rocks, Earth Planet. Sci. Lett., 14(3), 281–304, doi:https://doi.org/10.1016/0012-821X(72)90128-8, 1972.

Villa, I. M.: Lead isotopic measurements in archeological objects, Archaeol. Anthropol. Sci., 1(3), 149–153, doi:10.1007/s12520-009-0012-5, 2009.

Wehrens, P., Berger, A., Peters, M., Spillmann, T. and Herwegh, M.: Deformation at the frictional-viscous transition: Evidence for cycles of fluid-assisted embrittlement and ductile deformation in the granitoid crust, Tectonophysics, 693, 66–84, doi:10.1016/j.tecto.2016.10.022, 2016.

Wehrens, P., Baumberger, R., Berger, A. and Herwegh, M.: How is strain localized in a meta-granitoid, mid-crustal basement section? Spatial distribution of deformation in the central Aar massif (Switzerland), J. Struct. Geol., 94, 47–67, doi:10.1016/j.jsg.2016.11.004, 2017.

Weis, D., Kieffer, B., Maerschalk, C., Barling, J., De Jong, J., Williams, G. A., Hanano, D., Pretorius, W., Mattielli, N., Scoates, J. S., Goolaerts, A., Friedman, R. M. and Mahoney, J. B.: High-precision isotopic characterization of USGS reference materials by TIMS and MC-ICP-MS, Geochemistry, Geophys. Geosystems, 7(8), doi:10.1029/2006GC001283, 2006.

Williams, I.S.: U-Th-Pb geochronology by ion microprobe, in: Application of microanalytical techniques to understanding mineralizing processes, edited by: McKibben, M.A., Shanks III, W.C., and Ridley, W.I., Reviews in Economic Geology, 7(1), 1-35, 1998.

Wyllie, P. J.: Crustal anatexis: An experimental review, Tectonophysics, 43(1–2), 41–71, doi:10.1016/0040-1951(77)90005-1, 1977.

Zanoni, D., Rebay, G. and Spalla, M. I.: Ocean floor and subduction record in the Zermatt-Saas rodingites, Valtournanche, Western Alps, J. Metamorph. Geol., 34(9), 941–961, doi:10.1111/jmg.12215, 2016.

3.

Epidote U–Pb geochronology and Pb–Sr–O–H isotope geochemistry reveal Eo-Alpine fluid circulation in the Err nappe (Eastern Swiss Alps)

Veronica Peverelli[1], Alfons Berger[1], Martin Wille[1], Andreas Mulch[2,3], Benita Putlitz[4], Pierre Lanari[1], Thomas Pettke[1] & Marco Herwegh[1]

[1]Institute of Geological Sciences, University of Bern, Switzerland

[2]Senckenberg Biodiversity and Climate Research Centre (SBiK-F), 60325 Frankfurt, Germany

[3]Institute of Geosciences, Goethe University Frankfurt, 60438 Frankfurt, Germany

[4]Institute of Earth Sciences, University of Lausanne, Switzerland

"The very nature of science is discoveries, and the best of those discoveries are the ones you don't expect."

Neil deGrasse Tyson, 1958–Present

ABSTRACT The rate and mechanisms of metamorphism and deformation in the granitic crust at greenschist-facies conditions strongly depend on the availability of fluids in granitoids. Since these rocks have low primary water contents, the addition of fluids exerts important control on such processes. It is therefore of great interest to determine the timing of hydration reactions relative to deformation and metamorphic processes. Different geochronometers and fluid tracers record fluid circulation at different times, thus providing a comprehensive picture of hydration of the continental crust before, during and even after orogeny.

In this study, we date and trace hydration events in the continental crust of the Err nappe in the Albula Pass area (eastern Swiss Alps) by using U–Pb geochronology and Pb–Sr–O–H isotope geochemistry of epidote in hydrothermal veins. This area is part of the Adriatic hyper-extended passive continental margin (Err nappe), which was extensively affected by seawater infiltration during continental rifting in Jurassic times. Our results show that fluid circulation in the Err nappe continued after tectonic inversion in the Late Cretaceous until at least the Paleocene. Epidote Pb–Sr isotope geochemistry constrains the pathways of the epidote forming fluids. Isotopic equilibration of the fluids mainly occurred with the host granitoids and to a more limited extent with carbonatic rocks, which are locally overthrusted by the granitic rock. Hydrogen isotope data are in agreement with fluids that had a modified seawater or formation/connate water origin, and whose oxygen isotope composition was variably modified by fluid–rock interaction processes during percolation in the crust. The data returned by epidote as a geochronometer and isotope tracer complement the history of fluid circulation in the inverted Adriatic passive continental margin. Epidote is thus proven to record information on hydration events in rifted continental margins and to retain it across orogenic processes. This work supports the combination of different geochronometers and fluid tracers to comprehensively describe the hydration history of the continental crust in orogens.

3.1 Introduction

Fluid circulation in, and fluid-driven alteration of, granitoids are fundamental processes. These rocks dominate the continental crust and they are mechanically strong in their pristine state. However, their hydrothermal alteration induces prominent weakening, thus having important implications for the structural evolution of the continental crust during orogeny, particularly for strain localization (e.g., Ferry, 1979; Morad et a., 2010; Oliot et al., 2010; Bellahsen et al., 2019; Airaghi et al., 2020; Manatschal et al., 2015). A question arises as to how and when water is introduced into these rocks so as to allow the stabilization of hydrous minerals during metamorphism and deformation (e.g., Goncalves et al., 2012; Wehrens et al., 2016; 2017; Bellahsen et al., 2019; Airaghi et al., 2020; Grambling et al., 2021). In this respect, a compilation of time spans separating hydration and structural imprint of the continental crust in orogens globally, as well as of the types of water mediating hydrothermal alteration, is highly sought for. By comparing such data, we may better comprehend the role that fluids play in determining the structural evolution of the granitic crust. Moreover, we may gain better understanding of the fluid budget and cycle in the continental crust, which have substantial implications for economic mineralization as well.

To reconstruct fluid circulation in crustal rocks, numerous studies make use of trace element, isotopic and geochronological data (e.g., Dempster, 1986; Kralik et al., 1992; Marquer and Burkhard, 1992; Marquer and Peucat, 1994; Manatschal et al., 2000; Hofmann et al., 2004; Mulch et al., 2006; Pinto et al., 2015; Incerpi et al., 2017; 2018; 2019; Ricchi et al., 2019; 2020; Grambling et al., 2021; Peverelli et al., 2022; Chapter 4 of this thesis). One advantage of targeting vein-filling minerals for this purpose is that they precipitate directly from the mineralizing fluid, whose geochemical and isotopic characteristics are thus recorded and can be used to investigate fluid pathways (e.g., Pettke et al., 2000; Bons et al., 2002; Elburg et al., 2002). In the Alps, one common vein-filling mineral that is stable throughout the metamorphic evolution of the orogen at greenschist-facies conditions is epidote [i.e., $Ca_2Al_2(Al,Fe^{3+})Si_3O_{12}(OH)$]. This mineral is also related to seawater-driven alteration of the crust during rifting of passive continental margins (e.g., Iberian Margin; Gardien and Paquette, 2004). The wide range of pressures, temperatures and geodynamic settings across which epidote can form (Bird and Spieler, 2004; Enami et al., 2004; Franz and Liebscher, 2004; Grapes and Hoskin, 2004; Schmidt and Poli, 2004) make this mineral particularly appealing to study fluid circulation in inverted passive continental margins in orogens.

The high preservation potential of epidote in hydrothermal veins to retain its crystallization age across deformation events was recently proven by the occurrence of variably deformed Permian epidote veins in the central Swiss Alps (Peverelli et al., 2022; Chapter 4 of this thesis). In addition to dating fluid circulation events, this mineral has a complex crystal structure, such that the chemical composition of fluid(s) can be mirrored by hydrothermal epidote geochemistry (see Frei et al., 2004; Feineman et al., 2007; Anenburg et al., 2015). Strontium and Pb can substitute for Ca in the epidote crystal structure. These elements are readily incorporated by epidote from the epidote-forming fluids. Their isotopes can therefore be used in combination with those of O and H in the epidote hydroxyl group to trace the geochemical characteristics of the epidote-forming fluids. This contribution presents *in-situ* U–Pb geochronology and Pb–Sr–O–H isotopic compositions of epidote in hydrothermal veins from the Albula area (Err nappe, Eastern Swiss Alps) with the scope of reconstructing timing and paths of fluid circulation in the area. The Err nappe represents a classical example of hyperextended continental crust (Mohn et al., 2011; 2012; Manatschal et al., 2015). It is therefore a great target area to explore if and to what extent the continental crust was infiltrated by water during Jurassic rifting and (Eo-)Alpine inversion.

3.2 Geological context

The sampling location is in the Albula Pass area, which is located on the boundary between the Err and Ela nappes (Figs. 3.1 and 3.2). Here, frequent epidote ± quartz veins are hosted by the

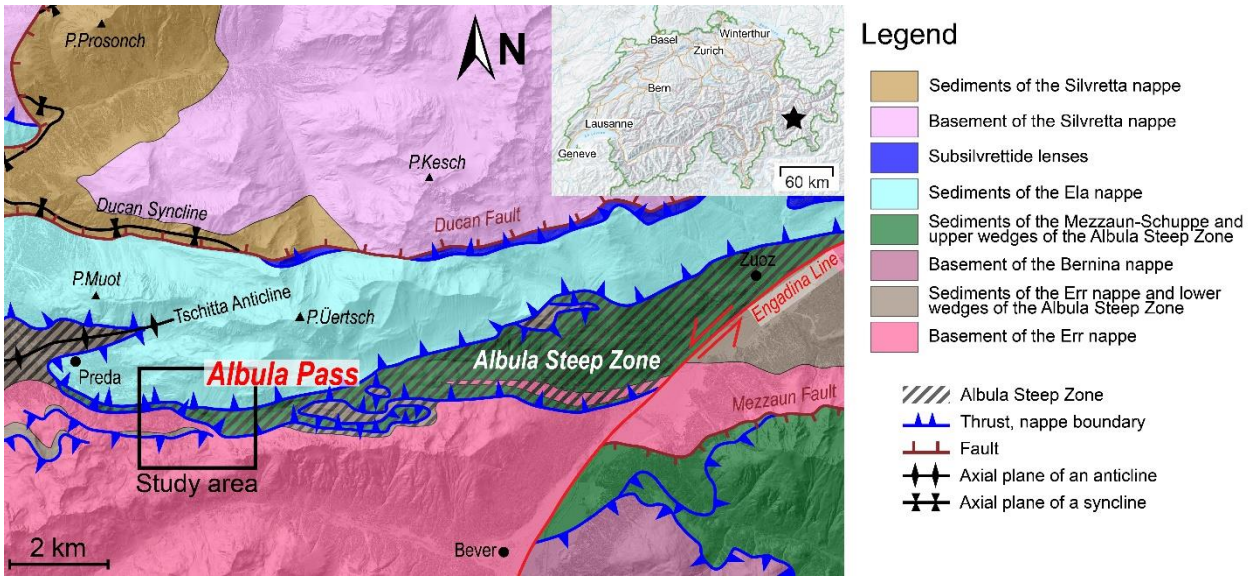

Fig. 3.1 *Geological map of the Albula Pass area including the sampling location shown in Fig. 3.2 (black rectangle). Redrawn from Furrer et al. (2015); the digital elevation model is from map.geo.admin.ch.*

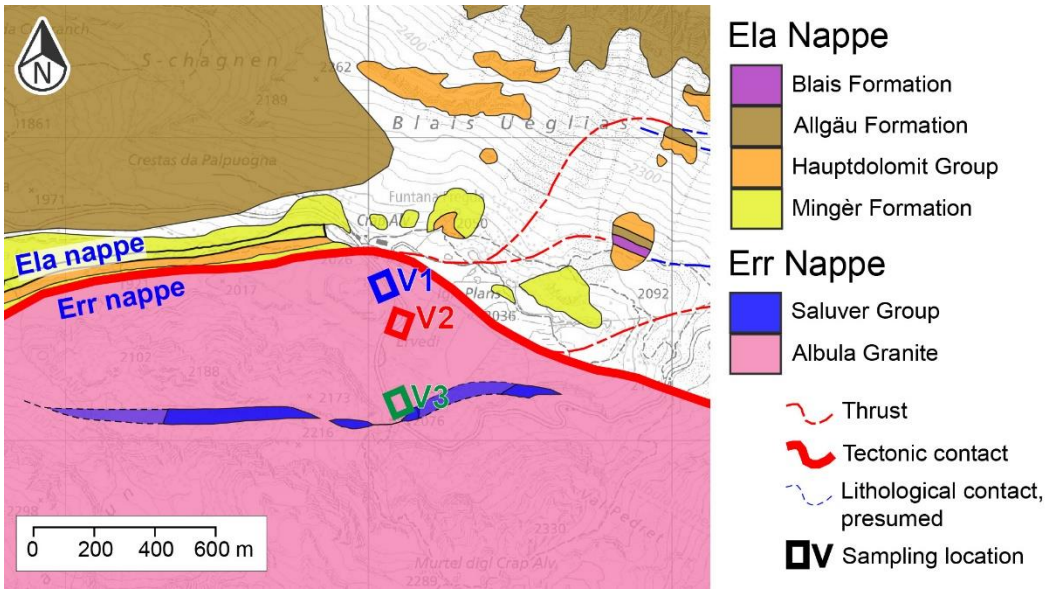

Fig. 3.2 *Geological map of the sampling location in the Albula Pass area. Redrawn from map.geo.admin.ch.*

Albula Granite, a calcalcaline granodiorite that represents the most common lithology in the Albula Pass area (e.g., Manatschal & Nievergelt, 1997; Furrer et al., 2015; Şengör, 2016). The Albula Granite intruded the metamorphic basement of the Err nappe in the late Carboniferous–early Permian at a depth of < 3 km (Mohn et al., 2011). Besides Late- to Post-Variscan granitoids, the Err nappe includes pre- and syn-rift Early to Middle Jurassic siliciclastic sediments such as the Saluver Formation (Froitzheim et al., 1994; Mohn et al., 2011). The Ela nappe, on the other hand, is dominated by thick pre-rift (e.g., Triassic Mingér Formation and Hauptdolomit Group) and syn-rift (e.g., Allgäu Formation) sediments (Mohn et al., 2011), which are underlain by the Err nappe (Froitzheim et al., 1994). Mohn et al. (2011) relate this difference in sedimentary record to the position of these nappes during rifting, with the Err and Ela nappes representing, respectively, the distal and proximal margins. The rift evolution produced a hyper-extended continental margin and an "ocean-continent transition", as recorded west of the study area (Froitzheim and Manatschal, 1996; Manatschal and Nievergelt, 1997; Mohn et al., 2011). This Lower Jurassic rifting stage is recorded by large-scale normal faults dissecting the basement, and by syn-rift breccias such as the Saluver breccia (Froitzheim et al., 1994; Manatschal and Nievergelt, 1997; Mohn et al., 2011). This hyperextended passive margin was hydrothermally altered during Jurassic rifting when seawater percolated into the crustal units exploiting rift-related structures (e.g., Manatschal et al., 2000; 2015; Pinto et al., 2015; Incerpi et al., 2017; 2018; 2019).

The Alpine history of the inverted Adriatic passive continental margin is recorded in the study area by three main deformational phases (hereafter named D1–3 after Handy et al., 1996; Table 3.1). Throughout its Alpine evolution, the area experienced lower greenschist-facies conditions, with the D1–2 phases in the stability field of epidote at 300–350 °C and 250–300 °C, respectively, and D3 deformation occurring at 150–250 °C (Handy et al., 1996). Pressures were estimated on the basis of phengite geobarometry (i.e., Si in mica) at 800–900 MPa for D1 and at 400–500 MPa for D2 at the base of the Err nappe (Handy et al., 1996). The D1 phase (or Trupchun phase of Froitzheim et al., 1994) is related to the inversion of the passive continental margin with W- to NW-directed nappe stacking (Froitzheim et al., 1994; Handy et al., 1996; Mohn et al., 2011). K/Ar ages in white mica forming the S1 schistosity indicate that greenschist-facies metamorphism related to the D1 phase occurred between 80–88 Ma (Handy et al., 1996). The following D2 phase (Ducan–Ela phase of Froitzheim et al., 1994) took place between 80–67 Ma, as indicated by white mica K/Ar dating, and led to top-to-the-E normal faulting and extensional uplift (Froitzheim et al., 1994; Handy et al., 1996). This deformation phase is interpreted as resulting from extension in the hanging wall during subduction (Handy et al., 1996; Mohn et al., 2011). The D1–D2 structures accommodated deformation related to the Eo-Alpine orogeny. Finally, the D3 (Blaisun of Froitzheim et al., 1994) structures formed as a response to the N–S-directed shortening upon continental collision between Adria and Europe, which led to the N-directed thrusting of the Cretaceous nappe stack on top of the Lower and Middle Penninic in Eocene time (Handy et al., 1996; Mohn et al., 2011; and references therein). However, the subsequent Cenozoic tectono-metamorphic overprint in the Err nappe was weak and allowed the preservation of the earlier D1 and D2 structures (e.g., Mohn et al., 2011; Epin et al., 2017). The Albula Pass area includes the "Albula steep zone" (Fig. 3.1), which is a late D1 structure: Here, the Ela nappe lies tectonically below the Err nappe (Froitzheim et al., 1994). The formation of this zone and its role in accommodating D2 deformation is debated to date, and it is beyond the scope of this work to discuss or to propose alternative scenarios to that illustrated in Froitzheim et al. (1994).

In the study area, aside from the Albula Granite (described in Sect. 3.3), the Mingér Formation, the Hauptdolomit Group, the Saluver (i.e., Salamun) Breccia and the Allgäu Formation are found in the field (Figs. 3.1 and 3.2; see also Furrer et al., 2015): The Mingér Formation belongs to the Raibl Group, which is constituted by dolomitic and evaporitic rocks deposited in Ladinian to Carnian times. The Hauptdolomit Group is of Carnian to Norian age, and it is dominated by

massive to brecciated dolomite. Neither the Raibl Group nor the Hauptdolomit Group contain fossils. The Salamun Breccia contains clasts of Albula Granite, limestones and dolomite, and it was deposited in the Middle Jurassic. Finally, the Middle Jurassic Allgäu Formation does not contain fossils in the study area, and it is made of limestones and marls (Furrer et al., 2015).

TABLE 3.1

Main characteristics of the D1–D3 deformation phases that affected the study area between the Late Cretaceous and the Eocene. Unless specified, data are from Handy et al. (1996). Pressure and temperature refer to the base of the Err nappe. Ep = epidote.

	Phase	Process	Age	Temperature	Pressure	Ep stability field
D1	(Trupchun)	W-directed thrusting and folding	88–80 Ma[2]	300–350 °C	8–9 kbar	Yes
D2	(Ducan–Ela)	E–W extension	80–67 Ma[2]	250–300 °C	4–5 kbar	Yes
D3	(Blaisun)	N–S shortening	Eocene	150–250 °C	2–3 kbar	No

[1]In parentheses: nomenclature of Froitzheim et al. (1994).

[2]White mica K/Ar.

3.3 Description of the studied epidote-vein samples

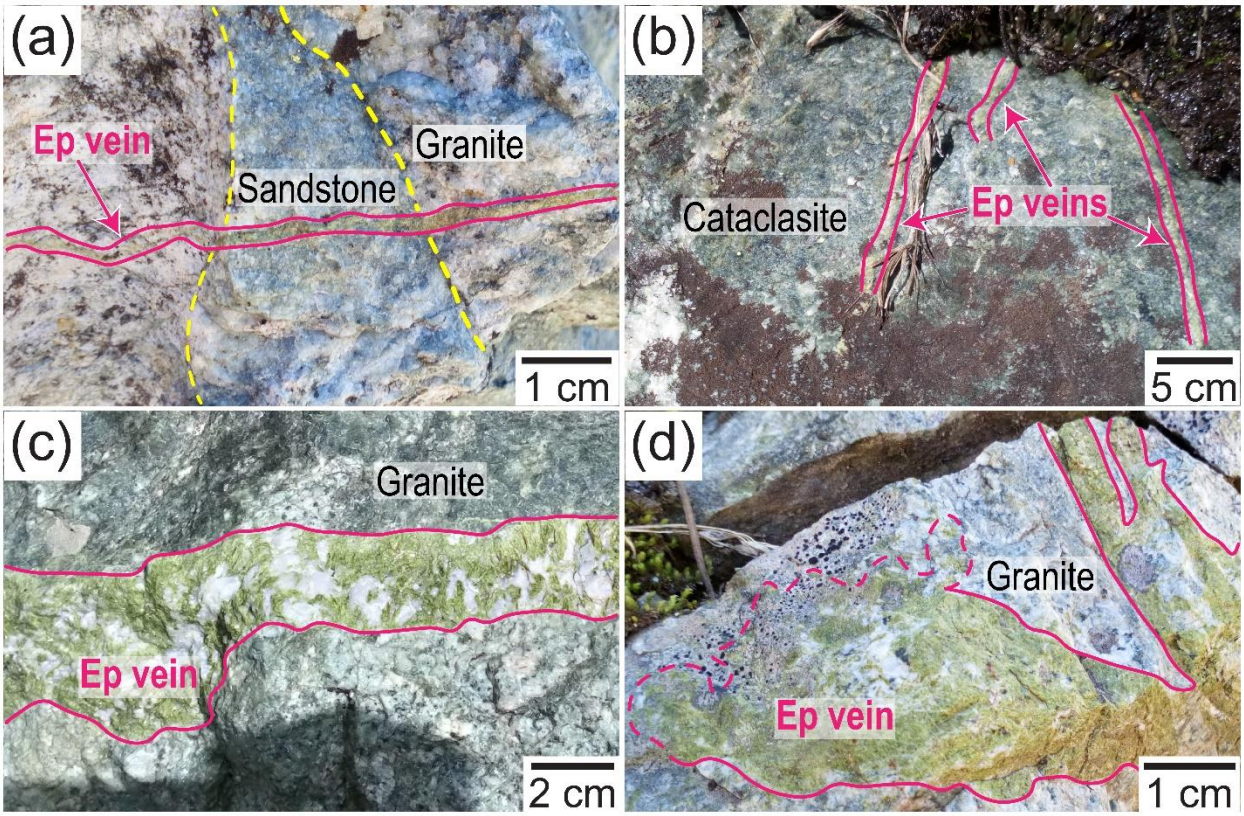

Fig. 3.3 *Field relations of the studied epidote vein samples. (a) V1 vein ALB19-1 crosscutting a sandstone pocket enclosed in the Albula Granite. (b) V2 veins ALB19-4 in cataclastic Albula Granite. V3 veins (c) Albula-1 and (d) ALB19-11 in weakly foliated and deformed Albula Granite. Cataclasite = cataclastic Albula Granite. Granite = weakly foliated and deformed Albula Granite.*

The studied epidote vein samples were collected along a ca. 400 m long profile (Fig. 3.2). The sampling location of V1 veins is the closest to the Ela–Err nappe boundary, that of V3 veins is in the vicinity of the carbonatic/dolomitic clast-bearing breccia of the Saluver Formation (i.e., Salamun Breccia), and that of V2 veins is in-between. The distinction of each epidote vein sample into V1, V2 and V3 vein groups is based on the appearance of the host rock in the field (Table 3.2): the one V1 vein collected is hosted by the Albula Granite, here coarse-grained and pale gray in color (Fig. 3.3a), and cuts through an enclosure of sandstone that is also contained by the Albula Granite (Sect. 3.3.1; Fig. 3.3a). This sandstone enclave is ca. 1–4 cm wide and is a local feature. V2 and V3 veins are hosted by the Albula Granite only, but with differing characteristics at the scale of the hand specimen: (V2 samples) fine-grained and dark green granitoid (Fig. 3.3b), and (V3 samples) coarse-grained and pale gray granitoid (Fig. 3.3c–d). Only one V1 vein was sampled. At the outcrop scale, this can reach a few mm in width, and has sharp, straight boundaries (Fig. 3.3a). V2 veins display sharp, linear

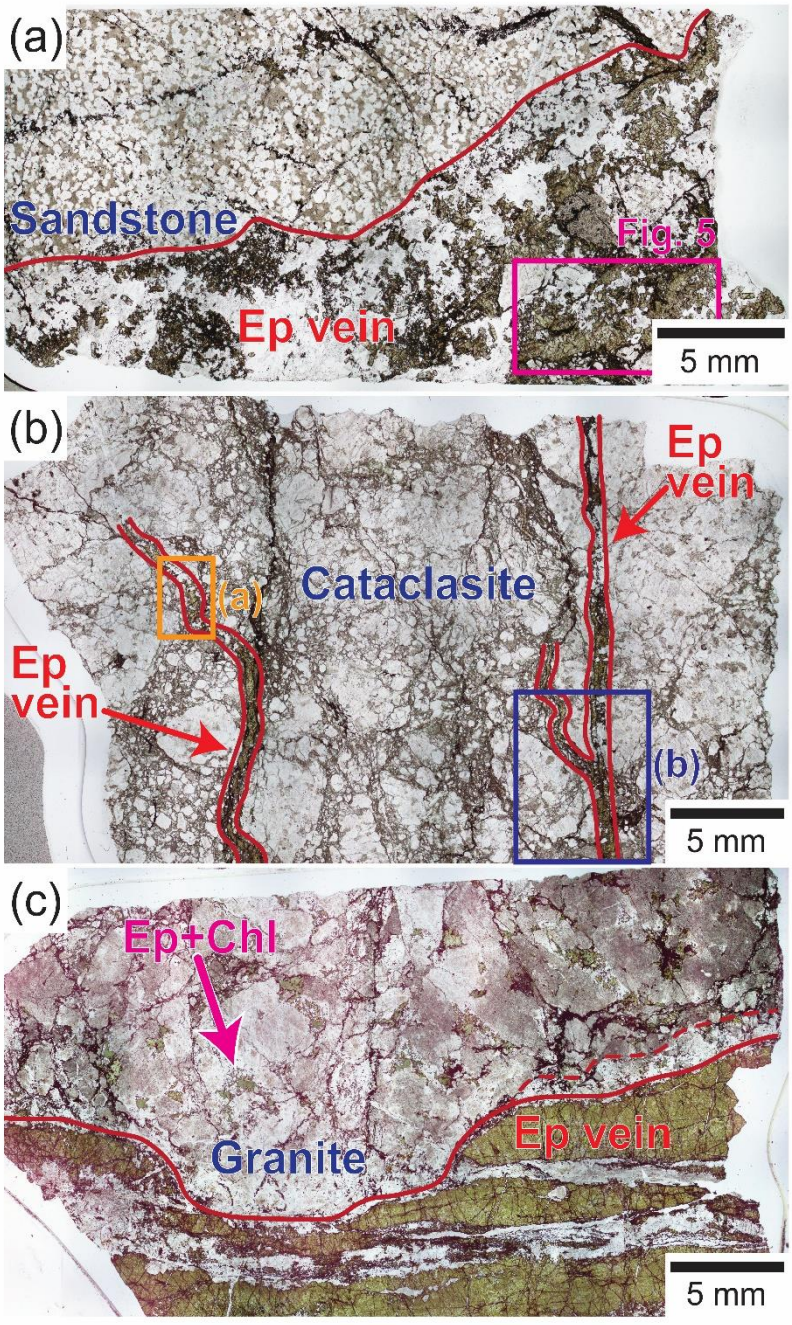

Fig. 3.4 *Transmitted light microphotographs of (a) V1 vein ALB19-1 in its host sandstone, (b) V2 veins ALB19-4 in their host cataclastic Albula Granite, and (c) V3 vein ALB19-11 in weakly deformed Albula Granite with weak foliation of chlorite + epidote ("Ep+Chl"; pink arrow). Ep = epidote. Rectangles in a–b indicate the locations of the microphotographs of Figs. 3.5–3.7. Plane-polarized light.*

boundaries and reach a maximum aperture of ca. 1 mm (Fig. 3.3b). V3 veins can reach a width of a few cm and run through the Albula Granite with different geometries: (1) sharp, straight boundaries (Fig. 3.3c) and constituted by epidote + quartz ± plagioclase, (2) locally blurred and convoluted in which only epidote can be distinguished in the hand specimen (Fig. 3.3d), or (3) a combination of both (Figs. 3.3c). To assess the equilibration paths of the epidote-forming fluids through measurements of Sr and Pb isotopes, a gneissic hand sample of the Albula Granite and carbonatic rocks of the Ela nappe (i.e., Allgäu and Mingér Formations, and Hauptdolomit Group) were collected in the surroundings of the epidote veins sampling locations. The collected samples of the Allgäu and Mingér Formations are dark gray with few calcite veins, which, on the other hand, are frequent in our light gray Hauptdolomit sample. The Albula Granite sample is collected from the sampling location of V3 epidote veins: the hand sample used for analyses (see Sect. 3.4.3) does not contain epidote veins but it is intensely altered into saussurite.

TABLE 3.2

Epidote vein samples studied here, with the subdivision into V1, V2 and V3 veins based on the appearance of their host rock.

Epidote vein sample	Vein group	Host rock
ALB19-1	V1	Albula Granite + Sandstone
ALB19-4	V2	Cataclastic Albula Granite
Albula-1		
ALB19-11	V3	Weakly foliated and deformed Albula Granite
ALB19-18		

3.3.1 V1 epidote vein group

The V1 epidote vein (sample ALB19-1; Fig. 3.4a) studied here is constituted by epidote and quartz. In thin section, the host rock is a sandstone composed of rounded quartz and altered (i.e., sericitized and saussuritic) feldspars of roughly the same dimensions (quartz:

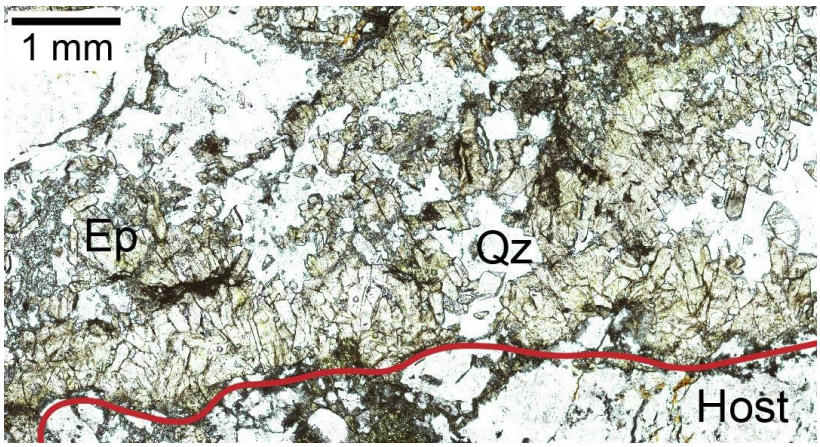

Fig. 3.5 *Transmitted light microphotograph of V1 vein ALB19-1. Ep = epidote; Qz = quartz. Red curve = vein–host boundary. Plane-polarized light.*

ca. 200–800 µm in diameter; feldspars: 200–300 µm in diameter). Vein growth microstructures are preserved, with the vein morphology ranging between blocky and elongate (Fig. 3.5; nomenclature after Bons et al., 2012). Epidote is euhedral to subhedral, with grain sizes ranging between a few to ca. 800 µm. Vein quartz is ca. 0.2–2 mm in size and has undulose extinction. In backscattered electron (BSE) images (Fig. 3.8a), epidote grains display regular chemical zoning and rare cracks.

3.3.2 V2 epidote vein group

The host of V2 epidote veins (sample ALB19-4) is the Albula Granite with a cataclastic texture (Fig. 3.4b). The host rock is composed of quartz, feldspars and white mica, mostly present in fine-grained polymineralic aggregates defining the cataclasites. Outside the cataclastic portions of the host granitoid, quartz (0.2–1.2 mm in size) is anhedral and has undulose extinction. Feldspar grains (80 µm to 3.5 mm in size) are anhedral and only slightly altered. White mica dominates the fine-grained polymineralic aggregates and it wraps feldspar relicts, although a few grains (80–800 µm in size) with undulose extinction are disseminated in the rock. The veins have similar orientation, as well as morphological and mineralogical characteristics. The morphology of V2 epidote veins varies between blocky to elongate (Fig. 3.6). These veins are made of euhedral to subhedral epidote grains of a few to ca. 500 µm in size, and quartz. Quartz is ca. 100–200 µm in size and has slight undulose extinction. Epidote-quartz grain boundaries are sharp (Figs. 3.3b, 3.4b and 3.6). Cataclastic portions are crosscut by V2 veins (Fig. 3.6b, red arrow), indicating that the veining event took place after cataclasis. The veins preserve their growth microstructures, as also indicated by regular chemical zoning in BSE images (Fig. 3.8b), although a few cracks occur in epidote.

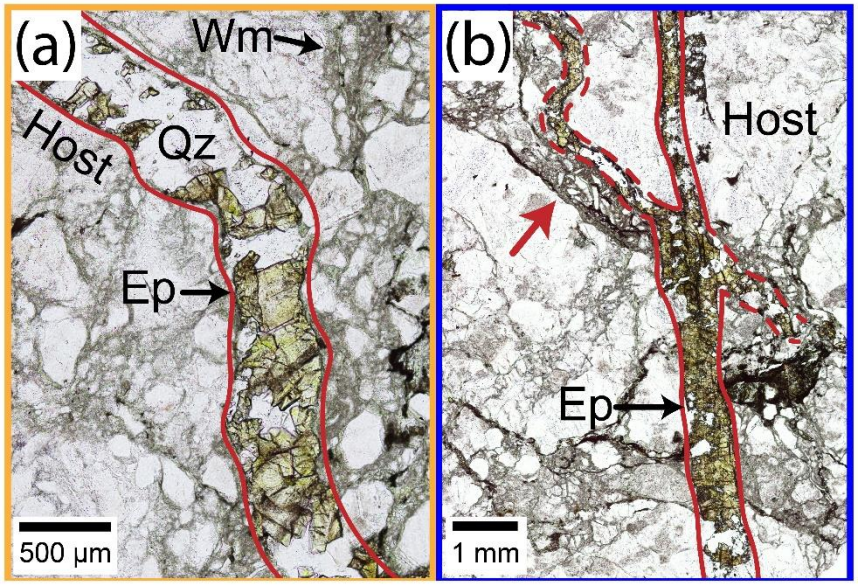

Fig. 3.6 *Transmitted light microphotograph of V2 veins in sample ALB19-4 cutting a cataclasite (red arrow). Ep =epidote; Wm = white mica. Dashed red lines indicate ill-defined vein-host boundaries. Red arrow = cataclasite. Plane-polarized light.*

3.3.3 V3 epidote vein group

V3 epidote veins are hosted by weakly foliated and deformed Albula Granite (Figs. 3.3c and 3.4c). Magmatic feldspars (ca. 0.2–3 mm in size) are highly altered into sericite and saussurite, with only rare plagioclase relicts recognizable. A slight foliation is defined by chlorite + epidote ± plagioclase (Fig. 3.4c, pink arrow), indicative of greenschist-facies conditions. Quartz (ca. 0.2–1 mm in size) displays undulose extinction in all samples. In some cases, the boundary between vein

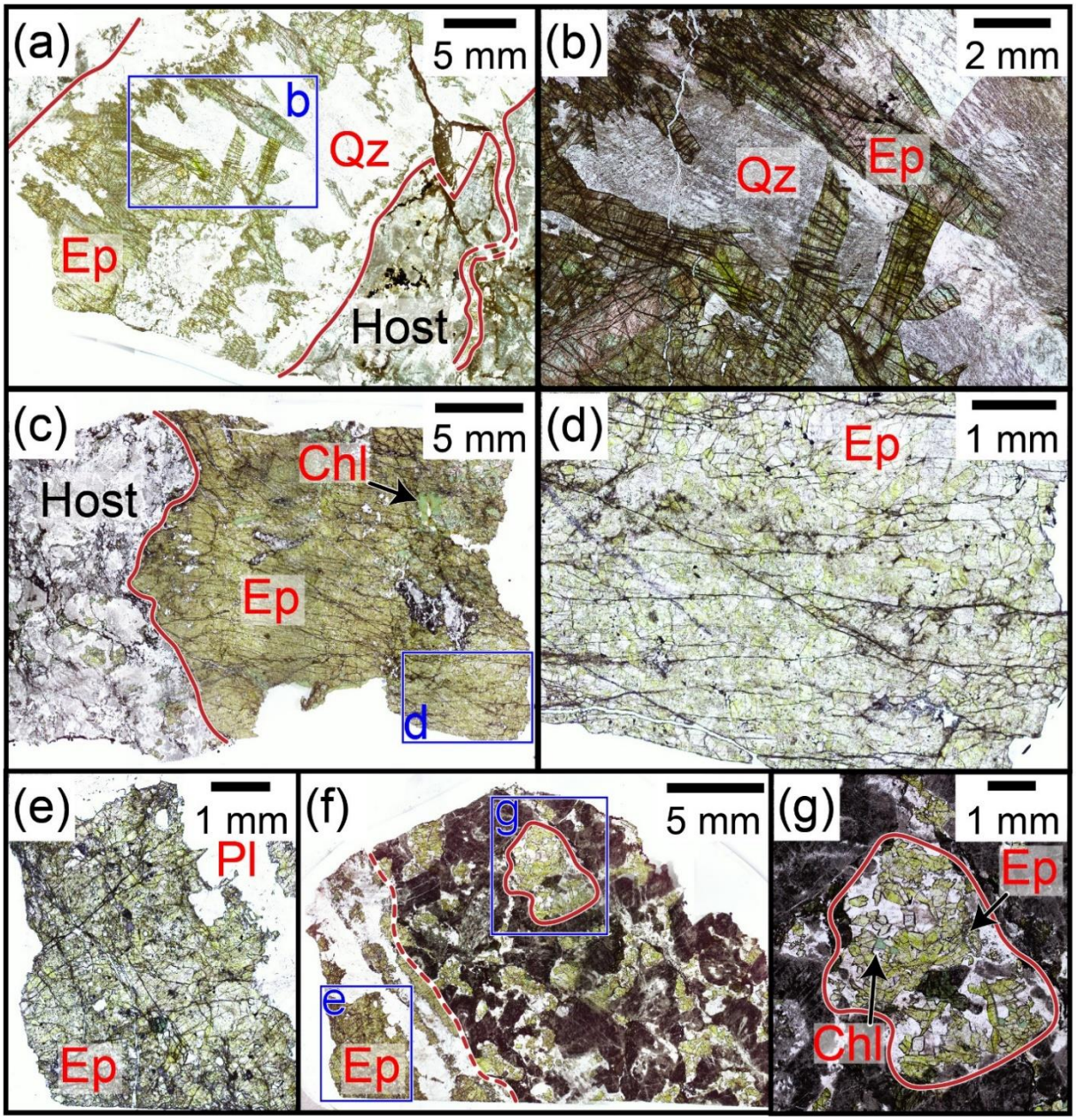

Fig. 3.7 *Transmitted light microphotographs of V3 veins (a–b) Albula-1, (c–d) ALB19-11, and (e–f) ALB19-18. Chl = chlorite; Ep = epidote; Pl = plagioclase; Qz = quartz. The letters in the blue rectangles indicate different panels. Plane-polarized light.*

and host is marked by a band of plagioclase with twinning perpendicular to the direction of vein opening (Fig. 3.4c, dashed red line). It is not always clear whether this band is part of the vein or part of the rock, but it may be interpreted as an alteration band due to fluid–rock interaction upon veining (i.e., salvage). Three types of gneiss-hosted veins are recognized (Fig. 3.7).

The first type is represented by sample Albula-1 (Fig. 3.7a–b). This vein has epidote grains with lengths between ca. 0.5 mm close to the vein boundaries and ca. 1 cm, and aspect ratios up to 7:1 in the center of the vein. The vein morphology varies from blocky at the vein rims to elongate

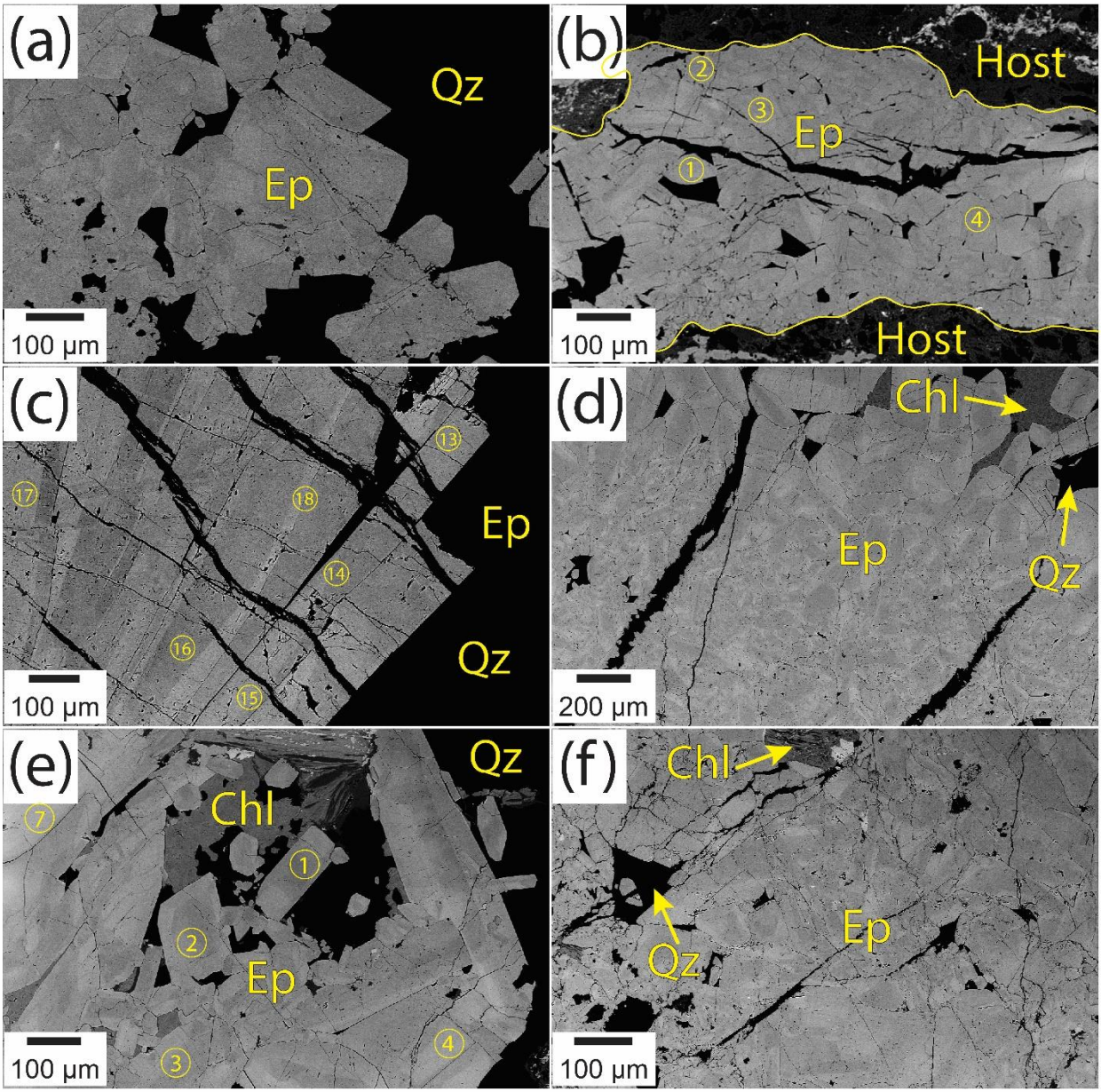

Fig. 3.8 *Backscattered electron (BSE) images of epidote in (b) V1 vein ALB19-1, (b) V2 vein ALB19-4, and V3 veins (c) Albula-1, (d) ALB19-11), (e) domain (b) of ALB19-18 and domain (a) of ALB19-18. Chl = chlorite; Ep =epidote; Qz = quartz. The numbered yellow circles indicate laser spots for U–Pb dating by LA-ICP-MS (Table 3B2).*

towards the center (Fig. 3.7b). The smaller epidote crystals define a band along the vein boundaries where epidote is associated with plagioclase (ca. 400–800 µm in size) with twinning perpendicular to the vein boundary. Outside this band, epidote is associated only with fractured quartz measuring ca. 1.2–6 mm. Epidote grains are mostly euhedral despite, attesting to the preservation of growth microstructures, which is also confirmed by regular chemical zoning in BSE images (Fig. 3.8c). Although only this main vein ("Vein1") is addressed and used for the isotope analyses presented in this contribution, a secondary one is recognized in sample Albula-1, with a width of ca. 1 mm in which euhedral to subhedral epidote grains with grain lengths of ca. 1–2 mm are associated with quartz and plagioclase. Peverelli et al. (2021; Chapter 2 of this thesis; Fig. 2.7a) obtained an LA-ICP-MS U–Pb age of 62.7 ± 3.0 Ma with an initial $^{207}Pb/^{206}Pb$ ratio of 0.8334 ± 0.0043 from in-situ analyses of epidote in both veins (Fig. 2.7a), which singularly yielded ages that are indistinguishable within uncertainty.

Sample ALB19-11 (Fig. 3.7c–d) exemplifies the second type of V3 veins, constituted mainly of euhedral and subhedral epidote grains, with minor and interstitial chlorite (ca. 150 µm to 1.5 mm in size), quartz (ca. 400–600 µm in size) and plagioclase (ca. 80–600 µm in size). Local fracturing causes ill-defined vein boundaries, which are otherwise sharp and sinuous (Fig. 3.7c). The maximum size of single epidote grains is difficult to estimate because of competition among single grains during crystallization into a blocky microstructure (Figs. 3.7d and 3.8c), whereas the minimum size is ca. 100 µm. The preservation of growth microstructures is supported by the observation that small epidote grains are perfectly euhedral and by the intact regular chemical zoning in BSE images of epidote grains (Fig. 3.8c).

Sample ALB19-18 (Fig. 3.7e–g) is the last type of V3 veins that we distinguish, and it can be subdivided into two domains: (a) an epidote + quartz + plagioclase vein (Fig. 3.7e) and (b) 1–5 mm wide pockets filled by epidote + chlorite + quartz ± plagioclase (Fig. 3.7g) disseminated throughout the country rock. In the host rock, magmatic feldspars are completely altered and it is not possible to adequately describe them, but feldspar pseudomorphs reaching up to 6 mm in size can be recognized (Fig. 3.7f–g). These grains are altered into sericite and saussurite. Domain (a) of the epidote vein shows epidote bands alternating with quartz + plagioclase ± minor chlorite bands in a blocky vein morphology (Fig. 3.7e). Epidote grains have minimum sizes of ca. 20 µm, but the largest sizes are difficult to estimate in the blocky microstructure. Quartz (ca. 0.4–4 mm in size) has undulose extinction, and the twinning of plagioclase (ca. 0.4–1.5 mm in size) is

perpendicular to the vein–host boundary. The vein morphology of domain (b) cannot be referred to any classical microstructures (Fig. 3.7g; see Bons et al., 2012). However, epidote in domain (b) is euhedral with lengths between ca. 200 µm and ca. 1 mm. In this domain, plagioclase, chlorite, and quartz are ca. 80 µm to 1.2 mm, 40–200 µm and 0.8–1 mm in size, respectively. Growth microstructures are preserved in both domains despite some fracturing, as supported by regular chemical zoning being intact in BSE images (Fig. 3.8e–f, showing domains (a) and (b), respectively). The mineral assemblage of both domains indicates greenschist-facies metamorphic conditions.

3.4 Methods

Analyses were carried out at the Institute of Geological Sciences, University of Bern, unless specified. The petrographic characterization (Sect. 3.3) of the samples was made on a ZEISS Axioplan microscope and on a Zeiss EVO50 scanning electron microscope (ca. 1 nA beam current, 20 kV acceleration voltage, and working distances of 8.5–9.5 mm).

3.4.1 Epidote U–Pb geochronology by LA-ICP-MS

The protocol outlined in Peverelli et al. (2021; Chapter 2 of this thesis) was employed for U–Pb geochronology of the studied epidote samples by laser ablation inductively coupled plasma mass spectrometry (LA-ICP-MS). Analytical conditions are reported in Table 3A1 (Appendix 3A1). Tara allanite (Gregory et al., 2007; Smye et al., 2014) was used as primary reference material. CAP (Barth et al., 1994; Gregory et al., 2007; Burn et al., 2017) and AVC (Barth et al., 2004; Gregory et al., 2007) allanite samples were analyzed as unknowns for quality control, obtaining U–Pb ages within uncertainty of their references values (see Table 3A1 in Appendix 3A). Data reduction was carried out in Iolite (version 7.08) and age calculation in Isoplot 3.7.5 (Ludwig, 2012). In addition to a U–Pb age, the Tera–Wasserburg plot gives the $^{207}Pb/^{206}Pb$ ratio of initial Pb (i.e., Pb assimilated by epidote during crystallization), which can be used to assess the nature of the epidote-forming fluids.

3.4.2 Epidote Sr data by TIMS

Measurements of Sr isotopes were carried out by thermal ionization mass spectrometry (TIMS) in epidote micro-separates produced from each epidote vein discussed here. Before ion

chromatography, the samples were digested in acids following the procedure in Peverelli et al. (2021) modified from Nägler and Kamber (1996). The SRM 987 standard was used for quality control, and for corrections for within-run mass bias and interference of ^{87}Rb during measurements by TIMS. A correction for ^{87}Rb-derived ^{87}Sr is not necessary in Sr isotope ratios measured in epidote due to Rb being highly incompatible in epidote (see Frei et al., 2004; Feineman et al., 2007). Analytical details are in Appendix 3A.

3.4.3 Strontium and Pb isotopes in Albula Granite and carbonatic rocks

Measurements of Pb and Sr isotopes were performed in weakly foliated and deformed Albula Granite and in the carbonatic rocks of the Ela nappe. The rock samples were dissolved in acids, although the silicate fraction of the carbonatic samples was not dissolved. Ion chromatography allowed to collect the Sr and Pb fractions in sequence. Strontium isotopes of the Albula Granite were measured by TIMS, with the same analytical protocol used for epidote samples (Appendix 3A). Lead isotope ratios of granitoid and carbonatic rocks, and Sr isotope data of the carbonatic samples were measured by solution MC-ICP-MS. For Pb isotope measurements, a Tl spike was used to correct for instrumental mass fractionation. The SRM 981 standard was used to assess external reproducibility of Pb isotope measurements. For quality control of Sr isotope data and for mass-bias correction, the SRM 987 standard (Weis et al., 2006) was measured at the beginning and at the end of the measurement sequence.

3.4.3.1 Lead and Sr isotope ratios of Albula Granite and carbonatic rocks at the time of veining

Granitoids and carbonatic rocks can contain appreciable mass fractions of Sr and Pb. In order to evaluate the fluid pathways of epidote-forming fluids, the Pb–Sr isotope composition of carbonatic rocks and Albula Granite at the time of fluid–rock interaction (i.e., the time of epidote-vein formation) have to be calculated from the measured Pb–Sr isotope ratios. This can be done by knowing the equations for radioactive decay of ^{235,238}U and ^{87}Rb into, respectively, ^{207,206}Pb and ^{87}Sr, as well as today's total U/Pb and Rb/Sr ratios. For this reason, an aliquot of the dissolved samples of Albula Granite and carbonatic rocks was collected before ion chromatography for measurements of Rb, Sr, U and Pb concentrations on a 7700x Agilent quadrupole ICP-MS at the Department of Geography of University of Bern.

3.4.4 Stable isotope data of epidote and estimations of crystallization temperature

Measurements of hydrogen isotopic ratios were performed using ca. 4 mg of epidote material at the Joint Goethe University Frankfurt–Senckenberg BiK-F Stable Isotope Facility (Frankfurt, Germany) on a Thermo high-temperature conversion elemental analyzer (TC/EA) coupled to a Thermo MAT 253 mass spectrometer in continuous flow mode. Repeated measurements of standards and unknowns resulted in an uncertainty of ±3 ‰ in δD values. Oxygen isotope ratios were measured at University of Lausanne (Switzerland) on single epidote grains handpicked from crushed vein material, using a CO_2-laser based extraction line coupled to a Finnigan MAT 253. Replicate measurements of unknowns indicate a precision of 0.3 ‰ or better. More details are given in Appendix 3A. Oxygen isotope data of carbonatic rocks of the Ela nappe and of the Albula Granite are reported in the comprehensive work of Manatschal et al. (2000). Hydrogen isotope data of carbonatic rocks of the Ela nappe are neither measured here nor reported anywhere due to negligible water contents of these lithologies. The hydrogen isotope system of hydrous minerals in granites are readily reset by fluid–rock interaction processes (Taylor, 1977; 1978). Thus, δD data are not acquired from our Albula Granite sample in that they do not allow significant comparisons with the investigated epidote-forming fluids.

For calculation of δD and $\delta^{18}O$ values of the epidote-forming fluids from the isotope data measured in epidote grains, the temperature of epidote crystallization has to be estimated. For V3 epidote, the chemical composition of chlorite in textural equilibrium with epidote in sample ALB19-11 was used to calculate the temperature of crystallization using the method of Vidal et al. (2005; 2006) implemented in the program ChlMicaEqui (Lanari, 2012). For calculation of the hydrogen and oxygen isotope compositions of the epidote-forming fluids, we used the fractionation equations of Chacko et al. (1999) and Zheng (1993), respectively.

3.5 Results

Table 3.3 summarizes epidote U–Pb ages and isotopic ratios of all samples discussed here. Radiogenic isotope ratios of host Albula Granite and of the carbonatic rocks are presented as values at the time of epidote-forming fluid–rock interaction, and the measured uncorrected data are in Table 3B1 (Appendix 3B). All epidote U–Pb age uncertainties are given at 95 % confidence level, and all uncertainties on isotope ratios are 2 standard errors (2 SE) unless specified.

3.5.1 Epidote U–Pb ages

The obtained $^{238}U/^{206}Pb$ and $^{207}Pb/^{206}Pb$ ratios by LA-ICP-MS are presented in Table 3B2 (Appendix 3B). Vein epidote V1 (sample ALB19-1) gave a lower intercept of 22 ± 64 Ma (MSWD = 1.10) in a Tera–Wasserburg diagram (Fig. 3.9a). The large uncertainty on this value (±290 %) is too large for the lower intercept to yield a meaningful age.

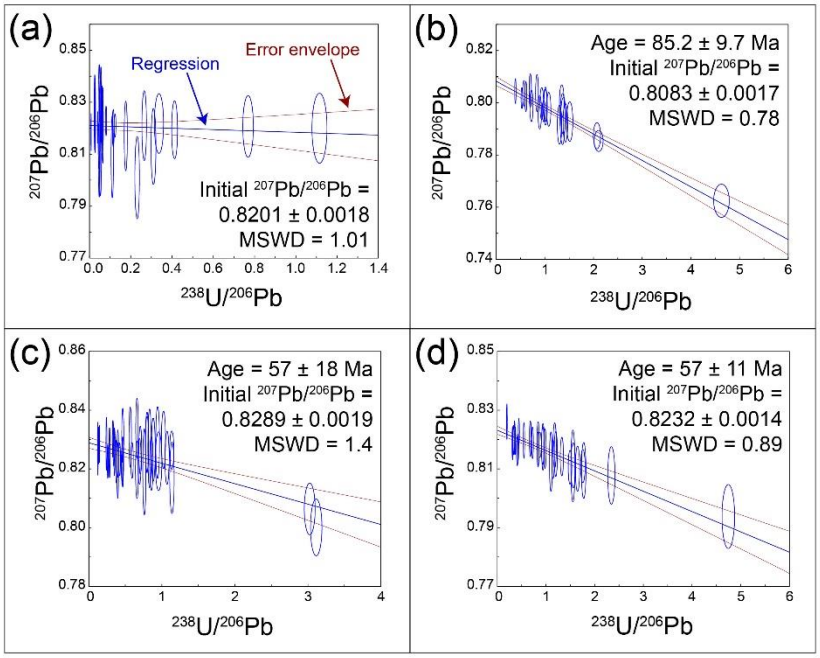

Fig. 3.9 *Tera–Wasserburg diagrams of (a) V1 vein epidote ALB19-1, (b) V2 vein epidote ALB19-4, and V3 vein epidote (c) ALB19-11 and (d) ALB19-18. Error ellipses are 2σ and age uncertainties are 95 % confidence. Plotted with Isoplot 3.5.7 (Ludwig, 2012).*

However, the initial $^{207}Pb/^{206}Pb$ ratio obtained from the Tera–Wasserburg plot of 0.8201 ± 0.0018 can be discussed (Sect. 3.6.2). Epidote V2 (sample ALB19-4) returned a Tera–Wasserburg age of 85.2 ± 9.7 Ma (MSWD = 0.78), and an initial $^{207}Pb/^{206}Pb$ ratio of 0.8083 ± 0.0017 (Fig. 3.9b). As for V3 epidote veins, ALB19-11 epidote yielded a Tera–Wasserburg age of 57 ± 18 Ma (MSWD = 1.4) with an initial $^{207}Pb/^{206}Pb$ ratio of 0.8289 ± 0.0019 (Fig. 3.9c), and ALB19-18 epidote an age of 57 ± 11 Ma (MSWD = 0.89) with an initial $^{207}Pb/^{206}Pb$ ratio of 0.8232 ± 0.0014 (Fig. 3.9d). No difference can be resolved either in age or in initial $^{207}Pb/^{206}Pb$ ratio in sample ALB19-18 by plotting the data obtained from microstructural domains (a) and (b) described in Sect. 3.3.3 (Fig. 3.7e–g). The Tera–Wasserburg age and initial $^{207}Pb/^{206}Pb$ ratio of sample Albula-1 of, respectively, 62.7 ± 3.0 Ma and 0.8334 ± 0.0043 are taken from Peverelli et al. (2021; Chapter 2 of this thesis; Fig. 2.7a). If the datasets obtained from V3 epidote samples (i.e., ALB19-11, ALB19-18 and Albula-1) are combined in a single Tera–Wasserburg plot, an age of 59.9 ± 2.7 Ma and an initial $^{207}Pb/^{206}Pb$ ratio of 0.8260 ± 0.0010 are obtained with an MSWD of 2.2. Although these three samples should be considered separately due to their significantly different initial $^{207}Pb/^{206}Pb$ ratios, the fact that the MSWD value of the combined dataset remains sufficiently low permits to infer that these three samples formed during a vein-forming deformation stage at ca. 60 Ma.

3.5.2 Strontium and Pb isotope data

The initial $^{207}Pb/^{206}Pb$ ratios of epidote are obtained from the Tera–Wasserburg diagram, as outlined in Sect. 3.5.1. The Sr isotope ratios of epidote obtained by TIMS are reported in Table 3.3. For epidote Sr isotope data, no age correction is necessary in that Rb is highly incompatible in epidote (see also Frei et al., 2004; Feineman et al., 2007). Therefore, ingrown ^{87}Rb-derived ^{87}Sr is negligible, the measured and the initial $^{87}Sr/^{86}Sr$ are equal, and the Sr isotope composition of epidote is entirely inherited from the epidote-forming fluid during crystallization.

The Albula Granite contains enough Rb and U (i.e., $^{87}Rb/^{87}Sr$ of 0.40 and $^{238}U/^{204}Pb$ of 21.8) to produce noticeable evolution curves of its Pb and Sr isotope composition from today ($^{207}Pb/^{206}Pb$ = 0.811302 ± 0.000018; $^{87}Sr/^{86}Sr$ = 0.718021 ± 0.000007) until the time of pluton emplacement ($^{207}Pb/^{206}Pb$ = 0.854313 ± 0.000018; $^{87}Sr/^{86}Sr$ = 0.716324 ± 0.000007). Therefore, in order to compare the Pb and Sr isotope compositions of the epidote-forming fluids with those of the host Albula Granite, and to evaluate fluid pathways, the Pb and Sr isotope compositions of the Albula Granite have to be calculated for the time of epidote-forming fluid–rock interaction. The $^{207}Pb/^{206}Pb$ and $^{87}Sr/^{86}Sr$ ratios of the Albula Granite presented in Table 3.3 are average values of the same isotope ratios calculated at 60 Ma and 85 Ma (i.e., respectively, the times of V3 and V2 vein formation). Similar considerations are valid for the Pb isotope composition of the carbonatic rocks of the Ela nappe, given that the total $^{238}U/^{204}Pb$ ratios (0.6–6.8) of these rocks produce noticeable variations in $^{207}Pb/^{206}Pb$ ratios over the considered time span. Hence, the $^{207}Pb/^{206}Pb$ ratios of the selected samples (Table 3.3) were calculated at 60 Ma and 85 Ma as well. Conversely, the low total $^{87}Rb/^{87}Sr$ ratios (0.002–0.018) entail that corrections for the contribution of ^{87}Rb-derived ^{87}Sr cause changes on the fifth decimal digit. Hence, the differences in $^{87}Sr/^{86}Sr$ ratios among the measured (i.e., today's) value, and those calculated at 60 Ma and 85 Ma are within the uncertainty of the measurements. Therefore, the $^{87}Sr/^{86}Sr$ data of the carbonatic rocks of the Ela nappe are given as uncorrected values in Table 3.3. The uncorrected isotope data of all rocks are reported in Table 3B1.

The samples of Allgäu and Mingér limestones returned $^{87}Sr/^{86}Sr$ ratios of 0.707448 ± 0.000014 (2 SE) and 0.707745 ± 0.000012, respectively, that are consistent with their formation in equilibrium with seawater in Triassic to Jurassic times ($^{87}Sr/^{86}Sr$ ratios of 0.7068–0.7080; McArthur et al., 2012). Conversely, our Hauptdolomit sample gave an $^{87}Sr/^{86}Sr$ value of 0.712967 ± 0.00013, which is far more radiogenic than Triassic seawater and published data (e.g., Faure et al., 1978).

This may be due to the presence of calcite veins in the hand samples (see Sect. 3.4.3), which may have inherited radiogenic Sr from the calcite-forming fluid. The lack of published Pb isotope data of the studied carbonatic rocks of the Ela nappe to do allow to assess our results against literature data. The $^{87}Sr/^{86}Sr$ value (0.718021 ± 0.000007), with Rb and Sr mass fractions (11 and 78 µg g^{-1}, respectively; Table 3B1) measured in our Albula Granite sample return an initial $^{87}Sr/^{86}Sr$ value (300 Ma) of 0.716324 ± 0.000007. This value is within the range of initial $^{87}Sr/^{86}Sr$ ratios obtained from the data of Pinto (2014) and Pinto et al. (2015). No Pb isotope data are available in the literature for the Albula Granite. The Pb–Sr isotope data of the studied epidote vein are within the range of Pb–Sr isotope values defined by the Albula Granite and the carbonatic rocks of the Ela nappe between the time of emplacement or deposition, respectively, and today.

TABLE 3.3

Isotope data of epidote vein samples, and those of host Albula Granite and carbonatic rocks of the Ela nappe at the time of epidote vein formation (i.e., 85–60 Ma; subscript "in"). Oxygen and hydrogen data measured in epidote are relative to the Vienna standard mean ocean water (V-SMOW). Age uncertainties are at 95 % confidence level, and uncertainties on isotope ratios are 2 standard errors (2 SE) which are propagated for average values calculated between 85 and 60 Ma. Carb. = carbonatic; Ep = epidote. The ages of Albula Granite and carbonatic rocks are taken from available literature (Manatschal and Nievergelt, 1997; strati.ch).

	Sample	Age	$(^{207}Pb/^{206}Pb)_{in}$	$(^{87}Sr/^{86}Sr)_{in}$	$\delta^{18}O_{V\text{-}SMOW}$ [‰]	$\delta D_{V\text{-}SMOW}$ [‰]
V1 Ep	ALB19-1	(22 ± 64 Ma)	0.8201 ± 0.0018	0.713812 ± 0.000006	8.5	-59
V2 Ep	ALB19-4	85.2 ± 9.7 Ma	0.8083 ± 0.0017	0.714963 ± 0.000011	12.7	-52
V3 Ep	ALB19-11	57 ± 18 Ma	0.8289 ± 0.0019	0.713060 ± 0.000006	7.4	-49
	ALB19-18 (a)	57 ± 11 Ma	0.8232 ± 0.0014	0.713235 ± 0.000007	9.4	-47
	ALB19-18 (b)			0.712983 ± 0.000004	-	-49
	Albula-1[1]	62.7 ± 3.0 Ma	0.8334 ± 0.0043	0.713835 ± 0.000005	7.6	-48
Host	Albula Granite	Permian	0.821157 ± 0.000025 (propagated 2 SE)	0.717611 ± 0.000011 (propagated 2 SE)	-[2]	10.4–12.7[3]
Carb. rocks	Allgäu Fm.	Jurassic	0.836553 ± 0.000028 (propagated 2 SE)	0.707448 ± 0.000014	-[2]	26.2–30.4[3]
	Mingér Fm.	Triassic	0.821744 ± 0.000019 (propagated 2 SE)	0.707745 ± 0.000012	-[2]	26.2–30.4[3]
	Hauptdolomit	Triassic	0.836220 ± 0.000030 (propagated 2 SE)	0.712967 ± 0.000013	-[2]	26.2–30.4[3]
					All ±0.3 ‰	All ±3 ‰

[1]Only "Vein1" of Peverelli et al. (2021; Chapter 2 of this thesis; Sect. 2.4.1).
[2]Data not available; see Sect. 3.4.3 for details.
[3]From Manatschal et al. (2000).

3.5.3 Epidote $\delta^{18}O$ and δD data

The O and H isotope data obtained from epidote in the studied veins are reported in Table 3.3 relative to Vienna standard mean ocean water (V-SMOW). The oxygen isotope composition of

domain (b) of V3 epidote vein ALB19-18 (see Sect. 3.3.3) could not be measured because pure epidote separates, which are required for measurements, could not be produced for this microstructural domain. The data measured in epidote microseparates (Table 3.3) are used to calculate the oxygen and hydrogen isotope composition of the epidote-forming fluids (Table 3.4), as outlined in the following (Sect. 3.5.3.1).

3.5.3.1 Temperature estimates and $\delta^{18}O$–δD data of V1–V3 epidote-forming fluids

TABLE 3.4

Calculated δD and $\delta^{18}O$ values of the epidote-forming fluids. The ranges include uncertainties of ±3 ‰ (δD) and ±0.3 ‰ ($\delta^{18}O$). Albula-1 refers to "Vein1" of Peverelli et al. (2021; Sect. 2.4.1).

	Epidote	δD (220–270 °C)	δD (300–350 °C)	$\delta^{18}O$ (220–270 °C)	$\delta^{18}O$ (300–350 °C)
V1 fluid	ALB19-1	-38 to -21 ‰	-	5.1–8.2 ‰	-
V2 fluid	ALB19-4	-	-21 to -11 ‰	-	11.4–12.8 ‰
V3 fluids	ALB19-11	-28 to -11 ‰	-	4.0–7.1 ‰	-
	ALB19-18 (a)	-26 to -9 ‰	-	6.0–9.1 ‰	-
	Albula-1	-24 to -10 ‰	-	4.3–7.3 ‰	-

The $\delta^{18}O$ and δD data of the epidote-forming fluids (Table 3.4) are calculated from the $\delta^{18}O$ and δD values measured in each epidote sample (Table 3.3) following Zheng (1993) and Chacko et al. (1999), respectively. The estimated temperature of crystallization of V3 epidote veins is calculated from the chemical composition of chlorite in V2 vein ALB19-11, measured by EPMA (Sect. 3.4.4). The chlorite structural formula is reported in Table 3C1 (Appendix 3C), along with the temperature of crystallization calculated or each analysis. An average temperature of 270 (± 50) °C is obtained, and interpreted as corresponding to the temperature of epidote formation during the veining event at ca. 60 Ma (obtained from V3 epidote samples Albula-1, ALB19-11 and ALB19-18 together; see Sect. 3.5.1).

The temperature of epidote crystallization in V2 vein ALB19-4 can only be estimated through geodynamic constraints and assuming thermal equilibration of the V2 epidote-forming fluid with the country rock. Hence, the temperature range existing at the base of the Err nappe during the D2 phase of 300–350 °C (see Handy et al., 1996) is used to calculate the $\delta^{18}O$ and δD of the V2 epidote-forming fluid. Because we do not have an age for V1 vein ALB19-1, we use the same temperature estimated for V3 veins (270 ± 50 °C). The use of this temperature is justified because

(1) only the D1 and D2 phases occurred in the stability field of epidote, thus excluding that this vein formed in the following lower-temperature D3 phase, (2) the isotope data of V1 epidote ALB19-1 suggest that the formation of this epidote vein occurred during the same veining event of V3 epidote veins at ca. 60 Ma (see Sect. 3.6.2). The estimated δD and $\delta^{18}O$ data of the epidote-forming fluids are plotted in Fig. 3.10 with the meteoric line and the seawater field from Sheppard (2018). $\delta^{18}O$ values of Albula Granite and carbonatic rocks are taken from Manatschal et al. (2000; Table 3.3). No δD data are available for these units. The δD values of all epidote samples are within uncertainty of each other. On the other hand, the $\delta^{18}O$ data of V3+V1 and V2 epidote-forming fluids are clearly different, and there are marked differences also among V3 epidote samples.

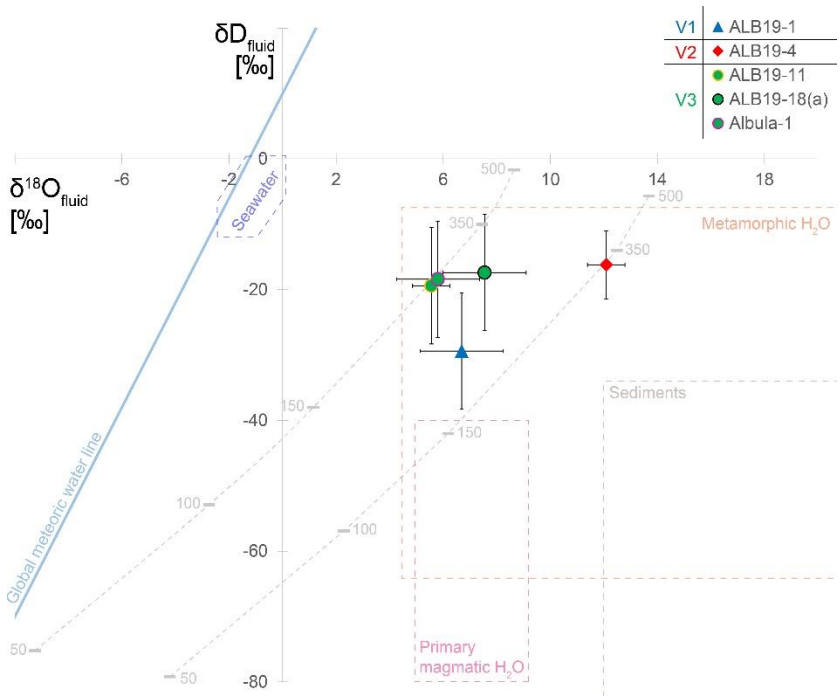

Fig. 3.10 *Hydrogen (δD) versus oxygen ($\delta^{18}O$) isotope data of the epidote-forming fluids, calculated from measurements in epidote grains and relative to Vienna Standard Mean Ocean Water (V-SMOW). The error bars of each datum-point and the shaded fields define the ranges of δD and $\delta^{18}O$ values obtained considering a temperature of crystallization of 220–320 °C (V3+1) and 300–350 °C (V2), and include analytical uncertainties. The dashed gray lines indicate the $\delta^{18}O$–δD evolution of the epidote-forming fluids at varying temperatures (50–500 °C; fractionation factors from Zheng, 1993 and Chacko et al., 1999). Redrawn from Sheppard et al. (2018).*

3.6 Discussion

3.6.1 Eo-Alpine fluid circulation

The Err nappe is a typical hyper-extended rifted continental margin (see Fig. 5 of Mohn et al., 2011; 2012; Manatschal et al., 2015) with indisputable evidence for fluid circulation in Jurassic times by means of seawater exploiting syn-rift faults for percolation into the crust (Manatschal et al., 2000; 2015; Pinto et al., 2015; Incerpi et al., 2017; 2018; 2019). In our study area, evidence for Jurassic faulting is provided by the presence of the Saluver breccia (Froitzheim et al., 1994; Mohn et al., 2011). At a first glance, one could assume that all hydrothermal features nearby,

including the studied epidote veins, are related to rifting and thus Jurassic in age. The Late Cretaceous to Paleocene ages obtained in our study show that this is not the case, however, and that hydration of the granitic crust of the Err nappe is at least a two-chapter story: (1) one related to rifting in the Jurassic (Manatschal et al., 2000; 2015; Pinto et al., 2015; Incerpi et al., 2017; 2018; 2019), and (2) another one related to the Eo-Alpine orogeny in Late Cretaceous to Paleocene times as shown here. The V2 epidote age of 85.2 ± 9.7 Ma is consistent with the D1 phase (88–80 Ma; Handy et al., 1996) of west-directed nappe stacking, while the formation of V3 epidote veins at ca. 60 Ma can be ascribed to the D2 extensional phase (80–67 Ma; Handy et al., 1996) in the opposite direction (top-to-the-E; Froitzheim et al., 1994; Handy et al., 1996). Both D1 and D2 occurred in the epidote stability field (Table 3.1; Handy et al., 1996), lending support for the interpretation of the presented ages.

Although the sampling location is in an area affected by Jurassic rifting, where seawater-driven alteration can produce epidote (see Humphris and Thompson, 1978; Gardien and Paquette, 2004; Brett-Adams et al., 2021), all epidote ages are related to the Eo-Alpine inversion history of the Err nappe. Surprisingly, no epidote samples yielded Jurassic ages. Only one epidote sample (V1 epidote in vein ALB19-1) did not return a geologically meaningful date because all data-points contain large amounts of initial Pb. Hence, all analyses plot close to the upper end of the Tera–Wasserburg regression (Fig. 3.9a), causing a highly imprecise lower intercept between regression and concordia (22 ± 64 Ma), which cannot be considered a meaningful age. The presence of chemical zoning (Fig. 3.8) and the preservation of growth microstructures (Figs. 3.5–3.3) are evidence that these Late Cretaceous–Paleocene ages date the formation of epidote during veining, and not the resetting of the U–Pb system during – for example – fluid-driven recrystallization of epidote. In this respect, thermal diffusion of Pb and other trace elements would require much higher temperatures than those of < 350 °C recorded by the study area during its geological history (see Dahl, 1997; Franz and Liebscher, 2004). In addition to this, no microstructural evidence suggests that the epidote veins may have been affected by secondary fluids after crystallization. Hence, fluid-driven disturbance of epidote's geochemical and isotopic systems is highly unlikely. Although all epidote veins studied here are Late Cretaceous to Paleocene in age and formed during the Eo-Alpine orogeny, the existence of rift-related Jurassic ones cannot be ruled out. The combination of our data with previous work (see Manatschal et al., 2000; 2015; Pinto et al., 2015; Incerpi et al., 2017; 2018; 2019) indicates multi-stage hydrothermal activity in the Err nappe

between Jurassic times and at least the Paleocene, as recorded by different geochronometers and isotope tracers. It is enticing that a so-far undetected event of fluid circulation in an area where hydrothermal activity has already been well characterized is revealed thanks to a newly established geochronometer like epidote.

3.6.2 Pb–Sr isotope data of epidote veins and rocks

The fact that the oldest epidote veins (i.e., V2 veins) that we detect in the Albula Pass area are of Late Cretaceous age and related to the Eo-Alpine D1 deformation phase provides constraints as to the possible fluid equilibration pathways. During the D1 deformation phase, (1) the Ela nappe was thrusted on top of the Err nappe, and (2) the Albula Steep Zone formed (Froitzheim et al., 1994). This means that the present-day stratigraphic sequence with the carbonatic rocks of the Ela nappe both beneath and above the Err nappe existed before the formation of V2 epidote veins. Lead and Sr are common trace elements in granitic an carbonatic rocks. These elements are fluid-mobile and they are readily incorporated into the epidote crystal structure during veining (Frei et al., 2004; Feineman et al., 2007). Therefore, the Pb–Sr isotope compositions of the studied epidote samples are equal to those of the epidote-forming fluids, and the latter reflect the lithologies with which the epidote-forming fluids interacted during percolation. The Sr–Pb isotope data of the studied epidote samples are outside the uncertainty of the age-corrected (i.e., 85–60 Ma) $^{87}Sr/^{86}Sr$–$^{207}Pb/^{206}Pb$ ratios of the Albula Granite (Table 3.3). This indicates that the Pb–Sr isotope system of epidote-forming fluids was not in complete equilibrium with the veins' host Albula Granite, and indicates a fluid source external to the Albula Granite. The dominant lithologies at Albula Pass area are the Albula Granite and the carbonatic rocks of the Ela nappe, with minor siliciclastic sediments (i.e., Saluver Breccia) of the Err nappe (Figs. 3.1 and 3.2). A first hypothesis may be that the epidote-forming fluids interacted mainly with these lithologies.

The Pb and Sr isotope ratios of V1 and V3 epidote samples plot in a field defined by isotope mixing curves with the carbonatic rocks of the Ela nappe (i.e., 5×Allgäu : 4×Hauptdolomit : 1×Mingér, in mass fractions) and the Albula Granite as end-members in a $^{207}Pb/^{206}Pb$ *vs.* $^{87}Sr/^{86}Sr$ plot (Fig. 3.11). This allows that the Pb–Sr isotope composition of the V1 and V3 epidote-forming fluids results from interaction with the Albula Granite after circulation through the carbonatic rocks of the Ela nappe. As shown by the mixing curves (Fig. 3.11), the Sr isotope composition of all of our V1–V3 epidote samples is dominated by the input of the carbonatic rocks of the Ela nappe, given

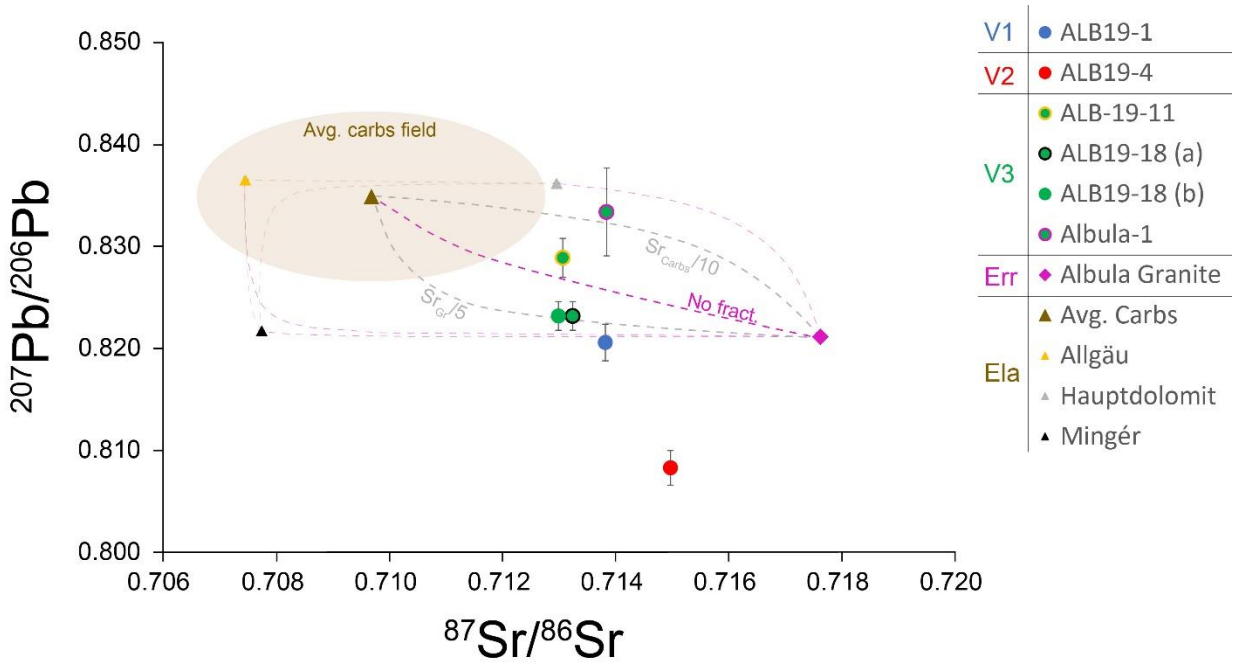

Fig. 3.11 *Sr–Pb isotope compositions of epidote samples, Albula Granite (Gr.) and carbonatic rocks (carbs.) from the Ela nappe. The dashed lines indicate mixing curves between rock end-members. Avg = average; fract. = fractionation.*

the high Sr mass fractions in these sedimentary rocks relative to the Albula Granite. Epidote Pb isotope composition, on the other hand, is controlled both by the Albula Granite (i.e., ALB19-1(a–b) and ALB19-1 epidote samples) and by the carbonatic rocks of the Ela nappe (i.e., Albula-1 epidote). One of the V3 epidote samples (i.e., ALB19-11) lies on a mixing curve which assumes that Pb and Sr are not fractionated from either the Albula Granite or the carbonatic rocks of the Ela nappe. All other epidote samples, instead, require fractionation of Sr and Pb during leaching upon fluid–rock interaction by an unknown process: (a) the Pb–Sr isotope composition of epidote sample Albula-1 can be accounted for by a depletion of Sr leached from the carbonatic rocks of the Ela nappe by a factor of 10, whereas (b) that of epidote samples ALB19-1 and ALB19-18(a–b) by depletion of Sr from the Albula Granite by a factor of 5. The fact that V1 epidote is isotopically similar to V3 epidote samples suggests that the undatable V1 epidote vein may have also formed in Paleocene times during the V3 veining event.

The Sr isotope composition of V2 epidote is similar to that of V1 and V3 epidote samples, suggesting that the V2 epidote-forming fluid also percolated through the Ela nappe before reaching the V2 veining location in the Albula Granite. The V2 epidote initial $^{207}Pb/^{206}Pb$ ratio is markedly different than those of V1 and V3 epidote samples, and even more radiogenic than that of the Albula Granite itself. This suggests that the V2 epidote-forming fluid interacted either (1) with a

lithology that concentrates U-bearing minerals which cannot be constrained with the present data, or (2) with U-rich accessory minerals in the Albula Granite itself. These Pb–Sr isotope data suggest that the equilibration pathway of the fluid forming V2 epidote veins was not the same as that of the V3+V1 epidote-forming fluids.

3.6.3 Stable isotope data of paleofluids

Since oxygen is the most abundant element in rocks and fluids, the oxygen isotope composition of the epidote-forming fluids inherited at their source is variably modified during fluid circulation, fluid–rock interaction, and fluid mixing (e.g., Hoefs, 2018; Sheppard, 2018). Therefore, the measured $\delta^{18}O$ values reflect the lithologies with which the epidote-forming fluids interacted. In contrast to oxygen, hydrogen is less abundant in granitic and carbonatic rocks, and it is mainly stored in hydrous minerals. However, hydrogen is prone to diffusion due to its small size (e.g., Zhao and Xheng, 2007; Farver, 2010). Nevertheless, a hydrogen-bearing phase has to exchange hydrogen with epidote in order for the measured epidote δD values to be affected by diffusion processes. Since the V1+V3 epidote-bearing veins are dominated by epidote (Sects. 3.3.1 and 3.3.3), such a process is unlikely within the veins themselves. V2 epidote veins are made of epidote and quartz, and they cut white mica-rich cataclastic domains of the Albula Granite (Sect. 3.3.2). This means that cataclasis and related enrichment in white mica occurred before V2 veining. It has been demonstrated that the hydrogen isotope system of hydrous phases in rocks is readily reset by interaction with percolating fluids (Taylor, 1977; 1978). Therefore, hydrous minerals in the Albula Granite, and any others present in the carbonatic rocks of the Ela nappe, most likely reflect the hydrogen isotope composition of the epidote-forming fluids. For these reasons, hydrogen isotope data of epidote can be used to investigate the epidote-forming fluid sources, while oxygen isotopes to assess fluid–rock interaction.

The δD and $\delta^{18}O$ data of the epidote-forming fluids (Fig. 3.10) also support different fluid pathways for the V2 and V3+V1 epidote-forming fluids. We can rule out that the differences in $\delta^{18}O$ values between V2 and V3+V1 epidote-forming fluids are due to temperature effects because this would require a crystallization temperature of 140–180 °C (fractionation factors of 5.6–7.9; see Zheng, 1993) for V2 epidote to have precipitated from a fluid with the same $\delta^{18}O$ value of the V3+V1 epidote-forming fluids. This temperature interval for the crystallization of V2 epidote is highly unlikely, since temperatures ranged between 300–350 °C during the D2 deformation phase

in the Err nappe (Handy et al., 1996). Therefore, the difference in oxygen isotope composition between the Late Cretaceous and Paleocene epidote-forming fluids reflects different equilibration histories. The $\delta^{18}O$ values of the V2 epidote-forming fluid (11.4–12.8 ‰; Table 3.4) overlap with those of the Albula Granite (10.4–12.7 ‰; Table 3.3) measured by Manatschal et al. (2000), suggesting complete re-equilibration of this fluid with the vein's host Albula Granite. The oxygen isotope composition of V3+V1 fluids (4.0–9.1 ‰) do not overlap with the $\delta^{18}O$ values of either the Albula Granite or carbonates (26.2–30.4 ‰; Manatschal et al., 2000). This indicates a more elaborate equilibration history of oxygen isotopes in these fluids which cannot be explained by simple interaction of the V3+V1 fluids with the rocks that they percolated through.

The δD values of all epidote-forming fluids are rather uniform (-38 to -11 ‰) and overlap with the field of fluids produced by prograde metamorphic reactions ("metamorphic fluids" in Fig. 10; compare with Sheppard, 2018). In the study area, fluids may be released by dehydrating serpentinites in the underlying Platta–Lizun–Malenco superunit, although this may have been difficult to achieve due to the relatively low temperatures reached by the Malenco unit (e.g., Clément et al., 2019; Picazo et al., 2019). Similar $\delta^{18}O$–δD values are also related to formation/connate waters and to seawater–hydrothermal waters (see Sheppard, 2018). Given the proximity and the involvement of sedimentary rocks of marine origin in the Late Cretaceous orogen, the release of modified seawater (i.e., formation/connate water) cannot be excluded. Finally, the input of other end-member waters (e.g., meteoric water; see Sheppard, 2018) may also account for the calculated $\delta^{18}O$–δD composition of the epidote-forming fluids, provided that their role can be reconciled with the geodynamic setting existing in Eo-Alpine times.

3.6.4 Eo-Alpine fluid pathways

During the D1 phase of the Eo-Alpine orogeny, the sedimentary units of the Ela nappe were stacked on top of the Err nappe (Fig. 3.12; Handy et al., 1996; Mohn et al., 2011). Moreover, the formation of the Albula steep zone at the end of the D1 stage entails that the Err nappe is underlain by the Ela nappe from the Late Cretaceous onwards (Froitzheim et al., 1994; Handy et al., 1996; Furrer et al., 2015). In addition, the Err–Ela nappe system as a whole lies on top of the Platta–Lizun–Malenco superunit (e.g., Froitzheim et al., 1994; Handy et al., 1996). Because it is not know whether the study area was above of below the seawater surface in Late Cretaceous to Paleocene times, in the following both options will be considered, along with the additional unknown of the

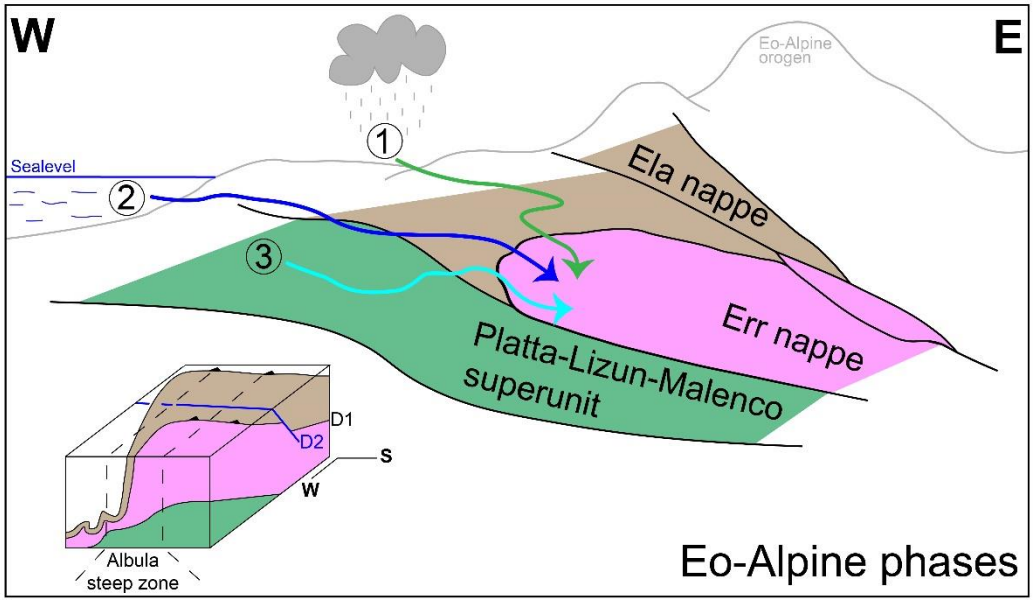

Fig. 3.11 *Sketch of fluid circulation and veining in the study area during the Eo-Alpine orogeny. The blue and green arrows indicate possible fluid pathways (1–3) described in the text. Not to scale. The cross section is redrawn from Mohn et al. (2011; their Fig. 12a); the block diagram is redrawn from Froitzheim et al. (1994; their Fig. 16).*

elevation of the Eo-Alpine orogen. Pb–Sr isotope data of epidote (Fig. 3.11), show that the epidote-forming fluids interacted with the carbonatic rocks of the Ela nappe before reaching the Albula Granite. The geochemical input by the carbonatic rocks of the Ela nappe is consistent with fluid circulation through the Ela nappe and into the Albula Granite in light of the stratigraphic relations between the Ela and Err nappes resulting from the D1 compressional tectonics (Fig. 3.12; Froitzheim et al., 1994; Handy et al., 1996; Furrer et al., 2015). As outlined in Sect. 3.6.3, three possible fluid sources can be identified as end-members during V1–3 vein formation, as shown in Fig. 3.12: (1) meteoric water, (2) modified seawater or formation/connate waters, or (3) metamorphic fluids. Meteoric water can be accepted as a plausible fluid source if the Eo-Alpine orogen had a low elevation, in that high elevation implies highly negative $\delta^{18}O$–δD values (see Sheppard, 2018; Campani et al., 2012; Krsnik et al., 2021). Modified seawater of formation/connate waters are likely water sources if one envisages the release of water from, for example, the carbonatic rocks of the Ela nappe during their involvement in D1 deformation, since these lithologies formed by sedimentation in marine environment (Furrer et al., 2015). Additionally, sweater infiltration itself may have been possible if the study area was below sea level in Eo-Alpine times. The third hypothesis seems the least favored in light of the temperatures required for serpentinite dehydration, as outlined in Sect. 3.6.3.

3.6.4.1 Early thrusting and V2 veins

Given the pressures of 8–9 kbar existing at the base of the Err nappe during the D1 phase and the V2 veining event at ca. 85 Ma, it seems more likely that the V2 epidote-forming fluids originated from deeper stratigraphic levels than the veining location. The preferred hypothesis for the source of the V2 epidote-forming fluids, thus, is that these fluids were expelled from the underlying carbonatic rocks of the Ela nappe (fluid pathway (3) in Fig. 3.12). Whether or not these fluids contained a contribution from dehydrating serpentinites from the Platta–Lizun–Malenco nappe cannot be constrained with the present data. The presence of non-cohesive fault rocks may have provided sufficient permeability for fluid circulation in the existing D1 compressional regime (e.g., Sibson, 1994; 1996; Bucher and Stober, 2010; Yardley and Bodnar, 2014).

3.6.4.2 Normal faulting and V3+V1 veining event

The V3+V1 veining event occurred during the D2 extensional phase, in which normal faults dissected all stratigraphic levels (Froitzheim et al., 1994; Handy et al., 1996). In this geodynamic context, it is possible that fluid percolation exploited extensional normal faults. Similar scenarios of downward fluid circulation along faults are a likely occurrence (e.g., Manatschal et al., 2000; Incerpi et al., 2018; 2019; Grambling et al., 2021). The fact that the $\delta^{18}O$ values of the V3+V1 epidote-forming fluids are lower than both carbonatic rocks of the Ela nappe and host Albula Granite argues for a fluid source with an even lower $\delta^{18}O$ value. Among the considered potential fluid sources (Fig. 3.12), (modified) seawater or formation/connate waters, or meteoric water might provide the sufficiently low $\delta^{18}O$ values for fluid–rock interaction with Albula Granite (10.4–12.7 ‰) and/or carbonatic rocks of the Ela nappe (26.2–30.4 ‰) to shift the oxygen isotope composition of the epidote-forming fluids to the calculated $\delta^{18}O$ values of 4.0–9.1 ‰. Either fluid source cannot be ascertained or ruled out based on the present data. However, it must be mentioned that a role of meteoric water during the D2 phase and the V3+V1 veining event can only be accepted if the elevation of the Eo-Alpine orogen was sufficiently low (Fig. 3.12). If this was not the case, the only possible fluid source for the V3+V1 veining event was modified seawater or formation/connate waters. In should be once again pointed out that it is not known if the study area was above or below the surface of the sea at this time. In a scenario where the Err nappe was below sea level during the Eo-Alpine orogeny, the presented δD–$\delta^{18}O$ and Pb–Sr isotope data (Figs. 3.10–3.11) may indicate that seawater was the ultimate source of the epidote-forming fluids, which

modified its isotope compositions by interacting with carbonatic rocks and Albula Granite to different extents during the D2 deformation phase (fluid pathway (2) in Fig. 3.12). In any of the presented scenarios, the V3+V1 epidote-forming fluids may have percolated into the Albula Granite by exploiting either newly formed D2 normal faults or inherited rift-related structures such as the Saluver breccia (Figs. 3.1 and 3.2): the clasts themselves of this breccia are made of carbonatic rocks from the Ela nappe and of Albula Granite. A fluid pathway along either syn-extensional or inherited normal faults accounts for the Pb–Sr–O–H isotope characteristics of the V3+V1 epidote-forming fluids during the D2 extensional phase (Fig. 3.12).

3.7 Conclusions

We present U–Pb geochronology and Pb–Sr–O–H isotope geochemistry of epidote in hydrothermal veins from the Albula Pass area. The obtained Late Cretaceous to Paleocene ages of epidote crystallization during veining are unexpected in the study area, which is a typical example of a hyperextended passive continental margin. Here, the continental crust was infiltrated and hydrothermally altered by seawater during Jurassic rifting (e.g., Incerpi et al., 2017; 2018; 2019). Therefore, hydration of the continental crust of the Adriatic passive margin started before tectonic inversion and, as shown here, continued across the Eo-Alpine orogeny. Epidote Pb–Sr isotope data show that, before reaching the veining locations in the Albula Granite, the Eo-Alpine fluids interacted with carbonatic rocks of the Ela nappe. This nappe was thrust on top of the Err nappe during the D1 phase of Eo-Alpine orogeny and shortly before the formation of the oldest epidote veins presented here. Stable isotope geochemistry of epidote suggests a role for modified seawater or formation/connate waters during these orogenic events. It is possible that these fluid were released by carbonatic rocks which formed in a marine environment and that were involved in Eo-Alpine deformation processes. Alternatively, our data may indicate that the Late Cretaceous orogeny occurred under submarine conditions, although a role of meteoric water cannot be rule out provided that the Eo-Alpine orogen had low elevation.

Our work supports the need to combine geochronological and isotope data from different geochemical tools and systems in order to comprehensively describe the hydration history of the continental crust. Such a multimethodological approach allows for more thorough insight into the role of fluid circulation in deformation of crustal rocks. This is especially relevant for primarily water-poor granitoids, which dominate the continental crust and are prominently weakened by

hydrothermal alteration of magmatic minerals (e.g., saussuritization and sericitization of feldspars; e.g., Oliot et al., 2010; Bellahsen et al., 2019; Airaghi et al., 2020; Malatesta et al., 2021). In this respect, using epidote to date and trace hydrothermal events in the crust may add useful information about lower greenschist-facies fluid cycling, which is common in orogens.

Appendix 3A: Methods

3A1 Epidote U–Pb geochronology by LA–ICP–MS

TABLE 3A1

Measurement conditions of Agilent 7900 for U–Pb isotope data by LA-ICP-MS.

RF power	15 October 2020: 1350 W
	3 June 2021: 1400 W
	8 June 2021: 1400 W
Fluence	3 J cm^{-2}
Repetition rate	5 Hz
Cell gas flow	All sessions: 3 ml min^{-1} N_2 and 400 ml min^{-1} He
Sensitivity on mass 232 in NIST612	15 October 2020: 4700 cps ppm^{-1}
(beam size 50 µm, fluence 2.5 J cm^{-2},	3 June 2021: 8150 cps ppm^{-1}
repetition rate 5 Hz, scan rate 5 µm s^{-1})	8 June 2021: 7200 cps ppm^{-1}
232/238 ratio	> 0.97
248/232 ratio	< 0.002
Background	30 s
Pre-cleaning	6 pulses; beam size 64 µm
Ablation time	40 s; beam size 50 µm
Measured masses	206, 207, 208, 232, 238 (all dwell times 40 ms)
Primary reference material	Tara allanite (Smye et al., 2014)
Secondary reference materials	All sessions: CAP and AVC allanite (Barth et al., 1994; Gregory et al., 2007; Burn et al., 2017)

For LA-ICP-MS epidote U–Pb geochronology, a RESOlutionSE 193 nm excimer laser system (Applied Spectra, USA) was used, equipped with a S-155 large-volume constant-geometry chamber (Laurin Technic, Australia) coupled with an Agilent 7900 ICP–QMS. Analytical conditions are as per Table A1. Tara allanite (Smye et al., 2014) was used as primary reference material with the reference values in Table 2 of Peverelli et al. (2021) for correction for downhole fractionation (DF) and for normalization of the measured isotopic ratios. Raw data were reduced using the software Iolite (version 7.08) by the VisualAge_UcomPbine Data Reduction Scheme

(Chew et al., 2014), applying a ^{207}Pb correction to Tara allanite primary reference material. Allanite samples CAP (Barth et al., 1994; Gregory et al., 2007), CAP^{b} (Burn et al., 2017) and AVC (Barth et al., 1994; Gregory et al., 2007), used as secondary reference materials for quality control, returned the U–Pb ages reported in Table 3A2 in Tera–Wasserburg diagrams anchored to an initial $^{207}Pb/^{206}Pb$ ratio of 0.854 ± 0.015 (275 Ma; Stacey and Kramers, 1975; see Barth et al., 1994; Gregory et al., 2007; Smye et al., 2014; Burn et al., 2017).

TABLE 3A2

Tera–Wasserburg and weighted average ^{207}Pb-corrected $^{238}U/^{206}Pb$ ages of CAP, CAP^{b} and AVC allanite reference materials. Age uncertainties are given at 95 % confidence level. All ages are calculated with Isoplot 2.7.5 (Ludwig, 2012). Tera–W. = Tera–Wasserburg.

Analytical session	CAP allanite		CAP^{b} allanite		AVC allanite	
	Tera–W. age[1]	^{207}Pb-corrected $^{238}U/^{206}Pb$ age[2]	Tera–W. age[1]	^{207}Pb-corrected $^{238}U/^{206}Pb$ age[2]	Tera–W. age[1]	^{207}Pb-corrected $^{238}U/^{206}Pb$ age[2]
15 October 2020	285.1 ± 2.5 Ma	285.3 ± 1.9 Ma	284.4 ± 2.7 Ma	284.4 ± 2.2 Ma	282.9 ± 3.1 Ma	283.2 ± 1.7 Ma
3 June 2021	289.4 ± 3.5 Ma	288.3 ± 2.5 Ma	-		281.2 ± 3.5 Ma	282.0 ± 1.8 Ma
8 June 2021	-		282.2 ± 4.0 Ma	283.0 ± 2.7 Ma	282.1 ± 3.4 Ma	282.4 ± 1.5 Ma
Reference Tera–W. age[3]	275.0 ± 4.7 Ma (Gregory et al., 2007)		284.9 ± 2.8 Ma (Burn et al., 2017)		289.6 ± 5.6 Ma (Gregory et al., 2007)	

[1]Anchored to a $^{207}Pb/^{206}Pb$ value of 0.854 ± 0.015 (275 Ma; Stacey and Kramers, 1975; see Gregory et al., 2007).

[2]Weighted average ages calculated from single-spot ^{207}Pb-corrected ages. The $^{207}Pb/^{206}Pb$ value of 0.854 ± 0.015 (275 Ma; Stacey and Kramers, 1975; see Gregory et al., 2007) was used for ^{207}Pb corrections.

The studied epidote vein samples were dated on three different days. On 15 October 2020, epidote in V3 veins ALB19-11 and ALB19-18 were dated. In this analytical session, CAP, CAP^{b} and AVC allanite samples were used as secondary standard, yielding ages of, respectively, 285.1 ± 2.5 Ma, 284.4 ± 2.7 Ma and 282.9 ± 3.1 Ma from anchored Tera–Wasserburg plots. Their weighted average ^{207}Pb-corrected $^{238}U/^{206}Pb$ ages are, respectively, 285.3 ± 1.9 Ma, 284.4 ± 2.2 Ma and 283.2 ± 1.7 Ma. One V2 epidote vein (epidote sample ALB19-4) was analyzed on 3 June 2021. In this second analytical session, secondary standards CAP and AVC allanite gave ages of 289.4 ± 3.5 Ma and 281.2 ± 3.5 Ma, respectively, in anchored Tera–Wasserburg diagrams. These allanite grains returned weighted average ^{207}Pb-corrected $^{238}U/^{206}Pb$ ages of 288.3 ± 2.5 Ma and 282.0 ± 1.8 Ma, respectively. Finally, the V1 epidote vein (epidote sample ALB19-1) was dated on 8 June 2021. In this analytical session, CAP^{b} and AVC allanite samples gave anchored Tera–Wasserburg ages of 282.2 ± 4.0 Ma and 282.1 ± 3.4 Ma, respectively. Their calculated weighted average ^{207}Pb-

corrected $^{238}U/^{206}Pb$ ages are 283.0 ± 2.7 Ma (CAP^b) and 282.4 ± 1.5 Ma (AVC). Although CAP allanite is older than its reference age (see Gregory et al., 2007), CAP^b and AVC allanite samples are within uncertainty of their reference ages (see Burn et al., 2017 and Gregory et al., 2007).

3A2 Measurements of Sr and Pb isotope ratios in epidote by TIMS

Based on LA-ICP-MS data of Sr mass fractions of epidote, samples were prepared from the epidote micro-separates corresponding to ca. 250 ng of Sr and they were weighed in Teflon beakers pre-cleaned with HCl. Samples from standards AGV-2 and GSP-2 (Weis et al., 2006) corresponding to ca. 250 ng of Sr were also prepared. A powdered sample of weakly deformed Albula Granite was also digested in acids by the same procedure used for epidote samples. The Sr fraction was separated by ion chromatography after sample dissolution in acids, and 1 µl of it – corresponding to 250 ng Sr – was loaded on Re filaments by using 1.5 µl Ta-oxide activator. The SRM 987 Sr standard (Weis et al., 2006) was also loaded on filaments and measured for quality control. Measurements of $^{87}Sr/^{86}Sr$ were carried out on a ThermoFisher Triton thermal ionization mass spectrometer (TIMS). The cup configuration was calibrated to detect masses 84, 85, 86 (center cup), 87 and 88. Corrections were applied to account for interference of ^{87}Rb using the IUPAC $^{87}Rb/^{85}Rb$ ratio of 0.385617, and for within-run mass fractionation by using the IUPAC $^{88}Sr/^{86}Sr$ ratio of 8.735209. The SRM 987 standard gave an $^{87}Sr/^{86}Sr$ of 0.710279 ± 0.000020 (2 standard deviation, SD; number of replicates, n = 12).

3A3 Measurements of Pb isotopes in Albula Granite, and Pb–Sr isotopes in carbonatic rocks by solution MC-ICP-MS

The Albula Granite sample was digested in acids as outline in Appendix A2, whereas the carbonatic rocks were dissolved in 7 M HCl. The silicate fraction of the carbonatic samples was not dissolved. Ion chromatography allowed to collect the Sr and Pb fractions in sequence from all samples. After drying, the Pb fractions of all samples (i.e., carbonatic rocks and Albula Granite) contained organics, which were removed with a combination of inverted aqua regia and H_2O_2. Strontium isotope ratios in the granitoid sample were also measured by TIMS, as described in Appendix A2. Strontium isotope data of the carbonatic samples, and Pb isotope ratios of granitoid and carbonatic rocks were measured on a ThermoFisher Neptune Plus MC-ICP-MS in desolvated plasma mode coupled to a CETAC Aridus 2 desolvating system. A Tl spike was used to correct

for instrumental mass fractionation during Pb isotope measurements. The SRM 981 standard was used for quality control, obtaining Pb isotope ratios identical within uncertainties to those reported by Rehkämper and Mezger (2000; their Table 4).

For Sr isotope measurements, the IUPAC $^{87}Rb/^{85}Rb$ and $^{88}Sr/^{86}Sr$ values of 0.385617 and 8.735209 were used to correct for the interference of ^{87}Rb and within-run mass bias, respectively. To assess external reproducibility, the SRM 987 standard (Weis et al., 2006) was measured at the beginning and at the end of the measurement sequence, obtaining 0.723745 ± 0.000014 (2 SE) and 0.723640 ± 0.000012.

3A4 Stable isotope data

Measurements of hydrogen isotopic ratios were carried out in ca. 4 mg of epidote material at the Joint Goethe University Frankfurt–Senckenberg BiK-F Stable Isotope Facility (Frankfurt, Germany) on a Thermo high-temperature conversion elemental analyzer (TC/EA) coupled to a Thermo MAT 253 mass spectrometer in continuous flow mode. For sample preparation, epidote grains were handpicked and then ground in ethanol. Standards USGS57 (biotite), USGS58 (muscovite), NBS22 (oil) and CH7 (polyethylene foil) were used for quality control, obtaining δD values of, respectively, -28.4 ‰, -91.9 ‰, -100.0 ‰ and -116.9 ‰ after correction for mass bias, daily drift of the thermal combustion reactor and offset from the certified reference. An in-house standard ("epidote_1867m"; Bird et al., 1988) gave a δD of -95 ‰.

For measurements of oxygen isotope ratios on single epidote grains, a CO_2-laser extraction line and fluorination coupled to a Finnigan MAT 253 mass spectrometer was used at University of Lausanne (Switzerland). For details on the procedure, see Lacroix and Vennemann (2015). A total of three CO_2-laser fluorination analysis sessions were carried out. All results were corrected to session values of the in-house quartz standard LS-1. Daily replicates of the LS-1 quartz standard report better than 0.1 ‰ (standard deviation, 1 SD); deviation from the accepted $\delta^{18}O$ value of 18.1 ‰ report better than 0.2 ‰ (1 SD). Unknowns replicates are within 0.3 ‰ or better.

Oxygen and hydrogen stable isotope data are reported as δD and $\delta^{18}O$, respectively, relative to the Vienna Standard Mean Ocean Water (V-SMOW):

$$\delta^{18}O = \frac{(^{18}O/^{16}O)_{sample} - (^{18}O/^{16}O)_{V-SMOW}}{(^{18}O/^{16}O)_{V-SMOW}} \times 1000\ ‰.$$

$$\delta D = \frac{(D/H)_{sample} - (D/H)_{V-SMOW}}{(D/H)_{V-SMOW}} \times 1000\ ‰.$$

3A5 Temperature of crystallization of V3 vein epidote

For calculation of the hydrogen and oxygen isotope compositions of the epidote-forming fluids, we used the fractionation equations of Chacko et al. (1999) and Zheng (1993), respectively. These calculations, however, require an estimate of the temperature of crystallization of epidote. In sample ALB19-11, epidote and chlorite are in textural equilibrium, allowing to estimate the temperature of crystallization from the chemical composition of chlorite (see Lanari et al., 2012; and references therein). The chemical composition of chlorite was measured on a JEOL-8200 electron probe micro-analyzer (EPMA) with a specimen current of 20 nA, using the following standards for calibration: albite (Na_2O), orthoclase (Si_2O and K_2O), anorthite (Al_2O_3 and CaO), forsterite (MgO), rutile (TiO_2), magnetite (FeO) and pyrolusite (MnO). For temperature estimation, the method of Vidal et al. (2005; 2006) implemented in the program ChlMicaEqui (Lanari, 2012) was applied. The temperature was determined when convergence of two independent reactions involving chlorite end-members, quartz and H_2O was less than 30 °C at a pressure of 5 kbar, based on the maximum pressure conditions reached at the base of the Err nappe during the D2 phase (see Handy et al., 1996). Slightly lower pressure conditions (e.g., 3 kbar) would not affect temperature estimated by more than a few degrees Celsius.

Appendix 3B: Raw Pb and Sr, and U–Pb isotope data.

TABLE 3B1

Raw $^{207}Pb/^{206}Pb$ and $^{87}Sr/^{86}Sr$ data, and Rb, Sr, U and Pb mass fractions in Albula Granite and carbonatic rocks. All uncertainties are 2 standard errors (2 SE). Isotope measurements are by Neptune MC-ICP-MS unless specified ([1]), and trace element contents by quadrupole ICP-MS. Superscript 1: measured by TIMS.

	Sample	$^{87}Sr/^{86}Sr$	2 SE	$^{207}Pb/^{206}Pb$	2 SE	Rb [µg g^{-1}]	Sr [µg g^{-1}]	U [µg g^{-1}]	Pb [µg g^{-1}]
Host	Albula Granite	0.718021[1]	0.000008	0.811293	0.000018	11	78	2.7	8.8
Carb. rocks	Mingér Fm.	0.707745	0.000012	0.818635	0.000013	1.0	330	0.21	2.2
	Hauptdolomit Gr.	0.712967	0.000013	0.835936	0.000021	1.1	170	1.0	120
	Allgäu Fm.	0.707448	0.000014	0.833177	0.000020	1.2	1950	0.25	2.5

TABLE 3B2

$^{238}U/^{206}Pb$ and $^{207}Pb/^{206}Pb$ ratios, and their uncertainties as 2 standard errors (2 SE) measured by LA-ICP-MS in the studied epidote samples in veins V1–V3.

Vein V1				
Epidote sample ALB19-1				
Analysis	**$^{238}U/^{206}Pb$**	**2 SE**	**$^{207}Pb/^{206}Pb$**	**2 SE**
1	0.124	0.004	0.821	0.004
2	0.176	0.006	0.817	0.011
3	0.080	0.002	0.8228	0.0047
4	0.265	0.009	0.821	0.011
5	0.059	0.002	0.8208	0.0047
6	0.115	0.003	0.82	0.006
7	0.769	0.021	0.8207	0.0097
8	0.027	0.002	0.824	0.011
9	0.040	0.001	0.820	0.005
10	0.058	0.002	0.8289	0.0056
11	0.337	0.018	0.8218	0.0094
12	0.310	0.010	0.813	0.012
13	0.047	0.004	0.819	0.021
14	0.008	0.000	0.8185	0.0059
15	0.060	0.003	0.823	0.011
16	0.064	0.003	0.821	0.012
17	0.231	0.009	0.801	0.013
18	0.412	0.012	0.8194	0.0091
19	0.111	0.005	0.809	0.013
20	0.053	0.005	0.817	0.019
21	0.025	0.002	0.826	0.012
22	0.044	0.002	0.8131	0.0071
23	0.055	0.003	0.829	0.012
24	1.11	0.03	0.82	0.01
Vein V2				
Epidote sample ALB19-4				
Analysis	**$^{238}U/^{206}Pb$**	**2 SE**	**$^{207}Pb/^{206}Pb$**	**2 SE**
1	1.08	0.03	0.7975	0.0053
2	0.935	0.030	0.800	0.005
3	1.30	0.04	0.7916	0.0061
4	2.11	0.08	0.7854	0.0033
5	0.978	0.027	0.7968	0.0033
6	0.724	0.026	0.7988	0.0049
7	0.839	0.023	0.8037	0.0058
8	0.895	0.029	0.7964	0.0053
9	2.07	0.06	0.7874	0.0041
10	1.36	0.04	0.7938	0.008
11	4.63	0.13	0.7625	0.0052
12	0.610	0.017	0.8024	0.0048
13	1.35	0.04	0.8006	0.0051
14	0.700	0.019	0.8047	0.0053
15	1.38	0.04	0.795	0.006

16	1.012	0.031	0.7983	0.0056
17	0.570	0.021	0.804	0.004
18	1.51	0.05	0.7928	0.0062
19	0.528	0.014	0.8018	0.0033
20	1.01	0.03	0.7994	0.0054
21	0.395	0.011	0.8045	0.0039
22	1.42	0.04	0.792	0.006
Vein V3				
Epidote sample ALB19-11				
Analysis	**$^{238}U/^{206}Pb$**	**2 SE**	**$^{207}Pb/^{206}Pb$**	**2 SE**
1	0.797	0.018	0.8283	0.0079
2	0.592	0.013	0.823	0.005
3	1.14	0.02	0.8264	0.0053
4	0.831	0.019	0.827	0.011
5	1.14	0.02	0.82	0.01
6	0.567	0.014	0.8308	0.0084
7	0.760	0.018	0.819	0.012
8	0.660	0.014	0.8338	0.0084
9	3.02	0.06	0.8064	0.0072
10	0.284	0.006	0.826	0.007
11	1.02	0.02	0.830	0.008
12	0.331	0.007	0.8302	0.0052
13	0.123	0.003	0.8303	0.0046
14	0.956	0.037	0.8226	0.0082
15	0.883	0.020	0.8266	0.0088
16	0.706	0.015	0.8264	0.0067
17	3.11	0.06	0.8001	0.0079
18	0.660	0.016	0.820	0.008
19	1.07	0.02	0.8238	0.0074
20	0.797	0.018	0.8292	0.0083
21	0.423	0.009	0.8233	0.0046
22	0.352	0.008	0.8258	0.0067
23	0.464	0.011	0.8314	0.0076
24	0.396	0.009	0.8195	0.0078
25	0.144	0.003	0.8285	0.0052
26	0.378	0.009	0.823	0.006
27	0.464	0.010	0.822	0.007
28	0.259	0.005	0.8225	0.0047
29	0.457	0.010	0.8215	0.0057
30	0.695	0.017	0.8226	0.0064
31	0.123	0.003	0.8241	0.0051
32	0.342	0.009	0.8275	0.0054
33	0.857	0.018	0.822	0.008
34	0.397	0.009	0.8252	0.0066
35	0.136	0.003	0.828	0.005
36	0.241	0.005	0.8286	0.0074
37	0.943	0.021	0.83	0.01
Epidote sample ALB19-18				

Analysis	$^{238}U/^{206}Pb$	2 SE	$^{207}Pb/^{206}Pb$	2 SE
1	4.75	0.11	0.7938	0.0089
2	0.199	0.004	0.827	0.004
3	1.18	0.03	0.818	0.0063
4	1.56	0.04	0.8112	0.0063
5	1.55	0.03	0.81	0.01
6	0.356	0.008	0.8207	0.0047
7	1.20	0.03	0.8151	0.0063
8	0.548	0.011	0.820	0.005
9	0.725	0.015	0.8189	0.0044
10	0.935	0.022	0.8179	0.0053
11	1.76	0.04	0.811	0.005
12	0.334	0.009	0.8198	0.0041
13	0.199	0.004	0.8245	0.0037
14	0.940	0.024	0.8175	0.0065
15	0.371	0.007	0.8196	0.0038
16	0.443	0.010	0.8226	0.0038
17	1.49	0.03	0.8106	0.0047
18	0.980	0.020	0.8169	0.0055
19	0.679	0.015	0.820	0.005
20	0.875	0.024	0.8182	0.0035
21	1.33	0.03	0.8142	0.0054
22	1.10	0.02	0.8125	0.0083
23	0.839	0.019	0.8184	0.0063
24	0.840	0.017	0.817	0.005
25	2.34	0.06	0.8078	0.008
26	0.428	0.009	0.8174	0.0037
27	0.411	0.013	0.8161	0.0041
28	0.314	0.007	0.8182	0.0042
29	0.314	0.006	0.8193	0.0042
30	1.65	0.04	0.8101	0.0063
31	1.15	0.02	0.8133	0.0054
32	1.78	0.04	0.8095	0.0078

Appendix 3C: Chemical composition of chlorite by electron probe microanalyzer (EPMA).

Table 3C1

Chemical composition of chlorite in vein ALB19-11 by electron probe microanalyzer (EPMA). All data are in atoms per formula unit unless specified in brackets, calculated on a 14 anhydrous-oxygen basis including Fe^{3+}. Each element is indicated with the occupied crystallographic site in parentheses.

Spot	Si(T1+T2)	Al(T2)	Al(M1)	Mg(M1)	Fe^{2+}(M1)	V(M1)	Mg(M2+M3)	Fe(M2+M3)	Al(M2+M3)	Al(M4)	Fe^{3+}(M4)	XMg [-]	T [°C][1]
1	2.75	1.25	0.25	0.26	0.18	0.31	1.95	1.33	0.63	0.26	0.74	0.59	275
2	2.76	1.24	0.24	0.25	0.17	0.34	1.92	1.32	0.68	0.20	0.80	0.59	265
3	2.75	1.25	0.25	0.26	0.17	0.31	1.98	1.30	0.64	0.21	0.79	0.60	277
4	2.79	1.21	0.21	0.25	0.15	0.39	1.98	1.17	0.78	0.08	0.92	0.63	252
5	2.78	1.22	0.22	0.25	0.16	0.38	1.92	1.24	0.75	0.14	0.86	0.61	251
6	2.77	1.23	0.23	0.25	0.16	0.36	1.95	1.25	0.72	0.17	0.83	0.61	261
7	2.78	1.22	0.22	0.25	0.16	0.37	1.96	1.22	0.74	0.12	0.88	0.62	257
8	2.79	1.21	0.21	0.25	0.15	0.39	1.95	1.17	0.79	0.08	0.92	0.62	250
9	2.76	1.24	0.24	0.26	0.17	0.33	1.95	1.30	0.67	0.21	0.79	0.60	269
10	2.79	1.21	0.21	0.24	0.15	0.40	1.90	1.23	0.79	0.12	0.88	0.61	244
11	2.76	1.24	0.24	0.25	0.17	0.34	1.94	1.30	0.68	0.18	0.82	0.60	268
12	2.78	1.22	0.22	0.25	0.16	0.37	1.92	1.27	0.73	0.16	0.84	0.60	255
13	2.75	1.25	0.25	0.26	0.17	0.33	1.97	1.29	0.66	0.22	0.78	0.60	268
14	2.78	1.22	0.22	0.25	0.15	0.37	1.98	1.19	0.75	0.14	0.86	0.62	252
15	2.77	1.23	0.23	0.26	0.15	0.35	2.01	1.20	0.70	0.17	0.83	0.63	262
16	2.77	1.23	0.23	0.26	0.15	0.36	2.04	1.16	0.72	0.16	0.84	0.64	258
17	2.74	1.25	0.25	0.27	0.17	0.30	2.01	1.29	0.61	0.28	0.72	0.61	279
18	2.77	1.23	0.23	0.26	0.16	0.35	1.97	1.23	0.71	0.18	0.82	0.61	261
19	2.75	1.25	0.25	0.26	0.16	0.32	2.02	1.25	0.65	0.24	0.76	0.62	271
20	2.77	1.23	0.23	0.26	0.16	0.35	2.01	1.21	0.70	0.20	0.80	0.63	263
21	2.74	1.26	0.26	0.27	0.17	0.30	2.04	1.28	0.61	0.26	0.74	0.61	280
22	2.77	1.23	0.23	0.27	0.15	0.36	2.07	1.13	0.72	0.15	0.85	0.65	261
23	2.73	1.27	0.27	0.28	0.18	0.28	2.05	1.30	0.56	0.27	0.73	0.61	292
24	2.71	1.29	0.29	0.29	0.19	0.23	2.07	1.37	0.47	0.33	0.67	0.60	318
25	2.80	1.20	0.20	0.27	0.13	0.41	2.08	1.02	0.82	0.06	0.94	0.67	248
26	2.77	1.23	0.23	0.27	0.14	0.36	2.09	1.11	0.72	0.12	0.88	0.65	264
27	2.78	1.22	0.22	0.27	0.14	0.37	2.06	1.10	0.75	0.14	0.86	0.65	256
28	2.78	1.22	0.22	0.28	0.15	0.35	2.10	1.11	0.71	0.09	0.91	0.65	271
29	2.76	1.24	0.24	0.26	0.16	0.34	2.01	1.24	0.67	0.14	0.86	0.62	272
30	2.82	1.17	0.17	0.26	0.13	0.44	2.02	1.00	0.89	0.00	1.00	0.67	263
31	2.77	1.23	0.23	0.27	0.15	0.35	2.07	1.14	0.71	0.14	0.86	0.65	264
32	2.72	1.28	0.28	0.29	0.18	0.25	2.12	1.30	0.50	0.30	0.70	0.62	310
33	2.76	1.24	0.24	0.27	0.16	0.33	2.05	1.20	0.67	0.20	0.80	0.63	271

34	2.76	1.24	0.24	0.27	0.16	0.34	2.04	1.21	0.67	0.16	0.84	0.63	272
35	2.70	1.30	0.30	0.31	0.21	0.19	2.10	1.43	0.39	0.45	0.55	0.60	340
36	2.76	1.23	0.23	0.27	0.15	0.35	2.07	1.14	0.71	0.18	0.82	0.64	263
37	2.83	1.17	0.17	0.27	0.12	0.44	2.10	0.96	0.88	0.04	0.96	0.69	239
38	2.82	1.18	0.18	0.27	0.12	0.43	2.08	0.98	0.87	0.02	0.98	0.68	248
39	2.76	1.23	0.23	0.26	0.15	0.35	2.04	1.17	0.70	0.19	0.81	0.64	262
40	2.74	1.26	0.26	0.26	0.18	0.30	1.95	1.36	0.61	0.34	0.66	0.59	277
41	2.78	1.22	0.22	0.26	0.15	0.37	2.00	1.16	0.75	0.09	0.91	0.63	258
42	2.80	1.20	0.20	0.25	0.14	0.40	1.99	1.11	0.81	0.05	0.95	0.64	250
43	2.79	1.21	0.21	0.26	0.14	0.39	2.04	1.10	0.78	0.14	0.86	0.65	249
44	2.78	1.22	0.22	0.27	0.15	0.36	2.07	1.13	0.72	0.15	0.85	0.65	263
45	2.73	1.27	0.27	0.29	0.17	0.26	2.09	1.28	0.53	0.28	0.72	0.62	300
46	2.78	1.22	0.22	0.27	0.14	0.37	2.07	1.11	0.75	0.13	0.87	0.65	257
47	2.75	1.25	0.25	0.27	0.17	0.32	2.01	1.26	0.64	0.26	0.74	0.61	272

[1]Temperature calculated following Vidal et al. (2005; 2006).

References

Airaghi, L., Bellahsen, N., Dubacq, B., Chew, D., Rosenberg, C., Janots, E., Waldner, M., Magnin, V., 2020. Pre-orogenic upper crustal softening by lower greenschist facies metamorphic reactions in granites of the central Pyrenees. J. Metamorph. Geol. 38, 183–204. https://doi.org/10.1111/jmg.12520

Anenburg, M., Katzir, Y., Rhede, D., Jöns, N., Bach, W., 2015. Rare earth element evolution and migration in plagiogranites: a record preserved in epidote and allanite of the Troodos ophiolite. Contrib. to Mineral. Petrol. 169. https://doi.org/10.1007/s00410-015-1114-y

Barth, S., Oberli, F., Meier, M., 1994. ThPb versus UPb isotope systematics in allanite from co-genetic rhyolite and granodiorite: implications for geochronology. Earth Planet. Sci. Lett. 124, 149–159. https://doi.org/10.1016/0012-821X(94)00073-5

Bellahsen, N., Bayet, L., Denele, Y., Waldner, M., Airaghi, L., Rosenberg, C., Dubacq, B., Mouthereau, F., Bernet, M., Pik, R., Lahfid, A., Vacherat, A., 2019. Shortening of the axial zone, pyrenees: Shortening sequence, upper crustal mylonites and crustal strength. Tectonophysics 766, 433–452. https://doi.org/10.1016/j.tecto.2019.06.002

Bird, D.K., Spieler, A.R., 2004. Epidote in Geothermal Systems. Trace element geochemistry of epidote minerals. Rev. Mineral. Geochemistry 56, 235–300. https://doi.org/10.2138/gsrmg.56.1.235

Bons, P.D., Elburg, M.A., Gomez-Rivas, E., 2012. A review of the formation of tectonic veins and their microstructures. J. Struct. Geol. 43, 33–62. https://doi.org/10.1016/j.jsg.2012.07.005

Brett-Adams, A.C., Diamond, L.W., Petrini, C., Madonna, C., 2021. Influence of in-situ temperatures and pressures on the permeability of hydrothermally altered basalts in the oceanic crust. Tectonophysics 815, 228994. https://doi.org/10.1016/j.tecto.2021.228994

Bucher, K., Stober, I., 2010. Fluids in the upper continental crust. Geofluids 10, 241–253. https://doi.org/10.1111/j.1468-8123.2010.00279.x

Burn, M., Lanari, P., Pettke, T., Engi, M., 2017. Non-matrix-matched standardisation in LA-ICP-MS analysis: General approach, and application to allanite Th-U-Pb dating. J. Anal. At. Spectrom. 32, 1359–1377. https://doi.org/10.1039/c7ja00095b

Campani, M., Mulch, A., Kempf, O., Schlunegger, F., Mancktelow, N., 2012. Miocene paleotopography of the Central Alps. Earth Planet. Sci. Lett. 337–338, 174–185. https://doi.org/10.1016/j.epsl.2012.05.017

Chew, D.M., Petrus, J.A., Kamber, B.S., 2014. U-Pb LA-ICPMS dating using accessory mineral standards with variable common Pb. Chem. Geol. 363, 185–199. https://doi.org/10.1016/j.chemgeo.2013.11.006

Clément, M., Padrón-Navarta, J.A., Tommasi, A., 2020. Interplay between fluid extraction mechanisms and antigorite dehydration reactions (Val Malenco, Italian Alps). J. Petrol. 60, 1935–1962. https://doi.org/10.1093/petrology/egz058

Dahl, P. S.: A crystal-chemical basis for Pb retention and fissiontrack annealing systematics in U-bearing mineral, with implications for geochronology, Earth Planet. Sci. Lett., 150, 277–290, 1997.

Dempster, T.J., 1986. Isotope systematics in minerals: biotite rejuvenation and exchange during Alpine metamorphism. Earth Planet. Sci. Lett. 78, 355–367. https://doi.org/10.1016/0012-821X(86)90003-8

Elburg, M.A., Bons, P.D., Foden, J., Passchier, C.W., 2002. The origin of fibrous veins: constraints from geochemistry, in: Deformation Mechanisms, Rheology and Tectonics: Current Status and Future Perspectives, Geological Society of London, special publication, Vol. 200, pp. 103-118.

Enami, M., Liou, J.G., Mattinson, C.G., 2004. Epidote minerals in high P/T metamorphic terranes: Subduction zone and high- to ultrahigh-pressure metamorphism. Rev. Mineral. Geochemistry 56, 347–398. https://doi.org/10.2138/gsrmg.56.1.347

Epin, M.E., Manatschal, G., Amann, M., 2017. Defining diagnostic criteria to describe the role of rift inheritance in collisional orogens: the case of the Err-Platta nappes (Switzerland). Swiss J. Geosci. 110, 419–438. https://doi.org/10.1007/s00015-017-0271-6

Farver, J.R., 2010. Oxygen and hydrogen diffusion in minerals. Rev. Mineral. Geochemistry 72, 447–507. https://doi.org/10.2138/rmg.2010.72.10

Faure, G., Assereto, R., Tremba, E.L., 1978. Strontium isotope composition of marine carbonates of Middle Triassic to Early Jurassic age, Lombardic Alps, Italy. Sedimentology 25, 523–543. https://doi.org/10.1111/j.1365-3091.1978.tb02078.x

Feineman, M.D., Ryerson, F.J., DePaolo, D.J., Plank, T., 2007. Zoisite-aqueous fluid trace element partitioning with implications for subduction zone fluid composition. Chem. Geol. 239, 250–265. https://doi.org/10.1016/j.chemgeo.2007.01.008

Ferry, J.M., 1979. Reaction mechanisms, physical conditions, and mass transfer during hydrothermal alteration of mica and feldspar in granitic rocks from south-central Maine, USA. Contrib. to Mineral. Petrol. 68, 125–139. https://doi.org/10.1007/BF00371895

Franz, G., Liebscher, A., 2004. Physical and Chemical Properties of the Epidote Minerals-An Introduction-. Rev. Mineral. Geochemistry 56, 1–81. https://doi.org/10.2138/gsrmg.56.1.1

Frei, D., Liebscher, A., Franz, G., Dulski, P., 2004. Trace element geochemistry of epidote minerals. Rev. Mineral. Geochemistry 56, 553–605. https://doi.org/10.2138/gsrmg.56.1.553

Froitzheim, N., Schmid, S.M., Conti, P., 1994. Repeated change from crustal shortening to orogen-parallel extension in the Austroalpine units of Graubünden. Eclogae geol. Helv. 87(2), 559–612.

Froitzneim, N., Manatschal, G., 1996. Kinematics of Jurassic rifting, mantle exhumation, and passive-margin formation in the Austroalpine and Penninic nappes (eastern Switzerland). Bull. Geol. Soc. Am. 108, 1120–1133. https://doi.org/10.1130/0016-7606(1996)108<1120:KOJRME>2.3.CO;2

Furrer, H., Froitzheim, N., Maisch, M., and Heierli, H., 2015: Blatt 1237 Albulapass, Geol. Atlas Schweiz 1:25 000, Erläut. 81, Federal Office of Topography swisstopo, Bern, Switzerland.

Gardien, V., Paquette, J.L., 2004. Ion microprobe and ID-TIMS U-Pb dating on zircon grains from leg 173 amphibolites: Evidence for Permian magmatism on the West Iberian margin. Terra Nov. 16, 226–231. https://doi.org/10.1111/j.1365-3121.2004.00554.x

Goncalves, P., Oliot, E., Marquer, D., Connolly, J.A.D., 2012. Role of chemical processes on shear zone formation: An example from the grimsel metagranodiorite (Aar massif, Central Alps). J. Metamorph. Geol. 30, 703–722. https://doi.org/10.1111/j.1525-1314.2012.00991.x

Grambling, T.A., Jessup, M.J., Newell, D.L., Methner, K., Mulch, A., Hughes, C.A., Shaw, C.A., 2022. Miocene to modern hydrothermal circulation and high topography during synconvergent extension in the Cordillera Blanca, Peru. Geology 50, 106–110. https://doi.org/10.1130/G49263.1

Grapes, R.H., Hoskin, P.W.O., 2004. Epidote group minerals in low-medium pressure metamorphic terranes. Rev. Mineral. Geochemistry 56, 301–345. https://doi.org/10.2138/gsrmg.56.1.301

Gregory, C.J., Rubatto, D., Allen, C.M., Williams, I.S., Hermann, J., Ireland, T., 2007. Allanite micro-geochronology: A LA-ICP-MS and SHRIMP U-Th-Pb study. Chem. Geol. 245, 162–182. https://doi.org/10.1016/j.chemgeo.2007.07.029

Guillong, M., Meier, D.L., Allan, M.M., Heinrich, C.A, Yardley, B.W.D., 2008. SILLS: A Matlab-Based Program for the Reduction of Laser Ablation ICP–MS Data of Homogeneous Materials and Inclusions. Mineral. Assoc. Canada Short Course 40(June 2015), 328–333.

Halter, W.E., Pettke, T., Heinrich, C.A., Rothen-Rutishauser, B., 2002. Major to trace element analysis of melt inclusions by laser-ablation ICP-MS: Methods of quantification. Chem. Geol. 183, 63–86. https://doi.org/10.1016/S0009-2541(01)00372-2

Handy, M.R., 1996. The transition from passive to active margin tectonics: A case study from the Zone of Samedan (eastern Switzerland). Int. J. Earth Sci. 85, 832–851. https://doi.org/10.1007/s005310050115

Handy, M.R., Herwegh, M., Kamber, B.S., Tietz, R., Villa, I.M., 1996. Geochronologic, petrologic and kinematic constraints on the evolution of the Err-Platta boundary, part of a fossil continent-ocean suture in the Alps (eastern Switzerland). Schweizerische Mineral. und Petrogr. Mitteilungen 76, 453–474.

Hoef, J. 2018. Stable isotope geochemistry. Springer International Publishing AG, part of Springer Nature 2018. https://doi.org/10.1016/s0037-0738(97)00056-0

Hofmann, B.A., Helfer, M., Diamond, L.W., Villa, I.M., Frei, R., Eikenberg, J., 2004. Topography-driven hydrothermal breccia mineralization of Pliocene age at Grimsel Pass, Aar massif, Central Swiss Alps. Schweizerische Mineral. und Petrogr. Mitteilungen 84, 271–302.

Horwitz, E., Dietz, M.L., Chiarizia, R., 1992. The application of novel extraction chromatographic materials to the characterization of radioactive waste solutions. Journal of Radioanalytical and Nuclear Chemistry 161, 575–583

Humphris, S.E., Thompson, G., 1978. Hydrothermal alteration of oceanic basalts by seawater. Geochim. Cosmochim. Acta 42, 107–125. https://doi.org/10.1016/0016-7037(78)90221-1

Incerpi, N., Martire, L., Manatschal, G., Bernasconi, S.M., 2017. Evidence of hydrothermal fluid flow in a hyperextended rifted margin: the case study of the Err nappe (SE Switzerland). Swiss J. Geosci. 110, 439–456. https://doi.org/10.1007/s00015-016-0235-2

Incerpi, N., Martire, L., Bernasconi, S.M., Manatschal, G., Gerdes, A., 2018. Silica-rich septarian concretions in biogenic silica-poor sediments: A marker of hydrothermal activity at fossil

hyper-extended rifted margins (Err nappe, Switzerland). Sediment. Geol. 378, 19–33. https://doi.org/10.1016/j.sedgeo.2018.10.005

Incerpi, N., Martire, L., Manatschal, G., Bernasconi, S.M., Gerdes, A., Czuppon, G., Palcsu, L., Karner, G.D., Johnson, C.A., Figueredo, P.H., 2020. Hydrothermal fluid flow associated to the extensional evolution of the Adriatic rifted margin: Insights from the pre- to post-rift sedimentary sequence (SE Switzerland, N ITALY). Basin Res. 32, 91–115. https://doi.org/10.1111/bre.12370

Kralik, M., Clauer, N., Holnsteiner, R., Huemer, H., Kappel, F., 1992. Recurrent fault activity in the Grimsel Test Site (GTS, Switzerland) : revealed by Rb-Sr, K-Ar and tritium isotope techniques. J. - Geol. Soc. 149, 293–301. https://doi.org/10.1144/gsjgs.149.2.0293

Krsnik, E., Methner, K., Campani, M., Botsyun, S., Mutz, S.G., Ehlers, A., Kempf, O., Fiebig, J., Schlunegger, F., and Mulch, A., 2021. Miocene high elevation and high relief in the central Alps: Solid Earth 12, 2615–2631, https://doi .org /10 .5194 /se-12-2615-2021.

Lanari, P., 2012. P-T-e Micro-mapping in Metamorphic Rocks. Application to the Alps and the Himalaya. Ph.D. Thesis. University of Grenoble, pp. 544.

Ludwig, K.R., 2012. User's Manual for A Geochronological Toolkit for Microsoft Excel. Berkeley Geochronology Center. Options (5).

Malatesta, C., Crispini, L., Ildefonse, B., Federico, L., Lisker, F., Läufer, A., 2021. Microstructures of epidote-prehnite bearing damaged granitoids (northern Victoria Land, Antarctica): clues for the interaction between faulting and hydrothermal fluids. J. Struct. Geol. 147. https://doi.org/10.1016/j.jsg.2021.104350

Manatschal, G., Nievergelt, P., 1997. A continent-ocean transition recorded in the Err and Platta nappes (Eastern Switzerland). Eclogae Geol. Helv. 90, 3–27.

Manatschal, G., Marquer, D., Früh-Green, G.L., 2000. Channelized fluid flow and mass transfer along a rift-related detachment fault (Eastern Alps, Southeast Switzerland). Bull. Geol. Soc. Am. 112, 21–33. https://doi.org/10.1130/0016-7606(2000)112<21:CFFAMT>2.0.CO;2

Manatschal, G., Lavier, L., Chenin, P., 2015. The role of inheritance in structuring hyperextended rift systems: Some considerations based on observations and numerical modeling. Gondwana Res. 27, 140–164. https://doi.org/10.1016/j.gr.2014.08.006

Marquer, D., Burkhard, M., 1992. Fluid circulation, progressive deformation and mass-transfer processes in the upper crust: the example of basement-cover relationships in the External Crystalline Massifs, Switzerland. J. Struct. Geol. 14(8–9), 1047–1057.

Marquer, D., Peucat, J.J., 1994. Rb-Sr systematics of recrystallized shear zones at the greenschist-amphibolite transition: examples from granites in the Swiss central Alps. Schweizerische Mineral. und Petrogr. Mitteilungen 74, 343–358.

McArthur, J.M., Howarth, R.J., Shields, G.A., 2012. Strontium isotope stratigraphy. Geol. Time Scale 2012 127–144. https://doi.org/10.1016/B978-0-444-59425-9.00007-X

Mohn, G., Manatschal, G., Masini, E., Müntener, O., 2011. Rift-related inheritance in orogens: A case study from the Austroalpine nappes in Central Alps (SE-Switzerland and N-Italy). Int. J. Earth Sci. 100, 937–961. https://doi.org/10.1007/s00531-010-0630-2

Mohn, G., Manatschal, G., Beltrando, M., Masini, E., Kusznir, N., 2012. Necking of continental crust in magma-poor rifted margins: Evidence from the fossil Alpine Tethys margins. Tectonics 31, 1–28. https://doi.org/10.1029/2011TC002961

Morad, S., El-Ghali, M.A.K., Caja, M.A., Sirat, M., Al-Ramadan, K., Manurberg, H., 2010. Hydrothermal alteration of plagioclase in granitic rocks from Proterozoic basement of SE Sweden. Geol. J. 45, 105–116. https://doi.org/10.1002/gj.1178

Mulch, A., Teyssier, C., Cosca, M.A., Vennemann, T.W., 2006. Thermomechanical analysis of strain localization in a ductile detachment zone. J. Geophys. Res. Solid Earth 111, 1–20. https://doi.org/10.1029/2005JB004032

Nägler, T.F., Kamber, B.S., 1996. A new silicate dissolution procedure for isotope studies on garnet and other rock forming minerals. Schweizerische Mineral. und Petrogr. Mitteilungen 76, 75–80. https://doi.org/10.5169/seals-57688

Oliot, E., Goncalves, P., Marquer, D., 2010. Role of plagioclase and reaction softening in a metagranite shear zone at mid-crustal conditions (Gotthard Massif, Swiss Central Alps). J. Metamorph. Geol. 28, 849–871. https://doi.org/10.1111/j.1525-1314.2010.00897.x

Pettke, T., Diamond, L.W., Kramers, J.D., 2000. Mesothermal gold lodes in the north-western Alps: A review of genetic constraints from radiogenic isotopes. Eur. J. Mineral. 12, 213–230. https://doi.org/10.1127/ejm/12/1/0213

Pettke, T., Oberli, F., Audétat, A., Guillong, M., Simon, A.C., Hanley, J.J., Klemm, L.M., 2012. Recent developments in element concentration and isotope ratio analysis of individual fluid

inclusions by laser ablation single and multiple collector ICP-MS. Ore Geol. Rev. 44, 10–38. https://doi.org/10.1016/j.oregeorev.2011.11.001

Peverelli, V., Ewing, T., Rubatto, D., Wille, M., Berger, A., Villa, I.M., Lanari, P., Pettke, T., Herwegh, M., 2021. U−Pb geochronology of epidote by laser ablation inductively coupled plasma mass spectrometry (LA-ICP-MS) as a tool for dating hydrothermal-vein formation. Geochronology 3, 123–147. https://doi.org/10.5194/gchron-3-123-2021

Peverelli, V., Berger, A., Mulch, A., Pettke, T., Piccoli, F., Herwegh, M., 2022. Epidote U–Pb geochronology and H isotope geochemistry trace pre-orogenic hydration of mid-crustal granitoids. GEOLOGY, https://doi.org/10.1130/G50028.1

Picazo, S.M., Ewing, T.A., Müntener, O., 2019. Paleocene metamorphism along the Pennine–Austroalpine suture constrained by U–Pb dating of titanite and rutile (Malenco, Alps). Swiss J. Geosci. 112, 517–542. https://doi.org/10.1007/s00015-019-00346-1

Pinto, V.H.G., 2014. Linking tectonic evolution with fluid history in hyperextended rifted margins: examples from the fossil Alpine and Pyrenean rift systems, and the present-day Iberia rifted margin. Ph.D. Thesis. University of Strasbourg, pp. 256.

Pinto, V.H.G., Manatschal, G., Karpoff, A.M., Viana, A., 2015. The example of Alpine Tethyan rifted margins. Geochemistry Geophys. Geosystems 16, 3271–3308. https://doi.org/10.1002/2015GC005830.Received

Quistini, S., Oddone, M., Villa. I.M., 2017. Sustainability of aquifers in Mali: Sr and Pb isotopic signatures and tritium ages. Abstract, SGI Congress, Pisa 22-9, p. 25.

Ricchi, E., Bergemann, C.A., Gnos, E., Berger, A., Rubatto, D., Whitehouse, M.J., 2019. Constraining deformation phases in the Aar Massif and the Gotthard Nappe (Switzerland) using Th-Pb crystallization ages of fissure monazite-(Ce). Lithos 342–343, 223–238. https://doi.org/10.1016/j.lithos.2019.04.014

Ricchi, E., Bergemann, C., Gnos, E., Berger, A., Rubatto, D., Whitehouse, M., Walter, F., 2019. Cenozoic deformation in the Tauern Window (Eastern Alps, Austria) constrained by in-situ Th-Pb dating of fissure monazite. Solid Earth Discuss. 1–59. https://doi.org/10.5194/se-2019-162

Schmidt, M.W., Poli, S., 2004. Magmatic epidote. Rev. Mineral. Geochemistry 56, 399–430. https://doi.org/10.2138/gsrmg.56.1.399

Sheppard, S.M.F., 2018. Characterization and isotopic variations in natural waters. Stable Isot. High Temp. Geol. Process. 165–183.

Sibson, R.H., 1994. Crustal stress, faulting and fluid flow. Geol. Soc. Spec. Publ. 78, 69–84. https://doi.org/10.1144/GSL.SP.1994.078.01.07

Sibson, R.H., 1996. Structural permeability of fluid-driven fault-fracture meshes. J. Struct. Geol. 18 (8), 1031–1042. https://doi.org/10.1016/0191-8141(96)00032-6

Smye, A.J., Roberts, N.M.W., Condon, D.J., Horstwood, M.S.A., Parrish, R.R., 2014. Characterising the U-Th-Pb systematics of allanite by ID and LA-ICPMS: Implications for geochronology. Geochim. Cosmochim. Acta 135, 1–28. https://doi.org/10.1016/j.gca.2014.03.021

Stipp, M., Stünitz, H., Heilbronner, R., Schmid, S. M., 2002. Dynamic recrystallization of quartz: correlation between natural and experimental conditions. Geological Society, London, Special Publications, 200(1), 171-190.

Şengör, A.M.C., 2016. The structural evolution of the Albula Pass Region, Graubunden, Eastern Switzerland: The origin of the various vergences in the structure of the Alps. Can. J. Earth Sci. 53, 1279–1311. https://doi.org/10.1139/cjes-2016-0020

Taylor, H.P., 1977. Water/rock interactions and the origin of H2O in granitic batholiths. J. Geol. Soc. London. 133, 509–558. https://doi.org/10.1144/gsjgs.133.6.0509

Taylor, H.P., 1978. Oxygen and hydrogen isotope studies of plutonic granitic rocks. Dev. Petrol. 5, 177–210. https://doi.org/10.1016/B978-0-444-41658-2.50014-6

Tera, F., Wasserburg, G.J., 1972. U-Th-Pb systematics in three Apollo 14 basalts and the problem of initial Pb in lunar rocks. Earth Planet. Sci. Lett. 14, 281–304. https://doi.org/https://doi.org/10.1016/0012-821X(72)90128-8

Vidal, O., Parra, T., Vieillard, P., 2005. Thermodynamic properties of the Tschermak solid solution in Fe-chlorite: Application to natural examples and possible role of oxidation. Am. Mineral. 90, 347–358. https://doi.org/10.2138/am.2005.1554

Vidal, O., De Andrade, V., Lewin, E., Munoz, M., Parra, T., Pascarelli, S., 2006. P-T-deformation-Fe3+/Fe2+ mapping at the thin section scale and comparison with XANES mapping: Application to a garnet-bearing metapelite from the Sambagawa metamorphic belt (Japan). J. Metamorph. Geol. 24, 669–683. https://doi.org/10.1111/j.1525-1314.2006.00661.x

Villa, I.M., 2009. Lead isotopic measurements in archeological objects. Archaeol. Anthropol. Sci. 1, 149–153. https://doi.org/10.1007/s12520-009-0012-5

Wehrens, P., Berger, A., Peters, M., Spillmann, T., Herwegh, M., 2016. Deformation at the frictional-viscous transition: Evidence for cycles of fluid-assisted embrittlement and ductile deformation in the granitoid crust. Tectonophysics 693, 66–84. https://doi.org/10.1016/j.tecto.2016.10.022

Wehrens, P., Baumberger, R., Berger, A., Herwegh, M., 2017. How is strain localized in a meta-granitoid, mid-crustal basement section? Spatial distribution of deformation in the central Aar massif (Switzerland). J. Struct. Geol. 94, 47–67. https://doi.org/10.1016/j.jsg.2016.11.004

Weis, D., Kieffer, B., Maerschalk, C., Barling, J., De Jong, J., Williams, G.A., Hanano, D., Pretorius, W., Mattielli, N., Scoates, J.S., Goolaerts, A., Friedman, R.M., Mahoney, J.B., 2006. High-precision isotopic characterization of USGS reference materials by TIMS and MC-ICP-MS. Geochemistry, Geophys. Geosystems 7. https://doi.org/10.1029/2006GC001283

Yardley, B.W.D., Bodnar, R.J., 2014. Fluids in the continental crust. Geochemical Perspect. 3, I–127. https://doi.org/10.7185/geochempersp.3.1

Zhao, Z.F., Zheng, Y.F., 2007. Diffusion compensation for argon, hydrogen, lead, and strontium in minerals: Empirical relationships to crystal chemistry. Am. Mineral. 92, 289–308. https://doi.org/10.2138/am.2007.2127

Zheng, Y.-F., 1993. Calculation of oxygen isotope fractionation in hydroxyl-bearing silicates. Earth Planet. Sci. Lett. 120, 247-263. https://doi.org/10.1016/0012-821X(93)90243-3

4.

Epidote U–Pb geochronology and H isotope geochemistry trace pre-orogenic hydration of mid-crustal granitoids

Veronica Peverelli[1], Alfons Berger[1], Andreas Mulch[2,3], Thomas Pettke[1], Francesca Piccoli[1] & Marco Herwegh[1]

[1]*Institute of Geological Sciences, University of Bern, 3012 Bern, Switzerland*

[2]*Senckenberg Biodiversity and Climate Research Centre (SBiK-F), 60325 Frankfurt, Germany*

[3]*Institute of Geosciences, Goethe University Frankfurt, 60438 Frankfurt, Germany*

Published in *GEOLOGY*: https://doi.org/10.1130/G50028.1

"Geologists have a saying – Rocks remember."

Neil Armstrong, 1930–2012

ABSTRACT Hydrothermal veins and altered feldspar are evidence for fluid circulation in granitic rocks in the continental crust. The hydrothermal alteration of feldspar affects the deformation behavior of granitoids, especially if it occurs before orogeny. Geochronology permits to establish the timing of fluid circulation, thus to determine if this fluid-driven alteration plays a role in crustal deformation. Although existing dating techniques cannot be applied to feldspar alteration directly, absolute ages of fluid circulation can be obtained from hydrothermal veins. We combine U–Pb geochronology and hydrogen isotope data (δD) of epidote [$Ca_2Al_2(Al,Fe^{3+})Si_3O_{12}(OH)$] to unravel the hydration of post-Variscan granitoids in the Alpine orogen. The recent protocol for epidote U–Pb dating proves for the first time that fluids of meteoric origin infiltrated the granitoids in Permian times exploiting syn-rift faults, consistently with the δD values of the epidote-forming fluids. This hydration event caused at least some degree of feldspar hydration and weakening of the granitic rocks ca. 260 myr before their pervasive structural overprint upon Alpine orogeny. The preservation of Permian U–Pb ages despite Alpine orogenic processes confirms epidote as a powerful tool to unveil pre-orogenic hydration events in metagranitoids. Our analytical approach broadens our insight into the water cycle in the middle continental crust in orogens.

4.1 Introduction

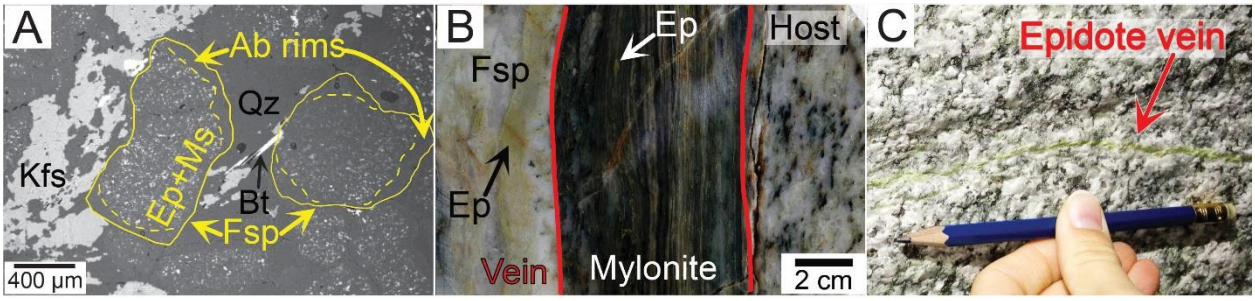

Fig. 4.1 *(A) Backscattered electron (BSE) image of albitized and saussuritic plagioclase. (B) Alpine shear zone in the Central Aar Granite associated with a feldspar-epidote vein. (C) Epidote vein in the Grimsel granodiorite. Ab = albite; Bt = biotite; Ep = epidote; Fsp = feldspar; Kfs = K-feldspar; Ms = muscovite; Qz = quartz.*

Fluid circulation in the Earth's (dominantly granitic) continental crust frequently produces hydrothermal veins and altered feldspar in metagranitoids (e.g., Ferry, 1979; Janecke and Evans, 1998; Plümper and Putnis, 2009; Morad et al., 2010; Incerpi et al., 2019; Airaghi et al., 2020; Peverelli et al., 2021a; 2021b). Veining occurs when a fracture is filled by a fluid from which minerals grow, and it introduces discontinuities in the host rock (Bons et al., 2012). Fluid–host rock interaction further leads to the substitution of feldspar grains by micrometer-sized crystals of hydrous minerals, commonly epidote and mica (i.e., saussurite; Morad et al., 2010). The timing of this low-grade alteration and veining relative to orogeny is seldom known (e.g., Bellahsen et al., 2019; Airaghi et al. 2020). Because feldspar is the most abundant mineral in the Earth's continental crust, its hydration weakens granitoids through (1) storage of water in hydrous alteration minerals, (2) addition of weak phyllosilicates, and (3) larger grain-surface area by generating numerous new grain boundaries that enhance the efficiency of dissolution–precipitation and diffusion processes (Fitz Gerald and Stünitz, 1993; Gueydan et al., 2003; Bürgmann and Dresen, 2008). An open question regards the fact that deformation at greenschist-facies conditions of granitoids requires addition of fluids to stabilize hydrous minerals in these primarily water-poor rocks. Thus, fluid circulation in these rocks before orogeny partakes in preconditioning granitoids for deformation (e.g., Bellahsen et al., 2019; Airaghi et al., 2020; Malatesta et al., 2021). This work presents U–Pb and H isotope data of vein-epidote to study the hydration of post-Variscan granitoids deformed during the Alpine orogeny. The timing of feldspar alteration (Fig. 4.1A) is inferred by dating hydrothermal vein-filling minerals (Fig. 4.1B–C), as at least some degree of microscale pervasive flow generally accompanies veining (e.g. Plümper and Putnis, 2009; Plümper et al., 2017).

4.2 Samples and methods

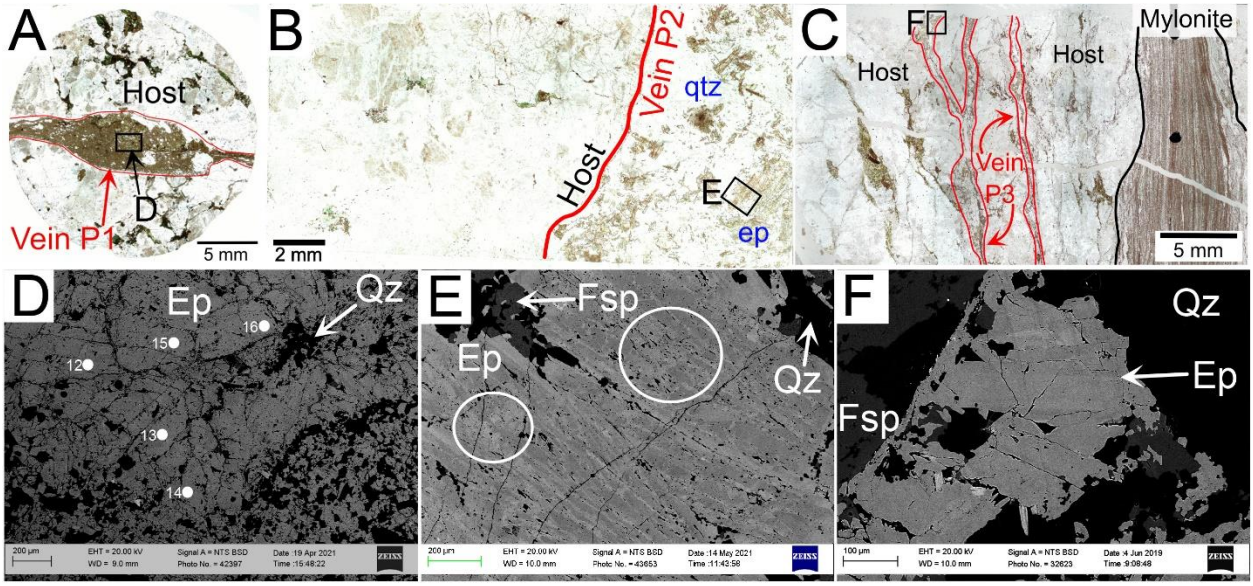

Fig. 4.2 *Transmitted light microscopy (A–C) and backscattered electron (BSE; D–F) images of epidote veins P1 (A, D), P2 (B, E) and P3 (C, F). Rectangles in panels A–C: locations of panels D–F. White spots in panel D: LA-ICP-MS analyses (Table 4.1); none were performed in the grains of panels E–F. White circles in panel E highlight areas of post-crystallization fluid–epidote interaction. Abbreviations as in Fig. 4.1.*

The investigated epidote veins P1, P2 and P3 (Fig. 4.2) were sampled in the Grimsel Test Site (GTS), the underground rock laboratory of Nagra at Grimsel Pass in the Haslital (46° 35' 27" N 8° 19' 17"; Fig. 4A1). Here, outcrops of post-Variscan Central Aar granite (299 ± 2 Ma) and Grimsel granodiorite (297 ± 2 Ma; Schaltegger and Corfu, 1992) reflect a typical mid-crustal section in collisional orogens (see Schneeberger et al., 2019). Starting ca. 22 Ma, numerous shear zones formed in these granitoids during the Alpine orogeny (Fig. 4.2B; e.g., Rolland et al., 2009; Herwegh et al., 2017; 2020; Wehrens et al., 2017; Schneeberger et al., 2019; Baumberger et al. 2022). Epidote veins (Fig. 4.1B–C) and intensely saussuritized (Fig. 4.1A) or sericitized magmatic feldspar provide evidence for fluid flow. The studied veins (Figs. 4.2 and 4A5–4A7) consist of epidote + quartz (± biotite) and are variably deformed (see Results). Their structural relations with dated structures (i.e., foliation, shear zones) do not reveal absolute ages of the veins, which can have formed at any time after the emplacement of the granitoids. Backscattered electron (BSE) images of epidote P1 and P3 reveal regular chemical zoning (Figs. 4.2D and 4.2F), commonly due to growth processes (see Franz and Liebscher, 2004). P2 epidote grains display patchy chemical zoning (Fig. 4.2E), suggesting that vein P2 includes a second epidote generation resulting from recrystallization of epidote upon interaction with a secondary fluid. Epidote U–Pb isotope data of P1–3 veins obtained by laser ablation inductively coupled plasma mass spectrometry (LA-ICP-

MS) at University of Bern are compared to those of vein-epidote Grimsel-1 and Grimsel-2 dated by Peverelli et al. (2021a; Chapter 2 of this thesis), whose protocol was followed for U–Pb dating. Grimsel-1–2 epidote samples gave Miocene ages and they are part of deformed epidote-quartz-biotite veins collected in the GTS (Fig. 4A1). To plan LA-ICP-MS analyses with a 50 µm spot size in all epidote samples avoiding contamination from cracks or mineral inclusions, BSE images (Fig. 4.2D–F) were used. To assess the nature of the epidote-forming fluids, hydrogen isotope data (δD) were measured in ca. 4–8 mg of P1, P2 and Grimsel-1 epidote separates by high-temperature conversion elemental analysis (TC/EA) at the Goethe University Frankfurt–Senckenberg BiK-F Stable Isotope Facility. LA-ICP-MS and TC/EA analyses sample ca. 20–24 × 10^3 µm^3 and ca. 1–2 × 10^9 µm^3, respectively. Thus, U–Pb isotope data of P2 vein exclude alteration patches (Fig. 4.2E). In contrast, TC/EA analyses return a homogenized δD signal from whole P2 epidote grains. *In-situ* dating of feldspar alteration minerals is not possible because of their small grain size. Since it cannot be assumed that all grains are coeval, bulk-feldspar analyses are also hampered. Epidote P1–3, sample preparation and analytical methods are described in Appendices 4A–4C at the end of this chapter. For description and U–Pb isotope data of Grimsel-1–2 veins see Peverelli et al. (2021a; Chapter 2 of this thesis).

4.3 Results

4.3.1 Meso- and microstructures

Low-grade brittle (e.g., fractures and altered feldspar; Figs. 4.1A and 4.1C) and greenschist-facies ductile (e.g., shear zones; Fig. 1B; e.g., Wehrens et al., 2016) features indicate multiphase and multiscale deformation in the area. Some veins (P1–2) show post-formation brittle overprinting (i.e., fracturing; Figs. 4.2 and 4A5–6), whereas veins in which quartz dynamically recrystallized by subgrain rotation (P3, Figs. 4.2 and 4A7; Grimsel-1–2, Peverelli et al., 2021a; Chapter 2 of this thesis; see also Sect. 2.4.1 and Fig. 2.1) are deformed in a ductile way. Hydrated feldspar is ubiquitous in the host granitoids and in Alpine mylonites as porphyroclast (Wehrens et al., 2016). Single hydrated feldspar grains contain up to ca. 50 vol. % epidote + white mica, but maintain their original shape.

4.3.1 Timing of vein formation

Epidote U–Pb ages of P1, P2 and P3 are 279 ± 29 Ma, 291 ± 50 Ma and 275 ± 18 Ma, respectively (Fig. 4C1), within uncertainty of each other. The mean squares of weighted deviation (MSWD) values of 2.0–2.3 reveal only one epidote generation in each vein at the current analytical precision. The timing of fluid–P2 epidote interaction (i.e., formation of a second epidote generation) remains unknown because alteration patches were not dated. The initial $^{207}Pb/^{206}Pb$ ratios ($^{207}Pb/^{206}Pb_{in}$) of 0.8296 ± 0.0028 (P1), 0.8316 ± 0.0031 (P2) and 0.8326 ± 0.0025 (P3) also overlap within uncertainty, allowing to calculate one age of 276 ± 13 Ma with an $^{207}Pb/^{206}Pb_{in}$ of 0.8311 ± 0.0015 by combining the U–Pb isotope data of all epidote samples (Permian regression; Fig. 4.3; Table 4.1). Based on the same criteria, the combined U–Pb isotope data of epidote Grimsel-1 (19.2 ± 4.3 Ma and $^{207}Pb/^{206}Pb_{in}$ of 0.7964 ± 0.0027) and Grimsel-2 (16.9 ± 3.7 Ma and $^{207}Pb/^{206}Pb_{in}$ of 0.7998 ± 0.0054; Peverelli et al., 2021a; Chapter 2 of this thesis; Fig. 2.7, Table 2.7 and Sect. 2.4.3) gave one age of 14.0 ± 1.8 Ma and one $^{207}Pb/^{206}Pb_{in}$ of 0.7942 ± 0.0017 (Alpine regression; Fig. 4.3). Only the combined Permian and Alpine ages of 276 ± 13 Ma and 14.0 ± 1.8 Ma, respectively, are discussed hereafter.

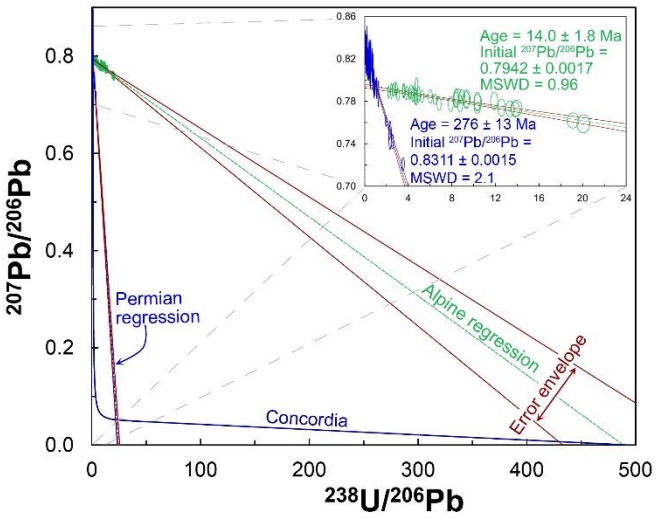

Fig. 4.3 *Tera–Wasserburg plot of U–Pb isotope data of Permian (blue) and Miocene (green; data from Peverelli et al., 2021a; Chapter 2 of this thesis; Table 2.7) epidote. Age uncertainties are 95 % confidence and data-point error ellipses 2σ. Plotted with Isoplot 3.7.5 (Ludwig, 2012).*

4.3.1 δD data

Epidote δD data reflect the vein-forming fluids, and permit a comparison of data obtained from (a) Permian epidote P1, (b) Alpine epidote Grimsel-1, and (c) Permian epidote P2 affected by post-veining fluid–epidote interaction at unknown times. Permian P1 epidote has a δD value of -77 ± 3 ‰, taken as representative of epidote formed by Permian fluids. The δD value of -55 ± 3 ‰ of Miocene Grimsel-1 epidote is used to represent Alpine vein epidote. Epidote P2 is Permian but has a δD value of -59 ± 3 ‰ that overlaps with Miocene epidote. The techniques for U–Pb dating and H isotope analyses sample different volumes of epidote (Sect. 4.2). Thus, this is consistent

with the H isotope data of P2 epidote grains being a mixed signal between (1) the δD value acquired by epidote during veining in the Permian and (2) that recorded in alteration patches during interaction with Alpine fluids in the Miocene (Figs. 4.2E and 4.4D).

From the δD values measured in Permian P1 and Miocene Grimsel-1 epidote samples, the δD data of the epidote-forming fluids are calculated following Chacko et al. (1999) with a temperature of epidote crystallization of 250 ± 50 °C for Permian epidote given by a normal geothermal gradient of 25 °C/km in the pluton intruded at ca. 10 km depth (Berger et al., 2017). For Alpine epidote, the temperature of crystallization of 400–600 °C is based on biotite being associated with epidote in the vein and the epidote–clinozoisite solid solution being stable up to 600 °C (Franz and Liebscher, 2004; Herwegh et al., 2020). The resulting δD values of Permian fluids are -57 to -44 (± 3) ‰, whereas those of the Alpine epidote-forming fluids -14 to -5 (± 3) ‰.

4.4 Discussion

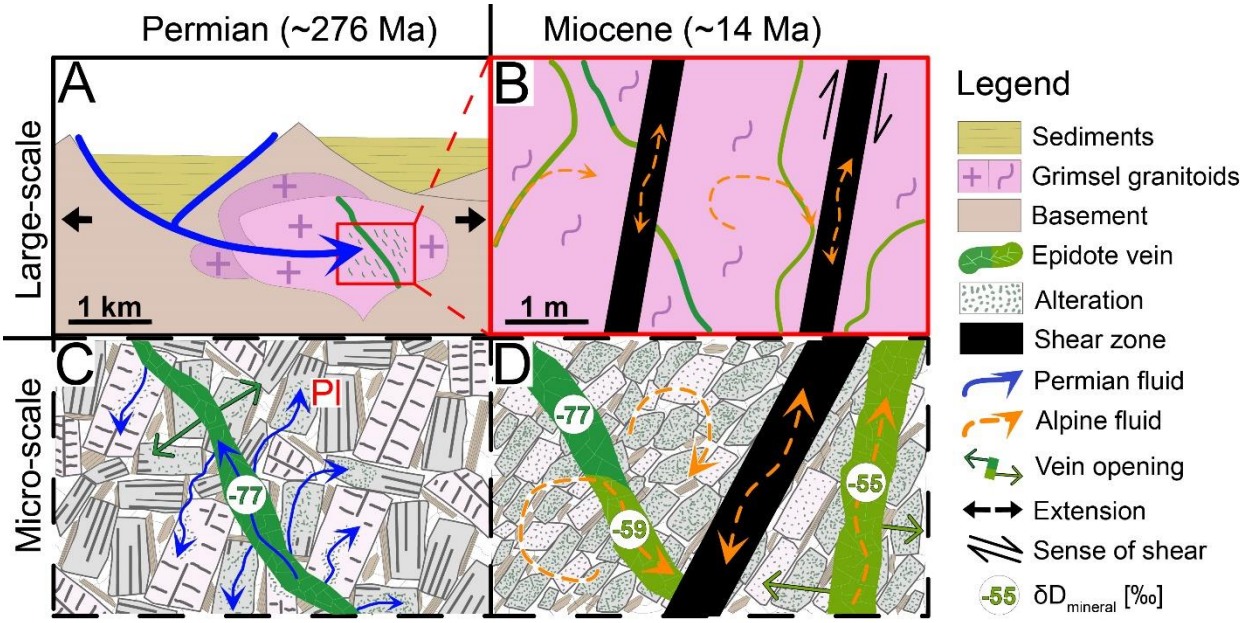

Fig. 4.4 *(A) Permian transtension and hydration, and (B) Alpine deformation in a portion of the granitoids (rectangle in Panel A) and Miocene veining. Panels C–D are hypothetical microstructures of the granitoids in A–B. Pl = plagioclase.*

4.4.1 Fluid sources

The δD values of the Permian fluids of -57 to -44 (± 3) ‰ overlap with those of primary magmatic, low-topography meteoric, sedimentary, or metamorphic waters (Sheppard, 2018; Fig. 4B1). Veining occurred at 276 ± 13 Ma, at least 6 myr after the emplacement of the granitoids. Primary magmatic water is thus excluded as source of the Permian fluids. The European continental crust,

including the investigated area, experienced a typical Permian transtensional regime as indicated by several small-scale sedimentary basins (Oberhänsli et al., 1988). Thus, the Permian fluids most likely originated as meteoric water that modified its hydrogen isotope composition by interacting with syn-tectonic sediments upon infiltrating the granitoids along syn-rift faults (Fig. 4.4A; Sheppard, 2018). The Alpine fluids have δD values of -14 to -5 (± 3) ‰ that overlap with those of hydrated oceanic crust (Sheppard, 2018), whose role is excluded in the studied continental setting. Pure meteoric water is an unlikely source, as in the Miocene the Grimsel Pass area already had high elevation (Campani et al., 2012; Krsnik et al., 2021), entailing low δD meteoric water. Thus, the δD values of Alpine fluids can only reflect a mixture of different waters. Nevertheless, Pb and H isotope data evidence that the Permian and Alpine fluids are strikingly different. Since Pb is fluid-mobile, epidote $^{207}Pb/^{206}Pb_{in}$ reflect the Pb isotope composition of the epidote-forming fluids. The $^{207}Pb/^{206}Pb_{in}$ of single samples overlapping within uncertainty in each age cluster hence reflect (1) a Permian fluid path into the crust along syn-rift faults, and (2) a Miocene one that is only constrained in terms of age.

4.4.2 Fluids and structural imprint

Hydration of the granitoids began upon Permian transtension, when fluids of meteoric origin formed epidote veins (Fig. 4.4A). Since at least some degree of pervasive flow follows veining (e.g., Plümper and Putnis, 2009; Plümper et al., 2017), it is likely that this fluid flow event altered some feldspar into epidote and mica (Fig. 4.4C). According to our results, veining and initial feldspar hydration took place ca. 260 myr before Alpine deformation in the Haslital granitoids, with substitution of coarse-grained feldspar by fine-grained aggregates of hydrous minerals (Fig. 4.4C). Feldspar hydration entails grain-size reduction via formation of fine-grained polymineralic aggregates within feldspar crystals, and storage of water in alteration (hydrous) minerals. In addition to Permian fluids stored in alteration minerals, primary (i.e., magmatic) biotite in the granitoids contains magmatic water. Upon deformation, these nominally hydrous minerals could release previously stored water (Fig. 4.4D). However, this recycled water alone is not sufficient to produce all hydration features observed in the granitoids, and addition of syn-orogenic fluids is evidenced by the Miocene epidote veins. In this context, the δD values of the Alpine vein-forming fluids are explained by a mixture of recycled water and syn-kinematic fluid components with a high δD value. Hydrated feldspar is found in granitoids worldwide (e.g., Ferry, 1979; Janecke and

Evans, 1998; Plümper and Putnis, 2009; Morad et al., 2010; Oliot et al., 2010; Bellahsen et al., 2019; Airaghi et al., 2020). In the Alpine realm, pre-Cenozoic hydration of the granitic crust occurred in the Bielsa pluton (Pyrenées) ca. 150–200 myr before the main Alpine phases (Airaghi et al., 2020), and in the Err nappe (eastern Swiss Alps) in the Jurassic and Late Cretaceous (Incerpi et al., 2019; Peverelli et al., 2021b; Chapter 3 of this thesis). Like the present example, other orogens (e.g., the Himalayas), whose middle continental crust was subjected to Mesozoic and/or Paleozoic rifting, may include granitic rocks that were hydrated before orogeny.

4.4.3 Hidden events require new geochemical tools

Our work reveals preserved Permian U–Pb ages in vein-epidote in metagranitoids affected by Mesozoic continental rifting, tectonic inversion and Alpine orogenic processes. Thus, it confirms the robustness of minerals of the epidote–clinozoisite solid solution series as U–Pb geochronometers to date hydrothermal events in the deformed continental crust in orogens (Peverelli et al., 2021a; Chapter 2 of this thesis). This is in line with microstructural observations suggesting that epidote does not dynamically recrystallize upon deformation and remains brittle across its stability field (see Franz and Liebscher, 2004). Epidote isotope geochemistry allows to date and trace hydration events in the primarily water-poor middle continental crust, provided that a representative epidote volume is sampled in the isotopic analyses (i.e., our epidote P2 gives a Permian U–Pb age but a mixed Permian–Alpine δD value). The fact that Permian veins in the Grimsel Pass area have only been revealed thanks to the new protocol for U–Pb dating of epidote is captivating: other hydration events in these granitoids may remain hidden until new methods are developed and applied to other structures. The high preservation potential of epidote shown here offers a powerful tool to lessen the hurdle posed by the rare preservation of pre-kinematic hydration features, and even to trace multistage (i.e., pre- and syn-kinematic, as shown here) fluid circulation in orogens. Larger age datasets may be obtained by merging geochronological data obtained from different geochronometers. The characterization of fluid circulation in crustal rocks in other orogens will allow to compare the time intervals between pre- and syn-orogenic hydration events, and fluid sources at a global scale. Thus, a multi-analytical study – like the one presented here – can contribute to the understanding of the role of fluids in geodynamic processes, and complement our understanding of the fluid budget and cycle in orogens.

Appendix 4A: Sampling area and studied epidote veins

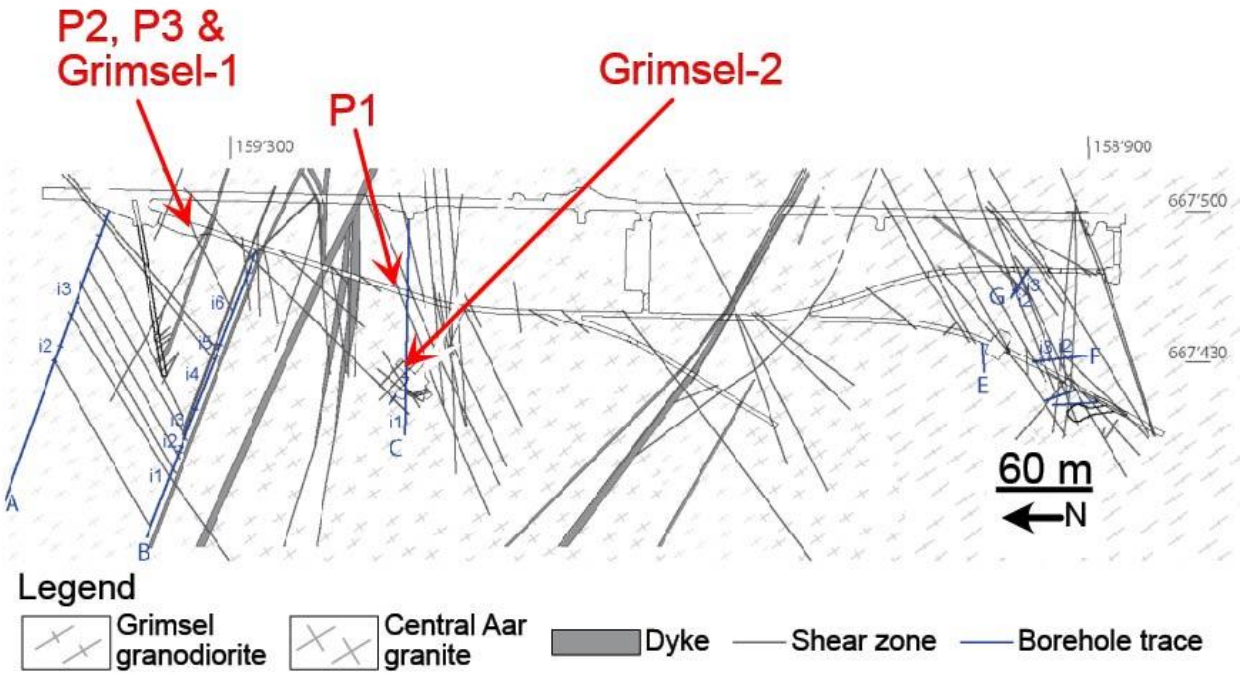

Fig. 4A1 *Map of the Nagra Grimsel Test Site at Grimsel Pass showing the sampling locations of the studied epidote vein samples (red arrows) and the position of Alpine shear zones. Modified from Schneeberger et al. (2019).*

The investigated epidote veins were sampled inside the Nagra Grimsel Test Site (GTS) at Grimsel Pass (Haslital), decimeters to centimeters away from Alpine shear zones (Fig. 4A1). The GTS is an underground rock laboratory with exposed undisturbed outcrops that are representative of the whole exhumed typical mid-crustal section exposed in the Haslital (Schneeberger et al., 2019). The veins studied here were sampled in different locations inside the GTS (Fig. 4A1), they are hosted by the Grimsel granodiorite (GG) and the Central Aar granite (ZAR; hereafter collectively referred to as granitoids), and they are either associated with Alpine shear zones (Fig. 4A2) or not. The granitoids belong to the calc-alkaline suite and

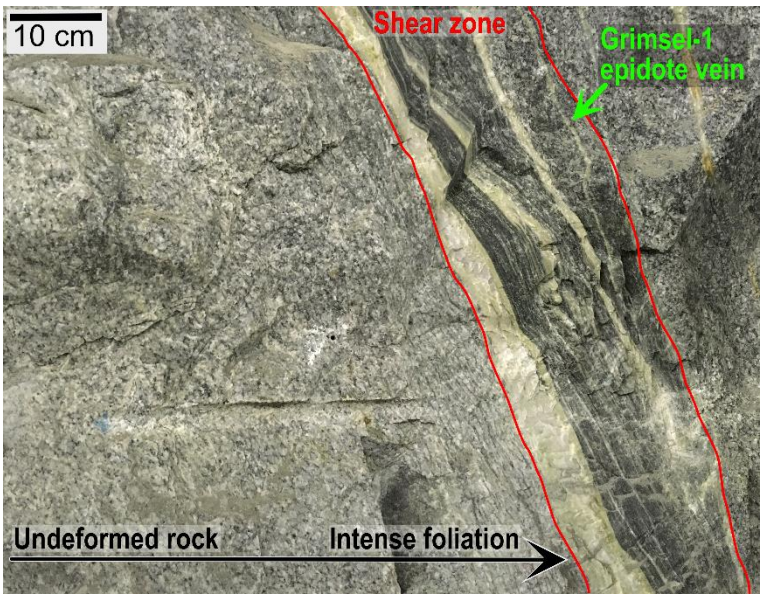

Fig. 4A2 *Outcrop photograph showing the transition between weakly deformed texture to intense foliation in the Central Aar Granite, and the Alpine shear zone near which epidote veins P2, P3 and Grimsel-1 were sampled.*

their emplacement is dated at 299 ± 2 Ma for the GG and at 297 ± 2 Ma for the ZAR (Schaltegger and Corfu, 1992). The depth of intrusion is ca. 10 km (Berger et al., 2017). Both granitoids are coarse-grained and they are composed of quartz, feldspars, biotite, chlorite, white mica, epidote, titanite and other accessory minerals. The abundance of biotite in the granitoids ranges between ca. 5–15 vol. % (Wehrens et al., 2017). Epidote contents are 2 vol. % in the GG and 0.4 wt. % in the ZAR (Schneeberger et al., 2019). In the granitoids, epidote is present as both vein-filling mineral (Figs. 4A3 and 4.1C) and as feldspar alteration product (Fig. 4.1A), in addition to metamorphic mineral in the foliation (Fig. 4A3). The granitoids were involved in the Alpine orogenesis, whose deformation products are expressed by variably intense foliation and by a large number of shear zones cutting the granitoids, whose activity began at 22 Ma (Rolland et al., 2009). The shear zones developed an anastomosing network that encloses undeformed portions of the granitoids, hence highlighting a gradation from the original magmatic textures to (ultra-) mylonites (Fig. 4A2; Wehrens et al., 2016; 2017; Schneeberger et al., 2019). The mineralogical composition of shear zones is similar to that of the undeformed granitoids with locally higher contents of sheet silicates (Wehrens et al., 2016; Schneeberger et al., 2019). Even where the original texture of the granitoids is preserved, pervasive alteration is evidenced by saussuritization and albitization of plagioclase (Fig. 4.1A) and sericitization of K-feldspar, although the latter is less pervasive than the former. These feldspar alteration features are observed both in the granitoids – with feldspar grains maintaining their original habit – and in porphyroclasts in mylonites, indicating that feldspar hydration occurred at least in part before the onset of Alpine deformation. In the area, the peak conditions during Alpine deformation were estimated by Goncalves et al. (2012) at 450 ± 30 °C

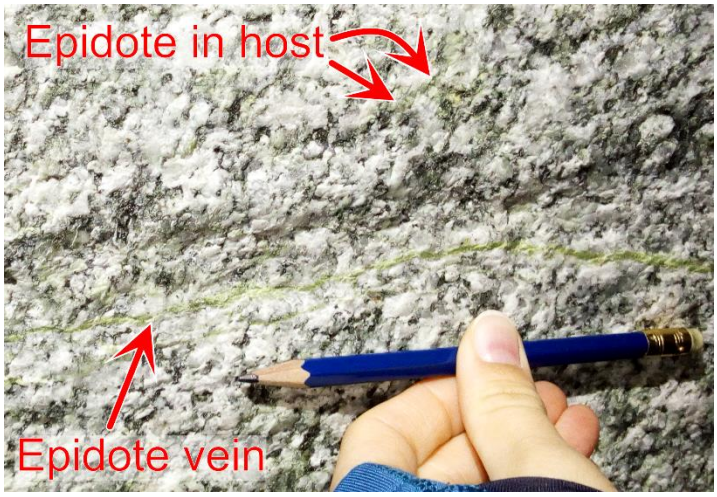

Fig. 4A3 *Outcrop figure showing an epidote vein and metamorphic and saussuritic epidote in the host granitoid.*

and 0.6 ± 0.1 kbar. A detailed characterization of granitoids and shear zones is given by Schneeberger et al. (2019; and references therein).

Epidote is here defined as minerals of the epidote–clinozoisite solid solution [$Ca_2Al_2Fe^{3+}Si_3O_{12}(OH)$–$Ca_2Al_3Si_3O_{12}(OH)$]. The occurrence of brittle epidote veins within the granitoids (Fig. 4A3) has been reported by Schneeberger et al. (2019; see their Fig. 4.2). The epidote veins range between decimeters to meters in length, and between ca. 1 mm to few centimeters in aperture. Their geometry is also highly variable, with some veins running rather straight and some being more sinuous. Altered feldspar and veins indicate the occurrence of fluid circulation at low temperature in the area, although the timing is unknown. A suggestion was made by Abrecht and Schaltegger (1988) that seawater infiltrated the granitoids in the Mesozoic based on whole rock (i.e., aplitic intrusions) Rb–Sr dating indicating resetting of the isotope system, possibly in Triassic or Jurassic times. The relationship between P1 epidote vein studied here and its host rock and associated shear zone is shown in Fig. 4A4. Veins P2 and P3 are located ca. 1 meter away from the Alpine shear zone near which sample Grimsel-1 was collected (Fig. 4A2). Grimsel-2 vein is also associated with Alpine shear zones, but no field photographs or hand samples were made available. Crosscutting relationships between veins and structures of known age (e.g., shear zones, foliation) do not allow to infer an absolute timing of vein formation, which may have occurred at any time after the emplacement of the granitoids. From field relations, it is impossible to ascertain if more than one generations of epidote veins are present, and how many.

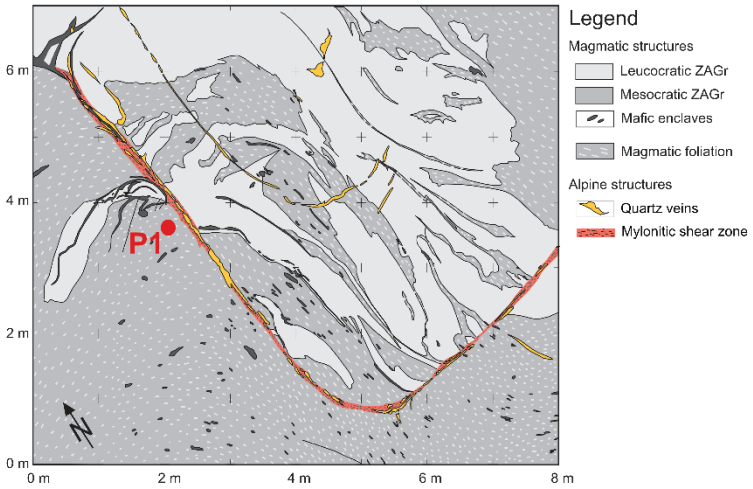

Fig. 4A4 *Outcrop map of the sampling location of epidote vein P1 and the Alpine shear zone nearby. Mapping by Marco Herwegh.*

Sample P1 (Fig. 4A5) is an epidote-quartz ± feldspar vein with an aperture of ca. 1–5 mm in a weakly deformed portion of the Grimsel Granodiorite with sharp contacts with the host. Epidote is euhedral to subhedral and highly fractured, with grain sizes ranging between ca. 20–300 µm in size. The grain-size distribution of epidote is bimodal, with epidote grains of up to few tens of

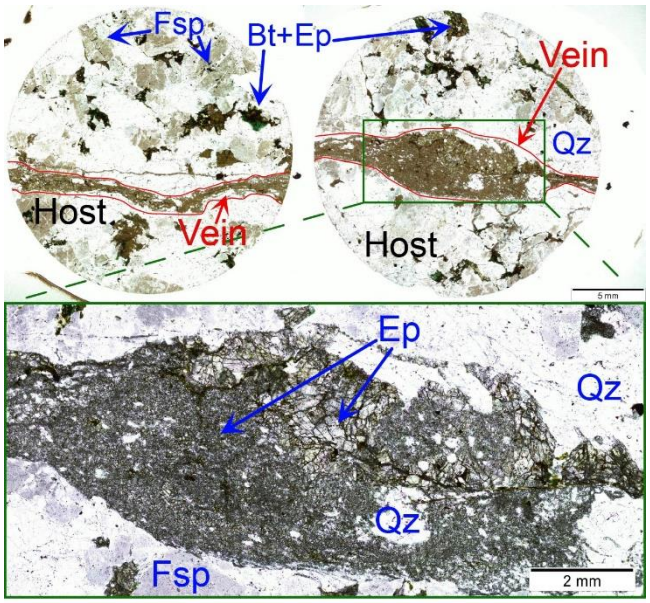

Fig. 4A5 *Transmitted light microscope images of epidote vein P1. All panels are in plane-polarized light. Bt = biotite; Ep = epidote; Fsp = feldspar; Qz = quartz.*

microns resulting from grain-size reduction of larger epidote relics (Fig. 4A5, lower panel; Fig. 4.2A and 4.2D). This indicates that the brittle process leading to the opening of the vein and to epidote mineralization was followed brittle deformation with epidote fracturing. The weak crystal zoning seen in backscattered electron (BSE) images indicates chemical zoning, whose regular pattern suggests that it results from growth processes (Fig. 4.2D; see Franz and Liebscher, 2004), with the higher BSE contrast generally due to higher Fe and REE contents. Along with quartz (ca. 50–400 µm in size), feldspar grains of ca. 10–50 µm in size are found among epidote fragments in the smaller-sized portion of the epidote vein.

Sample P2 (Fig. 4A6) is hosted by a weakly deformed sector of the Central Aar Granite and it is an epidote-quartz-feldspar vein with a sharp vein–host boundary. Epidote grains measure between ca. 50 µm and 2 mm, the crystals are subhedral to anhedral with frequent pores. Quartz grains measure ca. 40–400 m, with few larger grains reaching up to 3.2 mm in length. The patterns in BSE contrast within epidote grains are locally highly irregular and cannot be entirely ascribed to growth (Fig. 4.2E). Likely, these BSE patterns are due to epidote

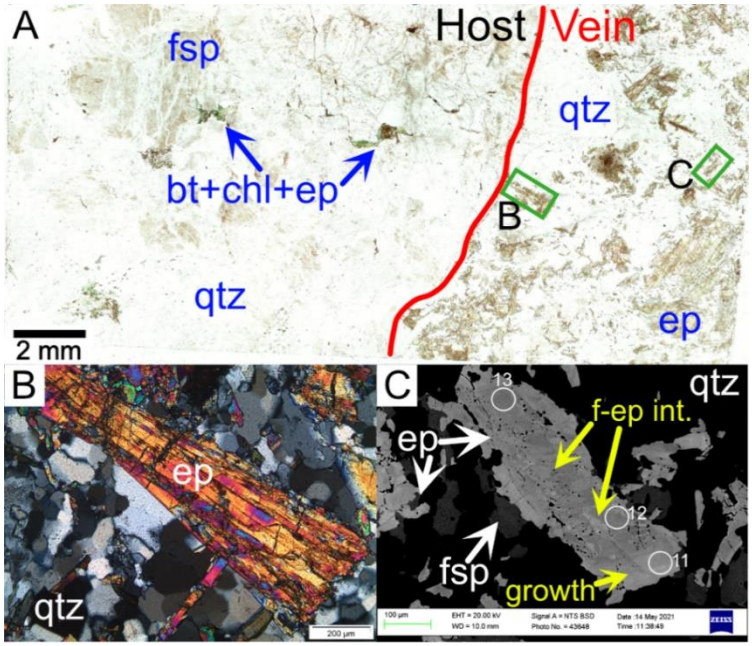

Fig. 4A6 *Transmitted light microscope (A-B) and BSE (C) images of sample P2. Panel A is in plane-polarized light, panel B in cross-polarized light. Green rectangles in A show the locations of panels B and C in the thin section. bt = biotite; chl = chlorite; ep = epidote; fsp = feldspar; e-ep int. = patchy zoning resulting from fluid–epidote interaction; growth = growth zoning; qtz = quartz. White circles are laser spots (Table 4.1).*

recrystallization upon post-crystallization interaction with a secondary fluid. No new mineral phases resulting from the fluid-driven alteration are recognized other than epidote. Brittle fracturing of epidote grains is observed.

Sample P3 (Fig. 4A7) is a highly deformed epidote-quartz vein hosted by a deformed portion of the Central Aar Granite, ca. 5 mm away from an ultramylonite (Fig. 4A7A). The vein is locally wrapped by a foliation made of biotite and epidote (Fig. 4A7C), which indicates that the deformation of the vein occurred in Alpine times (Wehrens et al., 2016; 2017), and the boundary between vein and host is locally ill-defined due to such deformation. Vein epidote is subhedral to anhedral and ranges between ca. 20–150 µm in size, with the smaller grains resulting grain-size reduction of larger ones. The fracturing of epidote and the dynamic recrystallization of quartz – with single grains measuring ca. 25–200 m in size –by subgrain rotation indicate that the brittle process of vein opening was overprinted by higher-temperature viscous deformation (e.g., Stipp et al., 2002). Regular zoning in BSE images (Fig. 4.2F) suggests chemical zoning related to epidote growth processes (see Franz and Liebscher, 2004).

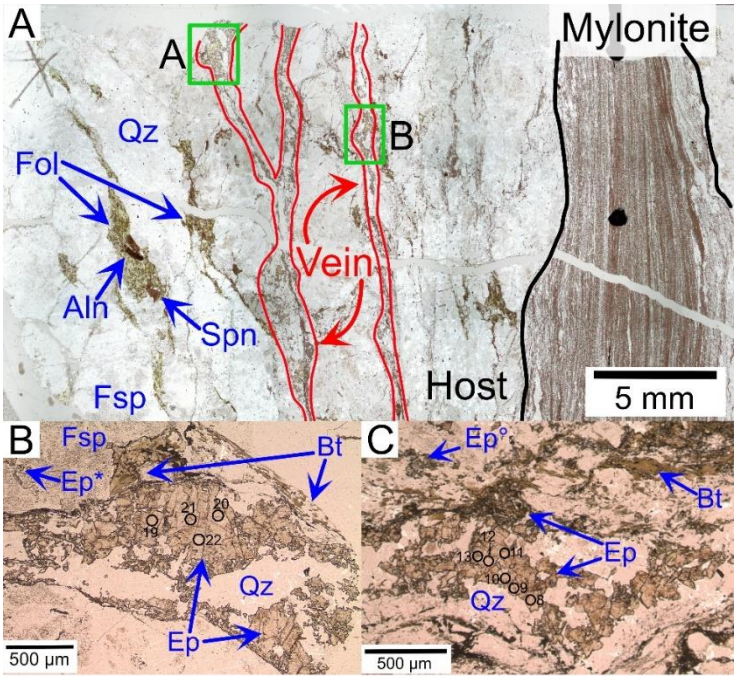

Fig. 4A7 *Transmitted light microscope images of sample P3 in plane-polarized light. Green rectangles in A indicate the locations of the microscopic images B and C, which are rotated by 90° to the right and to the left, respectively. aln = allanite; bt = biotite; ep = epidote; ep* = saussurite epidote; ep° = metamorphic epidote; fol = foliation; fsp = feldspar; qtz = quartz; ttn = titanite. Black circles indicate laser spots (Table 4.1).*

Samples Grimsel-1 and Grimsel-2 are described in detail in Peverelli et al. (2021; Chapter 2 of this thesis; Sect. 2.4.2). The characteristics of their host rock (Central Aar granite) are the same as those of samples P2 and P3.

Appendix 4B: Methods

Backscattered electron (BSE) images were acquired on a Zeiss EVO50 SEM with a beam current of ca. 1 nA, accelerating voltage of 20 kV and working distance of 9.5–10.0 mm in the laboratory facilities of the University of Bern.

Epidote U–Pb isotope data were measured at University of Bern using a Resonetics RESOlutionSE 193 nm excimer laser system (Applied Spectra, USA) equipped with an S-155 large-volume constant-geometry chamber (Laurin Technic, Australia) coupled to an Agilent 7900 ICP-QMS. Tara allanite (Smye et al., 2014) was used as primary reference material with the reference isotopic values presented in Peverelli et al. (2021; Table 2.2 of Chapter 2 of this thesis), and CAP and AVC allanite samples (Gregory et al., 2007) as secondary reference materials for quality control. Further details on the protocol can be found in Peverelli et al. (2021; Chapter 2 of this thesis) and the analytical conditions used for this work are as follows:

RF power:	1400 W
Fluence:	3 J cm^{-2}
Repetition rate:	5 Hz
Cell gas flow:	3 ml min^{-1} N_2 and 400 ml min^{-1} He
Sensitivity on mass 232 in NIST SRM612 beam size, fluence, repetition rate, scan rate:	7060 cps ppm^{-1} (samples P1 and P3)* and 6450 cps ppm^{-1} (sample P2)*; 50 µm, 2.5 J cm^{-2}, 5 Hz, 5 µm s^{-1}
232/238 ratio:	0.98
248/232 ratio:	0.002
Background:	40 s
Pre-cleaning (beam size in µm):	10 pulses (64)
Ablation time (beam size in µm):	40 s (50)
Measured masses (dwell times in ms):	206 (40), 207 (40), 208 (40), 232 (40), 238 (40)

*Samples P1 and P3 were measured on June 8th 2021, and sample P2 on June 9th 2021.

Hydrogen isotopic measurements were carried out in ca. 4–8 mg of epidote grains at the Joint Goethe University Frankfurt–Senckenberg BiK-F Stable Isotope Facility (Frankfurt, Germany) on a Thermo high-temperature conversion elemental analyzer (TC/EA) coupled to a Thermo MAT 253 mass spectrometer in continuous flow mode. For sample preparation, epidote grains were handpicked from hand samples of veins P1–2 and Grimsel-1 under a binocular microscope and then ground in ethanol to homogenize grain sizes. Two separates of epidote P1 were made from two separate hand samples (shown in Fig. 4A5, upper panels) collected ca. 5 cm away from each other along the P1 vein. The resulting δD value of -77 ± 3 ‰ is the average of the values obtained

from each epidote separate of -80 ± 3 ‰ and -74 ± 3 ‰, which overlap within uncertainty. Epidote separates could not be collected from sample P3 because a complete separation of epidote from biotite was not possible, and no hand specimen is available for sample Grimsel-2. Because multiphase fluid flow is inferred from epidote microstructures (Fig. 4.2E), H isotope analyses of feldspar hydration products – although technically feasible – are avoided as the data may represent a mixed signal between (1) fluids related to different hydration events and (2) the OH groups of epidote and mica. Effects on the measured values due to the size of the analyzed material (i.e., 4 *vs.* 8 mg) was ruled out in preliminary measurements of different aliquots of different grain sizes and weight of own samples (not presented here), obtaining the same δD value within uncertainty for all aliquots of each sample. Standards USGS57 (biotite), USGS58 (muscovite), NBS22 (oil) and CH7 (polyethylene foil) were analyzed for quality control, yielding δD values of, respectively, -28.4 ‰, -91.9 ‰, -100.0 ‰ and -116.9 ‰ after correction for mass bias, daily drift of the thermal combustion reactor and offset from the certified reference. An in-house standard ("epidote_1867m"; Bird et al., 1988) yielded a δD of -95 ‰. Repeated measurements of the various standards and unknowns resulted in a precision of ± 3‰ for δD. All isotope ratios are presented relative to the Vienna Standard Mean Ocean Water (V-SMOW) and $\delta D = \frac{(D/H)_{sample} - (D/H)_{reference}}{(D/H)_{reference}} \times 1000$ ‰.

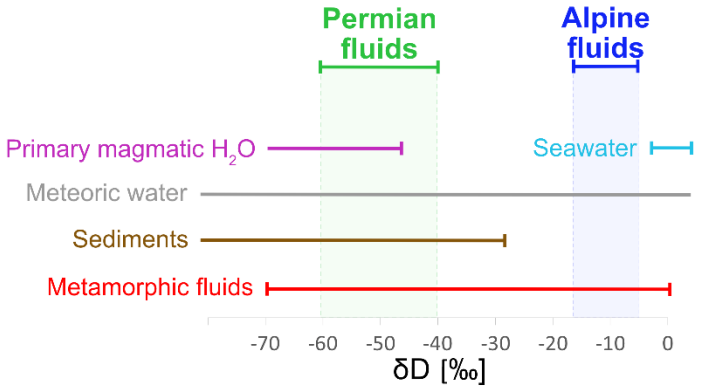

Fig. 4B1 *Hydrogen isotope composition of water reservoirs from Sheppard (2018) and comparison of the δD values calculated for the epidote-forming fluids investigated here. Open lines indicate that the field of possible values extends further.*

We used the fractionation equation of Chacko et al. (1999) for calculation of the hydrogen isotope compositions of all epidote-forming fluids at the estimated temperatures of epidote crystallization ranging from ca. 200 to 480 °C. More in detail, the temperature of crystallization of Permian epidote of 250 ± 50 °C is estimated based on the depth of intrusion of ca. 10 km of the host rock (Berger et al., 2017). Because temperature of host rocks does not automatically translate into temperature of fluids, we have tested the effect on δD values by assuming a temperature of 600 °C (breakdown of the epidote–clinozoisite solid solution; see Franz and Liebscher, 2004) to calculate

the maximum possible δD value of the Permian fluids. The fractionation factor calculated following Chacko et al. (1999) is -49.7, yielding a fluid δD of -27.3 (±3) ‰. This value is well outside uncertainty of the δD values calculated for the Alpine fluids of -14 to -10 (±3) ‰ and still consistent with a Permian fluid pathway from the surface into the granitoids exploiting syn-rift faults and interacting with syn-rift sediments. Hence, a fluid temperature of 600 °C is unlikely, and we accept the conservative estimate of 250 ± 50 °C for calculation of the δD values of the Permian fluids. It should be noted that we do not know if a normal geothermal gradient of 25 °C/km is valid for the area during Permian transtension. However, the Permian alteration cannot be high grade because of the shallow intrusion of the granite and of the basin-forming tectonics. Any uplift decreases the depth – and consequently the temperature – of the alteration, and an intrusion depth of 10 km is a conservative assumption. The large uncertainty included in these assumptions is reflected by that of ±50 °C of the estimated temperature. For Alpine epidote a temperature range of 400–600 °C is based on the breakdown temperature of the epidote–clinozoisite solid solution (Franz and Liebscher, 2004), and on the fact that the biotite is associated with epidote the veins (Peverelli et al., 2021; Chapter 2 of this thesis; Sect. 2.4.1), requiring a minimum temperature of ca. 400 °C (see Herwegh et al., 2020). The interpretation of the δD values of the epidote-forming fluids is based on a comparison with the data in Sheppard (2018; Fig. 4B1). A mention is necessary regarding the large δD range of meteoric waters, which is due to the dependence of H isotope fractionation with respect to topography – i.e., higher topography causes a larger extent of isotope fractionation and hence lower δD values, whereas lower-topography regions have rainwater that is closer to seawater δD values (the effect of latitude is not discussed here). Sedimentary waters refer to fluids trapped during sedimentation that equilibrate with the host sediments. Finally, the δD values of metamorphic waters are calculated from H isotopic measurements of metamorphic rocks, with metabasalts having δD values of ca. -35 to -70 ‰. Metamorphic waters extend to a δD value of 0 ‰, which is expected when seawater is released from hydrated rocks of the oceanic crust. The reader is referred to Hoefs (2018) for treatise on stable isotopes.

Appendix 4C: U–Pb isotopic data of samples P1, P2 and P3

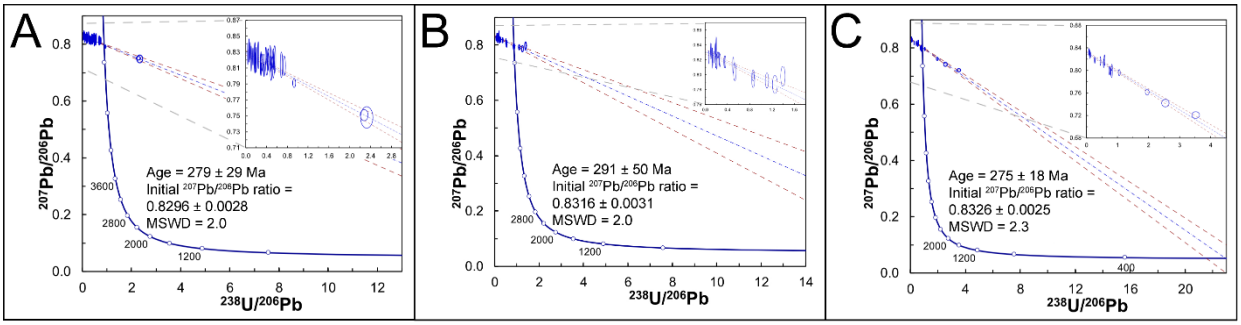

Fig. 4C1 *Tera–Wasserburg diagrams of samples (A) P1, (B) P2 and (C) P3. Ages are calculated from the lower intercept of the regressions through the analyses with the concordia, whereas initial $^{207}Pb/^{206}Pb$ ratios are calculated from the upper intercept of the regressions with the y axis. Dashed blue lines are regressions and dashed red lines are the error envelopes. Data-point error ellipses are 2σ, and age uncertainties are 95% confidence. The diagrams are plotted with Isoplot 3.7.5 (Ludwig, 2012).*

Epidote $^{238}U/^{206}Pb$ and $^{207}Pb/^{206}Pb$ ratios are given in Table 4.1, whereas the Tera–Wasserburg diagrams for sample P1, P2 and P3 are presented in Fig. 4C1. The age uncertainties, given at 95 % confidence level, are large due to high initial Pb contents in all of the single spot analyses causing the data-points to plot close to the upper end of the regression. More in detail, in epidote (or initial Pb-rich minerals in general) U–Pb geochronology with the Tera–Wasserburg approach (Tera and Wasserburg, 1972), the age uncertainty is determined by the spread of all data-points along a regression: analyses that are rich(er) in initial Pb plot closer to the upper end of the regression. Better precision is obtained if more data-points plot away from the upper end (i.e., are initial Pb-poorer), hence constraining the lower end of the regression and consequently the age (which is given by the lower intercept between regression and concordia). For initial Pb-rich minerals, like epidote, most data-points tend to plot close to the upper end of the regression, hence large age uncertainties. This is the main limitation of epidote U–Pb dating with the Tera–Wasserburg approach, which – in turn – yields highly precise initial $^{207}Pb/^{206}Pb$ ratios. The fact that all Permian ages and Permian initial $^{207}Pb/^{206}Pb$ ratios plot within uncertainty of each other offers the advantage of being able to combine the three datasets of single samples to obtain a more precise age: by comparing the Tera–Wasserburg diagrams of single samples (Fig. 4C1) with Fig. 4.3, the effect of initial Pb-poorer analyses in bettering age precision is evident. Samples P1 and P3 were measured on June 8th 2021, with AVC and CAP allanite samples giving anchored Tera–Wasserburg ages of, respectively, 282.1 ± 3.4 Ma and 282.4 ± 4.2 Ma. On June 9th 2021, only AVC allanite was used as secondary reference material in the analytical session of sample P2, yielding an anchored Tera–Wasserburg age of 280.7 ± 4.3 Ma. All allanite Tera–Wasserburg ages

are consistent with their published U–Pb ages (see Gregory et al., 2007). More details on the protocol are given in Peverelli et al. (2021; Chapter 2 of this thesis).

TABLE 4.1

$^{238}U/^{206}Pb$ and $^{207}Pb/^{206}Pb$ ratios and uncertainties as 2 standard errors (2 SE) measured by LA-ICP-MS.

Analysis number	$^{238}U/^{206}Pb$	2 SE	$^{207}Pb/^{206}Pb$	2 SE
		Sample P1		
1	0.489	0.014	0.8058	0.0094
2	0.085	0.003	0.831	0.009
3	0.175	0.008	0.823	0.016
4	0.346	0.010	0.814	0.011
5	0.242	0.009	0.826	0.014
6	0.194	0.006	0.8232	0.0083
7	0.526	0.013	0.8175	0.0059
8	0.292	0.009	0.8183	0.0088
9	0.488	0.012	0.817	0.007
10	2.28	0.062	0.7509	0.0056
11	0.040	0.002	0.8238	0.0077
12	0.740	0.020	0.81	0.01
13	0.388	0.011	0.825	0.009
14	0.317	0.009	0.817	0.009
15	0.189	0.005	0.8224	0.0074
16	0.686	0.020	0.814	0.013
17	0.176	0.006	0.819	0.008
18	0.471	0.013	0.8148	0.0081
19	0.424	0.012	0.8183	0.0099
20	0.531	0.017	0.816	0.015
21	0.062	0.003	0.832	0.012

22	0.139	0.006	0.824	0.009
23	0.429	0.012	0.822	0.01
24	0.107	0.005	0.822	0.013
25	0.039	0.002	0.828	0.011
26	0.540	0.013	0.8139	0.0045
27	0.554	0.019	0.821	0.014
28	0.472	0.013	0.826	0.01
29	0.203	0.006	0.826	0.008
30	2.32	0.97	0.748	0.011
31	0.201	0.006	0.8146	0.0081
32	0.929	0.025	0.7912	0.0047
33	0.352	0.010	0.8075	0.0068
34	0.405	0.015	0.8112	0.0083
35	0.290	0.008	0.8087	0.0068
36	0.293	0.009	0.816	0.012
		Sample P2		
1	0.229	0.008	0.8265	0.0036
2	0.102	0.003	0.8293	0.0068
3	0.191	0.008	0.8216	0.0062
4	0.130	0.004	0.8264	0.0081
5	0.106	0.006	0.8319	0.0083
6	0.100	0.003	0.8338	0.0073
7	0.189	0.004	0.8176	0.0069
8	0.861	0.014	0.7972	0.0043
9	0.198	0.005	0.835	0.013
10	0.209	0.006	0.8175	0.0083
11	1.25	0.04	0.79	0.01

12	0.132	0.004	0.822	0.011
13	0.069	0.003	0.8235	0.0072
14	0.344	0.007	0.8174	0.0066
15	0.534	0.021	0.80	0.01
16	0.165	0.004	0.8238	0.0066
17	0.862	0.022	0.7947	0.0097
18	1.11	0.025	0.7924	0.0083
19	0.360	0.009	0.8173	0.0067
20	0.506	0.010	0.8128	0.0089
21	0.252	0.005	0.8216	0.0067
22	0.266	0.010	0.8196	0.0072
23	0.184	0.004	0.8345	0.0071
24	1.40	0.03	0.798	0.011
		Sample P3		
1	0.552	0.014	0.8124	0.0063
2	0.266	0.007	0.8181	0.0047
3	0.450	0.012	0.8166	0.0064
4	0.071	0.002	0.8336	0.0044
5	0.809	0.022	0.7974	0.0082
6	0.742	0.021	0.7995	0.0063
7	1.96	0.05	0.7613	0.0042
8	3.52	0.10	0.7208	0.0049
9	0.585	0.015	0.8179	0.0079
10	0.134	0.004	0.8277	0.004
11	2.54	0.10	0.7421	0.0055
12	1.06	0.03	0.796	0.004
13	0.096	0.003	0.8304	0.0043

14	0.081	0.002	0.8329	0.0048
15	0.100	0.003	0.827	0.005
16	0.105	0.003	0.8303	0.0044
17	0.815	0.020	0.8053	0.0045

References

Abrecht, J., Schaltegger, U., 1988. Aplitic intrusions in the Central Aar massif basement: geology, petrography and Rb/Sr data. Eclogae Geol. Helv. 81, 227–239. http://doi.org/10.5169/seals-166177

Airaghi, L., Bellahsen, N., Dubacq, B., Chew, D., Rosenberg, C., Janots, E., Waldner, M., Magnin, V., 2020. Pre-orogenic upper crustal softening by lower greenschist facies metamorphic reactions in granites of the central Pyrenees. J. Metamorph. Geol. 38, 183–204. https://doi.org/10.1111/jmg.12520

Baumberger, R., Herwegh, M., Kissling, E., Survey, S.G., 2022. Remote sensing and field data based structural 3D modelling (Haslital , Switzerland) in combination with uncertainty estimation and verification by underground data 161–197.

Bellahsen, N., Bayet, L., Denele, Y., Waldner, M., Airaghi, L., Rosenberg, C., Dubacq, B., Mouthereau, F., Bernet, M., Pik, R., Lahfid, A., Vacherat, A., 2019. Shortening of the axial zone, pyrenees: Shortening sequence, upper crustal mylonites and crustal strength. Tectonophysics 766, 433–452. https://doi.org/10.1016/j.tecto.2019.06.002

Berger, A., Mercolli, I., Herwegh, M., and Gnos, E.: Geological Map of the Aar Massif, Tavetsch and Gotthard Nappes, Geol. spec. Map 1:100000, explanatory notes 129, Federal Office of Topography swisstopo, Bern, Switzerland, 2017.

Bird, D.K., Cho, M., Janik, C.J., Liou, J.G., Caruso, L.J., 1988. Compositional, order/disorder, and stable isotope characteristics of Al-Fe epidote, State 2-14 drill hole, Salton Sea geothermal system. J. Geophys. Res. 93, 135–144. https://doi.org/10.1029/jb093ib11p13135

Bürgmann, R., Dresen, G., 2008. Rheology of the lower crust and upper mantle: Evidence from rock mechanics, geodesy, and field observations. Annu. Rev. Earth Planet. Sci. 36, 531–567. https://doi.org/10.1146/annurev.earth.36.031207.124326

Campani, M., Mulch, A., Kempf, O., Schlunegger, F., Mancktelow, N., 2012. Miocene paleotopography of the Central Alps. Earth Planet. Sci. Lett. 337–338, 174–185. https://doi.org/10.1016/j.epsl.2012.05.017

Chacko, T., Riciputi, R., Cole, R., Horita, J., 1999. A new technique for determining equilibrium hydrogen isotope fractionation factors using the ion microprobe: Application to the epidote-water system. Geochim. Cosmochim. Acta 63, 1–10. https://doi.org/10.1016/S0016-7037(99)00007-1

Ferry, J.M., 1979. Reaction mechanisms, physical conditions, and mass transfer during hydrothermal alteration of mica and feldspar in granitic rocks from south-central Maine, USA. Contrib. to Mineral. Petrol. 68, 125–139. https://doi.org/10.1007/BF00371895

Fitz Gerald, J.D., Stünitz, H., 1993. Deformation of granitoids at low metamorphic grade. I: Reactions and grain size reduction. Tectonophysics 221, 269–297. https://doi.org/10.1016/0040-1951(93)90163-E

Franz, G., Liebscher, A., 2004. Physical and Chemical Properties of the Epidote Minerals-An Introduction-. Rev. Mineral. Geochemistry 56, 1–81. https://doi.org/10.2138/gsrmg.56.1.1

Gregory, C.J., Rubatto, D., Allen, C.M., Williams, I.S., Hermann, J., Ireland, T., 2007. Allanite micro-geochronology: A LA-ICP-MS and SHRIMP U-Th-Pb study. Chem. Geol. 245, 162–182. https://doi.org/10.1016/j.chemgeo.2007.07.029

Gueydan, F., Leroy, Y.M., Jolivet, L., Agard, P., 2003. Analysis of continental midcrustal strain localization induced by microfracturing and reaction-softening. J. Geophys. Res. Solid Earth 108. https://doi.org/10.1029/2001jb000611

Herwegh, M., Berger, A., Baumberger, R., Wehrens, P., Kissling, E., 2017. Large-Scale Crustal-Block-Extrusion During Late Alpine Collision. Sci. Rep. 7, 1–10. https://doi.org/10.1038/s41598-017-00440-0

Herwegh, M., Berger, A., Glotzbach, C., Wangenheim, C., Mock, S., Wehrens, P., Baumberger, R., Egli, D., Kissling, E., 2020. Late stages of continent-continent collision: Timing, kinematic evolution, and exhumation of the Northern rim (Aar Massif) of the Alps. Earth-Science Rev. 200, 102959. https://doi.org/10.1016/j.earscirev.2019.102959

Hoefs, J. 2018. Stable Isotope Geochemistry. Springer International Publishing AG, part of Springer Nature 2018. https://doi.org/10.1007/978-3-319-78527-1

Incerpi, N., Martire, L., Manatschal, G., Bernasconi, S.M., Gerdes, A., Czuppon, G., Palcsu, L., Karner, G.D., Johnson, C.A., Figueredo, P.H., 2020. Hydrothermal fluid flow associated to the extensional evolution of the Adriatic rifted margin: Insights from the pre- to post-rift sedimentary sequence (SE Switzerland, N ITALY). Basin Res. 32, 91–115. https://doi.org/10.1111/bre.12370

Janecke, S.U., Evans, J.P., 1988. Feldspar-influenced rock rheologies. Geology 16, 1064–1067. https://doi.org/10.1130/0091-7613(1988)016<1064:FIRR>2.3.CO;2

Krsnik, E., Methner, K., Campani, M., Botsyun, S., Mutz, S.G., Ehlers, A., Kempf, O., Fiebig, J., Schlunegger, F., Mulch, A., 2021: Miocene high elevation and high relief in the Central Alps. Solid Earth, 12, 2615–2631. https://doi.org/10.5194/se-12-2615-2021

Ludwig, K. R., 2012: User's Manual for A Geochronological Toolkit for Microsoft Excel, Berkeley Geochronology Center, Berkeley, CA, USA, 75 pp.

Malatesta, C., Crispini, L., Ildefonse, B., Federico, L., Lisker, F., Läufer, A., 2021. Microstructures of epidote-prehnite bearing damaged granitoids (northern Victoria Land, Antarctica): clues for the interaction between faulting and hydrothermal fluids. J. Struct. Geol. 147. https://doi.org/10.1016/j.jsg.2021.104350

Morad, S., El-Ghali, M.A.K., Caja, M.A., Sirat, M., Al-Ramadan, K., Manurberg, H., 2010. Hydrothermal alteration of plagioclase in granitic rocks from Proterozoic basement of SE Sweden. Geol. J. 45, 105–116. https://doi.org/10.1002/gj.1178

Oberhänsli, R., Schenker, F. and Mercolli, I., 1988. Indications of Variscan nappe tectonics in the Aar Massif. Schweizerische mineralogische und petrographische Mitteilungen, 68(3), pp.509-520.

Oliot, E., Goncalves, P., Marquer, D., 2010. Role of plagioclase and reaction softening in a metagranite shear zone at mid-crustal conditions (Gotthard Massif, Swiss Central Alps). J. Metamorph. Geol. 28, 849–871. https://doi.org/10.1111/j.1525-1314.2010.00897.x

Peverelli, V., Ewing, T., Rubatto, D., Wille, M., Berger, A., Villa, I.M., Lanari, P., Pettke, T., Herwegh, M., 2021a. U−Pb geochronology of epidote by laser ablation inductively coupled plasma mass spectrometry (LA-ICP-MS) as a tool for dating hydrothermal-vein formation. Geochronology 3, 123–147. https://doi.org/10.5194/gchron-3-123-2021

Peverelli, V., Berger, A., Wille, M., Rubatto, D., Putlitz, B., Pettke, T., Herwegh, M., 2021b. U–Pb geochronology and isotopic signatures of epidote in hydrothermal veins: evidence for Eo-Alpine fluid circulation in the Albula area (eastern Swiss Alps). https://doi.org/10.7185/gold2021.4577

Plümper, O., Putnis, A., 2009. The complex hydrothermal history of granitic rocks: Multiple feldspar replacement reactions under subsolidus conditions. J. Petrol. 50, 967–987. https://doi.org/10.1093/petrology/egp028

Plümper, O., Botan, A., Los, C., Liu, Y., Malthe-Sørenssen, A., Jamtveit, B., 2017. Fluid-driven metamorphism of the continental crust governed by nanoscale fluid flow. Nat. Geosci. 10, 685–690. https://doi.org/10.1038/ngeo3009

Rolland, Y., Cox, S.F., Corsini, M., 2009. Constraining deformation stages in brittle-ductile shear zones from combined field mapping and 40Ar/39Ar dating: The structural evolution of the Grimsel Pass area (Aar Massif, Swiss Alps). J. Struct. Geol. 31, 1377–1394. https://doi.org/10.1016/j.jsg.2009.08.003

Schaltegger, U., Corfu, F., 1992. The age and source of late Hercynian magmatism in the central Alps: evidence from precise U-Pb ages and initial Hf isotopes. Contrib. to Mineral. Petrol. 111, 329–344. https://doi.org/10.1007/BF00311195

Schneeberger, R.B., 2017. Interplay in 3D between faults and water flow paths in crystalline bedrock (Grimsel , Switzerland). PhD thesis.

Schneeberger, R., Kober, F., Lanyon, G.W., Mäder, U.K., Spillmann, T., Blechschmidt, I., 2019. Grimsel Test Site: Revisiting the site-specific geoscientific knowledge.

Sheppard, S.M.F., 2018. Characterization and isotopic variations in natural waters. Stable Isot. High Temp. Geol. Process. 165–183. https://doi.org/10.1515/9781501508936-011

Smye, A.J., Roberts, N.M.W., Condon, D.J., Horstwood, M.S.A., Parrish, R.R., 2014. Characterising the U-Th-Pb systematics of allanite by ID and LA-ICPMS: Implications for geochronology. Geochim. Cosmochim. Acta 135, 1–28. https://doi.org/10.1016/j.gca.2014.03.021

Stipp, M., Stünitz, H., Heilbronner, R., & Schmid, S. M., 2002. Dynamic recrystallization of quartz: correlation between natural and experimental conditions. Geological Society, London, Special Publications, 200(1), 171-190. https://doi.org/10.1144/GSL.SP.2001.200.01.11

Stünitz, H., Gerald, J.D.F., 1993. Deformation of granitoids at low metamorphic grade. II: Granular flow in albite-rich mylonites. Tectonophysics 221, 299–324. https://doi.org/10.1016/0040-1951(93)90164-F

Tera, F., Wasserburg, G.J., 1972. U-Th-Pb systematics in three Apollo 14 basalts and the problem of initial Pb in lunar rocks. Earth Planet. Sci. Lett. 14, 281–304. https://doi.org/https://doi.org/10.1016/0012-821X(72)90128-8

Wehrens, P., Berger, A., Peters, M., Spillmann, T., Herwegh, M., 2016. Deformation at the frictional-viscous transition: Evidence for cycles of fluid-assisted embrittlement and ductile

deformation in the granitoid crust. Tectonophysics 693, 66–84. https://doi.org/10.1016/j.tecto.2016.10.022

Wehrens, P., Baumberger, R., Berger, A., Herwegh, M., 2017. How is strain localized in a meta-granitoid, mid-crustal basement section? Spatial distribution of deformation in the central Aar massif (Switzerland). J. Struct. Geol. 94, 47–67. https://doi.org/10.1016/j.jsg.2016.11.004

5.

Epidote dissolution–precipitation during viscous granular flow: a micro-chemical and isotope study

Veronica Peverelli[1], Alfons Berger[1], Martin Wille[1], Thomas Pettke[1], Pierre Lanari[1], Igor M. Villa[1,2], & Marco Herwegh[1]

[1]*Institute of Geological Sciences, University of Bern, Switzerland*

[2]*Dipartimento di Scienze dell'Ambiente e della Terra, University of Milano-Bicocca, Italy*

In review for publication in EGU *Solid Earth*: https://doi.org/10.5194/egusphere-2022-311

"How wonderful that we have met with a paradox. Now we have some hope of making progress."

Niels Bohr, 1885–1962

ABSTRACT Deformation of polymineralic aggregates can be accommodated by viscous granular flow, a process mediated by the interplay among intracrystalline plasticity and dissolution–precipitation, each active in specific minerals at given *P–T* conditions. Common rock-forming minerals like quartz, feldspars and sheet silicates have been intensively studied in terms of deformation processes. Instead, the deformation behavior of epidote and its role during viscous granular flow is not well investigated, although this mineral is ubiquitous in granitic rocks deforming at greenschist-facies conditions. In this contribution, we provide microstructural and geochemical evidence for the occurrence of dissolution–precipitation of epidote during deformation of an epidote-quartz vein. The main part of the vein is deformed producing a fold, which is visible due to relicts of primary-growth layering inside the vein. The deformation mechanisms active during deformation include dynamic recrystallization of quartz by subgrain rotation recrystallization, producing grain-size reduction of the primary vein quartz. Recrystallization occurs contemporaneously with dissolution and (re)precipitation of epidote, and grain-boundary sliding, leading to a combined process described as viscous granular flow. The combination of intracrystalline plasticity, grain boundary sliding and dissolution locally and repeatedly produce creep cavities. These represent not only *loci* for nucleation of new epidote grains at the expenses of dissolved ones, but they also allow fluid-mediated transport of elements. The same trace element patterns between old epidote relicts and newly formed grains, with much narrower variability, indicate a process of chemical homogenization. The nature of the fluid mediating deformation is investigated using Pb–Sr isotope data of epidote, which suggest that deformation is assisted by internally recycled fluids with the addition of a syn-kinematic external fluid component.

5.1 Introduction

Deformation microstructures preserved in rocks are the result of the interplay of multiple microscale deformational processes, which may be identified and appreciated through careful petrographic studies (e.g., Passchier, 2005). These processes – which may be coupled to metamorphic reactions and diffusion (e.g., Pearce et al., 2013; Wintsch and Yeh, 2013; Bukovská et al., 2016; Giuntoli et al., 2018; Lanari and Duesterhoeft, 2019) – are the response of the grains to varying physico-chemical conditions in order to minimize the system's internal energy (e.g., Evans et al., 2001; Herwegh and Berger, 2004; Passchier, 2005; Karato, 2008; Herwegh et al., 2011; Hobbs et al., 2010). Microstructures of monomineralic aggregates are determined by the deformation behavior of the constituent mineral and by the physical conditions (e.g., temperature, stress, availability of fluids) existing during deformation. For example, Stipp et al. (2002) showed that the microstructures resulting from dynamic recrystallization of quartz can be linked to different recrystallization mechanisms active at increasing temperatures and strain rates. However, this type of interpretations is more complicated when dealing with polymineralic aggregates, where the modal amounts and specific deformation mechanisms of each mineral have an effect on the deformation behavior of the bulk rock (e.g., Handy, 1990; 1994; Olgaard, 1990; Stünitz and Fitz Gerald, 1993; Kruse and Stünitz, 1999; Tullis, 2002; Herwegh and Berger, 2004; Passchier, 2005; Herwegh et al., 2011; Wehrens et al., 2017). As an example, it has been shown that the grain size of calcite in mylonitic carbonates is determined by the grain size and volume abundance of second phases, such as sheet silicates (Olgaard, 1990; Herwegh and Berger, 2004; Herwegh et al., 2011). In this context, mass transfer processes like dissolution–precipitation play a fundamental role in that they enable the redistribution of material within the deforming system (e.g., Herwegh and Jenni, 2001; Konrad-Schmolke et al., 2018). The essential requisite for dissolution–precipitation processes to occur is the presence of a fluid phase (e.g., Putnis, 2009; Putnis and Austrheim, 2010; Putnis and John, 2010). In the presence of a fluid, dissolved material may precipitate into intragranular voids of an initially monomineralic aggregate during deformation. In this scenario, the process of dissolution–precipitation in combination with the presence of a second phase keeps the grain sizes of the deforming aggregate small in a process called viscous granular flow (Olgaard, 1990; Fitz Gerald and Stünitz, 1993; Stünitz and Fitz Gerald, 1993; Paterson, 1995; Herwegh and Berger, 2004; Herwegh et al., 2011). Viscous granular flow is a mechanism in which grains slide relative to one another: this process requires grain-size reduction, and plastic material

transfer and/or dissolution–precipitation processes (or solution transfer) at the scale of the deforming polymineralic aggregate in order to facilitate grain boundary sliding (Stünitz and Fitz Gerald, 1993; Paterson, 1995). Grain boundary sliding promotes the formation of creep cavities, hence allowing the nucleation of second-phase minerals (e.g., Herwegh and Jenni, 2001; Fusseis et al., 2009; Gilgannon et al., 2021). Fluids play a crucial role in deformation processes, but it is often unclear whether the fluids are newly added to the system during deformation (i.e., of external origin) or they are recycled (e.g., *via* dissolution of hydrous minerals). Hence, the interplay of recycled and newly added fluids, mass-transfer processes and deformation mechanisms to produce complex microstructures remains to be fully appreciated.

In this contribution, *via* combined microstructural observations geochemical data and Pb–Sr isotope geochemistry, we investigate the deformational processes affecting epidote [i.e., $Ca_2Al_2(Al,Fe^{3+})Si_3O_{12}(OH)$] and quartz defining a microfold in a deformed epidote-quartz hydrothermal vein. The nature of the fluid mediating dissolution–precipitation of epidote and the dynamic recrystallization of quartz is investigated using Pb and Sr isotope data. Epidote group minerals are widespread rock-forming, hydrothermal and alteration minerals in granitic rocks (e.g., Bird and Spieler, 2004; Enami et al., 2004; Franz and Liebscher, 2004; Grapes and Hoskin, 2004; Schmidt and Poli, 2004; Morad et al., 2010; Hentschel et al., 2020), and they allegedly behave similarly during deformation. Therefore, the occurrence of epidote dissolution–precipitation and its control on the deformation mechanisms of other rock-forming minerals (e.g., dislocation creep in quartz) has important implications for the structural evolution of granitoids, among other epidote-bearing rocks, during orogenic phases.

5.2 Geological setting

The Grimsel Pass area (Fig. 5.1; central Swiss Alps, Switzerland) is in the southern part of the Aar Massif, one of the External Crystalline Massifs of the Alps (e.g. Schneeberger et al., 2019; Berger et al., 2017). The Aar Massif consists of a Paleozoic polymetamorphic basement and Permian intrusives, including the post-Variscan Central Aar Granite. This granitoid was emplaced 299 ± 2 Ma (Schaltegger & Corfu, 1992; Ruiz et al., 2022) and bears clear evidence for Alpine deformation (e.g., Choukroune and Gapais, 1983; Bambauer et al., 2009; and references therein). This Alpine deformation is expressed by a large number of ductile shear zones, and in the southern Aar Massif it can be subdivided into two major phases: (1) a reverse faulting phase with green biotite stable

in the shear zones at < 400 °C (ca. 22–17 Ma; Challandes et al., 2008; Rolland et al., 2009; Wehrens et al., 2017) and (2) a strike-slip phase at lower temperatures with chlorite progressively replacing biotite in the shear zones (from ca. 14 Ma onwards; Rolland et al., 2009; Wehrens et al., 2017; Herwegh et al., 2020). The Alpine metamorphic overprint reached greenschist facies conditions in the area, with maximum temperatures and pressures of 450 ± 30 °C and 6 ± 1 kbar, respectively (Challandes et al., 2008; Goncalves et al., 2012; Villa and Hanchar, 2013). Hydrothermal activity upon exhumation in Alpine times is recorded in the area primarily by the Grimsel Breccia Fault hydrothermal system (e.g., Hofmann et al., 2004; Belgrano et al., 2016; Diamond et al., 2018; Egli et al., 2018). U–Pb geochronology of hydrothermal epidote in veins returned Miocene ages (19.2 ± 4.3 Ma and 16.9 ± 3.7 Ma; Peverelli et al., 2021; Chapter 2 of this thesis) related to fluid circulation occurring during the Alpine orogenic phases, already described on the basis of cleft mineralization (e.g., Mullis et al., 1994; Janots et al., 2012; Berger et al., 2013; 2022; Rossi and Rolland, 2014; Bergemann et al., 2017; Ricchi et al., 2019). In addition, Permian ages (279 ± 29 Ma, 291 ± 50 Ma and 275 ± 18 Ma) returned by other epidote veins revealed pre-orogenic fluid circulation in the Grimsel Pass area (Peverelli et al., 2022; Chapter 4 of this thesis).

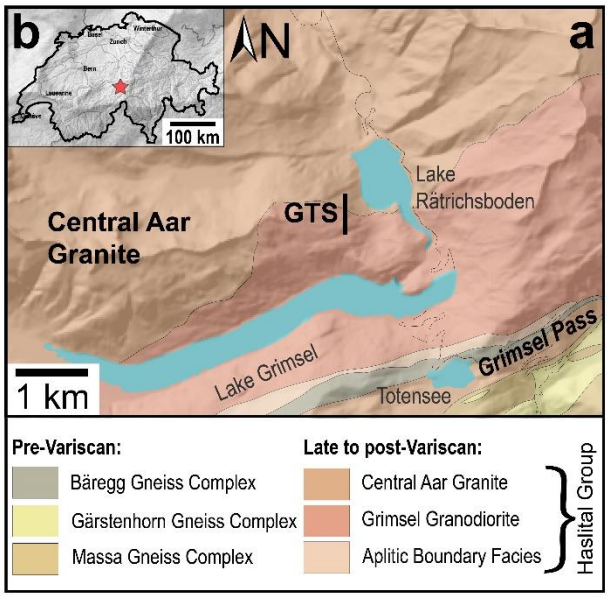

Fig. 5.1 *(a) Geological map of the Grimsel Pass area (redrawn from Wehrens et al., 2016). (b) Geographic location of the Grimsel Pass area (red star) in Switzerland (modified from map.geo.admin.ch). The digital elevation model of panel b is from map.geo.admin.ch.*

5.3 Field relations and sample description

The investigated sample is called Grimsel-1 and it is an epidote-quartz (±biotite) vein that was collected in the Grimsel Pass area inside the Grimsel Test Site (GTS), which is the underground rock laboratory of Nagra (Figs. 5.1 and 5.2a). The GTS is a ca. 500 m long tunnel designed to study rock properties and fluid circulation in the area (see Schneeberger et al., 2019). In the GTS, the anastomosing pattern of shear zones (e.g., Goncalves et al., 2012) is well exposed on the tunnel

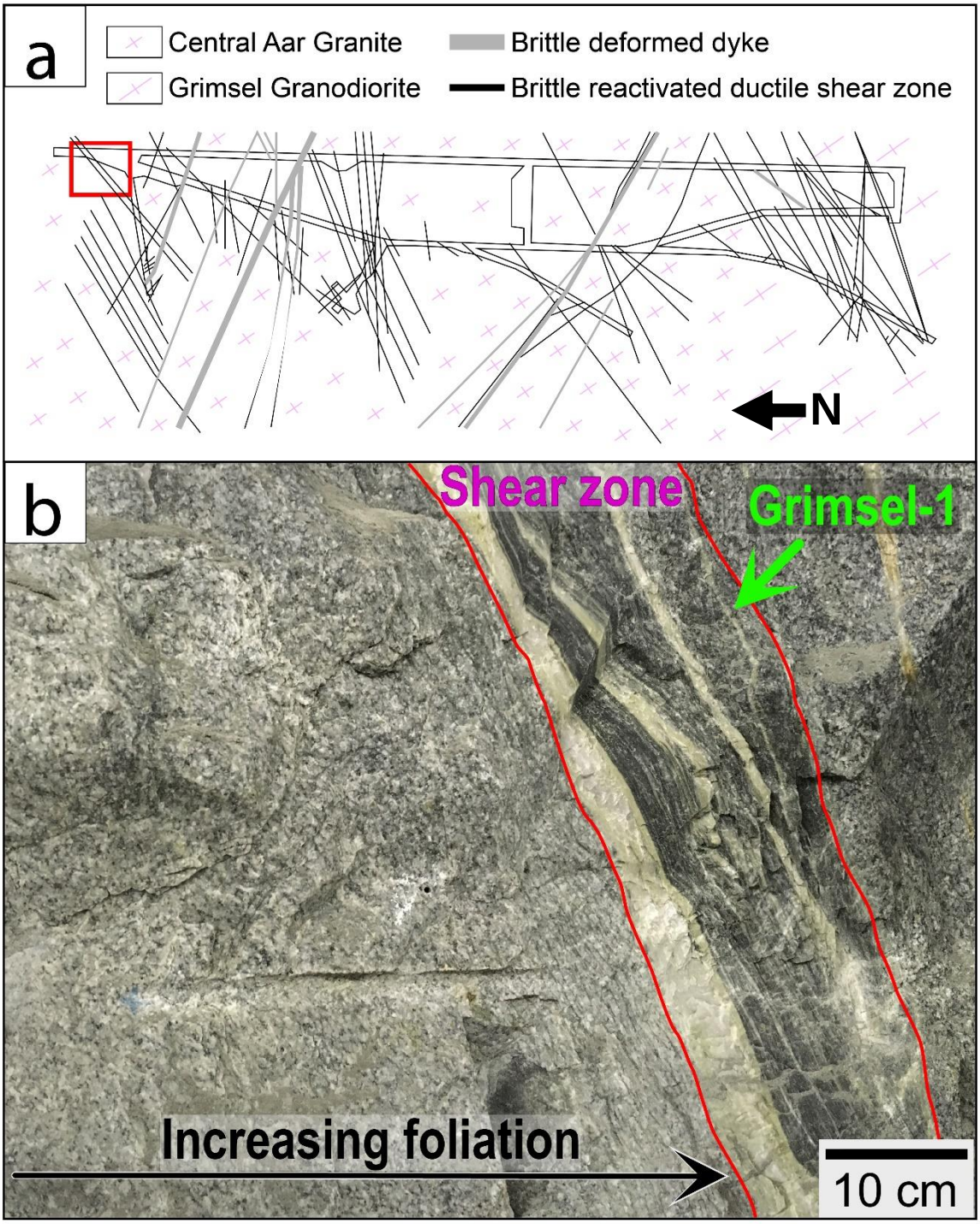

Fig. 5.2 *(a) Geological map of the Grimsel Test Site (GTS) of Nagra with the location of (b) shown in the red rectangle (redrawn from Schneeberger et al., 2019). (b) Field photograph of the location of the studied epidote-quartz vein (Grimsel-1) and the Alpine shear zone with which it is associated; both are in the Central Aar Granite, which shows increasing foliation towards the shear zone (modified from Peverelli et al., 2022; Chapter 4 of this thesis).*

walls. The studied epidote vein is associated to a WSW–ENE-striking and a steeply NNW-dipping shear zone of Alpine age hosted by the Central Aar Granite (Fig. 5.2b). The shear zone is ca. 10

cm wide, whereas the epidote vein (Grimsel-1 in Fig. 5.2b) reaches up to a couple of centimeters in width and ca. 50 cm in length on the tunnel wall.

The host Central Aar Granite displays a gradation from slightly to highly deformed: this is expressed by increasingly intense foliation and decreasing grain size moving towards the shear zone (Fig. 5.2b). In thin section (Fig. 5.3), the host rock mostly preserves its magmatic texture and it is made of ca. 55 vol. % of altered feldspar and 35 vol. % quartz. Feldspar grains are sometimes fractured, and quartz is mostly dynamically recrystallized by subgrain rotation recrystallization (SGR). Relict plagioclase and K-feldspar grains can be recognized by the different type and extent of alteration. Plagioclase (ca. 20 vol. %) is highly altered into epidote and white mica, to a larger extent in the cores than in the rims of the grains. Exsolution *lamellae* are preserved in K-feldspar grains (ca. 35 vol. %), which are moderately altered into sericite. Green biotite, epidote and minor chlorite define a weak foliation and make up ca. 10 vol. %, with a few accessory titanite grains completing the host rock's mineral assemblage. A detailed description of the host rock is outside the scope of this contribution and it is presented in Schneeberger et al. (2009).

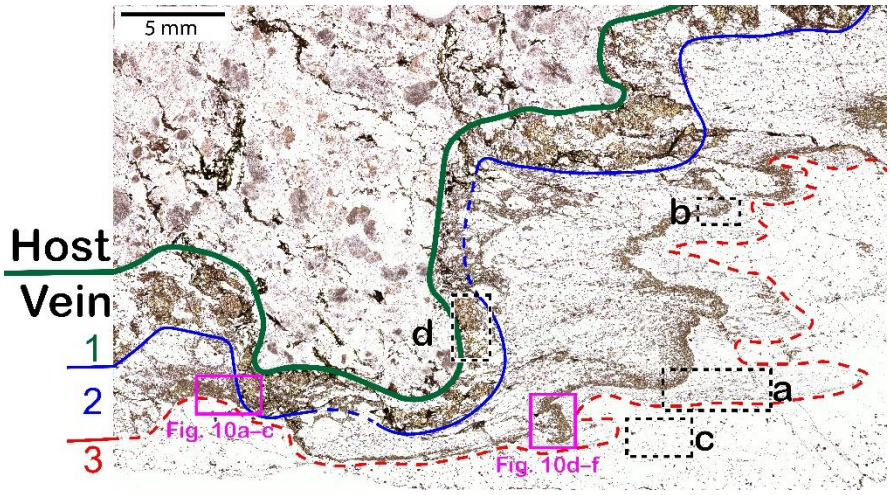

Fig. 5.3 *Transmitted-light microscope scan of the studied epidote-quartz (±biotite) vein and the host Central Aar Granite. The numbers 1–3 refer to the vein layers described in Sect. 5.5.1. Dashed rectangles a–d indicate the locations of the microstructural domains shown in Fig. 5.4a–d. The pink rectangles indicates the location of Fig. 5.10a–c (rotated by 90° clockwise) and Fig. 5.10d–f (rotated by 180°). Plane-polarized light.*

The sharp boundary between host and vein is marked by a change in modal abundances in epidote and quartz. The object of the present investigation is Grimsel-1 epidote-quartz vein (Fig. 5.3). This vein is subdivided into three layers: (1) layer with coarse-grained epidote (Fig. 5.4d), quartz and minor green biotite, (2) heavily deformed and finer-grained epidote-quartz layer (Fig. 5.4a–b), and (3) nearly pure quartz layer (Fig. 5.4c). Grain sizes and mineral proportions in each layer are given in Table 5.1. Layers 2–3 are strongly deformed and folded, as indicated by the spatial distribution of epidote and quartz (Figs. 5.3 and 5.4b). Layer 1, on the other hand, is less affected by this folding

process (Figs. 5.3 and 5.4d). The modal abundance of green biotite varies greatly among the three layers, with a sharp decrease from layer 1 to layer 2, and layer 3 being devoid of biotite (Table 5.1). The transition from layer 2 to layer 3 is marked by a change in the epidote/quartz ratio. This is up to ca. 40/60 in layer 2, whereas layer 3 is characterized by the near absence of epidote. Peverelli et al. (2021; Chapter 2 of this thesis) performed U–Pb dating by LA-ICP-MS of epidote grains in layer 1, obtaining a Tera–Wasserburg age of 19.2 ± 4.3 Ma (Fig. 2.7b). The Tera–Wasserburg regression revealed a single epidote generation at the current analytical precision (i.e., MSWD of 0.79), and the age is interpreted as the timing of epidote crystallization upon vein opening (Peverelli et al., 2021; Sect. 2.5.6 of this thesis). The focus of this manuscript are the deformation mechanisms in layers 2–3.

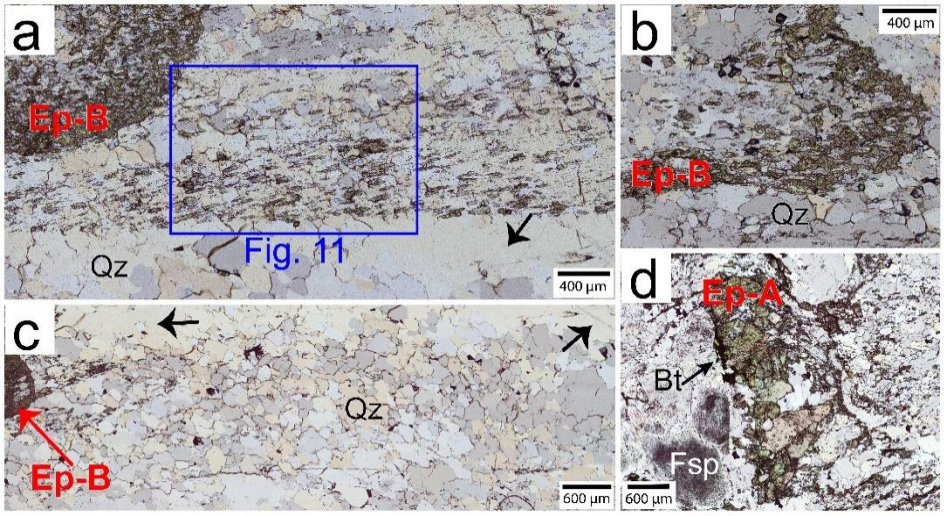

Fig. 5.4 *Transmitted-light scans of the microstructural domains described in Sect. 5.5.1. Microstructures (a–c) are used for microstructural analysis (Fig. 5.7; Sect. 5.5.1.2). The blue rectangle in (a) indicates the location of the cathodoluminescence image of Fig. 5.11. Bt = biotite; Ep = epidote; Fsp = feldspar; Qz = quartz. Plane-polarized light; the anomalous colors are due to the thickness of the section (ca. 60 µm).*

TABLE 5.1

Main characteristics of the vein layers. Ep = epidote; Qtz = quartz.

Layer	Minerals other than ep + qtz	Ep [vol. %]	Ep grain size	Qtz grain size (recrystallized)	Qtz grain size (relicts)
1	Green biotite (ca. 5 vol. %)	ca. 70	0.025–1.6 mm	80–400 µm	0.6–1.2 mm
2	Green biotite (ca. 1 vol. %)	ca. 5–40	5–90 µm	20–170 µm	1.4–2.5 mm
3	-	< 1	5–200 µm	30–400 µm	0.6–2 cm

5.4 Methods

Analyses were performed at the Institute of Geological Sciences of University of Bern (Switzerland). The petrographic characterization of the studied sample was done in a ca. 60 µm thick section on a Zeiss Axioplan petrographic microscope. For backscattered electron (BSE), forescattered electron (FSE) and cathodoluminescence (CL) images, and for electron backscatter diffraction (EBSD), a Zeiss EVO50 scanning electron microscope (SEM) was used with a beam current of ca. 1 nA and accelerating voltage of 20 kV.

5.4.1 Grain-size analysis

Microstructural analysis was performed combining transmission light and scanning electron microscopy to determine average grain sizes of epidote and quartz, as well as their volume fractions in selected microstructural domains. Grain size analysis was carried out in ImageJ (IJ 1.46r; Ferreira and Rasband, 2012) using sketches of the microstructures drawn on transmitted light, BSE and FSE images. In domains where the microstructure is not suitable for an automated grain size analysis by ImageJ (Figs. 5.4b, 5.6 and 5.7c), epidote and quartz areas were directly measured on a transmitted light microscope, approximated as ellipses. Epidote grains that are isolated among quartz grains are defined by the presence of epidote–quartz boundaries. Grain boundaries among or between epidote grains are defined as any irregular discontinuity between grains that is confirmed by different extinction angles at the optic microscope (i.e., misorientations of $\geq 2.5°$). Quartz grains are identified by the presence of visible grain boundaries in BSE images, and confirmed by observations of differences in extinction angles at the optic microscope. The equivalent diameter of each grain (D) is calculated from the grain areas (A) as $D = 2 \times \sqrt{A/\pi}$.

5.4.2 Chemical maps

X-ray compositional maps in wave-length dispersive mode of Si, Fe, Al, Ca, Mn and Sr were obtained by electron probe micro-analyzer (EPMA) on a JEOL-8200 microprobe. Accelerating voltage was 15 keV, specimen current 100 nA, the step size 4 µm, and dwell time was 190 ms (map of layers 1–3; Fig. 10a–c) and 180 ms (map of layer 2; Fig. 10d–f). For calibration of the X-ray maps, spot analyses were acquired with a specimen current of 10 nA, and calibrated using the following standards: wollastonite (SiO_2), olivine (MgO), anorthite (CaO, Al_2O_3), magnetite (FeO),

pyrolusite (MnO), tugtupite (Cl), rutile (TiO_2), and celestite (SrO). The processing of the X-ray compositional maps, including map calibration, was done by using XMapTools (Lanari et al., 2014; 2019). Minerals were identified based on the concentrations of specific elements (i.e., Ca, Fe and Al for epidote; Si for quartz; K for micas) and classified. Maps of the structural formula of epidote were calculated on 12.5 oxygen basis.

5.4.3 Trace elements

For trace element measurements, a RESOlutionSE 193 nm excimer laser system (Applied Spectra, USA) equipped with an S-155 large-volume constant-geometry chamber (Laurin Technic, Australia) coupled with an Agilent 7900 ICP-QMS was employed. During ablation, a He atmosphere was used, and Ar was admixed to the carrier gas before reaching the plasma of the ICP-MS. NIST SRM612 was used for optimization of the analytical conditions, ensuring that the ThO production rate was < 0.2 % and the Th/U sensitivity ratio > 97 %. On-sample fluence was 5 J cm^{-2} and repetition rate 5 Hz. The size of the analysis spots ranged between 20–30 µm, and BSE images were used to plan the analyses to avoid locating any spots across zones with heterogeneous composition (e.g., chemical zoning) or on inclusions. External standardization was done with USGS GSD-1G standard, and the SRM612 standard was measured as an unknown for quality control in absence of a well characterized epidote standard. Bracketing standardization enabled a true-time linear drift correction. Data reduction was carried out with the software SILLS (Guillong et al., 2008), using the sum of total oxides minus H_2O (98.3 % for epidote and 100 % for SRM612) as internal standard (see Halter et al., 2002). The formulation of Pettke et al. (2012) was employed to calculate limits of detection for each element in every analysis.

5.4.4 Pb isotope data

Measurements of $^{207}Pb/^{206}Pb$ (as well as $^{87}Sr/^{86}Sr$; Sect. 5.4.5) were made in epidote micro-separates following the procedure for sample digestion in acids and for column chemistry detailed by Peverelli et al. (2021; Sect. 2.3.3 of this thesis; modified from Nägler and Kamber, 1996). Two epidote micro-separates – each mixing Epidote-A and Epidote-B (see Sect. 5.5.1) in unknown and different proportions – were prepared (Ep_A+B_1 and Ep_A+B_2). After hand-picking, the material was finely ground and washed with MilliQ™ water. Two aliquots of each (Ep_A+B_1a and Ep_A+B_1b, and Ep_A+B_2a and Ep_A+B_2b) were weighed in as replicates for each micro-

separate ensuring ca. 300 ng of Pb in each aliquot. During column chemistry with a Sr-spec™ resin (Horwitz et al., 1992), the Sr and Pb fractions were collected in sequence (Haeusler et al., 2016). One large Epidote-A grain was also handpicked and ground, and an amount of the powder corresponding to 250 ng of Sr was digested in acids before the extraction of the Sr fraction by column chemistry. The Pb fraction of this Epidote-A grain was not collected since Pb isotopic data are available from *in-situ* U–Pb isotope measurements by LA-ICP-MS (Peverelli et al., 2021; Chapter 2 of this thesis). Procedural blank samples were used to assess contamination during work in the laboratories. Pb isotope ratios were measured on a Thermo Fisher Neptune Plus MC-ICP-MS in desolvated plasma mode equipped with a CETAC Aridus 2 desolvating system. Instrumental mass fractionation was corrected within-run by means of a Tl spike. External reproducibility of the measurements was quantified by measuring the NIST NBS981 standard. The measured Pb isotope ratios were identical to those obtained by Rehkämper and Mezger (2000; their Table 4).

5.4.5 Strontium isotope data

Strontium isotope ratios were measured on a ThermoFisher Triton™ thermal ionization mass spectrometer (TIMS) after loading 250 ng Sr diluted in 6.4 M HCl on Re filaments using 1.5 µl Ta-oxide activator. The SRM987 standard (200 ppm; Weis et al., 2006) was measured for quality control. The detected masses were 84, 85, 86 (center cup), 87 and 88. The interference of ^{87}Rb and within-run mass fractionation were corrected for by using the IUPAC ^{87}Rb/^{85}Rb and ^{88}Sr/^{86}Sr values of, respectively, 0.385617 and 8.735209. The SRM987 standard returned a weighted average ^{87}Sr/^{86}Sr ratio of 0.710279 ± 0.000020 (2 standard deviation, SD; number of replicates, n = 12), which is higher than the reference preferred value of 0.710248 (see Weis et al., 2006). Standards AGV-2 (n = 1) and GSP-2 (n = 2) of USGS were measured as unknowns for quality control and the returned, respectively, ^{87}Sr/^{86}Sr ratios of 0.704041 ± 0.000018 (2 standard error, 2 SE), and 0.765396 ± 0.000010 and 0.765202 ± 0.000008. These values are also higher than the reference preferred values of 0.703981 ± 0.00009 (2 SD) and 0.765144 ± 0.000075 (2 SD) for AGV-2 and GSP-2, respectively (see Weis et al., 2006). A correction based on the reference materials returning higher ^{87}Sr/^{86}Sr values than their reference values would produce the same shift in all measured ^{87}Sr/^{86}Sr ratios. Hence, we did not correct our data because only the variability among the samples is relevant in this study, while the interpretation of the absolute Sr isotope

ratios is beyond the scope of this work. Rubidium concentrations were not measured, as a correction for ^{87}Rb-derived ^{87}Sr is not necessary in epidote. This is a valid approach because the incompatibility of Rb in the epidote crystal structure results in negligible Rb concentrations (see Frei et al., 2004; Feineman et al., 2007).

5.5 Results

5.5.1 Microstructural analysis

The different characteristics of epidote and its microstructures in layers 1–3 (Figs. 5.3–5.4) allow the distinction of epidote into Epidote-A and Epidote-B as illustrated below. The microstructural characteristics of epidote – described below – suggest different formation mechanisms between epidote in layer 1 and in layers 2–3.

5.5.1.1 Layer 1: veining and Epidote-A

Layer 1 is characterized by coarse (ca. 0.2–1.6 mm) epidote grains associated with smaller angular ones (ca. 20–200 µm). The coarser epidote grains (Figs. 5.4d and 5.5a–b) form clusters with random shape orientations or are found as isolated crystals. Larger epidote grains are often surrounded by the smaller angular epidote grains (Fig. 5.5c; red arrow) as a result of brittle grain-size reduction upon deformation with brittle deformation behavior of epidote. Epidote is euhedral to anhedral. Anhedral/subhedral epidote has lobate grain boundaries (Fig. 5.5d), and smaller epidote crystals are found in the gaps among the larger ones as well ("Ep clasts" in Fig. 5.5d). Quartz is locally dynamically recrystallized, although some large quartz relicts are present displaying undulose extinction (Fig.

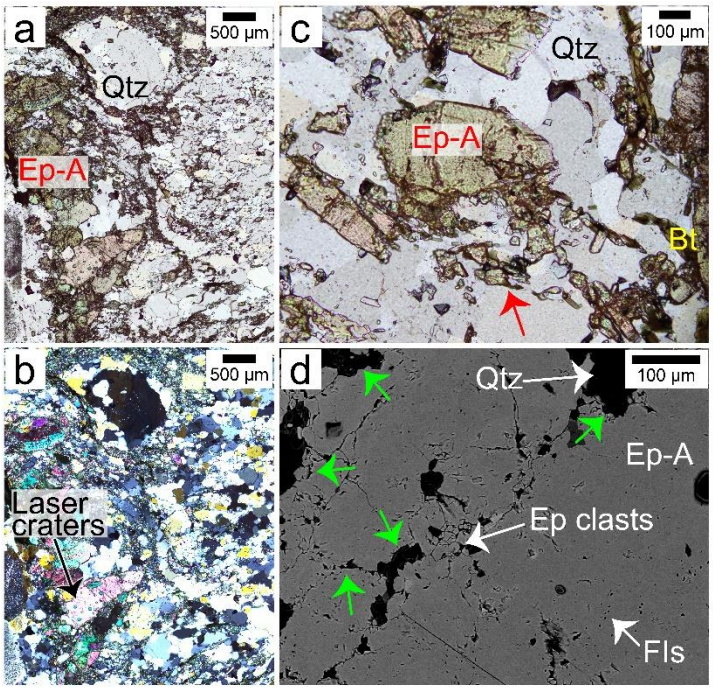

Fig. 5.5 *Details of epidote in layer 1. (a–b) Transmitted light microphotographs of epidote, dynamically recrystallized quartz and quartz; plane-polarized (a) and cross-polarized (b) light. (c) One isolated epidote grain surrounded by epidote clasts (red arrow). (d) Backscattered electron image of one epidote grain showing lobate grain boundaries and microporosity given by fluid inclusions (FIs). Bt = biotite; Ep = epidote; Qtz = quartz. Anomalous colors in panels a and c are due to the thickness of the thin section (ca. 60 µm).*

5.5a–b). Hereafter, we refer to epidote in layer 1 as Epidote-A. U–Pb dating of Epidote-A by LA-ICP-MS returned an age of 19.2 ± 4.3 Ma (Sect. 5.3; Table 2.7).

5.5.1.2 Layers 2–3: microfold and Epidote-B

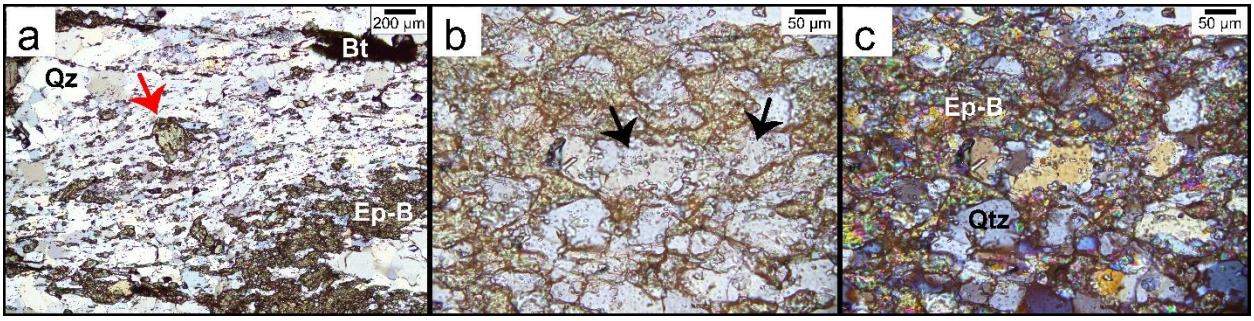

Fig. 5.6 *Transmitted light microphotographs of layer 2. (a) Detail of the epidote microfold, with oval epidote grains hosted by dynamically recrystallized quartz and their long axes oriented consistently with the microfold axial planes; red arrow: euhedral epidote grain. Overlapped imaged in plane-polarized and cross-polarized light. (b–c) Details of quartz enclosures among epidote grains in plane-polarized (b) and cross-polarized (c) light; the black arrows point at epidote and fluid inclusions in quartz. Bt = biotite; Ep = epidote; Qtz = quartz.*

In layers 2–3, the spatial distribution and the variable modal abundance of epidote define a fold (Figs. 5.3, 5.4b, 5.6 and 5A1). Smaller epidote grains with a shape-preferred orientation and quartz define axial planes and limbs (rectangle a in Fig. 5.3; Figs. 5.4a and 5.6). Epidote grain boundaries are mostly curved and irregular, but a few subhedral or euhedral epidote grains are also observed (Fig. 5.6, red arrow). Epidote grains vary between 5–90 µm in size, hampering U–Pb dating of epidote in layers 2–3. The modal abundance of epidote varies between ca. 5 to ca. 40 vol. % within the layer (Table 5.1), defining a quartz-supported microstructure.

Where epidote is most abundant, quartz confined as anhedral enclosures among epidote grains (Figs. 5.4b and 5.6). Small (ca. 1–20 µm in size) oval epidote grains and fluid inclusions

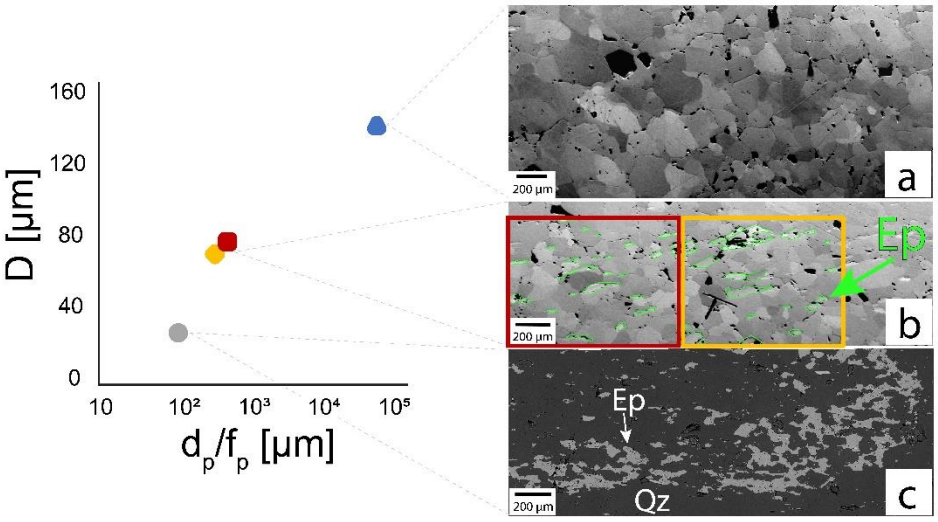

Fig. 5.7 *Correlation between quartz grain size (D) and Zener parameter (ratio between size and abundance of the second phase, p; d_p/f_p) of epidote as the second phase determined in the FS and BSE images of the microstructures in the microfold of layers 2–3. The green lines in the central BSE image contour epidote grains. Ep = epidote; Qz = quartz. Panels a, b and c correspond, respectively, to panels b, a and c of Fig. 5.4.*

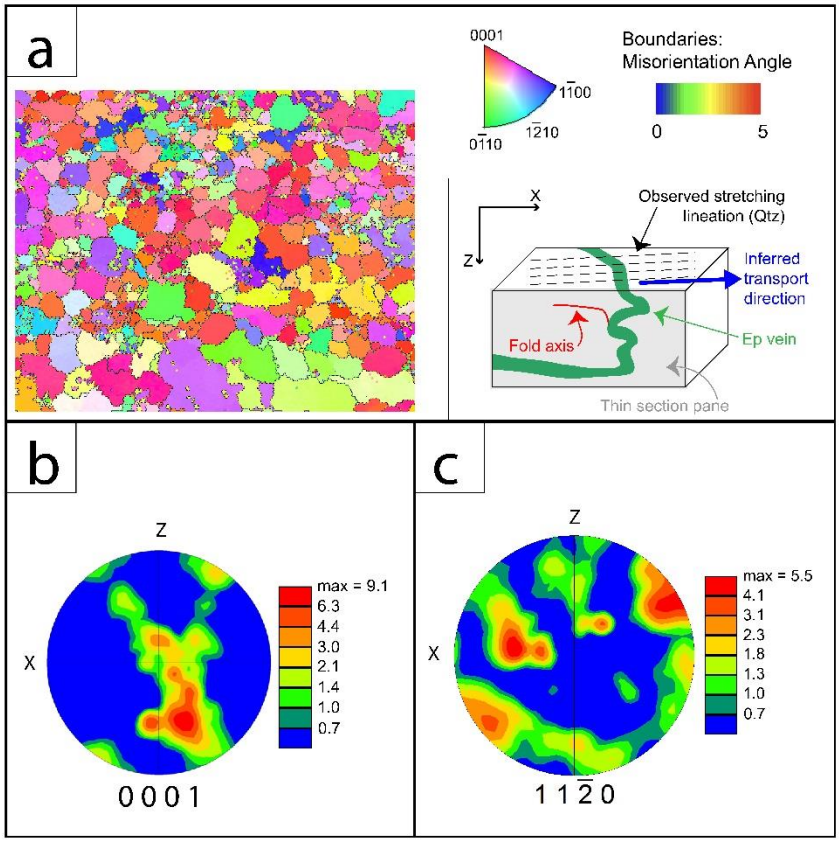

Fig. 5.8 *(a) Electron backscattered diffraction (EBSD) map of quartz in layer 3 and sketch of the thin section. (b) figure of quartz <c> axis, with density area spreading along a single girdle with relics of a cross-girdle. (c) Pole figure of quartz <a> axes.*

are observed within quartz grains (Fig. 5.6). The size of dynamically recrystallized quartz grains correlates with grain size and abundance of epidote (Fi. 5.7). Such a relation, referred to as "Zener relation", can be discussed with respect to the interplay of deformation mechanisms occurring in epidote and quartz simultaneously (see Herwegh et al., 2011). Dynamic recrystallization of quartz occurs by subgrain rotation (Figs. 5.4a–c and 5.7; compare with Stipp et al., 2002), leading to a crystallographic preferred orientation (CPO; Fig. 5.8). This orientation developed a <c> axis single girdle with related <a> axis distribution in the direction of transport (Fig. 5.8). These CPOs are interpreted as basal and rhomb slip systems as seen in Schmid and

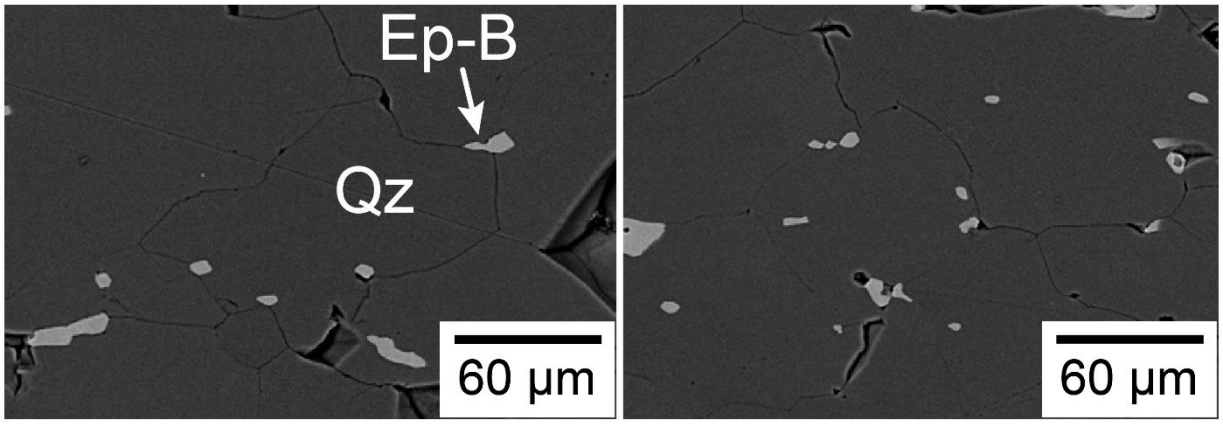

Fig. 5.9 *Backscattered electron images showing epidote (Ep) grains along quartz (Qz) grain boundaries and at triple junctions among quartz grains.*

Casey (1986) and Law (2014). A few quartz relicts are recognized thanks to their undulose extinction (black arrows in Figs. 5.4a, 5.4c and Fig. 5A1). Where minor epidote is present, anhedral epidote grains of few to ca. 10 µm in size are mostly interstitial and found at triple junctions among quartz subgrains (Fig. 5.9). We refer to subhedral to anhedral epidote grains in the microfold in layers 2–3 as Epidote-B.

5.5.2 Major and minor elements

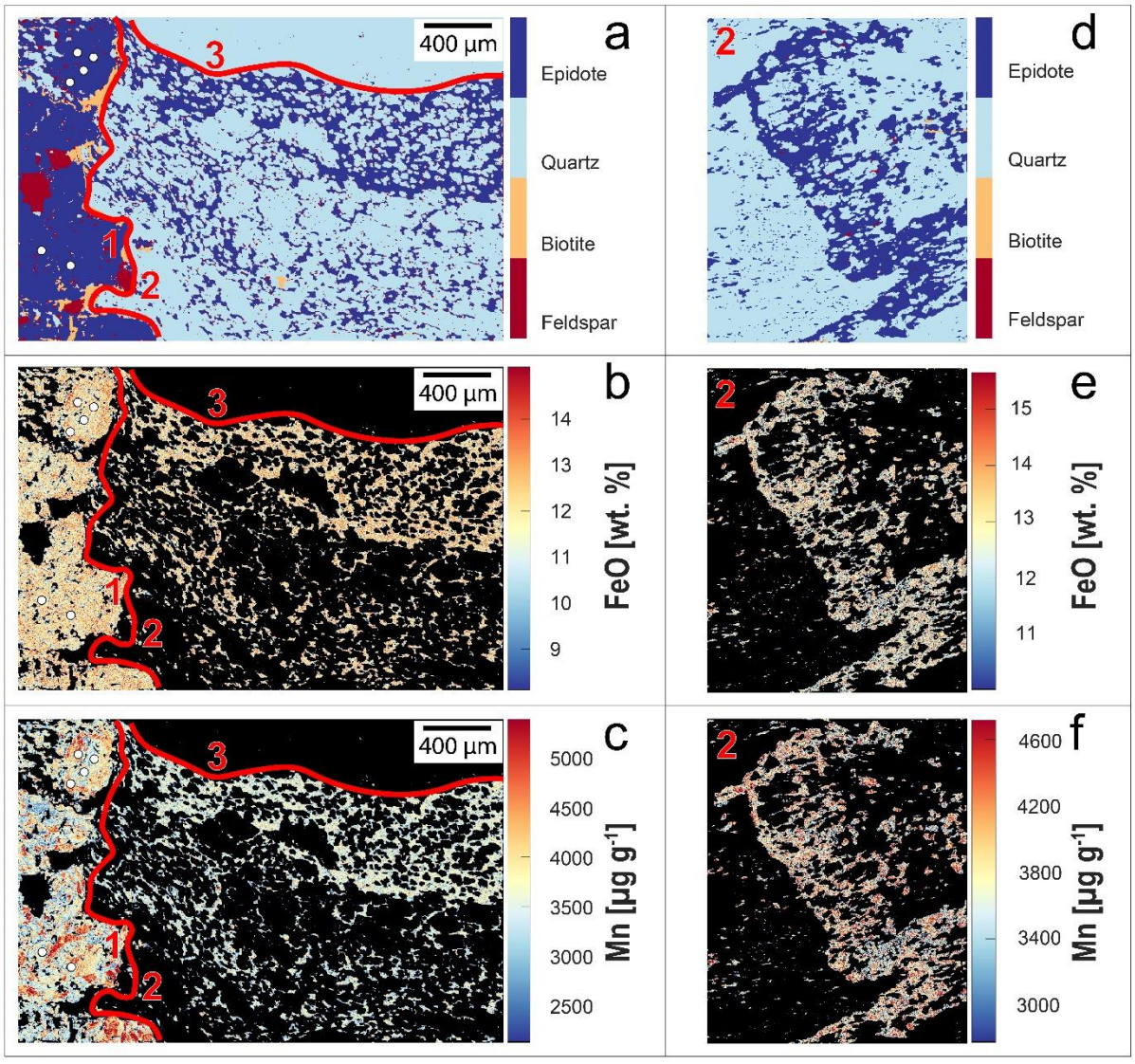

Fig. 5.10 *(a–c) X-ray compositional maps across layers 1–3 (Fig. 5.3; Sect. 5.5.1); white circles indicate spots for U–Pb dating by LA-ICP-MS of Peverelli et al. (2021; Chapter 2 of this thesis), and the pink line separates layer 1 from layers 2–3. (d–f) X-ray compositional maps of layer 2. Red numbers indicate vein layers.*

The compositional maps in Fig. 5.10 (locations shown in Fig. 5.3) cover layers 1–3. The compositions of FeO and Mn range between ca. 12.5–14 wt. % and ca. 2500–5000 µg g^{-1},

respectively, across all analyzed epidote grains. Larger Epidote-A grains in layer 1 are zoned, with FeO and Mn concentrations increasing from core to rim. Epidote in layers 2–3, on the other end, is characterized by uniform concentrations of FeO and Mn. It should be noted that, because the step size of the compositional maps is 4 µm, the chemical variability of epidote in layers 2–3 is better assessed among different grains across the overall microstructure rather than within each crystal (i.e., the majority of grains do not contain enough 4×4 µm pixels).

5.5.3 Trace elements

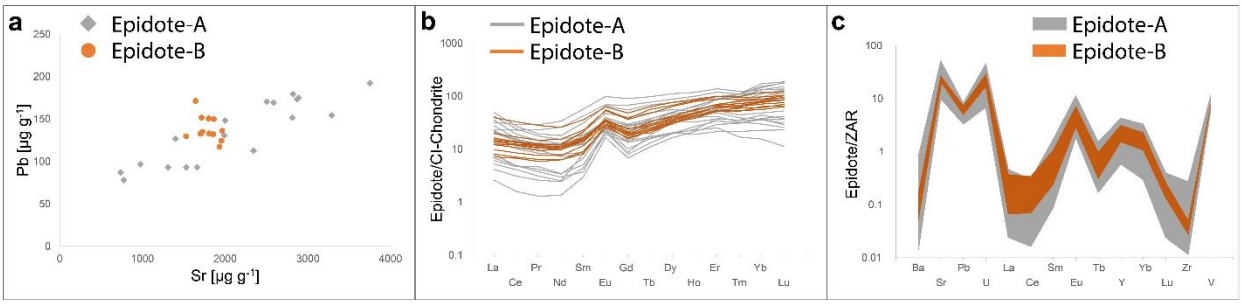

Fig. 5.11 *Epidote LA-ICP-MS data of (a) Pb and Sr, (b) CI-chondrite normalized (McDonough and Sun, 1995) rare earth element patterns (REE), and (c) trace elements normalized to the Central Aar Granite (ZAR; Schaltegger & Krähenbühl, 1990).*

The minimum spot size used for measurements by LA-ICP-MS is 20 µm, which is ca. four times larger than the smallest epidote grains. Therefore, chemical variability is assessed throughout each microstructural layer by relying on measurements in large-enough epidote grains to avoid contamination from grain boundaries. Epidote-A is also addressed here with no specific reference to intra-grain zoning but only across the overall Epidote-A microstructure (i.e., layer 1). Data of Epidote-B are collected in anhedral epidote grains in layer 2. The different extents of chemical variability between Epidote-A and Epidote-B noted in the compositional maps is reflected by trace element data (Table 5B1).

The concentrations of Sr and Pb in Epidote-B overlap with the trend defined by the same elements measured in Epidote-A, but they cover a more limited range of values (Fig. 5.11a). The CI chondrite-normalized rare earth elements (REE) patterns (Fig. 5.11b) of Epidote-A and Epidote-B have similar trends, characterized by positive slopes (La_N/Yb_N of 0.1–0.4 in Epidote-A and 0.03–0.5 in Epidote-B) and variably positive Eu anomalies (1.5–2.4 in Epidote-A and 1.2–2.3 in Epidote-B). The REE trends of Epidote-B fall within the range of Epidote-A and confirm the lesser extent of chemical variability of Epidote-B relative to Epidote-A. Selected elements, plotted as values normalized to the concentrations in the vein's host Central Aar Granite in Fig. 5.11c,

reinforce chemical affinity between Epidote-A and Epidote-B, as well as the lesser chemical variability of the latter relative to the former. Cathodoluminescence images of the recrystallized quartz grains (Fig. 5.12) qualitatively indicate trace element variability also in quartz grains (see Ramseyer et al., 1988; Götze et al., 2001; Nègre et al., 2022).

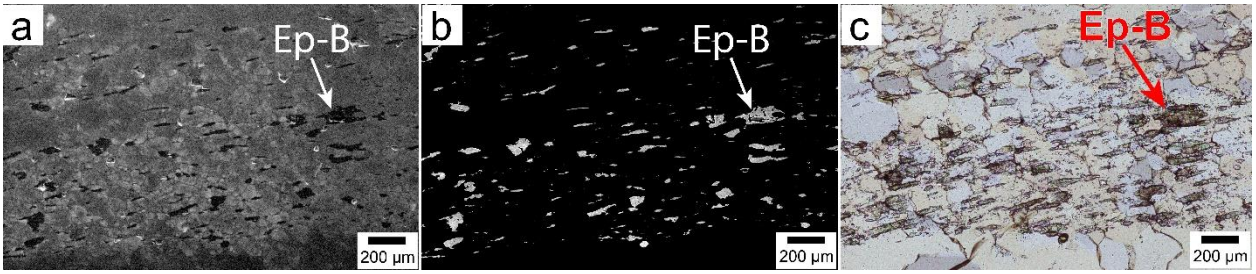

Fig. 5.12 *Cathodoluminescence (CL; a) and backscattered electron images (b) of the microstructural domain in the transmitted light microphotograph of panel c. The only minerals in the images are epidote (Ep) and quartz (unlabeled grains). The different CL contrasts in quartz (a) are due to variable trace element contents. The anomalous colors in panel c are due to the thickness of the thin section (ca. 60 µm).*

5.5.4 Isotope data

TABLE 5.2

Pb and Sr isotopic data. Uncertainties are 2 standard errors (2 SE).

	$^{207}Pb/^{206}Pb$	2 SE	$^{87}Sr/^{86}Sr$	2 SE
Ep_A+B_1a	0.79159	0.00001	0.727803	0.000011
Ep_A+B_1b	0.79108	0.00001	0.727807	0.000007
Ep_A+B_2a	0.79428	0.00001	0.726952	0.000010
Ep_A+B_2b	0.79391	0.00001	0.726830	0.000015
Epidote-A	0.7867[1]	0.0058[1]	0.726552	0.000007

[1]Datum-point #10 of Peverelli et al. (2021; Table 2.7 of this thesis) by LA-ICP-MS.

Strontium and Pb isotopic data (Table 5.2) of the epidote microseparates and those of the Epidote-A grain are plotted in Fig. 5.13. To compare the Pb and Sr isotopic characteristics of Epidote-A with those of the micro-separates mixing Epidote-A and Epidote-B, data obtained from different techniques are combined in a $^{207}Pb/^{206}Pb$ *versus* $^{87}Sr/^{86}Sr$ plot. Such a diagram takes the fundamental difference between the Pb and Sr isotope systems in epidote into account: Sr in epidote is entirely non-radiogenic due to negligible Rb contents of epidote. Instead, the measured $^{207}Pb/^{206}Pb$ ratios contain both initial and radiogenic (i.e., U-derived) Pb, since U mass fractions are 54–350 µg g^{-1} in this epidote sample (Table 2.6). This is true both for each *in-situ* U–Pb isotope

measurement by LA-ICP-MS and for bulk analyses by solution ICP-MS and TIMS. The epidote volume sampled in single LA-ICP-MS analyses is 20–24 × 10^3 µm^3, and in solution ICP-MS measurements it is ca. 9 × 10^9 µm^3. This implies that the extent of chemical homogenization is greatly different between *in-situ* and bulk measurements: $^{207}Pb/^{206}Pb$ ratios measured by LA-ICP-MS range between 0.774–0.794 (Table 2.7), while the same ratios are 0.726830–0.707807 (Table 5.2) by solution ICP-MS. Therefore, in order to directly compare LA-ICP-MS data with *bulk* solution ICP-MS ones, analysis #10 of Peverelli et al. (2021; see their Table 5; Table 2.7 of this thesis) is used to represent Epidote-A in a $^{207}Pb/^{206}Pb$ versus $^{87}Sr/^{86}Sr$ plot (Fig. 5.13). This is the datum-point closest to the average (0.786) and to the median (0.787) values of the $^{207}Pb/^{206}Pb$ ratios measured in Epidote-A by LA-ICP-MS.

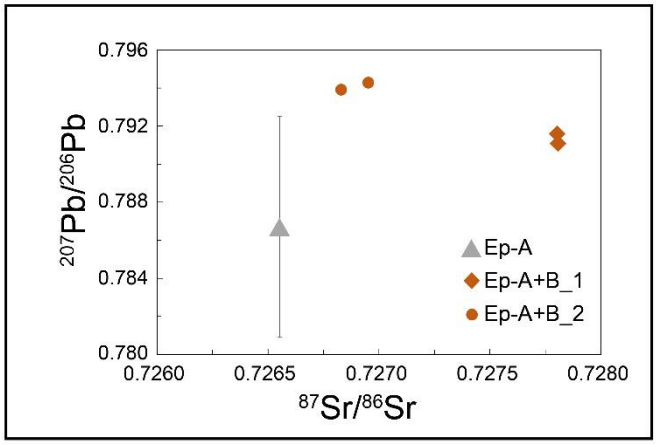

Fig. 5.13 *Total $^{207}Pb/^{206}Pb$ and initial $^{87}Sr/^{86}Sr$ data of Epidote-A and the epidote micro-separates; the $^{207}Pb/^{206}Pb$ ratio of Epidote-A is by LA-ICP-MS (analysis #10 of Peverelli et al., 2021; Table 2.7); all other $^{207}Pb/^{206}Pb$ ratios are by solution ICP-MS; $^{87}Sr/^{86}Sr$ ratios are by TIMS; error bars are smaller than the symbols where not shown.*

5.6 Discussion of the formation mechanisms for the epidote-quartz microfold

5.6.1 Interplay of epidote dissolution–precipitation and quartz dynamic recrystallization

The formation of a hydrothermal vein entails the crystallization of a mineral assemblage from a mineralizing fluid that fills a fracture (Bons et al., 2012). Although the original morphology of the studied epidote-quartz vein is obliterated by deformation, the euhedral, often elongate, shapes of Epidote-A grains (Fig. 5.4d) suggest that the formation of Epidote-A in layer 1 is related to vein-filling mineralization, with crystallization occurring in equilibrium with a fluid. The reasons why layer 1 is less deformed than layers 2–3 may be linked to the closer proximity of layer 1 to the host rock, to a role of mechanically strong epidote clusters forming a load-bearing network, or to a combination of both (Handy, 1990; 1994; Masuda, 1990; 1995; Tullis, 2002; Passchier, 2005). The microstructures in layers 2–3 differing from those in layer 1 (Sect. 5.5.1), along with the lesser extent of chemical variability across epidote grains in layers 2–3 compared to Epidote-A in layer 1 (Figs. 5.10–5.11), suggest that the mechanism of formation of Epidote-B is different than that of

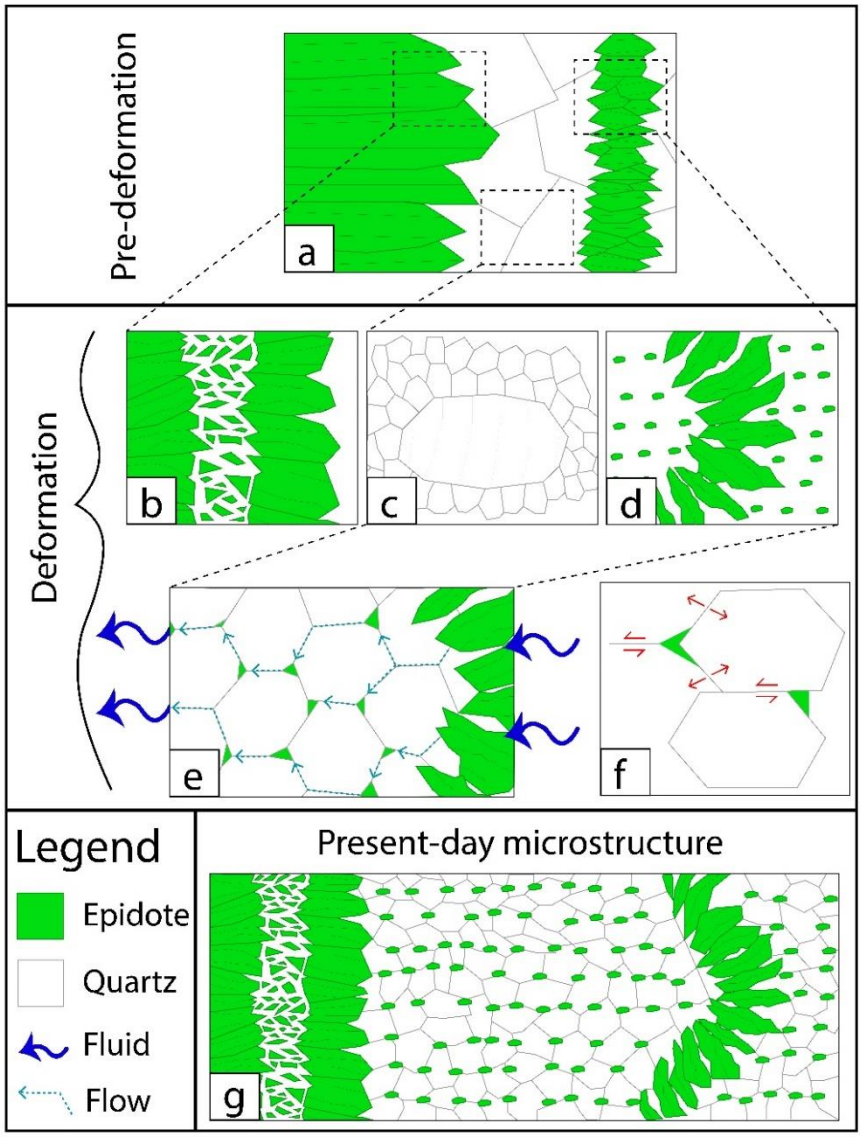

Fig. 5.14 *Sketches of the sequence of events affecting the studied epidote vein. (a) Original microstructure formed upon veining. (b) Detail of the fracturing occurring in Epidote-A in layer 1. (c) Dynamic recrystallization of quartz by subgrain rotation. (d) Folding of the epidote band in layer 2 and dissolution–precipitation of Epidote-B. (e) Detail of the viscous granular flow process and dynamic granular fluid pump allowing Epidote-B to precipitate in creep cavities along quartz grain boundaries. (f) Detail of quartz grain boundary sliding allowing dynamic granular fluid pump (modified from Fusseis et al., 2009). (g) Present-day microstructure. Not to scale.*

Epidote-A. The Zener relation between quartz and epidote in layers 2–3 indicate an interplay between epidote and quartz during the formation of this microstructural domain. At the same time, the alignment of Epidote-B grains along the microfold axial planes (Figs. 5.4a and 5.6), and the presence of minute Epidote-B along grain boundaries of dynamically recrystallized quartz grains (Fig. 5.9) suggest that quartz dynamic recrystallization and epidote-B formation are linked processes, thus that Epidote-B formed during deformation. The overlap in major and trace element compositions of Epidote-B and Epidote-A (Figs. 5.10–5.11), though, demonstrates that these epidote generations are chemically related. One way to reconcile this geochemical affinity with different formation mechanisms is a scenario in which Epidote-B formed *via* deformation-induced dissolution of Epidote-A grains and (re)precipitation. In fact, a few euhedral epidote grains can still be recognized in layer 2 (Fig. 5.6), which are interpreted as Epidote-A relicts inherited from the original vein

morphology. The gradation from epidote-rich/quartz-poor domains to virtually epidote-free/quartz dominated ones in layers 2–3 (Figs. 5.3, 5.4, 5.6a, 5.7 and 5.14g) suggests that the microstructure that formed upon veining was similar to that shown in Fig. 5.14a, and that the original vein morphology was subsequently deformed to form the present-day epidote–quartz spatial distribution. In fact, shifts between epidote-rich and quartz-rich domains are frequent in epidote-quartz veins (e.g., Peverelli et al., 2021; their Figs. 1a and 1c; Figs. 2.1a and 2.1c of this thesis). Further evidence for fluid-mediated mass transfer is also given by CL images of quartz (Fig. 5.12): these indicate trace element variability within single quartz grains, which is most likely the result of recrystallization in the presence of a fluid mediating mass-transfer processes (e.g., Ramseyer et al., 1988; Götze et al., 2001; Nègre et al., 2022). The presence of a fluid during deformation is also supported by fluid inclusions in dynamically recrystallized quartz (Fig. 5.6b–c).

The transport of dissolved epidote-forming material towards the microfold axial planes (Fig. 5.14d) calls for a mechanism allowing the fluid to move throughout the deforming microstructural domain. The presence of ca. 10 μm sized Epidote-B grains along quartz grain boundaries and at triple junctions (Fig. 5.9) implies that dissolved epidote-forming material is transported and precipitated into nucleation locations. This is achieved by the presence of an interconnected network hosting an intergranular fluid that allows mass transfer processes. Fluid circulation at the cm scale enabling mass transfer processes is possible by cavitation with the formation of nucleation sites (Fig. 5.14e–f; also described as "dynamic granular fluid pump"; see Fusseis et al., 2009; Menegon et al., 2015) among sliding dynamically recrystallized quartz grains (Figs. 9 and 12). A first deformation step in which quartz grain size is reduced by dynamic recrystallization via subgrain rotation (Fig. 5.14c) is suggested by a crystallographic preferred orientation in quartz-dominated domains (Fig. 5.8). Once the new quartz grains are formed, grain boundary sliding produces creep cavities (Fig. 5.14e–f; see Herwegh and Jenni, 2001; Fusseis et al., 2009; Gilgannon et al., 2017; 2021), thus creating nucleation *loci* for Epidote-B (Fig. 5.9), regardless of whether the dissolved epidote material is mobilized by diffusion or advection. A similar process is described by Gottardi and Hughes (2022) in quartzites deformed at the brittle–ductile transition in the crust, in which fluid inclusions are redistributed in the quartz matrix by dynamic recrystallization of quartz by subgrain rotation and grain-boundary migration. A similar microstructure and a similar interplay of processes are also discussed in mafic high-temperature mylonites (Kruse and Stünitz, 1999) and quartzites (Nègre et al., 2021; Pongrac et al., 2022). This

first step is followed by one in which the grain size and volume abundance of the newly precipitated Epidote-B grains control the grain size of quartz (Fig. 5.7), hence exerting control on quartz deformation mechanisms by pinning the migrating quartz boundaries (see Jessel, 1987; Olgaard, 1990; Humphreys and Ardakani, 1996; Bate, 2001; Herwegh and Berger, 2004; Herwegh et al., 2011; Cyprych et al., 2016). This allows to suggest a feedback process: (1) quartz grain boundary sliding creates creep cavities in which Epidote-B crystallizes, (2) Epidote-B keeps quartz grain size small, (3) more creep cavities are formed, and (4) more Epidote-B grains are formed. This process is referred to as viscous granular flow (e.g., Fitz Gerald and Stünitz, 1993;Stünitz and Fitz Gerald, 1993; Paterson, 1995; see also Kruse and Stünitz, 1999). The dissolution of epidote may have been facilitated by increased surface area achieved via brittle grain-size reduction of Epidote-A grains (Figs. 5.5 and 5.14a).

5.6.2 Open-system conditions and external fluids

Epidote dissolution–precipitation and the transport of dissolved epidote material to the *loci* of Epidote-B crystallization implies the presence of a fluid, whose nature can be assessed by Pb–Sr isotope data. We have mentioned that the epidote microseparates used for solution ICP-MS measurements mix Epidote-A and Epidote-B to unknown proportions, since the mechanical separation of pure Epidote-B is not feasible due to its small grain size. Therefore, the observation that the $^{207}Pb/^{206}Pb$ and $^{87}Sr/^{86}Sr$ ratios of the microseparates are different (Fig. 5.13) suggests that the microseparates include different epidote generations, hence that Epidote-A and Epidote-B crystallized from fluids with different Pb and Sr isotope compositions. This is supported by the Pb–Sr isotopic ratios of the microseparates being different than that measured in an Epidote-A grain (Fig. 5.13; Table 5.2). There are two principal processes that can induce changes in the Pb and Sr isotope compositions: (1) radioactive decay of $^{235,238}U$ into $^{207,206}Pb$ and ^{87}Rb into ^{87}Sr, or (2) open-system conditions allowing for advection of extraneous Pb and Sr with different isotopic compositions. Process (1) is unlikely in this case because ingrown radiogenic Pb and Sr of such young epidote are negligible. Consequently, the Pb–Sr isotope heterogeneity of the two epidote generations infers fluid-mediated addition of extraneous Sr and Pb during crystallization of Epidote-B. Because the vein microstructure carries evidence of a single deformation event (Fig. 5.14g), it is likely that a second fluid type entered the system during vein deformation and formation of Epidote-B (Fig. 5.14e–f). Thus, the differences in Pb and Sr isotopic data of Epidote-

A grain and microseparates are interpreted to document mixing between different contributions: (1) one reflecting the isotopic composition of Epidote-A incorporated upon vein formation, and (2) one reflecting the mixing of dissolved Epidote-A material with extraneous Pb and Sr brought to the site of Epidote-B crystallization. The existence of open-system conditions bears the potential for fluid-mediated transfer of chemical constituents (Figs. 5.14e–f). The fact that the major and trace element chemical composition of Epidote-B maintains the same patterns as, and represents a narrower range of, that of Epidote-A (Figs. 5.10–5.11) suggests similarly (either rock- or fluid-) buffered conditions during fluid mediated crystallization of Epidote-A and Epidote-B at closely comparable physico-chemical (e.g., *P, T, fO_2*) conditions and thus fluid composition. The initial compositional variability of Epidote-A got thereby homogenized upon dissolution and crystallization into Epidote-B. Considering that the 299 ± 2 Ma old host granitoid (Schaltegger and Corfu, 1992; Ruiz et al., 2022) contains minerals with high concentrations of U, Th and Rb (e.g., allanite, biotite), even slightly variable contributions of radiogenic Pb and Sr leached from these minerals may produce a measurable shift in Pb–Sr isotope ratios without a resolvable effect on Sr and Pb fluid concentrations. Also, crystallization of Epidote-A and Epidote-B most likely occurred at comparable *T* conditions (ca. 400–450 °C as inferred from the presence of biotite in the vein; see Goncalves et al., 2012). Hence, fluid/epidote partition coefficients of all measured elements remained similar between the two epidote crystallization events. Such a scenario can well account for the compositional uniformity but Pb and Sr isotopic differences between Epidote-A and Epidote-B, hence allowing that at least a fraction of the fluid involved in the deformation of layers 2–3 is of external origin. Peverelli et al. (2022; Chapter 4 of this thesis) measured the H isotope composition of epidote in this sample, obtaining values that can only be explained as a mixture of end-member waters (e.g., meteoric, seawater, etc.) as source for the epidote-forming fluids. In light of the present data, it is possible that their measured δD value reflects the mixing of internal and external fluids upon deformation of the epidote-quartz vein as described above.

5.6.3 Epidote geochemistry as a result of veining vs. of combined grain boundary sliding, cavitation, and nucleation

The present major and trace element data show that Epidote-B is geochemically similar to, and less variable than, Epidote-A (Figs. 5.10–5.11), and this result might be linked to differences in crystallization mechanisms between the two epidote generations. In a rock-dominated system, the

larger geochemical variability of Epidote-A may be due to (1) fluid distillation during epidote crystallization, (2) slight variations in physico-chemical conditions (e.g., *P*, *T*) throughout the veining processes, or (3) pulsating fluid fluxes. Trace element data (Fig. 5.11a–b) defining trends and not distinct epidote populations suggest that the geochemical variability of Epidote-A is most readily explained by an evolving epidote-forming fluid chemistry along with more and more epidote precipitating, thus readily removing compatible elements from the fluid (see also Anenburg et al., 2015). This does not exclude multiple pulses of the same fluid (i.e., same fluid source and chemistry) and a role for varying physico-chemical conditions. The lesser extent of chemical variation in Epidote-B indicates homogenization of the whole trace element budget dissolved into the Epidote-B-forming fluid. Viscous granular flow is a dynamic process in which continuous feedback exists among dissolution of minerals, grain boundary sliding, creep cavitation, mass transfer and mineral precipitation (e.g., Fitz Gerald and Stünitz, 1993; Stünitz and Fitz Gerald, 1993; Paterson, 1995). This implies that repeated dissolution and reprecipitation of the same material is likely to occur, and the chemical budget gets compositionally homogenized with ongoing deformation. Consequently, in the case of the epidote-quartz microfold in layers 2–3, such a mechanism may account for the chemical homogeneity of Epidote-B. If this respect, combined grain boundary sliding, cavitation, and nucleation promote recycling and homogenization of fluids in deforming polymineralic aggregates.

5.7 Consequences for epidote U–Pb ages

The inevitable question arising from the scenario developed above is what is the significance of the U–Pb age measured in Epidote-A. Temperature-driven resetting of the U–Pb system is excluded based on the peak temperature reached in the area (i.e., 450 ± 30 °C; Challandes et al., 2008; Goncalves et al., 2012) never exceeding the closure temperature for Pb diffusion in epidote (i.e., > 685 °C; Dahl, 1997). As a consequence, diffusional processes do not have the potential to affect Epidote-A U–Pb ages. However, the disturbance of the U–Pb isotope system may be affected by dissolution–precipitation mechanisms, as has been reported for many minerals (e.g., monazite; Tartèse et al., 2011; Williams et al., 2011; Seydoux-Guillaume et al., 2012; Grand'Homme et al., 2018). Fluid–rock interaction has been shown to affect other isotopic systems as well (e.g., K–Ar, B; Halama et al., 2014). The microstructural relationships between Epidote-A and biotite in layer 1 are consistent with both minerals forming together in Alpine times and before

vein deformation. Also, the U–Pb isotopic data presented in Peverelli et al. (2021; Chapter 2 of this thesis) resolve a single generation of Epidote-A when plotted in a Tera–Wasserburg diagram. Moreover, the time-resolved $^{206}Pb/^{238}U$ ratios corrected for downhole fractionation display flat trends when corrected for zoning in initial lead by applying a ^{208}Pb correction (see Fig. 5 of Peverelli et al., 2021; Fig. 2.6 of this thesis). This means that there is no resolvable isotopic zoning across the ca. 10–12 µm crater depth of the LA-ICP-MS measurements. The trace element data (Figs. 5.10c and 5.11; Table 5B1) reveal prominent chemical zoning. If any isotopic heterogeneity had been caused by interaction with the deformation-related fluid, the crystal rims would be affected to a greater extent than the cores. Consequently, if resolvable isotopic zoning existed in the dated Epidote-A grains, plotting data-points from different domains of isotopic zoning would create scatter of the data-points in a Tera–Wasserburg diagram. However, U–Pb isotope measurements cover all geochemically variable zones (Fig. 5.10; white circles) and they define a single Tera–Wasserburg regression regardless of their proximity to cores/rims of the analyzed epidote grains. This supports that the dissolution–precipitation processes during Epidote-B formation did not disturb the U–Pb isotope system in Epidote-A relicts to a noticeable extent.

5.8 Conclusions and outlook

This study combines microstructural and geochemical methods to investigate the formation mechanisms of an epidote-quartz microfold within an epidote-quartz (±biotite) vein. We have suggested the occurrence of epidote dissolution–precipitation processes, and that this mechanism coexists with quartz dynamic recrystallization, both contributing to grain-size reduction of the system. The genetic link between epidote grains being dissolved and those being reprecipitated is revealed by the overlap of the major and trace element compositions of both generations. We have shown that fluid circulation at the scale of the thin section and the formation of epidote nucleation *loci* in the deforming system are enabled by a combination of grain boundary sliding, creep cavitation, and mass transfer. Repeated dissolution and (re)precipitation processes of epidote in creep cavities formed among sliding quartz grain boundaries also cause chemical homogenization of the epidote-dissolving/forming fluid, and hence of the new epidote generation forming during deformation. This demonstrates the importance of fluid recycling in deformational processes, although the application of Pb–Sr isotope geochemistry recognizes a role for the addition of externally derived fluids mediating mass transfer processes in the studied epidote-quartz vein.

Epidote plays an active role in determining the deformation behavior of other minerals, hence in the deformation style of polymineralic aggregates and in producing the resulting microstructures. To our knowledge, before this study, only brittle deformation behavior of epidote had been proven (Masuda et al., 1990; 1995), but no other detailed studies had addressed epidote deformation mechanisms. In this respect, although Stünitz and Fitz Gerald (1993) do not observe any plastic deformation in clinozoisite, epidote dynamic recrystallization has never been either ruled out or demonstrated rigorously. However, since this mineral is widespread in crustal rocks (e.g., Bird and Spieler, 2004; Enami et al., 2004; Franz and Liebscher, 2004; Grapes and Hoskin, 2004; Schmidt and Poli, 2004; Morad et al., 2010), the occurrence of epidote ductile deformation may have effects on the deformation of the continental crust and it calls for a better understanding of this mineral.

Appendix 5A: Transmitted light microphotograph of the microfold in layers 2–3.

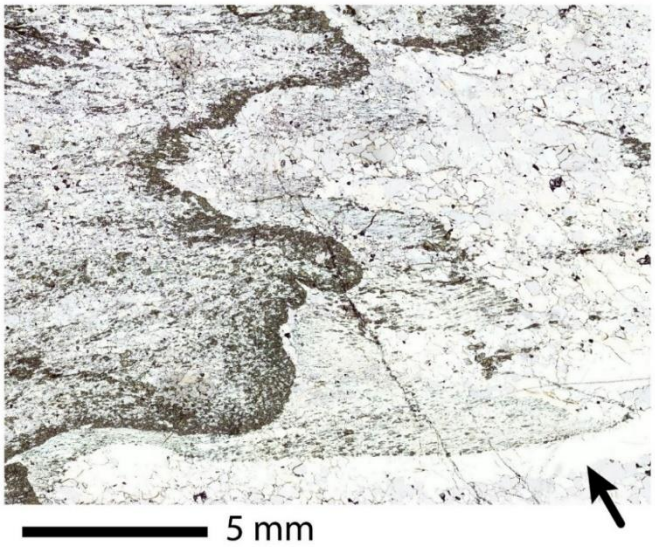

Fig. 5A1 *Transmitted light scan of layers 2–3. Plane-polarized light.*

Appendix 5B: Epidote trace element data by LA-ICP-MS.

Table 5B1

Trace element composition of epidote in µg g^{-1} measured by LA-ICP-MS.

Epidote-A

Spot	Ba	Sr	Pb	U	La	Ce	Pr	Nd	Sm	Eu	Gd	Tb	Dy	Y	Ho	Er	Tm	Yb	Lu	Zr	V
1	0.99	1400	130	79	5.6	14	2.2	12	6.3	3.9	14	2.8	22	200	5.5	19	2.7	19	2.7	3.6	140
2	1.2	1990	130	130	7.7	18	2.7	15	8.5	5.6	18	3.6	27	230	6.4	22	3.1	21	3.4	5.1	140
3	22	3290	150	350	4.8	8.8	1.2	5.6	2.5	2.0	5.7	1.2	12	120	3.6	14	2.5	21	3.8	22	110
4	21	2500	170	270	0.99	1.9	0.24	1.1	0.66	1.1	2.8	0.86	9.8	110	3.1	14	2.7	23	4.4	24	110
5	1.9	970	97	60	5.2	9.3	1.1	5.0	1.8	1.3	2.9	0.62	5.1	32	1.0	3.5	0.53	3.7	0.57	4.2	160
6	23	2590	170	130	10	15	1.6	7.0	2.8	1.9	5.6	1.3	9.9	71	2.3	9.2	1.6	15	3.1	51	130
7	0.98	740	87	140	5.0	9.3	1.2	5.3	2.7	1.6	5.5	1.1	8.4	53	1.8	6.0	0.88	5.8	0.77	4.5	200
8	21	2870	170	240	12	17	1.8	8.3	4.6	3.7	11	2.5	19	130	4.4	17	2.8	25	4.4	17	150
9	9.7	2000	150	100	8.5	12	1.4	5.9	3.2	2.7	8.0	1.8	14	82	2.9	8.7	1.1	7.8	1.3	9.6	140
10	24	2890	170	220	6.6	9.7	1.1	4.6	2.0	2.2	5.9	1.4	12	90	2.9	11	2.1	18	3.2	31	140
11	0.92	1660	93	100	3.4	7.2	0.90	3.3	1.2	1.4	2.7	0.59	5.1	41	1.3	4.1	0.42	2.5	0.28	2.2	110
12	34	3750	190	140	5.3	8.5	1.0	4.6	1.9	2.3	4.2	1.0	8.8	67	2.2	6.7	0.80	4.8	0.64	25	120
13	0.59	770	78	160	1.6	3.0	0.39	1.6	1.0	1.5	3.2	1.0	9.1	65	2.2	7.9	0.97	5.9	0.72	3.2	180
14	27	2820	180	260	1.3	2.5	0.29	1.2	1.2	1.5	4.6	1.3	12	120	3.5	14	2.8	28	4.6	42	130
15	5.8	1530	93	54	0.62	0.97	0.12	0.62	0.45	0.94	1.4	0.40	4.1	42	1.2	4.7	0.77	6.2	1.0	5.0	140
16	17	2810	150	140	1.9	3.0	0.35	1.4	0.55	1.3	1.7	0.66	7.8	77	2.3	9.3	1.6	14	2.3	18	130
17	5.2	1310	93	120	3.5	6.3	0.78	3.7	1.3	1.4	2.0	0.57	4.9	47	1.3	6.1	0.88	7.1	0.93	5.2	120
18	3.8	2340	110	110	1.5	2.9	0.43	1.6	0.76	1.2	1.6	0.47	4.9	47	5.5	5.5	0.78	5.8	0.90	3.1	120

Epidote-B

Spot	Ba	Sr	Pb	U	La	Ce	Pr	Nd	Sm	Eu	Gd	Tb	Dy	Y	Ho	Er	Tm	Yb	Lu	Zr	V
1	2.1	1640	171	130	4.7	10	1.4	7.1	3.4	3.0	7.3	1.7	16	150	4.4	14	2.1	14	2.3	5.2	130
2	2.9	1860	150	140	3.7	8.1	1.1	5.7	3.1	3.1	7.6	2.1	17	170	4.6	16	2.4	19	3.0	5.9	140
3	6.6	1950	120	190	1.7	4.2	0.55	2.9	1.2	1.6	3.1	0.81	8.1	85	2.1	8.6	1.5	9.7	1.7	8.2	120
4	5.0	1720	140	190	3.3	7.6	1.1	5.2	2.4	2.0	4.8	1.1	10	110	3.1	11	1.8	13	2.1	7.0	120
5	4.2	1700	130	170	3.0	7.4	0.97	5.0	2.3	2.1	4.2	1.2	11	120	3.0	11	2.0	14	2.5	7.7	120
6	5.1	1930	120	160	1.9	4.4	0.60	2.9	1.4	1.5	3.3	0.80	7.4	85	2.3	8.8	1.3	10	1.6	7.2	130
7	3.7	1530	130	160	2.9	6.6	0.88	4.5	2.1	1.7	4.1	0.73	7.9	84	2.3	8.3	1.3	9.0	1.6	5.2	130
8	6.5	1960	140	190	3.3	7.6	0.99	4.5	2.3	1.9	3.9	0.99	9.1	100	2.6	10	1.5	13	2.1	9.3	130
9	5.3	1850	130	190	3.4	8.2	1.1	4.7	2.2	1.9	3.7	0.91	8.4	100	2.7	9.9	1.5	13	2.1	8.6	130
10	5.4	1800	130	190	2.3	5.2	0.71	3.5	1.7	1.7	3.6	0.85	8.5	90	2.4	10	1.7	12	2.2	8.1	130
11	5.5	1800	150	180	3.9	8.5	1.2	5.6	2.5	1.9	4.9	0.99	9.8	100	2.7	10	1.6	12	1.9	8.0	130
12	4.8	1710	151	230	9.4	20	2.6	12	5.3	3.5	9.6	2.3	19	160	4.8	16	2.4	16	2.6	7.6	130

Central Aar Granite (Schaltegger and Krähenbühl, 1990)

KAW	Ba	Sr	Pb	U	La	Ce	Pr	Nd	Sm	Eu	Gd	Tb	Dy	Y	Ho	Er	Tm	Yb	Lu	Zr	V
2219	430	75	24	8	26	61	-	-	5.1	0.51	-	2.4	-	56	-	-	-	8.6	12	192	18

References

Anenburg, M., Katzir, Y., Rhede, D., Jöns, N., and Bach, W.: Rare earth element evolution and migration in plagiogranites: a record preserved in epidote and allanite of the Troodos ophiolite, Contrib. to Mineral. Petrol., 169, https://doi.org/10.1007/s00410-015-1114-y, 2015.

Bambauer, H. U., Herwegh, M., and Kroll, H.: Quartz as indicator mineral in the Central Swiss Alps: The quartz recrystallization isograd in the rock series of the northern Aar massif, Swiss J. Geosci., 102, 345–351, https://doi.org/10.1007/s00015-009-1319-z, 2009.

Barth, S., Oberli, F., Meier, M.: Th–Pb versus U–Pb isotope systematics in allanite from co-genetic rhyolite and granodiorite: implications for geochronology. Earth Planet. Sci. Lett. 124, 149–159, https://doi.org/10.1016/0012-821X(94)00073-5, 1994.

Bate, P.: The effect of deformation on grain growth in Zener pinned systems. Acta Mater. 49, 1453–1461, https://doi.org/10.1016/S1359-6454(01)00033-7, 2001.

Belgrano, T. M., Herwegh, M., and Berger, A.: Inherited structural controls on fault geometry, architecture and hydrothermal activity: an example from Grimsel Pass, Switzerland, Swiss J. Geosci., 109, 345–364, https://doi.org/10.1007/s00015-016-0212-9, 2016.

Bergemann, C., Gnos, E., Berger, A., Whitehouse, M., Mullis, J., Wehrens, P., Pettke, T., Janots, E.: Th-Pb ion probe dating of zoned hydrothermal monazite and its implications for repeated shear zone activity: An example from the central alps, Switzerland. Tectonics 36, 671–689, https://doi.org/10.1002/2016TC004407, 2017.

Berger, A., Gnos, E., Janots, E., Whitehouse, M., Soom, M., Frei, R., Waight, T.E.: Dating brittle tectonic movements with cleft monazite: Fluid-rock interaction and formation of REE minerals. Tectonics 32, 1176–1189, https://doi.org/10.1002/tect.20071, 2013.

Berger, A., Mercolli, I., Herwegh, M., Gnos, E.: Geological Map of the Aar Massif, Tavetsch and Gotthard Nappes. Geol. spec. Map 1:100 000, explanatory notes 129. Federal Office of Topogaphy swisstopo, Bern, Switzerland, 2017

Berger, A., Wehrens, P., Lanari, P., Zwingmann, H., Herwegh, M.: Microstructures, mineral chemistry and geochronology of white micas along a retrograde evolution: An example from the Aar massif (Central Alps, Switzerland). Tectonophysics 721, 179–195, https://doi.org/10.1016/j.tecto.2017.09.019, 2017.

Berger, A., Egli, D., Glotzbach, C., Valla, P.G., Pettke, T., Herwegh, M.: Apatite low-temperature chronometry and microstructures across a hydrothermally active fault zone. Chem. Geol. 588, 120633, https://doi.org/10.1016/j.chemgeo.2021.120633, 2022.

Bird, D. K. and Spieler, A. R.: Epidote in Geothermal Systems, Rev. Mineral. Geochemistry 56, 235–300, https://doi.org/10.2138/gsrmg.56.1.235, 2004.

Bons, P.D., Elburg, M.A., Gomez-Rivas, E.: A review of the formation of tectonic veins and their microstructures. J. Struct. Geol. 43, 33–62, https://doi.org/10.1016/j.jsg.2012.07.005, 2012.

Bukovská, Z., Jeřábek, P., Morales, F.G.: Major softening at brittle-ductile transition due to interplay between chemical and deformation processes: An insight from evolution of shear bands in the South Armorican Shear Zone. J. Geophys. Res. Solid Earth 1158–1182. https://doi.org/10.1002/2015JB012319, 2016

Challandes, N., Marquer, D., Villa, I.M.: P-T-t modelling, fluid circulation, and 39Ar-40Ar and Rb-Sr mica ages in the Aar Massif shear zones (Swiss Alps). Swiss J. Geosci. 101, 269–288, https://doi.org/10.1007/s00015-008-1260-6, 2008.

Choukroune, P. and Gapais, D.: Strain pattern in the Aar Granite (Central Alps): orthogneiss developed by bulk inhomogeneous flattening, 5, 411–418, https://doi.org/10.1016/b978-0-08-030273-7.50019-7, 1983.

Cyprych, D., Piazolo, S., Wilson, C.J.L., Luzin, V., Prior, D.J.: Rheology, microstructure and crystallographic preferred orientation of matrix containing a dispersed second phase: Insight from experimentally deformed ice. Earth Planet. Sci. Lett. 449, 272–281, https://doi.org/10.1016/j.epsl.2016.06.010, 2016.

Dahl, P. S.: A crystal-chemical basis for Pb retention and fission-track annealing systematics in U-bearing mineral, with implications for geochronology, Earth Planet. Sci. Lett., 150, 277–290, https://doi.org/10.1016/S0012-821X(97)00108-8, 1997.

Diamond, L. W., Wanner, C., and Waber, H. N.: Penetration depth of meteoric water in orogenic geothermal systems, Geology, 46, 1083–1066, https://doi.org/10.1130/G45394.1, 2018.

Egli, D., Baumann, R., Küng, S., Berger, A., Baron, L., and Herwegh, M.: Structural characteristics, bulk porosity and evolution of an exhumed long-lived hydrothermal system, 747–748, 239–258, https://doi.org/10.1016/j.tecto.2018.10.008, 2018.

Enami, M., Liou, J.G., Mattinson, C.G.: Epidote minerals in high P/T metamorphic terranes: Subduction zone and high- to ultrahigh-pressure metamorphism. Rev. Mineral. Geochemistry 56, 347–398, https://doi.org/10.2138/gsrmg.56.1.347, 2004.

Evans, B., Renner, J., and Hirth, G.: A few remarks on the kinetics of static grain growth in rocks, 90, 88–103, https://doi.org/10.1007/s005310000150, 2001.

Feineman, M. D., Ryerson, F. J., DePaolo, D. J., and Plank, T.: Zoisite-aqueous fluid trace element partitioning with implications for subduction zone fluid composition, 239, 250–265, https://doi.org/10.1016/j.chemgeo.2007.01.008, 2007.

Ferreira, T., Rasband, W.: ImageJ User Guide User Guide ImageJ. Image J user Guid. 1.46r. https://doi.org/10.1038/nmeth.2019, 2012.

Fitz Gerald, J.D., Stünitz, H.: Deformation of granitoids at low metamorphic grade. I: Reactions and grain size reduction. Tectonophysics 221, 269–297, https://doi.org/10.1016/0040-1951(93)90163-E, 1993.

Franz, G., Liebscher, A.: Physical and Chemical Properties of the Epidote Minerals-An Introduction-. Rev. Mineral. Geochemistry 56, 1–81, https://doi.org/10.2138/gsrmg.56.1.1, 2004.

Frei, D., Liebscher, A., Franz, G., Dulski, P.: Trace element geochemistry of epidote minerals. Rev. Mineral. Geochemistry 56, 553–605, https://doi.org/10.2138/gsrmg.56.1.553, 2004.

Gieré, R., Sorensen, S.S.: Allanite and other REE-rich epidote-group minerals. Rev. Mineral. Geochemistry 56, 431–493, https://doi.org/10.2138/gsrmg.56.1.431, 2004.

Gilgannon, J., Fusseis, F., Menegon, L., Regenauer-Lieb, K., and Buckman, J.: Hierarchical creep cavity formation in an ultramylonite and implications for phase mixing, 8, 1193–1209, https://doi.org/10.5194/se-8-1193-2017, 2017.

Gilgannon, J., Waldvogel, M., Poulet, T., Fusseis, F., Berger, A., Barnhoorn, A., and Herwegh, M.: Experimental evidence that viscous shear zones generate periodic pore sheets, 12, 405–420, https://doi.org/10.5194/se-12-405-2021, 2021.

Giuntoli, F., Menegon, L., Warren, C.J.: Replacement reactions and deformation by dissolution and precipitation processes in amphibolites. J. Metamorph. Geol. 36, 1263–1286, https://doi.org/10.1111/jmg.12445, 2018.

Goncalves, P., Oliot, E., Marquer, D., Connolly, J.A.D.: Role of chemical processes on shear zone formation: An example from the Grimsel metagranodiorite (Aar massif, Central Alps). J. Metamorph. Geol. 30, 703–722, https://doi.org/10.1111/j.1525-1314.2012.00991.x, 2012.

Gottardi, R., Hughes, B.: Role of fluids on deformation in mid-crustal shear zones, Raft River Mountains, Utah. Geol. Magazine, 1 – 13, doi:10.1017/S0016756822000231, 2022.

Götze, J., Plötze, M., Habermann, D.: Origin, spectral characteristics and practical applications of the cathodoluminescence (CL) of quartz - A review. Mineral. Petrol. 71, 225–250, https://doi.org/10.1007/s007100170040, 2001.

Grand'Homme, A., Janots, E., Seydoux-Guillaume, A.M., Guillaume, D., Magnin, V., Hövelmann, J., Höschen, C., Boiron, M.C.: Mass transport and fractionation during monazite alteration by anisotropic replacement. Chem. Geol. 484, 51–68, https://doi.org/10.1016/j.chemgeo.2017.10.008, 2018.

Grapes, R.H., Hoskin, P.W.O.: Epidote group minerals in low-medium pressure metamorphic terranes. Rev. Mineral. Geochemistry 56, 301–345, https://doi.org/10.2138/gsrmg.56.1.301, 2004.

Guillong, M., Meier, D.L., Allan, M.M., Heinrich, C.A., Yardley, B.W.D., 2008. SILLS: A Matlab-Based Program for the Reduction of Laser Ablation ICP–MS Data of Homogeneous Materials and Inclusions. Mineral. Assoc. Canada Short Course 40, 328–333.

Haeusler M., Haas C., Lösch S., Moghaddam N., Villa I.M., Walsh S., Kayser M., Seiler R., Ruehli F., Janosa M., Papageorgopoulou C.: Multidisciplinary identification of the controversial freedom fighter Jörg Jenatsch, assassinated 1639 in Chur, Switzerland. PLOS ONE, 11(12): e0168014, 1-22, doi: 10.1371/journal.pone.0168014, 2016.

Halama, R., Konrad-Schmolke, M., Sudo, M., Marschall, H.R., Wiedenbeck, M.: Effects of fluid-rock interaction on 40Ar/39Ar geochronology in high-pressure rocks (Sesia-Lanzo Zone, Western Alps). Geochim. Cosmochim. Acta 126, 475–494, https://doi.org/10.1016/j.gca.2013.10.023, 2014.

Halter, W.E., Pettke, T., Heinrich, C.A., Rothen-Rutishauser, B.: Major to trace element analysis of melt inclusions by laser-ablation ICP-MS: Methods of quantification. Chem. Geol. 183, 63–86, https://doi.org/10.1016/S0009-2541(01)00372-2, 2002.

Handy, M. R.: The solid-state flow of polymineralic rocks, J. Geophys. Res.-Earth, 95, 8647–8661, https://doi.org/10.1029/JB095iB06p08647, 1990.

Handy, M. R.: Flow laws for rocks containing two non-linear viscous phases: A phenomenological approach, J. Struct. Geol., 16, 287–301, https://doi.org/10.1016/0191-8141(94)90035-3, 1994.

Hentschel, F., Janots, E., Trepmann, C.A., Magnin, V., Lanari, P., 2020. Corona formation around monazite and xenotime during greenschist-facies metamorphism and deformation. Eur. J. Mineral. 32, 521–544. https://doi.org/10.5194/ejm-32-521-2020

Herwegh, M., & Berger, A.: Deformation mechanisms in second-phase affected microstructures and their energy balance. Journal of Structural Geology, 26(8), 1483–1498, https://doi.org/10.1016/j.jsg.2003.10.006, 2004.

Herwegh, M. and Jenni, A.: Granular flow in polymineralic rocks bearing sheet silicates: New evidence from natural examples, 332, 309–320, https://doi.org/10.1016/S0040-1951(00)00288-2, 2001.

Herwegh, M., Linckens, J., Ebert, A., Berger, A., Brodhag, S.H.: The role of second phases for controlling microstructural evolution in polymineralic rocks: A review. J. Struct. Geol. 33, 1728–1750, https://doi.org/10.1016/j.jsg.2011.08.011, 2011.

Herwegh, M., Berger, A., Baumberger, R., Wehrens, P., Kissling, E.: Large-Scale Crustal-Block-Extrusion During Late Alpine Collision. Sci. Rep. 7, 1–10, https://doi.org/10.1038/s41598-017-00440-0, 2017.

Herwegh, M., Berger, A., Glotzbach, C., Wangenheim, C., Mock, S., Wehrens, P., Baumberger, R., Egli, D., and Kissling, E.: Late stages of continent-continent collision: Timing, kinematic evolution, and exhumation of the Northern rim (Aar Massif) of the Alps, Earth-Science Rev., 200, 102959, https://doi.org/10.1016/j.earscirev.2019.102959, 2020.

Hobbs, B.E., Ord, A., Spalla, M.I., Gosso, G., Zucali, M.: The interaction of deformation and metamorphic reactions. Geol. Soc. Spec. Publ. 332, 189–223, https://doi.org/10.1144/SP332.12, 2010.

Hofmann, B. A., Helfer, M., Diamond, L. W., Villa, I. M., Frei, R., and Eikenberg, J.: Topography-driven hydrothermal breccia mineralization of Pliocene age at Grimsel Pass, Aar massif, Central Swiss Alps, Schweizerische Mineral. und Petrogr. Mitteilungen, 84, 271–302, 2004.

Horwitz, E. P., Dietz, M. L., and Chiarizia, R.: The application of novel extraction chromatographic materials to the characterization of radioactive waste solutions, J. Radioanal. Nucl. Ch., 161, 575–583, https://doi.org/10.1007/bf02040504, 1992.

Humphreys, F.J., Ardakani, M.G.: Grain boundary migration and zener pinning in particle-containing copper crystals. Acta Mater. 44, 2717–2727, https://doi.org/10.1016/1359-6454(95)00421-1, 1996.

Janots, E., Berger, A., Gnos, E., Whitehouse, M., Lewin, E., Pettke, T.: Constraints on fluid evolution during metamorphism from U-Th-Pb systematics in Alpine hydrothermal monazite. Chem. Geol. 326–327, 61–71, https://doi.org/10.1016/j.chemgeo.2012.07.014, 2012.

Jessell, M.W.: Grain-boundary migration microstructures in a naturally deformed quartzite. J. Struct. Geol. 9, 1007–1014, https://doi.org/10.1016/0191-8141(87)90008-3, 1987.

Karato, S.-I.: Deformation of Earth Materials: An Introduction to the Rheology of Solid Earth, Cambridge University Press, https://doi.org/10.1007/s00024-009-0536-8, 2009.

Kruse, R., Stünitz, H.: Deformation mechanisms and phase distribution in mafic high-temperature mylonites from the Jotun Nappe, southern Norway. Tectonophysics 303, 223–249, https://doi.org/10.1016/S0040-1951(98)00255-8, 1999.

Konrad-Schmolke, M., Halama, R., Wirth, R., Thomen, A., Klitscher, N., Morales, L., Schreiber, A., Wilke, F.D.H.: Mineral dissolution and reprecipitation mediated by an amorphous phase. Nat. Commun. 9, https://doi.org/10.1038/s41467-018-03944-z, 2018.

Lanari, P., Duesterhoeft, E.: Modeling Metamorphic Rocks Using Equilibrium Thermodynamics and Internally Consistent Databases: Past Achievements, Problems and Perspectives. J. Petrol. 60, 19–56, https://doi.org/10.1093/petrology/egy105, 2019.

Lanari, P., Vidal, O., De Andrade, V., Dubacq, B., Lewin, E., Grosch, E.G., Schwartz, S.: XMapTools: A MATLAB©-based program for electron microprobe X-ray image processing and geothermobarometry. Comput. Geosci. 62, 227–240, https://doi.org/10.1016/j.cageo.2013.08.010, 2014.

Lanari, P., Vho, A., Bovay, T., Airaghi, L., Centrella, S.: Quantitative compositional mapping of mineral phases by electron probe micro-analyser. Geol. Soc. Spec. Publ. 478, 39–63, https://doi.org/10.1144/SP478.4, 2019.

Ludwig, K. R., 2012: On the treatment of concordant uranium-lead ages, Geochim. Cosmochim. Ac., 62, 665–676, https://doi.org/10.1016/S0016-7037(98)00059-3, 1998.

Marquer, D. and Burkhard, M.: Fluid circulation, progressive deformation and mass-transfer processes in the upper crust: the example of basement – cover relationships in the External Crystalline Massifs, Switzerland, J. Struct. Geol., 8–9, 1047–1057, 1992.

Marquer, D. and Peucat, J. J.: Rb-Sr systematics of recrystallized shear zones at the greenschist-amphibolite transition: examples from granites in the Swiss central Alps, 74, 343–358, 1994.

Masuda, T., Shibutani, T., Kuriyama, M., Igarashi, T.: Development of microboudinage: an estimate of changing differential stress with increasing strain. Tectonophysics 178, 379–387, https://doi.org/10.1016/0040-1951(90)90160-A, 1990.

Masuda, T., Shibutani, T., Yamaguchi, H.: Comparative rheological behaviour of albite and quartz in siliceous schists revealed by the microboudinage of piedmontite. J. Struct. Geol. 17, 1523–1533, https://doi.org/10.1016/0191-8141(95)00060-Q, 1995.

McClay, K. R.: Pressure solution and Coble creep in rocks and minerals: A review, J. Geol. Soc. London., 134, 57–70, https://doi.org/10.1144/gsjgs.134.1.0057, 1977.

McDonough, W.F., Sun, S.S.: The composition of the Earth. Chem. Geol. 120, 223–253, https://doi.org/10.1016/0009-2541(94)00140-4, 1995.

Menegon, L., Fusseis, F., Stünitz, H., Xiao, X.: Creep cavitation bands control porosity and fluid flow in lower crustal shear zones. Geology 43, 227–230, https://doi.org/10.1130/G36307.1, 2015.

Morad, S., El-Ghali, M.A.K., Caja, M.A., Sirat, M., Al-Ramadan, K., Manurberg, H.: Hydrothermal alteration of plagioclase in granitic rocks from Proterozoic basement of SE Sweden. Geol. J. 45, 105–116, https://doi.org/10.1002/gj.1178, 2010.

Mullis, J., Dubessy, J., Poty, B., O'Neil, J.: Fluid regimes during late stages of a continental collision: Physical, chemical, and stable isotope measurements of fluid inclusions in fissure quartz from a geotraverse through the Central Alps, Switzerland. Geochim. Cosmochim. Acta 58, 2239–2267, https://doi.org/10.1016/0016-7037(94)90008-6, 1994.

Nègre, L., Stünitz, H., Raimbourg, H., Lee, A., Précigout, J., Pongrac, P., Jeřábek, P.: Effect of pressure on the deformation of quartz aggregates in the presence of H2O. J. Struct. Geol. 148. https://doi.org/10.1016/j.jsg.2021.104351, 2021.

Passchier, C.W. and Trouw, R.A.: Microtectonics. Springer Science & Business Media, 2005.

Paterson, M. S.: A theory for granular flow accommodated by material transfer via an intergranular fluid, 245, 135–151, https://doi.org/10.1016/0040-1951(94)00231-W, 1995.

Pearce, M.A., Timms, N.E., Hough, R.M., Cleverley, J.S.: Reaction mechanism for the replacement of calcite by dolomite and siderite: Implications for geochemistry, microstructure

and porosity evolution during hydrothermal mineralisation. Contrib. to Mineral. Petrol. 166, 995–1009, https://doi.org/10.1007/s00410-013-0905-2, 2013.

Pettke, T., Oberli, F., Audétat, A., Guillong, M., Simon, A.C., Hanley, J.J., Klemm, L.M.: Recent developments in element concentration and isotope ratio analysis of individual fluid inclusions by laser ablation single and multiple collector ICP-MS. Ore Geol. Rev. 44, 10–38, https://doi.org/10.1016/j.oregeorev.2011.11.001, 2012.

Peverelli, V., Ewing, T., Rubatto, D., Wille, M., Berger, A., Villa, I.M., Lanari, P., Pettke, T., Herwegh, M.: U−Pb geochronology of epidote by laser ablation inductively coupled plasma mass spectrometry (LA-ICP-MS) as a tool for dating hydrothermal-vein formation. Geochronology 3, 123–147, https://doi.org/10.5194/gchron-3-123-2021, 2021.

Peverelli, V., Berger, A., Mulch, A., Pettke, T., Piccoli, F., and Herwegh, M.: Epidote U–Pb geochronology and H isotope geochemistry trace pre-orogenic hydration of mid-crustal granitoids, GEOLOGY, 2022. https://doi.org/10.1130/G50028.1

Pongrac, P., Jeřábek, P., Stünitz, H., Raimbourg, H., Heilbronner, R., Racek, M., Nègre, L.: Mechanical properties and recrystallization of quartz in presence of H2O: Combination of cracking, subgrain rotation and dissolution-precipitation processes. J. Struct. Geol. 160. https://doi.org/10.1016/j.jsg.2022.104630, 2022.

Putnis, A.: Mineral replacement reactions: from macroscopic observations to microscopic mechanisms. Mineral. Mag. 66, 689–708, https://doi.org/10.1180/0026461026650056, 2002.

Putnis, A.: Mineral replacement reactions. Rev. Mineral. Geochemistry 70, 87–124, https://doi.org/10.2138/rmg.2009.70.3, 2009.

Putnis, A., Austrheim, H.: Fluid-induced processes: Metasomatism and metamorphism. Geofluids 10, 254–269. https://doi.org/10.1111/j.1468-8123.2010.00285.x, 2010.

Putnis, A., John, T.: Replacement processes in the earth's crust. Elements 6, 159–164. https://doi.org/10.2113/gselements.6.3.159, 2010.

Putnis, A., Putnis, C. V.: The mechanism of reequilibration of solids in the presence of a fluid phase. J. Solid State Chem. 180, 1783–1786, https://doi.org/10.1016/j.jssc.2007.03.023, 2007.

Ramseyer, K., Baumann, J., Matter, A., Mullis, J.: Cathodoluminescence Colours of α -Quartz . Mineral. Mag. 52, 669–677, https://doi.org/10.1180/minmag.1988.052.368.11, 1988.

Rehkämper, M., Mezger, K.: Investigation of matrix effects for Pb isotope ratio measurements by multiple collector ICP-MS: Verification and application of optimized analytical protocols. J. Anal. At. Spectrom. 15, 1451–1460, https://doi.org/10.1039/b005262k, 2000.

Ricchi, E., Bergemann, C.A., Gnos, E., Berger, A., Rubatto, D., Whitehouse, M.J.: Constraining deformation phases in the Aar Massif and the Gotthard Nappe (Switzerland) using Th-Pb crystallization ages of fissure monazite-(Ce). Lithos 342–343, 223–238, https://doi.org/10.1016/j.lithos.2019.04.014, 2019.

Rolland, Y., Cox, S.F., Corsini, M.: Constraining deformation stages in brittle-ductile shear zones from combined field mapping and 40Ar/39Ar dating: The structural evolution of the Grimsel Pass area (Aar Massif, Swiss Alps). J. Struct. Geol. 31, 1377–1394, https://doi.org/10.1016/j.jsg.2009.08.003, 2009.

Rossi, M. and Rolland, Y.: Stable isotope and Ar/Ar evidence of prolonged multiscale fluid flow during exhumation of orogenic crust: Example from the mont blanc and Aar Massifs (NW Alps), 33, 1681–1709, https://doi.org/10.1002/2013TC003438, 2014.

Ruiz, M., Schaltegger, U., Gaynor, S.P., Chiaradia, M., Abrecht, J., Gisler, C., Giovanoli, F., Wiederkehr, M.: Reassessing the intrusive tempo and magma genesis of the late Variscan Aar batholith : U-Pb geochronology, trace element and initial Hf isotope composition of zircon. Swiss J. Geosci. 1–24. https://doi.org/10.1186/s00015-022-00420-1, 2022.

Schaltegger, U., Krähenbühl, U.: Heavy rare-earth element enrichment in granites of the Aar Massif (Central Alps, Switzerland). Chem. Geol. 89, 49–63, https://doi.org/10.1016/0009-2541(90)90059-G, 1990.

Schaltegger, U., Corfu, F.: The age and source of late Hercynian magmatism in the central Alps: evidence from precise U-Pb ages and initial Hf isotopes. Contrib. to Mineral. Petrol. 111, 329–344, https://doi.org/10.1007/BF00311195, 1992.

Schmidt, M.W., Poli, S.: Magmatic epidote. Rev. Mineral. Geochemistry 56, 399–430, https://doi.org/10.2138/gsrmg.56.1.399, 2004.

Schneeberger, R., Kober, F., Lanyon, G.W., Mäder, U.K., Spillmann, T., Blechschmidt, I.: Grimsel Test Site: Revisiting the site-specific geoscientific knowledge, 2019.

Seydoux-Guillaume, A., Montel, J., Bingen, B., Bosse, V., Parseval, P. De, Paquette, J., Janots, E., and Wirth, R.: Low-temperature alteration of monazite : Fluid mediated coupled dissolution

– precipitation , irradiation damage , and disturbance of the U – Pb and Th – Pb chronometers, Chem. Geol., 330–331, 140–158, https://doi.org/10.1016/j.chemgeo.2012.07.031, 2012.

Stipp, M., Stünitz, H., Heilbronner, R., & Schmid, S. M.: Dynamic recrystallization of quartz: correlation between natural and experimental conditions. Geological Society, London, Special Publications, 200(1), 171-190. https://doi.org/10.1144/GSL.SP.2001.200.01.11, 2002.

Stünitz, H., Fitzgerald, J.D.F.: Deformation of granitoids at low metamorphic grade. II: Granular flow in albite-rich mylonites. Tectonophysics 221, 299–324, https://doi.org/10.1016/0040-1951(93)90164-F, 1993.

Tartèse, R., Ruffet, G., Poujol, M., Boulvais, P., Ireland, T.R.: Simultaneous resetting of the muscovite K-Ar and monazite U-Pb geochronometers: A story of fluids. Terra Nov. 23, 390–398, https://doi.org/10.1111/j.1365-3121.2011.01024.x, 2011.

Tullis, J.: Deformation of granitic rocks: Experimental studies and natural examples, Rev. Mineral. Geochemistry, 51, 51–95, https://doi.org/10.2138/gsrmg.51.1.51, 2002.

Villa, I.M., Hanchar, J.M.: K-feldspar hygrochronology. Geochim. Cosmochim. Acta 101, 24–33, https://doi.org/10.1016/j.gca.2012.09.047, 2013.

Wehrens, P., Berger, A., Peters, M., Spillmann, T., and Herwegh, M.: Deformation at the frictional-viscous transition: Evidence for cycles of fluid-assisted embrittlement and ductile deformation in the granitoid crust, Tectonophysics 693, 66–84, https://doi.org/10.1016/j.tecto.2016.10.022, 2016.

Wehrens, P., Baumberger, R., Berger, A., Herwegh, M.: How is strain localized in a meta-granitoid, mid-crustal basement section? Spatial distribution of deformation in the central Aar massif (Switzerland). J. Struct. Geol. 94, 47–67, https://doi.org/10.1016/j.jsg.2016.11.004, 2017.

Weis, D., Kieffer, B., Maerschalk, C., Barling, J., De Jong, J., Williams, G.A., Hanano, D., Pretorius, W., Mattielli, N., Scoates, J.S., Goolaerts, A., Friedman, R.M., Mahoney, J.B.: High-precision isotopic characterization of USGS reference materials by TIMS and MC-ICP-MS. Geochemistry, Geophys. Geosystems 7, https://doi.org/10.1029/2006GC001283, 2006.

Williams, M.L., Jercinovic, M.J., Harlov, D.E., Budzyń, B., Hetherington, C.J.: Resetting monazite ages during fluid-related alteration. Chem. Geol. 283, 218–225, https://doi.org/10.1016/j.chemgeo.2011.01.019, 2011.

Wintsch, R.P., Yeh, M.W.: Oscillating brittle and viscous behavior through the earthquake cycle in the Red River Shear Zone: Monitoring flips between reaction and textural softening and hardening. Tectonophysics 587, 46–62, https://doi.org/10.1016/j.tecto.2012.09.019, 2013.

6. Conclusions

This thesis develops and makes use of epidote as a novel U–Pb geochronometer and isotope tracer. A multimethodological approach was employed to successfully extract geochemical information from this mineral in veins, including U–Pb geochronology and Pb isotope geochemistry by LA-ICP-MS, Sr isotope measurements by solution-based ICP-MS and TIMS, O–H isotope data, major and trace element data, and microstructural analysis. The combination of these techniques allows to gain new insight into the hydration of the granitic continental crust in the Alps and into the role of epidote as a ubiquitous greenschist-facies mineral in deforming granitoids.

After having confirmed the suitability of allanite as reference material for U–Pb dating of epidote by LA-ICP-MS (Chapter 2), we have shown that epidote can return geologically meaningful ages and useful initial $^{207}Pb/^{206}Pb$ ratios provided that (1) the Tera–Wasserburg approach is used, and (2) the U/Pb ratio of single analysis allow for large-enough spread of all the LA-ICP-MS data-points along the Tera–Wasserburg regression. Finally, we proposed that the initial $^{207}Pb/^{207}Pb$ ratios yielded by the Tera–Wasserburg plot should be used to investigate the isotope characteristics of the epidote-forming fluids.

The protocol for epidote U–Pb geochronology and Pb isotope geochemistry, combined with classical Sr–O–H isotope geochemistry provides so-far unknown information on the hydration history of the granitic continental crust of the Aar Massif and the Err nappe. In this respect, the full potential of epidote as a geochronometer and fluid tracer is shown in the study of epidote veins from the Albula Pass area (Chapter 3). Here, the analyzed epidote veins revealed so-far undetected fluid circulation events related to the Eo-Alpine orogeny in the granitic continental crust of the Err nappe. These data beautifully complement previous work that demonstrated seawater circulation along syn-rift faults during Jurassic rifting (e.g., Manatschal et al., 2000; 2015; Pinto et al., 2015; Incerpi et al., 2017; 2018; 2019). These and our data provide evidence for multi-stage fluid circulation in the granitic continental crust during inversion of the former Adriatic passive continental margin.

At Grimsel Pass (Aar Massif), the preservation of Permian U–Pb ages in epidote in veins that were overprinted by Alpine brittle and viscous deformation processes (Chapter 4) confirms that epidote can retain geochronological and isotopic information across orogenic cycles. In addition to this, evidence is provided for pre-orogenic hydration of granitoids in the Aar Massif. These data prove that the Aar Massif granitoids were hydrated and altered ca. 260 myr before the onset of Alpine deformation in the area. It follows that hydrothermally altered – i.e., weakened – domains of the Aar Massif granitoids may have been exploited for strain localization. The occurrence of pre-orogenic softening of granitic rocks has been proven by previous work in other study areas (Pyrenées; Bellahsen et al., 2019; Airaghi et al., 2020). In this respect, a compilation of time spans separating hydrothermal alteration and orogenic overprint of granitoids in orogens worldwide, as well as of the type of fluids driving their hydration, may shed light into the water cycle in the granitic continental crust. This chapter proves that epidote is a robust and reliable geochronometer, able to return new geochronological data which survive deformation processes.

Finally, Chapter 5 documents the occurrence of epidote dissolution–precipitation processes combined with quartz dynamic recrystallization during viscous granular flow in an epidote-quartz vein. Epidote is a widespread mineral: not only is it stable throughout a broad range of pressures and temperatures, but it is also present in a wide variety of geodynamic contexts and diverse lithologies. Thus, its response to deformation can be relevant not only in the Aar Massif granitoids, but also, for example, in deforming hydrothermally altered basalts or in epidote amphibolites. Dissolution–precipitation processes allow to recycle water stored in the hydroxyl groups of hydrous minerals. This is crucial in the tectono-metamorphic evolution of granitoids, in that it may provide new perspective on the relative importance of recycled pre-kinematic and newly added syn-kinematic fluids in mediating orogenic processes in the granitic continental crust.

Going back to the scientific questions of this thesis outlined in the Introduction (Chapter 1), we can now provide an answer to each one of them:

1 Epidote can be used as a U–Pb geochronometer dating vein formation to date and trace hydration of the continental crust in orogens, despite being involved in deformation. The prerequisite for successful epidote U–Pb dating is that the analyses are characterized by

sufficient variability in total U/Pb ratios, hence are sufficiently spread-out along the Tera–Wasserburg regression.

2 Pre-orogenic fluid-driven alteration and rock softening did occur in granitoids of the continental crust in the Swiss Alps as early as in Permian times. This early hydration partly affected strain localization in this continental crust during subsequent stages of deformation.

3 We have greatly enhanced our understanding of hydration of the granitic continental crust in the Swiss Alps by using epidote as a geochronometer and fluid tracer. Our data prove that the recycling of water is a multistage process which repeatedly occurs during different stages of the evolution of the Swiss Alps.

4 Epidote undergoes dissolution–precipitation processes during deformation and it is an active participant in viscous granular flow. Hence, epidote can also be an important fluid and time proxy for grain-scale deformation processes.

To conclude, this thesis demonstrates the robustness of vein epidote as a geochronometer and fluid tracer in the granitic continental crust, providing a new powerful tool to investigate retrograde hydration of highly deformed granitoids in orogens. The application of epidote U–Pb geochronology and isotope geochemistry does not have to be limited to veins in the continental crust though. Instead, the tools presented in this thesis have great potential for applications to various epidote types and in diverse geological setting. In the continental crust, epidote is a common alteration mineral in feldspar. Just like the development of LA-ICP-MS allowed to successfully date epidote at all, the availability of more sensitive *in-situ* instruments coupled with efforts to develop an epidote standard may allow to target epidote in saussurite. Epidote is common in greenschist-, amphibolite- and blueschist-facies metamorphic rocks. Hence, the use of this mineral as a fluid tracer may provide complementary knowledge of fluid circulation in subduction. Because epidote is a product of plagioclase fluid-driven alteration, epidote may become a valuable water tracer in all feldspar-bearing rocks, the occurrence of which is not limited to Earth.

Author contribution

This PhD project was designed and supervised by Alfons Berger and Marco Herwegh. Many collaborators scientifically contributed to Chapters 2–5 of this thesis, as listed on the cover page of each chapter. In the following, the contribution of each author is indicated.

Chapter 2

Veronica Peverelli carried out sample preparation, most analytical work, and data reduction and evaluation. LA-ICP-MS measurements (U–Pb dating and trace element analyses), data reduction and data evaluation were supervised by Tanya Ewing, Daniela Rubatto and Thomas Pettke. The work in the clean lab for sample digestion and ion chromatography was supervised by Martin Wille. Lead isotope measurements by solution-based MC-ICP-MS were performed by Martin Wille and Igor M. Villa. Chemical analyses by EPMA were supervised by Pierre Lanari. The geological interpretation of epidote U–Pb ages includes valued input by Alfons Berger and Marco Herwegh, who also provided the epidote samples. All co-authors provided scientific feedback on the manuscript. Measurements of $^{238}U/^{206}Pb$ ratios were independently carried out at the Geography Department of University of Bern by Patrick Neuhaus. Technical assistance in the LA-ICP-MS and clean laboratories was provided by Francesca Piccoli and Gabriela Baltzer.

Chapter 3

Veronica Peverelli collected all samples except for samples Albula-1 (collected by Alfons Berger) and Hauptdolomit (provided by Marco Herwegh), prepared the samples for all analyses, and carried out petrographic characterization of the samples, SEM imaging, epidote U–Pb dating by LA-ICP-MS, sample digestion and ion chromatography in the clean lab, as well as TIMS, solution-based MC-ICP-MS and EPMA analyses. Alfons Berger supervised and greatly contributed to structuring the manuscript, and provided invaluable insight into the geological significance of geochronological and isotope data together with Marco Herwegh. Martin Wille supervised the work in the clean lab, and TIMS and solution-based MC-ICP-MS isotope measurements, and he

greatly contributed to the assessment of Pb and Sr isotope data. Andreas Mulch carried out most of the hydrogen isotope analyses, with a few samples analyzed by Veronica Peverelli. Benita Putlitz performed all oxygen isotope measurements. Pierre Lanari assisted chemical analyses of chlorite by EPMA and processed the data for calculation of crystallization temperatures. Thomas Pettke assisted LA-ICP-MS measurements, and contributed to data interpretation and to the structure of the manuscript. Technical assistance was provided by Francesca Piccoli in the LA-ICP-MS lab and by Ulrich Treffert for hydrogen isotope measurements.

Chapter 4

Veronica Peverelli acquired optic and SEM images of the samples, performed U–Pb dating of the epidote samples and prepared the samples for hydrogen isotope analyses. Francesca Piccoli and Thomas Pettke helped with the LA-ICP-MS analyses. Hydrogen isotope data were measured by Andreas Mulch and Veronica Peverelli at Goethe University Frankfurt (Germany), with technical assistance provided by Ulrich Treffert. Alfons Berger and Marco Herwegh designed the project, provided the epidote samples, and greatly contributed to structuring the manuscript, to data interpretation, and to outlining the implications of the work. All authors contributed scientifically to manuscript preparation.

Chapter 5

Veronica Peverelli performed petrographic description and grain-size analysis, carried out trace element measurements by LA-ICP-MS, planned chemical maps by EPMA, prepared the epidote microseparates, carried out acid digestion and ion chromatography, and measured Sr isotope data by TIMS. Alfons Berger and Marco Herwegh directed and provided invaluable input to the microstructural work, and they helped structure the manuscript. Alfons Berger carried out EBSD measurements and greatly contributed to their interpretation. Martin Wille supervised the work in the clean lab and TIMS measurements, and measured Pb isotopes by solution-based MC-ICP-MS with help by Igor M. Villa. Thomas Pettke assisted LA-ICP-MS work and contributed to the interpretation of trace element data. Pierre Lanari ran and processed the chemical maps by EPMA. All authors provided scientific feedback on the work. Technical assistance was provided by Francesca Piccoli during LA-ICP-MS analyses.

Appendix 1

In order to make the reading of the thesis chapters and manuscripts more fluent for the general reader, sample names used in this thesis are different than the official sample names (i.e., labels on hand samples and thin sections). Table A1 presents a sample list, with the sample names used in the chapters/manuscripts and the corresponding official sample names. The available data are indicated, as well as whether these are in an Appendix or in the (online) data repository.

TABLE A1 Sample list with corresponding sample names in chapters, and available data for each sample with corresponding electronic Appendix. Bt = biotite; Chl = chlorite; Ep = epidote; Fsp = feldspar; Qz = quartz.

				Data repository	Data repository	Data repository	Appendix 2	Appendix 3	Data repository		Appendix 4	Appendix 5	
		Sample name	Name in chapters	Petrographic data	Microstructural data	β scans	Microprobe data	Trace element data	Dated Ep	Ep ($^{207}Pb/^{206}Pb)_m$	Ep $^{87}Sr/^{86}Sr$	Ep δD data	$\delta^{18}O$ data
Albula Pass area		ALB13-1	Albula-1	yes	no	yes	yes (Ep)	yes (Ep)	yes	yes	yes	yes	yes (Ep, Qz)
		ALB13-6	-	yes	no	yes	no	no	no	no	no	no	no
		ALB13-7A	-	no	no	yes	no	no	no	no	no	no	no
		ALB13-7B	-	yes	no	yes	yes (Ep)	yes (Ep)	no	no	yes	yes	no
		ALB19-1-‖	ALB19-1	yes	no	no	no	yes (Ep)	yes	yes	yes	yes	yes (Ep, Qz)
		ALB19-4-1327A	ALB19-4	yes	no	no	yes (Ep, Wm)	yes (Ep)	yes	yes	yes	yes	yes (Ep)
		ALB19-11A1342	-	no	no	no	yes (Ep)	no	no	no	yes	yes	no
		ALB19-11A1343	-	yes	no	no	no	no	no	no	yes	yes	no
		ALB19-11B_A	-	no	no	no	no	yes (Ep)	no	no	no	no	no
		ALB19-11B_C	ALB19-11	yes	no	no	yes (Ep, Chl)	yes (Ep)	yes	yes	yes	yes	yes (Ep)
		ALB19-18	ALB19-18	yes	no	no	no	yes (Ep)	yes	yes	yes (a+b)[1]	yes (a+b)[1]	yes (Ep, a)[1]
		A4 Mingér (limestone)	Mingér	no	no	no	no	yes (bulk)	-	yes (bulk)	yes (bulk)	no	no
		A5 Allgäu (limestone)	Allgäu	no	no	no	no	yes (bulk)	-	yes (bulk)	yes (bulk)	no	no
		DM (dolomite)	Hauptdolomite	no	no	no	no	yes (bulk)	-	yes (bulk)	yes (bulk)	no	no
		ALB-G2 (granodiorite)	Albula Granite	yes	no	no	no	yes (bulk)	-	yes (bulk)	yes (bulk)	no	no
Aar Massif	**GTS**	P6-b	-	yes	no	no	yes (Ep)	yes (Ep)	yes	yes	no	no	no
		P8	-	yes	no	yes	yes (Ep)	yes (Ep)	yes	yes	no	no	no
		P9c	P1	yes	no	yes	yes (Ep)	yes (Ep)	yes	yes	yes	yes	no
		P9d	P1	yes	yes	yes	yes (Ep)	yes (Ep)	yes	yes	yes	yes	no
		Gr0-a	P3	yes	no	no	yes (Ep)	yes (Ep)	yes	yes	no	no	no
		Gr0-c	Gr0-c	yes	yes	yes	yes (Ep)	yes (Ep)	yes	yes	yes	yes	no
		Gr0-c2	-	no	no	no	no	yes (Ep)	yes	yes	yes	yes	no
		Gr0-d	Grimsel-1	yes	yes	yes	yes (Ep)	yes (Ep)	yes	yes	yes (+Bt)	yes	yes (Ep)
		Gr0-e	P2	yes	no	yes	no	yes (Ep)	yes	yes	yes	yes	yes (Ep)
		11.001 24.40 m	Grimsel-2	yes	yes	yes	yes (Ep)	yes (Ep)	yes	yes	no	no	no
		L106c	-	yes	no	yes	no	no	no	no	no	yes	no
		12.003-H-UL	-	no	no	yes	no	no	no	no	no	no	no
		11.003-H-ULa	-	no	no	yes	no	no	no	no	no	no	no
	Gelmersee	GE-4	-	yes	no	no	yes (Ep)	yes (Ep)	yes	yes	no	no	no
	Oberaletsch	OBA19-03A	-	yes	no	no	yes (Ep)	no	no	no	no	no	no
		OBA19-03B	-	yes	no	no	yes (Ep)	yes (Ep)	yes	yes	yes	yes	yes (Ep, Fsp)
		OBA19-03C	-	yes	no	no	no	no	yes	yes	no	no	no
	Lötschental	Lo20_1A	-	no	no	no	no	no	yes	yes	yes	yes	yes (Ep, Qz)
		Lo20_1B	-	no	no	no	no	no	no	no	no	no	no
		Lo20_2	-	no	no	no	no	no	no	no	no	yes	no
		Lo20_3A	-	no	no	no	no	no	no	no	no	no	no
		Lo20_3B	-	no	no	no	no	no	no	no	no	yes	no
		Lo20_4A	-	no	no	no	no	no	no	no	no	yes	no
		Lo20_4B	-	no	no	no	no	no	no	no	no	no	no
		Lo20_4C	-	no	no	no	no	no	no	no	no	no	no
		Lo20_4D	-	no	no	no	no	no	no	no	no	no	no
		Lo20_5A // _5B	-	no	no	no	no	no	yes (A)	yes (A)	no	no	no
		Lo20_5C	-	no	no	no	no	no	no	no	no	no	no
		Lo20_5D	-	no	no	no	no	no	no	no	no	yes (+Chl)	no
	Gasterntal	GAS19-01A	-	yes	no	no	no	no	no	no	no	yes	yes (Ep)
		GAS19-03A	-	yes	no	no	no	no	yes	yes	yes	no	no
	Clefts	Planggenstock	-	yes	no	no	no	yes (Ep)	yes	yes	yes	yes	yes (Ep)
		Aerlengletscher	-	yes	no	no	no	yes (Ep)	yes	yes	yes	yes	yes (Ep, Qz)
		Grosstal	-	yes	no	no	no	yes (Ep)	yes	yes	yes	yes	no
Heyuan Fault		HY17-5a2	Heyuan-1	yes	yes	yes	yes (Ep)	yes (Ep)	yes	yes	no	no	no
		HY17-19	-	no	no	yes	no	no	no	no	no	no	no

[1]See Sect. 3.3.3.

Appendix 2

Chemical data (in mass precent) of epidote measured by electron probe micro analyzer (EPMA) are reported hereafter.

6 June 2019												
No.		SiO2	MgO	CaO	FeO	Al2O3	F	MnO	Cl	TiO2	SrO	Total	Comment
	1	36.71	0	23.86	10.86	24.82	0	0.0493	0	0.1112	0.0723	96.4829	test-epidote
	2	36.9	0	23.73	11.73	24.08	0	0.2416	0	0.0115	0.0402	96.7334	test-epidote
	3	36.48	0	23.42	12.3	23.59	0	0.4236	0	0.0474	0	96.2611	test-epidote
	4	37.15	0	23.84	12.41	23.41	0	0.1971	0	0.0849	0	97.092	test-epidote
	5	36.38	0	23.63	12.13	23.6	0	0.1487	0	0.0245	0	95.9132	test-epidote
	6	36.89	0	23.33	11.1	24.4	0	0.4661	0.009	0.0299	0.3277	96.5528	test-epidote
	7	37.41	0	23.59	10.72	25.01	0	0.1346	0.0011	0.0476	0	96.9134	P9d_Area1_small1
	8	36.89	0	23.58	11.86	23.72	0	0.2709	0.0049	0.0412	0.0489	96.4159	P9d_Area1_small2
	9	36.26	0	23.8	11.32	24.37	0	0.3431	0.009	0.0159	0	96.1181	P9d_Area1_small3
	10	35.7	0	23.72	13.01	22.29	0	0.1333	0	0.0061	0.1167	94.9762	P9d_Area1_small4
	11	36.19	0	23.64	11.59	24.21	0	0.3219	0	0.015	0	95.9669	P9d_Area1_small5
	12	36.44	0	23.57	13.57	22.08	0	0.1778	0.0149	0.0255	0.0366	95.9149	P9d_Area1_small6
	13	36.31	0	23.99	10.7	24.22	0	0.0584	0	0.1845	0	95.463	P9d_Area1_small7
	14	35.69	0	23.5	10.36	24.43	0	0.2778	0.0064	0.0805	0.1094	94.4541	P9d_Area1_small8
	15	35.99	0	23.83	11.03	23.91	0	0.1661	0.0049	0.0639	0	94.9949	P9d_Area1_small9
	16	35.99	0	23.95	10.57	24.65	0	0.0633	0	0.145	0	95.3684	P9d_Area1_small10
	17	35.25	0	22.45	11.99	22.45	0	0.4486	0.0052	0.0658	0.1169	92.7766	P9d_Area1_small11
	18	37.46	0	23.64	13.67	22.41	0	0.0589	0.0056	0.03	0.0352	97.3097	P9d_Area2_small1
	19	36.58	0	23.43	12.39	23.16	0	0.3625	0.0049	0.026	0	95.9535	P9d_Area2_small2
	20	35.87	0	23.75	13.33	22.19	0	0.0825	0.0019	0	0.0772	95.3017	P9d_Area2_small2-core
	21	36.21	0	22.35	11.94	23.44	0	1.0305	0	0.0005	0.6351	95.6062	P9d_Area2_small2-rim
	22	36.54	0	24	10.52	24.77	0	0.1221	0.0082	0.0273	0	95.9877	P9d_Area3_1core
	23	36.18	0	23.71	12.83	22.83	0	0.1257	0	0.2948	0	95.9706	P9d_Area3_1rim-bright
	24	37.07	0	24.03	9.6	25.54	0	0.0633	0.0075	0.072	0.0509	96.4338	P9d_Area3_1rim-dark
	25	36.99	0	23.69	9.57	25.56	0	0.2646	0.0011	0.0585	0.0409	96.1752	P9d_Area3_2core-dark
	26	35.8	0	22.56	12.95	22.61	0	0.9212	0.0022	0.0108	0.36	95.2143	P9d_Area3_2core-bright
	27	37.35	0	23.83	11.43	24.11	0	0.2022	0	0.0919	0	97.0142	P9d_Area4_1
	28	37.26	0	23.6	12.57	23.13	0	0.1914	0.0097	0.0662	0	96.8273	P9d_Area4_2
	29	35.71	0	23.81	12.62	22.19	0	0.0355	0	0.0135	0.0044	94.3835	P9d_Area4_4
	30	35.49	0	23.38	13.53	21.68	0	0.4019	0.0034	0.0182	0.0021	94.5057	P9d_Area4_3

31	37.84	0	23.84	11.86	24.2	0	0.1695	0.0037	0.077	0	97.9903	P9d_Area4_5
32	37.22	0	23.55	9.59	25.96	0	0.3001	0	0.0313	0.1149	96.7664	Gr0-c_Area2_hydrothermal-struct-bottom
33	37.17	0	24.07	8.25	26.85	0	0.1475	0.0128	0.0309	0	96.5312	Gr0-c_Area2_hydroth-struc-cent-dark
34	36.3	0	22.95	10.67	24.73	0	0.4336	0.0128	0.0296	0.7713	95.8974	Gr0-c_Area2_hydroth-struc-cent-bright
35	36.55	0	23.86	10.05	25.28	0	0.2568	0	0.0246	0.0021	96.0235	Gr0-c_Area2_hydroth-struc-cent-up
36	37.03	0	23.91	10.59	24.74	0	0.1373	0.0015	0.0198	0	96.4286	Gr0-c_Area2_hydroth-struc-top
37	35.28	0	23.81	11.93	22.89	0	0.0958	0	0.038	0.0887	94.1326	Gr0-c_Area2_poss.overgrowth
38	36.06	0	23.93	10.11	24.33	0	0.0774	0.0008	0.0181	0.0034	94.5298	Gr0-c_Area2_bright
39	36.51	0	24.15	7.42	26.63	0	0.1738	0	0.0033	0.0681	94.9552	Gr0-c_Area2_dark1
40	37.13	0	24.14	8.98	25.93	0	0.1798	0.0008	0.0109	0	96.3716	Gr0-c_Area2_dark2
41	35.65	0	23.69	12.6	21.93	0	0.0719	0	0.0137	0.2004	94.1561	Gr0-c_Area2_bright2
42	37.44	0	23.94	10.89	24.97	0	0.1183	0.0049	0.0124	0	97.3756	Gr0-c_Area2_1
43	35.97	0	23.83	10.08	24.28	0	0.315	0	0.0926	0	94.5677	Gr0-c_Area2_2
44	36.44	0	23.19	12.6	22.51	0	0.5553	0	0.1179	0.0227	95.4359	Gr0-c_Area3_poss.overgrowth
45	35.86	0	23.3	12.63	22.6	0	0.1898	0.0019	0.0064	0.4347	95.0229	Gr0-c_Area3_1
46	36.72	0	23.37	10.93	24.18	0	0.4499	0.0079	0.0449	0	95.7028	Gr0-c_Area3_2
47	37.19	0	22.73	10.45	25	0	0.1306	0.0079	0.0488	0	95.5573	Gr0-c_Area3_3-dark
48	36.21	0	21.41	11.94	23.93	0	0.8894	0	0.0014	0.4367	94.8176	Gr0-c_Area3_3-bright
49	36.34	0	22.25	14.48	21.45	0	0.1618	0.0116	0.0069	0.1316	94.8319	Gr0-c_Area3_4-bright2
50	37.64	0	23.09	7.54	27.4	0	0.2427	0	0	0	95.9128	Gr0-c_Area3_4-dark2
51	36.75	0	22.56	10.71	24.96	0	0.1994	0	0.0998	0	95.2793	Gr0-c_Area3_4-dark1
52	37.21	0	22.69	9.94	25.58	0	0.2619	0.0011	0.0594	0.08	95.8225	Gr0-c_Area3_5
53	36.96	0	22.81	10.74	24.8	0	0.0962	0.0015	0.0389	0	95.4467	Gr0-c_Area3_6-dark-core
54	36.2	0	21.74	12.85	22.79	0	0.7443	0	0.089	0.2359	94.6493	Gr0-c_Area3_6-bright-rim
55	35.9	0	21.31	12.49	22.73	0	0.6945	0	0.0804	0.2477	93.4527	Gr0-c_Area1_1B_B-dark-ri,
56	35.5	0	21.26	14.38	21.76	0	0.4297	0.0389	0	0.6412	94.0099	Gr0-c_Area1_1B_B-bright-ri,
57	35.61	0	22.34	12.39	23.11	0	0.135	0.0026	0.0304	0.0335	93.6516	Gr0-c_Area1_1B_B-dark-core
58	35.52	0	22	14.96	20.73	0	0.0945	0.0146	0.0429	0	93.3621	Gr0-c_Area1_1B_B-bright-core
59	35.36	0	21.54	12.87	22.04	0	0.5057	0	0.0958	0.0051	92.4167	Gr0-c_Area1_1B_B-small-aside
60	35.4	0	21.78	12.79	22.95	0	0.5097	0.0011	0.0233	0	93.4541	Gr0-c_Area1_small-aside-dark-rim
61	35.28	0	21.66	14.91	21.15	0	0.1372	0.006	0	0.169	93.3122	Gr0-c_Area1_small-aside-bright-rim
62	35.76	0	21.95	12.61	22.87	0	0.2225	0.0075	0.0269	0.2001	93.6471	Gr0-c_Area1_small-aside-bright-core
63	35.8	0	22.34	13.05	22.73	0	0.0528	0	0.0287	0	94.0016	Gr0-c_Area1_chunk-dark-core
64	36.39	0	21.31	13.08	22.28	0	0.7086	0	0.0018	1.1524	94.9229	Gr0-c_Area1_chunk-bright-core
65	35.65	0	21.52	13.62	22.04	0	0.6669	0.0067	0.0048	0.5058	94.0143	Gr0-c_Area1_chunk-bright-infiltration1
66	35.74	0	21.9	13.14	22.87	0	0.3439	0.0097	0.0295	0.4312	94.4644	Gr0-c_Area1_chunk-bright-infiltration2
67	36.29	0	22.89	13.6	22.06	0	0.3147	0.0082	0.011	0.7236	95.8976	Gr0-c_Area1_chunk-bright-infiltration3
68	36.51	0	23.67	10.77	24.09	0	0.1274	0.003	0.0078	0.0671	95.2453	Gr0-c_Area1_chunk-dark-close-infiltrati
69	36.37	0	23.89	11.33	24.07	0	0.0552	0	0.1168	0	95.832	Gr0-c_Area1_chunk-dark-close-infiltrati
70	36.79	0	23.78	9.38	25.77	0	0.3364	0.0019	0.0052	0	96.0636	Gr0-c_Area1_chunk-dark-close-infiltrati
71	36.75	0	23.27	11.4	23.83	0	0.3102	0	0.0849	0.178	95.8232	11.001_Area1_1
72	36.6	0	23.38	11.12	23.93	0	0.281	0.0049	0.1411	0.1536	95.6106	11.001_Area1_2
73	36.54	0	23.29	11.42	23.9	0	0.3403	0.0131	0.0879	0.3681	95.9595	11.001_Area1_3

74	36.51	0	23.06	11.69	23.58	0	0.3287	0	0.0653	0.4395	95.6736	11.001_Area1_4
75	37.09	0	23.38	10.92	24.53	0	0.2807	0	0.0476	0.256	96.5043	11.001_Area1_5
76	36.49	0	23.28	11.37	23.84	0	0.3492	0.0176	0.1271	0.1104	95.5844	11.001_Area1_6
77	35.52	0	23.18	11.46	23.71	0	0.3906	0	0.1023	0.061	94.424	11.001_Area1_7
78	35.94	0	23.22	11.39	23.29	0	0.2701	0.0071	0.0349	0.3039	94.4561	11.001_Area1_8
79	35.99	0	23.33	11.6	23.52	0	0.257	0	0.0727	0.307	95.0768	11.001_Area1_9
80	36.41	0	22.99	12.1	23.37	0	0.284	0	0.0501	0.5698	95.774	11.001_Area1_10
81	35.9	0	23.13	11.71	23.29	0	0.4146	0	0.1462	0.0793	94.6702	11.001_Area2_1
82	36.11	0	22.72	12.31	23.07	0	0.383	0	0.0634	0.7537	95.4102	11.001_Area2_2
83	35.5	0	23.17	12.01	23.07	0	0.3841	0.012	0.0365	0.4721	94.6548	11.001_Area2_3
84	36.93	0	22.97	12.18	23.64	0	0.336	0	0.0384	0.5822	96.6767	11.001_Area2_4
85	36.28	0	23.32	11.62	24.01	0	0.3071	0	0.1067	0.0941	95.738	11.001_Area3_1
86	36.74	0	23.37	11.49	24.38	0	0.2739	0.0094	0.0967	0.1889	96.549	11.001_Area3_2
87	36.51	0	23.34	11.09	24.13	0	0.3323	0.0034	0.084	0.1399	95.6297	11.001_Area3_3
88	35.78	0	23.36	11.44	23.99	0	0.2931	0.0082	0.1029	0.2993	95.2736	11.001_Area3_4
89	36.01	0	23.43	11.32	23.41	0	0.3886	0	0.1342	0.2446	94.9375	11.001_Area3_5
90	36.4	0	23.49	11.34	23.95	0	0.2592	0	0.0489	0.2887	95.7768	11.001_Area4_1
91	36.14	0	23.52	11.32	23.89	0	0.2387	0.0179	0.0335	0.2208	95.381	11.001_Area4_2
92	36.19	0	23.34	11.2	23.74	0	0.279	0	0.0892	0.3468	95.1851	11.001_Area4_3
93	36.47	0	23.61	11.4	23.63	0	0.3799	0	0.1418	0.0924	95.7242	11.001_Area4_4
94	36.58	0	23.39	11.15	24.32	0	0.2501	0	0.0536	0.3487	96.0925	11.001_Area4_5
95	35.84	0	23.28	11.55	23.6	0	0.4016	0	0.1443	0.1078	94.9238	11.001_Area4_6core
96	36.14	0	23.29	11.27	23.76	0	0.3546	0	0.0204	0.4794	95.3145	11.001_Area4_7rim
97	36.11	0	23.04	11.89	23.39	0	0.3214	0	0.1137	0.7095	95.5747	11.001_Area4_8
98	36.49	0	23.59	11.24	24.09	0	0.2452	0.0011	0.0817	0.189	95.9271	11.001_Area4_9
99	35.7	0	23.47	11.33	23.17	0	0.2803	0.0056	0.0876	0.3417	94.3852	11.001_Area4_10
100	37.13	0	23.93	11.72	23.76	0	0.1648	0.0011	0.1067	0	96.8127	Spots4Map_01
101	35.91	0	23.87	10.98	24.23	0	0.2266	0	0.0221	0	95.2387	Spots4Map_2
102	36.06	0	23.94	12.22	23.57	0	0.1002	0.003	0.0237	0	95.9169	Spots4Map_3
103	36.2	0	23.47	12.41	23.5	0	0.3767	0	0.0254	0	95.9822	Spots4Map_4
104	36.06	0	22.86	13.29	23.26	0	0.794	0	0.0013	0.1522	96.4175	Spots4Map_5
105	36.67	0	23.73	11.38	24.62	0	0.1924	0.0041	0.0429	0.1569	96.7963	Spots4Map_6
106	37	0	23.82	9.46	26.12	0	0.21	0	0.0363	0.1347	96.7811	Spots4Map_7
107	35.51	0	22.54	12.8	22.97	0	0.9634	0.0176	0.0097	0.1596	94.9704	Spots4Map_8
108	35.95	0	23.74	11.12	24.53	0	0.1443	0.021	0.0357	0.1345	95.6756	Spots4Map_9
109	34.86	0	23.03	13.21	22.18	0	0.6716	0	0.0897	0.1411	94.1824	Spots4Map_10
110	35.78	0	24.11	10.57	24.77	0	0.0561	0	0.111	0	95.3971	Spots4Map_11
111	36.03	0	23.75	11.64	23.54	0	0.2026	0	0.0216	0	95.1842	Spots4Map_12
112	35.91	0	23.5	12.77	23.52	0	0.1297	0.006	0.0517	0.0817	95.9691	Spots4Map_13
113	34.26	0	23.45	13.26	21.83	0	0.1393	0	0.0238	0.1231	93.0863	Spots4Map_14
114	35.63	0	22.05	13.34	22.12	0	0.86	0	0.006	1.014	95.0201	Spots4Map_15
115	35.54	0	22.82	13.26	22.15	0	0.5597	0	0.0462	0.3794	94.7554	Spots4Map_16
116	36.39	0	24.06	10.49	24.81	0	0.0642	0.0053	0.1268	0	95.9464	Spots4Map_17

117	35.76	0	23.79	11.17	23.87	0	0.1026	0.0064	0.1577	0	94.8568	Spots4Map_18
118	35.39	0	22.95	12.9	22.27	0	0.5095	0	0.089	0	94.1085	Spots4Map_19
119	35.15	0	23.76	11.5	23.63	0	0.1037	0.0108	0.0296	0.1415	94.3257	Spots4Map_20
120	34.91	0	23.28	11.21	22.89	0	0.1775	0.0075	0.0163	0.4852	92.9765	Spots4Map_21
121	35.85	0	24	9.63	24.98	0	0.0703	0	0.1527	0	94.683	Spots4Map_22
122	35.96	0	23.97	9.58	24.6	0	0.0684	0	0.1031	0	94.2816	Spots4Map_23
128	37.43	0	23.76	10.51	23.59	0	0.0728	0.0547	0.0911	0.0744	95.5831	test_22
129	35.91	0	23.54	11.12	22.72	0	0.1929	0	0.0051	0.3482	93.8363	test_21
Minimum	34.26	0	21.26	7.42	20.73	0	0.0355	0	0	0	92.4166	
Maximum	37.84	0	24.15	14.96	27.4	0	1.0305	0.0547	0.2948	1.1524	97.9902	
Average	36.2548	0	23.2588	11.6312	23.6943	0	0.2894	0.0041	0.0564	0.1701	95.359	
Sigma	0.6422	0	0.7035	1.3374	1.1874	0	0.2086	0.0074	0.0488	0.2278	1.0485	
No. of data 124												

8 June 2019

No.	Al2O3	Na2O	CaO	K2O3	SiO2	MnO	FeO	MgO	TiO2	Total	Comment
1	20.79	0.0175	22.43	0	37.81	0.4568	13.74	0	0.0368	95.2812	ALB13-7B-eptestr1
2	20.3	0.0227	22.68	0.0149	38.48	0.3971	13.9	0	0.0215	95.8163	ALB13-7B_1
3	19.95	0	22.7	0	37.38	0.2403	14.05	0	0.0416	94.362	ALB13-7B_2
4	21.49	0	23.22	0	37.86	0.1712	12.74	0	0.1052	95.5865	ALB13-7B_3
5	21.46	0.0264	23.12	0	38.08	0.2643	12.51	0	0.1125	95.5733	ALB13-7B_4
6	21.9	0.0057	22.4	0.0128	37.81	0.234	12.26	0	0.0436	94.6662	ALB13-7B_5
7	21.22	0	23.3	0	37.49	0.1444	13.01	0	0.1434	95.3079	ALB13-7B_6
8	21.85	0.0485	22.38	0	37.49	0.3456	12.49	0	0.0695	94.6737	ALB13-7B_7
9	22.38	0.0272	21.7	0.0007	36.49	0.427	12.42	0	0.0855	93.5305	ALB13-7B_8
10	21.26	0.0001	23.02	0.0004	37.16	0.2987	12.87	0	0.1139	94.7232	ALB13-7B_9
11	20.3	0.0061	21.03	0.0107	40.3	0.439	11.76	0	0.0758	93.9217	Line 1 map1-ep
12	19.84	0.0195	22.16	0.0561	36.31	0.4607	12.65	0	0.1472	91.6436	Line 2 map1-ep
13	21.81	0.0311	22.4	0.0369	36.93	0.6616	13.37	0	0.2328	95.4725	Line 3 map1-ep
14	21.77	0.0352	22.86	0.0188	38.09	0.445	12.36	0	0.0972	95.6763	Line 4 map1-ep
15	18.93	0.0114	22.55	0.0796	37.77	0.358	11.36	0	3.34	94.3991	Line 5 map1-ep
16	16.75	0.0222	18.17	0.0323	41.28	0.2701	11.96	1.83	0.04	90.3547	Line 6 map1-ep
17	20.74	0.0451	22.11	0.0188	37.47	0.4579	12.63	0	0.0355	93.5073	Line 7 map1-ep
18	20.97	0.0178	22.99	0.0114	37.17	0.3738	12.87	0	0.0559	94.459	Line 8 map1-ep
19	22.37	0.0222	23.05	0.0089	37.89	0.2949	12.68	0	0.1039	96.4199	Line 9 map1-ep
20	21.14	0.0637	22.91	0	37.33	0.2648	13.33	0	0.0428	95.0814	Line 10 map1-ep
21	22.32	0	22.91	0.0139	37.93	0.4666	12.17	0	0.1581	95.9687	Line 11 map1-ep
22	21.21	0.0237	22.3	0	36.74	0.417	12.2	0	0.0883	92.979	Line 12 map1-ep
23	22.57	0	23.41	0	37.77	0.2433	12.61	0	0.1248	96.7282	Line 13 map1-ep
24	21.47	0.0087	22.98	0.0174	37.99	0.4788	12.99	0	0.0989	96.0338	Line 14 map1-ep
25	21.54	0	23.05	0	37.47	0.3976	12.87	0	0.0921	95.4198	Line 15 map1-ep
26	21.86	0.0214	23.28	0.0099	38.24	0.2907	12.47	0	0.1102	96.2823	Line 16 map1-ep

27	19.23	0.0541	22.09	0.0609	39.55	0.3062	12.2	0	0.0379	93.5292	Line 17 map1-ep
28	22.09	0	22.41	0.0213	38	0.617	12.54	0	0.0448	95.7232	Line 18 map1-ep
29	21.25	0.0368	23.08	0	38.26	0.2037	12.2	0	0.1358	95.1664	Line 19 map1-ep
30	21.66	0.0059	23	0.005	37.55	0.2648	12.68	0	0.05	95.2158	Line 20 map1-ep
31	19.73	0.0047	22.64	0.0117	36.64	0.4085	13.16	0	0.1233	92.7182	Line 21 map1-ep
32	17.34	0.0312	18.08	0.0123	53.01	0.4338	9.99	0	0.0675	98.9648	Line 22 map1-ep
33	21.41	0.0265	22.89	0.0189	38.81	0.2428	11.91	0	0.0585	95.3668	Line 23 map1-ep
34	22.31	0	23.59	0	37.79	0.1439	11.94	0	0.062	95.836	ALB13-1-ep1
35	23.6	0.0262	23.74	0	37.72	0.1782	11.21	0	0.084	96.5584	ALB13-1-ep2
36	22.38	0.0081	22.01	0	37.36	0.762	11.95	0	0.0455	94.5157	ALB13-1-ep3
37	22.37	0.0433	22.08	0.0061	37.92	0.7269	11.83	0	0.069	95.0454	ALB13-1-ep4
38	22.52	0.0218	23.47	0	38.09	0.0583	11.84	0	0.1829	96.183	ALB13-1-ep5
39	24.46	0	23.6	0.0029	38.5	0.1115	9.71	0	0.1719	96.5564	ALB13-1-ep6
40	22.53	0	22.12	0	37.94	0.7788	11.84	0	0.0398	95.2487	ALB13-1-ep7
41	22.73	0	23.87	0	37.85	0.0358	12.41	0	0.023	96.9189	ALB13-1-ep8
42	22.08	0.0021	21.95	0	37.34	0.7905	12.69	0	0.0513	94.904	ALB13-1-ep9
43	21.63	0	22.39	0.0032	36.84	0.5187	13.32	0	0.0398	94.7418	ALB13-1-ep10
44	22.08	0	23.41	0.0167	37.18	0.1156	13.07	0	0.0441	95.9165	ALB13-1-ep11
45	22.45	0	22.31	0.0011	36.48	0.7529	12.58	0	0.0456	94.6197	Line 1 map2-ep
46	23.3	0.0149	23.5	0.0039	38.93	0.0916	9.18	0	0.1491	95.1695	Line 2 map2-ep
47	24.69	0	23.42	0.005	37.47	0.1422	9.75	0	0.1159	95.5932	Line 3 map2-ep
48	24.42	0	23.43	0.0014	37.69	0.1392	9.79	0	0.1155	95.5862	Line 4 map2-ep
49	23.06	0.0147	23.47	0	37.24	0.0659	11.41	0	0.1571	95.4178	Line 5 map2-ep
50	21.81	0	22.64	0.0021	36.47	0.3889	12.58	0	0.0681	93.9592	Line 6 map2-ep
51	22.12	0.017	21.98	0.0178	36.78	0.7318	11.92	0	0.0656	93.6322	Line 7 map2-ep
52	21.65	0.0522	21.75	0.0011	39.38	0.7738	11.75	0	0.0773	95.4345	Line 8 map2-ep
53	22.62	0.0047	22.23	0	36.89	0.7401	11.5	0	0.0781	94.063	Line 9 map2-ep
54	22.27	0	21.9	0.0046	36.99	0.7729	12.28	0	0.0611	94.2786	Line 10 map2-ep
55	22.46	0.0306	22.09	0.0036	36.54	0.8155	12.19	0	0.0524	94.1822	Line 11 map2-ep
56	22.15	0	21.81	0.0334	37.05	0.76	12.04	0	0.0443	93.8877	Line 12 map2-ep
Minimum	16.75	0	18.08	0	36.31	0.0358	9.18	0	0.0215	90.3546	
Maximum	24.69	0.0637	23.87	0.0796	53.01	0.8155	14.05	1.83	3.34	98.9648	
Average	21.6534	0.0156	22.5368	0.0103	37.982	0.3959	12.2095	0.0327	0.1425	94.9785	
Sigma	1.4536	0.017	1.0551	0.0163	2.2427	0.2284	1.0018	0.2445	0.4374	1.3348	
No. of data 56											

9 December 2019

No.	SiO2	MgO	CaO	FeO	Al2O3	F	MnO	Cl	TiO2	SrO	Total	Comment
1	33.92	0	22.71	13.09	21.3	0	0.1692	0	0.0847	0	91.274	ALB13-1_1_rim
2	35.95	0	23.19	14.6	21.38	0	0.2317	0.0045	0.0144	0.1977	95.5683	ALB13-1_1_rim
3	35.51	0	23.17	12.67	22.5	0	0.2091	0.015	0.0286	0.1087	94.2115	ALB13-1_3
4	36.38	0	23.35	13.12	22.58	0	0.0713	0	0.0384	0.237	95.7768	ALB13-1_4

5	35.64	0	23.2	12.44	23.11	0	0.1011	0.0056	0.0098	0.2488	94.7554	ALB13-1_5
6	34.81	0	23.12	12.94	22.31	0	0.1217	0.0008	0.0394	0.3218	93.6637	ALB13-1_6
7	35.98	0	22.67	14.32	21.31	0	0.196	0	0.0067	0.9604	95.4432	ALB13-1_7
8	35.21	0	22.62	14.85	20.94	0	0.0733	0.0149	0.0166	0.6981	94.423	ALB13-1_8
9	34.39	0	22.99	13.34	21.99	0	0.1221	0	0.0484	0.178	93.0586	ALB13-1_9
10	35.51	0	22.28	13.08	22.44	0	0.3144	0	0.0388	1.34	95.0033	ALB13-1_rim2
11	35.39	0	22.73	13.03	22.26	0	0.2397	0.0008	0.0478	0.7879	94.4863	ALB13-1_11
12	34.77	0	23.05	11.84	23.33	0	0.0589	0	0.1641	0.6936	93.9067	ALB13-1_12
13	35.87	0	23.31	12.48	23.1	0	0.1143	0.009	0.017	0.1948	95.0952	ALB13-1_core2
14	35.74	0	23.32	13.35	22.58	0	0.1091	0.0078	0.0186	0.2252	95.3508	ALB13-1_14
15	36.03	0	23.33	13.63	22.22	0	0.1762	0	0.011	0.3661	95.7634	ALB13-1_15
16	34.95	0	22.68	15.05	20.78	0	0.1532	0	0	0.4259	94.0392	ALB13-1_rim2
17	35.51	0	23.26	14.39	21.57	0	0.1035	0	0.0083	0.0718	94.9137	ALB13-2_1
18	34.4	0	23.14	12.88	22.3	0	0.1149	0.0041	0	0.1722	93.0113	ALB13-2_2
19	35.11	0	22.28	13.13	22.22	0	0.923	0	0.0411	0.5659	94.2701	ALB13-2_5
20	35.97	0	22.06	12.8	22.88	0	0.8305	0.0056	0.0789	1.0907	95.7158	ALB13-2_4
21	35.75	0	23.5	12.91	22.25	0	0.1596	0	0	0.23	94.7997	ALB13-2_3
22	34.79	0	23.3	15.34	20.28	0	0.2282	0	0	0.1172	94.0555	ALB13-4_1
23	35.07	0	23.79	13.29	21.84	0	0.1625	0	0.0122	0.0534	94.2182	ALB13-4_2
24	34.96	0	23.47	14.14	21	0	0.1261	0.0168	0.0399	0.1341	93.887	ALB13-4_3
25	34.46	0	23.05	15.53	20	0	0.1483	0.0004	0.0003	0.3795	93.5686	ALB13-4_4
26	35.09	0	23.15	15.13	20.36	0	0.1076	0	0.0206	0.6119	94.4701	ALB13-4_5
27	34.55	0	23.25	15.01	19.66	0	0.1086	0.0123	0	0.4667	93.0576	ALB13-4_6
28	35.46	0	23.04	14.44	20.77	0	0.0981	0.0116	0.0229	0.5277	94.3704	ALB13-11_1
29	36.33	0	23.11	10.64	24.35	0	0.1642	0.0004	0.1763	1.0523	95.8232	ALB13-11_2
30	35.62	0	22.02	14.32	21.24	0	0.5591	0.0109	0.0863	1.1488	95.0052	ALB13-11_3
31	34.48	0	22.17	14.62	20.2	0	0.6267	0.0034	0.043	1.19	93.3332	ALB13-11_4
32	35.33	0	23.79	13.14	21.81	0	0.1589	0.0038	0.0561	0.3744	94.6632	ALB13-11_5
33	36.38	0	23.37	12.81	22.7	0	0.1425	0.0157	0.0295	0.1401	95.5879	ALB13-1_A_1
34	34.84	0	23.73	12.7	21.56	0	0.1611	0.0157	0.112	0.1065	93.2253	ALB13-1_A_2
35	34.69	0	23.26	12.17	22.05	0	0.2279	0.0344	0.1141	0.5467	93.0931	ALB13-1_A_3
36	35.74	0	23.59	10.9	24.16	0	0.0429	0	0.1726	0.3173	94.9229	ALB13-1_A_4
37	34.19	0	22.44	14.59	20.44	0	0.6365	0	0.0103	1.24	93.5469	ALB13-1_A_5
38	35.33	0	23.2	13.15	22.01	0	0.4675	0.0164	0.0586	0.075	94.3076	Gr0-d_8_1
39	36.1	0	23.38	13.81	22.4	0	0.6748	0.0023	0.0562	0.1981	96.6214	Gr0-d_8_2
40	36.22	0	23.27	12.6	22.95	0	0.5033	0	0.0699	0.1864	95.7997	Gr0-d_8_3
41	35.19	0	23.12	12.96	22.19	0	0.577	0.0142	0.1059	0	94.1572	Gr0-d_8_4
42	35.53	0	23.23	13.19	22.6	0	0.5791	0	0.0482	0.1222	95.2996	Gr0-d_1_1
43	33.7	0	23.43	11.78	22.43	0	0.4115	0	0.1144	0	91.866	Gr0-d_1_2
44	35.04	0	23.04	12.55	22.13	0	0.5502	0	0.0474	0.2149	93.5726	Gr0-d_1_3
45	34.83	0	23.45	12.47	22.7	0	0.4739	0.0086	0.1544	0	94.087	Gr0-d_1_4
46	35.23	0	23	12.77	23.14	0	0.5329	0	0.046	0.3221	95.041	Gr0-d_1_5
47	34.07	0	23.1	13.1	21.74	0	0.5832	0.0034	0.048	0	92.6446	Gr0-d_4_1

48	35.55	0	23.5	12.49	22.78	0	0.4404	0	0.04	0	94.8005	Gr0-d_4_2
49	36.21	0	23.19	12.21	23.46	0	0.5352	0.0008	0.0016	0.1084	95.7161	Gr0-d_4_3
50	35.52	0	22.95	12.76	22.81	0	0.6755	0	0.0748	0.3046	95.095	Gr0-d_4_4
51	34.43	0	22.68	13.16	22.07	0	0.7614	0.0082	0.063	0.4398	93.6125	Gr0-d_1_1
52	34.86	0	22.93	12.84	22.25	0	0.656	0.0019	0.1655	0.185	93.8885	Gr0-d_1_2
53	35.98	0	23.55	12.48	23.03	0	0.3282	0	0.0636	0	95.4318	Gr0-d_1_3
54	35.63	0	23.31	12.93	22.87	0	0.6363	0	0.0201	0.0604	95.4569	Gr0-d_1_4
55	35.11	0	23.59	12.05	23.1	0	0.3822	0.0045	0.1172	0	94.354	Gr0-d_1_5
56	35.09	0	23.69	12.72	22.25	0	0.2101	0	0.0266	0.1313	94.1181	HY17-5az_2_1
57	36.64	0	23.55	10.31	24.91	0	0.6648	0	0.0674	0.0978	96.2401	HY17-5az_2_2
58	35.56	0	22.92	11.08	23.59	0	1.0045	0.0004	0.0618	0.3896	94.6064	HY17-5az_2_3
59	36.36	0	24.03	8.46	26.65	0	0.2687	0.0161	0.016	0.3057	96.1066	HY17-5az_2_4
60	35.26	0	23.74	11.91	23.51	0	0.2054	0.0075	0.0255	0.0629	94.7214	HY17-5az_2_5
61	35.07	0	23.54	10.46	24.59	0	0.2523	0	0.0161	0.0538	93.9823	HY17-5az_2_6
62	34.82	0	23.55	11.92	22.82	0	0.1565	0	0.2118	0	93.4784	HY17-5az_3_1
63	35.51	0	23.14	10.65	24.88	0	0.5826	0	0.0061	0.0685	94.8372	HY17-5az_3_2
64	36.16	0	23.38	8.27	26.48	0	0.534	0	0.1058	0.2432	95.173	HY17-5az_3_3
65	35.61	0	23.64	9.06	25.91	0	0.2958	0	0.0273	0.1544	94.6976	HY17-5az_3_4
66	35.64	0	23.79	10.67	24.51	0	0.1829	0.0056	0.0419	0	94.8405	HY17-5az_3_5
67	35.53	0	23.74	11.51	23.5	0	0.0783	0.0142	0.3091	0.0527	94.7343	HY17-5az_3_6
68	35.1	0	23.41	12.74	22.8	0	0.4467	0	0.025	0.1036	94.6254	OBA19-03A_3_1
69	34.65	0	23.18	12.7	22.68	0	0.6092	0	0.0901	0.0417	93.9511	OBA19-03A_3_2
70	35.42	0	23.42	12.83	22.75	0	0.482	0	0.0569	0.0643	95.0233	OBA19-03A_3_3
71	35.8	0	23.6	13.38	22.6	0	0.4351	0	0.0986	0.1034	96.0172	OBA19-03A_3_4
72	34.95	0	23.02	13.84	21.67	0	0.6208	0	0.1671	0.2125	94.4805	OBA19-03A_3_5
73	35.96	0	22.64	13.52	22.34	0	0.6378	0.0116	0.063	0.6677	95.8401	OBA19-03A_3_6
74	34.67	0	23.04	13.88	21.2	0	0.6344	0	0.098	0.2002	93.7226	OBA19-03A_3_7
75	35.39	0	23.24	13.71	22.45	0	0.4756	0.0033	0.0948	0.1167	95.4805	OBA19-03A_3_8
76	34.5	0	22.55	14.16	21.69	0	0.4938	0.0037	0.0406	1.1029	94.5411	OBA19-03A_3_9
77	35.05	0	22.5	13.91	21.42	0	0.5361	0.0004	0.0142	1.21	94.6407	OBA19-03A_3_10
78	34.79	0	23.11	13.18	22.5	0	0.5245	0.0015	0.0434	0.1127	94.2622	OBA19-03A_3_11
79	34.99	0	22.61	13.95	21.54	0	0.508	0	0.0526	0.6797	94.3304	OBA19-03A_3_12
80	34.52	0	22.49	14.27	21.19	0	0.4781	0.009	0.0364	1.0773	94.0709	OBA19-03A_3_13
81	34.93	0	22.97	14.12	21.32	0	0.5109	0	0.0566	0.5066	94.4142	OBA19-03A_3_14
82	34.26	0	23.3	13.55	21.41	0	0.429	0	0.0532	0.1206	93.1229	OBA19-03A_3_15
83	35.87	0	22.93	13.65	21.97	0	0.4872	0	0.0989	0.268	95.2741	OBA19-03A_3_16
84	34.16	0	23.06	13.51	21.54	0	0.4541	0.0436	0.066	0.1774	93.0112	OBA19-03A_3_17
85	34.69	0	21.99	13.54	20.84	0	0.3766	0.0105	0.03	0.1572	91.6344	OBA19-03A_3_18
86	35.72	0	23.26	14.24	21.75	0	0.3614	0	0.0415	0.3908	95.7637	OBA19-03A_3_19
87	34.6	0	23.45	11.83	22.65	0	0.5	0.0022	0.1004	0.0994	93.2321	OBA19-03A_2_1
88	34.43	0	23.32	12.35	22.44	0	0.3934	0	0.0687	0.1256	93.1278	OBA19-03A_2_2
89	35.01	0	23.12	13.01	22.08	0	0.4109	0	0.0621	0.2238	93.9169	OBA19-03A_2_3
90	34.87	0	23.3	13.34	22.19	0	0.4481	0	0.0778	0.1171	94.343	OBA19-03A_2_4

91	34.8	0	22.76	13.63	21.56	0	0.5425	0.0127	0.0444	0.7631	94.1128	OBA19-03A_2_5
92	35.32	0	22.99	12.91	22.02	0	0.5964	0.0101	0.1087	0.1466	94.1019	OBA19-03A_2_6
93	34.1	0	22.99	13.75	21.52	0	0.5134	0.009	0.0439	0.4829	93.4093	OBA19-03A_2_7
94	34.07	0	22.61	14.07	20.91	0	0.5544	0.0015	0.0392	0.9998	93.255	OBA19-03A_2_8
95	34.5	0	23.06	13.4	21.92	0	0.3774	0.0101	0.0502	0.3231	93.6409	OBA19-03A_2_9
96	33.9	0	22.86	13.35	21.75	0	0.6064	0.0004	0.0546	0.1083	92.6298	OBA19-03A_2_10
97	34.02	0	22.61	14.02	21.31	0	0.5553	0	0.0569	0.6794	93.2516	OBA19-03A_1_1
98	34.68	0	23.2	13.17	21.78	0	0.5984	0	0.1112	0.2017	93.7413	OBA19-03A_1_2
99	35.27	0	23.07	13.4	21.67	0	0.6784	0	0.0975	0.1957	94.3817	OBA19-03A_1_3
100	34.52	0	22.94	13.28	21.83	0	0.5669	0	0.1288	0.2017	93.4675	OBA19-03A_1_4
101	34.29	0	22.68	13.67	20.89	0	0.5486	0.0015	0.0594	0.7077	92.8473	OBA19-03A_1_5
102	35.61	0	22.93	13.21	22.27	0	0.5147	0.0011	0.0658	0.4922	95.0939	OBA19-03A_1_6
103	34.25	0	22.76	13.42	21.37	0	0.4984	0	0.0706	0.55	92.9191	OBA19-03A_1_7
104	34.71	0	22.92	13.22	21.54	0	0.4229	0	0.063	0.3613	93.2373	OBA19-03A_1_8
105	34.38	0	23.32	12.32	22.62	0	0.4275	0	0.0549	0.0434	93.1659	OBA19-03A_1_9
106	33.68	0	22.71	13.76	21.21	0	0.5249	0	0.0614	0.7562	92.7026	OBA19-03A_1_10
107	35.3	0	22.8	13.18	21.84	0	0.5758	0.0022	0.0618	0.4505	94.2103	OBA19-03A_1_11
108	33.38	0	22.86	13.38	21.39	0	0.4431	0.0078	0.0552	0.4572	91.9734	OBA19-03A_1_12
109	33.44	0	23.01	12.85	21.79	0	0.571	0	0.101	0.2054	91.9674	OBA19-03A_1_13
110	33.12	0	22.85	13.05	21.72	0	0.5655	0	0.0344	0.58	91.92	OBA19-03A_1_14
111	33.54	0	22.66	13.73	21.15	0	0.3807	0	0.0456	1.1324	92.6388	ALB19-11B_A_1_1
112	33.01	0	23.65	13.46	21.55	0	0.1126	0	0.106	0	91.8887	ALB19-11B_A_1_2
113	34.06	0	23.9	13.56	21.73	0	0.081	0.0056	0.0671	0.0024	93.4062	ALB19-11B_A_1_3
114	33.67	0	23.49	13.4	21.63	0	0.114	0	0.0994	0	92.4035	ALB19-11B_A_1_4
115	33.68	0	22.94	13.36	21.74	0	0.2656	0.0007	0.2738	0.7457	93.0059	ALB19-11B_A_1_5
116	32.57	0	21.86	16.45	18.83	0	0.6464	0	0.0326	1.4	91.7891	ALB19-11B_A_1_6
117	33.71	0	23.55	13.65	21.2	0	0.1305	0.0045	0.1047	0	92.3498	ALB19-11B_A_1_7
118	33.5	0	23.52	13.76	21.45	0	0.092	0	0.0891	0	92.4112	ALB19-11B_A_1_8
119	33.48	0	23.76	13.78	21.11	0	0.1103	0.0063	0.1254	0.1082	92.4802	ALB19-11B_A_1_9
120	33.45	0	23.5	13.4	20.88	0	0.1174	0.0019	0.0717	0.2458	91.6668	ALB19-11B_A_1_10
121	33.62	0	23.64	14.05	20.9	0	0.1788	0.0056	0.0478	0.2906	92.7329	ALB19-11B_A_1_11
122	33.48	0	23.24	14.69	20.31	0	0.2635	0	0.0472	0.2709	92.3017	ALB19-11B_A_1_12
123	33.6	0	23.38	14.97	20.3	0	0.0965	0.0033	0.163	0.0894	92.6023	ALB19-11B_A_1_13
124	33.19	0	23.2	14.91	20.4	0	0.2237	0.0227	0.0476	0.2862	92.2803	ALB19-11B_A_1_14
125	33.63	0	23.51	13.41	21.09	0	0.1195	0	0.0993	0	91.8588	ALB19-11B_A_1_15
126	33.64	0	23.36	14.43	20.71	0	0.1834	0.0067	0.0698	0.1109	92.5109	ALB19-11B_A_1_16
127	33.84	0	23.39	14.89	20.9	0	0.1631	0.0156	0.0329	0.3027	93.5344	ALB19-11B_A_1_17
128	34.73	0	23.38	14.8	20.43	0	0.1219	0.0097	0.1682	0.3255	93.9654	ALB19-11B_A_1_18
129	34.28	0	23.49	14.77	20.49	0	0.1183	0	0.1406	0	93.2889	ALB19-11B_A_1_19
130	35.11	0	22.58	14.02	21.69	0	0.4164	0.0265	0.096	1.0985	95.0375	ALB19-11B_A_1_20
131	34.37	0	23.73	12.62	22.49	0	0.101	0	0.1899	0.0141	93.5151	ALB19-11B_A_1_21
132	35.11	0	23.09	13.25	21.6	0	0.5086	0	0.0442	0.1256	93.7284	OBA3_1_4_1
133	34.51	0	22.91	14.13	21.1	0	0.5592	0.0104	0	0.1839	93.4035	OBA3_1_4_2

134	35.39	0	23.16	13.24	22.32	0	0.4843	0.006	0.0754	0.2292	94.905	OBA3_1_4_3
135	35.14	0	22.6	13.48	22.11	0	0.6797	0	0.092	0.8083	94.9101	OBA3_1_4_4
136	35.06	0	23.55	13.53	21.98	0	0.3838	0	0.0486	0.25	94.8024	OBA3_1_4_5
137	34.39	0	23.31	13.57	22.23	0	0.4999	0	0.177	0.181	94.358	OBA3_1_4_6
138	34.91	0	22.6	14.05	21.91	0	0.9531	0	0.0388	0.2407	94.7027	OBA3_1_4_7
139	35.77	0	23.29	13.07	22.59	0	0.3798	0	0.1799	0.2496	95.5294	OBA3_1_2_1
140	34.46	0	23.02	13.32	22.15	0	0.4771	0	0.0627	0.3605	93.8503	OBA3_1_2_2
141	34.46	0	22.6	14.03	21.18	0	0.7213	0	0.0575	0.5434	93.5923	OBA3_1_2_3
142	34.32	0	23.01	13.76	21.7	0	0.5346	0.0119	0.0504	0.2976	93.6846	OBA3_1_2_4
143	34.68	0	23.11	13.78	22.08	0	0.503	0.0045	0.0022	0.3578	94.5176	OBA3_1_2_5
144	35.32	0	22.82	14.23	21.49	0	0.8314	0.006	0.0505	0.3226	95.0705	OBA3_1_2_6
145	34.6	0	23.33	13.23	22.1	0	0.4474	0	0.099	0.0536	93.8601	OBA3_1_2_7
146	35.1	0	23.25	13.57	22.14	0	0.3852	0	0.0712	0.4015	94.9179	OBA3_1_2_8
147	34.54	0	23.23	12.56	22.1	0	0.4158	0	0.1003	0.1091	93.0553	OBA3_1_2_9
148	33.95	0	22.94	13.76	20.61	0	0.6482	0	0.163	0.105	92.1763	OBA3_1_2_10
149	35.31	0	23	13.67	21.48	0	0.523	0	0.033	0.3493	94.3654	OBA3_1_2_11
150	35.26	0	22.69	14.09	20.96	0	0.5185	0	0.0684	0.5505	94.1374	OBA3_1_1_1
151	34.6	0	23.4	14.15	21.4	0	0.5485	0	0.0443	0.2075	94.3503	OBA3_1_1_2
152	34.3	0	22.64	13.59	21.11	0	0.5339	0	0.0282	0.546	92.7481	OBA3_1_1_3
153	34.96	0	22.91	13.8	21.44	0	0.5372	0.0004	0.056	0.5417	94.2454	OBA3_1_1_4
154	34.57	0	22.66	13.74	21.17	0	0.508	0	0.0508	0.7236	93.4225	OBA3_1_1_5
155	35.03	0	23.03	12.89	21.67	0	0.5463	0	0.1014	0.0792	93.347	OBA3_1_1_6
156	34.43	0	23.05	12.65	21.73	0	0.5094	0.0082	0.0376	0.022	92.4373	OBA3_1_1_7
157	35.01	0	22.69	13.9	21.49	0	0.5093	0	0.0695	0.6086	94.2775	OBA3_1_1_8
158	34.15	0	23.24	12.79	21.78	0	0.4885	0.0097	0.0505	0.2622	92.771	OBA3_1_1_9
159	35.05	0	23.14	13.02	21.66	0	0.6216	0	0.121	0.0375	93.6501	OBA3_1_1_10
Minimum	32.57	0	21.86	8.27	18.83	0	0.0429	0	0	0	91.2739	
Maximum	36.64	0	24.03	16.45	26.65	0	1.0045	0.0436	0.3091	1.4	96.6214	
Average	34.8475	0	23.1104	13.2468	21.9762	0	0.4008	0.0038	0.068	0.3337	93.9873	
Sigma	0.7975	0	0.4018	1.174	1.1381	0	0.2143	0.0067	0.0519	0.3274	1.124	
No. of data 159												

9 March 2020

No.	SiO2	MgO	CaO	FeO	Al2O3	F	MnO	Cl	TiO2	SrO	Total	Comment
1	68.42	0	0.0542	0	17.41	0	0	0.0021	0	0	85.8864	B31
2	32.77	0.0162	0.0385	0	0	0	70.17	0.0027	0.0189	0	103.0163	B32
3	32.43	0.0089	0.0315	0	0.0282	0	70.45	0	0	0	102.9485	B33
4	32.36	0	0.0364	0	0	0	70.27	0.0043	0.0119	0	102.6825	B34
5	46.1	0	19.79	0.123	34.64	0.0696	0	0	0.0226	0	100.7451	B35
6	47.18	0	19.98	0.1328	34.86	0	0	0	0.0104	0	102.1631	B36
7	37.18	0.0071	0.0439	42.96	19.81	0	0.002	0	0	0	100.0029	B37
8	37.44	0.0222	0.0054	42.4	19.92	0	0	0.0027	0.0119	0	99.8023	B38

9	41.75	49.84	0.1188	8.8	0	0	0.1399	0.0025	0.0223	0	100.6734	B39
10	41.9	50.01	0.0952	8.65	0.0419	0	0.0846	0.007	0.0083	0	100.797	B40
11	51.79	0	49.06	0.0428	0	0	0	0.044	0	0	100.9368	B41
12	52.01	0	48.83	0.0184	0.0323	0	0.0314	0.0023	0	0	100.9243	B42
13	46.91	0	19.55	0.091	38.05	0	0	0	0	0	104.6009	H81
14	40.83	0	23.59	8.87	26.02	0	0.2948	0.0108	0.0724	0.0031	99.6912	test
15	37.41	0	23.34	10.88	22.85	0	0.1592	0.0145	0.023	0	94.6768	test
16	38.92	0	23.45	9.28	24.46	0	0.2676	0.0045	0.1084	0.0613	96.5519	test
17	38.73	0	23.31	11.85	23.3	0	0.4955	0.0094	0.0435	0.1993	97.9378	test
18	40.02	0	23.78	8.7	25.97	0	0.2824	0	0.1402	0.0616	98.9543	P8_1_tail1
19	39.57	0	23.89	8.78	26.35	0	0.2524	0.0099	0.0871	0	98.9395	P8_1_tail2
20	39.57	0	23.91	8.71	26.53	0	0.2976	0	0.0858	0.1374	99.2409	P8_1_tail3
21	39.25	0	23.53	9.07	25.51	0	0.2669	0	0.0812	0.0634	97.7716	P8_1_tail4
22	37.89	0	22.75	12.11	22.53	0	0.6274	0	0.1302	0.1428	96.1805	P8_1_rim1
23	37.57	0	23.04	12.21	22.43	0	0.5072	0	0.0806	0.0691	95.907	P8_1_rim2
24	39.26	0	23.33	12.05	23.73	0	0.4939	0.0048	0.0475	0.2054	99.1216	P8_1_core1
25	37.94	0	23.08	12.1	23.53	0	0.4572	0.0132	0.0667	0.2632	97.4503	P8_1_core2
26	38.4	0	23.09	12.49	23.34	0	0.5175	0.007	0.0548	0.1168	98.0162	P8_1_core3
27	37.72	0	23.13	12.83	22.63	0	0.2724	0.0026	0.0373	0.1089	96.7313	P8_1_core4
28	40.18	0	23.89	8.62	26.92	0	0.3096	0	0.0953	0	100.0148	P8_1_rim3
29	39.12	0	23.62	9.18	26.56	0	0.3889	0.007	0.1224	0.161	99.1594	P8_1_rim4
30	39.5	0	23.63	8.96	26.7	0	0.3374	0.0062	0.1145	0	99.2482	P8_1_rim5
31	38.94	0	23.5	9	26.02	0	0.3149	0.0074	0.1255	0.1109	98.0188	P8_1_tail5
32	42.43	0	23.86	12.41	24.34	0	0.1608	0.0022	0.0171	0.1103	103.3303	P8_2_grain1
33	39.18	0	23.18	12.12	23.45	0	0.629	0	0.0423	0	98.6014	P8_2_grain2
34	38.52	0	23.71	11.75	22.15	0	0.1809	0	0.0188	0	96.3298	P8_2_grain3
35	38.52	0	22.71	12.6	21.97	0	0.752	0.0015	0.0424	0.2094	96.8054	P8_2_grain4
36	38.49	0	22.81	12.37	22.11	0	0.707	0	0.0482	0.1793	96.7146	P8_2_grain5
37	38.69	0	23.58	12.18	22.2	0	0.1268	0.0033	0.0093	0	96.7895	P8_2_grain6
38	39.17	0	23.57	10.32	23.9	0	0.2405	0.0073	0.1848	0	97.3927	P8_4_grain1
39	39.02	0	23.5	11.52	23.01	0	0.2159	0.0029	0.0328	0.0209	97.3225	P8_4_grain2
40	38.73	0	23.4	10.95	23.39	0	0.4644	0	0.1012	0	97.0356	P8_4_grain3
41	38.59	0	23.47	10.93	23.71	0	0.3092	0.008	0.0562	0.2356	97.3091	P8_4_grain4
42	39.05	0	23.84	9.12	24.96	0	0.31	0	0.0871	0.0914	97.4585	P8_4_grain5
43	38.91	0	23.67	8.81	25	0	0.3136	0.0033	0.0892	0.0352	96.8314	P8_4_grain6
44	40.94	0	23.6	9.01	26.73	0	0.2614	0.0051	0.0763	0	100.6227	P8_4_grain7
45	38.89	0	23.49	11.93	23.34	0	0.2758	0	0.0249	0	97.9508	P8_5_tail1
46	41.07	0	23.35	10.34	25.49	0	0.386	0.008	0.1067	0.0921	100.8427	P8_5_tail2
47	0.0133	0	56.37	0.0766	0.0395	0	0.0564	0.0047	0.0307	0.0662	56.6575	P8_5_tail3
48	40.46	0	23.73	8.92	26.19	0	0.3236	0	0.0928	0.0193	99.7358	P8_5_grain1
49	40.1	0	23.7	8.98	25.63	0	0.2905	0	0.0564	0	98.7569	P8_5_grain2
50	38.74	0	23.56	11.84	23.51	0	0.3523	0.0174	0	0	98.0198	P8_5_grain3
51	39.21	0	23.75	11.59	23.27	0	0.1944	0.0076	0.0568	0	98.0789	P8_5_grain4

52	38.66	0	23.49	11.1	21.17	0	0.3471	0	0.0731	0.2511	95.0913	P8_6_tail1
53	37.47	0	22.85	12.13	22.5	0	0.5767	0	0.0342	0.056	95.617	P8_6_tail2
54	38.27	0	23.43	11.93	22.53	0	0.3437	0	0.0389	0.07	96.6127	P8_6_tail3
55	38.67	0	23.68	9.64	25.48	0	0.3432	0.0044	0.0791	0.1851	98.0819	P8_6_tail4
56	38.55	0	23.19	11.9	23.46	0	0.4702	0	0.1494	0.1515	97.8711	P8_6_tail5
57	38.59	0	23.42	12.97	22.66	0	0.2664	0	0.0266	0.1577	98.0908	P8_6_tail6
58	38.13	0	23.7	11.48	23.42	0	0.1688	0.0076	0.0184	0.0408	96.9657	P8_6_core1
59	38.2	0	23.1	12.25	22.63	0	0.5847	0	0.041	0	96.8058	P8_6_core2
60	38.59	0	23.94	9.28	25.81	0	0.2596	0.0421	0.0636	0.0152	98.0005	P8_6_core3
61	37.86	0	23.4	11.83	22.73	0	0.3961	0.0072	0.02	0.0221	96.2655	P8_6_core4
62	38.65	0	23.89	11.15	23.68	0	0.1795	0.0166	0.3755	0	97.9417	P8_8_core1
63	38.27	0	22.96	10.95	24.45	0	0.6924	0.0065	0.1473	0.2549	97.7312	P8_8_core2
64	37.58	0	22.88	11.83	22.92	0	0.6349	0.012	0.0923	0.2937	96.243	P8_8_core3
65	40.14	0	23.87	8.63	26.68	0	0.2326	0.0007	0.0368	0	99.5901	P8_8_core4
66	38.13	0	23.15	12.65	23.06	0	0.4807	0.0029	0.0285	0	97.5022	P8_8_core5
67	38.31	0	23.47	11.25	23.67	0	0.3912	0.0025	0.0485	0.0656	97.2078	P8_8_core6
68	39.38	0	23.8	9.25	25.78	0	0.2176	0.0065	0.0694	0.2891	98.7926	P8_8_tail1
69	39.73	0	23.89	8.66	26.65	0	0.3045	0.0127	0.0976	0.0516	99.3965	P8_8_tail2
70	38.32	0	22.71	9.91	25.1	0	0.8428	0.0051	0.1445	0.1479	97.1804	P8_26_grain1
71	38.16	0	23.69	12.98	21.93	0	0.1843	0	0	0	96.9444	P8_26_grain2
72	38.35	0	23.69	8.84	26.24	0	0.3268	0	0.0781	0	97.525	P8_26_tail1
73	38.8	0	23.83	8.64	26.06	0	0.2564	0.0054	0.0405	0	97.6323	P8_26_tail2
74	38.5	6.92	0	23.26	17.08	0	0.5527	0.0145	1.2262	0	87.5535	P8_16_grain1
75	39.97	0	23.64	10.53	25.76	0	0.2694	0.0076	0.0384	0.1312	100.3465	P8_16_grain2
76	39.42	0	23.13	12.34	23.98	0	0.3618	0.0025	0.0386	0.2321	99.5051	P8_16_grain3
77	38.94	0	23.62	10.45	25.16	0	0.332	0.0043	0.0585	0.0156	98.5805	P8_16_grain4
78	40.12	0	23.35	9.03	26.49	0	0.4486	0.0004	0.1289	0.0754	99.6433	P8_19_1
79	38.09	0	23.27	10.71	24.06	0	0.3258	0.0025	0.0529	0.1933	96.7046	P8_19_2
80	39.86	0	23.38	10.72	25	0	0.3282	0.0025	0.0561	0.2189	99.5658	P8_19_3
81	38.86	0	23.43	12.17	23.1	0	0.2384	0	0.0325	0.0065	97.8375	P8_22_1
82	38.08	0	22.93	12.73	22.88	0	0.5839	0	0.032	0.2338	97.4698	P8_22_2
83	41.16	0	23.73	8.91	27.66	0	0.1335	0	0.0336	0	101.6271	P9c_1A_1
84	40.74	0	23.88	8.83	27.12	0	0.1663	0.0044	0.0582	0.0707	100.8696	P9c_1A_2
85	40.05	0	23.65	11.29	24.39	0	0.3776	0.0004	0.034	0	99.792	P9c_1A_3
86	39.37	0	23.63	13.15	22.61	0	0.0868	0.0094	0.0302	0	98.8865	P9c_1B1
87	41.3	0	23.51	11.52	25.33	0	0.3622	0.0094	0	0	102.0315	P9c_1B2
88	0.1132	0	55.69	0.1113	0.063	0	0.03	0	0	0.1361	56.1437	P9c_2_1
89	40.85	0	23.77	9.92	26.2	0	0.0808	0	0.0359	0.1275	100.9841	P9c_2_2
90	40.82	0	23.08	12.33	23.68	0	0.3778	0.0015	0.0233	0.1933	100.5059	P9c_7_1
91	41.01	0	24.16	4.21	30.88	0	0.1407	0	0.1058	0	100.5064	P9d_1_1
92	67.91	0.0025	0	0.0507	17.77	0	0	0.0321	0	0	85.7654	P9d_1_1
93	40.64	0	23.25	10.83	25.28	0	0.2985	0	0.0647	0.1883	100.5514	P9d_2_1
94	42.55	0	23.84	11.33	24.56	0	0.1852	0	0.0586	0	102.5238	P9d_3_1

95	40.02	0	23.25	11.71	24.57	0	0.4967	0	0.0619	0.0134	100.1219	P9d_3_2
96	40.92	0	23.29	12.4	23.65	0	0.4809	0	0.1028	0	100.8437	P9d_3_3
97	39.65	0	22.67	11.96	23.82	0	0.8089	0	0.0294	0.5311	99.4695	P9d_4_1
98	27.06	10.75	0.0954	30.85	17.3	0	1.0575	0.0135	0.0176	0	87.1441	P9d_6_1
99	39.37	0	23.38	10.13	25.29	0	0.2085	0	0.0628	0.4778	98.9192	P9d_6_2
100	39.43	0	23.25	11.08	24.45	0	0.2804	0.0094	0.03	0.3216	98.8515	P9d_6_3
101	39.36	0	22.59	11.97	23.58	0	0.8296	0.008	0	0.5807	98.9184	P9d_14_1
102	42.26	0	23.96	10.24	26.02	0	0.0991	0.008	0.0555	0.0314	102.6739	P9d_14_2
103	33.16	0	28.44	1.5	3.17	0	0.1124	0	31.33	0	97.7124	P9d_15_1
104	32.86	0	28.52	1.52	3.31	0	0.1196	0.0007	31	0	97.3304	P9d_15_2
105	39.28	7.91	0.0202	21.67	16.64	0	0.6061	0.0326	1.4169	0	87.5759	P9d_12_B_1
106	40.74	0	23.2	13.65	22.65	0	0.3027	0	0.0396	0.1856	100.7678	P9d_12_C_2
107	40.16	0	23.72	14.32	22.24	0	0.088	0	0.0142	0	100.5421	P9d_12_D_4
108	40.23	0	24.09	13.55	22.5	0	0.1723	0.0014	0.0081	0.0298	100.5816	P9d_12_D_5
109	26.38	9.54	0.0242	31.55	21.15	0	1.1097	0.0055	0.029	0	89.7885	P9d_9_C_1
110	43.35	0	23.59	9.82	26.92	0	0.2892	0	0.0737	0.1065	104.1493	P9d_9_A_1
111	32.16	0	28.98	1.6	2.87	0	0.1507	0	32.12	0	97.8808	P9d_9_A_2
Minimum	0.0133	0	0	0	0	0	0	0	0	0	56.1436	
Maximum	68.42	50.01	56.37	42.96	38.05	0.0696	70.45	0.044	32.12	0.5807	104.601	
Average	39.003	1.2165	21.8053	10.5393	21.7329	0.0006	2.2129	0.0049	0.9279	0.0803	97.5237	
Sigma	7.3577	6.8343	9.7131	6.757	7.9098	0.0066	11.4009	0.0078	5.1193	0.1156	6.4997	
No. of data 111												

10 March 2020

No.	SiO2	MgO	CaO	FeO	Al2O3	MnO	SrO	TiO2	Cl	Total	Comment
1	32.25	0	29.2	1.46	3.54	0.1392	0	33.63	0.0075	100.2266	
2	42.77	0	23.63	9.65	26.28	0.2466	0	0.0475	0.0034	102.6274	
3	38.82	0	23.71	10.84	23.61	0.0647	0	0.1106	0	97.1553	
4	38.14	0	23.57	9.21	25.75	0.4151	0.0653	0.1441	0.0119	97.3064	P6b_1_1
5	35.62	7.45	0.0466	24.08	16.2	0.587	0	0.863	0.0301	84.8768	P6b_1_2
6	39.79	0	23.51	9.11	26.67	0.403	0	0.1081	0	99.5912	P6b_1_3
7	38.4	0	23.58	9.92	25.29	0.4194	0.0274	0.1435	0.0007	97.7811	P6b_2_1
8	38.51	0	23.54	9.85	25.4	0.3592	0	0.0424	0.0056	97.7073	P6b_2_2
9	38.78	0	23.47	8.43	27.1	0.4088	0	0.0705	0.0082	98.2676	P6b_2_3
10	40.52	0	23.25	8.22	27.23	0.3583	0.0197	0.1104	0	99.7085	P6b_7_tail1
11	37.9	0	23.3	8.75	26.51	0.3487	0.0564	0.1132	0	96.9783	P6b_7_tail2
12	38.31	0	23.66	10.13	25.22	0.3189	0.0267	0.0555	0	97.7212	P6b_7_tail3
13	38.28	0	23.44	10.17	24.63	0.3311	0.0688	0.0514	0	96.9714	P6b_7_tail4
14	39.17	0	23.72	8.79	26.94	0.2421	0	0	0	98.8622	P6b_7_rim1
15	38.3	0	22.57	10.88	24.74	0.7695	0.1409	0.0984	0	97.4988	P6b_7_rim2
16	38.65	0	23.22	11.53	23.98	0.3803	0	0.0159	0	97.7763	P6b_7_rim3
17	38.03	0	23.24	10.23	24.93	0.4494	0.2462	0.1201	0	97.2458	P6b_7_rim4

18	38.7	0	23.83	7.39	27.75	0.2129	0.1175	0.0556	0.0112	98.0673	P6b_7_core1
19	38.95	0	23.95	8.67	26.49	0.2342	0	0.0321	0	98.3263	P6b_7_core2
20	38.78	0	23.63	9.33	26	0.3379	0.0752	0.0429	0	98.1961	P6b_6_tail1
21	40.22	0	23.52	8.28	27.67	0.3022	0.0221	0.0859	0.0116	100.1117	P6b_6_tail2
22	38.28	0	23.68	9.28	25.84	0.2989	0.088	0.0942	0.0022	97.5633	P6b_6_tail3
23	38.96	0	23.39	8.94	26.66	0.3127	0.0855	0.094	0.006	98.4482	P6b_6_tail4
24	39.88	0	23.47	10.69	25.71	0.307	0.247	0.0449	0	100.3488	P6b_6_tail5
25	38.73	0	23.01	12.39	23.84	0.4202	0.3155	0.1066	0.0045	98.8168	P6b_6_tail6
26	38.34	0	22.93	11.75	24.85	0.4719	0.1018	0.0074	0.0007	98.4519	P6b_6_rim1
27	38.46	0	23.42	11.94	23.88	0.095	0.0512	0.0371	0	97.8834	P6b_6_rim2
28	40.22	0	23.81	8.97	27.22	0.102	0	0.2041	0.0105	100.5365	P6b_6_rim3
29	38.45	0	23.22	10.81	24.62	0.2911	0.3068	0.0754	0	97.7734	P6b_6_core1
30	37.93	0	23.01	11.88	23.94	0.5394	0.1554	0.1155	0	97.5704	P6b_6_core2
31	38.25	0	23.55	10.38	24.92	0.2131	0.1218	0.1171	0.0119	97.564	P6b_5_corona1
32	38.23	0	23.69	10.22	24.69	0.2893	0.1972	0.0831	0.0119	97.4116	P6b_5_corona2
33	40.94	0	23.08	8.66	27.56	0.3423	0.0293	0.0786	0	100.6901	P6b_5_1
34	39.09	0	23.57	9.05	26.51	0.2647	0.0574	0.0689	0.0067	98.6178	P6b_5_2
35	38.41	0	23.28	10.54	25.03	0.272	0.0465	0.0322	0	97.6108	P6b_5_3
36	38.94	0	23.2	10.19	25.97	0.4075	0.0104	0.0591	0	98.7771	P6b_4_1
37	38.49	0	23.7	10.33	25.03	0.2294	0	0.0557	0.0067	97.8419	P6b_4_2
38	38.42	0	23.26	10.89	25.4	0.442	0.0306	0.0143	0.0938	98.5508	P6b_4_3
39	38.75	0	23.58	9.31	26.42	0.2621	0.0909	0.0662	0	98.4792	P6b_4_4
40	39.43	0	23.71	9.62	27.3	0.2495	0.0662	0.0295	0	100.4051	P6b_3_1
41	38.83	0	23.54	11.97	24.24	0.1538	0.0069	0.0072	0	98.748	P6b_3_2
42	38.36	0	23.49	9.28	26.41	0.2824	0.0114	0.0464	0	97.8802	P6b_9_tail1
43	39.16	0	23.48	9.18	26.99	0.3976	0	0.105	0.0034	99.3161	P6b_9_tail2
44	39.34	0	23.72	10.98	24.53	0.158	0.0408	0.0572	0.0048	98.8308	P6b_9_tail3
45	38.57	0	23.29	12.29	23.33	0.4393	0.0809	0.0239	0	98.0242	P6b_9_tail4
46	39.33	0	23.38	11.31	24.8	0.3611	0.0795	0.0655	0.0078	99.3339	P6b_9_1
47	39.16	0	22.74	10.57	25.07	0.7552	0.235	0.1725	0	98.7028	P6b_9_2
48	39.23	0	22.67	10.53	25.2	0.808	0.1494	0.1321	0.0015	98.7211	P6b_9_3
49	31.7	0	25.73	2.91	3.06	0.3774	0	30.3	0.006	94.0835	Gr0a_4_1
50	31.59	0	26.86	2.47	3.97	0.2405	0	31.03	0	96.1606	Gr0a_4_2
51	31.65	0	27.06	2.79	3.28	0.2897	0	31.29	0.0032	96.363	Gr0a_4_3
52	26.73	10.5	0.0957	31.64	18.34	1.35	0	0.0802	0.0079	88.7438	Gr0a_3_1
53	7.99	1.98	38.29	9.1	4.44	0.3913	0.0279	0.0671	0.0051	62.2915	Gr0a_3_2
54	38.53	0	23.54	12.02	23.63	0.2181	0.0329	0.0604	0	98.0314	Gr0a_2_1
55	30.92	0	26.77	2.47	2.87	0.3	0	31.02	0.0081	94.3582	Gr0a_2_2
56	40.53	0	23.17	12.12	24.88	0.4238	0.1585	0.0367	0	101.3189	Gr0a_2_3
57	39.27	0	23.56	12.28	23.42	0.1333	0.0094	0.0716	0.0067	98.7511	Gr0a_5_1
58	37.57	0	23.62	12.41	22.65	0.2194	0.023	0.0194	0.0093	96.5212	Gr0a_5_2
59	38.78	0	23.28	12.61	22.88	0.3288	0	0.022	0	97.9008	Gr0a_5_3
60	39.98	0	23.4	11.93	23.93	0.2122	0.001	0.1413	0.0138	99.6083	Gr0a_5_4

61	38.64	0	22.74	11.13	24.29	1.0227	0	0.0724	0	97.8951	Gr0a_5_tail1
62	41.18	0	23.73	9.02	26.97	0.3896	0	0.046	0.0071	101.3427	Gr0a_5_tail2
63	36.16	0	25.14	8.09	17.32	0.23	0.1033	11.96	0.0102	99.0136	Gr0a_6_1
64	39.03	9.02	0.0153	20.76	16.39	0.7452	0	1.439	0.0153	87.4149	Gr0a_6_2
65	39.05	0	23.47	12.24	23.57	0.3385	0	0.0444	0.0078	98.7207	Gr0a_6_3
66	39.28	0	23.44	11.13	24.1	0.3582	0	0.1268	0.0045	98.4396	Gr0a_7_1
67	39.86	0	23.87	10.31	25.29	0.163	0	0.1065	0	99.5996	Gr0a_7_2
68	39.41	0	23.53	12.27	23.66	0.3785	0	0.0749	0.0141	99.3376	Gr0a_7_3
69	40.51	10.76	0.002	19.61	16.21	0.6772	0	1.4412	0.0252	89.2356	Gr0a_9_1
70	39.11	0	23.39	12.53	23.5	0.1342	0	0.0449	0.0033	98.7125	Gr0a_9_2
71	39.1	10.49	0.0085	19.54	16.02	0.6721	0	1.3807	0.0099	87.2212	Gr0a_9_3
72	38.38	0	23.03	11.3	24.28	0.557	0.0265	0.0536	0.0004	97.6275	Gr0a_10_1
73	40.7	0	23.29	10.76	25.54	0.5117	0	0.045	0	100.8466	Gr0a_10_2
74	39.89	0	23.78	11.72	24.97	0.0941	0	0.0216	0.0019	100.4775	Gr0a_10_3
75	39.23	0	23.31	11.57	23.58	0.2861	0.0812	0.0724	0	98.1298	Gr0a_11_1
76	38.48	0	23.33	12.41	23.03	0.042	0.2016	0	0.0004	97.494	Gr0a_11_2
77	38.37	0	23.46	11.41	23.74	0.1138	0	0.0285	0	97.1224	Gr0a_11_3
78	39.5	0	23.78	9.56	25.82	0.2793	0.135	0.0136	0.0022	99.0901	Gr0c_1
79	38.39	0	23.23	11.8	23.41	0.4454	0.0762	0.0171	0	97.3688	Gr0c_2
80	37.53	7.51	0.0265	24.26	16.17	0.677	0	0.7008	0.0118	86.8862	Gr0c_3
81	39.16	0	23.71	11.32	24.49	0.0903	0.208	0.0533	0.0074	99.0391	Gr0c_4_1
82	38.31	0	23.99	11.02	23.59	0.0421	0.01	0.0004	0	96.9626	Gr0c_4_2
83	39.21	0	23.37	10.51	25.12	0.5854	0.0662	0.0371	0	98.8988	Gr0c_5_1
84	38.49	0	23.28	11.79	23.39	0.4883	0.1596	0.0969	0	97.6949	Gr0c_5_2
85	37.96	0	23.53	12.3	24.34	0.2717	0.0544	0.0375	0.0093	98.503	Gr0c_5_3
86	38.95	0	23.35	10.24	25.77	0.5508	0.1094	0.0213	0.0011	98.9926	Gr0c_5_4
87	38.01	0	23.83	11.23	24.07	0.1712	0.0537	0.1089	0	97.4739	Gr0c_6_1
88	39.51	0	23.26	8.49	26.84	0.5678	0.344	0.0496	0.009	99.0704	Gr0c_6_2
89	39.81	0	23.27	10.08	25.7	0.3643	0.6889	0.0219	0	99.9352	Gr0c_6_3
90	38.37	0	23.5	9.49	26.3	0.2496	0.3449	0.022	0.0179	98.2945	Gr0c_6_4
91	40.6	0	24.13	9.41	27.35	0.1694	0.0689	0.0235	0	101.7517	Gr0c_6_5
92	38.81	0	23.81	12.94	23.11	0.0715	0	0.0035	0.0126	98.7577	Gr0c_7_1
93	37.98	0	23.65	10.46	25.15	0.3465	0.0463	0.0034	0	97.6363	Gr0c_7_2
94	38.27	0	23.3	11.95	23.97	0.3017	0.1853	0.0353	0.0569	98.0693	Gr0c_7_3
95	38.54	0	23.29	12.14	24.05	0.441	0.2378	0.0652	0	98.7641	Gr0c_11_1
96	39.3	0	23.79	11.07	24.5	0.0838	0.1407	0.183	0.0056	99.0732	Gr0c_11_2
97	38.6	0	22.8	11.99	24.02	0.4403	0.0311	0.2061	0	98.0876	Gr0c_11_3
98	38.36	0	23.07	13.02	22.43	0.4776	0.1409	0.0602	0	97.5588	Gr0c_10_1
99	37.22	7.16	0.0465	23.83	15.78	0.7673	0	1.3858	0.011	86.2007	Gr0c_10_2
100	39.58	0	24.05	10.7	25.49	0.0114	0.0127	0.1268	0.0108	99.9818	Gr0c_10_3
101	38.8	0	23.68	10.2	25.5	0.354	0.0405	0.0266	0	98.6012	Gr0c_13_1
102	38.26	0	23.22	11.29	23.77	0.1769	0.1569	0.0308	0.0033	96.908	Gr0c_13_2
103	39.62	0	24.16	10.08	25.7	0.2076	0	0.0916	0	99.8593	Gr0c_13_3

Minimum	7.99	0	0.002	1.46	2.87	0.0114	0	0	0	62.2914
Maximum	42.77	10.76	38.29	31.64	27.75	1.35	0.6889	33.63	0.0938	102.6275
Average	38.1343	0.6298	22.1989	11.0543	23.1411	0.3527	0.0723	1.7714	0.0056	97.3604
Sigma	3.7031	2.3087	6.2485	4.109	5.55	0.2115	0.1051	6.8477	0.0117	4.7027
No. of data 103										

15 January 2021

No.	Al2O3	SiO2	CaO	FeO	MgO	MnO	SrO	TiO2	Cl	Total	Comment
1	23.39	37.76	23.07	12.99	0	0.4849	0.1172	0.0433	0.0056	97.8611	test-1
2	24.08	38.03	23.34	12.24	0	0.3937	0.1146	0.0271	0	98.2254	test-2
3	23.59	37.83	23.07	12.36	0	0.4022	0	0.0514	0.0011	97.3048	Map1_Spots1
4	23.56	37.28	23.1	12.37	0	0.567	0.3121	0.0634	0	97.2526	Map1_Spots2
5	24.49	37.71	23.43	11.4	0	0.3888	0	0.131	0.01	97.5599	Map1_Spots3
6	23.4	37.58	23.04	12.62	0	0.5013	0.0381	0.1176	0.01	97.3071	Map1_Spots4
7	23.11	37.22	22.97	13.06	0	0.5094	0.1014	0.0371	0	97.008	Map1_Spots5
8	23.78	37.96	22.75	12.58	0	0.5792	0.0393	0.112	0.0108	97.8114	Map1_Spots6
9	23.3	37.58	23.17	12.75	0	0.5306	0.1469	0.0176	0.0011	97.4963	Map1_Spots7
10	23.64	37.99	23.16	12.28	0	0.4772	0	0.1616	0.0152	97.7241	Map1_Spots8
11	23.55	37.76	23.05	12.27	0	0.4343	0.0098	0.0433	0.003	97.1205	Map1_Spots9
12	23.18	37.18	23.15	12.83	0	0.4642	0	0.0916	0.0041	96.9	Map1_Spots10
13	23.1	37.7	23.09	12.48	0	0.4168	0.1941	0.0254	0	97.0063	Map1_Spots11
14	23.14	37.69	22.99	12.88	0	0.4254	0.0958	0.0192	0	97.2405	Map1_Spots12
15	23.49	37.73	22.96	12.92	0	0.495	0.1566	0.0689	0	97.8206	Map1_Spots13
16	23.05	37.42	23.1	12.86	0	0.4826	0	0.0403	0	96.9529	Map1_Spots14
17	22.84	37.79	22.88	12.36	0	0.4907	0.1713	0.0355	0	96.5676	Map1_Spots15
18	22.97	37.98	22.97	12.81	0	0.497	0.0527	0.0546	0.007	97.3414	Map1_Spots16
19	22.23	37.66	22.88	13.33	0	0.4977	0.1344	0.0282	0	96.7604	Map2_spot1
20	23.01	37.74	23.11	12.65	0	0.5705	0.0487	0.1013	0	97.2306	Map2_spot2
21	22.74	37.78	22.85	13.04	0	0.5586	0	0.1016	0	97.0703	Map2_spot3
22	23.23	37.57	22.99	12.57	0	0.6048	0.0671	0.0617	0	97.0937	Map2_spot4
23	23.24	38.11	22.36	12.8	0	0.4804	0.0336	0.0761	0.0063	97.1065	Map2_spot5
24	23.15	37.83	22.35	12.66	0	0.5151	0	0.0424	0	96.5476	Map2_spot6
25	22.89	37.6	22.28	13.11	0	0.4803	0.0851	0.0892	0	96.5347	Map2_spot7
26	22.6	37.55	22	13.03	0	0.543	0.1004	0.0478	0.1397	96.011	Map2_spot8
27	23.08	37.98	22.42	12.63	0	0.3661	0.2256	0.0318	0.0022	96.7357	Map2_spot9
28	23.76	38.31	22.33	12.45	0	0.4242	0.0846	0.0592	0.0242	97.4423	Map2_spot10
29	22.78	38.32	22.1	13.01	0	0.4931	0.0025	0.0482	0	96.7539	Map2_spot11
30	23.9	38.03	22.43	12.24	0	0.4257	0.1138	0.0645	0.0022	97.2062	Map2_spot12
31	23.65	38.49	22.32	12.32	0	0.4958	0.0372	0.1052	0.0004	97.4186	Map2_spot13
32	22.56	37.84	22.23	13.3	0	0.5725	0.1082	0.099	0.0134	96.7232	Map2_spot14
33	23.23	38.07	22.56	12.97	0	0.4997	0.0453	0.1327	0.0082	97.516	Map2_spot15
34	23.64	38.3	21.88	12.41	0	0.7469	0.2836	0.0723	0.006	97.3389	Map3_Spot1

35	23.47	37.97	22.22	12.41	0	0.6618	0.3332	0.0748	0.0145	97.1544	Map3_Spot2
36	23.02	37.66	22.09	12.66	0	0.345	1.1047	0	0.0127	96.8925	Map3_Spot3
37	25.32	38.46	23.26	10.49	0	0.0847	0.1503	0.0118	0.0015	97.7784	Map3_Spot4
38	22.38	37.71	22.42	13.49	0	0.0864	0.0499	0.0388	0	96.1751	Map3_Spot5
39	25.92	38.25	22.83	9.76	0	0.1401	0.1074	0.0142	0	97.0218	Map3_Spot6
40	24.6	38.28	22.82	11.45	0	0.2286	0.0932	0.0262	0.0145	97.5126	Map3_Spot7
41	25.5	38.24	22.94	10.31	0	0.1713	0	0.0348	0.0011	97.1973	Map3_Spot8
42	24.95	38.48	22.72	10.68	0	0.4675	0.0039	0.0245	0.0075	97.3335	Map3_Spot9
43	24.75	37.28	23.63	10.74	0	0.1721	0	0.0035	0.0112	96.5868	Map3_Spot10
44	25.37	36.81	23.88	9.88	0	0.1583	0	0.0784	0.0149	96.1917	Map3_Spot11
45	22.08	36.34	23.57	13.83	0	0.0885	0	0.0508	0	95.9594	Map3_Spot12
46	23.63	36.64	23.33	11.81	0	0.1423	0.0413	0.0039	0.0093	95.6068	Map3_Spot13
47	21.91	37.36	23.28	13.98	0	0.1733	0.0318	0.0578	0	96.793	Map3_Spot14
48	24.67	36.46	22.62	10.8	0	0.9803	0.2623	0.0566	0.0108	95.8601	Map3_Spot15
Minimum	21.91	36.34	21.88	9.76	0	0.0847	0	0	0	95.6068	
Maximum	25.92	38.49	23.88	13.98	0	0.9803	1.1047	0.1616	0.1397	98.2254	
Average	23.5192	37.7356	22.8331	12.3515	0	0.4316	0.1062	0.0579	0.0077	97.0427	
Sigma	0.8955	0.4884	0.4566	0.9648	0	0.18	0.1713	0.0371	0.0203	0.5587	
No. of data 48											

30 April 2021

No.	Al2O3	SiO2	CaO	FeO	MgO	MnO	SrO	TiO2	Cl	Total	Comment
1	24.48	36.44	23.69	11.16	0	0.1589	0.0526	0.0305	0.0142	96.0263	Map1_Ep1
2	26.22	36.91	23.79	9.05	0	0.2375	0.0945	0.0448	0.0179	96.3648	Map1_Ep2
3	25.05	37.05	23.37	10.46	0	0.445	0.172	0.0997	0.0045	96.6513	Map1_Ep3
4	23.72	36.13	23.49	12.21	0	0.3139	0.1362	0.0383	0.0045	96.0429	Map1_Ep4
5	24.11	36.56	22.75	12.05	0	0.6836	0.1355	0.0739	0.006	96.369	Map1_Ep5
6	23.84	36.49	23.5	11.95	0	0.167	0.0866	0	0.013	96.0467	Map1_Ep6
7	24.91	36.32	23.4	10.9	0	0.3958	0.0797	0.0725	0	96.078	Map1_Ep7
8	26.02	36.89	23.83	9.26	0	0.2787	0	0.0582	0	96.337	Map1_Ep8
9	23.6	36.41	22.94	12.43	0	0.5572	0.3237	0.0663	0	96.3273	Map1_Ep9
10	25.29	36.17	23.85	10.72	0	0.1846	0	0.0608	0	96.2755	Map1_Ep10
11	25.45	36.44	23.21	9.2	0	0.2929	0.09	0.0825	0	94.7654	Map1_Ep11
12	25.7	36.07	23.54	9.49	0	0.3636	0.0699	0.0233	0.0161	95.2729	Map1_Ep12
13	23.69	36.72	23.25	12.35	0	0.452	0	0.0075	0	96.4696	Map1_Ep13
14	25.27	36.69	23.67	9.75	0	0.1847	0.0491	0.2704	0.0064	95.8907	Map1_Ep14
15	26.04	36.47	23.62	9.42	0	0.3633	0.1309	0.0423	0.0026	96.0891	Map1_Ep15
16	24.85	35.75	23.33	10.78	0	0.4076	0.2057	0.0376	0	95.361	Map1_Ep16
17	24.64	36.12	23.15	11.11	0	0.3894	0	0.0851	0	95.4945	Map1_Ep17

18	26.16	35.75	23.99	9.67	0	0.2433	0.0251	0.0318	0.0075	95.8778	Map1_Ep18
19	24.2	35.75	23.64	11.9	0	0.2479	0	0.1142	0	95.8521	Map1_Ep19
20	24.51	36.1	23.67	11.05	0	0.4087	0.0047	0.2348	0.0149	95.9932	Map1_Ep20
21	23.69	36.19	22.4	11.4	0	1.0863	0	0.0932	0.0168	94.8764	Map2_Ep1
22	23.58	36.32	23.55	11.42	0	0.2471	0.0175	0.0262	0.006	95.1668	Map2_Ep2
23	24.04	36.4	23.71	11.4	0	0.1857	0	0.0458	0.0034	95.785	Map2_Ep3
24	23.64	36.03	23.17	11.97	0	0.3769	0	0.046	0.0037	95.2366	Map2_Ep4
25	23.78	36.43	23.38	11.86	0	0.3459	0	0.031	0	95.827	Map2_Ep5
26	23.59	36.65	22.97	11.46	0	0.4669	0	0.0422	0	95.1792	Map2_Ep6
27	24.13	35.65	23.72	11.82	0	0.085	0.0074	0.0343	0	95.4468	Map2_Ep7
28	24.35	35.93	22.96	11.21	0	0.9139	0.0039	0.0464	0.0093	95.4236	Map2_Ep8
29	23.62	35.64	23.08	11.82	0	0.5831	0.0212	0.0975	0.0078	94.8697	Map2_Ep9
30	23.64	36.52	23.67	12.03	0	0.2058	0.0646	0.0374	0.0134	96.1813	Map2_Ep10
31	24.03	36.44	23.19	11.41	0	0.5596	0.0375	0.0181	0.003	95.6883	Map2_Ep11
32	24.77	36.39	22.2	10.69	0	1.57	0.0003	0.1516	0.0071	95.7791	Map2_Ep12
33	24.7	35.71	22.19	10.79	0	1.4	0.1058	0.1386	0.0022	95.0367	Map2_Ep13
34	26.41	36.5	23.35	8.98	0	0.6077	0	0.0621	0.0019	95.9118	Map2_Ep14
35	23.92	36.03	23.56	11.6	0	0.1525	0.0103	0.0391	0.0022	95.3141	Map2_Ep15
36	23.85	36.16	23.22	11.72	0	0.6936	0	0.0723	0.0112	95.7272	Map2_Ep16
37	24.17	36.15	23.66	11.44	0	0.194	0	0.0285	0.003	95.6456	Map2_Ep17
38	23.95	36.21	22.96	11.3	0	0.5972	0.0847	0.0164	0.0011	95.1195	Map2_Ep18
39	23.6	36.24	23.38	11.24	0	0.1342	0	0.0339	0	94.6282	Map2_Ep19
40	23.02	36.01	23.16	12.08	0	0.2758	0	0.0763	0.0041	94.6263	Map2_Ep20
41	24.13	36.41	22.83	11.63	0	0.3771	0.5162	0.0533	0.0041	95.9507	Map3_Spot1
42	23.95	36.55	23.27	11.64	0	0.4419	0	0.1362	0	95.9882	Map3_Spot2
43	24.21	36.13	22.45	11.45	0	0.5529	0.8748	0.0732	0	95.741	Map3_Spot3
44	23.97	36.68	22.72	11.52	0	0.4558	0.6633	0.0922	0.003	96.1044	Map3_Spot4
45	24.07	36.43	23.14	11.49	0	0.4212	0.4385	0.0921	0	96.0819	Map3_Spot5
46	23.54	36.48	22.7	11.89	0	0.3691	0.7342	0.1066	0	95.82	Map3_Spot6
47	23.68	36.55	23.17	11.83	0	0.4305	0.2573	0.1357	0	96.0536	Map3_Spot7
48	23.54	36.52	22.81	12.38	0	0.308	0.8573	0.0613	0.0082	96.4849	Map3_Spot8
49	24.22	36.3	23.38	11.27	0	0.2928	0.1992	0.1267	0	95.7888	Map3_Spot9
50	23.93	36.24	23.2	11.56	0	0.4207	0.1038	0.1193	0	95.5739	Map3_Spot10
51	24.21	36.36	22.87	11.35	0	0.4451	0.6231	0.0829	0.0004	95.9416	Map3_Spot11
52	24.03	36.41	22.76	11.22	0	0.5033	0.6531	0.0778	0	95.6543	Map3_Spot12
53	24.48	36.43	23.29	11.46	0	0.3525	0.2723	0.1008	0.0056	96.3913	Map3_Spot13
54	23.81	36.36	23.11	11.84	0	0.448	0.1733	0.1073	0.0037	95.8523	Map3_Spot14
55	24.26	36.54	23.04	11.57	0	0.4406	0.5374	0.0521	0.0101	96.4503	Map3_Spot15
56	24.25	36.55	23.49	11.54	0	0.3543	0.1559	0.1199	0.0067	96.4669	Map3_Spot16
57	24.28	36.31	23.09	11.68	0	0.3273	0.3084	0.0896	0.0093	96.0947	Map3_Spot17
58	23.75	36.2	22.9	12.08	0	0.4468	0.4306	0.0546	0.0026	95.8647	Map3_Spot18
59	24.1	36.43	23.24	11.52	0	0.382	0.282	0.0434	0.0019	95.9994	Map3_Spot19
60	23.94	36.18	23.03	11.73	0	0.4602	0.224	0.075	0	95.6393	Map3_Spot20

61	24.35	36.69	23.29	11.5	0	0.3237	0.3058	0.0717	0	96.5313	Map3_Spot21
62	23.86	36.38	23.28	11.91	0	0.4377	0.2141	0.1252	0.0007	96.2078	Map3_Spot22
63	23.7	36.26	23.27	11.81	0	0.435	0.3274	0.1175	0.0097	95.9296	Map3_Spot23
64	24.02	36.32	23.29	11.61	0	0.4608	0.3602	0.0494	0	96.1105	Map3_Spot24
Minimum	23.02	35.64	22.19	8.98	0	0.085	0	0	0	94.6262	
Maximum	26.41	37.05	23.99	12.43	0	1.57	0.8748	0.2704	0.0179	96.6512	
Average	24.2892	36.3209	23.2309	11.2817	0	0.4273	0.18	0.0746	0.0042	95.8089	
Sigma	0.7485	0.296	0.3892	0.8438	0	0.2585	0.2287	0.0483	0.005	0.4879	
No. of data 64											

Appendix 3

Trace element data by LA-ICP-MS are reported hereafter. Sample names are as per Table A1, The first column of each table reports the denomination of single spot analyses: where no column labeled "Analysis #" or "Info" is present, the first column corresponds to the analysis label/number. The location of each analysis spot is shown in thin section scans available in the online data repository. Mass fractions of Fe_2O_3 are calculated as 1.11×FeO. Analysis below limit of detection (available in the online data repository) follow the symbol <. When the signal was split, (copy) appears in the analysis label.

Albula Pass Area

Sample: ALB13-1	Time	Analysis #	Spot size	SiO2	TiO2	Al2O3	Fe2O3	FeO	MnO	MgO	CaO	Na2O	K2O	Li7	B11	V51	Cr53	As75	Rb85	Sr88	Y89	Zr90	Nb93	Ba137	La139	Ce140	Pr141	Nd146	Sm147	Eu151	Gd157	Tb159	Dy163	Ho165	Er167	Tm169	Yb173	Lu175	W182	Pb208	Th232	U238
			um	wt.%	wt.%	wt.%	wt.%	wt.%	wt.%	wt.%	wt.%	wt.%	wt.%	µg/g	µg/g	µg/g	µg/g	µg/g	µg/g	µg/g	µg/g	µg/g	µg/g	µg/g	µg/g	µg/g	µg/g	µg/g	µg/g	µg/g	µg/g	µg/g	µg/g	µg/g	µg/g	µg/g	µg/g	µg/g	µg/g	µg/g	µg/g	µg/g
24ryb07.xl	13:58	7	32	43.6	0.02	18.3	16.3	14.7	0.09	0.004	21.6	0.0010	<0.0045619	0.75	<1.4743	104	<18.4724	2.3	<0.17555	5686	21.1	12.5	0.04	11.0	5.22	12.65	1.70	9.27	2.78	0.89	3.48	0.69	4.62	0.74	2.04	0.23	1.33	0.20	<0.07143	43.9	0.67	26.4
24ryb07.xl (copy)	13:58	8	24	43.2	0.05	19.0	15.5	14.0	0.19	0.007	21.8	0.0054	<0.0081168	<0.90284	6.8	84	<32.7481	6.2	<0.30385	11145	117.1	15.6	0.12	94.0	32.81	67.11	10.17	52.76	18.96	1.98	25.14	4.21	27.28	5.37	12.39	1.20	7.01	0.87	0.39	63.7	14.19	140.0
24ryb09.xl	14:06	9	24	42.9	0.04	18.2	16.7	15.1	0.72	0.006	21.3	0.0011	<0.0070265	<0.9851	<1.9964	89	<28.2868	<1.6353	<0.2416	9901	19.2	3.3	<0.11823	36.6	125.07	271.46	30.59	119.57	20.68	1.59	15.03	1.47	6.51	0.69	1.42	0.10	0.65	0.06	<0.21067	24.5	4.02	35.7
24ryb09.xl (copy)	14:06	10	32	42.6	0.04	20.0	15.6	14.1	0.24	0.009	21.3	0.0011	<0.0036931	<0.47465	<0.99854	111	<14.8057	6.0	<0.12257	1580	121.8	6.7	<0.057619	1.3	2.96	6.35	1.03	5.46	2.44	3.00	8.48	1.94	17.43	4.19	11.12	1.27	7.34	0.75	<0.099369	17.4	0.02	89.1
24ryb11.xl	14:16	11	32	43.4	0.02	19.7	15.6	14.1	0.26	0.010	20.9	0.0021	0.007	0.80	<1.2599	111	<17.2407	7.5	<0.17442	1332	60.7	2.5	<0.049832	1.4	2.43	5.34	0.71	4.55	2.33	1.43	4.39	1.03	8.19	2.00	5.36	0.58	2.64	0.32	<0.057285	19.0	0.04	21.8
24ryb11.xl (copy)	14:16	12	32	42.4	0.02	20.0	15.7	14.1	0.17	0.007	21.5	0.0006	0.006	1.78	<1.5051	129	<20.427	<1.2035	<0.20768	2833	32.9	7.4	<0.060208	2.0	0.39	0.59	0.06	0.41	0.42	1.33	0.73	0.32	2.56	0.73	2.92	0.31	1.87	0.33	0.10	6.5	<0.025338	11.0
24ryb13.xl	14:24	13a	44	41.2	0.12	21.2	14.4	12.9	0.07	0.011	22.8	0.0016	0.005	1.04	<0.75327	166	<9.1993	0.8	<0.08626	3962	24.8	2.4	0.65	3.7	0.39	0.51	0.10	0.55	0.31	0.56	1.21	0.25	2.44	0.66	2.34	0.36	3.12	0.46	0.04	7.9	0.05	11.9
24ryb13.xl (copy)	14:24	13b	44	48.2	0.11	19.2	11.4	10.3	0.10	0.005	20.4	0.0022	0.004	0.55	<1.1624	110	<13.5269	<0.8048	<0.13147	5101	15.2	0.8	0.14	7.7	0.50	0.98	0.11	0.46	0.52	0.54	1.02	0.15	1.73	0.37	1.26	0.15	1.48	0.15	0.10	7.9	0.03	8.9
24ryb14.xl	14:29	14	32	43.9	0.13	19.5	15.7	14.2	0.08	0.011	20.5	0.0007	0.005	0.22	1.9	156	<15.5799	3.0	<0.15748	1396	62.0	9.0	0.48	<0.65952	2.72	5.60	0.88	4.13	1.76	1.41	3.69	0.80	6.96	1.87	6.55	0.83	4.97	0.56	<0.039703	3.9	<0.014232	28.2
24ryb14.xl (copy)	14:29	15	60	39.2	0.02	21.3	15.8	14.2	0.18	0.007	23.4	0.0007	<0.0010708	2.03	1.2	122	<4.4614	0.8	<0.045619	3261	35.3	8.3	<0.017638	2.6	2.90	5.11	0.81	4.20	1.56	1.26	3.08	0.62	4.69	1.05	3.22	0.36	2.19	0.30	<0.012917	9.7	<0.0046305	28.1
24ryb16.xl	14:37	16	44	42.4	0.04	19.8	15.8	14.2	0.25	0.006	21.5	0.0013	0.01	1.58	0.6	105	<8.9829	1.5	<0.064359	1404	21.1	2.6	<0.035222	1.0	1.35	2.64	0.31	1.89	0.61	0.45	0.87	0.17	1.30	0.44	1.97	0.25	1.92	0.22	0.03	17.7	<0.022424	7.1
24ryb17.xl	14:44	17	44	42.0	0.03	18.7	16.9	15.2	0.52	0.006	21.8	0.0015	<0.0032591	2.31	1.2	89	<13.3957	1.0	<0.12515	7850	13.5	2.4	<0.033959	34.2	3.84	7.77	0.91	4.95	1.40	1.06	1.94	0.31	2.18	0.38	1.06	0.08	0.43	0.04	0.04	20.7	0.03	11.3
24ryb17.xl (copy)	14:44	18	60	39.0	0.03	21.4	15.9	14.3	0.09	0.006	23.4	0.0013	<0.0010153	0.68	0.5	139	<4.1714	0.6	<0.03885	3167	45.8	12.4	<0.010438	2.5	0.49	0.65	0.09	0.55	0.33	2.18	1.35	0.35	4.14	1.27	4.02	0.48	3.15	0.45	0.03	11.5	<0.0039709	16.5
24ryb19.xl	14:52	19	24	43.7	0.02	19.3	15.9	14.3	0.17	0.007	20.8	0.0014	<0.0067427	1.92	<1.7576	127	<28.0465	2.2	<0.27198	2623	32.1	6.9	<0.079146	2.1	0.17	0.15	<0.08103	<0.46769	0.43	1.35	0.88	0.25	2.06	1.05	2.75	0.41	2.13	0.26	<0.19997	8.2	<0.072023	11.1
24ryb20.xl	14:57	20	32	42.6	0.03	20.0	15.6	14.0	0.09	0.001	21.5	0.0005	<0.0031937	<0.13294	<0.96825	196	<13.3171	<0.77535	<0.1251	765	66.6	<0.078067	<0.04696	0.8	<0.034201	0.02	<0.011935	<0.068887	<0.17865	0.32	0.16	0.07	1.75	1.00	6.49	0.99	6.65	0.86	0.05	8.5	<0.030141	3.7
24ryb20.xl (copy)	14:57	21a	32	41.8	0.03	20.5	15.5	14.0	0.10	0.001	21.9	0.0009	<0.0037483	<0.28781	<1.2902	191	<15.8124	<0.92788	<0.1604	779	74.4	<0.1148	<0.069054	1.8	0.07	<0.033896	<0.025839	<0.14914	<0.28503	0.21	0.28	0.07	1.62	1.18	6.39	1.13	8.27	0.97	<0.077081	7.5	<0.048089	4.5
24ryb20.xl (copy) (copy)	14:57	21b	32	43.4	0.02	19.0	16.9	15.3	0.23	0.001	20.4	0.0004	0.005	<0.26151	<1.403	188	<18.0937	<1.058	<0.17735	1330	52.0	<0.11982	<0.072078	1.5	0.13	0.06	<0.023478	<0.13551	<0.2881	0.37	<0.13925	0.09	1.33	0.73	4.70	0.77	5.39	0.65	<0.070037	10.1	<0.048607	5.9
24ryb22.xl	15:04	22	32	42.8	0.03	19.2	16.6	14.9	0.25	0.005	21.1	0.0010	<0.0036726	0.89	<1.2305	119	<15.5383	<0.90466	<0.1363	1428	33.8	0.4	<0.051712	1.3	<0.04405	<0.022759	<0.043847	<0.25308	<0.27946	0.60	0.34	0.12	1.35	0.69	2.65	0.39	2.54	0.25	<0.051776	15.8	<0.03889	5.6
24ryb22.xl (copy)	15:04	23	24	43.5	0.01	19.0	16.5	14.9	0.25	0.005	20.7	0.0008	<0.0060826	1.78	<2.0302	91	<25.7256	2.6	<0.22505	1655	13.6	0.3	<0.084943	1.4	<0.072228	0.04	<0.072024	<0.41571	<0.45904	0.41	0.31	0.10	0.47	0.28	0.74	0.11	0.75	0.14	<0.083969	23.9	<0.063767	8.3
24ryb24.xl	15:12	24	24	44.1	0.03	19.8	15.4	13.9	0.10	0.011	20.4	0.0005	<0.0064526	<0.65862	<1.6524	128	<26.7287	2.3	<0.26426	2269	54.1	9.6	<0.097136	<1.0709	0.24	0.39	0.04	0.36	<0.17757	1.68	1.04	0.29	4.25	1.17	5.70	0.71	4.00	0.46	<0.17727	5.7	<0.030105	23.0
24ryb24.xl (copy)	15:12	25a	60	38.6	0.01	20.4	17.0	15.3	0.19	0.003	23.7	0.0008	<0.0011379	0.39	0.6	116	<4.7382	1.1	<0.048446	3601	10.9	0.4	<0.019024	6.3	0.02	0.02	<0.0065243	0.04	0.05	0.38	0.13	0.02	0.55	0.19	0.80	0.10	0.83	0.14	<0.036064	61.5	<0.0070476	6.0
24ryb24.xl (copy) (copy)	15:12	25b	60	39.0	0.02	19.7	18.1	16.3	0.50	0.003	22.8	0.0023	<0.001162	0.54	<0.29757	110	<4.8134	1.0	<0.047589	4994	16.7	0.3	<0.017493	16.7	0.07	0.05	0.02	0.05	0.07	0.79	0.37	0.07	0.95	0.32	1.04	0.10	0.60	0.09	<0.031923	46.2	<0.0054214	7.5
24ryb26.xl	15:18	26	44	41.7	0.05	20.8	14.9	13.4	0.19	0.011	22.1	0.0014	<0.0018566	1.12	1.7	129	<7.6953	4.4	<0.078587	1878	22.6	1.3	0.12	3.4	0.03	0.03	<0.016654	0.04	0.05	0.49	0.28	0.09	1.21	0.51	1.94	0.25	1.50	0.19	0.02	9.0	<0.018021	3.7
24ryb26.xl (copy)	15:18	27	24	44.3	0.02	19.8	15.1	13.6	0.11	0.007	20.5	0.0034	<0.0064364	<0.65583	<2.0703	125	<26.6998	<1.5573	<0.27411	2459	32.1	6.1	<0.030142	1.6	0.05	0.09	<0.059193	<0.14765	0.18	1.28	0.35	0.17	2.10	0.87	3.12	0.36	2.61	0.27	<0.076433	6.4	<0.064052	12.5
24ryb28.xl	15:25	28	44	41.6	0.04	20.9	14.7	13.2	0.13	0.008	22.5	0.0010	<0.0019304	1.22	0.9	104	<8.2583	1.8	<0.07977	3102	20.7	6.5	0.03	2.1	0.87	2.02	0.27	1.72	0.65	0.69	1.14	0.29	2.39	0.63	2.11	0.27	1.67	0.20	0.04	8.3	0.01	26.0
24ryb28.xl (copy)	15:25	29	44	41.0	0.02	21.4	14.7	13.2	0.12	0.007	22.6	0.0010	<0.0018148	1.03	0.9	153	<7.7587	0.8	<0.074607	3093	56.1	11.9	<0.019128	1.9	0.51	0.68	0.07	0.67	0.46	1.90	1.61	0.37	4.03	1.44	5.11	0.63	3.87	0.52	<0.019948	7.6	<0.0072348	27.5
24ryb30.xl	15:33	30	44	42.5	0.04	20.2	15.7	14.2	0.17	0.009	21.2	0.0016	<0.0019319	1.54	1.8	142	8.8	1.8	<0.0902	2258	42.0	5.6	0.08	1.9	0.17	0.20	0.03	0.20	0.19	1.29	0.89	0.27	3.33	1.09	4.03	0.48	2.53	0.30	0.02	6.9	<0.0078697	9.6
24ryb31.xl	15:39	31	60	39.0	0.02	20.3	17.1	15.4	0.11	0.003	23.5	0.0009	<0.00099484	1.10	0.7	129	<4.2217	0.6	<0.042315	5799	17.1	4.0	0.02	12.4	0.05	0.06	0.01	0.11	0.05	0.99	0.35	0.09	1.24	0.43	1.24	0.14	0.90	0.16	0.04	25.5	<0.0035075	4.3
24ryb32.xl	15:45	32	32	43.0	0.09	19.9	15.6	14.0	0.11	0.002	21.2	0.0001	<0.0035587	<0.38586	<1.1857	141	<15.431	<0.88745	<0.1487	681	72.4	0.3	<0.041251	<0.78697	2.29	5.59	0.75	3.75	1.53	0.83	3.26	0.97	7.75	2.40	8.06	1.20	7.78	1.01	<0.105	7.6	0.05	3.3
24ryb32.xl (copy)	15:45	33	32	44.0	0.05	18.5	17.3	15.6	0.30	0.004	19.9	0.0006	<0.0047868	<0.48086	<1.5507	97	<20.7044	2.4	<0.19605	2711	28.9	3.0	<0.051407	4.3	13.32	27.63	3.07	12.31	3.00	1.14	4.51	0.75	4.46	0.85	2.94	0.42	2.69	0.40	<0.13085	21.3	0.30	10.5
24ryb32.xl (copy) (copy)	15:45	34	44	41.3	0.09	20.8	15.3	13.7	0.11	0.009	22.3	0.0023	<0.0016991	0.38	<0.53	144	<7.3254	1.2	<0.067762	2877	12.4	7.7	0.32	2.9	0.24	0.70	0.10	0.52	0.18	0.43	0.33	0.08	0.85	0.31	1.25	0.20	1.65	0.23	0.04	13.3	0.23	1.6
24ryb35.xl	15:54	35	32	41.7	0.03	18.5	17.4	15.7	0.47	0.005	21.9	0.0009	<0.0034068	1.13	1.5	120	<15.1532	2.4	<0.13371	6134	10.2	5.2	<0.065877	30.7	7.92	18.18	2.52	12.29	3.77	0.59	4.09	0.36	2.41	0.33	0.70	0.09	0.39	0.05	0.25	38.8	1.17	3.4

Sample: ALB13-7B	Time	Spot size	SiO2	TiO2	Al2O3	Fe2O3	FeO	MgO	CaO	K2O	P2O5	V51	Cr53	Sr88	Y89	Zr90	Nb93	Ba137	La139	Ce140	Pr141	Nd146	Sm147	Eu151	Gd157	Tb159	Dy163	Ho165	Er167	Tm169	Yb173	Lu175	Pb206	Pb208	Th232	U238
		um	wt.%	wt.%	wt.%	wt.%	wt.%	wt.%	wt.%	wt.%	wt.%	µg/g	µg/g	µg/g	µg/g	µg/g	µg/g	µg/g	µg/g	µg/g	µg/g	µg/g	µg/g	µg/g	µg/g	µg/g	µg/g	µg/g	µg/g	µg/g	µg/g	µg/g	µg/g	µg/g	µg/g	µg/g
4 ALB13-7B_1A_a.csv	14:39	20	38.17	0.12	20.72	16.9	15.23	0.01	24.06	0.001	0.01	331.32	32.84	2735.16	133.06	5.00	0.60	8.58	7.01	17.09	2.96	18.77	9.03	4.02	17.57	3.20	23.18	5.13	15.35	1.81	11.80	1.58	27.67	27.83	0.06	11.21
7 ALB13-7B_1C_a.csv	14:39	20	38.89	0.06	20.57	16.8	15.17	0.01	23.61	0.001	0.01	276.41	39.80	1981.07	124.28	6.55	0.03	3.18	7.34	23.65	4.51	29.10	13.58	3.19	19.90	3.54	23.15	4.72	14.89	1.98	12.80	1.63	22.61	21.93	0.07	14.28
7 ALB13-7B_1C_a.csv (copy)	14:39	20	38.03	0.07	20.90	16.8	15.10	0.01	24.19	0.001	0.01	281.35	38.72	2247.09	121.46	6.38	0.26	3.24	9.98	30.88	5.74	35.65	15.48	3.49	21.32	3.62	23.30	4.66	14.49	1.87	11.94	1.52	23.43	22.87	0.06	14.50
8 ALB13-7B_1C_b.csv	14:39	20	38.48	0.03	20.67	16.9	15.20	0.01	23.91	0.001	0.01	368.08	2.97	2218.42	44.23	6.94	0.03	3.46	0.35	0.43	0.09	0.53	0.40	1.00	1.83	0.42	4.33	1.32	4.23	0.53	3.26	0.44	27.81	27.53	0.04	3.68
15 ALB13-7B_4A_a.csv	14:39	20	37.05	0.09	21.21	16.4	14.78	0.01	25.16	0.001	0.01	294.64	41.84	2874.95	72.84	5.28	0.08	11.71	2.39	4.78	0.71	4.52	2.35	2.22	6.92	1.38	10.61	2.48	8.24	0.99	6.70	0.91	32.81	32.64	0.05	9.91
19 ALB13-7B_4A_b.csv	14:39	20	38.20	2.27	19.09	14.9	13.44	0.31	24.64	0.24	0.11	323.64	1210.62	5073.05	120.04	215.87	33.94	61.58	163.16	570.58	83.76	346.56	63.23	8.36	49.36	6.02	29.98	4.92	12.06	1.48	10.11	1.44	53.47	55.15	129.07	12.61
19 ALB13-7B_4A_b.csv (copy)	14:39	20	36.64	1.58	20.03	15.2	13.66	0.17	26.10	0.07	0.05	326.36	1139.50	5517.01	133.42	291.42	22.95	54.02	160.17	551.60	81.14	337.37	62.23	9.43	51.68	6.26	31.23	5.24	13.45	1.66	11.08	1.70	57.54	60.20	100.01	13.04
19 ALB13-7B_4A_b.csv (copy) (copy)	14:39	20	39.23	2.68	18.50	14.8	13.33	0.40	23.65	0.35	0.15	320.89	1255.60	4799.93	110.98	159.56	40.60	66.12	164.51	582.35	85.25	351.58	63.72	7.62	47.82	5.83	29.13	4.68	11.16	1.35	9.51	1.26	51.03	51.88	148.16	12.34
20 ALB13-7B_4A_c.csv	14:39	20	37.86	0.06	20.26	16.0	14.42	0.01	25.69	0.001	0.01	308.57	34.80	6638.15	127.07	3.81	0.06	21.94	115.71	320.93	47.98	224.94	50.65	9.29	47.84	5.87	29.87	5.04	11.48	1.44	9.63	1.56	44.12	46.62	0.51	12.71
21 ALB13-7B_4C_b.csv	14:39	20	37.21	0.15	21.99	16.0	14.39	0.01	24.55	0.001	0.01	540.70	7.01	1125.64	107.29	6.01	0.05	3.42	0.39	1.05	0.18	1.39	1.21	2.22	4.83	1.01	10.23	2.90	11.23	1.69	9.88	1.13	13.35	13.53	0.06	1.01
21 ALB13-7B_4C_b.csv (copy)	14:39	20	39.59	0.13	20.83	16.0	14.40	0.01	23.34	0.001	0.01	479.49	7.19	1905.52	87.43	4.17	0.04	6.14	2.61	5.24	0.80	4.65	1.92	2.32	4.82	1.05	9.02	2.40	8.94	1.33	6.85	0.85	19.47	18.54	0.06	1.67
21 ALB13-7B_4C_b.csv (copy) (copy)	14:39	20	38.44	0.14	21.39	16.0	14.40	0.01	23.92	0.001	0.01	507.94	7.08	1542.00	96.70	5.01	0.05	4.84	1.59	3.30	0.52	3.13	1.59	2.28	4.83	1.03	9.63	2.63	10.04	1.49	8.30	0.99	16.59	16.09	0.04	1.34
22 ALB13-7B_4C_a.csv	14:39	20	37.48	0.06	20.71	16.7	15.02	0.01	25.01	0.001	0.01	254.35	110.52	4030.22	104.77	5.66	0.04	12.98	12.81	30.26	4.72	24.82	8.67	4.51	15.33	2.44	18.04	3.85	10.87	1.37	9.28	1.26	32.86	33.04	0.05	12.91
23 ALB13-7B_5_a.csv	14:39	20	38.33	0.06	20.01	16.2	14.61	0.01	25.26	0.001	0.02	343.75	47.61	6367.27	186.80	4.23	0.04	21.19	154.16	418.71	64.48	305.78	76.15	13.80	76.24	9.66	47.79	7.76	18.24	2.19	16.08	2.27	42.97	43.63	0.05	21.07
26 ALB13-7B_5_b.csv	14:39	20	36.18	0.11	21.31	16.0	14.41	0.13	26.14	0.001	0.01	315.91	40.72	5907.07	54.24	5.76	0.79	32.16	7.28	10.64	2.02	10.09	2.97	2.71	5.68	0.90	6.62	1.61	5.11	0.70	4.70	0.71	49.72	50.67	0.05	3.78
26 ALB13-7B_5_b.csv (copy)	14:39	20	38.74	0.07	20.08	16.3	14.71	0.02	24.67	0.001	0.01	314.81	36.15	5654.42	36.03	4.66	0.07	28.79	5.06	5.53	1.31	4.79	1.69	1.26	2.39	0.38	3.09	0.85	3.06	0.54	3.19	0.48	44.71	47.65	0.06	2.55
26 ALB13-7B_5_b.csv (copy) (copy)	14:39	20	37.26	0.09	20.80	16.1	14.55	0.09	25.50	0.001	0.01	315.77	38.74	5782.31	46.60	5.30	0.50	30.99	6.36	8.47	1.72	7.80	2.43	2.11	4.28	0.69	5.12	1.29	4.26	0.62	4.05	0.61	47.54	49.43	0.04	3.27
27 ALB13-7B_5_c.csv	14:39	20	36.10	0.08	21.14	16.3	14.70	0.02	26.24	0.001	0.01	282.91	70.12	5485.06	87.07	5.02	0.16	26.22	5.89	11.94	2.03	11.23	4.24	3.96	9.42	1.78	12.10	2.93	8.74	1.12	7.27	1.13	45.34	47.18	0.06	7.22
27 ALB13-7B_5_c.csv (copy)	14:39	20	38.25	0.07	19.96	16.7	15.04	0.01	24.95	0.001	0.02	252.55	56.52	5288.29	89.58	5.54	0.13	27.81	8.72	18.46	2.98	16.66	6.12	5.16	12.97	1.93	13.81	3.07	8.89	1.17	7.31	1.10	46.71	46.59	0.06	6.44
27 ALB13-7B_5_c.csv (copy) (copy)	14:39	20	37.12	0.08	20.59	16.5	14.86	0.02	25.63	0.001	0.01	269.42	64.08	5406.16	88.42	5.32	0.14	27.03	7.22	14.98	2.49	13.77	5.11	4.54	11.11	1.84	12.88	2.98	8.80	1.15	7.32	1.11	45.96	46.93	0.04	6.86
28 ALB13-7B_5_e.csv	14:39	20	36.21	0.06	21.17	15.9	14.35	0.01	26.49	0.001	0.02	362.56	11.64	6181.04	243.05	5.31	0.08	19.83	54.15	155.51	24.11	120.32	36.27	11.72	53.55	8.18	52.76	9.57	23.58	2.59	16.16	2.39	45.23	46.05	0.25	21.32
28 ALB13-7B_5_e.csv (copy)	14:39	20	38.57	0.06	20.01	16.2	14.60	0.01	25.04	0.001	0.01	337.31	42.99	6583.20	264.54	4.43	0.06	19.56	144.03	431.10	66.59	315.98	80.68	16.10	88.98	11.89	66.71	11.01	25.28	2.84	18.03	2.60	48.87	49.08	0.74	27.35
28 ALB13-7B_5_e.csv (copy) (copy)	14:39	20	37.77	0.06	20.40	16.1	14.52	0.01	25.53	0.001	0.01	345.33	32.93	6473.35	257.89	4.70	0.05	19.92	114.96	342.30	52.88	252.86	66.32	14.67	77.56	10.68	62.29	10.53	24.82	2.76	17.36	2.54	47.74	48.19	0.56	25.51
29 ALB13-7B_5_d.csv	14:39	20	37.76	0.40	19.77	16.4	14.74	0.13	25.47	0.02	0.01	286.26	591.77	5613.28	92.59	10.56	5.17	26.12	66.96	222.20	33.11	141.19	30.24	5.52	25.50	3.51	18.27	3.46	9.44	1.14	6.84	1.01	60.14	60.21	1.46	9.12
34 ALB13-7B_5_g.csv	14:39	20	37.43	0.07	20.48	16.5	14.83	0.05	25.42	0.001	0.01	295.31	62.61	5351.44	75.81	6.04	0.17	42.70	15.06	28.23	5.04	25.28	7.80	3.55	10.77	1.78	11.48	2.39	7.62	0.98	6.81	1.03	54.77	55.87	0.03	6.34
34 ALB13-7B_5_g.csv (copy)	14:39	20	36.36	0.07	21.03	16.3	14.66	0.04	26.13	0.001	0.01	298.89	63.29	5343.53	82.41	6.30	0.17	44.75	16.76	32.19	5.82	29.20	9.16	3.80	12.24	1.98	12.74	2.67	8.58	1.02	7.70	1.12	54.71	57.14	0.04	7.07
34 ALB13-7B_5_g.csv (copy) (copy)	14:39	20	38.54	0.06	19.98	16.7	15.00	0.07	24.63	0.001	0.01	292.41	62.34	5366.42	69.36	5.77	0.17	40.72	13.42	24.19	4.28	21.40	6.47	3.29	9.24	1.58	10.28	2.12	6.69	0.93	5.97	0.96	54.39	54.21	0.04	5.53
35 ALB13-7B_5_h.csv	14:39	20	38.18	0.08	20.41	16.3	14.67	0.01	24.94	0.005	0.01	369.43	45.49	5028.16	50.86	6.02	0.23	36.60	4.73	7.63	1.31	6.13	1.40	1.89	2.92	0.53	4.50	1.23	4.53	0.69	4.80	0.71	53.90	55.00	0.03	3.12
5 ALB13-7B_1A_b.csv	14:39	30	37.50	0.11	20.58	16.5	14.86	0.01	25.23	0.0005	0.01	263.04	47.30	4380.56	90.19	5.68	0.21	27.30	9.53	22.51	3.43	19.43	7.22	2.52	11.68	2.07	14.67	3.16	10.31	1.38	8.78	1.22	47.69	48.49	0.01	13.36
6 ALB13-7B_1A_c.csv	14:39	30	37.56	0.14	20.22	16.4	14.77	0.01	25.58	0.003	0.01	225.71	61.48	5533.23	72.49	4.79	1.03	25.12	15.19	34.76	5.45	30.79	11.00	3.51	14.63	2.23	13.12	2.60	7.66	0.99	6.67	0.96	48.08	49.23	0.01	10.88
11 ALB13-7B_2A_a.csv	14:39	30	38.06	0.26	20.47	16.4	14.78	0.02	24.70	0.0005	0.01	696.90	124.46	3869.34	58.67	14.78	1.47	26.84	3.87	10.24	1.45	7.29	2.38	1.78	4.06	0.81	6.51	1.69	6.28	0.92	6.53	0.99	25.04	24.79	0.04	7.10
12 ALB13-7B_2A_b.csv	14:39	30	37.42	0.28	20.80	16.6	14.95	0.03	24.82	0.0004	0.01	838.37	85.63	3031.05	67.95	13.57	1.91	13.81	4.53	11.19	1.61	8.47	2.69	2.48	4.56	0.89	7.36	1.91	7.05	1.01	7.76	1.25	20.05	20.84	0.04	8.67
13 ALB13-7B_2B_b.csv	14:39	30	37.42	0.07	20.96	16.7	15.00	0.02	24.83	0.0003	0.00	550.50	148.43	2629.17	76.69	31.10	0.26	7.01	8.67	23.70	3.48	17.80	5.57	3.82	9.58	1.86	13.63	2.65	6.69	0.63	3.53	0.57	28.69	29.43	0.21	13.74
14 ALB13-7B_2B_a.csv	14:39	30	37.65	0.28	20.94	16.0	14.46	0.02	24.95	0.0004	0.01	804.78	139.77	3606.76	74.08	17.96	1.61	20.26	6.53	17.53	2.55	13.02	4.19	2.96	7.24	1.38	10.29	2.37	7.28	0.90	6.07	1.00	21.36	21.50	0.04	14.00
28 ALB13-7B_5_e.csv	14:39	30	36.79	0.06	20.98	16.0	14.39	0.01	26.06	0.001	0.02	363.21	12.03	6073.38	240.04	5.35	0.08	19.54	53.62	154.97	23.69	118.00	35.65	11.65	52.81	8.08	52.69	9.45	23.44	2.57	15.90	2.38	46.10	47.16	0.25	21.29
30 ALB13-7B_5_f.csv	14:39	30	36.34	0.74	21.02	15.6	14.08	0.09	25.86	0.15	0.01	351.34	115.23	5401.71	58.39	8.16	9.86	59.46	8.93	11.65	2.24	10.65	2.92	2.01	3.94	0.64	5.62	1.52	5.47	0.79	6.17	0.84	52.76	54.97	0.09	3.79
30 ALB13-7B_5_f.csv (copy)	14:39	30	38.99	1.03	19.79	15.5	13.93	0.17	24.04	0.34	0.01	328.26	123.99	4998.06	50.08	8.90	14.74	63.11	7.90	10.64	2.17	9.33	2.54	1.73	3.13	0.57	4.82	1.24	4.89	0.66	5.10	0.73	52.93	56.13	0.09	3.15
30 ALB13-7B_5_f.csv (copy) (copy)	14:39	30	37.97	0.93	20.25	15.5	13.99	0.14	24.73	0.27	0.01	337.02	120.65	5152.48	53.26	8.63	13.05	61.62	8.29	11.03	2.21	9.82	2.72	1.83	3.40	0.60	5.13	1.35	5.11	0.71	5.52	0.77	52.77	55.65	0.08	3.37

Sample: ALB19-1 ||	Time	Spot size	SiO2	TiO2	Al2O3	Fe2O3	FeO	MnO	MgO	CaO	Na2O	K2O	P2O5	Li7	B11	V51	Cr53	Sr88	Y89	Zr90	Nb93	Ba137	La139	Ce140	Pr141	Nd146	Sm147	Eu151	Gd157	Tb159	Dy163	Ho165	Er167	Tm169	Yb173	Lu175	Pb206	Pb207	Pb208	Th232	U238
			wt.%	wt.%	wt.%	wt.%	wt.%	wt.%	wt.%	wt.%	wt.%	wt.%	wt.%	µg/g	µg/g	µg/g	µg/g	µg/g	µg/g	µg/g	µg/g	µg/g	µg/g	µg/g	µg/g	µg/g	µg/g	µg/g	µg/g	µg/g	µg/g	µg/g	µg/g	µg/g	µg/g	µg/g	µg/g	µg/g	µg/g	µg/g
97 ALB19-1_1_1.csv	15:10	50	37.4	0.02	21.6	15.5	13.9	0.18	0.005	25.1	0.002	<0.00019543	0.004	1.20	4.59	83.8	<0.79569	4003	34.3	4.67	0.14	3.8	0.28	0.40	0.06	0.38	0.19	1.18	0.67	0.18	2.19	0.71	2.93	0.51	4.06	0.56	19.9	20.6	20.7	<0.0091796	1.46
98 ALB19-1_1_2.csv	15:10	50	36.6	0.02	21.4	15.0	13.5	0.07	0.003	26.7	0.001	<0.00021507	<0.0022913	0.25	15.73	55.6	0.9	7321	5.9	9.97	0.06	11.8	0.03	0.09	0.02	0.13	0.09	0.23	0.18	0.05	0.39	0.11	0.47	0.08	0.79	0.10	28.2	28.6	29.4	<0.0072936	0.19
99 ALB19-1_1_3.csv	15:10	50	37.8	0.03	22.9	14.1	12.7	0.10	0.007	24.8	0.001	<0.0002147	<0.0022914	0.42	4.06	63.5	<0.87552	3077	4.6	8.86	0.21	0.9	0.01	0.04	0.01	0.07	0.07	0.17	<0.101	0.04	0.36	0.11	0.41	0.06	0.96	0.12	7.9	8.3	8.0	<0.0092299	0.33
100 ALB19-1_1_4.csv	15:10	50	37.4	0.08	23.3	12.9	11.7	0.21	0.008	25.6	0.001	<0.00021149	<0.0022563	0.67	3.93	94.0	<0.86388	4973	6.0	2.48	0.70	5.8	0.03	0.03	0.01	0.04	<0.037343	0.15	0.10	0.03	0.38	0.08	0.40	0.10	1.01	0.17	14.6	15.2	15.1	<0.0087291	0.16
101 ALB19-1_1_5.csv	15:10	50	37.7	0.04	23.2	13.7	12.3	0.15	0.008	24.8	0.002	0.0006	<0.0025659	2.39	5.22	78.9	<0.9807	2440	5.2	3.42	0.25	2.0	0.04	0.07	0.01	0.09	0.04	0.13	0.07	0.03	0.29	0.11	0.40	0.09	0.75	0.12	10.2	10.7	10.7	<0.0099111	0.12
102 ALB19-1_1_6.csv	15:10	50	36.2	0.02	20.6	15.8	14.2	0.49	0.006	26.7	0.002	0.0052	0.0086	1.82	4.44	66.4	<0.80105	9086	12.7	2.83	0.05	33.3	0.76	1.01	0.15	0.91	0.39	0.70	1.03	0.16	1.24	0.27	0.94	0.11	0.72	0.14	25.4	26.7	26.6	<0.0073043	0.64
106 ALB19-1_1_7.csv	15:10	50	37.7	0.03	22.2	14.8	13.3	0.17	0.007	24.9	0.002	<0.00019961	0.0024	0.94	14.01	58.0	<0.8019	3082	20.4	0.61	0.40	3.0	0.16	0.21	0.03	0.17	0.10	0.68	0.42	0.10	1.42	0.58	2.30	0.45	3.89	0.60	20.9	21.4	21.8	<0.0084076	0.60
107 ALB19-1_1_8.csv	15:10	50	37.7	0.06	22.3	14.8	13.3	0.13	0.007	24.7	0.001	0.0003	0.0029	0.40	11.41	76.0	<0.83956	2621	37.1	4.04	0.41	1.2	0.22	0.38	0.06	0.40	0.27	1.19	0.68	0.21	2.45	0.79	3.44	0.55	4.26	0.61	9.0	9.4	9.6	<0.0087503	1.53
108 ALB19-1_1_9.csv	15:10	50	37.5	0.04	22.0	14.7	13.2	0.30	0.011	25.2	0.003	0.0062	0.0081	3.48	18.83	56.7	<0.90214	4604	22.6	0.43	1.36	11.3	0.76	1.00	0.15	0.81	0.27	0.86	0.65	0.16	1.75	0.59	2.77	0.45	3.67	0.64	39.9	40.2	41.0	0.04	0.63
109 ALB19-1_1_10.csv	15:25	50	37.6	0.04	22.0	15.3	13.7	0.15	0.009	24.8	0.003	0.0117	<0.0022029	0.98	4.96	95.4	<0.80579	2953	27.9	10.27	0.21	4.7	0.87	1.17	0.22	1.06	0.43	0.71	1.01	0.24	2.13	0.59	2.45	0.41	3.10	0.48	27.7	28.1	28.6	0.03	1.81
110 ALB19-1_2_1.csv	15:25	50	37.7	0.15	22.5	15.1	13.6	0.05	0.003	24.3	0.000	<0.00021079	<0.0022103	0.29	1.72	125.8	<0.83175	1261	14.1	17.25	1.06	0.4	0.03	0.09	0.02	0.13	0.10	0.27	0.24	0.09	0.75	0.25	1.41	0.32	2.72	0.46	2.8	3.0	3.0	<0.0077302	0.09
111 ALB19-1_2_2.csv	15:25	50	37.4	0.11	21.6	15.6	14.0	0.13	0.011	25.0	0.004	0.0006	<0.0021939	1.16	10.41	87.8	1.0	3033	24.9	3.31	4.82	7.2	1.02	1.84	0.32	1.83	0.95	0.77	1.33	0.30	2.33	0.69	2.77	0.49	4.52	0.74	27.0	27.9	28.3	<0.0079746	1.12
114 ALB19-1_2_3.csv	15:25	50	37.3	0.03	21.5	14.4	13.0	0.36	0.006	26.1	0.002	0.0010	0.007	1.91	5.26	55.0	<0.80963	7323	3.6	3.10	0.16	15.8	0.61	0.75	0.16	0.60	0.23	0.20	0.28	0.07	0.42	0.09	0.29	0.06	0.45	0.06	28.2	29.5	29.8	0.02	0.12
115 ALB19-1_2_4.csv	15:25	50	36.9	0.05	22.0	14.6	13.1	0.20	0.007	26.0	0.002	<0.0002008	0.004	0.91	15.88	61.8	<0.82904	5637	21.6	1.47	3.86	20.8	0.64	1.04	0.17	1.03	0.52	0.68	0.85	0.18	1.91	0.56	2.33	0.43	3.81	0.66	30.2	31.5	31.4	<0.0078829	0.89
116 ALB19-1_2_5.csv	15:25	50	37.5	0.03	22.3	14.7	13.2	0.22	0.008	25.0	0.005	0.0002	0.003	1.65	17.67	54.2	<0.86636	3322	19.5	1.09	0.50	4.7	0.96	1.74	0.31	1.78	0.80	0.86	1.18	0.23	2.13	0.62	2.38	0.37	2.85	0.44	20.1	20.9	21.2	<0.0093733	0.84
117 ALB19-1_2_6.csv	15:25	50	37.7	0.07	22.4	14.8	13.3	0.10	0.007	24.6	0.002	0.0004	<0.0021523	0.38	5.92	95.0	<0.86733	2261	31.5	12.43	0.80	2.1	0.52	0.93	0.17	0.91	0.49	0.62	1.29	0.28	2.61	0.74	3.09	0.49	3.92	0.57	9.6	9.8	9.7	<0.0087881	2.49
118 ALB19-1_2_7.csv	15:25	50	37.4	0.03	22.0	15.2	13.7	0.15	0.007	25.1	0.002	<0.00020572	0.003	0.70	8.20	57.2	<0.81548	3649	26.9	2.13	0.80	6.4	0.78	1.45	0.25	1.51	0.80	0.76	1.62	0.32	2.86	0.83	3.42	0.55	4.50	0.63	22.4	22.7	23.0	0.01	1.24

Sample: ALB19-4-1327A	Time	Spot size	SiO2	TiO2	Al2O3	FeO	FeO	MnO	MgO	CaO	Na2O	K2O	P2O5	Li7	B11	V51	Cr53	Sr88	Y89	Zr90	Nb93	Ba137	La139	Ce140	Pr141	Nd146	Sm147	Eu151	Gd157	Tb159	Dy163	Ho165	Er167	Tm169	Yb173	Lu175	Pb206	Pb207	Pb208	Th232	U238
		um	wt.%	wt.%	wt.%	wt.%	wt.%	wt.%	wt.%	wt.%	wt.%	wt.%	wt.%	µg/g	µg/g	µg/g	µg/g	µg/g	µg/g	µg/g	µg/g	µg/g	µg/g	µg/g	µg/g	µg/g	µg/g	µg/g	µg/g	µg/g	µg/g	µg/g	µg/g	µg/g	µg/g	µg/g	µg/g	µg/g	µg/g	µg/g
4 ALB19-4_1327A_1_1.csv	14:15	38	36.9	0.15	21.4	16.0	14.4	0.09	0.004	25.4	0.005	0.0007	<0.0029747	1.09	2.66	46.3	1.28	2781	122.9	5.94	8.38	6.61	0.8	1.7	0.3	1.5	1.2	0.2	3.8	1.2	12.4	3.3	11.7	1.7	10.1	1.3	15.4	14.8	15.3	0.02	12.11
4 ALB19-4_1327A_1_1.csv (copy)	14:15	38	37.5	0.25	20.4	17.1	15.4	0.06	0.007	24.6	0.006	0.0010	<0.0031727	1.66	2.08	67.8	1.38	2620	112.5	5.53	14.07	6.80	0.5	1.0	0.2	0.9	0.7	0.1	2.5	0.9	9.5	2.9	11.5	1.7	10.3	1.3	13.5	13.4	13.5	0.05	4.67
4 ALB19-4_1327A_1_1.csv (copy) (copy)	14:15	38	37.2	0.19	21.0	16.5	14.9	0.07	0.006	25.0	0.006	0.0008	<0.0023976	1.35	2.40	56.0	1.02	2707	118.2	5.77	10.97	6.66	0.7	1.4	0.2	1.2	1.0	0.2	3.2	1.1	11.1	3.1	11.6	1.7	10.2	1.3	14.5	14.2	14.5	0.03	8.77
5 ALB19-4_1327A_1_2.csv	14:15	38	36.0	0.04	20.2	16.9	15.2	0.31	0.002	26.5	0.005	0.0012	0.01	1.03	2.77	43.0	1.12	6763	162.5	6.91	1.57	25.32	8.8	13.7	1.7	6.6	2.9	0.9	7.6	2.0	18.1	4.1	12.9	1.6	9.7	1.2	97.5	96.6	97.8	1.01	15.79
6 ALB19-4_1327A_1_3.csv	14:15	38	36.1	0.03	20.7	16.4	14.7	0.47	0.003	26.3	0.002	0.0004	0.01	3.00	3.26	40.4	1.04	6593	127.2	6.25	0.40	26.68	6.9	10.5	1.2	4.3	1.8	0.7	4.7	1.3	12.5	3.0	9.6	1.2	7.2	1.0	104.5	103.5	104.6	1.12	10.40
7 ALB19-4_1327A_1_4.csv	14:15	38	35.9	0.05	20.7	15.6	14.1	0.51	0.003	26.9	0.009	0.0016	0.03	2.86	3.98	23.5	1.07	9046	101.3	1.98	1.61	51.48	7.1	11.8	1.7	8.0	4.1	1.4	9.2	2.2	15.8	2.7	6.8	0.9	5.0	0.6	30.3	30.3	31.5	0.16	8.89
8 ALB19-4_1327A_1_5.csv	14:15	38	36.0	0.02	20.1	16.9	15.2	0.08	0.001	26.9	0.001	0.0003	<0.0026583	0.28	1.09	28.3	1.17	7037	55.2	5.82	0.11	15.36	2.5	4.3	0.6	2.6	1.3	0.2	2.8	0.8	6.7	1.6	4.3	0.6	3.0	0.4	43.9	43.6	44.6	0.78	5.02
9 ALB19-4_1327A_1_6.csv	14:15	38	36.9	0.19	21.1	15.8	14.2	0.15	0.006	25.7	0.006	0.0010	0.004	1.65	4.05	48.9	1.09	4258	88.5	4.31	11.08	14.99	1.5	2.6	0.4	1.7	1.1	0.3	2.9	0.9	8.8	2.3	8.9	1.3	9.2	1.3	26.4	26.1	26.7	0.07	6.96
10 ALB19-4_1327A_1_7.csv	14:15	38	37.1	0.06	21.6	15.4	13.8	0.24	0.004	25.5	0.003	0.0004	0.009	1.74	4.87	31.4	1.09	4408	68.0	3.35	1.57	15.30	3.9	6.3	0.9	3.8	1.6	0.4	3.4	1.0	9.2	1.9	5.8	0.7	5.0	0.5	37.6	37.7	38.3	0.80	7.93
11 ALB19-4_1327A_1_8.csv	14:15	38	36.5	0.10	21.0	15.8	14.2	0.22	0.004	26.2	0.022	0.0701	0.020	0.99	5.14	31.9	1.11	6066	95.6	4.41	5.48	45.85	10.0	15.7	2.0	7.4	2.5	0.7	4.4	1.1	9.4	2.3	8.0	1.2	8.3	1.1	76.1	76.9	77.4	4.43	7.93
15 ALB19-4_1327A_2_1.csv	14:45	38	36.6	0.03	20.9	15.7	14.1	0.39	0.003	26.2	0.004	0.0004	0.007	2.83	10.09	26.8	1.24	6700	199.2	14.15	0.49	28.91	9.5	18.1	2.6	11.8	6.8	0.8	15.2	3.7	30.1	5.5	15.7	2.1	12.8	1.7	136.9	133.1	134.5	1.77	16.63
17 ALB19-4_1327A_2_3.csv	14:45	38	36.0	0.03	20.6	15.7	14.1	0.43	0.003	27.2	0.005	0.0007	0.009	2.49	10.75	23.5	1.11	8945	98.2	7.18	1.21	36.81	7.8	14.5	1.9	8.5	4.5	0.6	8.6	2.1	15.6	2.7	7.3	1.0	6.9	1.0	108.8	107.0	108.2	2.03	9.15
18 ALB19-4_1327A_2_4.csv	14:45	38	36.5	0.07	20.4	16.4	14.8	0.39	0.004	26.1	0.005	0.0009	0.011	1.78	11.77	38.8	1.09	6529	132.5	17.65	5.93	17.80	5.2	11.1	1.5	6.8	4.1	0.3	10.0	2.7	20.6	4.2	12.5	1.7	12.9	1.9	163.6	161.7	162.2	1.33	16.13
19 ALB19-4_1327A_2_5.csv	14:45	38	36.0	0.07	21.1	14.9	13.4	0.77	0.005	26.8	0.007	0.0032	0.029	2.56	19.37	25.8	1.10	8987	266.1	7.60	2.49	31.62	11.7	21.1	2.9	12.6	6.8	0.9	16.8	4.3	34.6	7.2	21.1	3.0	19.6	2.6	149.8	148.3	148.2	3.94	26.69
20 ALB19-4_1327A_2_6.csv	14:45	38	37.3	0.07	21.3	15.8	14.2	0.24	0.003	25.2	0.006	0.0007	0.003	1.36	11.83	30.5	1.15	4079	182.0	8.71	2.27	11.79	5.8	11.0	1.6	7.0	4.1	0.5	10.3	3.0	24.3	5.2	15.7	2.3	15.7	2.1	102.5	100.1	101.0	2.35	19.33
21 ALB19-4_1327A_2_7.csv	14:45	38	37.5	0.06	20.6	16.3	14.6	0.20	0.003	25.2	0.005	0.0005	0.005	1.02	9.92	30.9	1.13	4155	145.9	8.71	3.29	9.93	3.3	6.1	0.9	3.8	2.6	0.4	6.9	1.9	18.4	3.9	12.7	1.8	13.1	1.6	125.2	123.4	124.6	1.36	16.50
22 ALB19-4_1327A_3_1.csv	14:45	38	35.9	0.04	21.4	15.1	13.6	0.16	0.003	27.1	0.005	0.0008	0.004	0.84	25.51	26.9	1.40	6991	64.8	17.00	0.86	39.19	1.2	2.2	0.3	1.4	0.7	0.2	2.2	0.5	5.4	1.4	4.2	0.7	6.0	0.9	121.7	121.4	120.8	0.27	6.24
22 ALB19-4_1327A_3_1.csv (copy)	14:45	38	37.0	0.03	21.0	15.6	14.0	0.17	0.003	26.1	0.006	0.0010	0.005	0.81	27.01	26.7	1.39	6382	66.6	16.20	0.80	30.92	2.2	3.8	0.5	1.8	0.8	0.3	1.7	0.6	5.0	1.4	4.7	0.8	6.5	0.9	105.9	103.3	103.8	0.77	6.03
22 ALB19-4_1327A_3_1.csv (copy) (copy)	14:45	38	36.4	0.04	21.2	15.4	13.8	0.16	0.003	26.6	0.005	0.0009	0.004	0.83	26.30	26.8	1.09	6690	65.8	16.60	0.84	35.32	1.7	3.0	0.4	1.6	0.8	0.3	2.0	0.5	5.2	1.4	4.5	0.8	6.2	0.9	113.8	112.4	112.4	0.53	6.16
26 ALB19-4_1327A_3_2.csv	14:45	38	37.1	0.03	21.2	16.2	14.6	0.34	0.003	25.1	0.003	0.0003	0.006	2.21	7.38	34.4	1.13	3732	64.6	2.76	1.03	15.70	1.2	2.1	0.3	1.3	0.9	0.3	2.3	0.6	5.9	1.3	4.3	0.6	4.8	0.7	52.0	51.6	51.8	0.34	8.34
27 ALB19-4_1327A_3_3.csv	14:45	38	36.4	0.07	21.1	15.4	13.9	0.55	0.004	26.3	0.004	0.0025	0.017	1.66	10.51	27.7	1.93	7551	515.9	10.28	1.88	31.87	17.4	29.6	4.0	16.4	7.9	1.3	20.9	5.8	51.4	11.9	38.2	5.5	38.6	5.6	124.5	122.1	123.9	5.59	32.44
28 ALB19-4_1327A_3_4.csv	14:45	38	36.4	0.05	21.2	14.4	13.0	0.33	0.003	27.3	0.006	0.0030	0.010	2.16	22.99	24.0	1.43	9126	369.8	23.05	1.14	53.32	12.2	22.5	3.1	12.5	5.5	1.2	14.5	4.0	35.2	8.1	26.7	3.8	26.4	3.7	136.6	135.2	136.7	2.72	19.01
29 ALB19-4_1327A_3_5.csv	14:45	38	36.7	0.06	21.2	15.5	14.0	0.56	0.004	25.8	0.007	0.0007	0.015	1.95	13.41	33.7	1.05	5973	78.1	2.46	1.84	20.26	4.1	6.8	0.9	3.5	1.4	0.3	2.7	0.7	6.0	1.5	4.9	0.8	6.5	1.0	61.3	60.9	61.2	1.61	10.04
30 ALB19-4_1327A_3_6.csv	14:45	38	35.5	0.06	21.1	14.6	13.1	0.54	0.004	27.9	0.006	0.0119	0.023	1.28	22.46	22.0	1.16	10956	559.8	21.85	0.69	51.39	11.3	18.7	2.5	11.3	5.9	0.9	17.8	5.0	47.0	11.7	39.8	5.8	41.3	5.6	146.8	143.0	145.1	2.05	33.90
31 ALB19-4_1327A_3_7.csv	14:45	38	36.9	0.03	21.5	15.9	14.3	0.21	0.003	25.3	0.005	0.0008	0.004	1.15	9.96	33.4	1.44	3384	57.7	1.24	0.97	11.42	1.2	1.7	0.2	0.8	0.3	0.2	1.1	0.3	3.4	1.0	3.8	0.6	4.7	0.7	43.0	42.1	41.7	0.45	6.90
31 ALB19-4_1327A_3_7.csv (copy)	14:45	38	37.6	0.05	21.1	16.3	14.6	0.22	0.003	24.7	0.005	0.0006	0.005	1.07	8.88	34.6	1.37	3028	104.5	2.07	1.40	12.64	1.7	2.8	0.4	1.6	0.5	0.3	1.9	0.6	6.3	1.6	6.5	1.1	8.1	1.1	39.7	40.6	39.0	1.26	11.60
31 ALB19-4_1327A_3_7.csv (copy) (copy)	14:45	38	37.3	0.04	21.3	16.1	14.5	0.22	0.003	25.0	0.005	0.0007	0.005	1.09	9.36	34.1	1.08	3198	82.2	1.69	1.20	12.05	1.5	2.3	0.3	1.2	0.4	0.3	1.5	0.4	4.9	1.3	5.2	0.8	6.5	0.9	41.4	41.3	40.4	0.89	9.34
32 ALB19-4_1327A_3_8.csv	14:45	38	36.9	0.03	21.1	16.2	14.6	0.17	0.003	25.5	0.004	0.0007	0.003	1.04	8.76	31.2	1.10	3864	39.2	4.21	0.98	7.54	0.3	0.6	0.1	0.5	0.5	0.1	1.5	0.3	3.6	0.8	3.0	0.5	4.0	0.6	107.1	105.7	106.4	0.02	8.36
33 ALB19-4_1327A_3_9.csv	14:45	38	36.6	0.08	20.8	16.3	14.6	0.31	0.004	25.9	0.003	0.0005	0.007	1.74	7.73	43.0	1.15	4867	55.9	2.38	5.16	9.57	2.9	4.9	0.6	2.3	0.8	0.2	1.8	0.5	4.7	1.2	4.1	0.6	4.1	0.8	64.8	64.3	64.6	2.00	6.36
37 ALB19-4_1327A_3_10.csv	15:15	38	36.6	0.08	21.4	15.6	14.0	0.21	0.003	25.9	0.006	0.0015	<0.0027758	1.52	12.23	35.1	1.27	4863	254.0	13.03	2.22	23.62	3.9	8.0	1.1	5.0	2.8	0.8	8.1	2.4	21.0	5.0	18.4	2.7	20.1	2.8	101.4	98.4	99.1	0.70	17.37
37 ALB19-4_1327A_3_10.csv (copy)	15:15	38	37.1	0.09	21.3	15.5	13.9	0.21	0.004	25.7	0.006	0.0063	<0.0040128	1.27	17.16	34.3	1.88	5541	354.3	11.67	2.12	29.64	5.3	10.2	1.5	6.8	3.4	0.9	9.7	3.1	30.9	7.6	26.3	3.7	27.0	3.7	102.0	101.3	99.9	0.75	22.23
38 ALB19-4_1327A_4_1.csv	15:15	38	36.6	0.03	20.6	16.3	14.7	0.29	0.002	26.0	0.002	<0.00029722	0.005	2.03	7.02	28.6	1.16	5990	67.1	7.26	0.32	20.73	2.5	4.7	0.7	2.8	1.2	0.2	2.7	0.7	6.6	1.5	4.8	0.8	5.6	0.8	126.2	125.9	125.6	3.01	7.12
39 ALB19-4_1327A_4_2.csv	15:15	38	37.0	0.05	21.1	16.2	14.6	0.24	0.003	25.2	0.005	0.0007	0.005	1.37	9.80	29.6	1.16	3677	42.8	3.71	1.73	8.54	1.8	3.4	0.5	2.0	1.0	0.1	1.9	0.5	4.6	1.1	3.3	0.5	4.2	0.6	86.3	84.5	85.3	0.90	7.67
40 ALB19-4_1327A_4_3.csv	15:15	38	36.9	0.03	21.5	16.0	14.4	0.33	0.003	25.2	0.006	0.0007	0.01	2.58	11.12	37.9	1.50	3959	91.8	2.52	0.68	8.41	2.0	3.8	0.6	2.8	1.7	0.4	3.4	0.9	8.5	2.0	6.5	1.1	7.2	1.0	44.6	45.3	45.3	1.01	8.75
40 ALB19-4_1327A_4_3.csv (copy)	15:15	38	37.5	0.04	20.8	16.2	14.6	0.34	0.003	24.9	0.006	0.0007	0.01	3.00	10.84	37.9	1.42	4538	93.5	2.17	1.65	12.64	4.1	7.5	1.0	4.1	1.7	0.5	4.0	1.0	8.6	2.0	6.6	1.1	8.3	1.2	61.7	60.3	61.1	3.64	8.67
40 ALB19-4_1327A_4_3.csv (copy) (copy)	15:15	38	37.2	0.04	21.1	16.1	14.5	0.34	0.003	25.1	0.006	0.0007	0.01	2.83	10.99	37.9	1.13	4276	92.8	2.35	1.21	10.77	3.2	5.9	0.8	3.5	1.7	0.5	3.8	1.0	8.6	2.0	6.5	1.1	7.8	1.1	54.0	53.5	54.0	2.45	8.71
41 ALB19-4_1327A_4_4.csv	15:15	38	37.3	0.03	21.3	16.4	14.7	0.20	0.003	24.7	0.002	<0.00028954	<0.0025835	1.61	5.88	35.6	1.13	2591	73.6	2.79	0.63	3.61	1.4	2.7	0.4	1.9	0.9	0.3	2.7	0.7	6.6	1.6	5.4	0.8	6.8	1.0	48.0	47.8	47.9	0.46	10.78
42 ALB19-4_1327A_4_5.csv	15:15	38	37.1	0.03	21.0	16.4	14.8	0.23	0.002	25.2	0.003	0.0004	0.003	1.58	5.93	33.3	1.10	3310	105.3	7.68	0.57	4.58	1.6	3.2	0.5	2.5	1.5	0.3	4.0	1.2	10.8	2.5	7.9	1.3	9.7	1.5	101.2	99.0	99.6	0.16	12.06
43 ALB19-4_1327A_4_6.csv	15:15	38	37.1	0.02	21.3	16.3	14.6	0.28	0.003	25.0	0.004	0.0003	0.003	2.61	8.81	38.9	1.07	2998	72.1	1.57	0.46	4.54	1.5	3.0	0.5	2.1	1.2	0.3	2.8	0.8	6.3	1.6	5.5	0.7	6.2	0.9	43.7	43.9	43.8	0.15	8.75
44 ALB19-4_1327A_4_7.csv	15:15	38	36.7	0.03	21.1	16.6	14.9	0.14	0.003	25.5	0.002	<0.00033183	<0.002963	1.19	3.97	36.0	1.34	2902	69.9	3.48	0.71	2.95	3.0	5.8	0.7	2.8	1.1	0.2	2.2	0.7	7.2	1.7	5.4	0.8	6.7	1.1	82.4	82.6	83.2	1.66	10.89
44 ALB19-4_1327A_4_7.csv (copy)	15:15	38	37.4	0.03	20.7	16.8	15.1	0.16	0.003	24.8	0.002	<0.00035435	<0.0031645	1.51	4.51	35.7	1.44	3111	67.4	3.04	0.58	3.95	2.2	4.3	0.6	2.1	1.0	0.2	3.1	0.7	7.0	1.6	5.2	0.8	5.9	1.0	78.6	78.3	79.2	1.42	10.30
44 ALB19-4_1327A_4_7.csv (copy) (copy)	15:15	38	37.0	0.03	20.9	16.7	15.0	0.15	0.003	25.2	0.002	<0.00026869	<0.0023974	1.34	4.22	35.9	1.07	3002	68.8	3.26	0.65	3.45	2.6	5.1	0.7	2.5	1.0	0.2	2.6	0.7	7.1	1.7	5.3	0.8	6.3	1.0	80.7	80.6	81.4	1.58	10.60

Sample: ALB19-11B_A	Time	Spot size	SiO2	TiO2	Al2O3	FeO3	FeO	MnO	MgO	CaO	Na2O	K2O	P2O5	Li7	B11	V51	Cr53	Sr88	Y89	Zr90	Nb93	Ba137	La139	Ce140	Pr141	Nd146	Sm147	Eu151	Gd157	Tb159	Dy163	Ho165	Er167	Tm169	Yb173	Lu175	Pb206	Pb207	Pb208	Th232	U238
		um	wt.%	wt.%	wt.%	wt.%	wt.%	wt.%	wt.%	wt.%	wt.%	wt.%	wt.%	µg/g	µg/g	µg/g	µg/g	µg/g	µg/g	µg/g	µg/g	µg/g	µg/g	µg/g	µg/g	µg/g	µg/g	µg/g	µg/g	µg/g	µg/g	µg/g	µg/g	µg/g	µg/g	µg/g	µg/g	µg/g	µg/g	µg/g
67 ALB19-11B_A_1.csv	14:30	24	37.7	0.06	20.4	17.1	15.4	0.37	0.011	24.4	0.005	<0.00060046	<0.0084873	0.72	2.47	187.7	6.41	4558	31.0	3.98	0.044	7.42	0.92	3.73	0.71	3.95	1.39	0.62	1.98	0.29	3.01	0.87	3.77	0.44	3.43	0.46	23.0	23.8	23.2	0.155	8.33
71 ALB19-11B_A_2.csv	14:30	24	38.2	0.09	20.5	16.9	15.2	0.22	0.012	24.0	0.004	<0.00059456	<0.0078807	0.79	3.19	182.8	5.88	3100	36.7	5.78	0.065	6.28	0.50	2.10	0.45	2.67	1.28	0.57	1.80	0.37	3.07	0.93	4.52	0.62	4.69	0.64	20.8	21.1	20.6	0.085	10.81
72 ALB19-11B_A_3.csv	14:30	24	35.7	0.05	19.6	16.8	15.1	0.48	0.004	27.3	0.005	<0.00060569	0.009	0.24	2.67	170.4	4.33	12766	42.1	3.21	<0.0303347	30.32	8.42	15.77	2.03	10.14	2.81	1.68	4.38	0.67	5.97	1.30	4.33	0.61	4.39	0.84	43.8	44.3	44.8	0.976	9.83
73 ALB19-11B_A_4.csv	14:30	24	37.1	0.03	19.9	17.5	15.7	0.43	0.006	25.1	0.003	<0.00062957	<0.0083822	0.45	1.69	184.1	<2.7561	6031	13.5	1.80	<0.026436	12.26	0.80	2.71	0.48	2.75	1.11	0.58	1.61	0.19	2.00	0.37	1.29	0.14	0.88	0.10	39.1	40.9	40.0	<0.042593	2.47
74 ALB19-11B_A_5.csv	14:30	24	36.0	0.07	20.2	16.5	14.9	0.52	0.005	26.6	0.004	<0.00066379	0.020	0.27	1.45	165.5	7.43	9876	31.6	3.86	0.052	17.44	2.60	5.62	0.93	5.44	1.81	1.18	3.04	0.53	3.99	0.79	3.10	0.50	3.87	0.68	36.6	36.3	36.6	<0.034212	7.99
74 ALB19-11B_A_5.csv (copy)	14:30	24	37.3	0.07	19.6	16.9	15.2	0.47	0.005	25.6	0.003	<0.00073327	0.016	0.29	1.56	162.3	7.13	9816	28.9	4.42	0.122	18.77	3.80	6.84	0.95	5.45	1.76	1.18	2.54	0.56	3.80	0.84	3.25	0.36	3.43	0.57	42.1	41.9	43.9	<0.037793	8.19
75 ALB19-11B_A_6.csv	14:30	24	37.8	0.06	20.2	17.0	15.3	0.32	0.007	24.6	0.004	<0.00062006	0.009	0.60	1.60	200.8	4.05	4979	21.9	2.19	0.040	7.21	0.87	1.70	0.30	1.59	0.57	0.50	1.09	0.21	2.07	0.54	3.00	0.37	2.58	0.33	24.8	26.5	25.0	<0.036514	3.78
76 ALB19-11B_A_7.csv	14:30	24	37.1	0.04	19.1	17.9	16.1	0.43	0.004	25.5	0.002	<0.00057546	0.008	0.29	1.11	182.7	6.27	8080	18.2	5.62	<0.038743	17.68	0.99	2.45	0.43	2.58	0.97	0.64	1.56	0.30	2.43	0.53	1.78	0.19	1.37	0.23	43.9	46.4	46.0	0.026	6.06
77 ALB19-11B_A_8.csv	14:30	24	37.9	0.14	20.7	17.3	15.6	0.12	0.006	24.0	0.001	<0.00061874	<0.0081948	0.25	0.95	258.9	<2.749	1492	89.8	5.45	0.021	0.63	0.60	1.07	0.20	1.27	0.81	0.87	2.89	0.58	7.02	2.38	11.95	1.79	9.34	1.16	9.2	10.1	9.8	<0.032562	4.18
80 ALB19-11B_A_9.csv	14:30	24	38.1	0.07	19.9	17.3	15.6	0.31	0.008	24.3	0.014	0.001	0.012	0.36	2.87	201.3	4.50	4623	16.1	3.47	0.102	11.47	0.58	1.65	0.31	1.87	0.63	0.39	0.99	0.21	2.18	0.41	1.68	0.30	2.52	0.39	26.3	27.5	28.0	<0.046004	5.54
81 ALB19-11B_A_10.csv	14:30	24	37.0	0.06	19.9	16.2	14.6	0.39	0.004	26.3	0.002	<0.00057365	0.017	0.39	2.99	148.9	7.42	10439	25.7	3.38	<0.031127	43.15	3.69	9.42	1.56	8.31	2.57	0.91	2.99	0.53	3.66	0.78	2.97	0.44	2.50	0.43	64.9	66.8	65.7	<0.032928	5.87
82 ALB19-11B_A_11.csv	14:30	24	37.9	0.07	20.4	16.8	15.1	0.19	0.008	24.6	0.005	<0.00062571	<0.0082272	0.77	3.13	259.4	<2.8149	4653	54.2	3.40	0.193	13.55	28.74	61.69	8.56	43.47	13.55	4.59	17.75	2.42	12.99	2.19	5.28	0.59	3.63	0.49	31.3	31.8	31.8	<0.032267	15.40
83 ALB19-11B_A_12.csv	14:30	24	37.0	0.05	20.4	15.8	14.2	0.56	0.004	26.0	0.003	<0.00064259	0.022	<0.22579	2.56	135.2	<2.8063	10393	23.8	2.19	<0.042214	46.83	1.67	5.45	0.95	5.87	2.12	0.52	2.52	0.41	3.08	0.80	3.10	0.48	2.95	0.31	54.7	59.1	57.5	<0.026138	5.80
84 ALB19-11B_A_13.csv	14:30	24	38.5	0.10	20.6	16.3	14.7	0.26	0.005	24.1	0.005	0.0009	0.013	0.30	3.41	233.7	<2.9463	4058	36.5	2.85	0.155	12.73	3.74	9.28	1.47	8.11	3.19

Sample: ALB19_11B_C	Time	Spot size	SiO2	TiO2	Al2O3	Fe2O3	FeO	MnO	MgO	CaO	Na2O	K2O	P2O5	Li7	B11	V51	Cr53	Sr88	Y89	Zr90	Nb93	Ba137	La139	Ce140	Pr141	Nd146	Sm147	Eu151	Gd157	Tb159	Dy163	Ho165	Er167	Tm169	Yb173	Lu175	Pb206	Pb207	Pb208	Th232	U238
		um	wt.%	wt.%	wt.%	wt.%	wt.%	wt.%	wt.%	wt.%	wt.%	wt.%	wt.%	µg/g	µg/g	µg/g	µg/g	µg/g	µg/g	µg/g	µg/g	µg/g	µg/g	µg/g	µg/g	µg/g	µg/g	µg/g	µg/g	µg/g	µg/g	µg/g	µg/g	µg/g	µg/g	µg/g	µg/g	µg/g	µg/g	µg/g
19 ALB19-11B_C_1_1.csv	14:30	30	38.4	0.14	21.4	15.80	14.23	0.14	0.005	24.0	0.0052	0.0005	<0.0069818	0.56	2.42	212.6	2.03	2570	14.8	2.7	0.067	3.15	1.2	3.6	0.7	4.2	1.6	0.5	2.6	0.4	2.6	0.5	1.7	0.3	1.5	0.3	17.5	18.0	18.0	<0.013384	2.07
20 ALB19-11B_C_1_2.csv	14:30	30	37.4	0.06	20.5	16.12	14.53	0.59	0.002	25.2	0.0020	<0.00043168	0.020	<0.13336	1.49	129.5	<1.7914	8084	15.1	2.7	<0.0168	14.31	2.3	5.7	1.0	6.7	2.9	1.0	3.9	0.5	2.9	0.5	1.3	0.2	1.9	0.4	30.7	32.3	31.5	<0.020093	1.92
24 ALB19-11B_C_1_3.csv	14:30	30	36.9	0.05	20.0	17.07	15.38	0.32	0.005	25.7	0.0045	0.0022	0.010	0.32	1.48	208.0	4.00	7613	24.2	3.3	0.062	14.94	1.9	4.5	0.7	3.5	1.4	0.9	2.0	0.3	2.8	0.7	2.2	0.3	1.7	0.3	44.1	45.9	45.6	0.074	5.22
26 ALB19-11B_C_1_5.csv	14:30	30	38.2	0.09	21.7	15.91	14.33	0.11	0.002	23.9	0.0012	<0.00042646	<0.0064144	<0.14095	1.14	238.8	<1.8379	858	41.4	0.3	<0.016131	0.84	0.2	0.7	0.2	1.5	1.2	0.6	3.2	0.7	6.3	1.6	5.2	0.7	4.6	0.5	7.8	8.1	8.3	<0.01903	0.91
27 ALB19-11B_C_1_6.csv	14:30	30	37.5	0.05	20.2	17.18	15.47	0.47	0.004	24.6	0.0011	<0.00045335	0.013	0.27	1.39	196.9	4.14	5589	28.3	4.1	<0.025906	14.54	1.0	3.5	0.7	4.1	1.3	0.7	2.2	0.3	3.3	0.9	3.2	0.4	2.5	0.4	33.6	34.9	35.1	0.050	6.01
28 ALB19-11B_C_1_7.csv	14:30	30	36.7	0.06	19.9	16.91	15.23	0.76	0.003	25.7	0.0052	0.00048	0.021	0.32	1.90	149.8	6.13	8793	23.3	3.3	<0.023274	22.05	2.2	7.5	1.4	8.0	2.3	1.1	3.2	0.5	3.2	0.7	2.4	0.3	3.0	0.4	39.6	41.8	41.2	0.014	4.38
29 ALB19-11B_C_1_8.csv	14:30	30	37.9	0.10	21.5	16.01	14.43	0.19	0.004	24.2	0.0044	<0.00046455	<0.0069294	0.26	2.06	210.6	4.04	2219	15.7	1.2	0.048	2.94	0.1	0.7	0.2	1.0	0.5	0.2	0.8	0.2	2.0	0.5	2.0	0.3	2.0	0.2	14.9	14.1	14.5	<0.017643	1.49
30 ALB19-11B_C_1_9.csv	14:30	30	37.4	0.09	20.8	16.16	14.56	0.37	0.004	25.1	0.0011	<0.00044101	0.013	0.20	1.24	181.6	3.18	5926	13.8	2.6	0.034	10.85	2.0	6.2	1.1	6.6	2.4	0.7	3.1	0.4	2.9	0.5	1.7	0.3	1.8	0.3	28.4	29.3	28.9	<0.018725	2.27
33 ALB19-11B_C_1_10.csv	14:30	30	36.8	0.05	19.9	17.22	15.51	0.58	0.003	25.5	0.0022	<0.00042363	0.013	0.22	1.69	177.1	2.11	8394	15.9	2.8	0.071	18.74	1.6	5.3	0.9	5.8	1.8	0.7	1.9	0.4	2.2	0.5	1.7	0.2	1.4	0.2	39.0	41.3	40.8	0.065	3.10
34 ALB19-11B_C_1_11.csv	14:30	30	37.0	0.07	20.6	15.96	14.38	0.62	0.002	25.6	0.0012	<0.00041449	0.028	<0.14111	0.95	134.2	2.82	8613	17.0	3.6	<0.019789	14.31	3.6	11.5	2.0	11.7	3.5	0.9	3.3	0.4	2.5	0.5	1.7	0.3	2.8	0.5	32.3	33.8	33.2	<0.023361	2.96
35 ALB19-11B_C_1_12.csv	14:30	30	36.7	0.03	20.7	16.80	15.14	0.19	0.004	25.5	0.0012	<0.0005051	<0.0074635	0.31	1.26	223.4	2.78	5107	45.0	4.1	0.033	6.59	0.9	1.9	0.3	2.4	1.4	1.2	3.5	0.6	5.5	1.3	4.2	0.5	2.9	0.4	46.8	49.7	48.3	<0.024187	9.82
35 ALB19-11B_C_1_12.csv (copy)	14:30	30	37.9	0.04	20.3	17.08	15.39	0.20	0.005	24.5	0.0012	<0.00049331	<0.0072879	0.51	1.06	228.3	<1.9827	4132	47.7	4.1	0.028	7.50	0.7	1.6	0.3	2.0	1.4	1.2	2.8	0.7	5.5	1.5	4.4	0.5	2.8	0.4	38.9	39.7	40.8	<0.022652	10.81
35 ALB19-11B_C_1_12.csv (copy) (copy)	14:30	30	37.5	0.03	20.5	16.96	15.28	0.20	0.004	24.8	0.0012	<0.00042531	<0.0062813	0.44	1.10	225.4	1.93	4569	46.0	4.1	0.032	7.13	0.8	1.7	0.3	2.2	1.4	1.2	3.2	0.6	5.5	1.4	4.2	0.5	2.7	0.4	42.3	44.0	44.2	<0.017946	10.30
36 ALB19-11B_C_1_13.csv	14:30	30	36.7	0.05	19.7	17.12	15.43	0.68	0.002	25.7	0.0015	<0.00043655	<0.0064448	0.14	1.35	172.1	<1.8733	8776	15.5	3.3	<0.022381	22.40	2.9	8.4	1.5	8.8	3.2	0.9	3.1	0.5	2.6	0.5	1.5	0.2	0.8	0.1	42.2	44.0	43.1	<0.017076	2.91
37 ALB19-11B_C_1_14.csv	14:30	30	36.8	0.03	19.7	17.95	16.17	0.48	0.003	25.1	0.0019	<0.00042865	0.008	0.51	1.18	195.7	2.43	5636	10.6	2.8	0.138	11.91	0.7	3.0	0.6	3.4	1.3	0.4	2.0	0.3	2.2	0.4	0.9	0.1	0.5	0.1	41.7	41.7	42.4	<0.016391	1.64
38 ALB19-11B_C_1_15.csv	14:30	30	36.8	0.03	19.5	17.82	16.05	0.45	0.003	25.5	0.0038	<0.00041459	<0.0061222	0.24	0.99	209.0	<1.8263	7322	12.1	2.7	0.030	16.25	1.3	4.3	0.8	4.7	1.7	0.4	2.0	0.2	1.6	0.3	0.9	0.1	0.4	0.1	46.5	48.9	48.7	<0.021847	2.60
39 ALB19-11B_C_1_16.csv	14:30	30	35.8	0.03	20.1	17.68	15.92	0.46	0.002	26.0	0.0023	<0.00052087	<0.0076492	<0.19577	1.41	216.5	<2.3399	7236	14.2	2.7	<0.040767	16.29	1.2	4.3	0.8	4.9	1.9	0.6	2.3	0.3	1.8	0.4	1.0	0.1	0.7	0.1	45.7	46.1	46.7	<0.031788	2.87
42 ALB19-11B_C_1_17.csv	14:30	30	36.9	0.08	20.3	16.65	15.00	0.47	0.003	25.5	<0.0003973	<0.00043134	0.008	0.23	0.70	189.6	3.96	7426	13.4	2.3	<0.020837	13.69	1.2	4.4	0.8	5.1	1.9	0.5	2.8	0.4	2.5	0.5	1.5	0.1	0.6	0.1	35.5	36.8	36.8	<0.018958	1.75
43 ALB19-11B_C_1_18.csv	14:30	30	37.3	0.08	21.2	16.02	14.43	0.32	0.004	25.0	0.0031	0.0006	0.012	<0.15814	1.70	254.5	2.28	4608	44.1	2.4	0.052	6.40	1.8	5.4	1.0	5.9	2.1	0.8	2.9	0.4	3.0	1.1	4.8	0.7	5.2	0.7	21.2	21.1	21.2	<0.022381	5.69
44 ALB19-11B_C_1_19.csv	14:30	30	36.5	0.04	19.4	17.84	16.07	0.52	0.002	25.7	0.0007	<0.00044864	0.008	0.15	0.80	201.3	<1.9738	8345	9.8	2.7	0.011	21.43	1.8	5.7	1.0	6.4	2.4	0.6	2.4	0.3	1.9	0.3	0.9	0.1	0.4	<0.040423	43.6	45.3	46.0	<0.024518	1.57
45 ALB19-11B_C_1_20.csv	14:30	30	36.6	0.06	20.4	16.51	14.88	0.79	0.032	25.6	<0.0000449	<0.00043678	0.018	1.56	0.93	134.1	3.34	8698	19.3	3.7	<0.028661	15.46	3.4	11.0	2.0	11.0	3.6	0.9	3.7	0.5	3.2	0.7	1.9	0.3	2.1	0.4	33.4	34.9	35.0	0.017	3.45
46 ALB19-11B_C_1_21.csv	14:30	30	36.5	0.08	20.5	15.60	14.05	0.42	0.002	26.7	0.0037	<0.00043747	0.017	0.14	1.93	146.3	6.70	11097	28.9	4.2	0.023	22.71	3.0	10.5	1.9	10.7	3.5	1.0	3.5	0.5	3.4	0.8	2.7	0.5	4.0	0.7	35.5	37.6	36.7	<0.020513	5.22
47 ALB19-11B_C_1_22.csv	14:30	30	37.2	0.05	20.7	16.53	14.89	0.49	0.005	24.9	0.0024	<0.00043085	0.013	0.56	1.82	192.9	3.50	5322	19.3	2.7	<0.02497	7.95	1.8	6.4	1.1	6.4	2.3	0.6	2.7	0.5	3.6	0.6	2.1	0.3	2.2	0.3	25.3	25.7	25.2	<0.020078	2.42
48 ALB19-11B_C_1_23.csv	14:30	30	37.2	0.09	20.8	16.24	14.63	0.48	0.005	25.1	0.0028	<0.00041676	0.017	0.36	1.49	190.4	4.47	6358	15.6	2.8	0.055	10.76	1.8	6.1	1.1	6.4	2.3	0.6	2.7	0.4	2.5	0.5	1.9	0.3	2.7	0.4	26.5	27.1	27.1	<0.013265	3.41
52 ALB19-11B_C_2_1.csv	14:30	30	37.5	0.09	21.2	16.57	14.93	0.20	0.007	24.4	0.0080	0.00071	<0.0061103	0.46	2.05	278.8	3.81	2532	75.1	2.4	0.087	4.44	0.4	1.7	0.3	2.3	1.0	0.9	2.8	0.7	6.1	1.9	8.7	1.1	6.7	0.8	19.9	20.8	21.0	<0.020258	8.68
53 ALB19-11B_C_2_2.csv	14:30	30	37.2	0.08	20.8	16.30	14.69	0.38	0.005	25.1	0.0029	<0.00043284	0.011	0.33	2.54	214.7	2.64	6196	41.3	2.8	0.076	17.34	1.1	3.5	0.6	3.5	1.1	0.9	2.2	0.4	3.4	1.2	4.0	0.6	4.9	0.6	33.7	35.1	34.0	<0.014444	7.23
54 ALB19-11B_C_2_3.csv	14:30	30	37.0	0.04	19.7	17.34	15.62	0.48	0.007	25.5	0.0045	<0.00043639	0.010	0.83	2.12	208.2	<1.9706	7478	29.2	2.6	0.040	14.92	0.5	1.1	0.2	1.2	0.7	1.0	1.7	0.3	3.4	0.9	2.5	0.3	1.4	0.2	30.6	31.6	31.5	<0.017528	5.74
55 ALB19-11B_C_2_4.csv	14:30	30	37.4	0.07	21.0	16.68	15.03	0.23	0.006	24.6	0.0027	<0.00044158	<0.0063075	0.45	2.08	263.7	<1.952	3388	67.7	3.9	0.033	8.21	0.7	2.2	0.4	2.8	1.4	1.1	2.6	0.6	6.1	1.8	6.6	0.9	5.5	0.7	25.0	24.4	25.4	<0.020906	11.44
56 ALB19-11B_C_2_5.csv	14:30	30	38.0	0.11	20.6	17.35	15.63	0.16	0.015	23.8	<0.0003962	<0.00042132	<0.0060269	0.22	0.60	364.4	<1.8852	1074	13.0	1.0	0.084	<0.17556	0.3	1.2	0.2	1.7	0.9	0.3	1.2	0.2	1.0	0.3	1.3	0.2	2.1	0.5	13.3	13.5	13.8	<0.013683	5.50
57 ALB19-11B_C_2_6.csv	14:30	30	37.9	0.12	21.3	16.53	14.89	0.13	0.003	24.0	0.0016	<0.00042983	<0.0061339	0.13	1.22	226.0	5.42	853	37.6	1.8	<0.027209	0.75	0.1	0.4	0.1	0.8	0.5	0.2	1.4	0.4	3.3	1.0	5.2	0.8	5.2	0.6	8.3	8.8	8.5	<0.019526	1.16
58 ALB19-11B_C_2_7.csv	14:30	30	36.7	0.04	19.5	17.80	16.04	0.53	0.002	25.5	0.0004	<0.00039802	0.008	0.19	0.46	194.8	<1.8016	7512	10.8	2.4	<0.029289	16.76	1.6	4.4	0.8	5.4	2.0	0.7	2.7	0.4	2.0	0.4	0.7	0.1	0.4	0.0	39.3	41.2	41.0	<0.023766	1.35
61 ALB19-11B_C_2_8.csv	14:30	30	36.9	0.03	19.5	18.03	16.24	0.38	0.002	25.3	0.0028	<0.00035867	0.010	0.29	0.79	211.4	<1.5641	6445	14.8	3.0	<0.015741	14.92	2.3	6.3	1.2	7.8	3.2	1.0	3.9	0.6	3.4	0.6	1.3	0.1	0.6	0.1	42.8	44.6	44.1	<0.016917	3.30
62 ALB19-11B_C_2_9.csv	14:30	30	37.4	0.10	20.6	16.80	15.13	0.29	0.009	24.8	0.0011	<0.00041522	0.014	0.32	0.96	296.9	4.52	4300	31.0	3.2	0.094	5.54	0.7	2.5	0.4	2.7	1.2	0.6	2.0	0.4	3.5	0.9	3.1	0.5	3.8	0.7	21.4	21.9	22.4	<0.015792	7.15
63 ALB19-11B_C_2_10.csv	14:30	30	38.0	0.03	20.8	16.79	15.12	0.23	0.006	24.1	0.0028	<0.00041471	<0.0059115	0.64	1.92	207.1	1.93	3085	14.1	4.3	0.052	5.24	0.6	1.8	0.4	2.2	1.0	0.4	1.9	0.4	2.4	0.5	1.4	0.3	1.6	0.3	23.6	23.6	23.6	<0.024415	2.77
64 ALB19-11B_C_2_11.csv	14:30	30	37.3	0.03	20.2	17.42	15.69	0.29	0.004	24.8	0.0016	<0.00039669	<0.005645	0.48	1.09	195.1	<1.7817	4967	14.7	3.8	0.049	7.17	0.4	1.7	0.3	2.0	0.8	0.4	1.6	0.3	2.2	0.4	1.3	0.2	1.0	0.2	47.4	48.0	48.2	<0.018723	2.62
65 ALB19-11B_C_2_12.csv	14:30	30	37.7	0.11	20.6	17.48	15.75	0.16	0.015	24.0	0.0005	<0.00039517	<0.0055838	0.31	0.68	262.2	<1.7424	1466	11.5	1.7	0.061	0.44	0.3	1.0	0.2	1.5	1.1	0.4	1.6	0.3	1.6	0.3	1.2	0.2	1.9	0.4	14.5	15.2	15.0	<0.01737	3.49
66 ALB19-11B_C_2_13.csv	14:30	30	36.8	0.04	20.3	17.19	15.49	0.42	0.004	25.3	0.0057	0.00078	<0.0054758	0.30	2.64	198.7	<1.7313	6496	16.9	4.4	0.053	17.94	1.3	4.0	0.7	4.6	1.7	0.6	2.7	0.4	2.8	0.6	1.7	0.2	1.6	0.2	42.0	43.3	42.6	<0.0158	3.02

Sample: ALB19-18	Time	Analysis #	Spot size	SiO2	TiO2	Al2O3	Fe2O3	FeO	MnO	MgO	CaO	Na2O	K2O	P2O5	Li7	B11	V51	Cr53	Sr88	Y89	Zr90	Nb93	Ba137	La139	Ce140	Pr141	Nd146	Sm147	Eu151	Gd157	Tb159	Dy163	Ho165	Er167	Tm169	Yb173	Lu175	Pb206	Pb207	Pb208	Th232	U238
			um	wt.%	wt.%	wt.%	wt.%	wt.%	wt.%	wt.%	wt.%	wt.%	wt.%	wt.%	wt.%	µg/g	µg/g	µg/g	µg/g	µg/g	µg/g	µg/g	µg/g	µg/g	µg/g	µg/g	µg/g	µg/g	µg/g	µg/g	µg/g	µg/g	µg/g	µg/g	µg/g	µg/g	µg/g	µg/g	µg/g	µg/g	µg/g	µg/g
103.csv	11:30	1_4	38	35.0	0.061	20.4	15.2	13.7	0.859	0.004	28.3	0.002	<0.00025956	0.048	0.23	1.19	99.2	53.5	12322	22.8	4.05	<0.010006	15.90	1.61	2.94	0.38	1.89	0.56	1.09	1.05	0.20	1.80	0.49	2.26	0.48	4.91	0.86	29.4	29.3	30.1	2.89	7.18
103.csv (copy)	11:30	1_5_a	38	36.4	0.024	19.3	17.9	16.1	0.161	0.003	26.4	0.001	<0.00029506	0.041	2.10	162.2	24.9	7330	16.3	8.40	<0.01674	12.19	0.46	0.75	0.14	0.61	0.15	0.55	0.60	0.11	1.39	0.39	1.59	0.22	1.46	0.25	74.7	77.6	78.1	0.23	5.72
103.csv (copy) (copy)	11:30	1_5_b	38	36.0	0.027	19.5	17.5	15.8	0.177	0.006	26.7	0.002	0.026	0.003	0.49	3.57	157.8	24.6	7609	18.5	8.90	0.014	18.84	0.49	0.86	0.14	0.67	0.20	0.60	0.49	0.11	1.41	0.44	1.83	0.24	1.69	0.26	72.5	75.3	75.7	0.29	8.55
103.csv (copy) (copy) (copy)	11:30	1_7	38	35.6	0.053	19.7	16.7	15.1	0.497	0.005	27.4	0.001	<0.00025779	0.010	0.49	1.70	134.2	50.1	9770	35.4	5.50	<0.01601	30.78	1.05	1.98	0.26	1.34	0.41	1.08	0.85	0.20	2.18	0.76	3.44	0.46	2.94	0.43	57.4	58.3	59.0	0.90	13.63
103.csv (copy) (copy) (copy) (copy) (copy)	11:30	1_8	38	35.9	0.016	19.8	17.6	15.9	0.129	0.002	26.6	0.000	<0.00026479	<0.0022152	0.30	0.42	187.8	4.5	6749	16.6	3.87	0.019	8.70	0.86	1.07	0.16	1.00	0.50	0.56	1.36	0.26	2.04	0.49	1.30	0.15	1.10	0.18	95.1	99.6	97.9	0.03	4.57
103.csv (copy) (copy) (copy) (copy) (copy) (copy)	11:30	1_9	38	36.0	0.014	19.9	17.3	15.6	0.128	0.002	26.7	0.001	<0.00027674	0.002	0.27	1.22	214.8	9.6	6933	16.1	3.06	<0.014414	7.24	0.53	1.08	0.16	0.73	0.30	0.47	0.50	0.10	1.22	0.38	1.19	0.14	1.02	0.16	88.8	88.5	88.5	0.03	5.12
108.csv	11:30	1_10_a	38	36.4	0.098	20.1	16.6	14.9	0.170	0.005	26.6	0.001	0.004	0.005	0.55	1.32	178.4	42.6	7507	26.6	4.11	0.050	22.73	4.37	7.40	0.77	3.08	0.61	1.47	1.04	0.23	1.83	0.62	2.45	0.29	2.59	0.45	52.5	54.4	53.7	0.57	7.48
108.csv (copy)	11:30	1_10_b	38	36.0	0.094	20.3	16.5	14.9	0.178	0.006	26.9	0.001	0.008	0.004	0.49	1.38	181.9	38.6	7473	26.3	4.23	0.065	19.84	6.49	11.00	1.16	4.46	0.90	2.09	1.39	0.26	1.99	0.63	2.48	0.34	2.72	0.38	50.7	52.0	51.9	0.99	6.96
108.csv (copy) (copy)	12:30	1_15	38	36.4	0.037	19.9	17.2	15.5	0.549	0.006	26.0	0.002	<0.00030112	0.009	0.52	0.69	190.9	8.4	6867	31.7	3.26	<0.012016	16.07	0.54	1.24	0.18	0.96	0.30	0.79	0.87	0.17	2.35	0.75	2.29	0.23	1.17	0.13	35.2	36.1	37.0	0.26	4.54
108.csv (copy) (copy) (copy)	12:00	1_16	38	36.4	0.025	20.3	17.1	15.4	0.152	0.003	26.1	0.001	<0.00027243	0.003	0.34	1.13	184.1	5.6	5009	20.1	4.72	0.035	6.48	0.58	0.74	0.13	0.54	0.21	0.35	0.57	0.12	1.46	0.53	1.98	0.30	1.96	0.26	61.9	64.6	65.0	0.08	5.61
108.csv (copy) (copy) (copy) (copy)	12:00	1_17	38	35.5	0.056	20.5	15.8	14.2	0.857	0.003	27.1	0.001	<0.00032074	0.034	0.10	0.68	120.2	9.2	9283	59.1	3.59	<0.013331	14.79	2.53	3.93	0.53	2.68	1.01	2.58	2.81	0.55	4.54	1.50	4.94	0.89	7.85	1.40	32.1	32.4	32.7	0.09	16.57
116.csv	12:00	1_18	38	35.9	0.032	19.5	17.7	15.9	0.551	0.003	26.3	0.001	<0.00026756	0.009	0.18	0.76	216.0	14.2	7002	28.7	2.25	0.016	15.69	1.81	3.72	0.51	2.36	0.66	1.09	1.34	0.22	2.31	0.68	2.10	0.23	1.02	0.11	37.6	38.2	39.1	0.10	8.06
116.csv (copy)	12:00	1_19	38	34.8	0.047	19.2	15.8	14.3	0.597	0.003	29.3	0.002	<0.00029365	0.026	0.25	0.71	141.3	47.3	14516	59.0	3.99	0.016	32.13	10.17	14.71	1.48	5.54	1.31	2.57	2.05	0.41	4.30	1.33	6.07	1.00	6.85	1.17	48.2	49.6	50.7	3.80	11.95
116.csv (copy) (copy)	12:00	1_20	38	35.0	0.057	19.3	17.1	15.4	0.528	0.003	27.9	0.001	<0.00031004	0.010	0.32	0.55	195.1	23.8	10810	22.4	2.89	<0.026119	25.36	1.63	2.69	0.36	1.52	0.50	1.08	1.10	0.21	1.68	0.50	1.88	0.22	1.24	0.14	40.5	41.9	43.1	0.92	4.57
116.csv (copy) (copy) (copy)	12:00	1_21	38	35.5	0.035	19.0	17.6	15.9	0.517	0.006	27.4	0.001	0.014	0.010	0.44	1.26	168.5	5.8	10052	20.7	4.91	<0.015331	23.31	0.57	1.26	0.17	0.95	0.34	0.78	0.90	0.18	1.59	0.45	1.56	0.16	1.11	0.13	53.7	55.3	55.7	2.20	4.78
116.csv (copy) (copy) (copy) (copy)	12:00	3_1	38	37.8	0.087	22.1	15.6	14.1	0.110	0.002	24.2	0.002	<0.00029608	<0.0024608	<0.077317	0.44	215.0	11.7	809	29.4	0.33	<0.011915	0.50	0.29	0.77	0.11	0.77	0.42	0.46	1.17	0.29	2.63	0.81	3.78	0.61	4.11	0.63	6.9	7.1	7.2	<0.010506	0.70
121.csv	12:30	3_2	38	37.6	0.107	21.8	15.9	14.3	0.128	0.003	24.3	0.001	<0.00029162	<0.002425	0.08	0.69	230.4	<1.0897	1143	147.3	1.24	0.011	0.95	0.23	0.29	0.05	0.35	0.42	0.94	2.21	0.72	8.86	3.79	17.50	2.76	16.69	2.14	9.8	9.9	10.2	<0.0094551	5.98
121.csv (copy)	12:30	3_3	38	36.3	0.053	20.6	16.0	14.4	0.333	0.005	26.6	0.005	0.006	0.006	0.29	2.97	174.6	1.9	7361	70.9	3.24	0.024	18.22	7.64	10.46	1.29	6.68	2.20	2.29	5.23	0.87	7.77	2.07	6.43	0.82	5.43	0.71	44.8	45.1	45.7	0.08	21.79
121.csv (copy) (copy)	12:30	3_4	38	37.2	0.105	21.3	16.5	14.9	0.151	0.011	24.6	0.001	<0.00029717	<0.0024675

Aar Massif – GTS

Sample: 11.001 24.40 m	Time	Spot size	SiO2	TiO2	Al2O3	Fe2O3	FeO	MgO	CaO	K2O	P2O5	V51	Cr53	Sr88	Y89	Zr90	Nb93	Ba137	La139	Ce140	Pr141	Nd146	Sm147	Eu151	Gd157	Tb159	Dy163	Ho165	Er167	Tm169	Yb173	Lu175	Pb206	Pb208	Th232	U238
		um	wt.%	wt.%	wt.%	wt.%	wt.%	wt.%	wt.%	wt.%	wt.%	µg/g	µg/g	µg/g	µg/g	µg/g	µg/g	µg/g	µg/g	µg/g	µg/g	µg/g	µg/g	µg/g	µg/g	µg/g	µg/g	µg/g	µg/g	µg/g	µg/g	µg/g	µg/g	µg/g	µg/g	µg/g
38 11.001_24.40m_4A_A.csv	14:39	20	80.3	0.05	1.7	1.1	1.0	5.09	10.0	0.22	<0.011872	7	<3.7574	69	8	44.2	1.01	67.8	6.4	11.2	1.4	5.7	1.1	0.2	1.3	0.2	1.0	0.2	0.7	0.1	0.6	0.1	14.0	14.9	1.5	1.2
24 11.001_24.40m_2B_b.csv	17:30	20	40.5	0.07	21.9	13.4	12.1	0.05	23.6	0.07	<0.0076659	148	10.5	3440	352	6.2	0.37	5.9	417.3	827.1	98.9	411.4	99.0	17.8	92.5	11.9	64.1	11.7	35.1	4.9	35.1	5.7	91.9	89.4	428.8	287
24 11.001_24.40m_2B_b.csv (copy)	17:30	20	35.8	0.08	24.2	14.0	12.6	0.01	25.5	<0.0011358	<0.014586	160	11.3	3496	386	6.6	0.10	0.9	371.9	777.0	96.4	419.4	108.2	20.4	103.3	13.0	70.2	13.0	40.4	6.0	45.5	7.9	88.1	83.4	269.7	301
24 11.001_24.40m_2B_b.csv (copy) (copy)	17:30	20	41.2	0.07	21.5	13.2	11.9	0.07	23.4	0.10	<0.0084379	147	11.1	3426	334	5.8	0.43	7.5	378.1	764.4	92.2	384.7	93.4	16.8	87.3	10.9	59.4	10.9	32.6	4.7	32.6	5.4	90.6	88.6	450.1	282
24 11.001_24.40m_2B_b.csv (copy) (copy) (copy)	17:30	20	42.7	0.06	21.0	13.3	12.0	0.03	22.5	0.04	<0.011357	141	9.2	3449	373	7.1	0.42	6.0	561.3	1040.2	119.0	474.6	107.5	18.7	98.0	13.2	70.5	12.5	37.2	4.6	33.0	5.0	97.5	97.0	485.3	291
25 11.001_24.40m_2A_a.csv	17:30	20	39.5	1.83	18.9	21.1	19.0	0.69	18.4	0.01	<0.010346	444	17.6	1739	2230	10.3	1.92	64.8	52657.5	103253.1	10396.5	33530.9	3743.8	67.7	1743.1	152.5	599.6	83.6	190.9	22.2	146.2	23.0	97.5	292.6	12730.6	261
25 11.001_24.40m_2A_a.csv (copy)	17:30	20	28.9	0.95	12.4	14.4	13.0	0.43	32.7	0.01	9.90	284	11.8	1131	3713	7.1	1.10	28.7	33615.9	63138.7	6203.2	19892.0	2399.2	58.1	1336.8	138.5	668.4	119.4	338.8	45.0	304.9	49.2	67.0	182.5	6787.7	132
29 11.001_24.40m_3A_a.csv	17:30	20	39.0	0.07	22.4	13.9	12.5	0.03	24.2	0.10	0.01	146	11.6	3993	228	7.6	0.25	11.3	440.2	875.3	109.6	479.6	102.3	15.2	72.9	8.0	38.9	7.3	23.0	3.1	20.7	3.3	84.7	82.6	480.2	358
29 11.001_24.40m_3A_a.csv (copy)	17:30	20	37.7	0.07	22.8	14.0	12.6	0.01	25.1	0.001	0.01	151	12.5	4416	232	8.7	0.08	2.7	496.4	986.8	123.3	537.3	111.5	12.7	77.8	8.5	39.6	7.5	24.1	3.2	21.7	3.7	80.1	77.8	545.9	386
29 11.001_24.40m_3A_a.csv (copy) (copy)	17:30	20	40.5	0.07	22.0	13.8	12.4	0.07	23.1	0.23	0.01	138	10.9	3521	223	6.3	0.45	23.0	380.8	753.4	94.6	416.0	91.4	18.5	67.3	7.5	38.2	7.0	21.8	3.0	19.4	3.0	90.5	87.9	421.4	332
32 11.001_24.40m_4A_B_a.csv	17:30	20	39.2	0.07	22.2	14.2	12.8	0.01	24.0	<0.00062831	<0.0080059	176	<3.0672	2841	230	4.8	0.06	1.2	4.9	10.4	1.6	8.1	4.3	11.3	10.0	2.3	21.4	5.9	23.4	3.9	31.5	5.3	76.5	74.9	0.1	217
37 11.001_24.40m_4B_A_a.csv	17:30	20	38.7	0.13	23.0	13.8	12.4	0.01	24.0	<0.00065738	<0.0083672	209	<2.9779	2274	196	5.8	<0.028125	0.9	3.1	6.8	1.0	5.7	3.3	13.0	7.9	2.0	18.9	5.1	19.3	2.9	18.3	2.5	69.4	68.5	0.3	159
37 11.001_24.40m_4B_A_a.csv (copy)	17:30	20	38.4	0.11	22.8	14.0	12.7	0.01	24.3	<0.00058861	<0.0074862	198	<2.7154	2657	163	6.1	0.03	0.8	3.4	7.1	1.0	5.9	3.5	10.0	7.0	1.7	15.1	4.2	16.4	2.8	19.2	3.0	73.3	74.7	0.2	151
41 11.001_24.40m_4B_B_a.csv	17:30	20	39.4	0.08	22.4	14.3	12.9	0.10	23.4	0.001	<0.0098066	163	<3.7429	2395	203	5.0	<0.041481	0.8	2.5	5.2	0.8	4.3	2.9	9.6	7.4	1.9	17.7	5.3	20.2	2.9	17.1	2.4	51.2	50.7	<0.0612	121
42 11.001_24.40m_4B_C_a.csv	17:30	20	39.4	0.10	22.4	14.5	13.1	0.01	23.3	<0.00083577	<0.010586	181	<4.0326	2317	176	5.4	<0.032626	0.5	2.0	4.4	0.6	3.5	2.1	10.1	6.4	1.6	15.6	4.4	16.8	2.5	15.3	2.0	60.8	61.6	<0.048136	117
43 11.001_24.40m_4B_C_b.csv	17:30	20	39.3	0.10	22.3	14.5	13.1	0.01	23.4	0.002	<0.010267	194	<3.6521	2402	168	4.9	0.06	0.8	3.2	6.8	1.1	5.2	3.3	9.9	7.1	1.8	15.6	4.3	16.3	2.5	17.1	2.4	72.2	73.7	0.1	161
41 11.001_24.40m_4A_A_a.csv	14:39	30	37.9	0.09	22.3	13.7	12.3	0.01	25.8	0.01	0.01	152	<2.0166	6116	312	21.9	0.06	7.5	7.9	14.3	1.9	9.9	5.0	16.4	11.8	2.8	26.8	7.7	30.9	4.6	31.2	4.9	101.2	99.2	0.1	269
41 11.001_24.40m_4A_A_a.csv (copy)	14:39	30	37.8	0.09	22.4	13.7	12.3	0.01	25.6	0.004	0.01	152	<2.5082	6112	314	21.9	0.05	7.6	8.0	14.5	2.0	10.0	5.2	16.8	12.0	2.8	27.7	7.9	31.7	4.7	31.5	4.9	99.9	97.1	0.1	273
42 11.001_24.40m_4A_A_a_Incl.csv	14:39	30	38.0	0.05	22.5	13.7	12.4	0.01	25.3	0.001	<0.0060299	151	<2.0108	4416	164	4.9	0.12	1.8	9.5	17.8	2.4	11.8	5.0	10.5	9.6	2.0	16.4	4.3	15.9	2.2	15.1	2.3	95.0	94.7	0.1	266
23 11.001_24.40m_2B_a.csv	17:30	30	40.3	0.04	22.1	13.1	11.8	0.01	24.0	0.002	0.01	147	8.4	3979	318	5.7	<0.025027	1.4	524.3	1037.8	127.0	535.4	125.7	20.5	109.2	12.4	61.9	10.8	29.6	3.8	25.5	4.1	84.8	86.0	142.1	187
23 11.001_24.40m_2B_a.csv (copy)	17:30	30	41.2	0.04	21.6	12.9	11.7	0.02	23.7	0.01	0.01	144	9.0	3901	308	5.7	0.03	1.8	501.7	994.4	121.1	510.3	121.3	19.6	104.3	11.7	59.0	10.3	29.0	3.7	24.5	3.9	84.9	85.5	130.3	177
30 11.001_24.40m_3B_a.csv	17:30	30	37.3	0.09	23.7	13.0	11.7	0.04	25.3	0.18	<0.0052072	127	10.0	4021	227	6.9	0.31	20.8	252.2	486.0	62.0	283.9	71.6	15.6	64.9	8.2	42.6	7.6	23.5	3.3	22.9	3.8	83.7	81.8	142.5	380
30 11.001_24.40m_3B_a.csv (copy)	17:30	30	46.8	0.06	23.4	10.1	9.1	0.33	17.1	1.54	<0.0042512	91	6.6	2710	130	4.5	1.99	213.6	154.0	302.4	37.9	168.9	39.0	10.9	32.6	4.0	20.9	3.9	12.2	1.9	14.1	2.2	68.6	67.7	143.1	160
30 11.001_24.40m_3B_a.csv (copy) (copy)	17:30	30	42.5	0.08	23.6	11.4	10.3	0.20	20.7	0.93	0.004	107	8.2	3296	174	5.5	1.25	128.0	199.2	387.1	49.1	221.9	54.1	13.0	47.6	5.9	31.0	5.6	17.5	2.6	18.1	3.0	75.1	73.8	141.6	261
31 11.001_24.40m_4A_A_b.csv	17:30	30	37.1	0.06	21.6	14.1	12.7	0.01	26.8	0.01	<0.0049928	141	<1.7994	8331	153	8.0	0.15	2.9	9.7	16.5	2.1	9.3	3.9	8.4	6.9	1.7	14.5	4.1	15.6	2.5	17.3	3.0	66.5	65.4	0.2	284
33 11.001_24.40m_4A_C_a.csv	17:30	30	36.4	0.06	22.4	14.0	12.6	0.01	26.9	<0.00051999	<0.0067248	165	<2.6172	7325	308	15.3	<0.023588	5.5	3.9	6.9	1.0	5.4	3.4	15.1	9.1	2.5	25.8	7.6	30.5	5.1	38.4	6.5	92.9	94.4	<0.032477	233
33 11.001_24.40m_4A_C_a.csv (copy)	17:30	30	38.2	0.05	21.4	14.3	12.9	0.01	25.7	<0.00047856	<0.0061896	160	<2.4187	7358	195	9.3	<0.022799	4.0	2.8	5.2	0.7	3.8	2.8	10.5	6.3	1.7	16.6	4.7	19.0	2.8	19.3	3.0	79.8	81.3	<0.03139	118
33 11.001_24.40m_4A_C_a.csv (copy) (copy)	17:30	30	37.3	0.06	21.9	14.1	12.7	0.01	26.3	<0.00041369	<0.0053482	163	<2.0547	7340	253	12.4	<0.015775	4.7	3.4	6.1	0.9	4.6	3.1	12.9	7.8	2.1	21.4	6.2	24.9	4.0	29.1	4.8	86.4	88.0	<0.02172	177
34 11.001_24.40m_4A_C_b.csv	17:30	30	38.4	0.11	22.9	14.1	12.7	0.01	24.3	<0.00041709	<0.0053636	205	<1.9536	2989	184	6.9	0.04	1.5	4.6	9.5	1.4	7.1	3.4	12.9	7.0	1.7	15.2	4.4	18.3	2.4	91.4	93.4	<0.033771	109
35 11.001_24.40m_4A_D_b.csv	17:30	30	37.5	0.06	22.0	14.0	12.6	0.01	26.2	<0.0004205	<0.0054013	144	<1.9593	6897	244	10.2	0.03	3.8	16.3	28.6	3.8	16.7	6.7	13.3	12.8	2.8	24.1	6.5	23.9	3.5	25.2	4.0	77.5	74.6	0.5	535
36 11.001_24.40m_4A_D_a.csv	17:30	30	38.5	0.10	22.7	14.0	12.6	0.01	24.4	<0.0004218	<0.0054624	173	<1.9855	2882	133	4.9	0.03	0.8	4.9	10.4	1.4	6.5	3.2	6.7	5.7	1.3	11.9	3.4	14.6	2.7	20.5	3.3	65.2	62.5	0.4	311

Sample: Gr0-a	Time	Spot size	SiO2	TiO2	Al2O3	Fe2O3	FeO	MgO	CaO	K2O	P2O5	V51	Cr53	Sr88	Y89	Zr90	Nb93	Ba137	La139	Ce140	Pr141	Nd146	Sm147	Eu151	Gd157	Tb159	Dy163	Ho165	Er167	Tm169	Yb173	Lu175	Pb206	Pb208	Th232	U238
		um	wt.%	wt.%	wt.%	wt.%	wt.%	wt.%	wt.%	wt.%	wt.%	µg/g	µg/g	µg/g	µg/g	µg/g	µg/g	µg/g	µg/g	µg/g	µg/g	µg/g	µg/g	µg/g	µg/g	µg/g	µg/g	µg/g	µg/g	µg/g	µg/g	µg/g	µg/g	µg/g	µg/g	µg/g
37 Gr0-a_3B_b_20.csv	14:39	20	37.8	0.05	23.1	14.3	12.9	0.05	24.29	0.11	0.02	122.2	<4.9552	790	5.5	14.3	1.46	3.80	0.89	1.94	0.27	1.41	0.62	0.06	0.85	0.12	0.80	0.17	0.57	0.12	0.78	0.11	57.7	58.4	22.6	1.76
37 Gr0-a_3B_b_20.csv (copy)	14:39	20	39.6	0.04	22.5	14.7	13.2	0.03	22.78	0.09	0.03	106.9	<5.6343	773	5.3	12.7	1.07	3.31	0.64	1.75	0.27	1.26	0.74	0.11	0.81	0.15	0.90	0.22	0.44	0.07	0.68	0.12	55.5	62.5	16.6	2.18
37 Gr0-a_3B_b_20.csv (copy) (copy)	14:39	20	38.6	0.05	22.9	14.5	13.0	0.04	23.63	0.10	0.02	115.7	<4.1643	782	5.5	13.7	1.30	3.45	0.78	1.85	0.26	1.37	0.67	0.08	0.86	0.13	0.86	0.19	0.52	0.10	0.76	0.12	56.8	60.3	20.0	1.96
44 Gr0-a_2_a.csv	17:30	20	38.1	0.03	23.0	14.5	13.1	0.01	24.07	0.001	0.02	124.5	<3.0838	927	23.6	5.1	0.34	<0.34932	137.30	252.66	28.31	111.38	21.31	2.53	18.33	1.84	6.97	0.80	1.36	0.14	1.09	0.22	53.4	54.1	2.04	3.03
44 Gr0-a_2_a.csv (copy)	17:30	20	39.9	0.02	22.1	14.8	13.4	0.01	22.81	0.002	0.02	154.3	<3.6926	1250	49.3	4.7	0.35	1.24	60.98	107.60	11.79	47.53	9.68	1.85	9.37	1.28	7.23	1.47	3.66	0.44	3.23	0.56	54.9	53.9	1.37	11.8
44 Gr0-a_2_a.csv (copy) (copy)	17:30	20	38.8	0.03	22.7	14.7	13.2	0.01	23.59	0.002	0.02	136.2	<2.6602	1052	33.9	5.0	0.35	0.62	109.61	199.88	22.31	88.31	17.08	2.30	15.14	1.65	7.15	1.07	2.28	0.26	1.92	0.35	54.0	53.9	1.80	6.47
46 Gr0-a_2_c.csv	17:30	20	40.4	0.02	22.4	13.7	12.4	0.01	23.10	0.002	<0.0076675	132.0	<2.8294	960	28.2	4.2	0.35	0.63	28.27	50.20	5.42	22.02	5.16	1.31	6.00	0.75	4.08	0.74	2.17	0.24	1.65	0.37	32.9	34.1	2.25	6.67
36 Gr0-a_3B_b_30.csv	14:39	30	38.5	0.03	23.0	14.5	13.1	0.02	23.62	0.02	0.02	114.2	<2.081	803	3.0	13.8	0.49	1.14	2.97	5.81	0.73	3.50	0.97	0.16	1.23	0.11	0.54	0.10	0.24	0.04	0.32	0.07	53.6	55.8	<0.044226	1.10
45 Gr0-a_2_b.csv	17:30	30	37.4	0.04	23.7	13.7	12.4	0.02	24.80	0.002	0.01	161.9	<2.8143	1075	50.4	9.8	1.52	1.22	69.20	124.64	13.94	53.55	9.89	2.00	8.85	1.20	7.43	1.45	3.99	0.46	3.94	0.65	37.1	38.8	0.91	14.1
45 Gr0-a_2_b.csv (copy)	17:30	30	39.3	0.06	22.7	14.4	13.0	0.08	23.14	0.05	0.01	184.2	<2.0893	1064	46.8	9.6	2.77	2.33	73.01	135.00	14.95	56.70	10.62	1.84	9.50	1.17	6.81	1.26	3.23	0.44	2.84	0.57	40.3	40.9	1.51	13.2
45 Gr0-a_2_b.csv (copy) (copy)	17:30	30	38.6	0.05	23.1	14.2	12.8	0.06	23.73	0.04	0.01	175.6	<1.9049	1066	47.9	9.7	2.32	1.91	71.73	131.55	14.60	55.84	10.42	1.89	9.23	1.18	7.07	1.33	3.50	0.45	3.25	0.60	39.2	40.3	1.28	13.5

Sample: Gr0-c	Time	Spot size	SiO2	TiO2	Al2O3	Fe2O3	FeO	MnO	MgO	CaO	K2O	P2O5	V51	Cr53	Sr88	Y89	Zr90	Ba137	La139	Ce140	Pr141	Nd146	Sm147	Eu151	Gd157	Tb159	Dy163	Ho165	Er167	Tm169	Yb173	Lu175	Pb208	Th232	U238
		um	wt.%	wt.%	wt.%	wt.%	wt.%	wt.%	wt.%	wt.%	wt.%	wt.%	µg/g	µg/g	µg/g	µg/g	µg/g	µg/g	µg/g	µg/g	µg/g	µg/g	µg/g	µg/g	µg/g	µg/g	µg/g	µg/g	µg/g	µg/g	µg/g	µg/g	µg/g	µg/g	µg/g
13 Gr0-c_4A_a.csv	14:44	20	37.3	0.05	20.6	17.5	15.7	0.18	0.02	24.45	<0.00075335	<0.011628	111	4.90	2769	9.6	23.9	8.1	1.06	2.46	0.41	2.43	1.86	0.99	3.63	0.52	2.35	0.36	1.16	0.14	1.39	0.29	8.9	1.29	79.21
13 Gr0-c_4A_a.csv (copy)	14:44	20	39.3	0.04	19.8	17.8	16.0	0.23	0.02	22.89	<0.000772	<0.011916	92	6.22	2848	10.2	20.8	6.9	45.54	54.49	5.28	18.19	4.12	1.51	5.50	0.67	2.98	0.34	1.15	0.21	1.08	0.24	8.6	1.69	92.78
5 Gr0-c_1A_A_a.csv	14:44	30	38.1	0.08	22.1	14.9	13.4	0.60	0.01	23.99	0.001	<0.0112404320876975	150	<1.3361	2563	47.5	7.9	9.8	0.12	0.12	0.01	0.07	<0.044502	0.16	0.21	0.11	1.56	0.73	4.81	1.13	11.04	2.05	122.7	<0.026216	14.23
6 Gr0-c_1A_B_a.csv	14:44	30	37.2	0.06	21.2	15.9	14.4	0.56	0.01	24.93	<0.00033932	<0.0103591895741472	117	<1.3213	4525	147.7	32.1	20.4	2.15	2.44	0.31	1.79	1.42	1.66	4.92	1.14	11.36	3.40	14.87	2.91	28.88	5.22	113.0	<0.028707	92.10
7 Gr0-c_1A_B_b.csv	14:44	30	37.5	0.04	22.0	15.4	13.8	0.39	0.005	24.56	<0.00031928	<0.0049278	123	<1.3025	2471	118.3	5.1	4.8	5.00	3.37	0.34	1.88	0.83	1.44	4.14	1.12	10.67	3.09	11.08	1.48	10.01	1.61	55.6	0.03	21.59
8 Gr0-c_2A_a.csv	14:44	30	38.8	0.03	24.0	12.5	11.3	0.23	0.02	23.96	0.001	0.02	139	<1.8169	1100	6.2	6.5	0.8	5.03	4.27	0.39	1.59	0.25	0.27	0.61	0.13	0.76	0.13	0.36	0.06	0.45	0.06	47.4	0.78	4.81
8 Gr0-c_2A_a.csv (copy)	14:44	30	38.0	0.02	24.2	12.6	11.3	0.28	0.01	24.44	<0.00060956	0.03	134	<2.3774	1316	6.3	4.7	0.6	4.31	3.95	0.38	1.57	0.26	0.27	0.57	0.12	0.74	0.12	0.39	0.07	0.49	0.08	47.8	0.64	5.22
8 Gr0-c_2A_a.csv (copy) (copy)	14:44	30	39.5	0.04	23.7	12.5	11.3	0.18	0.02	23.52	0.002	0.01	143	<2.1279	894	6.1	8.2	0.9	5.67	4.56	0.41	1.58	0.26	0.26	0.64	0.14	0.76	0.12	0.34	0.05	0.41	0.05	47.1	0.89	4.39
9 Gr0-c_2A_b.csv	14:44	30	38.2	0.03	22.6	14.4	12.9	0.24	0.01	24.31	0.01	0.01	192	<1.8337	2473	14.1	5.2	1.7	1.44	1.70	0.18	0.87	0.23	0.40	0.76	0.17	1.45	0.33	1.21	0.16	1.34	0.20	70.1	2.49	8.33
9 Gr0-c_2A_b.csv (copy)	14:44	30	37.0	0.03	23.7	13.7	12.4	0.19	0.01	24.97	0.001	<0.010016	197	<2.5834	1899	11.4	6.7	1.4	0.70	0.83	0.12	0.55	0.15	0.32	0.57	0.14	1.00	0.27	0.90	0.13	1.20	0.18	43.2	0.38	7.77
9 Gr0-c_2A_b.csv (copy) (copy)	14:44	30	39.0	0.02	21.9	14.7	13.3	0.28	0.01	23.86	0.01	0.01	189	<2.0193	2854	15.6	4.2	1.9	1.90	2.23	0.22	1.05	0.29	0.45	0.88	0.18	1.74	0.37	1.41	0.17	1.40	0.21	87.7	3.82	8.57
10 Gr0-c_2A_c.csv	14:44	30	38.8	0.10	23.5	12.9	11.6	0.58	0.02	23.63	0.002	0.04	159	<1.9521	1693	6.2	25.0	1.1	2.87	2.25	0.19	0.78	0.13	0.36	0.37	0.06	0.57	0.15	0.54	0.06	0.88	0.13	44.9	0.51	3.19
11 Gr0-c_2A_d.csv	14:44	30	38.1	0.09	24.1	12.8	11.5	0.19	0.02	24.23	<0.00032232	0.01	214	<1.2462	991	2.9	13.2	0.4	0.61	0.46	0.05	0.16	0.05	0.08	0.16	0.02	0.27	0.07	0.25	0.04	0.37	0.05	24.1	<0.023573	2.05
12 Gr0-c_3A_a.csv	14:44	30	37.8	0.06	21.9	15.9	14.4	0.56	0.01	23.60	<0.00047478	<0.0072976	113	<1.9002	1078	37.8	2.0	1.9	0.34	0.75	0.11	0.55	0.25	0.35	0.57	0.21	2.24	0.77	3.80	0.68	4.90	0.71	104.3	<0.010956	66.18
14 Gr0-c_4A_b.csv	14:44	30	41.3	2.71	15.6	24.1	21.7	1.37	0.88	14.69	0.01	0.04	183	3.74	720	4091	10	64	67223	143396	15398	52126	6926	38	3335	306	1214	167	359	39	225	28	414	17087	135
18 Gr0-c_4D_c.csv	14:44	30	42.4	1.83	16.3	23.0	20.8	1.16	0.77	15.10	0.01	0.01	245	4.76	698	2663	12	35	56741	114600	11797	38849	4647	107	2324	206	783	106	221	24	139	18	362	11701	247
18 Gr0-c_4D_c.csv (copy)	14:44	30	40.9	1.89	17.4	21.7	19.6	1.07	0.81	16.58	0.01	0.01	247	9.55	986	2709	16	40	57517	114397	11820	38836	4549	76	2274	202	784	107	229	25	143	19	313	11860	200

Sample: Gr0-c2	Time	Info	Spot size	SiO2	TiO2	Al2O3	Fe2O3	FeO	MnO	MgO	CaO	Na2O	K2O	Li7	B11	V51	Cr53	Sr88	Y89	Zr90	Ba137	La139	Ce140	Pr141	Nd146	Sm147	Eu151	Gd157	Tb159	Dy163	Ho165	Er167	Tm169	Yb173	Lu175	Pb208	Th232	U238
			um	wt.%	wt.%	wt.%	wt.%	wt.%	wt.%	wt.%	wt.%	wt.%	wt.%	wt.%	µg/g	µg/g	µg/g	µg/g	µg/g	µg/g	µg/g	µg/g	µg/g	µg/g	µg/g	µg/g	µg/g	µg/g	µg/g	µg/g	µg/g	µg/g	µg/g	µg/g	µg/g	µg/g	µg/g	µg/g
29 Gr0-c_30um_1 - Copy.csv	11:45	29 Gr0-c_30um_1	30	39.0	0.03	24.1	12.6	11.3	0.13	0.01	23.6	0.00	0.00	0.24	0.93	154.8	<1.9199	936	1.0	17.4	0.22	26.54	21.62	1.77	7.09	0.50	0.09	0.34	0.02	0.11	0.03	0.08	0.01	0.19	0.04	13.31	0.02	2.52
29 Gr0-c_30um_1 - Copy.csv (copy)	11:45	30 Gr0-c_30um_2	30	38.4	0.09	22.1	15.5	13.9	0.58	0.01	23.2	0.00	<0.0092282	0.12	0.54	176.6

Sample Gr0-d	Time	Spot size	SiO2	TiO2	Al2O3	Fe2O3	FeO	MgO	CaO	K2O	P2O5	V51	Cr53	Sr88	Y89	Zr90	Nb93	Ba137	La139	Ce140	Pr141	Nd146	Sm147	Eu151	Gd157	Tb159	Dy163	Ho165	Er167	Tm169	Yb173	Lu175	Pb206	Pb208	Th232	U238
			wt.%	wt.%	wt.%	wt.%	wt.%	wt.%	wt.%	wt.%	wt.%	µg/g	µg/g	µg/g	µg/g	µg/g	µg/g	µg/g	µg/g	µg/g	µg/g	µg/g	µg/g	µg/g	µg/g	µg/g	µg/g	µg/g	µg/g	µg/g	µg/g	µg/g	µg/g	µg/g	µg/g	µg/g
7 Gr0-d_2A_a.csv	17:30	20	38.9	0.05	21.7	15.7	14.2	0.01	23.5	<0.00064066	<0.0082929	128	<3.0835	1804	93.3	8.1	0.69	5.4	2.33	5.24	0.71	3.49	1.73	1.68	3.58	0.85	8.50	2.43	10.37	1.67	12.22	2.15	134	133	0.12	195
8 Gr0-d_2A_b.csv	17:30	20	39.8	0.05	21.3	16.0	14.4	0.01	22.7	0.001	<0.011335	127	<4.0401	1800	98.9	8.0	0.61	5.5	3.88	8.46	1.16	5.57	2.46	1.91	4.92	0.99	9.76	2.67	10.05	1.57	11.51	1.87	148	151	7.63	182
18 Gr0-d_7B_a.csv	17:30	20	38.8	0.06	21.3	16.1	14.5	0.01	23.6	0.001	<0.0071695	111	<2.5768	2503	107.5	24.3	0.27	20.8	0.99	1.91	0.24	1.12	0.66	1.07	2.76	0.86	9.75	3.12	13.89	2.69	23.36	4.44	169	171	0.15	266
19 Gr0-d_8B_a.csv	17:30	20	39.8	0.05	21.6	15.5	14.0	0.01	22.8	<0.00082892	<0.010733	127	<3.9332	1714	160.4	7.6	1.25	4.8	9.40	20.20	2.62	11.86	5.33	3.54	9.64	2.29	18.82	4.80	16.08	2.36	15.66	2.56	155	152	0.99	226
20 Gr0-d_9A_a.csv	17:30	20	39.7	0.04	21.7	15.6	14.1	0.01	22.8	<0.00082634	<0.010663	141	<3.9473	1401	202.2	3.6	<0.031808	1.0	5.62	14.09	2.16	11.96	6.30	3.90	13.57	2.80	21.77	5.47	19.14	2.73	18.58	2.72	126	127	0.47	79
21 Gr0-d_10A_a.csv	17:30	20	39.0	0.06	21.8	15.6	14.0	0.01	23.3	<0.00083187	<0.010725	141	<3.9886	1988	233.0	5.1	0.04	1.2	7.66	18.08	2.70	15.47	8.48	5.57	18.07	3.55	27.46	6.47	22.19	3.06	21.29	3.38	131	131	<0.093666	129
22 Gr0-d_11A_a.csv	17:30	20	39.4	0.05	21.0	15.8	14.3	0.00	23.6	<0.00081929	<0.010467	108	<4.0104	3288	117.3	21.7	0.15	22.0	4.78	8.85	1.21	5.64	2.52	1.95	5.68	1.16	12.08	3.61	13.78	2.46	21.34	3.76	158	155	0.82	353
43 Gr0-d_1A_a.csv	14:39	30	39.0	0.10	22.2	15.3	13.7	0.01	23.3	<0.00044761	<0.0066529	159	<2.1005	974	32.1	4.2	0.09	1.9	5.19	9.32	1.14	5.04	1.81	1.26	2.89	0.62	5.05	1.04	3.45	0.53	3.68	0.57	98	97	0.07	60
44 Gr0-d_1A_b.csv	14:39	30	38.6	0.11	21.9	15.2	13.7	0.004	24.0	<0.0004118	0.03	130	2.47	2588	71.1	51.0	0.09	22.5	9.97	14.84	1.64	7.03	2.77	1.93	5.62	1.25	9.86	2.28	9.18	1.64	15.48	3.09	170	169	0.71	125
4 Gr0-d_1B_a.csv	17:30	30	38.2	0.14	22.4	14.9	13.5	0.02	24.0	0.0003	0.01	200	<0.89324	737	53.3	4.5	0.20	1.0	4.99	9.34	1.21	5.27	2.72	1.61	5.47	1.10	8.41	1.79	6.01	0.88	5.77	0.77	88	87	0.30	137
5 Gr0-d_1C_a.csv	17:30	30	38.1	0.06	21.9	15.7	14.2	0.00	24.0	<0.00041454	0.01	151	<2.0167	2867	125.0	17.0	0.04	21.2	11.71	16.62	1.81	8.31	4.65	3.70	10.97	2.47	18.86	4.37	15.63	2.76	24.71	4.37	173	174	0.56	242
6 Gr0-d_1C_b.csv	17:30	30	38.8	0.06	22.4	14.8	13.4	0.01	23.7	<0.00040177	0.01	143	<1.893	2002	82.0	9.6	0.19	9.7	8.45	11.71	1.36	5.85	3.19	2.70	8.02	1.76	13.79	2.86	8.67	1.10	7.82	1.30	147	148	2.57	102
9 Gr0-d_3C_a.csv	17:30	30	38.5	0.10	21.7	15.5	14.0	0.01	24.0	<0.00040446	0.01	138	<1.9555	2886	89.7	30.8	0.06	23.7	6.57	9.71	1.06	4.63	1.97	2.22	5.91	1.37	11.60	2.91	10.92	2.06	17.81	3.24	175	175	0.47	225
10 Gr0-d_4B_a.csv	17:30	30	38.8	0.02	22.2	15.2	13.7	0.01	23.5	<0.00041647	<0.0055084	113	<1.9362	1661	40.5	2.2	<0.026507	0.9	3.38	7.18	0.90	3.34	1.23	1.43	2.68	0.59	5.05	1.25	4.05	0.42	2.51	0.28	94	93	4.88	103
11 Gr0-d_5B_a.csv	17:30	30	38.4	0.07	22.0	15.2	13.7	0.00	24.1	<0.0004058	0.01	121	<2.0161	3749	67.4	24.6	0.02	33.5	5.34	8.52	1.04	4.58	1.93	2.25	4.24	1.03	8.77	2.18	6.71	0.80	4.81	0.64	194	193	0.81	136
12 Gr0-d_6B_B_a.csv	17:30	30	39.4	0.14	22.0	15.2	13.7	0.01	23.1	0.001	<0.0053515	180	<1.9109	774	64.6	3.2	0.17	0.6	1.61	3.02	0.39	1.55	1.01	1.51	3.22	1.00	9.06	2.21	7.87	0.97	5.93	0.72	79	78	1.88	158
13 Gr0-d_7A_a.csv	17:30	30	37.2	0.09	22.1	15.6	14.1	0.01	24.8	0.002	0.01	135	<2.9491	2820	122.9	41.6	0.06	27.3	1.25	2.52	0.29	1.16	1.21	1.46	4.63	1.34	12.46	3.47	14.34	2.77	27.75	4.59	183	179	0.14	263
13 Gr0-d_7A_a.csv (copy)	17:30	30	40.4	0.10	21.6	15.0	13.5	0.01	22.7	0.005	0.01	135	<2.2262	1886	74.7	15.5	0.08	12.8	0.89	1.82	0.23	1.05	0.76	1.10	3.08	0.83	7.76	2.17	8.40	1.44	11.57	2.07	133	131	0.16	165
16 Gr0-d_7A_b.csv	17:30	30	39.1	0.10	22.2	14.9	13.4	0.01	23.4	0.01	0.01	145	<1.8336	1527	41.8	5.0	0.25	5.8	0.62	0.97	0.12	0.62	0.45	0.94	1.36	0.40	4.08	1.18	4.70	0.77	6.17	1.02	93	93	0.04	54
16 Gr0-d_7A_b.csv (copy)	17:30	30	38.8	0.10	22.4	14.7	13.3	0.01	23.6	0.02	0.01	147	<2.3495	1343	41.0	3.8	0.23	3.2	0.48	0.85	0.12	0.52	0.33	0.94	1.28	0.39	4.12	1.21	4.54	0.72	5.55	0.87	88	91	<0.044865	54
16 Gr0-d_7A_b.csv (copy) (copy)	17:30	30	39.3	0.09	22.1	15.0	13.5	0.01	23.3	0.004	0.01	143	<2.2169	1655	42.5	5.8	0.27	7.6	0.71	1.07	0.12	0.68	0.52	0.93	1.41	0.40	4.10	1.15	4.83	0.80	6.59	1.13	96	94	0.05	54
17 Gr0-d_7B_b.csv	17:30	30	38.6	0.06	21.9	15.3	13.7	0.01	23.9	<0.00041019	0.01	130	1.97	2813	77.1	18.0	0.11	16.7	1.87	2.99	0.35	1.37	0.55	1.26	1.73	0.66	7.83	2.32	9.31	1.64	13.62	2.29	152	152	0.84	140

Sample: Gr0-d (Mar. 15, 2021 analyses)	Time	Info	Spot size	SiO2	TiO2	Al2O3	Fe2O3	FeO	MnO	MgO	CaO	Na2O	K2O	Li7	B11	V51	Cr53	Sr88	Y89	Zr90	Ba137	La139	Ce140	Pr141	Nd146	Sm147	Eu151	Gd157	Tb159	Dy163	Ho165	Er167	Tm169	Yb173	Lu175	Pb208	Th232	U238
			um	wt.%	wt.%	wt.%	wt.%	wt.%	wt.%	wt.%	wt.%	wt.%	wt.%	µg/g	µg/g	µg/g	µg/g	µg/g	µg/g	µg/g	µg/g	µg/g	µg/g	µg/g	µg/g	µg/g	µg/g	µg/g	µg/g	µg/g	µg/g	µg/g	µg/g	µg/g	µg/g	µg/g	µg/g	µg/g
86 P9d_24um_6.csv (copy)	15:45	87 Gr0-d_20um - 1	20	38.3	0.04	22.2	15.1	13.6	0.49	0.01	23.6	0.002	0.003	0.360	1.0	132	<3.3324	1642	150.5	5.24	2.14	4.70	10.42	1.38	7.10	3.39	3.04	7.32	1.73	15.82	4.35	14.30	2.14	14.15	2.32	171.5	8.92	133.2
86 P9d_24um_6.csv (copy) (copy)	15:45	88 Gr0-d_20um - 2 - 1st	20	37.2	0.05	22.5	14.9	13.4	0.49	0.01	24.7	0.002	<0.00075825	0.297	<1.0979	136	<4.4238	1861	172.3	5.87	2.95	3.65	8.14	1.14	5.67	3.10	3.13	7.58	2.05	16.59	4.57	15.90	2.42	19.20	3.01	150.1	0.18	137.4
95 Gr0-d_20um_6.csv	0.677083333	95 Gr0-d_20um - 6	20	38.7	0.05	21.6	15.6	14.1	0.56	0.01	23.4	0.002	0.001	<0.18579	<0.81129	124	<3.7093	1954	85.3	8.16	6.61	1.70	4.15	0.55	2.89	1.22	1.63	3.11	0.81	8.09	2.09	8.61	1.47	9.74	1.74	124.6	0.15	188.2
95 Gr0-d_20um_6.csv (copy)	0.677083333	96 Gr0-d_20um - 7	20	39.4	0.05	21.2	15.7	14.2	0.55	0.01	23.0	0.003	0.001	0.368	<1.0779	123	<4.5491	1723	109.9	7.04	5.00	3.28	7.62	1.08	5.17	2.36	1.97	4.81	1.06	10.38	3.07	10.85	1.80	12.90	2.13	135.0	0.30	186.5
95 Gr0-d_20um_6.csv (copy) (copy)	0.677083333	97 Gr0-d_20um - 8 1st	20	39.0	0.05	21.6	14.9	13.4	0.52	0.01	23.7	0.003	<0.00063811	<0.20886	<0.86536	121	<3.7991	1702	115.3	7.65	4.17	2.99	7.38	0.97	4.95	2.30	2.06	4.24	1.20	10.51	2.98	11.31	1.97	14.22	2.51	132.7	0.26	174.1
98 Gr0-d_20um_9.csv	0.677083333	98 Gr0-d_20um - 9 1st	20	37.1	0.05	22.5	15.1	13.6	0.54	0.01	24.5	0.001	<0.00066498	<0.2127	<0.92029	131	<4.1908	1930	85.2	7.21	5.09	1.93	4.35	0.60	2.88	1.35	1.46	3.29	0.80	7.40	2.27	8.81	1.29	10.31	1.60	117.5	0.14	164.0
98 Gr0-d_20um_9.csv (copy)	0.677083333	98 Gr0-d_20um - 9 2nd	20	39.7	0.05	21.2	15.7	14.2	0.55	0.01	22.6	0.003	<0.00078799	0.296	<1.0905	130	<4.966	1525	83.7	5.16	3.68	2.88	6.62	0.88	4.53	2.10	1.67	4.13	0.73	7.93	2.28	8.28	1.32	9.04	1.56	129.9	0.36	160.5
98 Gr0-d_20um_9.csv (copy) (copy)	0.677083333	99 Gr0-d_20um - 10	20	38.3	0.05	21.8	15.7	14.2	0.55	0.01	23.4	0.002	0.001	0.435	1.1	128	<4.1803	1964	102.7	9.32	6.55	3.31	7.60	0.99	4.47	2.32	1.91	3.92	0.99	9.12	2.59	10.05	1.51	13.22	2.13	136.2	2.18	185.2
101 Gr0-d_20um_11.csv	0.677083333	104 Gr0-d_20um - 11	20	37.9	0.05	22.2	15.5	14.0	0.55	0.01	23.7	0.002	0.001	0.279	0.8	129	<3.395	1856	95.7	8.61	5.28	3.43	8.24	1.05	4.69	2.21	1.85	3.72	0.91	8.42	2.65	9.89	1.54	12.67	2.07	132.2	2.02	192.4
101 Gr0-d_20um_11.csv (copy)	16:45	104 Gr0-d_20um - 12	20	37.2	0.08	22.5	15.4	13.9	0.57	0.01	24.0	0.003	0.008	0.210	<0.76435	123	<3.7288	1311	47.4	5.23	5.24	3.47	6.26	0.78	3.69	1.30	1.37	2.01	0.57	4.84	1.29	6.06	0.88	7.08	0.93	93.1	0.83	118.0
101 Gr0-d_20um_11.csv (copy) (copy) (copy)	16:45	106 Gr0-d_20um - 14	20	37.0	0.06	22.5	15.3	13.7	0.54	0.01	24.5	<0.00039071	<0.00061025	<0.18136	<0.87143	119	<3.6194	2343	46.5	3.08	3.82	1.45	2.88	0.43	1.59	0.76	1.20	1.60	0.47	4.91	1.47	5.48	0.78	5.84	0.90	112.7	3.02	105.2

Sample: Gr0-e	Time	Spot size	SiO2	TiO2	Al2O3	Fe2O3	FeO	MnO	MgO	CaO	K2O	P2O5	V51	Cr53	Sr88	Y89	Zr90	Ba137	La139	Ce140	Pr141	Nd146	Sm147	Eu151	Gd157	Tb159	Dy163	Ho165	Er167	Tm169	Yb173	Lu175	Pb208	Th232	U238
		um	wt.%	wt.%	wt.%	wt.%	wt.%	wt.%	wt.%	wt.%	wt.%	wt.%	µg/g	µg/g	µg/g	µg/g	µg/g	µg/g	µg/g	µg/g	µg/g	µg/g	µg/g	µg/g	µg/g	µg/g	µg/g	µg/g	µg/g	µg/g	µg/g	µg/g	µg/g	µg/g	µg/g	µg/g
24 Gr0-e_1A_a_e.csv	14:44	20	38.4	0.05	22.3	15.1	13.6	0.13	0.01	23.8	<0.00058701	<0.0088895	158	<2.3435	988	0.90	13.61	0.38	0.39	0.71	0.06	0.26	0.13	0.08	<0.094307	0.02	0.08	0.03	0.11	<0.01266	<0.095572	0.03	6.29	<0.059804	2.13
25 Gr0-e_1A_a_f.csv	14:44	20	38.8	0.01	21.5	16.2	14.6	0.21	0.01	23.3	<0.00079836	<0.012261	163	<3.1432	1202	0.09	13.78	<0.41484	0.09	0.13	0.02	<0.11569	<0.12552	<0.041457	<0.13668	<0.019656	<0.076682	<0.019427	<0.099526	<0.018595	<0.11974	<0.014246	10.69	<0.062118	1.38
33 Gr0-e_1A_b_e.csv	14:44	20	39.4	0.02	23.6	12.7	11.5	0.19	0.02	23.5	<0.00082369	<0.012365	158	<3.4179	1041	7.53	32.70	0.64	25.04	33.87	3.15	11.30	1.59	0.14	1.07	0.15	0.79	0.20	0.57	0.10	0.74	0.14	42.30	<0.077752	2.31
34 Gr0-e_1A_b_f.csv	14:44	20	39.3	0.02	23.5	13.1	11.8	0.25	0.01	23.3	<0.00079543	<0.01195	106	<3.3278	1340	1.19	16.25	0.37	10.40	18.28	1.72	6.39	0.86	0.07	0.27	0.03	0.18	0.04	<0.10563	0.02	0.26	0.04	38.97	<0.049977	1.36
5 Gr0-e_2A_b.csv	16:12	20	39.3	0.03	24.8	11.8	10.6	0.23	0.01	23.2	0.003	0.03	160	<3.1188	812	2.53	9.19	<0.53577	0.58	1.11	0.10	0.42	<0.14143	0.07	0.17	0.04	0.38	0.07	0.25	0.05	0.27	0.06	33.27	<0.055978	0.78
5 Gr0-e_2A_b.csv (copy)	16:12	20	38.3	0.03	25.7	11.3	10.2	0.13	0.01	24.0	<0.00087793	0.02	134	<3.7948	645	2.18	9.55	<0.71794	0.07	0.19	<0.030591	<0.14358	<0.18645	<0.045993	<0.11652	0.02	0.42	0.07	0.23	0.06	0.24	0.06	35.43	<0.079002	0.80
5 Gr0-e_2A_b.csv (copy) (copy)	16:12	20	40.6	0.02	23.9	12.4	11.1	0.35	0.02	22.3	0.01	0.04	188	<4.0942	993	2.86	8.88	<0.78121	1.12	2.09	0.18	0.78	<0.2026	0.09	0.23	0.05	0.31	0.07	0.26	0.04	0.29	0.07	30.83	<0.086326	0.78
7 Gr0-e_2B_a.csv	16:12	20	37.3	0.02	23.3	13.8	12.4	0.69	0.01	24.6	<0.00090957	0.02	77	<3.7513	4272	0.22	6.55	1.41	0.57	0.92	0.09	0.56	<0.17677	0.06	<0.16875	<0.020187	<0.1005	<0.021488	<0.093353	<0.020498	<0.14859	<0.026524	11.96	<0.11441	0.49
7 Gr0-e_2B_a.csv (copy)	16:12	20	40.9	0.02	20.8	14.2	12.8	0.93	0.07	22.8	0.02	0.02	69	<4.3861	7023	1.36	2.94	4.19	0.63	0.77	0.11	0.26	<0.21611	<0.057037	<0.20707	<0.025052	0.25	0.05	0.17	0.03	0.28	0.05	28.83	9.82	2.06
8 Gr0-e_2B_b.csv	16:12	20	39.1	0.04	24.6	12.4	11.2	0.11	0.00	23.3	<0.00082866	<0.011636	94	<3.3072	460	2.23	6.33	<0.12964	0.07	0.26	0.05	0.26	0.15	<0.044575	0.19	0.06	0.34	0.06	0.14	0.03	0.20	0.03	48.00	<0.06726	0.63
19 Gr0-e_3_a_f.csv	16:12	20	39.0	1.02	22.3	13.8	12.5	0.49	0.17	22.7	0.18	<0.0077812	142	32.26	1966	316	8.61	9.40	96.10	242.08	35.21	168.12	55.52	7.01	65.83	9.53	56.57	10.80	28.75	3.31	20.77	2.83	63.47	57.34	153.76
19 Gr0-e_3_a_f.csv (copy)	16:12	20	39.8	1.08	22.0	13.8	12.5	0.52	0.24	22.0	0.25	<0.0088591	142	30.53	1943	356	7.30	10.80	103.81	262.10	38.24	180.61	60.03	7.43	72.50	10.53	61.36	11.86	30.85	3.58	21.68	2.79	67.57	34.72	143.57
19 Gr0-e_1A_a_a.csv	14:44	30	38.1	0.04	23.9	12.7	11.4	0.50	0.02	24.3	0.003	0.03	186	<1.8948	2304	16.24	9.40	2.25	4.46	7.82	0.93	4.18	1.14	0.49	1.43	0.29	1.98	0.48	1.50	0.23	1.35	0.24	36.39	3.45	8.21
20 Gr0-e_1A_a_b.csv	14:44	30	38.9	0.02	25.1	11.3	10.2	0.42	0.03	23.6	<0.00046468	0.04	107	<1.8374	216	1.96	9.59	0.26	0.17	0.51	0.09	0.68	0.34	0.04	0.33	0.06	0.37	0.07	0.17	0.04	0.26	0.05	15.34	<0.041778	1.04
21 Gr0-e_1A_a_c.csv	14:44	30	38.8	0.02	24.8	11.6	10.5	0.45	0.02	23.7	<0.00046814	0.03	110	<1.8083	241	2.05	11.30	<0.24516	0.12	0.42	0.07	0.44	0.20	0.04	0.39	0.06	0.38	0.09	0.24	0.04	0.23	0.05	17.77	<0.048116	1.22
23 Gr0-e_1A_a_d.csv	14:44	30	38.8	0.02	24.9	11.4	10.3	0.47	0.03	23.8	0.002	0.05	117	<1.7003	358	2.49	6.73	0.56	0.73	1.33	0.19	0.91	0.24	0.03	0.40	0.05	0.34	0.08	0.34	0.03	0.28	0.05	20.43	<0.030622	0.99
26 Gr0-e_1A_b_a.csv	14:44	30	38.3	0.02	24.7	12.1	10.9	0.46	0.02	23.8	<0.00045058	0.04	106	<1.8101	302	1.58	5.38	0.20	0.10	0.42	0.08	0.43	0.26	<0.025839	0.19	0.04	0.26	0.06	0.19	0.03	0.29	0.05	18.30	<0.048553	0.78
27 Gr0-e_1A_b_b.csv	14:44	30	38.1	0.34	22.5	14.5	13.0	0.26	0.06	24.0	<0.00042321	0.01	528	<1.6058	391	5.73	23.43	<0.21332	0.63	1.35	0.19	0.79	0.27	0.12	0.51	0.11	0.66	0.16	0.73	0.11	0.87	0.19	27.25	<0.037407	1.84
27 Gr0-e_1A_b_b.csv (copy)	14:44	30	37.4	0.35	22.9	14.4	13.0	0.25	0.07	24.3	<0.00049786	0.01	537	<1.9167	396	5.63	23.99	<0.28235	0.68	1.36	0.21	0.86	0.27	0.12	0.45	0.10	0.68	0.17	0.74	0.12	0.87	0.20	26.82	<0.048758	1.78
27 Gr0-e_1A_b_b.csv (copy) (copy)	14:44	30	39.2	0.33	21.9	14.6	13.1	0.29	0.06	23.4	<0.00053852	0.02	515	<2.1024	384	5.80	22.60	<0.33846	0.56	1.29	0.14	0.67	0.27	0.10	0.59	0.12	0.61	0.15	0.71	0.11	0.88	0.18	27.88	<0.057741	1.86
28 Gr0-e_1A_b_c.csv	14:44	30	38.9	0.03	24.5	11.9	10.7	0.41	0.02	23.7	0.001	0.02	106	<1.6971	491	8.31	9.77	0.30	9.60	14.94	1.60	6.36	1.15	0.12	1.08	0.16	1.16	0.24	0.81	0.09	0.83	0.14	16.82	<0.027073	2.75
32 Gr0-e_1A_b_d.csv	14:44	30	38.3	0.02	24.5	12.5	11.3	0.54	0.02	23.6	<0.00039606	0.05	93	<1.595	422	1.87	7.46	0.53	0.17	0.49	0.08	0.47	0.19	<0.021528	0.30	0.07	0.30	0.06	0.19	0.03	0.22	0.06	24.51	0.04	1.07
39 Gr0-e_1B_e.csv	14:44	30	36.3	0.02	22.0	14.1	12.7	0.53	0.00	26.7	0.001	0.01	76	<1.1138	8878	16.77	4.84	9.35	5.58	5.86	0.56	2.17	0.50	0.57	1.18	0.24	1.79	0.42	1.14	0.16	1.05	0.21	24.14	0.52	15.43
41 Gr0-e_2A_a.csv	14:44	30	38.6	0.02	23.7	12.9	11.6	0.43	0.02	23.7	0.25	0.01	133	<2.1168	1395	2.16	13.08	26.83	1.17	1.60	0.17	0.72	0.18	0.03	0.18	0.04	0.28	0.06	0.22	0.03	0.33	0.05	44.49	0.36	2.64
41 Gr0-e_2A_a.csv (copy)	14:44	30	38.8	0.02	23.6	12.8	11.6	0.44	0.02	23.5	0.32	0.01	131	<2.1717	1399	1.88	12.70	34.11	1.23	1.65	0.16	0.73	0.20	<0.026506	0.19	0.04	0.26	0.06	0.17	0.03	0.27	0.05	42.46	0.35	2.47
6 Gr0-e_2A_c.csv	16:12	30	38.7	0.03	23.2	14.0	12.6	0.27	0.02	23.4	0.001	<0.0058719	165	2.35	640	0.29	28.78	0.91	0.03	0.03	<0.01091	<0.061927	<0.038716	<0.021971	<0.095969	<0.01141	<0.055114	<0.012157	0.05	<0.010181	<0.070518	0.03	20.47	4.48	0.72
9 Gr0-e_2B_c.csv	16:12	30	38.7	0.04	23.9	13.3	12.0	0.10	0.00	23.5	<0.00043451	<0.0060809	102	<1.7115	463	1.63	7.81	<0.17866	0.05	0.20	0.03	0.30	0.13	0.02	0.23	0.04	0.19	0.04	0.14	0.02	0.16	0.04	47.27	<0.034963	0.45
10 Gr0-e_2B_d.csv	16:12	30	38.2	0.03	23.8	13.9	12.5	0.09	0.00	23.7	<0.00042317	<0.0059432	79	<1.6814	452	1.13	6.98	<0.28828	0.04	0.11	0.01	0.13	0.10	<0.028212	0.11	0.02	0.14	0.03	0.10	<0.011378	0.09	0.02	46.60	<0.044782	0.69
11 Gr0-e_3_a_a.csv	16:12	30	36.8	0.11	22.1	15.2	13.7	0.36	0.01	25.2	0.004	<0.0040982	121	154.86	5077	357	19.56	5.53	100.50	199.20	27.56	134.48	49.24	8.71

Sample: P6-b	Time	Spot size	SiO2	TiO2	Al2O3	Fe2O3	FeO	MnO	MgO	CaO	K2O	P2O5	V51	Cr53	Sr88	Y89	Zr90	Ba137	La139	Ce140	Pr141	Nd146	Sm147	Eu151	Gd157	Tb159	Dy163	Ho165	Er167	Tm169	Yb173	Lu175	Pb208	Th232	U238
		um	wt.%	wt.%	wt.%	wt.%	wt.%	wt.%	wt.%	wt.%	wt.%	wt.%	µg/g	µg/g	µg/g	µg/g	µg/g	µg/g	µg/g	µg/g	µg/g	µg/g	µg/g	µg/g	µg/g	µg/g	µg/g	µg/g	µg/g	µg/g	µg/g	µg/g	µg/g	µg/g	µg/g
34 P6-b_4_a_a.csv	16:12	20	39.0	0.05	24.7	11.9	10.7	0.30	0.01	23.2	0.30	0.04	198	<2.5422	1489	51.2	6.54	95.44	6.65	9.30	0.99	3.95	1.31	4.01	2.13	0.47	4.05	1.18	4.91	0.86	5.84	0.79	114.6	0.02	24.2
35 P6-b_4_a_b.csv	16:12	20	37.5	0.06	25.1	12.4	11.2	0.63	0.02	23.8	<0.00066997	0.06	149	<2.728	1475	22.4	3.39	3.18	9.79	11.22	1.06	3.64	1.02	3.67	1.49	0.22	1.87	0.43	1.79	0.36	3.17	0.60	53.8	<0.060437	5.2
36 P6-b_4_a_c.csv	16:12	20	38.7	0.06	23.9	13.2	11.9	0.51	0.01	23.3	0.002	0.04	169	<2.6853	2270	11.9	5.85	2.47	1.90	2.30	0.25	1.14	0.34	1.82	0.39	0.08	0.75	0.25	1.17	0.22	2.69	0.53	79.2	<0.018396	8.1
37 P6-b_4_a_d.csv	16:12	20	38.3	0.04	24.9	12.2	11.0	0.29	0.01	23.8	<0.00061268	0.01	150	<2.4552	1162	27.0	4.41	1.73	5.01	6.38	0.64	2.56	0.70	2.32	1.12	0.23	1.96	0.57	2.58	0.45	3.38	0.55	84.0	<0.067034	8.3
37 P6-b_4_a_d.csv (copy)	16:12	20	37.0	0.04	25.5	12.3	11.0	0.27	0.01	24.5	<0.00079337	0.02	147	<3.262	1132	14.7	3.29	1.48	1.12	1.50	0.13	0.52	<0.16927	1.75	0.45	0.11	0.62	0.19	1.26	0.22	1.90	0.42	66.8	<0.10206	3.1
37 P6-b_4_a_d.csv (copy) (copy)	16:12	20	39.3	0.05	24.5	12.1	10.9	0.31	0.01	23.2	0.001	0.01	153	<2.8627	1189	35.6	5.15	1.89	7.72	9.74	0.99	3.93	1.08	2.70	1.58	0.31	2.88	0.83	3.49	0.60	4.48	0.65	96.6	0.10	12.0
38 P6-b_4_a_e.csv	16:12	20	38.3	0.03	25.1	12.1	10.9	0.25	0.01	23.7	<0.00059849	0.01	155	<2.269	1354	19.0	2.92	1.74	0.56	0.89	0.10	0.54	0.21	2.20	0.66	0.10	1.24	0.38	1.66	0.29	2.46	0.36	60.1	<0.039027	4.0
39 P6-b_4_a_f.csv	16:12	20	38.0	0.06	25.3	11.3	10.2	0.50	0.01	24.1	<0.00060005	0.05	177	<2.2797	2687	43.0	2.99	6.19	1.86	2.47	0.33	1.32	0.50	5.22	1.19	0.29	2.73	0.90	3.99	0.69	5.55	0.83	97.8	<0.014184	17.8
40 P6-b_4_b_b.csv	16:12	20	46.0	0.04	23.6	8.0	7.3	0.24	0.01	16.3	4.85	0.02	136	<2.2953	1122	32.3	4.58	1704.82	2.98	4.21	0.45	1.64	0.67	2.88	1.00	0.24	2.08	0.72	2.93	0.59	4.22	0.60	109.5	<0.048589	12.9
41 P6-b_4_b_a.csv	16:12	20	38.3	0.03	24.8	12.2	11.0	0.29	0.01	23.9	<0.00062727	0.02	156	<2.5429	1576	21.3	2.39	2.44	0.50	0.70	0.08	0.57	0.27	2.76	0.53	0.17	1.52	0.41	2.07	0.34	2.67	0.38	67.1	<0.042609	5.6
46 P6-b_4_b_c.csv	16:12	20	38.6	0.05	26.0	10.2	9.2	0.29	0.01	24.1	<0.00055538	0.01	117	<2.4536	2204	41.9	1.50	6.28	2.41	2.79	0.30	1.48	0.66	6.36	1.30	0.28	2.44	0.68	2.97	0.54	4.13	0.65	176.4	<0.061	7.7
47 P6-b_4_c_a.csv	16:12	20	37.7	0.13	23.9	13.6	12.3	0.81	0.22	22.7	0.50	0.06	205	<2.5555	2707	21.6	11.02	12.52	7.27	19.00	3.19	14.75	4.23	3.54	4.37	0.59	3.20	0.63	2.17	0.44	4.01	0.78	45.9	0.08	17.1
49 P6-b_4_c_c.csv	16:12	20	38.8	0.07	24.3	12.4	11.1	0.33	0.01	23.7	0.01	<0.0083603	206	<2.4363	1459	74.0	7.94	2.03	17.11	33.55	3.70	13.84	3.83	3.90	4.24	0.82	6.73	1.90	7.99	1.22	8.76	1.23	119.4	0.52	40.4
21 P6-b_2_a_a.csv	16:12	30	38.5	0.04	23.3	13.7	12.3	0.35	0.01	23.7	0.001	0.01	168	<1.8905	1887	177.8	4.31	1.54	1.48	2.08	0.30	1.94	1.68	5.06	7.39	1.74	16.07	4.17	13.78	1.75	11.96	1.89	39.3	<0.042966	180.4
22 P6-b_2_a_b.csv	16:12	30	38.9	0.06	24.9	11.2	10.1	0.29	0.01	24.0	<0.00044748	0.01	127	<1.8139	2249	74.2	4.25	3.76	0.92	1.69	0.26	1.27	0.73	5.41	1.87	0.42	4.06	1.20	4.69	0.72	5.67	0.90	109.4	<0.029046	28.9
24 P6-b_2_a_c.csv	16:12	30	39.1	0.05	24.9	11.4	10.3	0.23	0.01	23.8	0.001	0.01	125	<1.81	1415	57.1	6.55	1.79	0.76	1.60	0.23	1.32	0.65	3.80	1.60	0.34	2.96	0.83	3.46	0.64	5.12	0.91	74.9	<0.036382	11.4
25 P6-b_2_a_d.csv	16:12	30	38.6	0.13	23.8	13.0	11.7	0.73	0.01	23.3	0.001	0.07	177	<1.6875	2562	34.0	16.64	3.91	3.47	6.09	0.82	4.32	1.51	3.52	2.60	0.40	3.13	0.74	2.84	0.54	5.39	1.20	56.2	0.25	42.8
26 P6-b_2_a_e.csv	16:12	30	37.7	0.07	23.2	14.6	13.1	0.23	0.14	23.6	0.28	0.01	161	1.47	1429	40.4	7.86	7.48	2.23	4.60	0.70	3.78	1.40	1.44	2.59	0.49	4.07	1.04	3.45	0.48	3.04	0.53	50.5	0.60	39.8
27 P6-b_3_a.csv	16:12	30	38.6	0.02	22.3	15.1	13.6	0.30	0.01	23.5	<0.00044582	<0.0062235	176	<1.6808	1389	23.9	4.69	1.04	0.46	0.69	0.09	0.68	0.37	1.54	1.17	0.27	2.62	0.71	2.44	0.27	1.70	0.22	33.4	<0.043825	42.3
28 P6-b_3_b.csv	16:12	30	38.7	0.03	22.9	14.2	12.8	0.33	0.01	23.5	0.001	<0.0060284	154	<1.6225	1695	70.0	5.57	1.41	0.95	1.58	0.24	1.49	1.15	4.53	3.17	0.86	7.62	2.13	7.89	1.03	6.79	0.90	34.0	<0.035451	174.1
32 P6-b_3_c.csv	16:12	30	38.5	0.07	23.8	13.3	12.0	0.69	0.01	23.2	0.001	0.07	197	<1.591	2120	15.8	9.12	2.83	2.29	3.59	0.55	3.01	1.22	2.55	1.54	0.25	1.93	0.45	1.50	0.30	3.21	0.62	31.6	0.04	12.1
33 P6-b_3_d.csv	16:12	30	38.7	0.02	22.7	14.6	13.2	0.34	0.01	23.3	0.002	<0.0061264	171	<1.6955	1141	33.6	4.32	0.71	0.95	0.99	0.10	0.43	0.21	2.06	0.69	0.22	2.41	0.78	3.21	0.44	2.52	0.32	40.6	<0.010655	39.5
48 P6-b_4_c_b.csv	16:12	30	38.7	0.04	24.7	12.2	11.0	0.26	0.02	23.6	0.001	0.01	159	2.30	1132	33.5	11.59	1.63	1.81	6.22	1.16	6.57	2.63	2.11	3.74	0.62	4.43	1.05	3.73	0.58	4.56	0.68	59.3	<0.053424	9.1

Sample: P8	Time	Spot size	SiO2	TiO2	Al2O3	Fe2O3	FeO	MnO	MgO	CaO	K2O	P2O5	V51	Cr53	Sr88	Y89	Zr90	Ba137	La139	Ce140	Pr141	Nd146	Sm147	Eu151	Gd157	Tb159	Dy163	Ho165	Er167	Tm169	Yb173	Lu175	Pb208	Th232	U238
		um	wt.%	wt.%	wt.%	wt.%	wt.%	wt.%	wt.%	wt.%	wt.%	wt.%	µg/g	µg/g	µg/g	µg/g	µg/g	µg/g	µg/g	µg/g	µg/g	µg/g	µg/g	µg/g	µg/g	µg/g	µg/g	µg/g	µg/g	µg/g	µg/g	µg/g	µg/g	µg/g	µg/g
6 P8_2_a_b.csv	17:17	20	37.5	0.14	22.4	14.8	13.4	0.58	0.01	24.2	<0.00058782	0.04	231	3.50	3359	213.8	37.0	8.21	13.98	20.50	2.81	14.23	4.91	3.53	7.78	1.47	13.65	4.40	20.99	4.04	37.72	6.72	53.4	3.31	465
7 P8_2_a_c.csv	17:17	20	37.8	0.09	22.2	14.9	13.4	0.66	0.01	24.1	0.001	0.02	237	5.96	3590	104.1	21.5	4.50	11.62	22.34	3.32	17.64	6.13	4.23	7.69	1.24	9.76	2.40	9.29	1.74	15.98	3.02	44.1	11.2	237
8 P8_2_a_d.csv	17:17	20	45.9	0.06	22.6	9.3	8.4	0.24	0.01	21.1	<0.00079663	<0.01082	75	<3.2127	951	28.0	5.5	<0.54446	2.29	4.44	0.55	2.55	0.94	1.98	1.70	0.31	2.82	0.64	2.63	0.32	2.49	0.21	108.8	0.10	2.64
8 P8_2_a_d.csv (copy)	17:17	20	66.8	0.11	15.8	5.4	4.9	0.12	0.49	7.5	2.57	<0.0082345	43	<2.4135	338	12.8	1.9	325.38	2.75	5.60	0.65	2.85	0.73	0.70	1.28	0.21	1.49	0.33	0.87	0.17	0.79	0.11	47.0	0.28	1.90
9 P8_2_a_e.csv	17:17	20	38.1	0.17	25.8	10.8	9.7	0.33	0.04	24.0	0.15	<0.0086185	94	<2.5109	1265	13.0	5.0	13.89	1.19	2.25	0.25	1.07	0.29	1.71	0.48	0.12	0.94	0.32	1.16	0.23	1.76	0.27	140.3	0.05	1.04
10 P8_2_a_f.csv	17:17	20	38.7	0.02	22.1	15.2	13.7	0.18	0.01	23.5	<0.00075564	<0.010308	189	3.87	1296	75.1	5.7	0.58	3.95	6.97	1.04	5.11	2.38	1.81	3.91	0.80	6.43	1.76	6.04	0.69	3.74	0.47	31.5	0.54	111
11 P8_2_a_g.csv	17:17	20	38.9	0.02	21.8	15.5	13.9	0.30	0.01	23.3	<0.00083727	<0.011458	212	<3.4425	1447	105.0	4.7	0.56	5.23	9.59	1.51	7.90	2.90	3.26	5.37	0.99	9.08	2.42	8.86	1.08	7.32	1.01	28.2	0.46	163
50 P8_1_a_a.csv	16:12	30	37.6	0.08	21.7	16.3	14.7	0.15	0.06	24.0	0.03	<0.0055772	276	5.96	1496	84.1	5.3	1.73	6.48	16.54	2.89	15.35	7.01	7.58	9.90	1.56	10.47	2.10	5.92	0.67	4.27	0.74	1.84	154	
51 P8_1_a_c.csv	16:12	30	27.1	0.01	20.7	43.2	39.0	1.24	10.24	0.0	0.01	<0.004503	138	22.09	2	0.1	<0.026149	0.89	<0.0083887	<0.0056292	<0.0076308	<0.054159	<0.063698	<0.01463	<0.055757	<0.0079807	<0.039176	<0.01065	<0.037858	<0.0088849	<0.069446	0.01	0.1	<0.022873	0.07
52 P8_1_a_f.csv	16:12	30	27.6	0.14	21.0	42.0	37.9	1.19	9.37	0.0	1.12	<0.0045356	101	12.95	2	0.0	<0.045775	21.56	<0.0099889	<0.009854	<0.010358	<0.040245	<0.040766	<0.014279	<0.054416	<0.009157	<0.03823	<0.0082983	<0.040355	<0.0099418	<0.067765	<0.010794	0.2	0.01	0.08
53 P8_1_a_b.csv	16:12	30	37.3	1.39	21.5	14.5	13.1	0.56	0.01	24.5	0.0003	0.02	193	7.13	3126	133.6	14.3	2.65	107.56	140.32	15.81	69.35	18.29	9.31	20.16	3.03	18.97	3.95	12.16	1.90	15.55	2.97	37.1	27.3	345
54 P8_1_a_c.csv	16:12	30	37.7	0.05	22.2	15.5	14.0	0.25	0.03	24.1	<0.00029103	0.01	232	5.20	1284	105.6	5.7	0.63	4.67	10.26	1.70	9.21	4.49	2.08	8.22	1.70	13.29	3.40	10.14	1.17	6.58	1.08	32.1	4.92	309
55 P8_1_a_d.csv	16:12	30	38.2	0.04	22.6	14.7	13.2	0.35	0.01	23.9	<0.00031507	<0.0042917	135	12.38	1880	85.2	6.3	3.30	6.85	20.15	3.58	20.92	9.08	2.09	12.74	2.11	14.04	2.89	8.04	1.14	7.63	1.15	68.4	4.07	79.6
5 P8_2_a_a.csv	17:17	30	39.5	0.11	24.9	11.0	9.9	0.30	0.14	23.3	0.19	0.01	207	7.66	1038	249.9	7.8	5.81	373.83	727.69	81.08	288.78	52.17	9.66	47.91	6.81	41.16	8.10	22.28	2.49	12.31	1.40	133.6	181	79.1
12 P8_3_a.csv	17:17	30	39.2	0.11	23.6	12.6	11.4	0.40	0.01	23.6	<0.00043518	<0.0056915	294	7.06	1313	203.5	6.2	0.43	49.80	102.81	13.28	57.10	17.48	8.38	21.65	3.79	26.67	6.17	20.10	2.79	18.51	2.66	70.3	2.69	215
13 P8_3_b.csv	17:17	30	38.7	0.12	23.5	13.0	11.7	0.42	0.02	23.8	0.001	<0.0058589	190	5.21	1298	106.4	6.5	0.36	11.27	22.93	3.36	16.83	7.62	3.72	12.54	2.28	15.72	3.41	10.23	1.32	9.34	1.22	67.8	0.03	59.5
14 P8_3_c.csv	17:17	30	38.3	0.04	23.4	12.7	11.5	0.55	0.01	24.6	<0.00042571	<0.005603	126	3.39	4324	196.6	13.7	2.98	21.08	36.36	5.33	29.12	14.09	6.83	24.41	4.14	29.37	6.21	18.23	2.17	12.21	1.58	82.0	0.03	95.5
19 P8_3_d.csv	17:17	30	39.0	0.09	23.3	12.9	11.6	0.39	0.01	23.9	0.001	0.01	176	6.09	2463	109.5	6.9	2.20	13.22	26.28	3.59	18.31	7.41	3.30	11.43	2.06	14.81	3.25	10.80	1.71	14.19	2.37	65.0	0.34	57.3
20 P8_3_e.csv	17:17	30	39.1	0.11	23.8	12.4	11.2	0.40	0.01	23.6	<0.00041765	<0.0054174	296	7.71	1378	207.9	6.5	0.52	50.78	103.28	13.22	56.20	17.46	8.35	22.49	4.04	28.34	6.32	19.66	2.77	18.42	2.70	74.7	5.14	185
21 P8_3_f.csv	17:17	30	83.5	0.52	4.2	6.7	6.0	0.14	1.66	<0.027957	2.26	<0.0054712	25	2.08	0	<0.027043	<0.034078	77.48	0.004	<0.011453	<0.010428	<0.057777	<0.068449	<0.028299	<0.092214	<0.0090302	<0.057969	<0.010738	<0.047597	<0.0092799	<0.082985	<0.013006	0.4	<0.037535	<0.036916
24 P8_4_a_c.csv	17:17	30	39.0	0.03	23.1	13.7	12.4	0.22	0.01	23.6	<0.00042338	0.01	136	<1.6785	1078	71.6	10.6	0.81	0.42	0.78	0.14	0.67	0.70	2.27	2.10	0.47	4.72	1.38	5.48	0.70	4.66	0.78	25.6	<0.040191	30.24
25 P8_4_a_d.csv	17:17	30	38.0	0.13	22.9	13.7	12.3	0.59	0.01	24.3	<0.00029766	0.05	192	<1.2041	2940	129.7	25.2	6.39	2.04	3.45	0.54	3.38	1.79	6.30	4.12	0.88	8.35	2.47	9.92	1.67	14.21	2.80	52.7	0.22	201
26 P8_4_a_e.csv	17:17	30	38.4	0.10	22.8	13.8	12.4	0.56	0.01	23.9	<0.00030055	0.02	238	<1.247	2599	80.0	13.5	2.97	3.44	4.69	0.67	3.23	1.61	5.57	3.51	0.72	5.90	1.58	5.82	1.07	9.40	2.17	35.5	0.08	66.54
27 P8_4_b_a.csv	17:17	30	38.2	0.04	23.9	13.0	11.7	0.22	0.01	24.3	0.001	<0.0039673	140	<1.1629	1746	45.2	8.3	1.80	0.82	1.52	0.24	1.46	0.86	3.06	1.76	0.39	3.32	0.88	3.29	0.46	3.03	0.56	57.7	0.01	24.44
28 P8_4_b_b.csv	17:17	30	38.8	0.03	23.3	13.6	12.3	0.48	0.01	23.3	<0.00042742	0.02	154	<1.6806	1055	30.2	3.6	1.94	0.73	1.18	0.22	1.07	0.64	2.06	1.24	0.26	2.27	0.61	2.16	0.27	1.66	0.31	25.5	<0.030072	15.47
33 P8_4_b_c.csv	17:17	30	38.4	0.05	24.0	12.3	11.1	0.36	0.01	24.4	<0.00028371	0.01	150	<1.1435	2239	135.2	4.7	2.85	1.30	2.39	0.40	2.48	1.81	6.61	4.73	1.05	9.57	2.58	9.44	1.33	8.88	1.45	58.2	<0.032833	78.81
36 P8_5_a_c.csv	17:17	30	39.4	0.08	25.3	10.3	9.3	0.27	0.01	24.0	<0.00044276	<0.0056841	106	<1.7089	1347	36.6	10.6	1.86	1.51	2.86	0.49	2.89	1.36	4.73	2.68	0.47	3.65	0.78	2.73	0.41	2.66	0.44	67.8	0.05	10.96
39 P8_5_b_b.csv	17:17	30	38.6	0.04	23.7	12.7	11.5	0.36	0.01	24.1	0.001	0.01	140	<1.1752	1847	42.9	4.6	2.94	0.73	0.89	0.15	0.74	0.51	4.01	1.27	0.30	2.89	0.82	3.34	0.46	3.52	0.50	55.7	<0.020982	26.61
40 P8_5_b_c.csv	17:17	30	39.1	0.06	24.2	12.3	11.1	0.38	0.01	23.5	<0.00042826	0.03	121	<1.6467	1209	31.2	8.8	2.46	3.84	6.93	1.01	5.50	2.28	2.80	3.36	0.59	4.05	0.87	2.76	0.38	2.49	0.42	51.9	<0.042548	7.09
34 P8_5_a_a.csv	17:17	50	37.9	0.04	23.9	13.1	11.8	0.35	0.01	24.3	<0.00017831	0.004	160	<0.74405	2039	97.7	5.7	1.88	1.03	1.18	0.15	0.72	0.48	5.63	1.73	0.49	5.42	1.77	7.43	1.16	8.29	1.33	44.6	<0.012501	70.83
35 P8_5_a_b.csv	17:17	50	37.7	0.03	23.6	13.8	12.4	0.29	0.01	24.3	0.0002	0.01	167	<0.75999	1628	101.3	7.8	1.27	0.62	0.72	0.08	0.44	0.29	4.65	1.53	0.43	5.28	1.76	7.43	1.12	7.66	1.22	34.4	<0.021237	57.30
37 P8_5_a_d.csv	17:17	50	37.9	0.04	24.5	12.6	11.4	0.27	0.01	24.2	<0.0001847	0.01	123	<0.77812	1594	40.0	10.4	2.12	0.70	0.94	0.13	0.77	0.40	3.47	1.34	0.28	2.64	0.77	3.12	0.48	3.30	0.51	47.7	<0.018804	18.18
38 P8_5_b_a.csv	17:17	50	37.6	0.03	23.7	13.9	12.5	0.39	0.01	24.0	0.001	0.01	161	<0.79476	1563	40.9	5.5	1.81	0.76	0.94	0.12	0.64	0.31	3.12	1.03	0.26	2.57	0.75	3.04	0.45	3.10	0.44	29.5	0.06	24.04

Sample: P9d	Time	Analysis #	Spot size	SiO2	TiO2	Al2O3	Fe2O3	FeO	MnO	MgO	CaO	Na2O	K2O	Li7	B11	V51	Cr53	As75	Rb85	Sr88	Y89	Zr90	Nb93	Ba137	La139	Ce140	Pr141	Nd146	Sm147	Eu151	Gd157	Tb159	Dy163	Ho165	Er167	Tm169	Yb173	Lu175	W182	Pb208	Th232	U238
				wt.%	wt.%	wt.%	wt.%	wt.%	wt.%	wt.%	wt.%	wt.%	wt.%	µg/g	µg/g	µg/g	µg/g	µg/g	µg/g	µg/g	µg/g	µg/g	µg/g	µg/g	µg/g	µg/g	µg/g	µg/g	µg/g	µg/g	µg/g	µg/g	µg/g	µg/g	µg/g	µg/g	µg/g	µg/g	µg/g	µg/g	µg/g	µg/g
24/p9d7.xl	10:29	7	24	41.7	0.05	22.5	13.7	12.3	0.41	0.01	21.3	0.0004	<0.0098592	<1.1762	<2.6355	98.4	<55.9952	<2.4232	<0.38928	917.7	31.13	3.04	0.50	4.94	0.55	1.24	0.32	1.04	1.06	1.30	2.07	0.49	2.87	0.86	3.04	0.52	3.36	0.52	0.15	22.63	0.23	2.79
24/p9d7.xl (copy)	10:29	8	24	43.2	0.04	21.5	13.6	12.2	0.35	0.01	21.0	0.001	<0.91704	1.48	90.4	<27.1057	<1.8259	<0.30359	1178.9	19.12	2.26	0.57	2.54	0.33	1.02	0.21	0.94	0.51	0.96	1.29	0.22	2.48	0.42	1.54	0.25	1.98	0.34	0.20	31.74	0.10	4.82
25/p9d7.xl (copy) (copy)	10:29	9	24	41.1	0.02	20.7	16.6	14.9	0.50	0.02	21.0	0.0011	0.01	<0.74828	7.50	164.4	<23.5999	1.81	<0.25966	920.3	4.14	<0.03	0.34	9.98	1.30	2.92	0.52	1.95	0.78	0.72	0.48	0.11	0.87	0.09	0.42	0.07	0.57	0.09	<0.082888	25.67	0.24	0.69
26/p9a10.xl	10:38	10	24	42.1	0.02	20.5	16.0	14.4	0.43	0.02	20.8	0.0017	<0.0071768	<0.33058	2.11	181.4	<25.6127	<1.6996	<0.29407	321.7	6.75	27.77	0.25	1.59	0.45	1.60	0.30	1.21	0.65	0.78	1.16	0.19	1.67	0.21	0.82	0.14	1.12	0.17	<0.19398	13.20	0.08	1.77
27/p9a10.xl (copy)	10:38	11	24	40.6	0.02	21.0	16.3	14.7	0.20	0.01	21.8	0.0002	<0.0072522	0.48	<2.0529	145.7	<26.0229	<1.7305	<0.30792	705.2	<0.10005	8.45	<0.12041	<1.5811	<0.050261	<0.10157	<0.077241	<0.52548	<0.25919	<0.071483	<0.23134	<0.030261	<0.31116	<0.070469	<0.12633	<0.026422	<0.16136	<0.031171	<0.2237	27.69	<0.041494	0.24
28/p9a12.xl	10:45	12	44	40.3	0.02	22.4	14.6	13.2	0.46	0.02	21.9	0.0014	<0.0019619	<0.22667	1.63	162.9	<7.0881	0.47	<0.067469	388.0	1.30	14.64	0.15	1.62	0.10	0.20	0.04	0.25	0.17	0.11	0.34	0.03	0.18	0.03	0.18	0.04	0.22	0.05	<0.060995	12.43	0.01	0.92
29/p9a12.xl (copy)	10:45	13	44	40.0	0.03	22.2	14.8	13.4	0.19	0.02	22.5	0.0012	<0.0019252	<0.22003	2.03	165.2	<6.9522	0.61	<0.065955	471.0	7.08	58.19	0.15	1.31	0.18	0.47	0.08	0.45	0.28	0.47	0.51	0.10	0.69	0.21	0.58	0.09	0.89	0.19	<0.059208	22.92	0.06	2.38
30/p9a14.xl	10:52	14

Aar Massif – Gelmersee

Sample: GE-4	Time	Info	Spot size	SiO2	TiO2	Al2O3	Fe2O3	FeO	MnO	MgO	CaO	Na2O	K2O	Li7	B11	V51	Cr53	Sr88	Y89	Zr90	Ba137	La139	Ce140	Pr141	Nd146	Sm147	Eu151	Gd157	Tb159	Dy163	Ho165	Er167	Tm169	Yb173	Lu175	Pb208	Th232	U238
			um	wt.%	wt.%	wt.%	wt.%	wt.%	wt.%	wt.%	wt.%	wt.%	wt.%	µg/g	µg/g	µg/g	µg/g	µg/g	µg/g	µg/g	µg/g	µg/g	µg/g	µg/g	µg/g	µg/g	µg/g	µg/g	µg/g	µg/g	µg/g	µg/g	µg/g	µg/g	µg/g	µg/g	µg/g
7 GE4_30um_3.csv	10:45	7 GE4_30um_3	30	38.7	0.09	22.4	14.4	13.0	0.41	0.02	23.7	0.002	<0.0003065	0.67	2.09	141.6	<1.613	1241	281.6	21.5	0.61	10.35	27.98	3.48	14.93	6.03	1.77	11.49	3.23	30.06	8.24	31.14	4.88	36.81	5.84	38.20	0.00	79.6
7 GE4_30um_3.csv (copy)	10:45	8 GE4_30um_4_1st	30	38.0	0.02	22.7	14.6	13.2	0.63	0.01	23.8	0.004	0.001	1.72	1.74	103.0	<1.8672	1247	93.0	4.8	0.40	1.04	2.06	0.31	1.40	1.13	1.74	2.68	0.67	7.11	2.01	8.53	1.31	10.71	1.48	29.92	<0.0058314	20.4
7 GE4_30um_3.csv (copy) (copy)	10:45	8 GE4_30um_4_2nd	30	39.4	0.02	22.0	15.0	13.5	0.65	0.01	22.8	0.002	<0.00042413	0.55	1.10	93.5	<2.2708	1140	53.3	4.6	0.59	0.28	0.55	0.07	0.47	0.28	1.17	0.74	0.25	3.17	0.99	4.78	0.86	6.56	1.09	29.87	<0.0077015	11.0
7 GE4_30um_3.csv (copy) (copy) (copy)	10:45	9 GE4_30um_5	30	38.4	0.01	22.2	15.0	13.6	0.31	0.01	23.8	0.001	<0.00029832	0.13	1.58	120.4	<1.6025	1639	214.0	5.4	0.25	0.38	0.84	0.12	0.53	0.41	2.43	1.70	0.75	10.53	4.13	18.21	2.60	14.90	1.88	31.10	<0.0067562	41.4
10 GE4_30um_6.csv	10:45	10 GE4_30um_6	30	38.0	0.05	22.5	14.4	13.0	0.86	0.01	23.9	0.001	<0.00030366	0.34	8.25	108.5	<1.5579	2637	313.2	10.8	0.81	1.58	3.11	0.50	3.30	2.87	6.07	7.69	2.09	21.00	6.42	27.78	4.94	39.46	5.52	60.51	0.02	162.0
10 GE4_30um_6.csv (copy)	11:15	11 GE4_30um_7	30	37.1	0.04	21.2	15.6	14.0	0.92	0.00	25.1	0.001	<0.00030426	0.21	0.79	140.9	<1.6044	6728	27.2	3.2	4.57	0.25	0.38	0.05	0.21	0.10	0.33	0.10	0.03	0.41	0.24	1.95	0.56	6.84	1.20	57.56	0.01	5.4
10 GE4_30um_6.csv (copy) (copy)	11:15	13 GE4_30um_8	30	36.7	0.05	22.1	15.1	13.6	0.92	0.01	24.9	0.001	0.0007	0.56	4.44	132.6	<2.2261	4836	581.5	11.6	2.12	48.62	84.02	8.64	31.85	9.47	9.63	17.33	4.36	43.77	13.46	55.89	10.53	89.33	14.06	63.45	1.32	147.1
10 GE4_30um_6.csv (copy) (copy) (copy)	11:15	16 GE4_30um_9	30	38.3	0.12	21.4	16.0	14.4	0.26	0.02	23.7	0.001	0.0004	0.56	1.78	289.1	<1.5778	1168	250.8	29.0	0.17	0.91	1.71	0.25	1.29	0.98	3.29	4.14	1.56	18.31	5.62	22.27	3.76	29.73	4.75	43.00	0.07	160.4
17 GE4_30um_10.csv	11:15	17 GE4_30um_10	30	36.2	0.08	21.8	15.4	13.8	0.96	0.00	25.4	0.001	<0.00037903	0.26	<0.52933	139.6	<2.0577	7104	300.3	25.7	5.44	1.51	2.13	0.29	1.52	1.22	1.63	3.58	1.21	16.49	5.89	31.59	7.28	70.44	11.19	63.02	0.06	76.1
17 GE4_30um_10.csv (copy)	11:15	18 GE4_30um_11	30	37.7	0.02	22.0	15.3	13.8	0.41	0.01	24.4	0.001	0.0004	0.40	0.66	114.9	<1.6411	3053	255.2	4.0	1.01	0.72	2.00	0.39	2.82	3.54	3.05	11.14	2.93	27.68	7.18	24.11	2.98	16.42	1.90	76.50	0.01	53.2
17 GE4_30um_10.csv (copy) (copy)	11:15	19 GE4_30um_12	30	38.5	0.08	22.5	14.7	13.3	0.51	0.02	23.4	0.001	<0.00029584	0.61	3.22	122.3	<1.6337	1311	224.5	24.6	0.30	1.04	2.09	0.31	2.00	1.97	3.10	6.78	2.08	22.42	6.31	25.18	4.18	32.88	5.19	29.19	<0.0049401	71.8
17 GE4_30um_10.csv (copy) (copy) (copy)	11:15	20 GE4_30um_13	30	37.7	0.03	22.1	15.2	13.7	0.40	0.01	24.3	0.001	0.0004	0.42	0.80	162.5	<1.7253	2607	223.5	5.6	0.78	0.49	1.20	0.16	0.80	0.76	2.15	3.79	1.37	16.50	5.15	21.42	2.90	18.31	2.13	61.71	0.03	48.3
21 GE4_30um_14.csv	11:45	21 GE4_30um_14	30	38.3	0.02	22.6	14.6	13.2	0.42	0.01	23.8	0.002	0.0010	0.71	1.85	63.8	3.00	1543	111.2	6.9	0.57	2.24	5.63	0.87	4.89	4.46	0.90	10.44	2.59	19.60	4.04	12.77	1.57	9.04	1.15	42.92	0.56	20.1
21 GE4_30um_14.csv (copy)	11:45	22 GE4_30um_15	30	37.9	0.16	23.0	14.2	12.8	0.24	0.01	24.1	0.001	<0.00032901	0.48	0.49	129.1	<1.7713	649	483.9	10.4	0.50	0.08	0.11	0.02	0.11	0.24	1.34	3.03	1.82	29.41	12.08	64.74	11.37	79.32	10.11	17.89	0.00	15.0
21 GE4_30um_14.csv (copy) (copy)	11:45	24 GE4_30um_16	30	38.1	0.09	21.6	15.8	14.2	0.46	0.02	23.8	0.004	0.0016	1.14	2.03	264.9	<1.5464	2145	405.1	9.0	0.43	0.50	1.27	0.18	1.13	1.12	3.66	5.67	2.16	27.88	8.95	37.12	5.48	40.48	6.18	47.42	0.11	181.9
21 GE4_30um_14.csv (copy) (copy) (copy)	11:45	27 GE4_30um_17	30	37.6	0.05	21.8	15.4	13.9	0.89	0.01	24.0	0.008	0.0040	3.60	3.24	129.4	<1.6482	4398	391.3	13.2	3.71	0.47	1.32	0.22	1.33	1.42	1.51	6.65	2.37	29.79	9.20	39.29	7.07	58.53	8.55	66.37	0.01	106.7

Aar Massif – Oberaletsch

Sample: OBA19-03B	Time	Spot size	SiO2	TiO2	Al2O3	Fe2O3	FeO	MnO	MgO	CaO	Na2O	K2O	P2O5	Li7	B11	V51	Cr53	Sr88	Y89	Zr90	Nb93	Ba137	La139	Ce140	Pr141	Nd146	Sm147	Eu151	Gd157	Tb159	Dy163	Ho165	Er167	Tm169	Yb173	Lu175	Pb206	Pb207	Pb208	Th232	U238
		um	wt.%	wt.%	wt.%	wt.%	wt.%	wt.%	wt.%	wt.%	wt.%	wt.%	wt.%	µg/g	µg/g	µg/g	µg/g	µg/g	µg/g	µg/g	µg/g	µg/g	µg/g	µg/g	µg/g	µg/g	µg/g	µg/g	µg/g	µg/g	µg/g	µg/g	µg/g	µg/g	µg/g	µg/g	µg/g	µg/g	µg/g	µg/g
5 OBA19-03_1_2.csv	14:30	50	37.1	0.04	20.8	15.6	14.1	0.5	0.006	25.7	0.0027	0.0004	0.0061	0.18	0.78	92.5	<1.0922	6493	403.6	17.7	0.062	22.11	0.8	1.7	0.2	1.3	0.8	1.6	2.4	1.1	20.0	8.8	43.6	8.0	60.5	8.9	188	188	189	<0.0105	363
6 OBA19-03_1_3.csv	14:30	50	38.2	0.08	21.7	15.5	14.0	0.6	0.011	23.7	0.0007	<0.00027647	0.0026	0.11	0.53	129.7	1.25	2307	559.6	4.4	<0.011095	1.34	2.3	6.4	1.1	6.9	6.8	6.7	21.7	6.7	63.2	15.6	56.0	9.3	68.8	10.0	127	127	128	0.0099	263
7 OBA19-03_1_4.csv	14:30	50	37.0	0.05	20.7	15.6	14.0	0.5	0.006	26.0	0.0009	0.0003	0.0032	0.10	0.80	97.3	1.06	7339	863.4	20.7	<0.013625	28.67	3.9	8.8	1.5	9.6	10.4	10.1	32.6	9.7	91.9	23.2	78.7	10.8	66.3	8.6	200	201	200	<0.0072974	475
8 OBA19-03_1_5.csv	14:30	50	36.9	0.05	21.0	15.6	14.0	0.5	0.006	25.8	0.0009	<0.00027626	0.0027	0.16	0.78	95.4	<0.92583	6612	911.4	16.7	0.057	18.20	1.6	3.8	0.7	5.0	6.7	9.4	26.8	8.7	90.3	24.1	82.7	11.6	68.3	8.4	171	168	168	<0.0097849	531
9 OBA19-03_1_6.csv	14:30	50	37.9	0.05	21.8	15.4	13.8	0.5	0.011	24.2	0.0022	<0.00028102	<0.0025138	0.16	0.72	113.8	3.93	2858	1026.8	3.9	0.016	1.26	159.4	364.9	50.5	237.1	97.3	14.6	125.8	22.9	156.1	31.5	92.7	11.6	65.8	7.3	128	128	127	7.92	365
10 OBA19-03_1_7.csv	14:30	50	37.2	0.06	21.3	15.3	13.8	0.5	0.008	25.3	0.0007	<0.0002645	0.0028	0.09	0.55	98.4	1.47	5406	1096.1	5.9	0.015	4.87	37.4	80.7	11.3	53.5	26.6	13.5	55.7	14.1	126.3	30.4	100.1	12.5	66.9	7.3	117	113	114	1.72	604
13 OBA19-03_1_8.csv	14:30	50	36.9	0.05	21.0	15.4	13.8	0.5	0.006	25.9	0.0006	<0.00024076	0.0050	0.10	0.59	94.3	<0.81438	6993	726.1	16.5	0.065	21.73	0.6	1.3	0.2	1.6	2.9	6.6	15.8	5.8	65.7	18.7	68.3	9.5	60.3	8.0	174	173	175	<0.0067971	415
14 OBA19-03_1_9.csv	14:30	50	37.4	0.04	21.1	15.4	13.9	0.4	0.006	25.5	0.0012	<0.00027813	<0.0024521	0.09	0.55	93.6	<0.92462	5907	845.3	7.4	0.066	4.89	2.6	6.2	1.1	6.7	7.2	8.5	26.9	8.4	85.1	22.4	77.8	10.2	58.2	6.3	153	151	151	0.0161	439
15 OBA19-03_1_10.csv	14:30	50	37.7	0.03	21.6	15.5	14.0	0.5	0.011	24.5	0.0013	<0.00027707	0.0038	0.12	0.54	114.1	2.48	3440	1091.2	4.3	0.030	2.05	144.7	320.6	43.9	207.1	81.7	17.6	115.1	21.2	154.2	32.6	100.9	14.0	96.7	13.6	152	151	151	13.3	452
16 OBA19-03_2_1.csv	14:30	50	37.5	0.01	21.2	16.0	14.5	0.6	0.009	24.5	0.0009	<0.00026112	0.0044	0.07	0.53	56.2	<0.8593	3877	181.2	2.3	0.008	1.47	0.1	0.3	0.0	0.2	0.1	0.4	0.4	0.3	7.8	3.8	18.9	2.5	13.9	1.5	116	116	116	0.041	313
17 OBA19-03_2_2.csv	14:30	50	37.1	0.06	21.3	15.7	14.1	0.4	0.008	25.3	0.0015	0.0004	0.0040	0.21	0.72	65.1	<0.94014	5146	57.0	3.0	0.039	3.42	0.5	1.0	0.1	0.6	0.2	0.1	0.6	0.1	1.7	0.9	6.7	1.3	9.3	1.3	146	148	148	0.037	124
18 OBA19-03_2_3.csv	14:30	50	37.2	0.04	21.2	15.4	13.8	0.5	0.008	25.5	0.0006	<0.00026193	0.0028	0.09	0.66	105.9	3.44	5671	934.2	7.3	<0.008918	2.67	164.3	331.2	44.1	204.4	81.6	12.5	108.4	19.7	136.8	28.4	83.5	10.6	60.5	7.3	118	119	118	1.53	330
19 OBA19-03_2_4.csv	14:30	50	37.7	0.11	21.1	16.3	14.7	0.7	0.010	24.0	0.0003	<0.00029054	0.0042	0.08	0.64	86.3	<0.94343	2686	202.6	3.9	<0.0084729	1.34	0.1	0.3	0.0	0.1	0.1	0.3	0.2	0.2	6.5	3.9	25.1	5.5	45.9	6.9	117	117	117	0.019	245
22 OBA19-03_2_5.csv	14:30	50	37.6	0.10	21.3	16.0	14.4	0.5	0.009	24.3	0.0003	<0.0002447	0.0035	<0.056607	0.43	85.9	<0.82174	2861	92.4	3.8	0.029	1.67	0.1	0.2	0.0	0.1	<0.032737	0.1	0.1	0.1	2.0	1.5	11.8	3.2	27.6	4.1	118	118	120	0.023	158
24 OBA19-03_2_6.csv	14:30	50	36.0	0.05	20.5	15.3	13.8	0.4	0.004	27.5	0.0009	0.0005	0.0041	0.13	0.54	64.9	<0.77328	10088	52.4	4.1	0.015	10.29	0.1	0.3	0.0	0.1	0.1	0.1	0.1	0.0	0.8	0.7	6.4	1.6	15.6	3.0	133	134	134	0.033	101
25 OBA19-03_3_1.csv	14:30	50	38.0	0.05	22.5	14.7	13.2	0.5	0.011	24.0	0.0005	<0.00027166	0.0024	<0.061141	0.42	127.2	3.28	2219	707.3	6.7	0.034	1.13	109.2	240.3	29.8	123.2	40.3	8.9	55.0	11.5	89.4	20.4	69.9	10.7	74.8	9.6	163	164	164	12.3	191
26 OBA19-03_3_2.csv	14:30	50	37.9	0.05	22.0	15.0	13.5	0.5	0.012	24.3	0.0008	<0.0002604	0.0035	0.09	0.37	124.6	2.71	2804	979.9	5.4	0.044	1.48	189.6	421.9	55.7	245.7	84.9	13.6	107.5	20.2	141.7	29.8	89.8	12.1	76.1	10.0	166	167	166	2.903	345
27 OBA19-03_3_3.csv	14:30	50	37.9	0.09	22.0	15.2	13.7	0.5	0.010	24.1	0.0006	<0.00028658	0.0033	0.07	0.63	121.2	1.31	2477	388.5	4.6	0.019	1.50	11.0	24.8	3.5	17.2	9.8	5.0	20.9	5.3	48.1	12.1	41.1	5.8	39.8	5.4	146	146	146	0.432	224
28 OBA19-03_3_4.csv	14:30	50	36.5	0.05	21.0	15.4	13.9	0.5	0.006	26.4	0.0005	<0.00025359	0.0030	0.08	0.35	96.2	1.60	7397	846.6	21.7	<0.0088278	29.46	6.8	15.3	2.6	16.0	14.2	10.3	37.6	10.3	94.8	23.0	78.2	10.6	66.7	8.5	197	196	197	0.014	456
29 OBA19-03_3_5.csv	14:30	50	36.7	0.05	21.0	15.5	13.9	0.5	0.006	26.2	0.0010	0.0003	0.0043	0.20	0.47	99.5	1.05	6497	906.1	18.7	0.016	22.76	7.3	17.0	2.8	16.7	13.7	10.5	38.5	10.7	97.3	24.4	85.7	12.1	82.9	11.4	185	185	186	0.134	466
32 OBA19-03_3_6.csv	14:30	50	37.3	0.07	21.5	15.5	14.0	0.6	0.008	25.0	0.0004	<0.00025422	0.0028	0.07	0.33	104.6	<0.85038	4481	406.3	8.2	0.041	7.15	0.1	0.2	0.0	0.2	0.1	1.3	1.0	0.9	19.5	9.2	47.1	8.8	66.8	9.5	137	137	137	<0.0073537	342
33 OBA19-03_4_1.csv	14:30	50	37.6	0.09	22.0	15.1	13.6	0.5	0.009	24.4	0.0008	0.0003	<0.002271	0.11	0.53	122.1	<0.89346	3012	574.5	5.4	0.071	1.46	1.4	3.6	0.6	4.0	5.1	6.7	19.4	6.5	63.9	15.9	54.5	7.8	50.6	6.4	117	116	116	<0.0095861	249
34 OBA19-03_4_2.csv	14:30	50	37.0	0.04	21.3	15.7	14.1	0.5	0.007	25.4	0.0006	<0.00026402	<0.0022004	<0.057778	0.49	90.9	<0.88571	5100	268.2	5.1	0.038	3.20	0.0	0.1	0.0	0.1	0.1	1.0	0.8	0.6	12.6	5.8	29.6	4.5	28.6	3.6	143	143	142	<0.010587	247
35 OBA19-03_4_3.csv	14:30	50	37.5	0.10	22.4	15.1	13.6	0.6	0.010	24.2	0.0014	0.0004	0.0047	0.20	0.53	125.9	<0.92891	2240	467.8	5.0	0.088	1.40	2.9	6.2	0.9	4.6	4.3	5.2	14.6	4.7	50.0	12.9	46.5	6.8	43.3	5.7	115	115	115	0.019991683	246
36 OBA19-03_4_4.csv	14:30	50	37.5	0.10	21.6	16.0	14.4	0.7	0.010	24.0	<0.00023267	<0.00027004	0.0031	0.10	0.40	104.5	<0.87759	2373	278.4	4.1	<0.0078151	1.16	0.0	0.0	0.0	0.0	<0.03612	0.7	0.7	0.6	13.7	6.2	36.5	8.1	71.2	10.9	115	116	116	<0.0051242	241
37 OBA19-03_4_5.csv	14:30	50	37.0	0.03	20.8	16.1	14.5	0.5	0.008	25.5	0.0007	<0.00024862	0.0062	<0.050914	0.55	64.7	<0.80005	5316	222.8	3.9	0.014	7.08	0.0	0.0	0.0	0.0	0.1	0.7	0.8	0.6	13.5	5.5	23.3	3.6	23.7	3.3	191	190	191	<0.010049	221

Aar Massif – Clefts

Sample: Planggenstock	Time	Spot size	Notes	SiO2	TiO2	Al2O3	Fe2O3	FeO	MnO	MgO	CaO	Na2O	K2O	P2O5	Li7	B11	V51	Cr53	Sr88	Y89	Zr90	Nb93	Ba137	La139	Ce140	Pr141	Nd146	Sm147	Eu151	Gd157	Tb159	Dy163	Ho165	Er167	Tm169	Yb173	Lu175	Pb206	Pb207	Pb208	Th232	U238
		um		wt.%	wt.%	wt.%	wt.%	wt.%	wt.%	wt.%	wt.%	wt.%	wt.%	wt.%	µg/g	µg/g	µg/g	µg/g	µg/g	µg/g	µg/g	µg/g	µg/g	µg/g	µg/g	µg/g	µg/g	µg/g	µg/g	µg/g	µg/g	µg/g	µg/g	µg/g	µg/g	µg/g	µg/g	µg/g	µg/g	µg/g	µg/g
65 Planggenstock_1_core-rim1.csv	14:10	50	Dated	37.5	0.08	23.5	12.1	10.9	0.36	0.0050	26.0	0.0002	<0.0002875	0.0081	<0.055174	0.35	248	2.6	6441	66.5	13.5	<0.010511	10.91	114.4	156.3	16.0	63.5	15.4	28.9	16.0	2.4	13.8	2.5	6.0	0.8	5.9	1.0	102.8	105.1	104.7	0.27	44.2
66 Planggenstock_1_core-rim2.csv	14:10	50	Dated	37.1	0.08	23.6	11.8	10.6	0.37	0.0053	26.5	<0.00019579	<0.0002122	0.0054	<0.053848	0.36	218	2.1	7483	64.3	8.3	<0.009717	6.05	57.6	82.0	8.9	37.0	9.9	20.3	11.4	1.8	11.5	2.3	6.4	0.8	6.3	1.1	67.0	68.1	69.0	0.14	35.3
67 Planggenstock_1_core-rim3.csv	14:10	50	Dated	37.1	0.08	23.4	11.8	10.6	0.41	0.0046	26.7	0.0002	<0.00021203	0.0159	<0.050718	0.44	206	1.9	8188	47.1	14.8	<0.009799	15.41	34.6	50.0	5.6	23.8	6.5	13.1	7.5	1.1	7.8	1.6	4.7	0.7	6.4	1.3	86.3	87.7	89.3	0.04	27.1
68 Planggenstock_1_core-rim4.csv	14:10	50	Dated	38.5	0.06	24.7	11.4	10.2	0.36	0.0079	24.4	0.0002	<0.00022123	0.0067	<0.060716	0.45	227	36.2	2490	68.7	2.0	<0.0068969	1.26	26.6	62.0	9.2	47.4	16.1	8.6	18.6	2.7	15.1	2.5	5.8	0.5	2.5	0.3	43.2	43.9	44.0	0.10	29.9
72 Planggenstock_1_core-rim5.csv	14:10	50	Dated	37.0	0.07	23.4	11.8	10.6	0.39	0.0046	26.9	<0.00018581	<0.00020163	0.0096	<0.055944	0.39	337	32.6	8375	102.4	9.0	<0.0074035	4.61	34.5	84.1	12.6	64.7	20.7	7.9	23.9	3.5	19.8	3.6	9.6	1.3	11.0	2.2	55.7	56.8	57.3	0.11	45.1
73 Planggenstock_1_core-rim6.csv	14:10	50	Dated	36.7	0.07	23.3	11.8	10.7	0.37	0.0049	27.2	<0.00019578	<0.00021148	0.0075	<0.058682	0.42	352	21.0	8804	100.5	7.1	<0.0023615	3.33	25.6	63.8	9.8	51.0	17.2	6.1	20.8	3.1	18.5	3.5	9.7	1.4	11.9	2.6	52.6	53.9	53.5	0.04	33.1
74 Planggenstock_1_core-rim7.csv	14:10	50	Dated	36.8	0.07	23.3	11.8	10.7	0.37	0.0048	27.1	<0.00019182	<0.00020753	0.0069	<0.055217	0.40	382	8.4	8865	95.1	6.0	<0.0020994	1.82	15.9	39.0	6.0	31.6	11.5	3.7	15.3	2.6	15.8	3.3	9.7	1.5	13.0	2.8	47.7	47.8	47.9	0.02	20.7
75 Planggenstock_1_core-rim8.csv	14:10	50	Dated	36.8	0.07	23.2	12.0	10.8	0.33	0.0043	27.1	<0.00018337	<0.00019837	0.0034	<0.051499	0.31	393	5.8	8678	93.3	5.1	<0.010204	0.93	14.4	34.8	5.3	28.5	10.4	3.2	14.2	2.3	15.6	3.1	9.3	1.4	12.8	2.7	39.3	40.4	40.4	0.02	18.0
76 Planggenstock_1_core-rim9.csv	14:10	50	Dated	37.8	0.09	24.5	11.4	10.3	0.23	0.0049	25.4	0.0002	<0.00019336	0.0031	<0.051816	0.45	375	5.3	4209	71.8	2.4	<0.0086379	0.16	8.5	22.1	3.5	18.8	7.2	2.0	10.3	1.7	11.7	2.3	6.9	0.8	6.1	1.0	24.3	24.8	24.8	0.02	15.5
77 Planggenstock_1_core-rim+1.csv	14:10	50	Dated	38.3	0.15	24.3	12.1	10.9	0.34	0.0141	24.3	<0.00020475	<0.00022034	0.0027	<0.056144	0.35	540	16.9	1843	79.7	6.4	<0.0088272	0.23	20.2	59.1	9.3	48.9	16.7	4.9	19.7	2.7	15.7	2.8	6.9	0.7	3.9	0.5	46.6	46.6	47.2	0.02	51.4
80 Planggenstock_1_core-rim+2.csv	14:40	50	Dated	38.1	0.13	24.5	11.7	10.5	0.33	0.0110	24.7	0.0007	<0.00019337	<0.0020692	0.11	0.42	445	23.2	2590	76.5	4.8	<0.007503	0.27	16.6	47.6	7.6	40.4	14.5	4.9	16.7	2.5	15.2	2.6	6.6	0.7	4.1	0.6	42.4	42.8	43.3	0.04	44.4
81 Planggenstock_1_core-rim+3.csv	14:40	50	Dated	38.0	0.08	24.6	11.7	10.5	0.15	0.0057	24.9	<0.00019232	<0.00020705	<0.0021842	<0.050629	0.40	369	3.9	2480	54.1	1.4	<0.0090973	<0.064095	13.2	27.4	3.8	19.0	6.7	3.6	8.5	1.3	8.6	1.9	5.1	0.5	2.8	0.4	15.5	15.3	15.4	0.08	29.0
82 Planggenstock_1_core-rim+4.csv	14:40	50	Dated	38.2	0.07	24.5	11.4	10.3	0.17	0.0043	25.1	<0.00019972	<0.00021503	0.0037	<0.06061	0.34	336	4.2	3340	53.3	1.6	<0.012023	<0.087207	7.7	17.5	2.6	13.9	5.1	2.1	6.7	1.2	8.6	1.8	5.1

Sample: Aerlengletscher	Time	Spot size	SiO2	TiO2	Al2O3	Fe2O3	FeO	MnO	MgO	CaO	Na2O	K2O	P2O5	Li7	B11	V51	Cr53	Sr88	Y89	Zr90	Nb93	Ba137	La139	Ce140	Pr141	Nd146	Sm147	Eu151	Gd157	Tb159	Dy163	Ho165	Er167	Tm169	Yb173	Lu175	Pb206	Pb207	Pb208	Th232	U238
		um	wt.%	wt.%	wt.%	wt.%	wt.%	wt.%	wt.%	wt.%	wt.%	wt.%	wt.%	µg/g	µg/g	µg/g	µg/g	µg/g	µg/g	µg/g	µg/g	µg/g	µg/g	µg/g	µg/g	µg/g	µg/g	µg/g	µg/g	µg/g	µg/g	µg/g	µg/g	µg/g	µg/g	µg/g	µg/g	µg/g	µg/g	µg/g
4 Ar01-1_core-rim.csv	12:25	50	39.3	0.12	26.9	7.4	6.7	0.14	0.01	25.1	<0.00021247	<0.00023732	0.008	<0.073939	0.57	774	76.7	3105	79.3	39.1	<0.0098001	8.73	60.85	116.74	13.72	54.52	12.01	10.33	12.33	1.90	12.30	2.61	8.33	1.17	7.76	1.23	68.7	71.6	71.7	1.82	9.8
5 Ar01-1_core-rim.csv	12:25	50	39.4	0.13	27.0	7.1	6.4	0.15	0.02	25.1	0.0003	<0.00024451	0.024	<0.067762	0.59	594	66.5	3702	55.9	43.6	<0.0073985	7.28	52.91	97.78	11.11	43.54	8.83	9.46	8.64	1.31	8.79	1.96	6.17	0.97	7.41	1.38	80.4	84.1	84.2	1.06	5.9
6 Ar01-1_core-rim.csv	12:25	50	39.9	0.30	27.8	6.8	6.1	0.18	0.03	24.0	<0.00023579	<0.00026072	0.005	<0.0817	0.57	760	110.7	983	50.4	15.1	0.003	0.57	42.10	92.88	11.08	44.27	8.94	11.92	8.33	1.27	8.62	1.84	5.85	0.83	5.57	0.83	57.9	60.3	60.5	0.76	9.7
7 Ar01-1_core-rim.csv	12:25	50	40.0	0.10	27.8	6.7	6.1	0.17	0.03	24.2	0.0005	<0.00023818	0.007	<0.075163	1.19	441	46.2	1207	62.7	11.1	<0.0121115	0.62	29.15	60.75	7.35	30.58	7.27	9.95	7.65	1.32	9.73	2.20	6.97	0.95	5.52	0.69	62.2	64.9	65.4	0.26	7.3
8 Ar01-1_core-rim.csv	12:25	50	39.8	0.05	27.2	7.6	6.8	0.12	0.02	24.4	<0.00022241	<0.00024634	<0.003078	<0.071098	0.80	654	58.7	1593	59.2	5.8	<0.0112193	0.58	34.85	69.21	8.07	32.73	8.12	7.57	9.40	1.53	10.12	2.14	6.35	0.71	4.12	0.54	36.9	38.1	38.3	0.50	5.9
9 Ar01-1_core-rim.csv	12:25	50	39.8	0.16	27.0	7.8	7.0	0.04	0.01	24.3	<0.00023312	<0.00025846	<0.0032177	<0.074473	0.66	614	28.5	1131	6.1	5.4	<0.0111873	<0.0843665	0.46	0.75	0.08	0.39	0.12	2.31	0.23	0.06	0.60	0.17	0.80	0.15	1.37	0.25	3.8	3.9	3.9	<0.0086031	0.5
12 Ar01-1_core-rim+.csv	12:25	50	39.6	0.17	27.1	7.9	7.1	0.04	0.01	24.3	<0.00021771	<0.0002399	<0.0029634	<0.0708	0.40	628	32.2	1119	9.0	6.6	<0.0071709	<0.0755553	1.08	1.56	0.15	0.65	0.24	3.02	0.41	0.09	0.93	0.27	1.08	0.26	2.43	0.47	4.6	4.7	4.8	<0.0084529	0.7
13 Ar01-1_core-rim+.csv	12:25	50	39.5	0.05	26.9	8.1	7.3	0.08	0.01	24.4	<0.00021865	<0.00024055	<0.0029687	<0.06941	0.63	1142	42.0	1312	142.7	1.8	<0.0092158	<0.11315	60.04	107.51	12.46	52.74	14.12	23.42	18.63	3.18	21.79	4.89	14.76	1.72	8.91	1.06	8.6	8.9	9.0	0.36	23.9
14 Ar01-1_core-rim++.csv	12:25	50	39.8	0.09	27.7	7.0	6.3	0.20	0.03	24.2	0.0005	<0.00024424	0.004	<0.075642	0.59	585	54.7	1295	78.4	6.0	<0.0097396	0.81	45.37	93.59	11.28	45.42	10.59	13.66	11.25	1.86	12.28	2.71	8.42	1.04	6.04	0.84	63.3	65.6	66.2	0.99	8.6
15 Ar01-1_core-rim++.csv	12:25	50	39.9	0.27	27.3	7.3	6.6	0.18	0.04	24.0	<0.00025026	<0.00027549	0.007	<0.079022	0.58	716	95.5	969	58.2	20.9	<0.0091908	0.75	34.57	72.17	8.66	34.15	7.59	13.39	7.93	1.35	9.24	2.05	6.35	0.97	7.06	1.09	69.8	73.3	72.9	0.02	12.2
16 Ar01-1_core-rim++.csv	12:25	50	40.0	0.29	27.4	7.2	6.5	0.18	0.04	23.9	<0.00022395	<0.00024558	0.008	<0.071551	0.45	637	22.1	951	53.0	23.3	<0.0092268	0.83	18.39	29.02	3.22	13.55	3.76	12.58	5.36	1.01	7.85	1.87	6.13	0.93	6.58	1.00	68.4	71.3	71.7	<0.010757	8.2
17 Ar01-1_core-rim++.csv	12:25	50	40.2	0.06	27.7	6.7	6.0	0.17	0.03	24.1	0.0004	<0.00029543	0.008	<0.077767	0.46	351	7.6	1290	58.0	6.7	<0.0110377	0.47	15.65	23.36	2.60	10.91	3.73	14.16	5.85	1.04	8.93	2.07	6.10	0.75	4.03	0.50	43.8	46.2	45.8	<0.0097945	6.3
21 Ar01-1_core-rim++.csv	12:55	50	40.1	0.06	27.7	6.8	6.2	0.16	0.03	24.1	0.0003	<0.0002315	0.005	<0.075376	0.76	369	13.3	1394	53.8	7.1	<0.0110189	0.41	23.10	36.64	4.15	16.93	4.44	13.34	6.35	1.13	8.46	1.94	5.99	0.73	3.89	0.51	45.7	48.2	47.9	<0.0116036	6.4
22 Ar01-1_core-rim++.csv	12:55	50	40.0	0.06	27.8	6.8	6.1	0.16	0.03	24.1	0.0005	<0.00026242	0.007	<0.071348	0.61	355	12.1	1341	56.7	6.7	<0.0082925	0.29	19.33	30.94	3.54	14.60	4.28	13.07	5.72	1.20	8.63	1.94	6.50	0.72	3.99	0.51	44.9	46.5	47.1	0.01	6.4
23 Ar01-1_core-rim.csv	13:25	50	39.8	0.12	27.2	7.0	6.3	0.15	0.01	24.7	<0.00022856	<0.00024844	0.008	<0.073167	0.58	746	92.7	3019	96.2	30.6	<0.0120225	5.95	94.94	181.05	20.89	85.00	18.26	11.54	17.97	2.62	16.88	3.29	9.78	1.23	8.25	1.15	62.2	66.8	65.6	3.15	14.0
24 Ar01-1_core-rim.csv	13:25	50	40.0	0.24	27.5	7.0	6.3	0.19	0.03	24.0	<0.00022929	<0.00024965	0.005	<0.079084	0.55	1001	173.6	1110	84.3	11.6	<0.0113744	0.60	81.78	188.77	23.15	95.30	20.30	10.74	18.93	2.63	15.90	2.99	8.56	1.06	7.19	1.02	63.7	67.1	66.7	4.67	16.5
25 Ar01-1_core-rim.csv	13:25	50	40.1	0.25	27.5	6.9	6.3	0.19	0.03	24.0	<0.00022417	<0.00024382	0.006	<0.070551	0.57	1045	186.8	1072	79.6	12.4	<0.0074408	0.62	87.13	196.49	23.70	97.73	20.57	10.71	18.54	2.58	15.63	2.92	8.27	1.07	7.33	1.01	60.8	64.6	63.8	4.43	16.8
26 Ar01-1_core-rim.csv	13:25	50	39.9	0.11	27.6	7.0	6.3	0.17	0.02	24.1	0.0003	<0.00023235	0.008	<0.065836	0.62	722	128.3	1205	108.6	5.8	<0.0098361	0.73	112.29	234.76	28.30	117.64	27.41	12.39	26.99	3.78	21.53	4.10	11.05	1.37	8.18	1.11	62.4	66.2	65.6	1.21	16.0
29 Ar01_2_core-rim.csv	13:55	50	39.9	0.10	27.7	6.9	6.2	0.14	0.03	24.2	0.0003	<0.00026213	0.019	<0.078701	0.52	735	123.0	1061	96.7	5.2	<0.010608	0.45	81.05	173.61	21.33	90.42	21.82	9.47	22.90	3.20	19.60	3.69	10.20	1.46	9.91	1.48	57.1	61.2	60.0	0.51	12.0
30 Ar01_2_core-rim+.csv	13:55	50	39.8	0.12	26.8	8.1	7.3	0.13	0.02	24.1	<0.00022658	<0.00024452	<0.0027488	<0.07002	0.44	1066	88.8	1391	117.3	5.6	<0.0076433	0.58	113.42	249.38	29.75	125.59	28.98	15.94	29.64	4.47	26.69	4.48	10.82	1.13	6.56	0.85	30.6	32.7	31.9	5.21	26.1
31 Ar01_2_core-rim+.csv	13:55	50	39.9	0.19	27.0	7.7	6.9	0.18	0.02	24.1	<0.00023466	<0.00025421	0.006	0.07	0.61	1092	171.5	1270	85.2	10.7	<0.0141168	0.78	59.44	136.87	16.77	70.54	15.48	11.91	15.26	2.31	15.61	2.99	8.98	1.11	7.60	1.10	65.6	69.1	68.8	1.47	16.0
32 Ar01_2_core-rim+.csv	13:55	50	40.1	0.09	27.4	7.1	6.4	0.17	0.03	24.0	0.0003	<0.00025421	<0.002832	<0.075923	0.66	702	106.2	1302	106.5	7.2	<0.0114431	0.88	73.50	154.50	18.63	79.03	19.17	10.17	20.46	3.20	20.80	3.99	10.98	1.34	7.77	0.97	62.7	67.4	66.9	0.65	14.1
33 Ar01_2_core-rim+.csv	13:55	50	39.7	0.22	27.3	7.5	6.7	0.20	0.03	24.1	<0.00021733	<0.00023559	0.006	<0.064181	0.51	1006	107.2	1121	84.5	14.1	0.003	0.75	40.91	94.24	11.85	49.84	11.75	13.82	12.15	1.93	13.48	2.83	9.50	1.26	9.23	1.44	75.2	81.3	78.6	2.02	14.2
34 Ar01_2_core-rim+.csv	13:55	50	39.2	0.14	26.7	7.2	6.4	0.15	0.02	25.6	<0.0002605	<0.0002832	0.011	<0.080427	0.45	572	57.8	5118	55.4	17.0	<0.0112646	6.44	23.94	45.42	5.41	22.39	5.43	8.21	6.23	1.02	8.19	1.76	6.32	1.06	10.03	2.34	76.9	82.2	81.6	0.13	3.4
38 Ar01_2_core-rim+.csv	14:25	50	39.9	0.29	27.8	6.6	6.0	0.17	0.03	24.1	0.0003	<0.00025834	0.005	<0.080099	0.51	854	119.5	1046	52.1	13.1	<0.0113994	0.55	45.56	97.74	11.56	47.90	10.08	12.04	8.73	1.42	9.39	1.83	5.65	0.74	4.65	0.66	61.8	65.8	64.8	0.17	10.4

Sample: Grosstal	Time	Spot size	SiO2	TiO2	Al2O3	Fe2O3	FeO	MnO	MgO	CaO	Na2O	K2O	P2O5	Li7	B11	V51	Cr53	Sr88	Y89	Zr90	Nb93	Ba137	La139	Ce140	Pr141	Nd146	Sm147	Eu151	Gd157	Tb159	Dy163	Ho165	Er167	Tm169	Yb173	Lu175	Pb206	Pb207	Pb208	Th232	U238
		um	wt.%	wt.%	wt.%	wt.%	wt.%	wt.%	wt.%	wt.%	wt.%	wt.%	wt.%	µg/g	µg/g	µg/g	µg/g	µg/g	µg/g	µg/g	µg/g	µg/g	µg/g	µg/g	µg/g	µg/g	µg/g	µg/g	µg/g	µg/g	µg/g	µg/g	µg/g	µg/g	µg/g	µg/g	µg/g	µg/g	µg/g	µg/g
39 Grosstal_1_core-rim.csv	13:25	50	38.6	0.012	26.2	7.5	6.8	0.40	0.05	26.2	0.0003	<0.00022123	0.049	0.16	9.8	160	<0.92876	7242	1.3	2.7	<0.006219	<0.128	0.14	0.38	0.07	0.30	0.10	0.35	0.13	0.02	0.10	0.03	0.10	<0.010867	4.06	3.96	4.06	0.011	0.071
40 Grosstal_1_core-rim.csv	13:25	50	38.4	0.017	26.4	7.5	6.7	0.33	0.06	26.3	0.0002	<0.00022975	0.038	0.17	8.0	157	<0.89165	6647	2.8	7.3	<0.012338	<0.091288	0.11	0.32	0.06	0.34	0.11	0.37	0.17	0.02	0.22	0.07	0.23	0.05	0.34	0.05	3.98	3.95	3.92	<0.0094262	0.242
41 Grosstal_1_core-rim.csv	13:25	50	39.2	0.018	27.5	6.7	6.0	0.07	0.04	25.4	0.0003	<0.00024602	<0.0027949	<0.061672	6.6	111	<1.023	3255	1.0	29.2	<0.010027	<0.025803	0.03	0.09	0.02	0.07	<0.043082	0.15	<0.081243	<0.013044	0.09	0.02	0.06	0.02	0.17	0.03	2.73	2.85	2.76	<0.00833	0.187
42 Grosstal_1_core-rim.csv	13:25	50	39.6	0.055	27.6	6.7	6.0	0.09	0.04	24.9	0.0004	<0.00023485	0.006	0.11	15.5	139	<0.93823	2738	1.6	18.6	0.035	<0.094392	0.04	0.12	0.02	0.15	0.04	0.23	0.08	0.03	0.14	0.02	0.17	0.02	0.28	0.06	2.79	2.66	2.65	<0.00837	0.067
46 Grosstal_1_core-rim.csv	13:25	50	38.7	0.018	26.7	7.5	6.8	0.15	0.04	25.9	0.0027	<0.00022751	0.007	0.06	10.9	164	<0.88773	4969	2.3	10.8	0.020	<0.099897	0.09	0.26	0.05	0.27	0.10	0.34	0.18	0.02	0.23	0.07	0.20	0.04	0.36	0.06	2.75	2.72	2.73	<0.0088279	0.186
47 Grosstal_1_core-rim.csv	13:25	50	37.2	0.011	26.8	7.4	6.7	0.41	0.05	27.1	0.0003	<0.0002757	0.031	<0.089019	8.1	183	<1.1374	7794	2.0	2.6	<0.012497	<0.14807	0.19	0.45	0.07	0.41	0.12	0.55	0.17	0.02	0.17	0.04	0.24	0.03	0.19	0.02	3.68	3.59	3.59	<0.012828	0.087
48 Grosstal_1_core-rim.csv	13:25	50	39.2	0.043	27.5	6.9	6.2	0.11	0.05	25.1	0.0004	<0.00021878	0.008	0.08	26.5	118	<0.87937	2871	1.2	13.7	<0.010833	<0.12331	0.05	0.11	0.02	0.14	0.06	0.22	<0.075068	0.01	0.07	0.03	0.12	0.02	0.15	0.03	2.97	2.87	2.90	<0.0068943	0.079
49 Grosstal_1_core-rim.csv	13:25	50	37.4	0.012	26.5	7.2	6.5	0.44	0.05	27.3	0.0005	<0.00026837	0.034	0.13	5.3	149	<1.0653	9686	0.9	3.9	<0.013409	<0.13979	0.12	0.27	0.05	0.27	0.08	0.33	<0.092917	<0.011551	0.10	0.02	0.05	0.01	<0.098717	<0.01514	5.24	5.12	5.29	<0.011509	0.065
50 Grosstal_1_core-rim.csv	13:25	50	39.3	0.018	27.7	6.5	5.9	0.07	0.04	25.4	<0.00021598	<0.00023374	<0.002608	<0.065006	6.0	86	<0.9456	3376	0.9	21.9	<0.0087671	<0.10576	0.02	0.07	0.01	0.06	<0.040648	0.12	<0.070299	<0.011211	0.06	0.02	0.13	0.02	0.10	0.02	3.33	3.52	3.48	<0.0072079	0.088
51 Grosstal_2_core-rim.csv	13:25	50	39.5	0.038	28.1	6.0	5.4	0.12	0.05	25.1	0.0005	<0.00023605	0.006	0.12	17.7	117	<0.96864	2784	0.7	40.5	<0.013686	<0.093959	0.04	0.12	0.02	0.13	0.06	0.13	<0.080777	<0.0089364	0.05	<0.013334	0.08	0.01	0.14	<0.013162	5.01	5.08	5.05	0.015	0.154
55 Grosstal_2_core-rim.csv	13:55	50	39.3	0.056	28.1	6.3	5.7	0.13	0.05	25.0	0.0008	<0.00021867	0.013	0.13	32.0	121	<0.89961	2674	0.7	17.9	0.023	<0.092131	0.06	0.18	0.03	0.18	0.07	0.13	<0.085472	0.01	<0.053819	0.02	0.07	0.01	0.13	0.02	5.31	5.55	5.42	<0.008708	0.069
56 Grosstal_2_core-rim.csv	13:55	50	39.2	0.144	27.7	6.6	5.9	0.11	0.09	25.2	0.0004	<0.00023483	0.007	0.10	13.9	244	<0.92041	2603	0.8	28.8	0.096	<0.093777	0.04	0.13	0.02	0.14	0.05	0.11	0.09	0.01	0.07	0.01	0.09	<0.013042	0.15	0.03	5.13	5.42	5.40	<0.0097091	0.056
57 Grosstal_2_core-rim.csv	13:55	50	39.4	0.027	28.5	5.6	5.0	0.10	0.05	25.2	0.0005	<0.00024326	0.005	<0.070385	8.6	103	<0.94706	2812	0.6	52.9	0.005	<0.011433	0.03	0.12	0.02	0.13	<0.044679	0.11	<0.065975	<0.012218	0.06	0.01	<0.062423	0.02	0.11	0.02	3.95	4.00	3.80	<0.012311	0.214
58 Grosstal_2_core-rim.csv	13:55	50	39.5	0.104	27.6	6.8	6.2	0.13	0.07	24.7	0.0004	<0.00023095	0.010	0.17	28.8	124	<0.93929	2046	1.0	34.2	0.018	<0.091834	0.04	0.13	0.03	0.11	0.06	0.13	0.10	<0.012417	0.12	0.02	0.10	0.02	0.17	0.06	4.02	4.17	4.08	<0.01143	0.093
59 Grosstal_2_core-rim.csv	13:55	50	39.4	0.094	28.2	6.1	5.5	0.10	0.06	24.9	0.0003	<0.00024687	0.008	0.11	14.6	139	<0.9927	2532	1.0	43.1	0.056	<0.011965	0.04	0.11	0.02	0.10	0.05	0.12	<0.080258	0.02	0.11	<0.014849	0.14	0.02	0.31	0.04	3.91	4.11	4.16	<0.012209	0.132
60 Grosstal_2_core-rim.csv	13:55	50	39.4	0.039	28.1	6.1	5.5	0.10	0.05	25.1	0.0005	<0.00022027	0.006	0.10	17.3	105	<0.90221	2739	0.7	31.3	0.019	<0.10581	0.03	0.11	0.01	0.12	0.05	0.13	<0.063847	<0.011011	0.08	0.01	<0.058738	0.02	0.11	0.02	4.37	4.44	4.37	<0.0089832	0.095
63 Grosstal_2_core-rim.csv	13:55	50	38.1	0.044	27.5	6.2	5.6	0.17	0.02	26.9	0.0005	<0.00022107	0.002	0.10	131.1	122	<0.87647	6807	2.9	6.3	<0.0077651	<0.10413	0.14	0.40	0.07	0.49	0.15	0.54	0.24	0.03	0.29	0.06	0.27	0.04	0.33	0.06	21.15	21.07	20.95	0.018	0.147
64 Grosstal_2_core-rim	13:55	50	38.7	0.056	27.7	6.3	5.7	0.14	0.04	25.9	0.0005	<0.00022003	0.007	0.07	68.6	123	<0.89721	4642	1.8	21.5	0.013	<0.068661	0.09	0.29	0.06	0.26	0.09	0.33	0.14	0.02	0.16	0.03	0.17	0.02	0.25	0.05	11.87	11.70	11.86	0.032	0.153

Heyuan Fault

Sample: HY17-Sa2	Time	Spot size	SiO2	TiO2	Al2O3	Fe2O3	FeO	MnO	MgO	CaO	Na2O	K2O	P2O5	Li7	B11	V51	Cr53	Sr88	Y89	Zr90	Nb93	Ba137	La139	Ce140	Pr141	Nd146	Sm147	Eu151	Gd157	Tb159	Dy163	Ho165	Er167	Tm169	Yb173	Lu175	Pb206	Pb207	Pb208	Th232	U238
		um	wt.%	wt.%	wt.%	wt.%	wt.%	wt.%	wt.%	wt.%	wt.%	wt.%	wt.%	µg/g	µg/g	µg/g	µg/g	µg/g	µg/g	µg/g	µg/g	µg/g	µg/g	µg/g	µg/g	µg/g	µg/g	µg/g	µg/g	µg/g	µg/g	µg/g	µg/g	µg/g	µg/g	µg/g	µg/g	µg/g	µg/g	µg/g
38 HY17-5az_2_1.csv	14:30	30	37.2	0.04	24.6	12.2	11.0	0.65	0.02	24.7	0.00	0.00	0.08	0.18	1.84	9.85	1.12	2353.97	8.03	9.87	0.13	0.64	6.39	12.79	1.49	5.81	1.35	0.91	1.31	0.19	1.22	0.24	0.80	0.11	1.25	0.19	17.91	18.56	18.59	0.48	8.37
41 HY17-5az_2_2.csv	14:30	30	36.6	0.07	21.7	15.4	13.9	0.59	0.01	25.4	0.00	<0.0002336	0.00	0.06	0.34	103.27	<0.77811	4591.25	408.43	8.11	0.03	7.08	0.10	0.21	0.04	0.22	0.16	1.38	0.96	0.88	19.69	9.28	47.12	8.83	67.95	9.61	140.26	139.10	140.38	<0.0068284	335.95
42 HY17-5az_2_3.csv	14:30	30	38.3	0.07	25.3	10.8	9.7	0.36	0.02	24.5	0.00	0.00	0.02	0.38	1.81	12.89	<2.4236	1252.01	10.12	8.17	0.35	0.47	2.44	4.93	0.55	2.51	0.71	0.74	0.76	0.15	1.20	0.27	1.01	0.20	1.66	0.25	12.89	12.23	12.06	0.30	17.74
42 HY17-5az_2_3.csv (copy)	14:30	30	39.0	0.05	23.9	12.1	10.9	0.69	0.02	23.6	0.01	0.01	0.08	0.56	2.91	9.95	<2.4754	2281.66	7.81	8.53	0.20	0.81	4.93	8.69	0.94	3.30	0.94	1.03	0.77	0.12	1.10	0.18	0.51	0.14	1.27	0.31	16.47	16.06	15.82	0.38	8.73
43 HY17-5az_2_4.csv	14:30	30	38.1	0.04	24.1	12.2	11.0	0.79	0.02	24.2	<0.0005316	<0.00062395	0.10	<0.12911	2.48	6.38	<2.139	2621.71	5.34	9.40	0.12	0.95	2.76	4.61	0.54	2.32	0.64	0.93	0.85	0.11	0.66	0.16	0.61	0.07	0.95	0.21	15.24	15.60	15.46	0.42	8.37
44 HY17-5az_2_5.csv	14:30	30	38.7	0.03	23.4	13.3	12.0	0.38	0.02	23.7	0.00	0.01	0.02	0.25	1.68	16.41	<2.6729	1768.65	15.27	7.42	0.32	<0.38157	23.11	47.78	5.20	19.28	3.86	0.91	2.44	0.32	1.74	0.48	1.67	0.26	1.88	0.35	26.45	26.39	27.14	0.67	7.48
45 HY17-5az_2_6.csv	14:30	30	37.3	0.04	24.6	12.8	11.5	0.25	0.02	24.6	0.00	0.00	<0.0054803	<0.12144	1.35	12.95	<2.2101	1178.56	14.39	15.84	0.47	<0.29304	4.23	8.99	1.02	4.17	1.12	0.66	1.29	0.26	1.89	0.48	1.70	0.27	2.66	0.46	16.52	16.00	16.10	0.05	13.01
46 HY17-5az_2_7.csv	14:30	30	37.3	0.08	25.4	10.8	9.8	0.44	0.02	25.3	0.00	0.00	0.06	<0.18789	1.21	10.14	<3.0241	2453.97	14.25	8.65	0.65	0.91	16.76	33.41	3.75	14.38	2.99	1.46	2.53	0.43	1.90	0.42	1.69	0.19	1.78	0.35	22.44	20.45	20.86	16.94	24.25
46 HY17-5az_2_7.csv (copy)	14:30	30	38.8	0.09	24.2	11.6	10.4	0.50	0.03	24.2	0.00	0.01	0.07	0.34	1.60	14.93	<2.5453	2374.86	16.13	9.09	1.42	0.53	36.08	72.87	8.11	29.46	5.54	1.58	4.45	0.44	2.64	0.50	1.35	0.26	1.95	0.41	20.15	18.89	19.78	37.92	34.36
4 HY17-5az_2_8.csv	14:30	30	39.2	0.04	24.4	11.4	10.3	0.27	0.02	24.0	0.00	<0.00051113	<0.0084943	0.22	4.92	4.60	<2.2815	2241.96	17.26	9.78	0.11	0.47	1.25	2.34	0.30	1.57	0.92	1.51	1.52	0.23	1.92	0.50	1.90	0.23	2.23	0.32	25.89	25.51	26.17	0.08	18.35
5 HY17-5az_2_9.csv	14:30	30	38.1	0.02	23.7	13.5	12.1	0.54	0.03	23.7	0.00	<0.00050533	0.03	0.21	2.49	6.08	2.06	1460.95	6.13	8.31	0.16	0.31	0.71	1.18	0.14

Appendix 4

The measured Sr isotope data by TIMS and Neptune MC-ICP-MS are reported hereafter. The complete datasets with all measurement cycles are in the online data repository.

TIMS

10-11 August 2020									
	84Sr	**85Rb**	**86Sr**	**87Sr**	**88Sr**	**87Sr/86Sr (1)**	**84Sr/86Sr (2)**	**88Sr/86Sr (3)**	**85Rb/86Sr (4)**
Cup	L2	L1	C	H1	H2	H1 | C	L2 | C	H2 | C	L1 | C
					SRM987 (1)				
Info	tbdgy	tbdgy	tbdgy	tbdgy	tbdgy	ON1e I1 tbdgy - St	ON1e tbdgy - St	O tbdgy - St	ON1e tbdgy - St
Mean	0.038146	0.000002	0.671232	0.475440	5.590568	0.710297	0.056508	8.328943	0.000003
StdErr (%)	0.122869	51.388514	0.121896	0.121498	0.121271	0.000551	0.002924	0.001670	53.837493
StdErr (abs)	0.000047	0.000001	0.000818	0.000578	0.006780	0.000004	0.000002	0.000139	0.000001
StdDev (%)	1.504833	629.378195	1.492915	1.488039	1.485265	0.006591	0.034849	0.020178	648.289263
StdDev (abs)	0.000574	0.000013	0.010021	0.007075	0.083035	0.000047	0.000020	0.001681	0.000017
Valid Values	150 (150)	150 (150)	150 (150)	150 (150)	150 (150)	143 (150)	142 (150)	146 (150)	145 (150)
					SRM987 (2)				
Mean	0.064359	0.000004	1.131643	0.801201	9.417443	0.710279	0.056502	8.321501	0.000004
StdErr (%)	0.346122	27.350334	0.351156	0.353479	0.355794	0.000409	0.001819	0.005087	23.413361
StdErr (abs)	0.000223	0.000001	0.003974	0.002832	0.033507	0.000003	0.000001	0.000423	0.000001
StdDev (%)	4.239116	334.971813	4.300760	4.329216	4.357568	0.004880	0.021758	0.061679	279.983073
StdDev (abs)	0.002728	0.000014	0.048669	0.034686	0.410371	0.000035	0.000012	0.005133	0.000011
Valid Values	150 (150)	150 (150)	150 (150)	150 (150)	150 (150)	142 (150)	143 (150)	147 (150)	143 (150)
					SRM987 (3)				
Mean	0.054009	0.000015	0.948935	0.671573	7.890315	0.710288	0.056496	8.314802	0.000013
StdErr (%)	0.218808	10.578114	0.222636	0.224542	0.226580	0.000462	0.002253	0.004465	11.197269
StdErr (abs)	0.000118	0.000002	0.002113	0.001508	0.017878	0.000003	0.000001	0.000371	0.000001
StdDev (%)	2.679834	129.554914	2.726728	2.750071	2.775022	0.005542	0.027031	0.054687	133.899864
StdDev (abs)	0.001447	0.000019	0.025875	0.018469	0.218958	0.000039	0.000015	0.004547	0.000018
Valid Values	150 (150)	150 (150)	150 (150)	150 (150)	150 (150)	144 (150)	144 (150)	150 (150)	143 (150)
					SRM987 (4)				
Mean	0.050762	0.000018	0.895427	0.634944	7.474860	0.710260	0.056501	8.347209	0.000020
StdErr (%)	0.575725	8.344452	0.585103	0.589791	0.594237	0.000466	0.002316	0.010565	7.278625
StdErr (abs)	0.000292	0.000001	0.005239	0.003745	0.044418	0.000003	0.000001	0.000882	0.000001
StdDev (%)	7.051164	102.198253	7.166016	7.223435	7.277884	0.005627	0.028081	0.129396	86.734830

StdDev (abs)	0.003579	0.000018	0.064166	0.045865	0.544012	0.000040	0.000016	0.010801	0.000017
Valid Values	150 (150)	150 (150)	150 (150)	150 (150)	150 (150)	146 (150)	147 (150)	150 (150)	142 (150)
				SRM987 (5)					
Mean	0.041346	0.000003	0.726284	0.513981	6.038508	0.710290	0.056505	8.313169	0.000003
StdErr (%)	0.040280	41.356686	0.038694	0.038237	0.037819	0.000529	0.002679	0.003516	50.323993
StdErr (abs)	0.000017	0.000001	0.000281	0.000197	0.002284	0.000004	0.000002	0.000292	0.000001
StdDev (%)	0.493324	506.513885	0.473904	0.468305	0.463183	0.006328	0.032144	0.041310	605.981124
StdDev (abs)	0.000204	0.000013	0.003442	0.002407	0.027969	0.000045	0.000018	0.003434	0.000015
Valid Values	150 (150)	150 (150)	150 (150)	150 (150)	150 (150)	143 (150)	144 (150)	138 (150)	145 (150)
				SRM987 (6)					
Mean	0.061349	0.000034	1.080876	0.766047	9.012935	0.710285	0.056504	8.336068	0.000024
StdErr (%)	1.091593	10.450621	1.100312	1.104822	1.109137	0.000367	0.002045	0.007674	10.171955
StdErr (abs)	0.000670	0.000004	0.011893	0.008463	0.099966	0.000003	0.000001	0.000640	0.000002
StdDev (%)	13.369223	127.993447	13.476017	13.531252	13.584102	0.004314	0.024107	0.091124	122.063459
StdDev (abs)	0.008202	0.000043	0.145659	0.103656	1.224326	0.000031	0.000014	0.007596	0.000029
Valid Values	150 (150)	150 (150)	150 (150)	150 (150)	150 (150)	138 (150)	139 (150)	141 (150)	144 (150)
				Gr0-d_A (see Peverelli et al., 2021; Chapter 2)					
Mean	0.028167	0.000006	0.499602	0.363575	4.193071	0.726952	0.056503	8.393631	0.000011
StdErr (%)	0.808615	18.151166	0.801650	0.798195	0.794865	0.000676	0.003344	0.022351	18.799743
StdErr (abs)	0.000228	0.000001	0.004005	0.002902	0.033329	0.000005	0.000002	0.001876	0.000002
StdDev (%)	9.903471	222.305480	9.818163	9.775848	9.735071	0.007996	0.039849	0.273740	224.812233
StdDev (abs)	0.002790	0.000014	0.049052	0.035543	0.408198	0.000058	0.000023	0.022977	0.000025
Valid Values	150 (150)	150 (150)	150 (150)	150 (150)	150 (150)	140 (150)	142 (150)	150 (150)	143 (150)
				Gr0-d_B (see Peverelli et al., 2021; Chapter 2)					
Mean	0.014654	0.000004	0.259220	0.188346	2.169569	0.726830	0.056495	8.368927	0.000014
StdErr (%)	0.954693	27.940165	0.953717	0.953485	0.953444	0.001033	0.006198	0.016560	26.073562
StdErr (abs)	0.000140	0.000001	0.002472	0.001796	0.020686	0.000008	0.000004	0.001386	0.000004
StdDev (%)	11.692556	342.195734	11.680599	11.677761	11.677256	0.012479	0.073861	0.200774	313.967260
StdDev (abs)	0.001713	0.000013	0.030278	0.021995	0.253346	0.000091	0.000042	0.016803	0.000045
Valid Values	150 (150)	150 (150)	150 (150)	150 (150)	150 (150)	146 (150)	142 (150)	147 (150)	145 (150)
				Gr0-d_C (see Peverelli et al., 2021; Chapter 2)					
Mean	0.025332	0.000071	0.448427	0.326427	3.756456	0.727803	0.056504	8.377791	0.000100
StdErr (%)	0.902920	16.722641	0.893484	0.888633	0.884835	0.000766	0.003649	0.029962	14.899131
StdErr (abs)	0.000229	0.000012	0.004007	0.002901	0.033238	0.000006	0.000002	0.002510	0.000015
StdDev (%)	11.058466	204.809691	10.942905	10.883485	10.836976	0.009218	0.043488	0.366960	178.167693
StdDev (abs)	0.002801	0.000145	0.049071	0.035527	0.407086	0.000067	0.000025	0.030743	0.000178
Valid Values	150 (150)	150 (150)	150 (150)	150 (150)	150 (150)	145 (150)	142 (150)	150 (150)	143 (150)
				Gr0-d_D (see Peverelli et al., 2021; Chapter 2)					
Mean	-0.000002	0.000003	-0.000006	0.000001	0.000047	0.749572	1.555538	-1.886727	0.766967
StdErr (%)	-202.487850	74.643858	-60.456582	614.053379	8.337327	142.136371	143.383055	-81.330091	151.248257
StdErr (abs)	0.000003	0.000002	0.000004	0.000004	0.000004	1.065415	2.230378	1.534477	1.160024
StdDev (%)	-784.232070	289.094419	-234.147335	2378.218511	32.290330	317.826588	320.614258	-293.239814	338.201384
StdDev (abs)	0.000012	0.000008	0.000014	0.000015	0.000015	2.382340	4.987277	5.532636	2.593893

Valid Values	15 (15)	15 (15)	15 (15)	15 (15)	15 (15)	5 (15)	5 (15)	13 (15)	5 (15)
					ALB19-18(a)				
Mean	0.054728	0.000001	0.962702	0.684541	8.014100	0.713235	0.056497	8.324286	0.000001
StdErr (%)	0.308202	71.303998	0.315303	0.318999	0.322725	0.000495	0.002045	0.014399	75.333848
StdErr (abs)	0.000169	0.000001	0.003035	0.002184	0.025863	0.000004	0.000001	0.001199	0.000001
StdDev (%)	3.774690	873.292056	3.861661	3.906922	3.952552	0.005897	0.024454	0.176353	900.861793
StdDev (abs)	0.002066	0.000011	0.037176	0.026744	0.316761	0.000042	0.000014	0.014680	0.000010
Valid Values	150 (150)	150 (150)	150 (150)	150 (150)	150 (150)	142 (150)	143 (150)	150 (150)	143 (150)
					Gr0-d				
Mean	0.039948	0.000436	0.703148	0.509625	5.856694	0.726552	0.056496	8.329330	0.000297
StdErr (%)	0.612440	13.175262	0.610972	0.608895	0.610210	0.000496	0.003065	0.014151	15.739473
StdErr (abs)	0.000245	0.000057	0.004296	0.003103	0.035738	0.000004	0.000002	0.001179	0.000047
StdDev (%)	7.500832	161.363352	7.482848	7.457408	7.473512	0.005926	0.037032	0.173314	180.832778
StdDev (abs)	0.002996	0.000704	0.052616	0.038005	0.437701	0.000043	0.000021	0.014436	0.000537
Valid Values	150 (150)	150 (150)	150 (150)	150 (150)	150 (150)	143 (150)	146 (150)	150 (150)	132 (150)
					Planggenstock				
Mean	0.045704	0.000006	0.806104	0.572037	6.727946	0.710868	0.056497	8.349224	0.000009
StdErr (%)	1.672311	15.771207	1.668106	1.666183	1.664339	0.000528	0.002655	0.006461	11.835804
StdErr (abs)	0.000764	0.000001	0.013447	0.009531	0.111976	0.000004	0.000001	0.000539	0.000001
StdDev (%)	20.481548	193.157049	20.430040	20.406489	20.383911	0.006355	0.032188	0.075069	142.029650
StdDev (abs)	0.009361	0.000011	0.164687	0.116733	1.371419	0.000045	0.000018	0.006268	0.000012
Valid Values	150 (150)	150 (150)	150 (150)	150 (150)	150 (150)	145 (150)	147 (150)	135 (150)	144 (150)
					ALB19-11A_1343				
Mean	0.054491	0.000002	0.960042	0.683028	8.004026	0.713086	0.056495	8.336328	0.000001
StdErr (%)	0.799508	50.807201	0.802098	0.803521	0.804874	0.000396	0.002248	0.005910	61.188319
StdErr (abs)	0.000436	0.000001	0.007700	0.005488	0.064422	0.000003	0.000001	0.000493	0.000001
StdDev (%)	9.791929	622.258587	9.823656	9.841085	9.857653	0.004737	0.026699	0.070917	734.259829
StdDev (abs)	0.005336	0.000011	0.094311	0.067217	0.789009	0.000034	0.000015	0.005912	0.000011
Valid Values	150 (150)	150 (150)	150 (150)	150 (150)	150 (150)	143 (150)	141 (150)	144 (150)	144 (150)
					P9c				
Mean	0.035232	0.000161	0.623892	0.443601	5.227726	0.710753	0.056499	8.377885	0.000178
StdErr (%)	1.424335	12.244705	1.428465	1.430833	1.433461	0.000662	0.003344	0.027216	12.562197
StdErr (abs)	0.000502	0.000020	0.008912	0.006347	0.074937	0.000005	0.000002	0.002280	0.000022
StdDev (%)	17.444466	149.966393	17.495050	17.524051	17.556240	0.007975	0.039988	0.331099	148.637915
StdDev (abs)	0.006146	0.000241	0.109150	0.077737	0.917792	0.000057	0.000023	0.027739	0.000265
Valid Values	150 (150)	150 (150)	150 (150)	150 (150)	150 (150)	145 (150)	143 (150)	148 (150)	140 (150)
					Grosstal				
Mean	0.028049	0.000014	0.492159	0.347172	4.086666	0.708453	0.056493	8.302771	0.000029
StdErr (%)	0.845530	11.083003	0.852588	0.856173	0.859840	0.000583	0.003909	0.007530	11.240239
StdErr (abs)	0.000237	0.000002	0.004196	0.002972	0.035139	0.000004	0.000002	0.000625	0.000003
StdDev (%)	10.355580	135.738510	10.442022	10.485939	10.530847	0.007001	0.047076	0.092224	135.350406
StdDev (abs)	0.002905	0.000020	0.051391	0.036404	0.430360	0.000050	0.000027	0.007657	0.000039
Valid Values	150 (150)	150 (150)	150 (150)	150 (150)	150 (150)	144 (150)	145 (150)	150 (150)	145 (150)

Aerlengletscher									
Mean	0.034746	0.000005	0.611253	0.432789	5.088778	0.710172	0.056497	8.325057	0.000007
StdErr (%)	0.444279	20.146583	0.446402	0.447289	0.448230	0.000553	0.003367	0.004635	21.396941
StdErr (abs)	0.000154	0.000001	0.002729	0.001936	0.022809	0.000004	0.000002	0.000386	0.000001
StdDev (%)	5.441285	246.744239	5.467288	5.478150	5.489675	0.006568	0.040540	0.056763	256.763290
StdDev (abs)	0.001891	0.000012	0.033419	0.023709	0.279357	0.000047	0.000023	0.004726	0.000017
Valid Values	150 (150)	150 (150)	150 (150)	150 (150)	150 (150)	141 (150)	145 (150)	150 (150)	144 (150)
ALB13-1									
Mean	0.075378	0.000003	1.331586	0.949628	11.131239	0.713835	0.056498	8.358958	0.000002
StdErr (%)	0.312800	32.624568	0.322921	0.328301	0.333989	0.000330	0.001916	0.022793	30.040436
StdErr (abs)	0.000236	0.000001	0.004300	0.003118	0.037177	0.000002	0.000001	0.001905	0.000001
StdDev (%)	3.830999	399.567717	3.954957	4.020848	4.090518	0.003931	0.023066	0.279156	360.485229
StdDev (abs)	0.002888	0.000011	0.052664	0.038183	0.455325	0.000028	0.000013	0.023334	0.000008
Valid Values	150 (150)	150 (150)	150 (150)	150 (150)	150 (150)	142 (150)	145 (150)	150 (150)	144 (150)
OBA19-03B									
Mean	0.042663	0.000039	0.750562	0.544507	6.248883	0.727619	0.056496	8.324683	0.000047
StdErr (%)	0.464787	5.497786	0.479848	0.487136	0.494658	0.000502	0.002846	0.019263	5.337265
StdErr (abs)	0.000198	0.000002	0.003602	0.002652	0.030911	0.000004	0.000002	0.001604	0.000002
StdDev (%)	5.692452	67.333850	5.876917	5.966173	6.058302	0.006047	0.033670	0.235921	63.376511
StdDev (abs)	0.002429	0.000026	0.044110	0.032486	0.378576	0.000044	0.000019	0.019640	0.000030
Valid Values	150 (150)	150 (150)	150 (150)	150 (150)	150 (150)	145 (150)	140 (150)	150 (150)	141 (150)
GSP-2									
Mean	0.019832	0.002031	0.349712	0.267973	2.918580	0.765396	0.056508	8.343111	0.004709
StdErr (%)	1.438099	9.243155	1.428127	1.425584	1.418153	0.000713	0.006014	0.009231	7.858257
StdErr (abs)	0.000285	0.000188	0.004994	0.003820	0.041390	0.000005	0.000003	0.000770	0.000370
StdDev (%)	17.613044	113.205069	17.490912	17.459762	17.368756	0.008440	0.072673	0.107258	93.311634
StdDev (abs)	0.003493	0.002300	0.061168	0.046787	0.506921	0.000065	0.000041	0.008949	0.004394
Valid Values	150 (150)	150 (150)	150 (150)	150 (150)	150 (150)	140 (150)	146 (150)	135 (150)	141 (150)
AGV-2									
Mean	0.010628	0.000009	0.186995	0.131262	1.556858	0.704041	0.056491	8.325299	0.000048
StdErr (%)	0.285531	11.137633	0.296413	0.301767	0.307044	0.001283	0.008450	0.010861	9.828547
StdErr (abs)	0.000030	0.000001	0.000554	0.000396	0.004780	0.000009	0.000005	0.000904	0.000005
StdDev (%)	3.497025	136.407594	3.630299	3.695879	3.760501	0.015341	0.100699	0.133015	117.120659
StdDev (abs)	0.000372	0.000012	0.006788	0.004851	0.058546	0.000108	0.000057	0.011074	0.000056
Valid Values	150 (150)	150 (150)	150 (150)	150 (150)	150 (150)	143 (150)	142 (150)	150 (150)	142 (150)

6-7 October 2020									
	84Sr	**85Rb**	**86Sr**	**87Sr**	**88Sr**	**87Sr/86Sr (1)**	**84Sr/86Sr (2)**	**88Sr/86Sr (3)**	**85Rb/86Sr (4)**
Cup	L2	L1	C	H1	H2	H1 | C	L2 | C	H2 | C	L1 | C
SRM987 (1)									
Mean	0.117481	-0.000004	2.080893	1.478656	17.443205	0.710273	0.056508	8.382789	-0.000002
StdErr (%)	0.251731	-22.584405	0.255082	0.257074	0.259115	0.000300	0.001094	0.012288	-18.644378

StdErr (abs)	0.000296	0.000001	0.005308	0.003801	0.045198	0.000002	0.000001	0.001030	0.000000
StdDev (%)	3.083066	-276.601341	3.124105	3.148505	3.173497	0.003574	0.012992	0.149487	-222.954331
StdDev (abs)	0.003622	0.000012	0.065009	0.046556	0.553560	0.000025	0.000007	0.012531	0.000005
Valid Values	150 (150)	150 (150)	150 (150)	150 (150)	150 (150)	142 (150)	141 (150)	148 (150)	143 (150)
				SRM987 (1) - Second measurement					
Mean	0.054209	-0.000001	0.960642	0.682825	8.057403	0.710274	0.056515	8.387152	-0.000001
StdErr (%)	0.673016	-89.973901	0.677793	0.680235	0.682602	0.000386	0.002265	0.008963	-82.902190
StdErr (abs)	0.000365	0.000001	0.006511	0.004645	0.055000	0.000003	0.000001	0.000752	0.000001
StdDev (%)	8.242731	-1101.950741	8.301239	8.331141	8.360137	0.004572	0.027176	0.109769	-987.893609
StdDev (abs)	0.004468	0.000011	0.079745	0.056887	0.673610	0.000032	0.000015	0.009206	0.000010
Valid Values	150 (150)	150 (150)	150 (150)	150 (150)	150 (150)	140 (150)	144 (150)	150 (150)	142 (150)
				SRM987 (2)					
Mean	0.092847	0.000002	1.627872	1.150962	13.510402	0.710277	0.056508	8.299093	0.000001
StdErr (%)	0.611590	46.056493	0.615988	0.618088	0.620183	0.000328	0.001479	0.004707	48.918047
StdErr (abs)	0.000568	0.000001	0.010027	0.007114	0.083789	0.000002	0.000001	0.000391	0.000001
StdDev (%)	7.490423	564.074538	7.544280	7.570003	7.595656	0.003908	0.017620	0.057653	580.869620
StdDev (abs)	0.006955	0.000011	0.122811	0.087128	1.026204	0.000028	0.000010	0.004785	0.000006
Valid Values	150 (150)	150 (150)	150 (150)	150 (150)	150 (150)	142 (150)	142 (150)	150 (150)	141 (150)
				SRM987 (3)					
Mean	0.042914	-0.000002	0.751551	0.531104	6.231356	0.710270	0.056516	8.291120	-0.000003
StdErr (%)	0.742269	-50.814449	0.744465	0.745489	0.746486	0.000436	0.002714	0.002837	-37.680427
StdErr (abs)	0.000319	0.000001	0.005595	0.003959	0.046516	0.000003	0.000002	0.000235	0.000001
StdDev (%)	9.090899	-622.347353	9.117799	9.130339	9.142545	0.005144	0.032337	0.034745	-449.014112
StdDev (abs)	0.003901	0.000011	0.068525	0.048492	0.569705	0.000037	0.000018	0.002881	0.000013
Valid Values	150 (150)	150 (150)	150 (150)	150 (150)	150 (150)	139 (150)	142 (150)	150 (150)	142 (150)
				SRM987 (4)					
Mean	0.096423	0.000000	1.695288	1.200224	14.107226	0.710277	0.056504	8.320988	0.000000
StdErr (%)	0.350251	-215.220402	0.360732	0.365804	0.370683	0.000347	0.001420	0.010276	-496.863058
StdErr (abs)	0.000338	0.000001	0.006115	0.004390	0.052293	0.000002	0.000001	0.000855	0.000000
StdDev (%)	4.289683	-2635.900832	4.418047	4.480163	4.539918	0.004183	0.016924	0.125849	-5941.618000
StdDev (abs)	0.004136	0.000010	0.074899	0.053772	0.640457	0.000030	0.000010	0.010472	0.000005
Valid Values	150 (150)	150 (150)	150 (150)	150 (150)	150 (150)	145 (150)	142 (150)	150 (150)	143 (150)
				SRM987 (5)					
Mean	0.090975	-0.000003	1.595353	1.128046	13.242300	0.710279	0.056505	8.299921	-0.000002
StdErr (%)	0.706151	-29.630986	0.712911	0.716241	0.719543	0.000362	0.001595	0.008035	-24.608061
StdErr (abs)	0.000642	0.000001	0.011373	0.008080	0.095284	0.000003	0.000001	0.000667	0.000000
StdDev (%)	8.648551	-362.903985	8.731346	8.772128	8.812571	0.004394	0.019141	0.098414	-293.238885
StdDev (abs)	0.007868	0.000010	0.139296	0.098954	1.166987	0.000031	0.000011	0.008168	0.000006
Valid Values	150 (150)	150 (150)	150 (150)	150 (150)	150 (150)	147 (150)	144 (150)	150 (150)	142 (150)
				SRM987 (6)					
Mean	0.041925	-0.000002	0.735005	0.519689	6.100714	0.710271	0.056518	8.300092	-0.000003
StdErr (%)	0.390991	-53.322773	0.393534	0.394941	0.396326	0.000474	0.002645	0.003184	-34.795201
StdErr (abs)	0.000164	0.000001	0.002892	0.002052	0.024179	0.000003	0.000001	0.000264	0.000001

StdDev (%)	4.788648	-653.067933	4.819793	4.837014	4.853976	0.005669	0.031964	0.039000	-416.090089
StdDev (abs)	0.002008	0.000012	0.035426	0.025137	0.296127	0.000040	0.000018	0.003237	0.000014
Valid Values	150 (150)	150 (150)	150 (150)	150 (150)	150 (150)	143 (150)	146 (150)	150 (150)	143 (150)
				Gr0-d_D (see Peverelli et al., 2021; Chapter 2)					
Mean	0.040364	-0.000001	0.713037	0.518558	5.962807	0.727807	0.056521	8.370215	-0.000001
StdErr (%)	1.512419	-87.893264	1.492074	1.482087	1.472233	0.000485	0.002751	0.020476	-85.208813
StdErr (abs)	0.000610	0.000001	0.010639	0.007685	0.087786	0.000004	0.000002	0.001714	0.000001
StdDev (%)	18.523270	-1076.468246	18.274101	18.151787	18.031093	0.005781	0.033125	0.241406	-1022.505755
StdDev (abs)	0.007477	0.000012	0.130301	0.094128	1.075159	0.000042	0.000019	0.020206	0.000015
Valid Values	150 (150)	150 (150)	150 (150)	150 (150)	150 (150)	142 (150)	145 (150)	139 (150)	144 (150)
				ALB19-11B_C					
Mean	0.083107	-0.000002	1.460926	1.038280	12.156272	0.713033	0.056509	8.319912	-0.000001
StdErr (%)	0.629890	-47.220682	0.642984	0.649422	0.655744	0.000409	0.001722	0.012963	-39.899239
StdErr (abs)	0.000523	0.000001	0.009394	0.006743	0.079714	0.000003	0.000001	0.001079	0.000001
StdDev (%)	7.714546	-578.332886	7.874917	7.953766	8.031186	0.004946	0.020594	0.158768	-475.454309
StdDev (abs)	0.006411	0.000012	0.115047	0.082582	0.976293	0.000035	0.000012	0.013209	0.000007
Valid Values	150 (150)	150 (150)	150 (150)	150 (150)	150 (150)	146 (150)	143 (150)	150 (150)	142 (150)
				ALB19-11A_1342					
Mean	0.04499	0.00000	0.79125	0.56253	6.58783	0.71306	0.05652	8.32527	-0.00001
StdErr (%)	0.34023	-21.46457	0.35342	0.35975	0.36617	0.00048	0.00234	0.01616	-17.22658
StdErr (abs)	0.00015	0.00000	0.00280	0.00202	0.02412	0.00000	0.00000	0.00135	0.00000
StdDev (%)	4.16689	-262.88617	4.32855	4.40598	4.48464	0.00578	0.02794	0.19792	-204.55435
StdDev (abs)	0.00187	0.00001	0.03425	0.02478	0.29544	0.00004	0.00002	0.01648	0.00001
Valid Values	150 (150)	150 (150)	150 (150)	150 (150)	150 (150)	144 (150)	142 (150)	150 (150)	141 (150)
				ALB1913-7					
Mean	0.036451	0.000137	0.639950	0.454890	5.319554	0.713338	0.056523	8.314009	0.000049
StdErr (%)	2.678200	19.647296	2.672595	2.672872	2.665960	0.001039	0.003384	0.006891	21.910250
StdErr (abs)	0.000976	0.000027	0.017103	0.012159	0.141817	0.000007	0.000002	0.000573	0.000011
StdDev (%)	32.801112	240.629246	32.732465	32.735861	32.651213	0.012202	0.040328	0.084393	257.387160
StdDev (abs)	0.011956	0.000331	0.209471	0.148912	1.736899	0.000087	0.000023	0.007016	0.000126
Valid Values	150 (150)	150 (150)	150 (150)	150 (150)	150 (150)	138 (150)	142 (150)	150 (150)	138 (150)
				ALB1919-18(b)					
Mean	0.037112	0.000367	0.650830	0.462154	5.403874	0.712983	0.056520	8.302972	0.000508
StdErr (%)	0.418856	4.527767	0.418724	0.417239	0.418351	0.000565	0.002901	0.000718	4.388305
StdErr (abs)	0.000155	0.000017	0.002725	0.001928	0.022607	0.000004	0.000002	0.000060	0.000022
StdDev (%)	5.129915	55.453590	5.128305	5.110117	5.123737	0.006754	0.034574	0.008500	51.737354
StdDev (abs)	0.001904	0.000204	0.033377	0.023617	0.276880	0.000048	0.000020	0.000706	0.000263
Valid Values	150 (150)	150 (150)	150 (150)	150 (150)	150 (150)	143 (150)	142 (150)	140 (150)	139 (150)
				GAS19-01A					
Mean	0.044951	0.001505	0.796221	0.579734	6.676150	0.726957	0.056520	8.370003	0.001520
StdErr (%)	1.213478	11.197812	1.248591	1.271640	1.283925	0.000467	0.002627	0.027645	11.359167
StdErr (abs)	0.000545	0.000169	0.009942	0.007372	0.085717	0.000003	0.000001	0.002314	0.000173
StdDev (%)	14.862005	137.144630	15.292049	15.574349	15.724809	0.005600	0.031522	0.320013	135.835875

StdDev (abs)	0.006681	0.002064	0.121758	0.090290	1.049812	0.000041	0.000018	0.026785	0.002065
Valid Values	150 (150)	150 (150)	150 (150)	150 (150)	150 (150)	144 (150)	144 (150)	134 (150)	143 (150)
				Gr0-e					
Mean	0.053002	0.000150	0.935074	0.668080	7.807745	0.715495	0.056507	8.349880	0.000131
StdErr (%)	0.571984	10.310684	0.572232	0.572899	0.572309	0.000413	0.002351	0.004962	10.649777
StdErr (abs)	0.000303	0.000015	0.005351	0.003827	0.044684	0.000003	0.000001	0.000414	0.000014
StdDev (%)	7.005339	126.279578	7.008380	7.016551	7.009326	0.004899	0.027922	0.060774	127.352811
StdDev (abs)	0.003713	0.000189	0.065534	0.046876	0.547270	0.000035	0.000016	0.005075	0.000167
Valid Values	150 (150)	150 (150)	150 (150)	150 (150)	150 (150)	141 (150)	141 (150)	150 (150)	143 (150)
				Gr0-c					
Mean	0.037541	-0.000001	0.660510	0.469688	5.500488	0.713145	0.056505	8.318404	-0.000002
StdErr (%)	2.145576	-77.242023	2.163248	2.172138	2.181026	0.000593	0.003033	0.017853	-57.867694
StdErr (abs)	0.000805	0.000001	0.014288	0.010202	0.119967	0.000004	0.000002	0.001485	0.000001
StdDev (%)	26.277836	-946.017721	26.494267	26.603148	26.712003	0.007064	0.036014	0.208202	-699.218008
StdDev (abs)	0.009865	0.000011	0.174997	0.124952	1.469291	0.000050	0.000020	0.017319	0.000016
Valid Values	150 (150)	150 (150)	150 (150)	150 (150)	150 (150)	142 (150)	141 (150)	136 (150)	146 (150)
				Lö20_1A					
Mean	0.03390	-0.00001	0.59405	0.41860	4.92796	0.70806	0.05650	8.29507	-0.00001
StdErr (%)	0.45496	-18.16635	0.45772	0.45889	0.46024	0.00062	0.00313	0.00220	-15.46914
StdErr (abs)	0.00015	0.00000	0.00272	0.00192	0.02268	0.00000	0.00000	0.00018	0.00000
StdDev (%)	5.57206	-222.49144	5.60596	5.62019	5.63679	0.00739	0.03770	0.02627	-184.33608
StdDev (abs)	0.00189	0.00001	0.03330	0.02353	0.27778	0.00005	0.00002	0.00218	0.00002
Valid Values	150 (150)	150 (150)	150 (150)	150 (150)	150 (150)	143 (150)	145 (150)	142 (150)	142 (150)
				GSP-2					
Mean	0.050411	0.002822	0.891268	0.682826	7.458705	0.765202	0.056514	8.370038	0.002175
StdErr (%)	0.957685	13.315383	0.947089	0.946284	0.938890	0.000493	0.002510	0.046723	12.987601
StdErr (abs)	0.000483	0.000376	0.008441	0.006461	0.070029	0.000004	0.000001	0.003911	0.000282
StdDev (%)	11.729195	163.079468	11.599425	11.589569	11.499004	0.005932	0.030330	0.572237	153.121559
StdDev (abs)	0.005913	0.004601	0.103382	0.079137	0.857677	0.000045	0.000017	0.047896	0.003330
Valid Values	150 (150)	150 (150)	150 (150)	150 (150)	150 (150)	145 (150)	146 (150)	150 (150)	139 (150)

12 June 2012

	84Sr	**85Rb**	**86Sr**	**87Sr**	**88Sr**	**87Sr/86Sr (1)**	**84Sr/86Sr (2)**	**88Sr/86Sr (3)**	**85Rb/86Sr (4)**
Cup	L2	L1	C	H1	H2	H1 | C	L2 | C	H2 | C	L1 | C
				SRM987 (1)					
Mean	0.029683	-0.000001	0.522346	0.369907	4.348999	0.710274	0.056484	8.326332	-0.000003
StdErr (%)	0.634041	-69.151836	0.627387	0.624427	0.621521	0.000616	0.003787	0.006763	-56.273635
StdErr (abs)	0.000188	0.000001	0.003277	0.002310	0.027030	0.000004	0.000002	0.000563	0.000002
StdDev (%)	7.765383	-846.933566	7.683888	7.647640	7.612043	0.007467	0.045283	0.082832	-675.283619
StdDev (abs)	0.002305	0.000011	0.040136	0.028289	0.331048	0.000053	0.000026	0.006897	0.000019
Valid Values	150 (150)	150 (150)	150 (150)	150 (150)	150 (150)	147 (150)	143 (150)	150 (150)	144 (150)
				SRM987 (1) - Second measurement (static)					

Mean	0.027641	0.000002	0.488190	0.346349	4.079407	0.710262	0.056490	8.356110	0.000005
StdErr (%)	0.121092	53.916734	0.124652	0.126784	0.129132	0.000669	0.003751	0.006700	33.709262
StdErr (abs)	0.000033	0.000001	0.000609	0.000439	0.005268	0.000005	0.000002	0.000560	0.000002
StdDev (%)	1.483068	660.342436	1.526667	1.552778	1.581539	0.008000	0.045014	0.082055	403.104144
StdDev (abs)	0.000410	0.000011	0.007453	0.005378	0.064517	0.000057	0.000025	0.006857	0.000019
Valid Values	150 (150)	150 (150)	150 (150)	150 (150)	150 (150)	143 (150)	144 (150)	150 (150)	143 (150)
				SRM987 (1) - Second measurement					
Mean	0.027641	0.000002	0.488190	0.346349	4.079407	0.710262	0.056490	8.356110	0.000005
StdErr (%)	0.121092	53.916734	0.124652	0.126784	0.129132	0.000669	0.003751	0.006700	33.709262
StdErr (abs)	0.000033	0.000001	0.000609	0.000439	0.005268	0.000005	0.000002	0.000560	0.000002
StdDev (%)	1.483068	660.342436	1.526667	1.552778	1.581539	0.008000	0.045014	0.082055	403.104144
StdDev (abs)	0.000410	0.000011	0.007453	0.005378	0.064517	0.000057	0.000025	0.006857	0.000019
Valid Values	150 (150)	150 (150)	150 (150)	150 (150)	150 (150)	143 (150)	144 (150)	150 (150)	143 (150)
				SRM987 (2)					
Mean	0.049848	0.000004	0.878917	0.623076	7.333234	0.710269	0.056495	8.343413	0.000005
StdErr (%)	0.755879	24.490218	0.756593	0.757075	0.757584	0.000461	0.002362	0.013197	19.623535
StdErr (abs)	0.000377	0.000001	0.006650	0.004717	0.055555	0.000003	0.000001	0.001101	0.000001
StdDev (%)	9.257594	299.942695	9.266334	9.272234	9.278476	0.005509	0.028345	0.161635	235.482417
StdDev (abs)	0.004615	0.000011	0.081443	0.057773	0.680412	0.000039	0.000016	0.013486	0.000011
Valid Values	150 (150)	150 (150)	150 (150)	150 (150)	150 (150)	143 (150)	144 (150)	150 (150)	144 (150)
				SRM987 (3)					
Mean	0.055127	0.078842	0.967759	0.715016	8.039898	0.710571	0.056493	8.309573	0.075209
StdErr (%)	2.563235	5.044340	2.557768	2.608254	2.553050	0.000855	0.002536	0.008072	3.631208
StdErr (abs)	0.001413	0.003977	0.024753	0.018649	0.205263	0.000006	0.000001	0.000671	0.002731
StdDev (%)	31.393092	61.780298	31.326130	31.944459	31.268354	0.010266	0.030745	0.098866	44.175554
StdDev (abs)	0.017306	0.048709	0.303162	0.228408	2.513944	0.000073	0.000017	0.008215	0.033224
Valid Values	150 (150)	150 (150)	150 (150)	150 (150)	150 (150)	144 (150)	147 (150)	150 (150)	148 (150)
				SRM987 (4)					
Mean	0.010868	0.000006	0.190391	0.134515	1.577899	0.710258	0.056464	8.288245	0.000040
StdErr (%)	7.379935	17.347984	7.375622	7.374648	7.373883	0.001673	0.010838	0.001507	16.204840
StdErr (abs)	0.000802	0.000001	0.014043	0.009920	0.116352	0.000012	0.000006	0.000125	0.000007
StdDev (%)	90.385371	212.468550	90.332551	90.320626	90.311259	0.019937	0.130510	0.018212	193.781706
StdDev (abs)	0.009823	0.000013	0.171985	0.121495	1.425021	0.000142	0.000074	0.001509	0.000078
Valid Values	150 (150)	150 (150)	150 (150)	150 (150)	150 (150)	142 (150)	145 (150)	146 (150)	143 (150)
				SRM987 (5)					
Mean	0.010273	0.000002	0.180082	0.127267	1.493240	0.710274	0.056462	8.292676	0.000009
StdErr (%)	6.343645	57.056499	6.338650	6.337520	6.336533	0.001391	0.010677	0.001910	64.034807
StdErr (abs)	0.000652	0.000001	0.011415	0.008066	0.094620	0.000010	0.000006	0.000158	0.000006
StdDev (%)	77.693464	698.796544	77.632290	77.618446	77.606365	0.016518	0.126332	0.023077	768.417684
StdDev (abs)	0.007982	0.000011	0.139802	0.098782	1.158849	0.000117	0.000071	0.001914	0.000072
Valid Values	150 (150)	150 (150)	150 (150)	150 (150)	150 (150)	141 (150)	140 (150)	146 (150)	144 (150)
				AGV-2					
Mean	0.021557	0.000011	0.381942	0.268990	3.201231	0.704001	0.056484	8.381357	0.000018

StdErr (%)	0.822026	18.278941	0.822930	0.823583	0.824147	0.000772	0.004524	0.010404	15.772029
StdErr (abs)	0.000177	0.000002	0.003143	0.002215	0.026383	0.000005	0.000003	0.000872	0.000003
StdDev (%)	10.067717	223.870396	10.078794	10.086791	10.093702	0.009292	0.054102	0.127419	189.264347
StdDev (abs)	0.002170	0.000025	0.038495	0.027132	0.323123	0.000065	0.000031	0.010679	0.000034
Valid Values	150 (150)	150 (150)	150 (150)	150 (150)	150 (150)	145 (150)	143 (150)	150 (150)	144 (150)
AGV-2 - Second measurement									
Mean	0.009506	0.000003	0.169296	0.119506	1.425543	0.703975	0.056459	8.420535	0.000017
StdErr (%)	0.434106	37.199554	0.431259	0.430035	0.429228	0.001128	0.009807	0.007006	33.895326
StdErr (abs)	0.000041	0.000001	0.000730	0.000514	0.006119	0.000008	0.000006	0.000590	0.000006
StdDev (%)	5.316689	455.599629	5.281822	5.266833	5.256952	0.013535	0.116447	0.085809	406.743915
StdDev (abs)	0.000505	0.000013	0.008942	0.006294	0.074940	0.000095	0.000066	0.007226	0.000067
Valid Values	150 (150)	150 (150)	150 (150)	150 (150)	150 (150)	144 (150)	141 (150)	150 (150)	144 (150)
ALB-G2									
Mean	0.044633	0.000009	0.791039	0.568327	6.633035	0.718021	0.056492	8.387873	0.000011
StdErr (%)	1.157193	11.103659	1.147317	1.142599	1.137996	0.000519	0.002923	0.018992	10.542066
StdErr (abs)	0.000516	0.000001	0.009076	0.006494	0.075484	0.000004	0.000002	0.001593	0.000001
StdDev (%)	14.172657	135.991497	14.051701	13.993926	13.937544	0.006268	0.035202	0.229479	126.504796
StdDev (abs)	0.006326	0.000012	0.111154	0.079531	0.924482	0.000045	0.000020	0.019248	0.000014
Valid Values	150 (150)	150 (150)	150 (150)	150 (150)	150 (150)	146 (150)	145 (150)	146 (150)	144 (150)
ALB19-1 ||									
Mean	0.044749	0.000003	0.791101	0.564632	6.617157	0.714189	0.056492	8.367749	0.000004
StdErr (%)	1.633534	30.890116	1.627493	1.624671	1.621831	0.000503	0.002282	0.007886	33.154402
StdErr (abs)	0.000731	0.000001	0.012875	0.009173	0.107319	0.000004	0.000001	0.000660	0.000001
StdDev (%)	20.006628	378.325109	19.932634	19.898074	19.863290	0.005990	0.027096	0.092980	400.606161
StdDev (abs)	0.008953	0.000012	0.157687	0.112351	1.314385	0.000043	0.000015	0.007780	0.000015
Valid Values	150 (150)	150 (150)	150 (150)	150 (150)	150 (150)	142 (150)	141 (150)	139 (150)	146 (150)
ALB19-4_1327A									
Mean	0.05339	0.00001	0.94239	0.67330	7.87072	0.71547	0.05649	8.35396	0.00001
StdErr (%)	0.62251	13.03085	0.59612	0.58363	0.57154	0.00041	0.00221	0.03707	12.87033
StdErr (abs)	0.00033	0.00000	0.00562	0.00393	0.04498	0.00000	0.00000	0.00310	0.00000
StdDev (%)	7.62420	159.59463	7.30098	7.14799	6.99986	0.00492	0.02639	0.45403	156.04442
StdDev (abs)	0.00407	0.00001	0.06880	0.04813	0.55094	0.00004	0.00001	0.03793	0.00001
Valid Values	150 (150)	150 (150)	150 (150)	150 (150)	150 (150)	142 (150)	142 (150)	150 (150)	147 (150)
SRM987 (6)									
Mean	0.013636	0.000004	0.239311	0.169244	1.987127	0.710291	0.056478	8.305927	0.000020
StdErr (%)	4.634037	27.083409	4.624688	4.620904	4.617761	0.001127	0.008638	0.004027	22.639158
StdErr (abs)	0.000632	0.000001	0.011067	0.007821	0.091761	0.000008	0.000005	0.000334	0.000004
StdDev (%)	56.755129	331.702666	56.640633	56.594287	56.555790	0.013432	0.104019	0.048159	270.724958
StdDev (abs)	0.007739	0.000012	0.135547	0.095783	1.123835	0.000095	0.000059	0.004000	0.000053
Valid Values	150 (150)	150 (150)	150 (150)	150 (150)	150 (150)	142 (150)	145 (150)	143 (150)	143 (150)
Gr0-c									
Mean	0.033870	0.000052	0.598284	0.426673	5.000091	0.713891	0.056489	8.360365	0.000073
StdErr (%)	0.984060	6.549413	0.972783	0.967705	0.962384	0.000538	0.003338	0.010313	4.972833

StdErr (abs)	0.000333	0.000003	0.005820	0.004129	0.048120	0.000004	0.000002	0.000862	0.000004
StdDev (%)	12.052222	80.213600	11.914113	11.851918	11.786746	0.006455	0.039638	0.122457	59.049123
StdDev (abs)	0.004082	0.000042	0.071280	0.050569	0.589348	0.000046	0.000022	0.010238	0.000043
Valid Values	150 (150)	150 (150)	150 (150)	150 (150)	150 (150)	144 (150)	141 (150)	141 (150)	141 (150)
					GSP-2				
Mean	0.001119	0.000049	0.019935	0.015251	0.167082	0.763806	0.058293	8.378584	0.001952
StdErr (%)	5.521534	6.214281	5.506456	5.508214	5.515957	0.012285	3.212252	0.039712	165.465598
StdErr (abs)	0.000062	0.000003	0.001098	0.000840	0.009216	0.000094	0.001873	0.003327	0.003230
StdDev (%)	67.624700	76.109088	67.440034	67.461572	67.556399	0.145878	38.412948	0.471550	1978.680764
StdDev (abs)	0.000757	0.000037	0.013444	0.010288	0.112875	0.001114	0.022392	0.039509	0.038631
Valid Values	150 (150)	150 (150)	150 (150)	150 (150)	150 (150)	141 (150)	143 (150)	141 (150)	143 (150)
					P9c				
Mean	0.053267	0.000106	0.942592	0.669907	7.892929	0.710732	0.056499	8.376460	0.000108
StdErr (%)	1.560998	4.523764	1.547567	1.541049	1.534538	0.000516	0.002494	0.024603	3.670121
StdErr (abs)	0.000831	0.000005	0.014587	0.010324	0.121120	0.000004	0.000001	0.002061	0.000004
StdDev (%)	19.118246	55.404571	18.953750	18.873915	18.794176	0.006210	0.029613	0.301325	44.041456
StdDev (abs)	0.010184	0.000059	0.178657	0.126438	1.483411	0.000044	0.000017	0.025240	0.000048
Valid Values	150 (150)	150 (150)	150 (150)	150 (150)	150 (150)	145 (150)	141 (150)	150 (150)	144 (150)
					RGM-2				
Mean	0.112596	0.000005	1.995177	1.405696	16.727825	0.704169	0.056494	8.385511	0.000002
StdErr (%)	1.216426	18.557069	1.210560	1.208041	1.205741	0.000287	0.001319	0.033531	18.132774
StdErr (abs)	0.001370	0.000001	0.024153	0.016981	0.201694	0.000002	0.000001	0.002812	0.000000
StdDev (%)	14.898112	227.276753	14.826271	14.795423	14.767257	0.003448	0.015719	0.410669	216.076938
StdDev (abs)	0.016775	0.000012	0.295810	0.207979	2.470241	0.000024	0.000009	0.034437	0.000005
Valid Values	150 (150)	150 (150)	150 (150)	150 (150)	150 (150)	144 (150)	142 (150)	150 (150)	142 (150)

Neptune MC-ICP-MS

23 September 2019														
	202Hg	**203Tl**	**204Pb**	**205Tl**	**206Pb**	**207Pb**	**208Pb**	**206Pb/204Pb (1)**	**207Pb/204Pb (2)**	**208Pb/204Pb (3)**	**205Tl/203Tl (4)**	**207Pb/206Pb (5)**	**208Pb/206Pb (6)**
Cup	L3	L2	L1	C	H1	H2	H3	H1 | L1	H2 | L1	H3 | L1	C | L2	H2 | H1	H3 | H1
							ALB13-1 U-Pb A						
Mean	-0.00001	0.21306	0.11345	0.51495	2.20723	1.81384	4.51103	19.21556	15.69413	38.79434	2.41695	0.81674	2.01889
StdErr (%)	-21.12841	0.80006	0.69159	0.80041	0.69230	0.69240	0.69250	0.00235	0.00268	0.00327	0.00148	0.00083	0.00149
StdErr (abs)	0.00000	0.00170	0.00078	0.00412	0.01528	0.01256	0.03124	0.00045	0.00042	0.00127	0.00004	0.00001	0.00003
StdDev (%)	-163.65993	6.19722	5.35705	6.19995	5.36257	5.36332	5.36407	0.01773	0.02023	0.02472	0.01096	0.00629	0.01133
StdDev (abs)	0.00001	0.01320	0.00608	0.03193	0.11836	0.09728	0.24197	0.00341	0.00317	0.00959	0.00026	0.00005	0.00023
Valid Values	60 (60)	60 (60)	60 (60)	60 (60)	60 (60)	60 (60)	60 (60)	57 (60)	57 (60)	57 (60)	55 (60)	57 (60)	58 (60)
							ALB13-1 U-Pb B						
Mean	-0.00001	0.21805	0.09817	0.52693	1.90953	1.56907	3.90160	19.21525	15.69372	38.78837	2.41657	0.81674	2.01867
StdErr (%)	-17.17015	0.75370	0.66671	0.75458	0.66749	0.66803	0.66869	0.00282	0.00324	0.00373	0.00174	0.00088	0.00149
StdErr (abs)	0.00000	0.00164	0.00065	0.00398	0.01275	0.01048	0.02609	0.00054	0.00051	0.00145	0.00004	0.00001	0.00003
StdDev (%)	-132.99940	5.83816	5.16433	5.84495	5.17035	5.17456	5.17965	0.02150	0.02449	0.02793	0.01317	0.00662	0.01131

StdDev (abs)	0.00001	0.01273	0.00507	0.03080	0.09873	0.08119	0.20209	0.00413	0.00384	0.01083	0.00032	0.00005	0.00023
Valid Values	60 (60)	60 (60)	60 (60)	60 (60)	60 (60)	60 (60)	60 (60)	58 (60)	57 (60)	56 (60)	57 (60)	57 (60)	58 (60)
						ALB13-1 H A							
Mean	0.00000	0.22109	0.09000	0.53440	1.75891	1.43917	3.58054	19.30193	15.69612	38.81219	2.41705	0.81319	2.01079
StdErr (%)	63.48913	1.14241	0.60321	1.14071	0.60370	0.60378	0.60373	0.00324	0.00372	0.00465	0.00212	0.00111	0.00197
StdErr (abs)	0.00000	0.00253	0.00054	0.00610	0.01062	0.00869	0.02162	0.00063	0.00058	0.00180	0.00005	0.00001	0.00004
StdDev (%)	491.78469	8.84907	4.67242	8.83591	4.67626	4.67685	4.67647	0.02427	0.02787	0.03480	0.01573	0.00836	0.01471
StdDev (abs)	0.00001	0.01956	0.00421	0.04722	0.08225	0.06731	0.16744	0.00468	0.00437	0.01351	0.00038	0.00007	0.00030
Valid Values	60 (60)	60 (60)	60 (60)	60 (60)	60 (60)	60 (60)	60 (60)	56 (60)	56 (60)	56 (60)	55 (60)	57 (60)	56 (60)
						ALB13-1 H B							
Mean	0.00001	0.21099	0.08747	0.50982	1.70874	1.39823	3.47844	19.30017	15.69843	38.82040	2.41634	0.81337	2.01138
StdErr (%)	23.73721	0.67583	0.67683	0.67618	0.67821	0.67866	0.67886	0.00236	0.00284	0.00329	0.00174	0.00093	0.00139
StdErr (abs)	0.00000	0.00143	0.00059	0.00345	0.01159	0.00949	0.02361	0.00046	0.00045	0.00128	0.00004	0.00001	0.00003
StdDev (%)	183.86767	5.23494	5.24268	5.23768	5.25343	5.25691	5.25842	0.01765	0.02196	0.02526	0.01311	0.00707	0.01062
StdDev (abs)	0.00001	0.01105	0.00459	0.02670	0.08977	0.07350	0.18291	0.00341	0.00345	0.00981	0.00032	0.00006	0.00021
Valid Values	60 (60)	60 (60)	60 (60)	60 (60)	60 (60)	60 (60)	60 (60)	56 (60)	60 (60)	59 (60)	57 (60)	58 (60)	58 (60)
						Gr0-d H A							
Mean	-0.00002	0.33221	0.12626	0.80333	2.53622	2.02051	5.10693	19.82923	15.69641	39.42235	2.41816	0.79159	1.98810
StdErr (%)	-9.66044	0.80245	0.65950	0.80270	0.65972	0.65982	0.66001	0.00234	0.00269	0.00319	0.00125	0.00067	0.00122
StdErr (abs)	0.00000	0.00267	0.00083	0.00645	0.01673	0.01333	0.03371	0.00046	0.00042	0.00126	0.00003	0.00001	0.00002
StdDev (%)	-74.82948	6.21573	5.10844	6.21771	5.11014	5.11095	5.11239	0.01782	0.02030	0.02433	0.00949	0.00499	0.00923
StdDev (abs)	0.00001	0.02065	0.00645	0.04995	0.12960	0.10327	0.26109	0.00353	0.00319	0.00959	0.00023	0.00004	0.00018
Valid Values	60 (60)	60 (60)	60 (60)	60 (60)	60 (60)	60 (60)	60 (60)	58 (60)	57 (60)	58 (60)	58 (60)	55 (60)	57 (60)
						Gr0-d H B							
Mean	-0.00002	0.32762	0.12715	0.79216	2.55532	2.03428	5.14292	19.84146	15.69652	39.43379	2.41782	0.79108	1.98740
StdErr (%)	-8.81451	0.90801	1.10668	0.90906	1.10879	1.10976	1.11084	0.00259	0.00334	0.00389	0.00319	0.00091	0.00161
StdErr (abs)	0.00000	0.00297	0.00141	0.00720	0.02833	0.02258	0.05713	0.00051	0.00052	0.00154	0.00008	0.00001	0.00003
StdDev (%)	-68.27691	7.03338	8.57228	7.04156	8.58862	8.59616	8.60457	0.01937	0.02520	0.02940	0.02430	0.00684	0.01215
StdDev (abs)	0.00001	0.02304	0.01090	0.05578	0.21947	0.17487	0.44253	0.00384	0.00396	0.01159	0.00059	0.00005	0.00024
Valid Values	60 (60)	60 (60)	60 (60)	60 (60)	60 (60)	60 (60)	60 (60)	56 (60)	57 (60)	57 (60)	58 (60)	56 (60)	57 (60)
						Gr0-d U-Pb A							
Mean	-0.00001	0.34495	0.09985	0.83422	1.99859	1.59769	4.03427	19.75805	15.69386	39.37561	2.41834	0.79428	1.99286
StdErr (%)	-25.69788	0.99333	0.89749	0.99325	0.89753	0.89765	0.89774	0.00247	0.00261	0.00315	0.00144	0.00089	0.00136
StdErr (abs)	0.00000	0.00343	0.00090	0.00829	0.01794	0.01434	0.03622	0.00049	0.00041	0.00124	0.00003	0.00001	0.00003
StdDev (%)	-199.05491	7.69427	6.95193	7.69366	6.95223	6.95315	6.95386	0.01884	0.01955	0.02402	0.01097	0.00675	0.01036
StdDev (abs)	0.00001	0.02654	0.00694	0.06418	0.13895	0.11109	0.28054	0.00372	0.00307	0.00946	0.00027	0.00005	0.00021
Valid Values	60 (60)	60 (60)	60 (60)	60 (60)	60 (60)	60 (60)	60 (60)	58 (60)	56 (60)	58 (60)	58 (60)	57 (60)	58 (60)
						Gr0-d U-Pb B							
Mean	-0.00001	0.45663	0.10285	1.10461	2.06007	1.64630	4.15701	19.76739	15.69346	39.36912	2.41903	0.79391	1.99163
StdErr (%)	-17.20358	0.77914	0.62642	0.77974	0.62686	0.62701	0.62729	0.00247	0.00249	0.00285	0.00111	0.00076	0.00104
StdErr (abs)	0.00000	0.00356	0.00064	0.00861	0.01291	0.01032	0.02608	0.00049	0.00039	0.00112	0.00003	0.00001	0.00002
StdDev (%)	-133.25835	6.03522	4.85226	6.03981	4.85566	4.85682	4.85895	0.01883	0.01879	0.02154	0.00849	0.00578	0.00783
StdDev (abs)	0.00001	0.02756	0.00499	0.06672	0.10003	0.07996	0.20199	0.00372	0.00295	0.00848	0.00021	0.00005	0.00016

Valid Values	60 (60)	60 (60)	60 (60)	60 (60)	60 (60)	60 (60)	60 (60)	58 (60)	57 (60)	57 (60)	58 (60)	58 (60)	57 (60)
							Blank						
Mean	0.00001	0.19321	0.03770	0.46672	0.72905	0.60171	1.48880	19.11429	15.68295	38.57843	2.41553	0.82050	2.01832
StdErr (%)	28.57891	1.01672	0.91308	1.01791	0.91293	0.91302	0.91429	0.00543	0.00541	0.00561	0.00261	0.00167	0.00237
StdErr (abs)	0.00000	0.00196	0.00034	0.00475	0.00666	0.00549	0.01361	0.00104	0.00085	0.00217	0.00006	0.00001	0.00005
StdDev (%)	198.00052	7.04405	6.32601	7.05231	6.32498	6.32562	6.33440	0.03682	0.03627	0.03765	0.01788	0.01118	0.01611
StdDev (abs)	0.00001	0.01361	0.00238	0.03291	0.04611	0.03806	0.09431	0.00704	0.00569	0.01453	0.00043	0.00009	0.00033
Valid Values	48 (48)	48 (48)	48 (48)	48 (48)	48 (48)	48 (48)	48 (48)	46 (48)	45 (48)	45 (48)	47 (48)	45 (48)	46 (48)
							NBS981						
Mean	0.00000	0.38118	0.09514	0.92161	1.63196	1.50172	3.57986	16.93678	15.48779	36.68863	2.41781	0.91444	2.16615
StdErr (%)	-127.24774	5.27451	5.19828	5.27599	5.19768	5.19937	5.19950	0.00364	0.00362	0.00443	0.00391	0.00211	0.00361
StdErr (abs)	0.00000	0.02011	0.00495	0.04862	0.08482	0.07808	0.18613	0.00062	0.00056	0.00163	0.00009	0.00002	0.00008
StdDev (%)	-708.48542	29.36723	28.94279	29.37546	28.93944	28.94886	28.94958	0.01961	0.01951	0.02388	0.02107	0.01119	0.01980
StdDev (abs)	0.00001	0.11194	0.02753	0.27073	0.47228	0.43473	1.03635	0.00332	0.00302	0.00876	0.00051	0.00010	0.00043
Valid Values	31 (31)	31 (31)	31 (31)	31 (31)	31 (31)	31 (31)	31 (31)	29 (31)	29 (31)	29 (31)	29 (31)	28 (31)	30 (31)

January 2022

	202Hg	**203Tl**	**204Pb**	**205Tl**	**206Pb**	**207Pb**	**208Pb**	**206Pb/204Pb (1)**	**207Pb/204Pb (2)**	**208Pb/204Pb (3)**	**205Tl/203Tl (4)**	**207Pb/206Pb (5)**	**208Pb/206Pb (6)**
Cup	L3	L2	L1	C	H1	H2	H3	H1 | L1	H2 | L1	H3 | L1	C | L2	H2 | H1	H3 | H1
							NBS981 (start 20 January)						
Mean	0.00002	0.28571	0.06858	0.68847	1.17234	1.07708	2.56346	16.93599	15.48781	36.69014	2.40968	0.91448	2.16642
StdErr (%)	9.09427	0.82033	0.80236	0.82024	0.80344	0.80343	0.80381	0.00457	0.00444	0.00477	0.00146	0.00132	0.00152
StdErr (abs)	0.00000	0.00234	0.00055	0.00565	0.00942	0.00865	0.02061	0.00077	0.00069	0.00175	0.00004	0.00001	0.00003
StdDev (%)	49.81135	4.49315	4.39473	4.49263	4.40061	4.40056	4.40262	0.02419	0.02305	0.02525	0.00771	0.00712	0.00806
StdDev (abs)	0.00001	0.01284	0.00301	0.03093	0.05159	0.04740	0.11286	0.00410	0.00357	0.00926	0.00019	0.00007	0.00017
Valid Values	30 (30)	30 (30)	30 (30)	30 (30)	30 (30)	30 (30)	30 (30)	28 (30)	27 (30)	28 (30)	28 (30)	29 (30)	28 (30)
							NBS981 (end 19 January)						
Mean	0.00002	0.24374	0.05824	0.58789	0.99666	0.91602	2.18106	16.93840	15.48840	36.69070	2.41194	0.91438	2.16614
StdErr (%)	10.75153	0.50515	0.51084	0.50534	0.51084	0.51113	0.51116	0.00569	0.00657	0.00723	0.00187	0.00148	0.00227
StdErr (abs)	0.00000	0.00123	0.00030	0.00297	0.00509	0.00468	0.01115	0.00096	0.00102	0.00265	0.00005	0.00001	0.00005
StdDev (%)	58.88856	2.76685	2.79798	2.76785	2.79797	2.79958	2.79975	0.03065	0.03537	0.03893	0.00989	0.00781	0.01201
StdDev (abs)	0.00001	0.00674	0.00163	0.01627	0.02789	0.02564	0.06106	0.00519	0.00548	0.01428	0.00024	0.00007	0.00026
Valid Values	30 (30)	30 (30)	30 (30)	30 (30)	30 (30)	30 (30)	30 (30)	29 (30)	29 (30)	29 (30)	28 (30)	28 (30)	28 (30)
							NBS981 (end 20 January)						
Mean	0.00002	0.29129	0.06984	0.70190	1.19404	1.09696	2.61079	16.93769	15.48841	36.69353	2.40963	0.91443	2.16634
StdErr (%)	11.80734	0.72040	0.70951	0.72008	0.70943	0.70974	0.71009	0.00337	0.00371	0.00520	0.00208	0.00145	0.00242
StdErr (abs)	0.00000	0.00210	0.00050	0.00505	0.00847	0.00779	0.01854	0.00057	0.00057	0.00191	0.00005	0.00001	0.00005
StdDev (%)	64.67146	3.94579	3.88616	3.94402	3.88568	3.88738	3.88931	0.01816	0.01996	0.02846	0.01122	0.00778	0.01280
StdDev (abs)	0.00001	0.01149	0.00271	0.02768	0.04640	0.04264	0.10154	0.00308	0.00309	0.01044	0.00027	0.00007	0.00028
Valid Values	30 (30)	30 (30)	30 (30)	30 (30)	30 (30)	30 (30)	30 (30)	29 (30)	29 (30)	30 (30)	29 (30)	29 (30)	28 (30)
							Blank						
Mean	0.00006	1.20173	0.00038	2.89336	0.00693	0.00590	0.01449	18.93551	16.04544	39.22616	2.40764	0.84693	2.07106

StdErr (%)	2.68030	0.60828	2.09570	0.60882	1.93438	1.97694	1.96064	0.38376	0.36748	0.37300	0.00087	0.04388	0.03384
StdErr (abs)	0.00000	0.00731	0.00001	0.01762	0.00013	0.00012	0.00028	0.07267	0.05896	0.14631	0.00002	0.00037	0.00070
StdDev (%)	20.76149	4.71169	16.23325	4.71588	14.98368	15.31330	15.18706	2.92262	2.79862	2.84068	0.00668	0.33127	0.25771
StdDev (abs)	0.00001	0.05662	0.00006	0.13645	0.00104	0.00090	0.00220	0.55341	0.44905	1.11429	0.00016	0.00281	0.00534
Valid Values	60 (60)	60 (60)	60 (60)	60 (60)	60 (60)	60 (60)	60 (60)	58 (60)	58 (60)	58 (60)	59 (60)	57 (60)	58 (60)
A4 Mingér													
Mean	0.00002	0.63043	0.08326	1.51916	1.61038	1.32447	3.29537	19.16261	15.68737	38.85105	2.40971	0.81864	2.02741
StdErr (%)	10.26921	0.46491	0.97604	0.46481	0.97624	0.97629	0.97646	0.00322	0.00330	0.00371	0.00086	0.00081	0.00102
StdErr (abs)	0.00000	0.00293	0.00081	0.00706	0.01572	0.01293	0.03218	0.00062	0.00052	0.00144	0.00002	0.00001	0.00002
StdDev (%)	68.88798	3.11871	6.54749	3.11807	6.54885	6.54919	6.55032	0.02136	0.02167	0.02431	0.00563	0.00536	0.00667
StdDev (abs)	0.00001	0.01966	0.00545	0.04737	0.10546	0.08674	0.21586	0.00409	0.00340	0.00945	0.00014	0.00004	0.00014
Valid Values	45 (45)	45 (45)	45 (45)	45 (45)	45 (45)	45 (45)	45 (45)	44 (45)	43 (45)	43 (45)	43 (45)	44 (45)	43 (45)
A5 Allgäu													
Mean	0.00002	0.17683	0.27723	0.42658	5.26813	4.41216	10.96809	18.80508	15.66804	38.74775	2.41235	0.83318	2.06049
StdErr (%)	6.05579	0.55837	0.54770	0.55926	0.54780	0.54780	0.54784	0.00241	0.00344	0.00442	0.00204	0.00118	0.00201
StdErr (abs)	0.00000	0.00099	0.00152	0.00239	0.02886	0.02417	0.06009	0.00045	0.00054	0.00171	0.00005	0.00001	0.00004
StdDev (%)	46.90793	4.32512	4.24244	4.33201	4.24320	4.24327	4.24357	0.01807	0.02576	0.03337	0.01523	0.00893	0.01501
StdDev (abs)	0.00001	0.00765	0.01176	0.01848	0.22354	0.18722	0.46544	0.00340	0.00404	0.01293	0.00037	0.00007	0.00031
Valid Values	60 (60)	60 (60)	60 (60)	60 (60)	60 (60)	60 (60)	60 (60)	56 (60)	56 (60)	57 (60)	56 (60)	57 (60)	56 (60)
ALB19-4 A (feldspar)													
Mean	0.00001	0.63811	0.09616	1.53918	1.84055	1.53271	3.75816	18.94443	15.69483	38.28683	2.41211	0.82846	2.02099
StdErr (%)	28.75795	0.91022	0.93588	0.91069	0.93640	0.93654	0.93628	0.00360	0.00366	0.00392	0.00102	0.00107	0.00117
StdErr (abs)	0.00000	0.00581	0.00090	0.01402	0.01723	0.01435	0.03519	0.00068	0.00057	0.00150	0.00002	0.00001	0.00002
StdDev (%)	157.51376	4.98550	5.12600	4.98806	5.12886	5.12966	5.12823	0.01904	0.01934	0.02076	0.00549	0.00575	0.00618
StdDev (abs)	0.00001	0.03181	0.00493	0.07678	0.09440	0.07862	0.19273	0.00361	0.00304	0.00795	0.00013	0.00005	0.00012
Valid Values	30 (30)	30 (30)	30 (30)	30 (30)	30 (30)	30 (30)	30 (30)	28 (30)	28 (30)	28 (30)	29 (30)	29 (30)	28 (30)
ALB19-4 B (feldspar; 3 January)													
Mean	0.00004	1.34579	0.00925	3.24063	0.18180	0.14719	0.36047	19.51399	15.72912	38.35585	2.40798	0.80602	1.96559
StdErr (%)	3.99615	0.42799	1.50857	0.42821	1.50983	1.50602	1.50608	0.01759	0.01485	0.01549	0.00073	0.00602	0.00622
StdErr (abs)	0.00000	0.00576	0.00014	0.01388	0.00274	0.00222	0.00543	0.00343	0.00234	0.00594	0.00002	0.00005	0.00012
StdDev (%)	30.95403	3.31517	11.68535	3.31692	11.69511	11.66559	11.66608	0.13165	0.11213	0.11693	0.00551	0.04505	0.04695
StdDev (abs)	0.00001	0.04462	0.00108	0.10749	0.02126	0.01717	0.04205	0.02569	0.01764	0.04485	0.00013	0.00036	0.00092
Valid Values	60 (60)	60 (60)	60 (60)	60 (60)	60 (60)	60 (60)	60 (60)	56 (60)	57 (60)	57 (60)	57 (60)	56 (60)	57 (60)
ALB19-4 B (feldspar; 20 January)													
Mean	0.00001	0.28571	0.07456	0.68848	1.46974	1.18902	2.91304	19.52839	15.72476	38.34682	2.40972	0.80524	1.96369
StdErr (%)	11.59260	1.04513	0.83555	1.04560	0.83554	0.83546	0.83558	0.00337	0.00393	0.00407	0.00140	0.00102	0.00142
StdErr (abs)	0.00000	0.00299	0.00062	0.00720	0.01228	0.00993	0.02434	0.00066	0.00062	0.00156	0.00003	0.00001	0.00003
StdDev (%)	77.76551	7.01098	5.60506	7.01407	5.60498	5.60442	5.60525	0.02186	0.02578	0.02666	0.00930	0.00670	0.00940
StdDev (abs)	0.00001	0.02003	0.00418	0.04829	0.08238	0.06664	0.16328	0.00427	0.00405	0.01022	0.00022	0.00005	0.00018
Valid Values	45 (45)	45 (45)	45 (45)	45 (45)	45 (45)	45 (45)	45 (45)	42 (45)	43 (45)	43 (45)	44 (45)	43 (45)	44 (45)
ALB19-11 A (feldspar)													
Mean	0.00002	1.13953	0.01070	2.74821	0.20455	0.17012	0.42223	18.93073	15.66380	38.68177	2.41172	0.82749	2.04343
StdErr (%)	8.86938	0.61398	0.58258	0.61418	0.58532	0.58560	0.58572	0.01229	0.01173	0.01205	0.00062	0.00149	0.00178

StdErr (abs)	0.00000	0.00700	0.00006	0.01688	0.00120	0.00100	0.00247	0.00233	0.00184	0.00466	0.00002	0.00001	0.00004
StdDev (%)	68.70191	4.75583	4.51268	4.75745	4.53384	4.53602	4.53701	0.09362	0.08781	0.09096	0.00475	0.01115	0.01366
StdDev (abs)	0.00001	0.05419	0.00048	0.13074	0.00927	0.00772	0.01916	0.01772	0.01375	0.03519	0.00011	0.00009	0.00028
Valid Values	60 (60)	60 (60)	60 (60)	60 (60)	60 (60)	60 (60)	60 (60)	58 (60)	56 (60)	57 (60)	58 (60)	56 (60)	59 (60)
ALB19-11 A (feldspar)													
Mean	0.00001	1.07287	0.00984	2.58785	0.18867	0.15670	0.38919	18.97921	15.68249	38.75117	2.41208	0.82629	2.04179
StdErr (%)	14.20696	0.43557	0.44008	0.43567	0.43867	0.43907	0.43887	0.01467	0.01456	0.01468	0.00065	0.00218	0.00200
StdErr (abs)	0.00000	0.00467	0.00004	0.01127	0.00083	0.00069	0.00171	0.00278	0.00228	0.00569	0.00002	0.00002	0.00004
StdDev (%)	110.04660	3.37392	3.40888	3.37466	3.39790	3.40103	3.39944	0.11361	0.11280	0.11374	0.00490	0.01671	0.01534
StdDev (abs)	0.00001	0.03620	0.00034	0.08733	0.00641	0.00533	0.01323	0.02156	0.01769	0.04407	0.00012	0.00014	0.00031
Valid Values	60 (60)	60 (60)	60 (60)	60 (60)	60 (60)	60 (60)	60 (60)	60 (60)	60 (60)	60 (60)	56 (60)	59 (60)	59 (60)
ALB-G2													
Mean	0.00004	1.26362	0.08617	3.04657	1.68486	1.37366	3.43095	19.36307	15.70929	39.04459	2.41099	0.81129	2.01647
StdErr (%)	3.47993	0.82023	1.40637	0.82007	1.40697	1.40610	1.40648	0.00310	0.00298	0.00343	0.00096	0.00108	0.00090
StdErr (abs)	0.00000	0.01036	0.00121	0.02498	0.02371	0.01931	0.04826	0.00060	0.00047	0.00134	0.00002	0.00001	0.00002
StdDev (%)	23.34407	5.50224	9.43423	5.50121	9.43821	9.43239	9.43497	0.02011	0.01934	0.02249	0.00638	0.00711	0.00602
StdDev (abs)	0.00001	0.06953	0.00813	0.16760	0.15902	0.12957	0.32371	0.00389	0.00304	0.00878	0.00015	0.00006	0.00012
Valid Values	45 (45)	45 (45)	45 (45)	45 (45)	45 (45)	45 (45)	45 (45)	42 (45)	42 (45)	43 (45)	44 (45)	43 (45)	45 (45)
DM Hauptdolomit													
Mean	0.00001	0.09463	0.24744	0.22804	4.68558	3.93524	9.74412	18.75837	15.68084	38.64779	2.40983	0.83594	2.06026
StdErr (%)	11.85228	0.49347	0.55454	0.49374	0.55456	0.55451	0.55458	0.00227	0.00333	0.00449	0.00230	0.00125	0.00226
StdErr (abs)	0.00000	0.00047	0.00137	0.00113	0.02598	0.02182	0.05404	0.00043	0.00052	0.00174	0.00006	0.00001	0.00005
StdDev (%)	79.50751	3.31032	3.71998	3.31211	3.72012	3.71976	3.72027	0.01491	0.02182	0.02978	0.01507	0.00822	0.01479
StdDev (abs)	0.00001	0.00313	0.00920	0.00755	0.17431	0.14638	0.36251	0.00280	0.00342	0.01151	0.00036	0.00007	0.00030
Valid Values	45 (45)	45 (45)	45 (45)	45 (45)	45 (45)	45 (45)	45 (45)	43 (45)	43 (45)	44 (45)	43 (45)	43 (45)	43 (45)
Gr0-d A													
Mean	0.00002	0.04520	0.05045	0.10893	0.99254	0.80268	2.02495	19.49067	15.68984	39.39531	2.40975	0.80496	2.02129
StdErr (%)	9.97818	0.60545	0.69975	0.60627	0.69994	0.69990	0.69995	0.00650	0.00879	0.01078	0.00459	0.00240	0.00466
StdErr (abs)	0.00000	0.00027	0.00035	0.00066	0.00695	0.00562	0.01417	0.00127	0.00138	0.00425	0.00011	0.00002	0.00009
StdDev (%)	77.29068	4.68979	5.42026	4.69615	5.42168	5.42139	5.42180	0.04910	0.06748	0.08212	0.03496	0.01829	0.03577
StdDev (abs)	0.00001	0.00212	0.00273	0.00512	0.05381	0.04352	0.10979	0.00957	0.01059	0.03235	0.00084	0.00015	0.00072
Valid Values	60 (60)	60 (60)	60 (60)	60 (60)	60 (60)	60 (60)	60 (60)	57 (60)	59 (60)	58 (60)	58 (60)	58 (60)	59 (60)
Gr0-d B													
Mean	0.00002	0.10398	0.07376	0.25058	1.44972	1.17366	2.95998	19.47017	15.68858	39.38101	2.41003	0.80577	2.02261
StdErr (%)	9.39567	0.47073	0.48968	0.47046	0.48966	0.48976	0.48978	0.00384	0.00513	0.00593	0.00303	0.00169	0.00289
StdErr (abs)	0.00000	0.00049	0.00036	0.00118	0.00710	0.00575	0.01450	0.00075	0.00080	0.00234	0.00007	0.00001	0.00006
StdDev (%)	63.02807	3.15773	3.28488	3.15592	3.28476	3.28541	3.28553	0.02519	0.03363	0.03843	0.01964	0.01109	0.01870
StdDev (abs)	0.00001	0.00328	0.00242	0.00791	0.04762	0.03856	0.09725	0.00490	0.00528	0.01514	0.00047	0.00009	0.00038
Valid Values	45 (45)	45 (45)	45 (45)	45 (45)	45 (45)	45 (45)	45 (45)	43 (45)	43 (45)	42 (45)	42 (45)	43 (45)	42 (45)
P9 A													
Mean	0.00003	1.12742	0.57906	2.71891	11.12760	9.21036	22.93063	19.02257	15.66578	38.80674	2.41165	0.82354	2.04003
StdErr (%)	4.11633	0.58627	0.69003	0.58653	0.69033	0.69049	0.69068	0.00091	0.00124	0.00142	0.00078	0.00053	0.00063
StdErr (abs)	0.00000	0.00661	0.00400	0.01595	0.07682	0.06360	0.15838	0.00017	0.00019	0.00055	0.00002	0.00000	0.00001

StdDev (%)	27.61315	3.93283	4.62889	3.93456	4.63091	4.63191	4.63321	0.00591	0.00805	0.00931	0.00511	0.00345	0.00420
StdDev (abs)	0.00001	0.04434	0.02680	0.10698	0.51531	0.42662	1.06242	0.00112	0.00126	0.00361	0.00012	0.00003	0.00009
Valid Values	45 (45)	45 (45)	45 (45)	45 (45)	45 (45)	45 (45)	45 (45)	42 (45)	42 (45)	43 (45)	43 (45)	43 (45)	44 (45)
							P9 B						
Mean	0.00002	0.85185	0.03888	2.05270	0.74529	0.61770	1.53608	18.99342	15.66836	38.78357	2.40971	0.82495	2.04201
StdErr (%)	9.66785	0.84170	0.83646	0.84150	0.83772	0.83760	0.83783	0.00496	0.00504	0.00510	0.00091	0.00125	0.00117
StdErr (abs)	0.00000	0.00717	0.00033	0.01727	0.00624	0.00517	0.01287	0.00094	0.00079	0.00198	0.00002	0.00001	0.00002
StdDev (%)	64.85392	5.64630	5.61112	5.64498	5.61962	5.61876	5.62037	0.03252	0.03267	0.03307	0.00596	0.00819	0.00770
StdDev (abs)	0.00001	0.04810	0.00218	0.11587	0.04188	0.03471	0.08633	0.00618	0.00512	0.01282	0.00014	0.00007	0.00016
Valid Values	45 (45)	45 (45)	45 (45)	45 (45)	45 (45)	45 (45)	45 (45)	43 (45)	42 (45)	42 (45)	43 (45)	43 (45)	43 (45)

Appendix 5

In the following tables, we report hydrogen and oxygen isotope data, measured at the Joint Goethe University Frankfurt–Senckenberg BiK-F Stable Isotope Facility (Frankfurt, Germany) by TC/EA and at University of Lausanne (Switzerland) using a CO_2-laser based extraction line coupled to a mass spectrometer. For details, see Chapter 3 of this thesis (Sect. 3.4.3).

2019 measurements					
Sample Name	dD ‰ VSMOW	"H_2O"* wt %	dD ‰ Mean duplicate	SD dD ‰ duplicate	Remark
ALB13-1_Chips	**-47**	2.1			
ALB13-1_Chips_B	**-51**	2.0	-49	2.8	
ALB13-1_ground	**-49**	2.1			
ALB13_1_ground_B	**-48**	1.9	-49	0.7	
VP_Alb13_1_not ground	**-49**	1.9			
ALB13-7	**-59**	1.2			
Gr0-c	**-59**	0.9			
Gr0-c_B	**-58**	0.6	-59	0.8	
Gr0-d	**-55**	0			
Gr0-d_B	**-54**	0.4	-55	1.0	
L016c	**-58**	0.8			
P9_Fsp	**-50**	1.4			
P9_Fsp_B	**-52**	1.3	-51	1.6	
P9c	**-74**	1.6			
P9d	**-80**	1.1			
Epidot_1867m	**-95**	2.0			
Epidot_1867m	**-90**	2.0	-93	3.7	
Standards	Ist-Wert	Sollwert	Abw.	SD	
NBS 30 (USGS2017)	-54.3	-54.3	0.0	0.6	
Nbs 22 (USGS2017)	-117.3	-116.9	-0.4	1.4	
CH7	-100.2	-100.3	0.1	1.4	
* water content calculated to NBS30					

After correction for mass bias, daily drift of the thermal combustion reactor and offset from the certified reference values, NBS30 (biotite), NBS22 (oil), CH7 (polyethylene foil) had δD = -54,3‰, -117,3‰, and -100.2‰, respectively. Repeated measurements of the various standards and unknowns resulted in a precision of ± 3‰ for δD. All isotopic ratios are reported relative to Vienna-Standard Mean Ocean Water (V-SMOW).

2021 measurements						
Sample Name	dD ‰ VSMOW	"H_2O"* wt %	dD ‰ Mean duplicate	SD dD ‰ duplicate	Remark	Remark VP
ALB13-1	-46	2.1				
ALB19-1	-59	1.1			replicate**	
ALB19-4_1327A	-50	1.2				epidot-rich 65%
ALB19-4_1327A	-54	1.1	-52	2.6	duplicate	
ALB19-11A_1342	-50	2.0				
ALB19-11A_1343	-50	2.1				
ALB19-11B_C	-46	2.1				
ALB19-18(b)	-49	2.6				epidot-rich 40%
ALB19-18(a)	-47	1.4				
ALB10-18(a)	-47	1.3	-47	0.0	duplicate	
Aerlengletscher	-28	2.2				
GAS19-01A	-97	1.9				
GAS19-01A	-97	1.7	-97	0.4	duplicate	
Gr0-d		0.4			signal too low***	
Gr0-d UPb		0.2			signal too low***	epidot-rich 50%
Gr0-e	-59	1.6				epidot-rich 65%
Grosstal	-82	2.2				
Lö20_5A (epidote	-57	2.0			replicate**	"chlorite"
Lö20_1	-37	1.8				epidot-rich 65%
Lö20_2	-75	1.4				
Lö20_2	-72	1.4	-73	1.7	duplicate	
Lö20_3	-101	1.9				
Lö20-4	-78	2.0				
Lö20-4	-74	2.0	-76	2.7	duplicate	
Lö20_5A (chlorite	-38	11.4			chlorite?, dark colored, replicate**	
OBA19-03B	-86	2.0				epidot-rich 65%
Planggenstock	-104	2.1				
KP Epidot 1867m	-97	2.0				
KP Epidot 1867m	-93	2.1	-95	2.9		

Standards	Sollwert	Ist-Wert	SD	Abw.
USGS 58	-28.4	-28.4	0.5	0.0
USGS 57	-91.5	-91.9	0.5	-0.4
CH-7	-100.3	-100.0	0.7	0.3
NBS 22	-116.9	-116.9	0.6	0.0

* water content calculated to USGS57

** replicate (sample weight)

*** signal too low: no data evaluation possible

After correction for mass bias, daily drift of the thermal combustion reactor and offset from the certified reference values, USGS57 (biotite), USGS58 (muscovite), NBS22 (oil), CH7 (polyethylene foil) had δD = -28,4‰, -91,9‰, -100,0‰, and -116,9‰, respectively. Repeated measurements of the various standards and unknowns resulted in a precision of ± 3‰ for δD. All isotopic ratios are reported relative to Vienna-Standard Mean Ocean Water (V-SMOW).

Sample	Type	Weight [mg]	$\delta^{18}O$ corrected to LS_1 qtz	Comment
Aerlengletscher	Ep	1.68	3.8	
ALB19-1 ||	Ep	1.44	8.5	
GAS19-01A	Ep	1.55	7.9	
Gr0_d	Ep	n.a.	6.5	
ALB19-11B	Ep	1.73	7.4	
ALB19-4_1327A	Ep	1.44	12.5	Repeat; 2nd "allochtone" small grain in pit ; contaminated
Aerlengletscher	Ep	1.49	3.2	
Gr0-e	Ep	2.12	-	Problem while lasing - sample jumped out - no result = to repeat
ALB19-18 (a)	Ep	1.46	-	Problem while lasing - sample jumped out - no result = to repeat
Gr0_e (A)	Ep	1.62	4.81	Sputter
ALB19-18 (a)	Ep	2.07	9.40	Nice smooth lasing
ALB19-4	Ep	1.46	12.69	Repeat previous run; long and hard lasing (almost mafic); some little sputter
Aerlengletscher	Ep	1.51	3.73	Repeat previous run; sputter; long and hard lasing
Gr0_e (B)	Ep	1.79	5.65	Ok lasing; some little sputter
Lö20_1	Ep	1.76	4.48	
ALB13_1	Ep	1.80	7.65	
Plaggenstock	Ep	1.93	4.35	Beautifull, clear grains, idomorphic
OBA19_03	Ep	1.53	4.35	
ALB13_1	Qtz	1.66	15.21	One milky grain
Plaggenstock	Qtz	1.08	9.37	One clear grain
OBA19_03	Qtz	1.52	9.37	Slight residuum: coating & brown spotz = not pure qtz
Lö20_1	Qtz	2.02	9.94	Residuum: coating & brown spotz = not pure qtz
Duplicate - 2 October 2020				
Arl_01	Ep	1.68	3.8	
Arl_01	Ep	1.49	3.4	
			3.6	
			0.27	
			(n=2)	

Declaration of consent

on the basis of Article 18 of the PromR Phil.-nat. 19

Name/First Name:

Registration Number:

Study program:

Bachelor ☐ Master ☐ Dissertation ☐

Title of the thesis:

Supervisor:

I declare herewith that this thesis is my own work and that I have not used any sources other than those stated. I have indicated the adoption of quotations as well as thoughts taken from other authors as such in the thesis. I am aware that the Senate pursuant to Article 36 paragraph 1 litera r of the University Act of September 5th, 1996 and Article 69 of the University Statute of June 7th, 2011 is authorized to revoke the doctoral degree awarded on the basis of this thesis.
For the purposes of evaluation and verification of compliance with the declaration of originality and the regulations governing plagiarism, I hereby grant the University of Bern the right to process my personal data and to perform the acts of use this requires, in particular, to reproduce the written thesis and to store it permanently in a database, and to use said database, or to make said database available, to enable comparison with theses submitted by others.

Place/Date

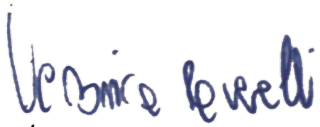

Signature